Forschungsbericht 2024-11

Design methodology for highly loaded composite bolted joints with local metal hybridization at low temperature

Josef Koord

Deutsches Zentrum für Luft- und Raumfahrt
Institut für Systemleichtbau
Stade

DLR Deutsches Zentrum für Luft- und Raumfahrt

Forschungsbericht 2024-11

Design methodology for highly loaded composite bolted joints with local metal hybridization at low temperature

Josef Koord

Deutsches Zentrum für Luft- und Raumfahrt
Institut für Systemleichtbau
Stade

320 Seiten
167 Bilder
45 Tabellen
245 Literaturstellen

Deutsches Zentrum
DLR für Luft- und Raumfahrt

Herausgeber:

Deutsches Zentrum
für Luft- und Raumfahrt e. V.
Wissenschaftliche Information
Linder Höhe
D-51147 Köln

ISSN 1434-8454
ISRN DLR-FB-2024-11
Erscheinungsjahr 2024

DOI: 10.57676/mzxc-3158

Bolzenverbindungen, lokale Metallhybridisierung, Auslegung, Simulation, statische Tests, analytische Methoden, Flugzeugstrukturen, Raumfahrtstrukturen

(Publiziert in Englisch)

Josef KOORD
DLR, Institut für Systemleichtbau, Stade

Auslegungsmethodik für hochbelastete Bolzenverbindungen mit lokaler Metallhybridisierung bei Niedertemperatur

Dissertation, Technische Universität Carolo-Wilhelmina zu Braunschweig

Bolzenverbindungen werden in Faserverbundstrukturen aufgrund ihrer einfachen Montage-, Demontage- und Reparaturmöglichkeiten breit eingesetzt. Jedoch haben sie Nachteile, wie die verringerte Effizienz bei der Lastübertragung aufgrund der hohen Kerbwirkung an Bohrungen. Diese Nachteile können durch lokale Metallhybridisierung im Verbindungsbereich hochbelasteter Strukturen überwunden werden. Dieses Konzept beschreibt die lokale Substitution von Einzellagen des Verbundmaterials durch Metalllagen, was zu einer höheren Tragfähigkeit führt. Der Verstärkungseffekt ist für Stahl- und Titanhybridisierung bei Raumtemperatur nachgewiesen.

In CFK-Stahl-Hybridlaminaten liegen hohe inter- und intralaminaren thermische Eigenspannungen vor, die das Materialverhalten insbesondere bei niedrigen Temperaturen beeinflussen. Das Ziel der vorliegenden Arbeit besteht darin, zu untersuchen, ob der Verstärkungseffekt durch Stahl-Hybridisierung auch bei niedrigen Temperaturen vorliegt. Darüber hinaus zielt die Arbeit darauf ab, festzustellen, ob der Auslegungsprozess für hybridisierte Bolzenverbindungen die Berücksichtigung thermischer Eigenspannungen erfordert.

Die Ergebnisse dieser Arbeit bestätigen, dass der Verstärkungseffekt durch Hybridisierung auch bei niedrigen Temperaturen, hier speziell für CFK-Stahl-Hybridlaminate, vorhanden ist. Darüber hinaus trägt die Arbeit zur Entwicklung von numerischen und analytischen Konstruktionswerkzeugen zum Zwecke der Vor- und Detailauslegung hybrider Verbindungen bei und stellt auf diese Weise einen Beitrag zur breiteren Anwendung der lokalen Metallhybridisierung in Verbundstrukturen dar.

Bolted joints, local metal hybridization, design, simulation, experimental testing, analytical methods, aircraft structures, aerospace structures

Josef KOORD
German Aerospace Center (DLR), Institute of Lightweight Systems, Stade

Design methodology for highly loaded composite bolted joints with local metal hybridization at low temperature

Doctoral Thesis, Technische Universität Carolo-Wilhelmina zu Braunschweig

Bolted joints are broadly utilized in composite structures due to their ease of assembly, disassembly, and repair. However, they also possess certain drawbacks including reduced load transfer efficiency resulting from high stress concentrations near holes. By local metal hybridization of the joining area in highly loaded structures these drawbacks can be overcome. The concept of local metal hybridization involves the substitution of specific layers of the composite with metal layers in the joining area, resulting in an overall higher bearing efficiency. The reinforcement effect through hybridization has been proven for steel and titanium hybridized composite laminates under room temperature conditions.

In CFRP-steel hybrid laminates, high inter- and intralaminar thermal residual stresses are present, which influence the material behavior especially at lower temperatures. The aim of this thesis is to investigate whether the reinforcement effect of steel hybridization is also present at low temperatures. Furthermore, the thesis aims to determine whether the design process for bolted joints with local metal hybridization requires consideration of thermal residual stresses.

The results of this work confirm that the reinforcement effect by hybridization is also present at low temperatures, specifically for CFRP-steel hybrid laminates. In addition, the work contributes to the development of numerical and analytical design tools for the purpose of preliminary and detailed design of hybridized bolted joints, thereby contributing to a broader application of local metal hybridization in composite structures.

TU Braunschweig – Niedersächsisches
Forschungszentrum für Luftfahrt

Berichte aus der Luft- und Raumfahrttechnik

Forschungsbericht 2024-10

Design Methodology for Highly Loaded Composite Bolted Joints with Local Metal Hybridization at Low Temperature

Josef Koord

Deutsches Zentrum für Luft- und Raumfahrt
Institut für Systemleichtbau
Stade

Diese Veröffentlichung wird gleichzeitig in der Berichtsreihe „NFL - Forschungsberichte“ geführt.

Diese Arbeit erscheint gleichzeitig als von der Fakultät für Maschinenbau der Technischen Universität Carolo-Wilhelmina zu Braunschweig zur Erlangung des akademischen Grades eines Doktor-Ingenieurs genehmigte Dissertation.

Design Methodology for Highly Loaded Composite Bolted Joints with Local Metal Hybridization at Low Temperature

Von der Fakultät für Maschinenbau

der Technischen Universität Carolo-Wilhelmina zu Braunschweig

zur Erlangung der Würde

eines Doktor-Ingenieurs (Dr.-Ing.)

genehmigte Dissertation

von:	Josef Koord
geboren in:	Hamburg

eingereicht am:	12.09.2023
mündliche Prüfung am:	24.04.2024

Vorsitz:	Prof. Dr.-Ing. Carsten Schilde
Gutachter:	Prof. Dr.-Ing. Christian Hühne Prof. Dr.-Ing. Paolo Ermanni

2024

Kurzfassung

Bolzenverbindungen werden in Faserverbundstrukturen aufgrund ihrer einfachen Montage-, Demontage- und Reparaturmöglichkeiten breit eingesetzt. Jedoch weisen sie auch bestimmte Nachteile auf, wie z.B. eine verringerte Effizienz bei der Lastübertragung aufgrund der hohen Kerbwirkung an Bohrungen. Durch lokale Metallhybridisierung im Verbindungsbereich hochbelasteter Strukturen können diese Nachteile überwunden werden. Das Konzept der lokalen Metallhybridisierung beschreibt die lokale Substitution von Einzellagen des Verbundmaterials im Verbindungsbereich durch Metalllagen, was zu einer insgesamt höheren Tragfähigkeit führt. Der Verstärkungseffekt ist für Stahl- und Titanhybridisierung bei Raumtemperatur nachgewiesen.

Diese Hybridlaminate, in der vorliegenden Arbeit CFK-Stahl, sind besonders anfällig für das Auftreten großer inter- und intralaminarer thermischer Eigenspannungen, die das Werkstoffverhalten signifikant beeinflussen können, insbesondere bei niedrigen Temperaturen. Dies ist auf die hohe Diskrepanz der thermischen Ausdehnungskoeffizienten und Steifigkeiten zwischen dem CFK und Stahl zurückzuführen.

Das Ziel der vorliegenden Arbeit besteht darin, zu untersuchen, ob der Verstärkungseffekt durch Stahl-Hybridisierung auch bei niedrigen Temperaturen vorliegt. Darüber hinaus zielt die Arbeit darauf ab, festzustellen, ob der Auslegungsprozess für hybride Bolzenverbindungen die Berücksichtigung thermischer Eigenspannungen erfordert. In herkömmlichen monolithischen Laminaten ist die Größenordnung der thermischen Eigenspannungen für die Festigkeitsprognose in der Regel vernachlässigbar, während hybride Laminate ihre Berücksichtigung im Konstruktionsprozess erfordern könnten. Folglich umfasst die Arbeit auch die Entwicklung von ingenieurtechnischen Werkzeugen für die Auslegung von Bolzenverbindungen in Hybridlaminaten.

Es erfolgen experimentelle Tests auf Coupon-Ebene zur Charakterisierung der inter- und intralaminaren Materialeigenschaften einschließlich der Korrektur von parasitären thermischen Einflüssen. Darüber hinaus werden umfangreiche Lochleibungsversuche bei verschiedenen Temperaturen durchgeführt, um die Forschungsfrage zu beantworten. Die Finite Elemente Methode wird verwendet, um das mesoskalige Schädigungsverhalten zu untersuchen, die Verbindungsfestigkeit vorherzusagen sowie zur virtuellen Kennwertermittlung. Basierend auf den Erkenntnissen aus den experimentellen und numerischen Analysen wird ein rein analytisches Vorauslegungstool entwickelt, um die Festigkeit in hybriden Bolzenverbindungen vorherzusagen.

Zusammenfassend bestätigen die Ergebnisse dieser Arbeit, dass der Verstärkungseffekt durch Hybridisierung auch bei niedrigen Temperaturen, hier speziell für CFK-Stahl-Hybridlaminate, vorhanden ist. Darüber hinaus trägt die Arbeit zur Entwicklung von numerischen und analytischen Konstruktionswerkzeugen zum Zwecke der Vor- und Detailauslegung hybrider Verbindungen bei und stellt auf diese Weise einen Beitrag zur breiteren Anwendung der lokalen Metallhybridisierung in Verbundstrukturen dar.

Abstract

Bolted joints are broadly utilized in composite structures due to their ease of assembly, disassembly, and repair. However, they also possess certain drawbacks including reduced load transfer efficiency resulting from high stress concentrations near holes. By local metal hybridization of the joining area in highly loaded structures these drawbacks can be overcome. The concept of local metal hybridization involves the substitution of specific layers of the composite with metal layers in the joining area, resulting in an overall higher bearing efficiency. The reinforcement effect through metal hybridization has been proven for steel and titanium hybridized composite laminates under room temperature conditions.

These hybrid laminates, in the present work CFRP-steel laminates, are particularly prone to the presence of large inter- and intralaminar thermal residual stresses that can significantly affect the material behavior, especially at lower temperatures. This is attributed to the large mismatch in coefficient of thermal expansion and stiffness between CFRP and steel.

Thus, the research goal is to investigate whether the reinforcement effect achieved by metal hybridization is also present at low temperatures in CFRP-steel laminates. Additionally, the study aims to determine whether the design process for hybridized bolted joints needs to incorporate thermal residual stresses. In traditional monolithic laminates, the magnitude of thermal residual stresses is generally negligible for strength prediction, whereas hybrid laminates may require their inclusion in the design process. Consequently, the thesis involves the development of engineering tools tailored to the design of bolted joints in hybrid laminates.

Experimental testing is conducted on coupon-level to characterize the inter- and intralaminar material properties including the correction of parasitic thermal effects. Furthermore, extensive bolt-bearing testing is performed at different temperature levels to address the research question. Finite element analysis is employed to analyze meso-scale progressive damage mechanisms, to predict strength, and to conduct virtual testing. Based on the conclusions drawn from the experimental and numerical analyses, a purely analytical design tool is developed for strength prediction in hybridized bolted joints.

In conclusion, the results confirm that the reinforcement effect achieved through hybridization extends to low temperature conditions, specifically in the case of CFRP-steel hybrid laminates. Additionally, the study contributes to the development of numerical and analytical design tools for preliminary and detailed design of hybridized joints. Consequently, this work represents a contribution towards the broader application of local metal hybridization in composite structures.

Acknowledgments

The present thesis was completed during my time as a researcher at the Institute of Lightweight Systems at German Aerospace Center (DLR) in Stade and partly funded by the Deutsche Forschungsgemeinschaft (DFG) under Germany´s Excellence Strategy – EXC 2163/1 - *Sustainable and Energy Efficient Aviation* – Project-ID 390881007.

First, I would like to express my gratitude to Prof. Dr. Christian Hühne for allowing me to be a part of the Composite Design department and for supervising this thesis. I am especially grateful for the trusting, encouraging and supportive work environment with tasks to grow on both professionally as an engineer and on a personal level. I would like to thank Prof. Dr. Paolo Ermanni for co-supervising the work as well as Prof. Dr. Carsten Schilde for taking on the responsibility as chairman of the thesis committee.

I would like to thank Dr. Daniel Stefaniak for introducing me to scientific working in my early career days, encouraging a critical yet always productive discussion culture, and sharing his insights on the newest productivity tools. Although not directly related to the thesis, jumping into the (for us) new topic of cryogenics in composites together with Philipp Sämann has been fun. Both my former and current team leaders, Dr. Daniel Stefaniak and Dr. Alexander Pototzky, have provided an enjoyable yet productive working environment, which I appreciate very much. I am grateful to Prof. Dr. Oliver Völkerink and Dr. Enno Petersen for the fruitful collaborative research, countless discussions on modeling and testing of composites as well as for proofreading the present thesis. I also wish to express my gratitude to Carmen Westphal for her help and advice during the experimental testing campaigns and Jens Kosmann for his support with optical measurements during testing. Moreover, I would like to thank Robert Prussak for the many discussions on thermal residual stresses as well as his assistance during experimental testing related to this topic.

I am very thankful to the technical staff, in particular Cordelia Koch, Christine König, Mareike Stegmaier amd Niklas Drews for their support during specimen manufacturing. Also, I am very grateful for the valuable contributions of my former students Luca Massera, Jan-Lukas Stüven and Joshua Moll to the analytical and numerical methods of the present work.

I wish to extend a special thanks to Dr. Christian Sikorski, my former high school physics teacher. He ignited my passion for the sciences, and without his impact, my career trajectory would have certainly taken a very different path.

Above all, I would like to express my profound gratitude to my family. My parents and siblings have always been there for me, offering unwavering understanding and support. Furthermore, from my early childhood on, my parents have instilled in me the value of education and encouraged me to do whatever I feel passionate about. They have often put aside their own interests to enable my siblings and me to pursue our own goals, and that is why I am infinitely grateful to them.

Contents

Notations

Abbreviations

Abbreviation	Description
aERR	Apparent energy release rate
AITM	Airbus testing method
ajaX	Analytical joint analysis tool
APC	Action plane criterion
ASTM	American society for testing materials
BT	Beam theory
BUS	Bearing ultimate strength
BYS	Bearing yield strength
CARALL/CARE	Carbon reinforced aluminum laminate
CC	Compliance calibration
cERR	Critical energy release rate
CFRP	Carbon fiber reinforced plastic
CLT	Classical lamination theory
CT	Cryogenic temperature
CTE	Coefficient of thermal expansion
CWB	Center wing box
CZM	Cohesive zone modeling
DCB	Double cantilever beam
DIC	Digital image correlation
DLR	German aerospace center
ENF	End-notched flexure
ERR	Energy release rate
ESA	European Space Agency

Abbreviation	Description
FE	Finite element
FEA	Finite element analysis
FF	Fiber failure
FI	Failure index
FMC	Failure mode concept
FML	Fiber metal laminate
GFEM	Global finite element model
GFRP	Glass fiber reinforced plastic
GLARE	Glass fiber reinforced laminate
HO	Highly-orthotropic
HTCL/TiGr	Titanium reinforced carbon fiber laminate
IF	Interface
IFF	Inter fiber failure
ILSS	Interlaminar shear strength
IM	Intermediate modulus
KDF	Knock-down factor
LC	Load case
LL	Limit load
LT	Low temperature
LWC	Lower wing cover
MBT	Modified beam theory
MCC	Modified compliance calibration
MMB	Mixed mode bending
MVF	Metal volume fraction
NASA	National aeronautics and space administration
NDI	Non-destructive investigation
OHT	Open hole tension
QI	Quasi-isotropic
QUADS	Quadratic stress criterion
RF	Reaction force
RP	Reference point
RT	Room temperature
SCF	Stress concentration factor

Abbreviation	Description
tERR	True energy release rate
TRS	Thermal residual stresses
UD	Unidirectional
UL	Ultimate load
UMAT	User-defined material model for Abaqus/Standard
US	Ultrasound
UWC	Upper wing cover
VCCT	Virtual crack closure technique
VERrSO	Virtual environment for structural optimization
VUMAT	User-defined material model for Abaqus/Explicit
w/	with
w/o	without
WH	Working hypothesis
WRJ	Wing root joint
XFEM	Extended finite element method

Symbols

Latin symbol	Description	Unit
a	Crack length	mm
A	Area	mm^2
b	Width	mm
d	Diameter	mm
d_i	Damage variable	mm
e	Edge distance	mm
E	Stiffness	N/mm^2
F_f^c ,F_f^c	Hashin fiber failure initiation criterion	-
F_m^c,F_m^c	Hashin matrix failure initiation criterion	-
G_{ft},G_{fc}	Intralam. fracture toughness in fiber direction	N/mm
G_{mt},G_{mc}	Intralam. fracture toughness in matrix direction	N/mm
G_s	Intralaminar fracture toughness in shear	N/mm
G_I,G_{II},G_{III}	Interlaminar fracture toughness in modes I, II, III	N/mm
I	Bending stiffness	N/mm^2
k	Spring stiffness	N/mm^2
k_b	Bearing stress intensity factor	-
k_t	Tensile stress intensity factor	-
l	Length	mm
L	Specimen length	mm
l_{cz}	Cohesive zone length	mm
p	Bolt pitch	mm
P	Load	N
PE	Plastic strain	-
$[Q]$	Laminate tiffness matrix	-
$[\hat{Q}]$	Ply stiffness matrix	-
r, R	Radius	mm
R_{oc}	Characteristic distance in compression	mm
R_{ot}	Characteristic distance in tension	mm
$R_{p,0.2}$	Yield strength at 0.2 % non-linearity	N/mm^2
S, R_{12}	Shear strength	N/mm^2
t	Thickness	mm
t^o	Interface traction	N/mm
T	Temperature	°C
$[T]$	Transformation matrix	-
u	Displacement	mm
w	Width	mm
X_c, R_1^c	Longitudinal compressive strength	N/mm^2
X_t, R_1^t	Longitudinal tensile strength	N/mm^2
Y_c, R_2^c	Transverse compressive strength	N/mm^2
Y_t, R_2^t	Transverse tensile strength	N/mm^2

Greek symbol	Description	Unit
α	Thermal expansion coefficient	$10^{-6}/\mathrm{mm}$
β_{HT}	Hashin-Train non-linear shear parameter	-
δ	Displacement	mm
ε	Strain	-
η_{BK}	Benzeggagh-Kenane interaction coefficient	-
γ	Shear strain	-
μ	Friction coefficient	-
ν	Poisson's ratio	-
σ	Normal stress	$\mathrm{N/mm^2}$
τ	Shear stress	$\mathrm{N/mm^2}$
θ	Angle	$^\circ$

Indices

Symbol	Description
$1, 2, 3$	Cartesian coordinates on ply level
all	Allowable
b	Bearing
c	Compression
C	Composite
eq	Equivalent
exp	Experimental
f	Failure
I, II, III	Delamination modes
is	In-situ
L	Laminate
m	matrix
M	Metal
op	Operating
pl	Plastic
ref	Reference
sf	Stress-free
s	Symmetric
t	Tension
th	Thermal
tot	Total
vM	von Mises
x, y, z	Cartesian coordinates on laminate level
y	Yield

Chapter 1

Introduction

1.1 History of Fiber-Metal-Laminates

The development of Fiber-Metal-Laminates (FML) was initially driven by the need to enhance the fatigue and damage tolerance properties of metallic components in aircraft structures. Developed at TU Delft in the Netherlands, FMLs were treated as a new material concept made up of thin metallic sheets and intermediate composite layers. Their superior fatigue behavior is mainly due to the *bridging effect*, wherein cracked metallic sheets are relieved through load transfer to adjacent composite layers, and thus crack growth in the structure is significantly reduced. In addition to the benefits with respect to fatigue behavior FMLs also exhibit lower density compared to their metallic counterparts and therefore appear predestined for application in lightweight aircraft structures [1].

Figure 1.1 Transition zone of a composite laminate with local metal hybridization

The first FML concept successfully implemented in an aircraft structure was ARALL (**A**ramid **R**einforced **Al**uminum **L**aminate). It was used on the cargo door of the military transport aircraft C-17 by McDonnell Douglas (now Boeing) in the 1980s. Further development of ARALL for fuselage applications, however, revealed its poor behavior when subjected to compressive loading cycles [2]. By using glass fibers with better compressive stability, the second generation FML labeled GLARE (**Gla**ss Fiber **Re**inforced Laminate) was created. The presumably most popular application of GLARE are the fuselage panels on the Airbus A380. In addition to around 800 kg in weight savings per aircraft and improved fatigue properties, the benefits of GLARE with respect to impact resistance and damage tolerance, burn-through resistance, and corrision resistance favored its application to primary fuselage structures [1–3]. Despite promising prospects regarding fatigue properties, FMLs based on carbon fibers and aluminum (CARALL/CARE) never were considered for actual structural applications. Their biggest drawback is the problem of galvanic corrosion due to the difference in chemical potential between the two constituents [4, 5].

Historically developed as a composite reinforcement concept for metallic structures, FMLs can alternatively be considered a composite structure being enhanced by the introduction of a metal component. By metal hybridization, the latter concept is applied to improve properties of a composite, e.g. temperature resistance, material stiffness and strength. In the early 1990s, titanium reinforced carbon fiber composites (HTCL/TiGr) were first investigated by NASA and Boeing for structural applications on supersonic aircraft [6, 7]. This new concept of FMLs combined high modulus carbon fibers with an elevated temperature epoxy and titanium sheets, resulting in an FML that exhibits high stiffness and strength, good impact behavior, and good fatigue behavior both at room temperature and elevated temperatures [8, 9]. Stainless steel is considered an alternative to titanium as metal reinforcement. Although steel exhibits higher density compared to titanium, superior stiffness and strength of steel alloys can lead to an advantageous load distribution within the laminate and improved mechanical properties especially with respect to bearing strength [10, 11]. Recent advances show the potential of hybridization of thin-ply CFRP laminates by steel layers in an effort to overcome a typical drawback of thin-ply material where stress-concentrations at holes represent a limiting factor in the design of structures [12]. As oppose to the first and second generation FMLs, namely ARALL and GLARE, which were mainly developed because of their advantageous fatigue and damage tolerance behavior, new generation FMLs, e.g. steel and titanium reinforced carbon fiber composites, promise an increase in material strength and temperature resistance in addition to good fatigue and damage tolerance behavior. However, none of the carbon fiber composite based intrinsic FMLs reached structural application yet. Granted, development effort for these types of FMLs are by far less pronounced than it was the case for GLARE. The present thesis, therefore, aims to contribute to paving the way of this promising new class of FML to structural application.

1.2 Research on FMLs at DLR Braunschweig

In literature, FMLs are often considered a material concept rather than a structural concept. As a consequence, oftentimes a certain material combination is investigated

(a) UD-CFRP-steel reinforcement struts [13]

(b) Erosion protection on leading-edge [13]

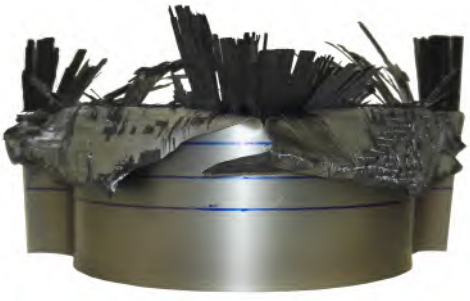

(c) Energy dissipation during crash [15]

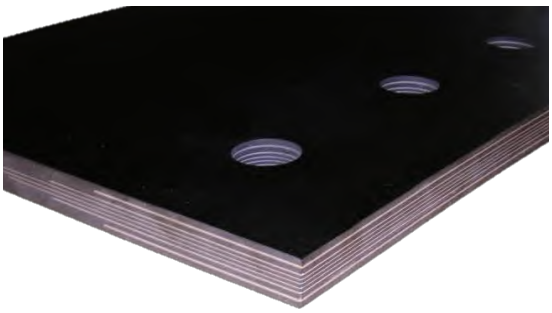

(d) Local hybridization for load transfer [16]

Figure 1.2 Current FML applications at DLR

with respect to a specific property without having a distinct application and its resulting set of requirements in mind. A more appropriate approach for FMLs consists in focussing on the actual structural application. Based on a set of requirements, the constituents of the FML can be selected accordingly and the resulting FML can be tuned as desired, e.g. by adjusting metal type and volume content, metal sheet thickness, or the layup of the laminate. A comprehensive approach also requires consideration of manufacturing as well as operational and maintenance aspects.

The Institute of *Lightweight Systems* at German Aerospace Center (DLR) in Braunschweig focuses on hybridization of composites for high performance applications. Depending on the application and requirements at hand, ply substitution or ply addition techniques are applied in order to design an FML. The former substitutes composite plies by metal sheets of equal thickness, thus avoiding laminate build-up, while the latter allows for variation of metal sheet and laminate thickness. Both approaches have in common that laminate integrity is achieved by direct adhesion between the constitutents without an additional adhesive film, thus resulting in an intrinsic FML [13]. A metal treatment process developed at DLR combines mechanical and chemical treatment by vacuum grit-blasting, sol-gel application as well as primer application in order to assure adequate bonding between composite and metal layers [14]. Currently, metal hybridization of composites is performed focusing on four fields: unidirectional (UD) CFRP-steel FML, function integration, crash energy absorption, and local metal hybridization.

Figure 1.2a shows metal hybridization at the example of unidirectionally loaded

struts. Increasing notch and impact sensitivity do not allow for full exploitment of the lightweight potential of the composite, since the applicable number of UD layers in loading direction is limited. By hybridization of a UD CFRP laminate with high strength steel layers of sheet thicknesses below 0.08 mm and metal volume fractions below 12 %, a UD-CFRP-steel laminate is formed exhibiting a weight-specific increase of stiffness and strength of up to 15 %. This reinforcement concept is most effective when using high strength steel sheets. Since their fracture strain and thus their formability is limited, application of the UD-CFRP-steel concept is recommended on struts with constant cross-section [13,14].

The field of function integration is presented at the example of a leading-edge demonstrator in Figure 1.2b. In this case, metal hybridization of the top layer is applied for abrasion protection, while a woven CFRP layer insulated by adjacent GFRP layers is used to electrically heat the structure for anti- and de-icing purposes. Another promising concept is the integration of electrically conductive paths within a structure by inserting a defined number of thin metallic sheets insulated by GFRP interlayers [17,18].

Composite materials, especially CFRP laminates, exhibit great potential for crash applications. Investigations have shown that substituting metallic crash elements by CFRP structures leads to significant mass savings at comparable energy absorption rates [19]. Monolithic CFRP crash elements have a relatively high peak force during the deformation process. Hybridization of CFRP crash elements with thin steel sheets of thicknesses below 0.12 mm can lead to a significant improvement in crash efficiency and overcome the issue of the undesireable high peak force. The FML structure shown in Figure 1.2c offers an increase in specific energy absorption rate of up to 60 % compared to the CFRP reference. In addition, metal hybridization allows for tuning of the crash behavior by alteration of the number, thickness, and position of the steel reinforcement layers [13,20].

Much development effort has been put into bolted joints in composite structures. In order to overcome the low bearing and shear capabilities, especially in highly orthotropic laminates, local metal hybridization of the joining region of highly loaded mechanically fastened composite structures has been introduced (see Figure 1.2d). By substituting composite layers with high strength metal layers of equal thickness, the efficiency of highly loaded joints is increased significantly. As a consequence, local laminate ramp-up can be avoided and the number of fasteners in the joining region reduced, resulting in a highly efficient joint design. A comprehensive design study at the example of the Ariane 5 composite booster has demonstrated the benefits of local metal hybridization using high strength titanium sheets: Approximately 500 kg could be conserved at each inter-segment joint, resulting in total weight savings of around 2 tons in both boosters of the launch system [10,16,21].

1.3 Research on Local Metal Hybridization

As indicated in the previous section, local metal hybridization of mechanically fastened composite joints exhibits promising prospects with respect to joint efficiency

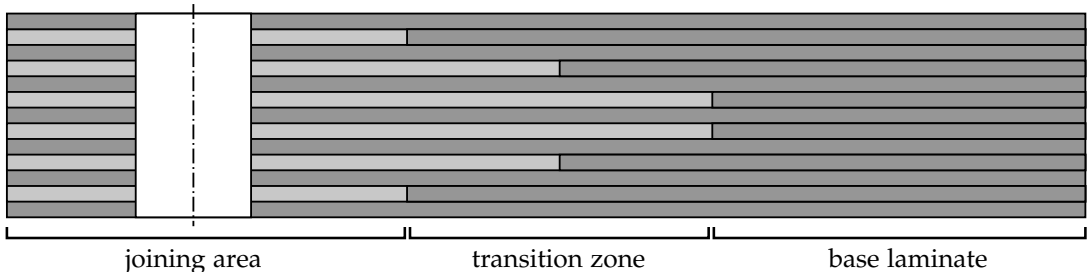

Figure 1.3 Local metal hybridization of a CFRP composite laminate

in highly loaded structures. Figure 1.3 shows the concept of local metal hybridization in detail. By ply-substitution in the transition zone, metal sheets are embedded into the laminate, thus dividing the laminate into three zones: The fully hybridized *joining area* increases the bearing capacity of the laminate and allows for a high local coupling efficiency at constant laminate thickness. Ply loads from the joining area are redistributed along the *transition zone* into the monolithic *base laminate*, which is in turn designed for the global loading case. The ply-substitution technique is most effective when replacing composite layers that contribute least to the material strength in loading direction, e.g. preferably 90° followed by $\pm 45^\circ$ layers. Remaining layers pass continuously through the transition zone into the fully hybridized zone, thus ensuring laminate adhesive integrity and contributing to the laminate strength. Given that this technology is developed for highly loaded structures, the FML consituents usually consist of CFRP laminates reinforced with steel or titanium sheets, resulting in CFRP-St and CFRP-Ti FMLs, respectively.

The superior bearing capacity of steel and titanium based FMLs over monolithic laminates has evoked a lot of research on the challenges of local metal hybridization. Main research activities and important results are summarized to give a brief overview on the field of research at hand: First major activities are originated in the U.S. where NASA at Langley Research Center, Boeing and several universities investigated CFRP-Ti laminates (namely HTCL, TiGr) for supersonic aircraft applications in the early 1990s. Research was initially focused on fatigue and damage tolerance behavior at room and elevated temperatures [22–27]. Hundley was first to investigate the static bearing behavior of titanium reinforced CFRP laminates and observed an increase in strength compared to a quasi-isotropic CFRP reference by a factor of 1.5 to 2.1 in addition to a decrease in minimum required edge and pitch distances [8,9,28].

In the late 1990s, Kolesnikov [29] investigated the bearing behavior of CFRP-Ti laminates at DLR in Germany. Research at DLR was then extended to considering high strength stainless steel sheets as reinforcement material in the subsequent decade. Thereby, an increase in static bearing strengh by a factor of up to 2.6 for CFRP-St laminates compared to monolithic CFRP as well as a reduction of the minimum edge and pitch distances could be achieved [10, 21, 30]. Several patents on this topic have been filed by Boeing [31], NASA [32], DLR [33–35] and Airbus [36]. The fundamental concept of integrating composite layers with metal remains consistent across the patents. However, the implementation differs based on choices related to material selection, reinforcement techniques, surface treatment, and manufacturing processes.

Fink [10] also investigated the fatigue behavior of single and multi-row bolted joints based on the MINITWIST[1] loading collective. Non-destructive investigation (NDI) by ultrasound scanning revealed no visible damage in the CFRP-Ti components after loading equivalent to a total number of 180.000 flights which equals about five times the lifespan of an A320 aircraft. The fatigue tests conducted by Fink also incorporated the transition zone of the hybridized laminates, thus proving that ply-substitution at the abutting points does not lead to premature failure due to crack initiation and propagation.

Recently, Petersen [38] presented a detailed investigation on the transition zone of locally hybridized CFRP-St laminates, thereby introducing design rules for an effective and efficient ply-substitution. Both [11] took a very practical approach in investigating environmental effects on the mechanical behavior of CFRP-St and CFRP-Ti FMLs in 2013. In a comprehensive experimental study, ageing effects on the material strength due to long time immersion in hydraulic fluids, aircraft propellant, and hot water as well as conditioning by thermal and thermo-mechanical cycling were investigated. Immersion in fluids leads to a decrease in strength for the CFRP-St laminates comparable to the CFRP reference, while the strength decrease in CFRP-Ti FMLs is larger. Therein, metal pre-treatment appears to have a significant influence on the ageing of the FMLs. Thermal and thermo-mechanical cycling is sustained better by the FMLs than is the case for the CFRP reference. Similar observations were made by Monden [39] for CFRP-St. Furthermore, Monden achieved an increase in material strength as well as improved corrosion resistance by surface coating with *diamond-like carbon* during the metal pre-treatment process. Most studies are conducted on coupon level, thus, not allowing for meaningful asssumptions regarding manufacturability of relevant structures. However, a performance study conducted by DLR under ESA supervision on CFRP-Ti hybrid bolted joints at the example of a spacecraft payload adaptor successfully demonstrated processability, inspectability, and compatibility of local metal hybridization with a standard industrial fibre placement process [37]. Another example for successfull local metal hybridization is a case study conducted on a wing rib of the Dornier Do 228NG [11]. Within the study, mechanical benefits under static and fatigue loading as well as manufacturing feasibility were demonstrated at the example of local metal hybridization by high strength stainless steel.

The overview on most relevant research on local metal hybridization by CFRP-St and CFRP-Ti suggests that many of the major fields of technology research have been covered. Mechanical benefits have been demostrated with respect to static and fatigue behavior as well as resistance to various environmental effects. Furthermore, manufacturing of highly complex structures has repeatedly been proven to be feasible. The vast majority of research on CFRP-St and CFRP-Ti FMLs was conducted at room temperature, while effects of high temperature were considered mainly during development of the original CFRP-Ti FMLs, namely HTCL and TiGr. Introduction of CFRP-St and CFRP-Ti laminates into air- and spacecraft structures, however, requires investigation of temperature effects within the entire range of operating temperatures.

[1]The MINITWIST loading collective is usually applied for investigating the dynamic behavior of a lower wing cover. The upper loading limit is equal to *Limit Load* while the lower loading limit is set to 15 % of *Limit Load* under compression. [37]

Currently, the development of a highly optimized composite upper stage as an upgrade to the Ariane 6 launch vehicle is pursued by ArianeGroup and MT Aerospace. In order to reduce cost and weight, and improve stage performance and payload capacity, comprehensive application of composite materials is considered. This includes composite cryogenic tanks for storage of liquid hydrogen and liquid oxygen at temperatures as low as -253°C and -183°C. Efforts in the aviation industry in the context of the ZEROe program by Airbus to develop the worlds first zero-emmision commercial aircraft by 2035 currently contemplate using liquid hydrogen as fuel for combustion with oxygen in a modified gas turbine. Storage of liquid hydrogen in composite cryogenic tanks in an aircraft is yet an open question. Wheather it is the use in the tank wall structure to fulfill tightness requirements or within the mounting of the tanks to assure joint strength, FMLs can present a valuable contribution to current problems. Considering the curing temperature of common aerospace grade resin systems of 180°C, there is substantial potential for thermal residual stresses to build up. Yet, there is no substantial research on low temperature effects on steel and titanium reinforced composite bolted joints. Given the findings on CARALL/CARE, where large thermal residual stresses due to the difference in the coefficient of thermal expansion (CTE) renders application of that type of FML very unlikely [2], it is remarkable that the effect of thermal residual stresses at low temperature on CFRP-St and CFRP-Ti hybridized composite bolted joints has not yet been addressed comprehensively.

1.4 Motivation

The presence of thermal residual stresses is inherent to FMLs. The driving force for their occurence is the difference in CTE of the constituents of an FML. For illustration purposes an FML consisting of UD composite and metal plies is considered in Figure 1.4. Since the CTE of the unidirectional composite ply in fiber direction is much smaller than the CTE of the metal constituent, cooling of an FML from high temperatures during curing (see Figure 1.4c) down to operating temperature usually results in tensile stresses in the metal plies and compressive stresses in the composite plies (see Figure 1.4b). The magnitude of thermal residual stresses within the individual plies is a function of CTE and stiffness of the constituents of an FML and largely depends on the laminate stacking, metal volume content, stress-free temperature, and operating temperature. Low temperature applications exhibit a large difference between curing and operating temperature, and therefore, large thermal residual stresses can be expected when considering an FML structure, as indicated in Figure 1.4a.

When dealing with thermal residual stresses a differentiation can be made with respect to the source of the thermal load inducing the stress state (see Figure 1.5). Thermal residual stresses that develop in the material during manufacturing when cooled from the curing temperature down to room temperature are generally referred to as *process induced stresses* or *curing stresses*. Furthermore, thermal residual stresses arise due to the difference between operating and room temperature. These stresses act in addition to the process induced stresses and can either aggravate or relieve the total thermal residual stress state depending on whether the operating temperature is smaller or larger than room temperature.

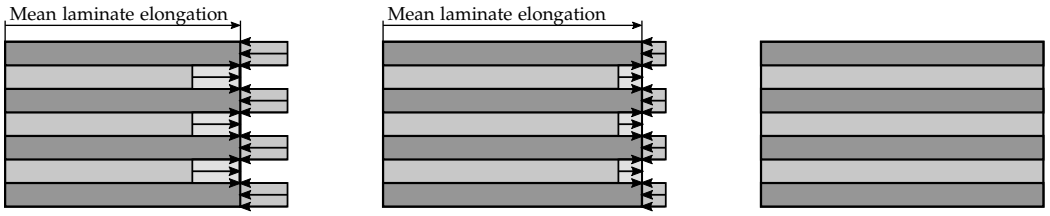

(a) Low temperature during operation

(b) Room temperature after manufacturing

(c) Stress-free temperature during curing

Figure 1.4 Thermal residual stresses in metal and composite layers of an FML

A numerical study by means of Finite-Element-Analysis (FEA) of a bolt hole in a CFRP-Ti FML at room temperature by Fink [10] shows residual stresses of around 135 MPa in a titanium ply and compressive longitudinal stresses of -192 MPa in a 0° composite ply, with no external bolt loads being applied. An analytical approach by Stefaniak [14] on an unnotched CFRP-St plate at -55 °C predicts tensile stresses of up to 550 MPa in steel plies and compressive stresses of up to -300 MPa in CFRP plies for relevant metal volume fractions between 20 - 50 %. Apparently, thermal residual stresses of significant magnitude can occur in FMLs at low temperatures. These stresses represent an intrisic loading and therefore limit the exploitable net-strength of the material. In addition, bolt loading and thermal shear and peel stresses at the free edge of a drilled hole superimpose and result in a complex stress distribution that influences failure in the laminate. Research on this specific problem is scarce.

Studies on monolithic CFRP indicate that the effect of thermal residual stresses may indeed be of high relevance. Walker [40] investigates monolithic CFRP pin-bearing specimens at -129 °C and draws three main conclusions. First, the change in material stiffness and strength at lower temperature levels influences the bearing strength. Second, interlaminar failure has a large influence on the failure behavior and should thus be considered during analysis. Third, the occurence of thermal residual stresses can reduce bearing strength at low temperature. Hirano et al. [41] and Takao [42] conduct CFRP pin-bearing tests at -100 °C and observe an increase in stiffness as well as strength for quasi-isotropic laminates. Fractographic analysis reaveals an increase in delamination effects at low temperature and thus confirms the findings of Walker. Interlaminar fracture toughness of CFRP laminates at -50 °C is quantified in detail by Asp [43] by means of Double-Cantilever Beam (DCB), End-Notched Flexure (ENF) and Mixed-Mode-Bending (MMB) tests. For a temperature decrease, the findings show an increase in apparent fracture toughness under pure interlaminar shear loading, while no obvious tendency under interlaminar peel loading could be observed. The effects of thermal residual stresses and asymmetrical laminate stacking are not considered in the study, since methods to account for the fraction of energy release rate due to said effects aren't introduced until after 2006 by Nairn [44] and Yokozeki et al. [45]. Petersen [38] as well as Monden [39] apply these methods to CFRP-St FMLs and present a compelling case for the need of their consideration, however, the effect of low temperature is not addressed.

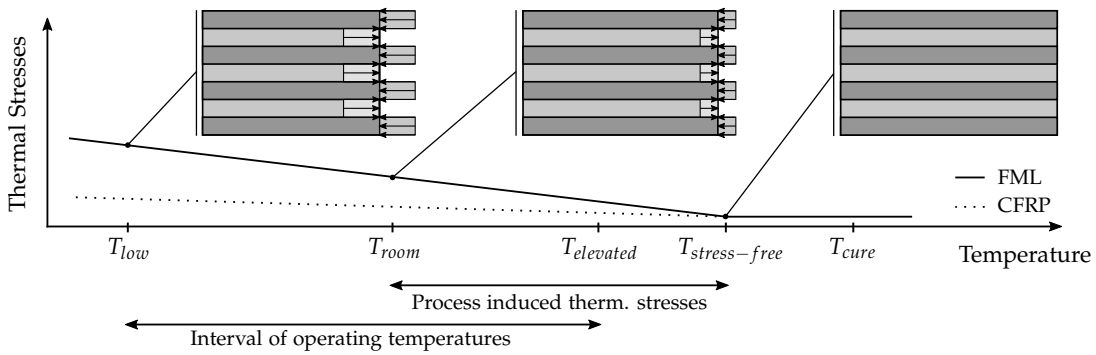

Figure 1.5 Representation of thermal residual stress levels in an FML at varying temperatures

At the example of monolithic CFRP laminates it can be seen that a temperature decrease greatly affects the material intra- and interlaminar behavior. In general, bearing stiffness and strength increase with decreasing temperature [40–42, 46], however, the presence of large thermal residual stresses can reduce the bearing capacity [40]. The failure characteristic is also influenced, indicating that an increase in delamination effects at low temperatures renders investigation of interlaminar properties more relevant. As a matter of fact, the field of low temperature bearing behavior and interlaminar properties of CFRP-St and CFRP-Ti FMLs is yet to be explored in detail. Due to the combination of large differences in CTE as well as material stiffness, inter- and intralaminar thermal residual stresses are expected to have significant influence on the material behavior. As a result, the question arises whether the increase in bearing strength by metal hybridization of monolithic CFRP laminates observed at room temperature also extends to low temperature conditions. This question defines the research hypothesis of the present work. Insight on this aspect and the capability to predict the behavior with engineering tools are deemed to be necessary for designing highly loaded hybridized composite joints.

1.5 Thesis Hypotheses

The considerations in the previous sections demonstrate that low temperature operation might represent a critical design point in the overall design of a metal hybridized mechanically fastened structure. Therefore, the question raised in the previous section, whether the superior mechanical behavior of metal hybridized composites at room temperature also extends to low temperature applications, defines the framework of the present thesis.

Research Hypothesis

> The benefits of local metal hybridization of highly loaded mechanically fastened joints in composite structures proven at room temperature extend to low temperature despite increasing thermal residual stresses in the FML and engineering tools are capable to capture this behavior for the purpose of joint design.

Working Hypothesis I

Altering interlaminar properties of a hybridized laminate at low temperature do not lead to a decrease in delamination strength of the FML.

Working Hypothesis II

Despite increasing thermal residual stresses, metal hybridized laminates exhibit an absolute bearing strength at low temperature superior to monolithic laminates.

Working Hypothesis III

Consideration of both thermal residual stresses and temperature dependent material properties is necessary for accurate numerical modeling of FMLs at low temperature.

Working Hypothesis IV

Consideration of both thermal residual stresses and temperature dependent material properties is necessary for accurate analytical modeling of FMLs at low temperature.

While working hypotheses WH-I and WH-II result from the discussion on the effects of intra- and interlaminar properties as well as thermal residual stresses on the bearing behavior of FMLs, WH-III is based on the necessity for detailed investigation on the nature and magnitude of thermal residual stresses around a loaded hole as well as the need for the capability to conduct detailed design analyses. In order to incorporate the effect of thermal residual stresses into preliminary design stages, WH-IV focuses on the prospects of a simplified analytical method for bearing analysis. In Section 3.4, a detailed derivation of the research and working hypotheses including a stragety for investigating the hypotheses is presented.

The investigation of the research hypothesis is conducted on the material combination CFRP-St for following reasons: Due to the large difference in CTE and material stiffness, steel reinforced FMLs exhibit larger thermal residual stresses than CFRP-Ti FMLs and thus present the more critical material combination. With respect to manufacturing cost and effort, the low price of relevant steel alloys (e.g. 1.4310) over titanium alloys (e.g. Ti6Al4V) as well as better processability of steel foil over titanium foil render steel hybridization more interesting for aviation applications [10, 38]. Furthermore, studies show that only about half the metal volume content is required when using steel instead of titanium in order to achieve the same reinforcement effect [10]. This results in a smaller number of required metal layers in the laminate thus decreasing the manufacturing effort when using steel as hybridization material.

The low temperature level considered in this thesis is set to -55 °C as it represents the lower bar of the temperature range for commercial aircraft application. Despite the limitations made with respect to material and temperature level, the methods developed within the present work are equally applicable to CFRP-Ti FMLs and for that matter to any FML on any operating temperature level, e.g. cryogenic.

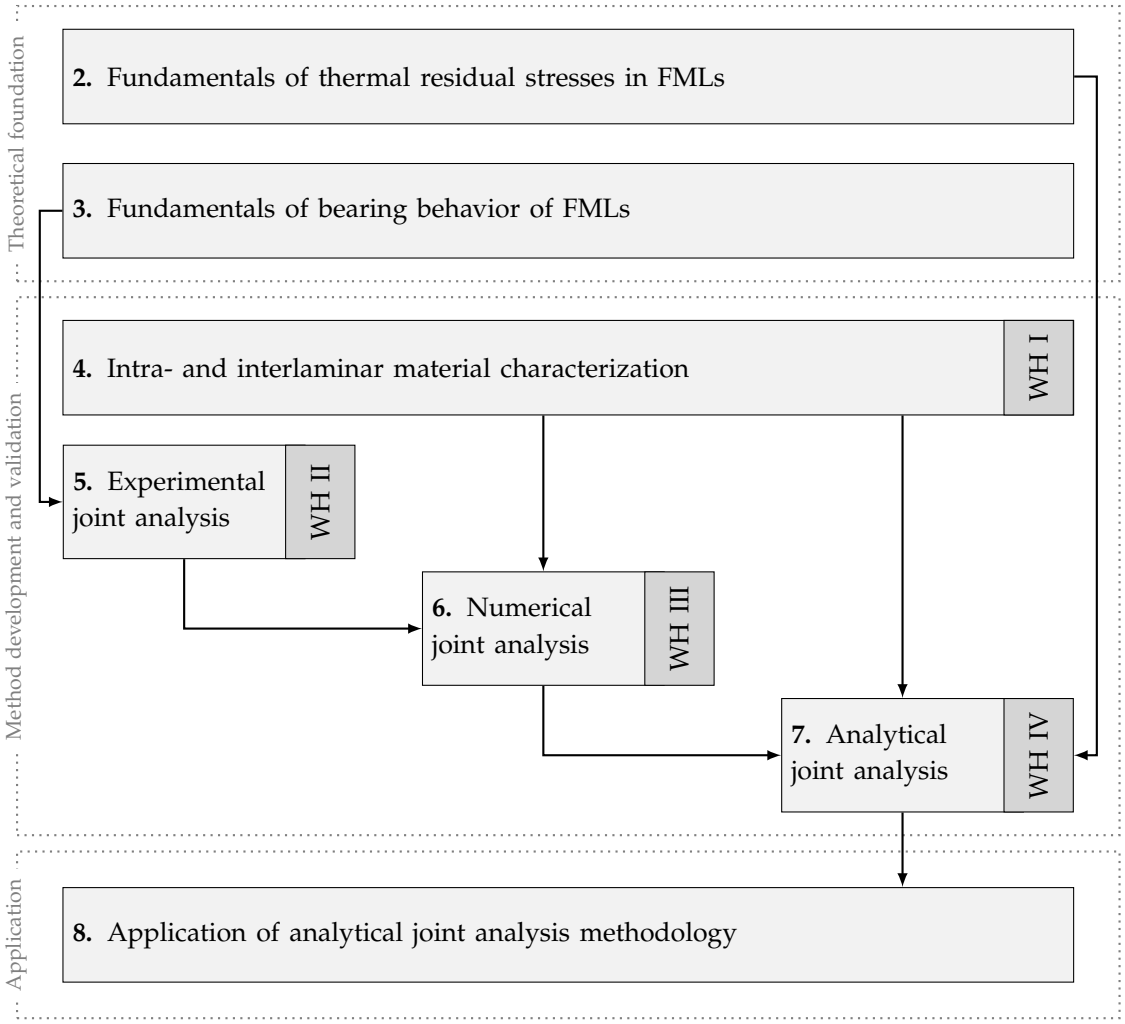

Figure 1.6 Thesis outline and the interlinkage of chapters

1.6 Thesis Outline

The present work aims for a comprehensive approach within the investigation of the bearing behavior of hybridized composite joints at low temperature. In Figure 1.6, the thesis outline is presented. The fundamental statements are based on experimental testing results at low temperature conditions. Following this phenomenological approach to build an understandig on the material behavior, requirements for a numerical modeling technique are then derived in order to be capable to simulate the structural behavior including damage initiation and progression and to conduct detailed design analyses. The findings of the experimental and numerical approach are subsequently used to develop an analytical model for preliminary design purposes, thus, providing a comprehensive set of tools for design and analysis of highly loaded hybridized composite joints under thermo-mechanical loading.

In order to build an understanding on the nature, influencing factors, and effects of thermal residual stresses in hybridized CFRP composites, the intra- and interlaminar

thermo-mechanical behavior of FMLs is discussed in Chapter 2. A literature review on the effects of metal hybridization and thermo-mechanical loading on mechanically fastened composite joints is presented in Chapter 3, including a detailed description on the approach taken to investigate the research hypothesis in the subsequent chapters.

On mesoscale, the FMLs considered in this work are composed of three entities, i.e. UD composite plies, metal plies and the interface between two single plies. The intralaminar stiffness and strength as well as the interlaminar properties govern the material behavior of the laminate - including the bearing behavior. In order to understand the material behavior on macroscale, for instance under bearing loading, an understanding of the material behavior of constituents is necessary in the first place. Therefore, an experimental characterization of the intra- and interlaminar material properties at low temperature is conducted in Chapter 4. The results allow for an initial qualitative estimate on the material behavior on macroscale and serve as input for the numerical and analytical models of this work.

The reinforcement effect by metal hybridization of mechanically fastened composite joints at low temperature is primarily investigated by experimental testing in Chapter 5. Therein, the reinforcement effect as such is determined for various metal volume fractions as well as laminate stackings with varying degrees of orthotropy. This allows for an assessment of the potential of metal hybridization based on both achievable strength and the effects of hybridization on representative laminate stackings, e.g. quasi-isotropic and highly-orthotropic laminates as well as their respective hybridized counterparts. Tangible benefits of metal hybridization become apparent when the reinforcement effect is related to design parameters, e.g. edge and pitch distances. Therefore, an experimental study on the minimum achievable edge-to-diameter and width-to-diameter ratios is conducted. In the course of this study, the effects of hybridization on failure modes are examined as well. Detailed analysis of progressive failure behavior in the bearing plane is conducted by application of ultrasound scanning and fractographic analysis methods in order to build an understanding on the failure characteristics of hybridized composites at low temperature.

Additional measurement methods during experimental testing (e.g. digital image correlation or acoustic emission) as well as post-testing evaluation methods (e.g. microscopy, ultrasound scanning or computer tomography) only allow to draw conclusions and make qualitative assumptions on the damage mechanisms, especially when considering bearing related damage with its high level of complexity. Numerical modeling, on the other hand, opens up the possibility to investigate the laminate on mesoscale so that strains, stresses, and damage can be quantified at any loading condition. This level of resolution is deemed necessary in particular when analyzing the effects of thermal residual stresses on the structural behavior of hybridized composite joints. In Chapter 6, the numerical modeling technique and the selection of material properties is presented and discussed with a focus on the peculiarities of thermo-mechanical loading of hybridized composite joints. The numerical models are validated using experimental bearing test data. This allows for a conclusive investigation of the stress state around a fastener hole due to solely thermal residual stresses

as well as combined thermo-mechanical loading cases that lead to complex superimposed stress states. Furthermore, the potential of the numerical model is studied with respect to virtual testing application.

When compared to analytical methods, experimental as well as numerial methods appear very cost and time consuming with respect to modeling of mechanically fastened joints. Although in general less versatile than its experimental and numerical counterparts, analytical methods exhibit high potential for application in certain design stages. This is why, based on the findings within the experimental and numerical work in the present thesis, an analytical modeling approach for mechanically fastened composite joints is introduced in Chapter 7. The analytical model is validated with respect to pin- and bolt-bearing loading cases at different temperature levels. In addition, an approach for incorporating the effects of thermal residual stresses is introduced and verified with the help of the numerical models from the previous chapter.

In Chapter 8, a design methodology for hybridization of composite joints is presented and applied for the design of a wing-root joint of a long-range aircraft in order to assess the benefits of local metal hybridization on large scale. Chapter 9 summarizes the fundamental findings of the thesis. The thesis hypotheses are briefly revisited and their verification is presented with concluding remarks.

Chapter 2

Thermo-Mechanical Behavior of Fiber-Metal-Laminates

2.1 Multi-scale Considerations on Thermal Residual Stresses

The presence of thermal residual stresses is inherent to composite materials. Their appearance and effects, however, are manifold depending on the entity under observation. Figure 2.1 illustrates the different levels on which effects of thermal residual stresses are present in composite materials. On micro-scale, different CTEs of fiber and matrix result in tensile hoop stresses and compressive radial stresses within the matrix in the area around a fiber after cooling of the material [47]. On meso-scale, a laminate is shown consisting of UD composite plies in different orientations, or metal plies in case of an FML. The difference in CTE of the individual plies in longitudinal and transverse direction results in intra- and interlaminar thermal residual stresses after cooling of the laminate. A cross-ply laminate $[0,90]_{ns}$, for instance, exhibits longitudinal compressive and transverse tensile intralaminar stresses in the single plies after cooling of the material. In combination with low transverse strengths of a UD ply, the sole presence of intralaminar thermal residual stresses can already lead to the occurence of matrix micro-cracks and fiber matrix debonding in transverse direction as observed repeatedly in literature [48–50]. On macro-scale, the example of a mechanically fastened structural joint is illustrated. Different CTEs of the plates result in different elongations. However, while the thermal effect in the former two cases is due to the temperature difference between operating temperature and stress-free temperature during curing, thermal effects on macro-scale result from temperature differences between operating temperature and the temperature at assembly. The free elongation of the plate area between the two fasteners is limited by the clearance of the fasteners. Once the plate elongation exceeds the clearance, thermally induced bearing stresses act on the plates. These bearing stresses are present in addition to the stresses on meso- and micro-scale, thus indicating the complexity of the occurence and effects of thermal residual stresses.

In order to understand the interaction between temperature and mechanical loads in FMLs, analytical models are introduced in this chapter to quantify thermal effects and discuss their influence on the mechanical behavior of a hybrid structure composed of a layered material and reinforced with high strength metals. Thereby, the

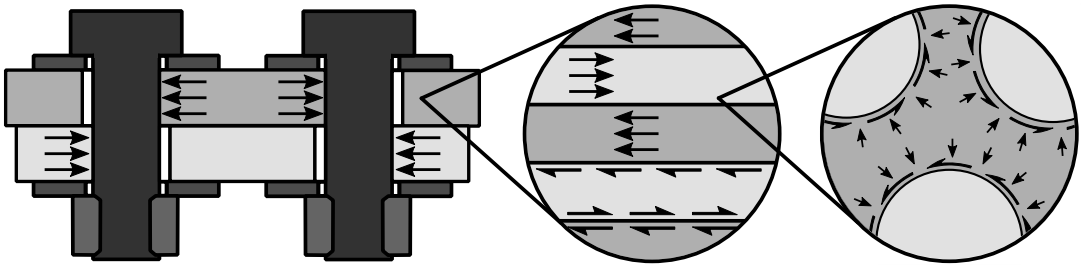

(a) Macro-scale (b) Meso-scale (c) Micro-scale

Figure 2.1 Thermal residual stresses on different scales; (a) Macro-scale: residual stresses acting on the structure at the fastener positions due to different thermal elongation of the plates, (b) Meso-scale: intra- and interlaminar residual stresses on ply level, (c) Micro-scale: thermal residual stresses in fiber and matrix

focus is set on stresses on meso-scale that influence the behavior on macro-scale. Accordingly, in a first step a detailed investigation on the biaxial thermal residual stress state in pure CFRP laminates and FMLs is conducted. Subsequently, the impact of thermal residual stresses on mechanical properties of an FML is discussed based on a new 2D approach for hybrid materials. As low temperatures are considered critical regarding the intralaminar thermal residual stress state in a structure, analysis within this chapter addresses different low temperature levels. Fundamental characteristics are discussed on the basis of generic FML consisting of UD-0° plies and metal sheets. However, in order to transfer the findings to practically relevant structures, the behavior of both pure CFRP as well as FMLs in quasi-isotropic and highly-orthotropic configuration are studied. Although the focus of this thesis is put on the material combination CFRP-St, additional material combinations, namely CFRP-Ti, are looked into in order to build a more profound understanding on the characteristics of different constituents.

2.2 Analytical Determination of Thermo-Mechanical Properties in FMLs

The present section introduces the analytical methods that are later applied for investigating the intralaminar thermal residual stress state as well as the mechanical properties of both pure CFRP and hybrid laminates under varying thermal conditions. Prediction of the intralaminar thermal residual stress state is based on the classical lamination theory (CLT), while estimating the mechanical properties of hybrid laminates is based on a 2D approach for FMLs.

2.2.1 Determination of Thermal Residual Stresses

The CLT builds on the assumption of a laminate that is free of imperfections and exhibits a perfect bond between single layers. The laminate as well as the single layers are considered in a plane-stress state. In case of a symmetric and balanced laminate, such that bending-torsion coupling is eliminated, only in-plane deformations are free to occur when thermal loads are applied. At the absence of external loads, the ther-

mal residual stresses for a given temperature gradient ΔT in the k-th ply within the laminate are denoted by the difference of the mean laminate thermal strain ε^{th} and the free thermal elongation of the respective ply [51]:

$$\begin{Bmatrix} \sigma_{xx} \\ \sigma_{yy} \\ \tau_{xy} \end{Bmatrix}_k = \begin{bmatrix} \hat{Q}_{11} & \hat{Q}_{12} & 0 \\ \hat{Q}_{21} & \hat{Q}_{22} & 0 \\ 0 & 0 & \hat{Q}_{66} \end{bmatrix}_k \left(\begin{Bmatrix} \varepsilon_{xx} \\ \varepsilon_{yy} \\ \gamma_{xy} \end{Bmatrix}^{th} - \Delta T \begin{Bmatrix} \alpha_{xx} \\ \alpha_{yy} \\ 2\alpha_{xy} \end{Bmatrix}_k \right) \tag{2.1}$$

Therein, the stiffness matrix of a UD-ply $[\hat{Q}]_k$ depends on the ply orientation with respect to the global coordinate system (x, y). The stiffness matrix of any given ply k in global coordinates can be calculated by rotating the stiffness matrix of the k-th ply $[Q]_k$ with the rotation matrix $[T]$ and the rotation angle θ:

$$[Q]_{UD} = \begin{bmatrix} \frac{E_1}{1-\nu_{12}\nu_{21}} & \frac{\nu_{21}E_1}{1-\nu_{12}\nu_{21}} & 0 \\ \frac{\nu_{12}E_2}{1-\nu_{12}\nu_{21}} & \frac{E_2}{1-\nu_{12}\nu_{21}} & 0 \\ 0 & 0 & G_{12} \end{bmatrix} \tag{2.2}$$

$$[\hat{Q}]_k = [T]^{-1}[Q]_k[T] \tag{2.3}$$

$$[T] = \begin{bmatrix} cos^2(\theta) & sin^2(\theta) & \frac{1}{2}sin(2\theta) \\ sin^2(\theta) & cos^2(\theta) & -\frac{1}{2}sin(2\theta) \\ -sin(2\theta) & sin(2\theta) & cos(2\theta) \end{bmatrix} \tag{2.4}$$

Similary, the vector of the coefficients of thermal expansion for the k-th ply in global coordinates can be obtained by:

$$\begin{Bmatrix} \alpha_{xx} \\ \alpha_{yy} \\ 2\alpha_{xy} \end{Bmatrix}_k = [R][T]^{-1} \begin{Bmatrix} \alpha_{11} \\ \alpha_{22} \\ 0 \end{Bmatrix}_k \tag{2.5}$$

Since the engineering shear strain ($\gamma_{xy} = \epsilon_{xy} + \epsilon_{yx}$) is considered, multiplication with the Reuter matrix $[R]$ results to $2\alpha_{xy}$ for the shear component of the CTE vector. The vector of mean CTE of the laminate is calculated by summation of the CTEs of the individual plies weighted by their stiffness and ply thickness:

$$\begin{Bmatrix} \hat{\alpha}_{xx} \\ \hat{\alpha}_{yy} \\ 2\hat{\alpha}_{xy} \end{Bmatrix} = [A]^{-1} \sum_{k=1}^{n} \hat{Q}_{i,j,k} h_k \begin{Bmatrix} \alpha_{xx} \\ \alpha_{yy} \\ 2\alpha_{xy} \end{Bmatrix}_k \tag{2.6}$$

$$A_{i,j} = \sum_{k=1}^{n} \hat{Q}_{i,j,k} h_k \tag{2.7}$$

The vector of mean CTE of the laminate is then applied for determining the laminate midplane strains due to the temperature change ΔT:

$$\begin{Bmatrix} \varepsilon_{xx} \\ \varepsilon_{yy} \\ \gamma_{xy} \end{Bmatrix}^{th} = \Delta T \begin{Bmatrix} \hat{\alpha}_{xx} \\ \hat{\alpha}_{yy} \\ 2\hat{\alpha}_{xy} \end{Bmatrix} \tag{2.8}$$

The magnitude of thermal residual stresses in the single plies of a laminate can now be determined using Equation 2.1. In case of an UD-CFRP FML only containing composite plies in 0° orientation and metal plies, the intralaminar longitudinal and transverse thermal residual stresses in the consitutents can be simplified to:

$$\sigma_{xx,M} = [\hat{Q}_{11,M}(\hat{\alpha}_{xx} - \alpha_{xx,M}) + \hat{Q}_{12,M}(\hat{\alpha}_{yy} - \alpha_{yy,M})]\Delta T \tag{2.9}$$

$$\sigma_{yy,M} = [\hat{Q}_{21,M}(\hat{\alpha}_{xx} - \alpha_{xx,M}) + \hat{Q}_{22,M}(\hat{\alpha}_{yy} - \alpha_{yy,M})]\Delta T \tag{2.10}$$

$$\sigma_{xx,C} = [\hat{Q}_{11,C}(\hat{\alpha}_{xx} - \alpha_{xx,C}) + \hat{Q}_{12,C}(\hat{\alpha}_{yy} - \alpha_{yy,C})]\Delta T \tag{2.11}$$

$$\sigma_{yy,C} = [\hat{Q}_{21,C}(\hat{\alpha}_{xx} - \alpha_{xx,C}) + \hat{Q}_{22,C}(\hat{\alpha}_{yy} - \alpha_{yy,C})]\Delta T \tag{2.12}$$

2.2.2 Determination of Mechanical Properties

The interaction between thermal and mechanical loads in an FML is discussed based on the stress-strain behavior under uniaxial tensile loading. Thermal loading in this case refers to the temperature difference between stress-free temperature and operating temperature, thus, describing the intralaminar thermal residual stress state in the composite and metal constituents.

A 1D approach has been used previously [10, 14] in order to determine the hybrid laminate's mechanical properties whilst taking into account the effects of thermal residual stresses. Calculation of the mean laminate CTE and the laminate stiffness are both solely based on the rule of mixture and hence neglect transverse coupling effects. While this simplification is acceptable for the metal ply due to the low transverse stiffness of the composite, the approach fails to capture the restraining effect of the metal layer on the composite ply. Especially, when considering laminates that are composed of plies with orientations different from 0° the error from neglecting the transverse coupling effect increases. Therefore, the 1D model is extended on the basis of the CLT in an effort to incorporate 2D effects, i.e. ply interaction and the 2D stress state, into the determination of the mechanical properties of a hybrid laminate.

When designing hybrid laminates the onset of plasticity is of main concern, which is why the focus is set on determination of the yield point in an FML. In FMLs that are reinforced with toughened high strength steels, the yield point is usually defined by the onset of plasticity in the metal component. Figure 2.2 shows a stress-strain curve for an FML by including strain hardening, necking, and effects of Luder's strain that occurs in low- to medium-carbon steels and is more pronounced at low temperatures that at higher temperatures. In the present case, the approach is used for determining the yield strain.

Calculation of the ply stiffness matrix $[\hat{Q}]_k$, the plate membrane stiffness matrix $[A]$ as well as the mean laminate CTE was previously introduced in Equation 2.2 throughout Equation 2.6. In case of a symmetric and balanced laminate the elastic properties of the laminate that are required for the subsequent steps can be derived from the $[A]$-matrix:

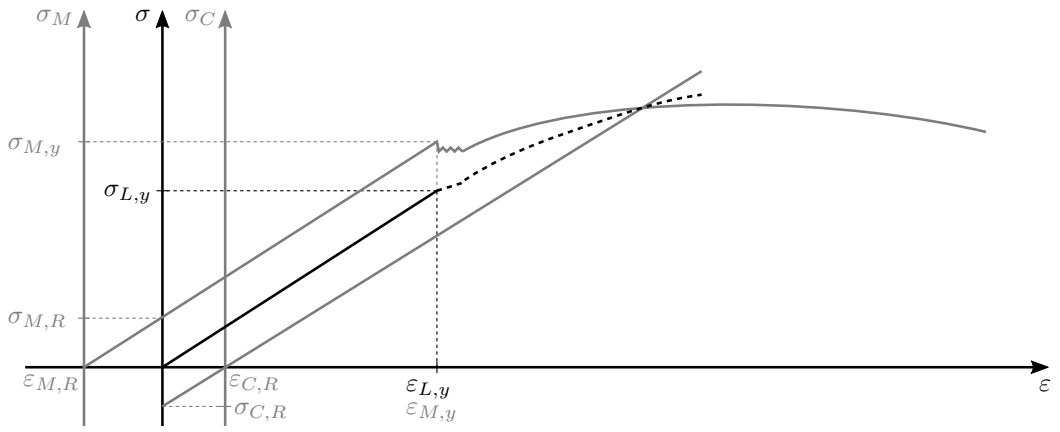

Figure 2.2 Stress-strain behavior of an FML an its metal and composite constituents under uniaxial tensile loading

$$\hat{E}_{xx} = \frac{1}{h_{tot}}\left(A_{11} - \frac{A_{12}^2}{A_{22}}\right); \quad \hat{E}_{yy} = \frac{1}{h_{tot}}\left(A_{22} - \frac{A_{12}^2}{A_{11}}\right); \quad \hat{\nu}_{xy} = \frac{A_{12}}{A_{22}} \tag{2.13}$$

At the presence of external forces acting on the laminate, the combined stress state of a ply k can be determined by evaluating the stresses due to thermal effects and external loading seperately and then combining them to the total stress state. The resulting total stress state in the metal ply is composed of a portion due to thermal strains $\{\varepsilon\}^{th}$ and a portion due to the laminate midplane strains $\{\varepsilon\}^{o}$ due to external loading:

$$\begin{Bmatrix}\sigma_{xx}\\ \sigma_{yy}\\ \tau_{xy}\end{Bmatrix}_k = \begin{bmatrix}\hat{Q}_{11} & \hat{Q}_{12} & 0\\ \hat{Q}_{21} & \hat{Q}_{22} & 0\\ 0 & 0 & \hat{Q}_{66}\end{bmatrix}_k \begin{Bmatrix}\varepsilon_{xx}\\ \varepsilon_{yy}\\ \gamma_{xy}\end{Bmatrix}_k^{th} + \begin{bmatrix}\hat{Q}_{11} & \hat{Q}_{12} & 0\\ \hat{Q}_{21} & \hat{Q}_{22} & 0\\ 0 & 0 & \hat{Q}_{66}\end{bmatrix}_k \begin{Bmatrix}\varepsilon_{xx}\\ \varepsilon_{yy}\\ \gamma_{xy}\end{Bmatrix}^{o} \tag{2.14}$$

Therein, the thermal strains in the k-th ply result from the difference between the mean laminate CTE and the CTE of the k-th ply while the midplane strains are due to external loading accompanied by transverse contraction due to Poisson's effect:

$$\begin{Bmatrix}\varepsilon_{xx}\\ \varepsilon_{yy}\\ \gamma_{xy}\end{Bmatrix}_k^{th} = \Delta T\left(\begin{Bmatrix}\hat{\alpha}_{xx}\\ \hat{\alpha}_{yy}\\ 2\hat{\alpha}_{xy}\end{Bmatrix} - \begin{Bmatrix}\alpha_{xx}\\ \alpha_{yy}\\ 2\alpha_{xy}\end{Bmatrix}_k\right); \qquad \begin{Bmatrix}\varepsilon_{xx}\\ \varepsilon_{yy}\\ \gamma_{xy}\end{Bmatrix}^{o} = \begin{Bmatrix}\varepsilon_{xx}\\ -\hat{\nu}_{xy}\varepsilon_{xx}\\ 0\end{Bmatrix}^{o} \tag{2.15}$$

Equation 2.14 can be rewritten to obtain the total stress state for a metal ply in a hybrid laminate:

$$\sigma_{xx,M} = \hat{Q}_{11,M}\cdot\varepsilon_{xx,M}^{th} + \hat{Q}_{12,M}\cdot\varepsilon_{yy,M}^{th} + \hat{Q}_{11,M}\cdot\varepsilon_{xx}^{o} - \hat{Q}_{12,M}\cdot\hat{\nu}_{xy}\varepsilon_{xx}^{o} \tag{2.16}$$

$$\sigma_{yy,M} = \hat{Q}_{21,M}\cdot\varepsilon_{xx,M}^{th} + \hat{Q}_{22,M}\cdot\varepsilon_{yy,M}^{th} + \hat{Q}_{21,M}\cdot\varepsilon_{xx}^{o} - \hat{Q}_{22,M}\cdot\hat{\nu}_{xy}\varepsilon_{xx}^{o} \tag{2.17}$$

$$\tau_{xy,M} = \hat{Q}_{66,M}\cdot\gamma_{xy,M}^{th} \tag{2.18}$$

For a symmetric and balanced laminate the thermal shear strain γ_{xy}^{th} vanishes. Once the stresses in the metal ply are defined, the von Mises yield criterion in 2D formulation is used to determine the onset of plasticity:

$$\sigma_{vM} = \sqrt{\sigma_{xx}^2 - \sigma_{xx}\sigma_{yy} + \sigma_{yy}^2 + 3\tau_{xy}^2} \tag{2.19}$$

The onset of plasticity in the hybrid laminate $\varepsilon_{xx}^o = \varepsilon_{xx,yield}^o$ occurs when the equivalent von Mises stress σ_{vM} in the metal layer reaches the metal yield stress $\sigma_{M,yield}$. Substituting the stress components of the metal layer due to thermal and mechanical loads (Equations 2.16-2.18) into the von Mises yield criterion in Equation 2.19 allows for determination of the laminate tensile yield strain $\varepsilon_{L,y}$:

$$\begin{aligned}\varepsilon_{L,y} = \varepsilon_{xx,yield}^o = &\sqrt{\left(\frac{2ab - ad - bc + 2cd}{2(b^2 - bd + d^2)}\right)^2 - \frac{a^2 - ac - bd - c^2 - \sigma_{M,yield}^2}{b^2 - bd + d^2}} \\ &- \frac{2ab - ad - bc + 2cd}{2(b^2 - bd + d^2)}\end{aligned} \tag{2.20}$$

with

$$\begin{aligned} a &= \hat{Q}_{11,M} \cdot \varepsilon_{xx,M}^{th} + \hat{Q}_{12,M} \cdot \varepsilon_{yy,M}^{th} \\ b &= \hat{Q}_{11,M} - \hat{Q}_{12,M} \cdot \hat{\nu}_{xy} \\ c &= \hat{Q}_{21,M} \cdot \varepsilon_{xx,M}^{th} + \hat{Q}_{22,M} \cdot \varepsilon_{yy,M}^{th} \\ d &= \hat{Q}_{21,M} - \hat{Q}_{22,M} \cdot \hat{\nu}_{xy} \end{aligned}$$

The corresponding laminate yield stress $\sigma_{L,y}$ reads:

$$\sigma_{L,y} = \sigma_{xx,yield}^o = \hat{E}_{xx} \cdot \varepsilon_{xx,yield}^o - \frac{\hat{\nu}_{xy}\hat{E}_{yy}}{1 - \hat{\nu}_{xy}\hat{\nu}_{yx}}\hat{\nu}_{xy}\varepsilon_{xx,yield}^o \tag{2.21}$$

By incorporating the effects of ply interaction, the 2D approach allows for application of the model to any given laminate stacking as oppose to the 1D approach which is only applicable to UD-CFRP FMLs. Determination of the yield point of an FML is done whilst taking into account the stiffness, CTE and strength of the individual constitutents. Furthermore, effects on the FML behavior arising from the difference between operating and stress-free temperature are considered. It is important to note that when applying the 2D approach it should be ensured that plasticity in the metal ply occurs at smaller strains than failure in the composite plies.

2.2.3 Limitations and Characterisitcs of Analytical Approach

When estimating the intralaminar stress state in a laminate the CLT approach is able to capture the biaxial residual stress state quite accurately by considering transverse coupling effects. Despite the limitations that come along with the simplifications of the CLT, the absolute accuracy of this method can be considered as rather good. Cowley and Beaumont [52] investigated the applicability of the CLT approach for

predicting thermal residual stresses in CFRP laminates. Analytically calculated and experimentally measured curvertures of asymmetric specimens were compared for a wide temperature range. Therein, it was concluded that the CLT approach yields very good results and is able to predict thermal effects in both quality and magnitude for CFRP based on thermoplastic as well as thermoset matrices. It addition, it was shown that the assumption of thermal residual stresses to build up linearly from the point of stress-free temperature is appropriate. Barnes and Byerly [53] as well as Walker [40] come to the same conclusion based on analytical/experimental and analytical/numerical studies, respectively. However, when applying the CLT approach for predicting thermal residual stresses, the appropriate choice of material properties is crucial.

Relaxation of Thermal Residual Stresses

The analytical models presented in this chapter both belong to the class of so called *elastic behavior models*. They assume that residual stresses build up linear-elastically with increasing difference between operating and stress-free temperature. This approach yields satisfactory results as shown in [40, 52, 53]. The class of *visco-elastic behavior models* allows for stress relaxation and creep to be taken into account but requires additional material properties. Models with varying degree of complexity have been proposed in literature. In addition to visco-elastic constitutive relations some of them also include thermo-elastic behavior as well as degree-of-cure dependent material properties, thus, allowing for a comprehensive study of chemical and thermal effects on the material behavior prior-, peri- and post-curing [54]. Application of these models is a trade-off between desired degree of detail and required input data for a model. Analytical models based on the elastic behavior approach successfully avoid detailed modeling by using the stress-free temperature as reference point, thereby implicitly accounting for manufacturing effects. However, they lack the ability to quantify stress relaxation in the laminate over time. In order to discuss in what ways the thermal residual stress prediction in hybrid laminates is affected, first, basic rheological spring-dashpot models describing time-dependent material behavior are introduced in Figure 2.3. These models are then combined to qualitatively describe the behavior of an FML in Figure 2.4.

Connecting a spring element that represents time-indepentend elastic material behavior and a dashpot element that represents time-dependent viscous material behavior in series yields the *Maxwell* model. In Figure 2.3 the strain and stress response of the Maxwell model subjected to a constant stress (creep experiment) and constant strain (relaxation experiment) are illustrated. The creep response is composed of a constant elastic strain and a viscous strain that increases with time. While the model yields acceptable results for small time intervals, the strain response becomes increasingly inaccurate for large time intervals. The relaxation response of the Maxwell model is characterized by a stress decay up to complete stress relaxation for very large times. However, for technical resin systems full relaxation of stresses is commonly not the case [52, 53]. The *Voigt-Kelvin* model consists of a spring and a dashpot connected in parallel. The creep response shows a strain curve with a degressive slope that approaches a finite value for very large time intervals. While the presence of a limit strain

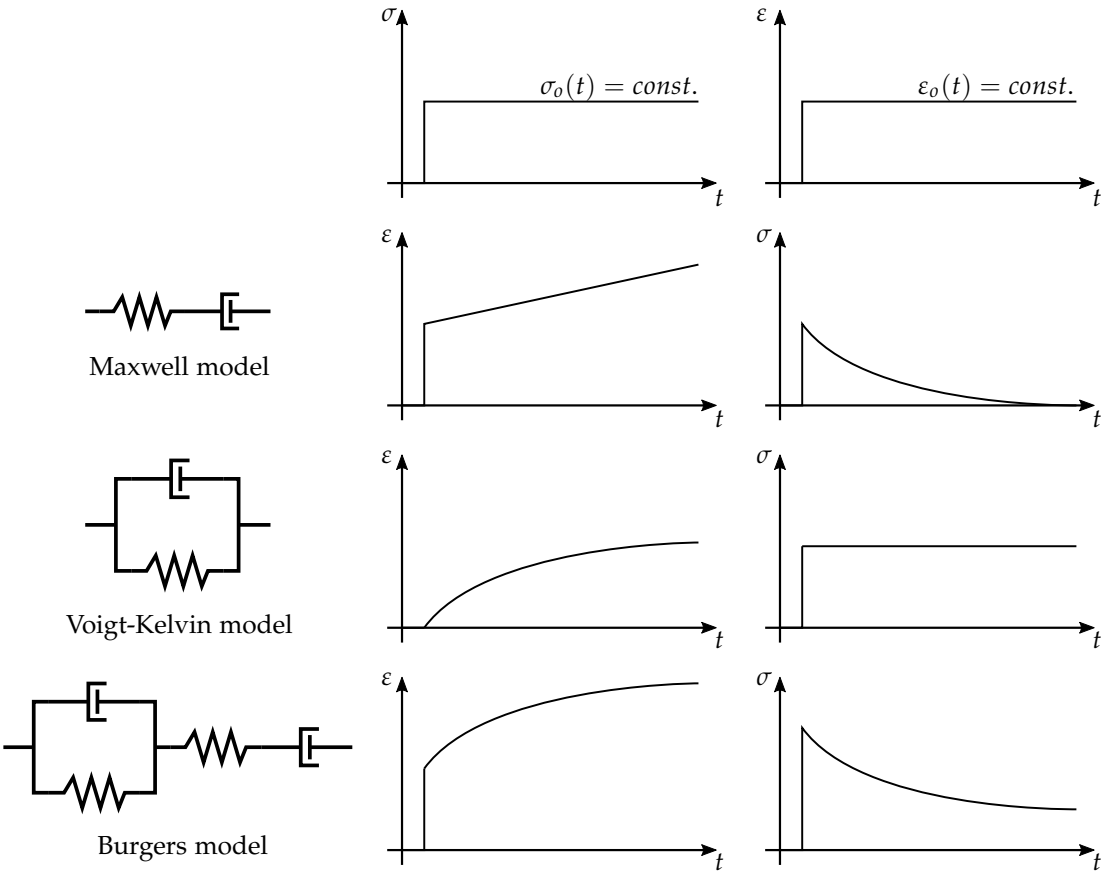

(a) Model representation **(b)** Creep behavior **(c)** Relaxation behavior

Figure 2.3 Qualitative representation of the capabilities of three basic rhelogical models to accurately capture the creep and relaxation material response of a viscoelastic material; (a) spring-dashpot representation, (b) strain response to imposed stress $\sigma_o(t) = const.$, (c) stress response to imposed strain $\varepsilon_o(t) = const.$

for large times is accurate, the Voigt-Kelvin model fails to capture the instantanious strain increase occuring in the beginning of a creep experiment. When considering the relaxation response, the material responds with a constant stress when subjected to a constant strain which makes the Voigt-Kelvin model unfit for describing relaxation in a material. By combining the Maxwell and Voigt-Kelvin model and connecting them in series the *Burgers* model is obtained. The Burgers model overcomes the shortcomings of the previous two models and is able to accurately describe both creep and relaxation in technical resin systems. As indicated in Figure 2.3, the Burgers model can be considered a superposition of the Maxwell and Voigt-Kelvin model. Thus, by assigning appropriate values for the moduli of elasticity of the individual springs as well as the dynamic viscosities of the individual dashpots, the Burgers model captures both the instantanious strain increase in the beginning of the creep experiment as well as the asymptotic behavior for large time intervals. Similarly, the relaxation response of the Burgers model accurately reflects the instantanious stress increase as well as the asymptotic decay toward a finite stress value that is typical for technical resins.

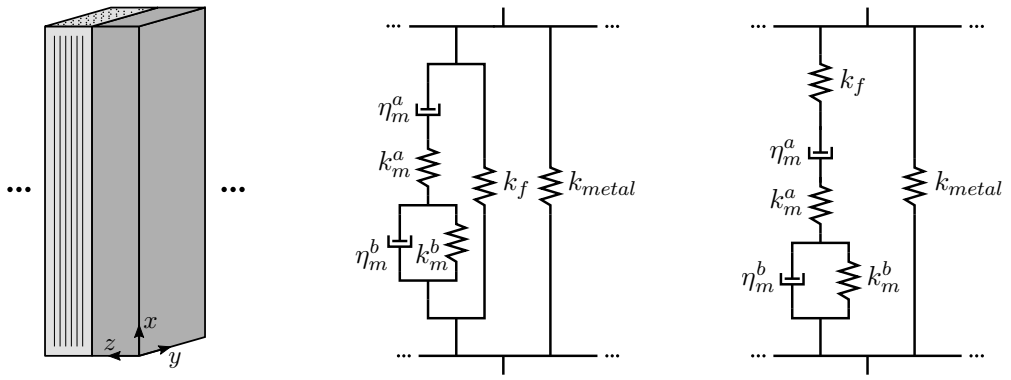

(a) FML-segment **(b)** Longitudinal direction **(c)** Transverse direction

Figure 2.4 Two-ply segment of a UD-CFRP/metal laminate (a) and simplified spring-dashpot model of the segment describing the intralaminar material relaxation behavior in longitudinal (b) and transverse (c) direction

After introducing the models to describe the matrix material behavior, a two-ply segment of a symmetric and balanced FML is considered in Figure 2.4a in order to discuss the effects of relaxation and creep in FMLs. The behavior of the two-ply segment in longitudinal and transverse direction is described in Figure 2.4b and Figure 2.4c, respectively. Metal and fiber stiffness are represented by ideally elastic springs (k_{metal}, k_f), whereas the matrix time-dependend viscoelastic behavior is described by the Burgers model consisting of two springs (k_m^a, k_m^b) and two dashpots (η_m^a, η_m^b). In longitudinal direction, a UD-CFRP ply is modeled by fibers (k_f) and matrix (k_m^a, k_m^b, η_m^a, η_m^b) connected in parallel, as illustrated in Figure 2.4b, while in transverse direction fibers (k_f) and matrix (k_m^a, k_m^b, η_m^a, η_m^b) can be considered in series, see Figure 2.4c. In both cases the UD-CFRP ply and metal ply are connected in parallel on laminate level. Transverse coupling as well as shear deformation effects are disregarded at this point.

As indicated in Figure 2.4b, creep and relaxation effects in longitudinal direction are assumed to take place solely on microlevel between fiber and matrix without affecting neighboring layers. The rearrangement and slippage of sequences of polymer chains on molecular level results in a redistribution of loads from the matrix (k_m^i, η_m^i) into the fibers (k_f) of a ply. Generally speaking this behavior is favorable since the load transfer occurs toward the element that exhibits the higher strength. However, since the magnitude of the stress redistribution is very low, amounting to only a few percent of the fiber strength, the effect is hardly measurable and often lies on the same order of magnitude as the standard deviation of the material strength during testing [55]. Hence, stress relaxation effects in fiber direction are assumed to be negligible as long as the stress analysis is not extended to the microlevel. Considering the transverse direction of the two-ply segment in Figure 2.4c, fiber (k_f) and matrix (k_m^i, η_m^i) of the UD ply are now connected in series. Time-dependent effects in the matrix are not compensated by the fibers within the respective layer anymore. In fact, creep and relaxation effects in the UD ply result in an alleviation of the stress level in transverse direction

of the UD ply. A number of experimental studies on relaxation effects in cross-ply thermoset CFRP laminates by application of the curvature method on assymmetric specimens have been carried out. The results indicate that the magnitude of thermal residual stresses due to manufacturing is reduced by 15 % to 25 % [52, 54, 56] depending on the specific matrix system, laminate configuration, storage time as well as load and temperature levels under consideration. Therein, the influence of temperature on creep and relaxation processes in polymer materials is of particular relevance. Temperature induces chain mobility that is required for the molecular rearrangement and slippage processes of chain sequences that are the basis of macroscopically visible creep and relaxation effects. The few studies conducted on stress relaxation in composites at low temperatures indicate that the effect is hardly present at all in many polymer systems at temperatures below -100°C [57] and becomes more relevant for temperatures close to and above room temperature level [54]. When discussing the stress relaxation of thermal residual stresses, care must be taken as to which portions of the thermal stress can be considered to relax. Process induced thermal residual stresses resulting from cooling of a part after curing can be assumed to relax due to the large time period between manufacturing and service. However, when thermal residual stresses result from temperature changes during operation, it has to be established whether the time intervall under consideration is sufficient for significant stress relaxation processes to occur, in particular, if low temperature applications are considered. In principal, moisture uptake in composites leads to a swelling of the matrix and thereby results in residual stresses, too. However, since highly cross-linked epoxy systems are considered in the present thesis and due to the fact that metal plies in FMLs act as shielding against moisture absorption, residual stresses due to moisture are not further considered. In Chapter 7.2.3, a detailed description on how to deal with relaxation in designing a joint is presented.

Selection of Model Input

After discussing the limitations of the analytical approach, the present section aims to demonstrate the necessity for an appropriate selection of the model input data when applying the models. First and foremost, it is important to employ temperature dependent material properties. Therefore, material stiffness and strength data need to be available for the operating temperature under investigation. Required material properties can either be determined through experimental testing or estimated through the micromechanical approach [55] based on fiber and matrix properties. Aside from material stiffness and strength, the correct definition of the CTE and the stress-free temperature are of particular relevance and will be adressed hereafter.

Coefficient of Thermal Expansion

The crucial interaction between temperature and strains in the laminate is marked by the CTE. In ISO 11359-2 two definitions of the CTE are proposed. The differential coefficient of thermal expansion $\alpha(T)$ at a given temperature T is obtained from thermomechanical analysis (TMA) data as:

$$\alpha(T) = \frac{dL}{dT} \cdot \frac{1}{L_{ref}} \tag{2.22}$$

The mean coefficient of thermal expansion $\bar{\alpha}$ between the temperature T and a reference temperature T_{ref} is defined as:

$$\bar{\alpha} = \frac{L - L_{ref}}{T - T_{ref}} \cdot \frac{1}{L_{ref}} \tag{2.23}$$

During thermo-mechanical analysis of a structure, e.g. when applying a temperature load as is done in the subsequent sections, the latter definition of the mean coefficient of thermal expansion $\bar{\alpha}$ is required to describe the material response due to a temperature change. In case the thermal strain ε_{th} needs to be calculated based on $\alpha(T)$, the relation between coefficient of thermal expansion and temperature reads as follows:

$$\varepsilon_{th} = \int_{T_{ref}}^{T} \alpha(T)\, dT = \alpha_{me}(T_{ref} - T) \tag{2.24}$$

with

$$\alpha_{me} = \frac{\int_{T_{ref}}^{T} \alpha(T) dT}{T - T_{ref}} \tag{2.25}$$

In order to simplifiy the application of temperature-dependent coefficients of thermal expansion, $\alpha(T)$ can be transformed into a mechanically effective coefficient of thermal expansion α_{me} as depicted in Equation 2.25. Thereby, the temperature dependency is incorporated and the mechanically effective coefficient of thermal expansion can be applied with the temperature change at hand as indicated in Equation 2.24. It should be noted that, similar to the mean coefficient of thermal expansion $\bar{\alpha}$, the mechanically effective coefficient of thermal expansion α_{me} is only valid for the temperature range ($T_{ref} \rightarrow T$) and is to be employed accordingly.

Stress-free Temperature

Introduced by Pagano and Hahn [58], the concept of a stress-free temperature refers to a condition during curing of a laminate that serves as a reference point regarding the development of thermal residual stresses. Above this temperature the matrix is assumed to be visco-elastic enough so that any residual stress built in the material is fully relaxed. Below this temperature the increase of thermal residual stresses with decreasing temperature is essentially linear [52,59,60]. Determination of the stress-free temperature can be conducted in several ways. Assuming the stress-free temperature to be equal to the maximum applied temperature during curing

$$T_{sf} = T_{cure} \tag{2.26}$$

is a simple but very conservative approach. A great number of commercially available prepreg systems consist of so-called 120°C or 180°C epoxy systems as matrix component. This temperature marks the recommended maximum temperature applied during curing. Typically, the recommended curing cycles aim for generating a high glass-transition temperature T_g and a high cross-linking level in order to achieve good thermo-mechanical properties. The glass-transition temperature by definition

seperates the energy-elastic brittle regime from the region of entropy-elastic soft material behavior. For epoxy resins T_g is often in a temperature range comparable to T_{cure}. Therefore, assuming $T_{sf} = T_{cure}$ is oftentimes an acceptable because conservative simplification [11]. An estimation of the stress-free temperature on the basis of T_g presents a more accurate approach since the load-bearing capacity of thermosets above T_g is drastically reduced. Thereby, setting the stress-free temperature equal to the glass-transition temperature

$$T_{sf} = T_g \tag{2.27}$$

is one possible formulation. The glass-transition temperature T_g, however, is merely a characteristic point in the glass-transition zone defined by $T_{g,onset}$ and $T_{g,offset}$ in between which molecular rearrangement processes take place. As a result, assuming that thermal residual stresses increase linearly with decreasing temperature from T_g on cannot be expected [11]. In order to allow for the assumption of linearly increasing thermal residual stresses, Schürmann [55] defines the stress-free temperature to be in the energy-elastic regime and introduces the relation

$$T_{sf} = T_{g,onset} - 20°C, \tag{2.28}$$

thereby allowing for immediate load transfer between fibers and different laminate plies through the matrix with decreasing temperature from T_{sf} on.

The preceding definitions of T_{sf} are all based on certain assumptions and represent simplified approaches when experimentally determined values are not available. Since a multitude of external effects during manufacturing influence the stress-free temperature, experimental approaches for determining the stress-free temperature are recommended [14, 60]. Therein, the curvature method using asymmetrical specimens or strain measurements by introducing fiber Bragg grating (FBG) sensors into the laminate are two rather accurate possibilities. The former method is based on laminates with a non-symmetric stacking which results in curved specimens after curing of the laminate. Reheating to a temperature where the curvature unwinds reveals the stress-free temperature. In the latter method FBG sensors are integrated within the laminate and monitor the strain during the manufacturing process. Analysis of the strain data allows for identification of the stress-free temperature. Both embedding of FBG sensors as well as applying the curvature method on asymmetrical laminates for residual stress measurements and determination of the stress-free temperature have been successfully demonstrated on CFRP-St FMLs [14, 15, 59–62].

2.3 Effects of Temperature on Thermo-Mechanical Properties

After introducing the analytical approaches for investigating thermo-mechanical properties of FMLs, the analytical models are applied to a number of steel and titanium hybridized laminates as well as monolithic laminates. Principle characteristics of the laminates' mechanical behavior at different temperatures are first explained at the example of pure 0°-UD-CFRP-FMLs. In addition to those laminates consisting solely of UD-0° plies and metal, in the following a quasi-isotropic (QI) laminate (25/50/25) and a highly-orthotropic (HO) laminate (60/30/10) as well as their respective hybridiza-

Table 2.1 Material properties at room temperature (RT) low temperature (LT) and cryogenic temperature (CT)

			T_{op} [°C]	E_1 [GPa]	E_2 [GPa]	ν_{12} [-]	G_{12} [GPa]	$\bar{\alpha}_1$ [10^{-6}/K]	$\bar{\alpha}_2$ [10^{-6}/K]	$R_{p,0.2}$ [MPa]
CFRP	M21/T700GC	CT	-196	128[1)]	11.9[1)]	0.130[1)]	10.2[1)]	0.23	26.9	-
		LT	-55	123	10.0	0.287	5.7	-0.25	34.0	-
		RT	23	124	8.4	0.291	4.3	-0.44	36.8	-
Steel	1.4310	CT	-196	213[2)]		0.292[2)]	82.4[5)]	11.4		1886[2)]
		LT	-55	196		0.302[2)]	75.3[5)]	12.6		1674[2)]
		RT	23	193		0.307[2)]	73.8[5)]	12.7		1579[2)]
Titanium	Ti-6Al-4V	CT	-196	131[3)]		0.298[3)]	54.5[5)]	7.9[4)]		1334[3)]
		LT	-55	117[3)]		0.315[3)]	44.5[5)]	8.5[4)]		1031[3)]
		RT	23	114[3)]		0.322[3)]	43.1[5)]	8.6[4)]		898[3)]

[1)] extrapolated based on data from [63], [2)] extrapolated based on data from [64], [3)] from [64], [4)] calculated based on data from [64]

tions (25/50/0/25) and (60/0/0/40) are considered.[1] The QI laminate is hybridized by substituting all 90° layers with metal layers, while in the HO laminate all but the 0° layers are substituted, conforming to hybridization design rules proposed by Fink [10], who suggests substitution of ply orientations that contribute least to the load bearing capacity, i.e. 90° followed by ±45° plies. Consideration of the QI and HO laminates allows for conclusions regarding more practically relevant laminate configurations.

The effect of different operating temperature levels is studied for conditions at room temperature 23°C (RT), low temperature -55°C (LT) and cryogenic[2] temperature -196°C (CT). Consideration of this large temperature range requires temperature dependent material properties to be taken into account. Table 2.1 shows the temperature dependent properties for the different materials under consideration. Stiffness and strength properties of CFRP and steel at RT and LT are based on experimental test data (see Chapter 4). In case of steel, stiffness and strength properties at CT are taken from [64]. The CFRP stiffness values at CT are extrapolated based on the strength increase from RT to CT observed by Haberle [63] for a material system with comparable fiber and matrix components. Stiffness and strength properties of titanium are taken from *The Cryogenic Materials Data Handbook* [64]. The linear coefficients of thermal expansion are determined based on data from TMA in case of CFRP and metal, while the calculation of CTE in case of titanium is done based on the material elongation behavior documented in [64]. In all cases, the CTE is determined between the operating temperature T_{op} and the stress-free temperature T_{sf} which is assumed to be 160°C ($T_{cure} - 20$°C). The metals are considered isotropic, while orthotropic behavior is taken into account for CFRP.

[1]Unless otherwise stated, the ply-distribution code for monolithic laminates and FMLs are given by (0°/±45°/90°) and (0°/±45°/90°/metal), respectively.

[2]Currently, no precise and unversally accepted definition for the cryogenic temperature range is available. The U.S. National Institute of Standards and Technology, however, considers temperatures below -180°C cryogenic, since the boiling point of permanent gases (e.g. hydrogen, helium, nitrogen, oxygen and neon) is below that temperature. Accordingly, cryogenic conditions in the present thesis are related to the boiling point of liquid nitrogen as it is a common coolant for cryogenic applications and therefore material properties are more accessible. However, much lower temperatures can be achieved when using for instance helium (-269 °C) as liquid coolant [64].

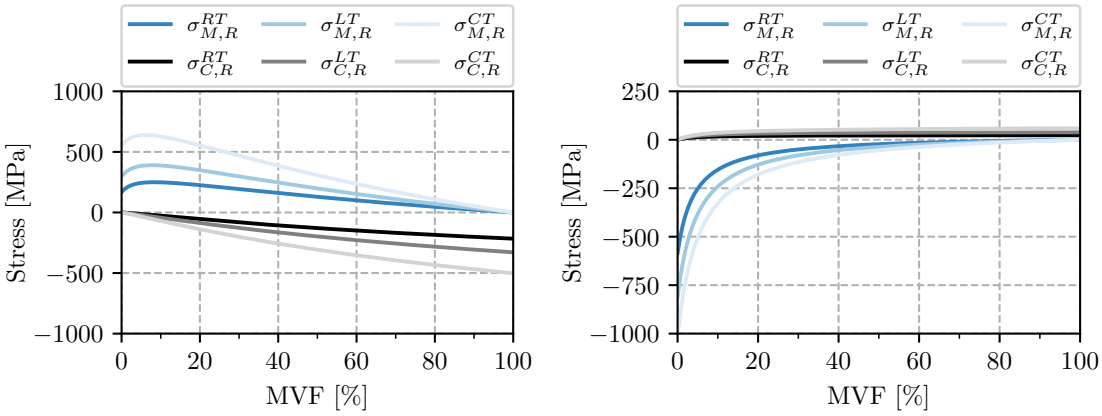

(a) Stress in longitudinal direction

(b) Stress in transverse direction

Figure 2.5 Intralaminar thermal residual stresses in CFRP-St with varying MVF at different temperature levels

2.3.1 Intralaminar Thermal Residual Stresses

The intralaminar state of thermal residual stresses in both longitudinal and transverse direction of a CFRP-St and a CFRP-Ti FML are shown in Figure 2.5 and Figure 2.6, respectively. Metal volume fractions (MVF) between 0 - 100% are considered. In Figure 2.5a, the difference in CTE results in tensile stresses in the steel layers and compressive stresses in the composite layers in longitudinal direction. With decreasing volume fraction of a respective constituent the magnitude of residual stress increases since the difference to the mean laminate thermal strain increases. As a result, thermal residual stresses in the metal component are largest for low MVF, while compressive stresses in the composite are largest for high MVF. At technically relevant MVF for bearing applications between 20 % and 50 %, considerable stresses are present in both steel and composite. Decreasing the operating temperature from room temperature significantly increases the stress state in the CFRP-St FML. At very low MVF the stresses in the metal layers slightly decrease. This is due to the fact that high compressive stresses in transverse direction of the metal ply (Figure 2.5b) result in a longitudinal contraction, thus, alleviating the thermal elongation in longitudinal direction. At low MVF in combination with cryogenic temperatures the steel reaches almost 50 % of its yield strength. Similary, the composite component at high MVF experiences significant stresses of about one third of its compressive strength. The large missmatch in intralaminar thermal residual stresses also hints at a severe interlaminar stress state which inidcates that the material combination CFRP-St might be prone to delamination at low temperatures.

The longitudinal and transverse thermal residual stresses in a CFRP-Ti FML are shown in Figure 2.6. The qualitative behavior of the residual stress state is quite similar to the previously presented CFRP-St FML. However, the longitudinal stresses present in the CFRP-Ti FML are significantly lower in magnitude. This is due to the better compatibility of titanium and CFRP with respect to stiffness and CTE as can be seen in Table 2.1. The decrease in longitudinal residual stresses for very low MVF in

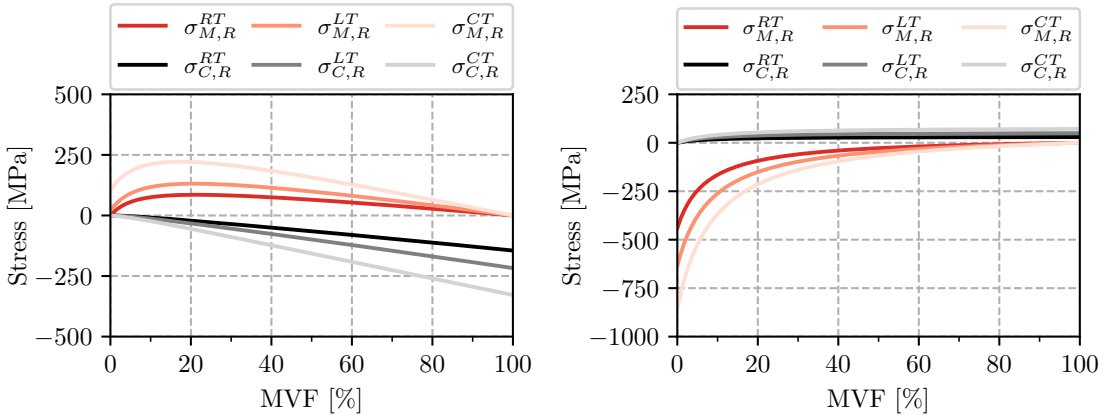

(a) Stress in longitudinal direction

(b) Stress in transverse direction

Figure 2.6 Intralaminar thermal residual stresses in CFRP-Ti with varying MVF at different temperature levels

Figure 2.6a results from the transverse coupling effect in the laminate as explained at the example of the CFRP-St FML. Due to the lower stiffness of titanium, this effect is more pronounced. The relatively large residual stresses in transverse direction in the CFRP-Ti FML in Figure 2.6b are a result of the mismatch in CTE in transverse direction, which is actually larger between CFRP and titanium compared to CFRP and steel.

The considerations in Figure 2.7 underline the necessity for taking into consideration the temperature-dependency of material properties during thermo-mechanical analysis. Based on the example of the CFRP-St FML from Figure 2.5, additional curves (dashed lines) are plotted in which RT material properties are used for calculating the thermal residual stress state at LT and CT conditions. In both cases the difference between T_{op} and T_{sf} is 160°C. The relative error between thermal residual stresses calculated based on these two appraches is plotted for LT and CT conditions. As can be seen, the relative error is largest for low MVF and becomes less sensitive to changes in the FML composition with increasing MVF. This is due to the fact that the temperature-dependency of CFRP is more pronounced than that of steel. Furthermore, since matrix dominated properties are affected the most by a temperature change, it is not surprising that the transverse stresses at low MVF exhibit the largest relative error. For MVF relevant to local metal hybridization between 20 % and 50 %, the error resulting from neglecting the temperature-dependency of material properties in Figure 2.7 reaches values of 2.4 % (LT) and 9.2 % (CT) in longitudinal direction and -3,5 % (LT) and 16,2 % (CT) in transverse direction. Therein, the error resulting from using CTEs at a certain temperature as oppose to calculating mechanically effective CTEs between the temperature levels under consideration is not taken into account and is likely to contribute to a significant increase in error.

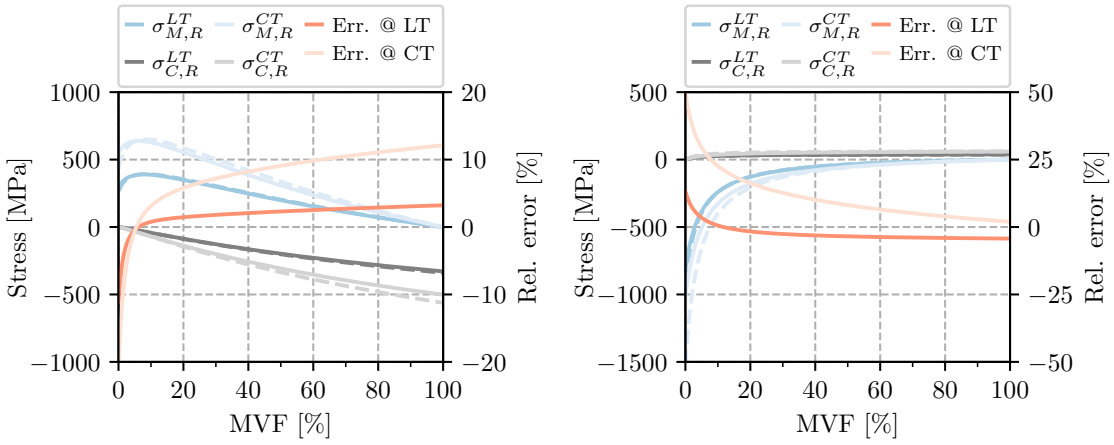

(a) Longitudinal direction **(b)** Transverse direction

Figure 2.7 Error resulting from neglecting the temperature-dependency of material properties in a CFRP-St FML: solid lines are based on temperature-dependent properties, dashed lines use RT values with ΔT=160°C

Multi-directional Laminates

In order to build a more differentiated understanding on the characteristics of thermal residual stresses in multi-directional laminates, the longitudinal and transverse residual stress state in the individual plies of a QI and HO laminate as well as the respective CFRP-St and CFRP-Ti hybridizations at room temperature are presented in Figure 2.8. The intralaminar thermal residual stress state in the QI laminate in Figure 2.8a and Figure 2.8b is typical with respect to both quantity and quality of thermal residual stresses. Due to the evenly distributed ply share of 0°, ±45° and 90° layers, absolute thermal residual stresses in both longitudinal and transverse direction are identical in magnitude. Therein, longitudinal compressive stresses are present since the fiber parallel CTE of a UD ply is smaller than the mean laminate CTE. In transverse direction, tensile stresses are present because the fiber perpendicular CTE is larger than the mean laminate CTE. Substituting the 90° layers with metal plies alters the residual stress state substantially. The metal exhibits high tensile stresses in both longitudinal and transverse direction. At the same time, significant compressive stresses are present in longitudinal direction of the 0° and ±45° plies. Although the qualitative behavior of CFRP-St and CFRP-Ti FMLs in longitudinal direction is identical, the better compatibility of titanium and CFRP in longitudinal direction results in a considerably lower overall stress state in the CFRP-Ti FML compared to the CFRP-St FML. With respect to the transverse behavior, however, stresses in the composite plies of the CFRP-Ti laminate are larger than in the CFRP-St FML. This is due to the fact that the tranverse CTE of the composite plies is closer to the steel CTE than to the titanium CTE. Thus, when considering the composite plies only, titanium hybridization leads to smaller thermal residual stresses in longitudinal direction, while steel hybridization introduces slightly less residual stresses considering the transverse residual stress state.

The intralaminar longitudinal and transverse stress state in the individual plies of a HO laminate as well as the respective CFRP-St and CFRP-Ti FMLs is shown in

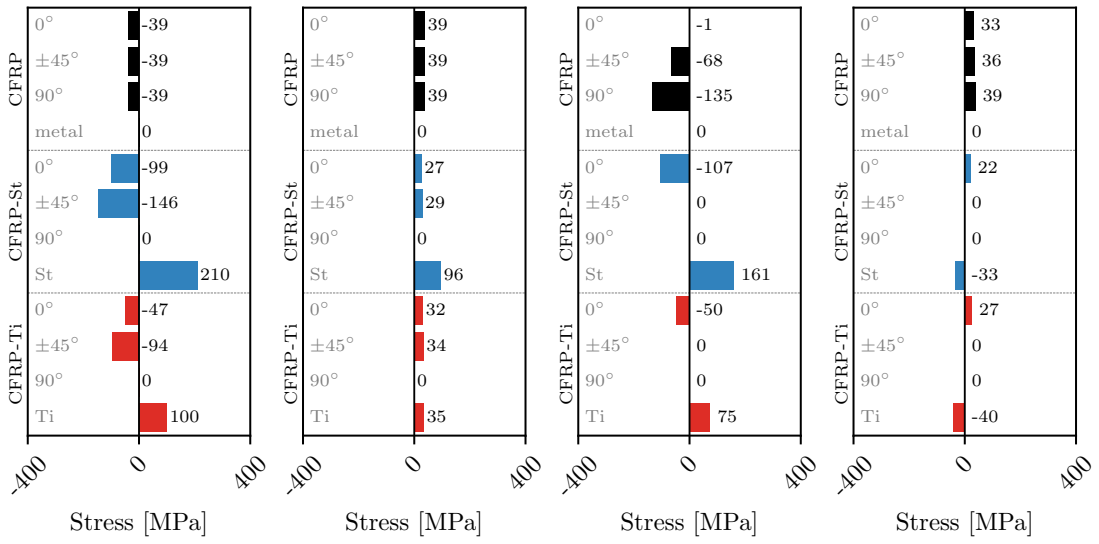

(a) Longitudinal Stress in QI-Laminates **(b)** Transverse Stress in QI-Laminates **(c)** Longitudinal Stress in HO-Laminates **(d)** Transverse Stress in HO-Laminates

Figure 2.8 Intralaminar thermal residual stresses in individual plies of a pure CFRP QI laminate (25/50/25) and HO laminate (60/30/10) as well as their respective CFRP-St and CFRP-Ti FMLs (60/0/0/40) in local ply coordinate system

Figure 2.8c and Figure 2.8d. As a result of the ply share, the mean laminate CTE is driven by the behavior of the 0° layers, thus the residual stresses in the monolithic CFRP laminate are the lowest in the 0° plies and the largest in the 90° plies. Hybridization of the HO laminate by substituting all but the 0° plies with metal results in similar effects with respect to the thermal residual stress state as observed at the example of the QI laminates. In longitudinal direction, significant compressive and tesile stresses are present in the composite plies and metal plies, respectively. Thereby, the stress state is much more severe in case of the CFRP-St FML compared to the CFRP-Ti FML. As the CTEs of both titanium and steel are lower than the CFRP transverse CTE, transverse thermal residual stresses in the composite plies are of tensile nature while compressive stresses are present in the metal transverse direction. Similar to the case of the QI laminates, the difference in longitudinal and transverse CTE between steel and titanium leads to larger stresses in the CFRP-St FML in longitudinal direction and lower stresses in transverse direction when compared to the CFRP-Ti FML.

In conclusion, hybridization of the monolithic QI and HO laminates leads to significant thermal residual stresses in both composite and metal plies of the QI- and HO-FMLs. Thus, the subject of thermal residual stresses is not only relevant for UD-CFRP FMLs but also plays a significant role when considering common multi-directional laminate layups. The analysis further shows that the effect of hybridization should be discussed by differentiating between longitudinal and transverse residual stresses. While metal hybridization leads to a severe increase in fiber parallel residual stresses, the thermal residual stress state perpendicular to the fiber direction is slighly relieved. This behavior, however, strongly depends on the individual CTEs of the constituents of an FML as well as the respective ply shares under consideration. Overall, CFRP-Ti

FMLs show better compatibility, thus, resulting in significantly lower thermal residual stresses when compared to CFRP-St FMLs. Thermal residual stresses in FMLs, typically in the hundreds of megapascals, are not very high compared to the metal strength as well as the fiber dominated strengths of the composite, which are in the thousands of megapascals. However, these stresses are significant when compared to the matrix-dominated strengths, also in the hundreds of megapascals. Therefore, it is important to analyze, in the course of this work, how residual stresses affect the material behavior.

Effect of Temperature in Multi-Directional Laminates

Based on the results in Figure 2.8 with respect to thermal residual stresses in QI and HO laminates at room temperature, Figure 2.9 reveals the effect of decreasing temperature on the intralaminar stress state in both monolithic and hybrid QI and HO laminates. Longitudinal and transverse thermal residual stresses in monolithic and hybrid QI laminates at room, low, and cryogenic temperatures are presented in Figure 2.9a and Figure 2.9b. In case of the pure CFRP laminate, the effect of temperature on the intralaminar thermal residual stress state is limited. However, when considering the QI FMLs the effect of decreasing temperature is significant. In case of the CFRP-St FML, longitudinal residual stresses in the composite plies can account for up to one third of its compressive strength at cryogenic temperature. Similarly, thermal residual stresses in the steel plies can make up about one quarter of the tensile strength of steel. Apparently, substantial thermal residual stresses are present and their consideration is critical for structural design. The CFRP-Ti FML exhibits a significant increase in thermal residual stresses compared to the pure CFRP laminate. In comparison with the CFRP-St FML, however, better compatibility of the CFRP-Ti FML results in intralaminar thermal residual stresses of about only one third in magnitude. In transverse direction, thermal residual stresses in the metal plies are again significant. When considering residual stresses in the composite plies, hybridization actually reduces the stress state as described previously. Since the present calculations take into account temperature dependent material properties, the effect of matrix embrittlement and reduction of CTE with decreasing temperature is visible. As the transverse CTE of the composite and the CTEs of steel and titanium approach with decreasing temperature, the missmatch in mean laminate elongation and free elongation of an individual ply decreases, too. Thus, partially compensating for the increasing difference between operating and stress free temperature.

In Figure 2.9c and Figure 2.9d, the intralaminar thermal residual stress state of HO laminates at different temperature levels is presented. Compared to the case of the monolithic QI laminate, thermal residual stresses in the pure CFRP HO laminate are higher an increase notably at low temperature levels. It should be noted that the transverse residual stresses approach the transverse strength, thus, indicating that especially highly orthotropic composites are prone to transverse matrix cracking at low temperatures - a phenomenon frequently observed in composites at low temperature levels [48–50]. Hybridization of the HO laminate results in large thermal residual stresses in longitudinal direction of both CFRP and metal which significantly

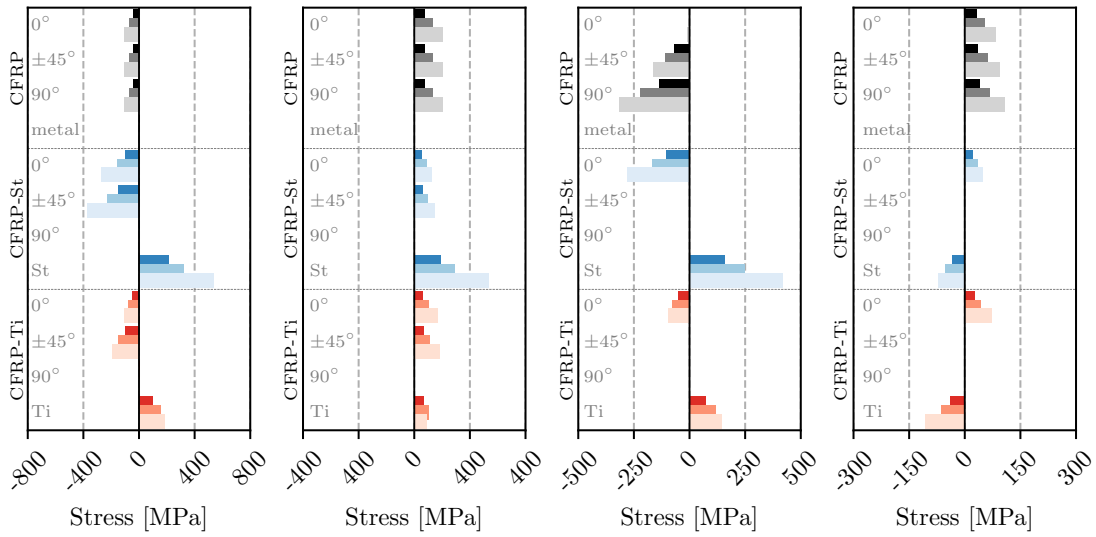

(a) Longitudinal Stress in QI-Laminates **(b)** Transverse Stress in QI-Laminates **(c)** Longitudinal Stress in HO-Laminates **(d)** Transverse Stress in HO-Laminates

Figure 2.9 Intralaminar thermal residual stresses in individual plies of a pure CFRP QI laminate (25/50/25) and HO laminate (60/30/10) as well as their respective CFRP-St and CFRP-Ti FMLs (60/0/0/40) in local ply coordinate system at RT, LT and CT conditions indicated by dark, medium and light shades

increase with decreasing temperature. When considering the transverse thermal residual stresses, hybridization again alleviates the stress state in the composite plies. Decreasing temperatures lead to an increase in residual stresses. In conclusion, the effect of temperature on the state of thermal residual stresses in the monolithic QI laminates is limited. The magnitude of thermal residual stresses at room temperature is relatively low to begin with and decreasing temperatures only lead to a small increase in residual stresses since the longitudinal and transverse CTE of the composite approach with decreasing temperature, thus, partially compensating for the increasing difference between operating and stress free temperature. In HO composites, however, thermal residual stresses are larger and increase notably with decreasing temperature. The thermal residual stress state in FMLs is severely affected by the change in temperature. The initial state of residual stresses in FMLs at room temperature is relatively high. Decreasing temperatures further increase the stress state substantially. In CFRP-St laminates, for instance, thermal residual stresses can account for up to one third of the material strength. This magnitude of residual stresses cannot be neglected when designing FML structures. In case of CFRP-Ti FMLs, the overall magnitude of thermal residual stresses amounts to about one third of the stresses in CFRP-St FMLs due to better compatibility of CFRP and titanium. Therein, the stress state is alleviated but yet still significant. When considering transverse thermal residual stresses, hybridization appears to have a beneficial effect on the residual stresses in the composite plies. Due to better compatibility of the CTEs of the composite and metals, transverse tensile stresses are reduced by hybridization, thus, reducing the composite's proneness to transverse matrix cracking. Since the CTEs of the constitutents approach with decreasing temperature, this effect is magnified at low temperature levels.

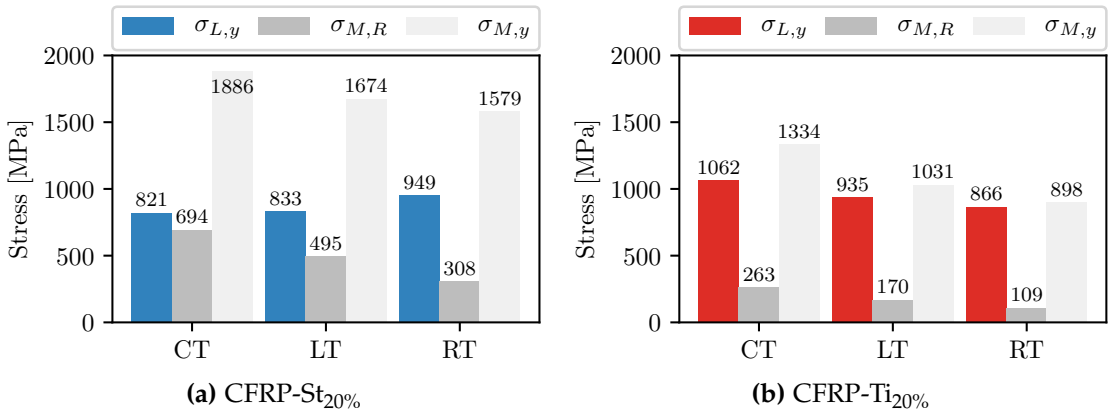

(a) CFRP-St$_{20\%}$ **(b)** CFRP-Ti$_{20\%}$

Figure 2.10 Influence of temperature on FML yield strength $\sigma_{L,y}$ for MVF = 20 %

Observations on UD-CFRP-FMLs in the beginning of the section shows the behavior of longitudinal and transverse thermal residual stresses with varying metal contents and material properties. Therein, especially the combination CFRP-St exhibits substantial thermal stresses that increase significantly with decreasing temperature. Due to the high magnitude of intralaminar stresses at all temperature levels it is expected that the strength of the FML is affected. Further studies on QI- and HO-FMLs show that common laminate stackings exhibit similarly high residual stresses. Therefore, in the subsequent section the FML strength is analyzed in order to assess the effect of thermal residual stresses on the mechanical behaviour of steel and titanium reinforced FMLs.

2.3.2 Damage Initiation in FMLs

As indicated in the previous section, the difference between operating and stress-free temperature has a significant influence on the state of intralaminar thermal residual stresses in an FML. In order to assess the effect of thermal residual stresses on the mechanical behavior of an FML, the laminate yield strength is considered herein. First, FMLs consisting solely of 0° plies and metal are investigated in Figure 2.10 and 2.11 at metal volume contents relevant to bearing applications. The results are based on the 2D analytical approach for determining the yield strength of an FML introduced in section 2.2.2.

Figure 2.10 illustrates the relation between laminate yield strength $\sigma_{L,y}$, intralaminar residual stress in the metal $\sigma_{M,R}$ and the metal yield strength $\sigma_{M,y}$ for the steel and titanium hybridized composites with a metal volume content of 20 %. Decreasing the temperature level has very different effects on the yield strength of the two FMLs under consideration. In the CFRP-Ti laminate, residual stresses in the metal increase but remain at an overall low level due to the good compatibility of the constituents. Since the metal yield strength increases with decreasing temperature, the overall hybrid laminate yield strength also increases. The CFRP-St laminate exhibits similar behavior with respect to metal yield strength and thermal residual stresses. However, the absolute values of the residual stresses in the metal are significantly larger. There-

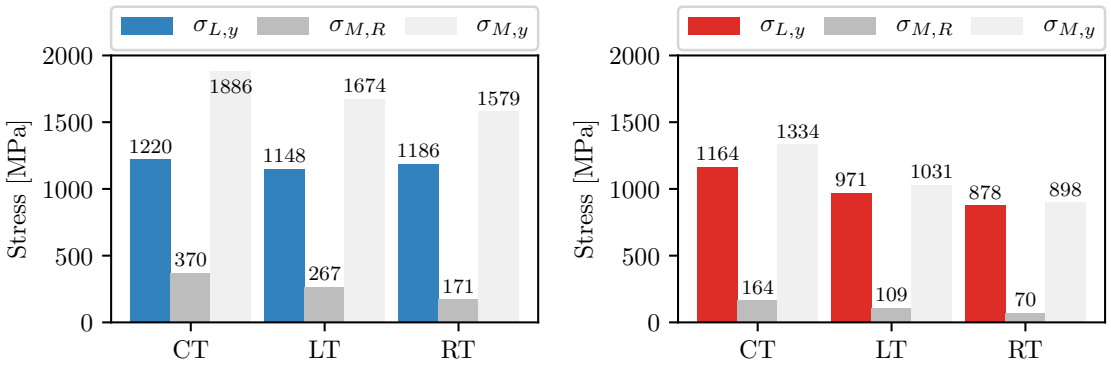

(a) CFRP-St$_{50\%}$ **(b)** CFRP-Ti$_{50\%}$

Figure 2.11 Influence of temperature on FML yield strength $\sigma_{L,y}$ for MVF = 50 %

fore, contrary to the CFRP-Ti FML, the laminate yield strength of the CFRP-St FML decreases with decreasing temperature despite the increase in yield strength of the metal. The correlation between magnitude of thermal residual stresses and laminate yield strength is also observed by Prussak et al. [61] for CFRP-St laminates manufactured with different curing cycles in order to alter the residual stress state.

When considering the same FMLs with higher metal volume content in Figure 2.11, the observations with respect to the CFRP-Ti laminate remain the same. The overall state of residual stresses is slightly lower due to the higher MVF, thus, the increase in yield strength of the metal component with decreasing temperature translates to increasing yield strength of CFRP-Ti. For the CFRP-St laminate, the increase in MVF leads to noticeably lower thermal residual stresses in the metal. The yield strength of the laminate, however, does not exhibt a clear tendency. Due to the marginal changes with decreasing temperature, the yield strength can be assumed as somewhat constant. Hence, the increase in metal yield strength again does not translate to an increase in laminate yield strength for the CFRP-St laminate.

In Figure 2.12 the yield strengths of the QI- and HO-FMLs are presented together with the data from Figure 2.10 and Figure 2.11. Consideration of these laminates shall allow for a better estimate on the influence of thermal residual stresses on the mechanical behavior of more commonly used laminate stacking patterns as they represent possible hybridization of a monolithic (25/50/25) and (60/30/10) laminate, respectively. The QI and HO CFRP-Ti laminates in Figure 2.12 both follow the trend of increasing yield strength with decreasing temperature as already observed in Figure 2.10 and Figure 2.11. The increase in yield strength of titanium thus directly translates to an increase in the FML yield strength. When considering the steel hybridized laminates in Figure 2.12, it can be seen that no continuous increase in yield strength with decreasing temperature is present. Unlike the CFRP-Ti laminates, the CFRP-St FMLs exhibit significant residual stresses that do not allow for full exploitment of the metal strength. This observation holds true for both QI and HO laminates with varying MVF. The observations with respect to yield strength in the CFRP-St FMLs contradict the common tendency of material strength to increase with decreasing temperature. Therefore the effect of thermal residual stresses on the mechanical properties of an

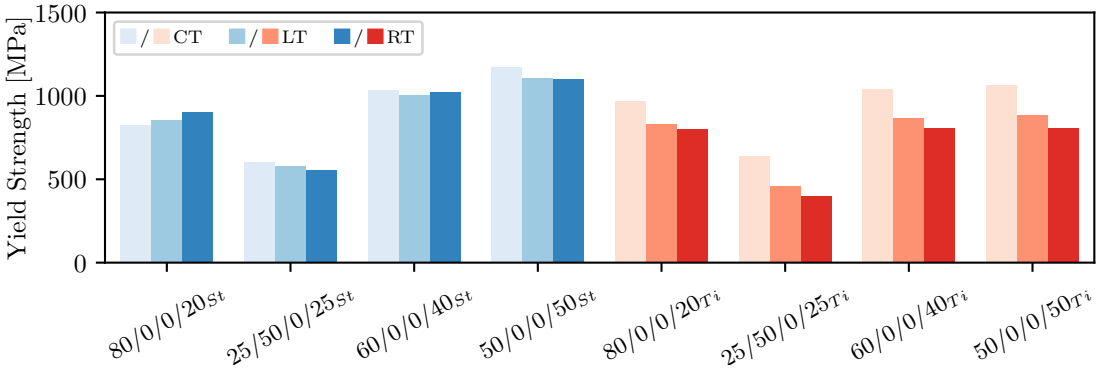

Figure 2.12 Influence of temperature on yield strength of various FMLs

FML should be taken into consideration when designing a structure. Depending on the material system, the effect of temperature on the mechanical behavior of FMLs can be very different. Good compatibility of the constituents with respect to CTE is deemed critical regarding the occurence of residual stresses. Low compatibility of CTE in combination with a high stiffness of the constituents results in large thermal residual stresses that can negatively affect the mechanical properties of the FML as seen at the example of the material combination CFRP-St.

2.4 Summary and Conclusions

In this chapter, the focus of the present thesis on meso-scale thermal residual stresses is described. An analytical calculation method for estimating thermal residual stresses in monolithic and hybrid laminates based on CLT is introduced. Additionally, a new analytical calculation method for determining the yield strength of FMLs is proposed. The novel method extends a previously proposed 1D model to the 2D case in order to incorporate effects such as transverse coupling into the analysis process. Furthermore, the theoretical basis for dealing with stress relaxation and modeling thermal residual stresses analytically, e.g. applying the stress-free tempeature and temperature dependent material properties, is introduced in preparation to be used in the subsequent chapters.

Application of the methods introduced in this chapter demonstrates that, contrary to monolithic CFRP laminates, FMLs exhibit significant thermal residual stresses. The magnitude of thermal residal stresses is especially high in CFRP-steel FMLs due to the large missmatch in CTE and stiffness. Therefore, thermal residual stresses need to be included into the design process. The use of temperature-dependent material properties also has a significant impact on the magnitude of thermal residual stresses. Furthermore, the determination of yield strength in FMLs reveals that an increase in metal and composite strength does not necessarily translate to an increase in yield strength of the laminate due to thermal residual stresses. It is therefore crucial to account for thermal residual stresses during analysis of FMLs, especially since neglecting thermal residual stresses in FMLs can be non-conservative.

Chapter 3

Effects of Metal Hybridization and Low Temperature on Bolted Joints in Composites

3.1 Fundamentals of Mechanically Fastened Joints

Structural coupling in composites can be avoided by means of integral design. However, limitations resulting from size, design, technological and logistic aspects often require structural joints within components. For composite parts, adhesive bonding and mechanical fastening remain the predominant joining methods. Despite higher joint efficiencies and lower part counts of adhesive bonding, mechanically fastened joints are generally preferred due to their suitability for thick and highly loaded laminates, their easy assembly and disassembly for maintenance, repair and inspection purposes, and their insensitivity to environmental effects compared to adhesively bonded joints. The drawbacks of mechanically fastened composite joints include effects that result from the anisotropic and laminated nature of composite materials, e.g. their lack of plasticity, their high notch sensitivity, the inherent complex fracture mechanics as well as the strong influence of geometrical and laminate configuration parameters on the material's performance [65–67]. Hence, meeting required joint efficiencies in highly loaded composite joints presents a challenging task.

The present chapter first provides a brief introduction to the fundamentals of mechanically fastened joints in composite structures. Subsequently, the characteristics of metal hybridized joints are discussed based on a literature review, followed by the topic of low temperature effects on composite joints. Therein, local metal hybridization and low temperature effects are initially discussed seperately due to the lack of comprehensive investigations combining these topics. At the end of the chapter the characteristics of both hybridized joints and low temperature effects are discussed in order to derive a strategy for investigating the effects of low temperature on mechanically fastened joints in CFRP-St hybrid laminates.

When analyzing mechanically fastened joints, usually a single-hole specimen is considered that can appear in either pin- or bolt-bearing configuration as a single-

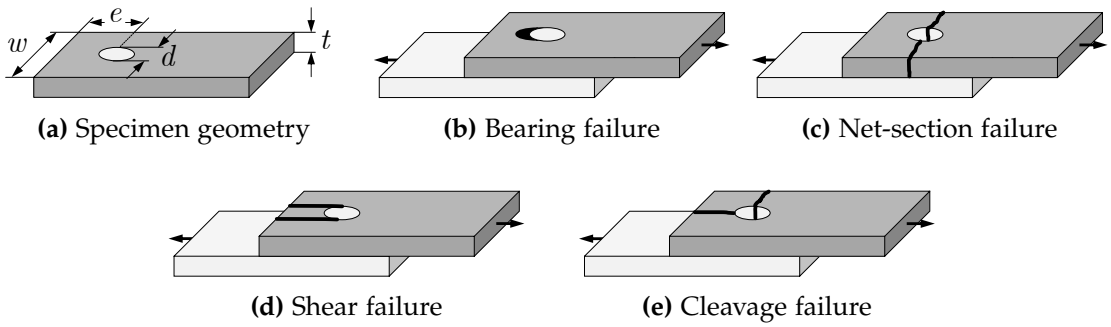

(a) Specimen geometry **(b)** Bearing failure **(c)** Net-section failure

(d) Shear failure **(e)** Cleavage failure

Figure 3.1 Mecanically fastened joint: Geometry and failure modes

or double-lap joint. Due to the lack of lateral constraint and load peaks caused by pin-tilting, the absolute strength of a pinned joint in single-lap configuration, for instance, is considerably smaller compared to the strength of a bolted double-lap joint. The occuring failure modes, however, are very similar. Apart from bolt or pin failure induced by extensive shear and/or bending of the fastener, the four common failure modes distinguished in the laminate are *bearing failure*, *net-section failure*, *shear-out failure*, and *cleavage failure*. Typically, mechanically fastened joints are designed for failure in bearing mode. Due to progressive elongation of the hole, this failure mode exhibits a somewhat ductile behavior while the other failure modes are sudden and catastrophic, and therefore undesireable. The occurence of a particular failure mode strongly depends on the joint design, therefore, the main influencing factors are addressed in the following.

Influence of Joint Geometry

As illustrated in Figure 3.1a, the joint geometry can be described by the fastener diameter d, the laminate thickness t, the edge distance e, and the specimen witdh w. Relating the dimensions to the bolt diameter gives three ratios that characterize a joint: width-to-diameter ratio w/d, edge-to-diameter ratio e/d and thickness-to-diameter ratio t/d. The choice of these ratios strongly influences the failure behavior of a joint. Small values of w/d, for instance, can result in net-section failure while joints with small e/d ratios tend to fail in shear mode. In order to assure failure in bearing mode, as a rule of thumb the values of w/d and e/d should be set to at least 4-5 and 3, respectively. Depending on the laminate thickness, however, these values may change. When t/d ratios are high the fastener is prone to shear failure in the fastener-shank. With decreasing t/d ratio failure in the laminate, e.g. bearing failure, becomes more likely. If the t/d ratio is too small, however, fastener pull-through can be present. In general, t/d ratios between 0.5 and 1.5 are recommended.

In addition to the dimensions of the joint, design of the connection in single- or double-lap configuration strongly influences the joint strength. Due to the double-sided support and symmetrical loading case, tilting of the bolt as well as bending and out-of-plane deformations of the laps in a double-lap joint are much less likely to occur than it is the case in single-lap joints. Hence, double-lap joints commonly

exhibit higher load bearing capabilities than single-lap joints.

Influence of Fiber Orientation and Stacking Sequence

Discussion on the influence of fiber orientation is most sensible when considering all failure modes at once since increasing resistance to one failure mode commonly is accompanied by lowering the resistance to another. While compressive and shear loads dominate in the region where the fastener is in contact with the laminate, tensile stresses are present in the smallest cross-section. As a result, a combination of $0°$, $\pm 45°$ and $90°$ layers is required for an optimum joint design. Therein, a minimum fraction of $0°$ layers is required due to their high compressive and tensile strength in fiber direction. Inclusion of $90°$ layers prevents splitting of the laminate resulting from the low transverse strength of $0°$ layers. In addition to contributing to resistance to shear failure and splitting, inclusion of $\pm 45°$ layers also decreases the degree of orthotropy of the laminate and thus leads to an alleviation of the stress peaks around the fastener hole. In general, laminate layups close to the quasi-isotropic pattern are favorable for bearing applications. Hart-Smith [68] suggests a general rule according to which there never should be more than $3/8$ nor less than $1/8$ of fibers in any of the principle laminate directions $0°$, $+45°$, $-45°$, and $90°$ in a highly loaded composite joint.

Although the effects of stacking sequence on the bearing strength are not as pronounced as effects resulting from joint geometry, fiber orientation or lateral constraint, consideration of some basic principles can help improving the joint behavior. It should be mentioned that the term stacking sequence solely refers to the position of plies in a laminate at constant ply shares. The general stacking rules advise symmetrical and balanced stacking sequences, uniform distribution of plies with different orientations within the laminate, and minimizing angles between adjacent plies. In addition to these recommendations that equally apply to bearing loading, it is advantageous to position $90°$ layers towards the surface of the laminate, thus producing compressive through-the-tickness stresses that can inhibit delamination and therefore increase the bearing strength of a joint [69, 70]. Especially in thin laminates, positioning $0°$ plies towards the center of the laminate where they are partly constrained by outer plies increases their load bearing capacity and hence the bearing strength of the joint [71].

Influence of Fastener Type and Lateral Constraint

Fastener types such as rivets or protruding and countersunk bolts can be categorized into pin- and bolt-bearing loading cases. While the former offers little to no lateral constraint, latter provides a lateral constraint in the vicinity of the fastener by clamping through a washer or the bolt head. The lateral constraint leads to a substantial increase in bearing strength since displacement of initially damaged material is suppressed and the material continues to withstand compressive loads introduced by the fastener shank. In case of pin-loading, however, the lack of both fastener head and nut allows for initially damaged material to delaminate. This material does not carry any load which, in turn, increases the bearing load on the remaining material. As a result the rate of failure in the joint is accelerated. Following this logic, the lower and upper bar of bearing strength is given by pure pin-loading and fully tightened bolt-loading,

respectively. Bearing strenghts of joints connected through rivets or countersunk fasteners are somewhere in between [68,72].

The effect of lateral constraint can also be extended to double-lap shear joints, where increased bearing strength of the center laminate compared to the laminates on the outer faces is observed [73]. This effect is related to better confinement of damage in the inner laminate which means that not only clamping but also the area over which clamping is induced is of relevance. As a result, it is recommended to design outer splices slightly thicker (by about 20 %) than the inner laminate and use large and stiff washers under the fastener head [68].

Multi-fastener Joints

In practical applications, multi-row fastener joints are widespread and single-bolt data is often used for their sizing. However, there are concurrent views on the practice of using single-bolt data for the design of multi-row joints. While results by Collings et al. [69] indicate that this approach is in fact valid for sufficiently large pitch distances resulting in negligible interference of stress fields between fastener rows, Matthews et al. [74] have found that equating the single-bolt specimen width with the pitch in a multi-row joint is not appropriate and results in overestimation of the multi-row joint strength. A feature that yet increases the complexity of multi-row joints is the fact that in addition to bearing loads also bypass loads have to be taken into account. For illustration purposes Figure 3.2a shows a four-row mechanically fastened joint in double-lap configuration. Due to the intrinsically uneven load distribution in multi-row joints, load transfer from the center plate to the outer splices results in high bearing loads at fasteners 1 and 4 compared to the fasteners 2 and 3. The portion of the total load that is not transferred through the fastener, passes the fastener rows as bypass loads, hence, the largest bypass loads occur at fastener 1 and gradually decrease until they vanish at fastener 4. The superposition of bearing and bypass loads leads to an excessive loading of the laminate at fastener 1, where failure is very likely to occur much earlier than at the subsequent fastener rows which results in an inefficient joint design. An advanced design with increased efficiency is shown in Figure 3.2b. The main objective during design of this joint is to alter the effective stiffness of the segments around a fastener in order to decrease the bearing loads at fastener 1, where there are large bypass loads, by shifting the bearing loads towards fastener 3 and 4, where there is little to no bypass load. As a result, there is a more even overall load distribution and the individual strength of each fastener row is exploited more effectively. In addition to adjusting the thickness of the outer plates, as demonstrated in Figure 3.2b, effective measures include alteration of the fastener diameter and material as well as changing the strip width in sinlge-strip joints and, if necessary, tapering both outer and inner laps [68] as shown in Figure 3.2c.

Mechanical Joint Efficiency

The joint efficiency relates the strength of a joint to the ultimate tensile strength of the unnotched laminate. Achieving satisfactory joint efficiencies in composite structures presents a challenging task as geometry and material related factors as well as environmental and manufacturing related effects strongly influence the joint behavior.

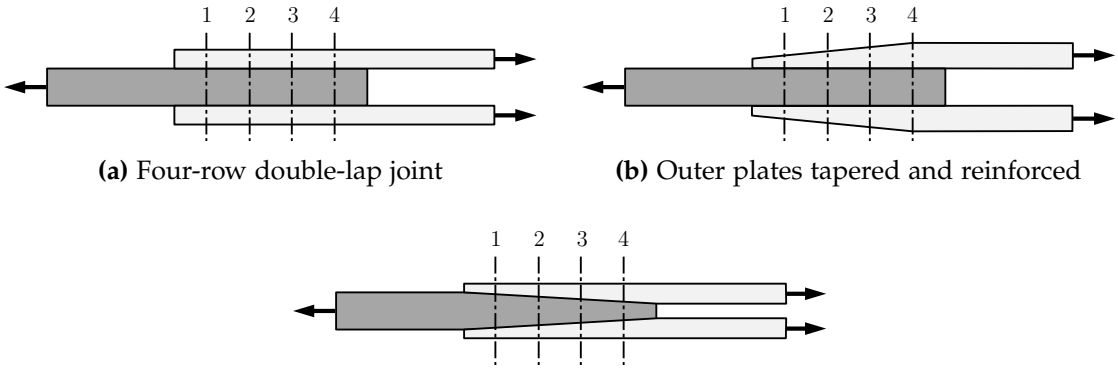

(a) Four-row double-lap joint

(b) Outer plates tapered and reinforced

(c) Inner and outer plates tapered

Figure 3.2 Four-row mechanically fastened joint design in basic configuration (a) and advanced design (b) and (c)

While common ductile metal alloys achieve joint efficiencies of up to 80 %, even well designed composite bolted joints exhibit a joint efficiency of no more than 50 % [68]. With respect to weight efficiency, the gap between mechanically fastened joints in composites and metallic structures increases even more, since composite joints commonly feature thicker skins, larger edge and pitch distances, a larger number of fasteners as well as larger and heavier fasteners and larger overlap lengths. In highly loaded mechanically fastened composite joints, it is common practice to locally increase the laminate thickness in the joining area in order to achieve the required joint strength. Due to design requirements, e.g. aerodynamic drag considerations, the local thickening often has to be implemented one sided resulting in eccentricities in the load path and additional secondary stresses that have to be accounted for. In addition, the local variation in laminate thickness increases the structural complexity and can even lead to reduced structural efficiency of adjacent parts, thus indicating significant structural weight penalties by local thickening [75].

3.2 Bearing Behavior of Hybridized Composite Joints

In order to overcome the aforementioned limitations of mechanically fastened joints in composite materials, local metal hybridization has been introduced. Therein, hybridization of the laminate is limited to the joining area and can be realized by applying either ply-addition or ply-substitution techniques. The former is based on the insertion of metal sheets of any desired thickness between continuous composite plies thus avoiding ply interruptions. This approach results in local thickening, however, significantly less pronounced than in pure composites. At the same time, this approach offers advantages due to flexibility with respect to the choice of metal sheet thickness and laminate integration. In order to avoid any local laminate thickening, ply-substitution techniques can be applied. Therein, composite plies in the joining area are replaced by metal sheets of equal thickness. As depicted in 1.3, the laminate can be divided into a hybrid region with incrased bearing capacity, a transition region and the base laminate. The superior bearing capacity in the joining area can result in a significant increase in joint efficiency due to preventing of laminate thickening,

Figure 3.3 Ariane 5 Composite Booster: Monolithic CFRP design of the inter-segment joint requiring two bolt rows and laminate thickening [10]

Figure 3.4 Ariane 5 Composite Booster: Locally metal hybridized CFRP joint with reduced bolt rows and fitting size while retaining basis laminate thickness [10]

decreasing of edge distances, and reducing the number of fastener rows and thus the overlap lengths. Hence, local metal hybridization offers a great weight saving potential. A design study by Fink [10] on the inter-segment joint of the Ariane 5 booster reveals a weight saving potential through local metal hybridization by ply-substitution using titatium sheets (Ti-15-3) of 500 kg per inter-segment joint – amounting to an overall weight reduction of around two tons for all inter-segment joints on both boosters. As can be seen in Figure 3.4, hybridization prevents laminate thickening, reduces the number of bolts and bolt-rows as well as the overlap of the metallic fitting, thus resulting in significant weight savings compared to the monolithic CFRP design in Figure 3.3 When designing a locally hybridized joint special care must be awarded to the transition region. In general, plies that contribute the least to the overall load carrying capacity of the laminate are substituted first. This ensures a gradual relief of load carrying plies with increasing metal content and prevents material damage and delamination onset due to load peaks at the ply-substitution points. A comprehensive investigation of the load carrying mechanism in the transition zone of a locally hybridized laminate including design guidelines can be found in the contribution by Petersen [38]. In the following, the fundamentals of local metal hybridization are presented briefly in an effort to give an overview of the technology. The most comprehensive studies on this topic are presented by Fink [10], Both [11], and Hundley [9]. Fundamental findings are reviewed and reprocessed in order to offer a concise yet comprehensive introduction into how metal hybridization influences the bearing behavior of composites.

Selection of Metal Component

The reinforcement effect through hybridization is mainly based on the relief of composite layers by adjacent metal plies. In order for this mechanism to be effective, high metal stiffness paired with high metal strength is required. High metal stiffness allows for a significant load relief of the composite plies while high metal strength assures

Table 3.1 Requirements for the choice of an adequate metal component

mechanical	thermal/chemical	manufacturing
• high stiffness	• low CTE	• availability as sheet/foil
• high yield strength	• corrosion resistance	• good cold formability
• high ultimate strength	• high chemical nobility	• good machinability
• sufficient ductility		

that the metal plies do not fail prematurely. A certain degree of ductility is required for the formation of a plastic zone at the notch root in order to avoid premature shear cracks that decrease the bearing strength. At the same time, adequate ductility is beneficial for good impact behavior and facilitates sheet forming of the metal. Aside from mechanical factors, thermal and chemical compatibility between metal and composite are of high relevance. Thermo-mechanical properties are highly dependent on the constituents' CTE and influence strength, fatigue resistance, and delamination resistance of the FML. Hence, the mismatch in CTE between metal and composite should be moderate. With respect to the long-term behavior corrosion resistance of the metal and galvanic compatibility between the FML costituents are required. In addition to the mechanical, chemical, and thermal requirements, the metal component also needs to feature certain manufacturing requirements such as good cold formability and machinability. Considering the collective of requirements titanium alloys and high strength stainless steel alloys present promising reinforcement metals for CFRP [10,75].

Principal Effects of Hybridization

The effect of hybridization on a composite bolted joint is explained on the basis of joint stiffness, joint yield strength[1] and the joint ultimate strength[2] in Figure 3.5, where the bearing behavior for UD-CFRP FMLs with increasing metal content is plotted against a reference CFRP laminate. It is obvious that hybridization by both steel and titanium leads to an increase of joint stiffness, bearing yield strength as well as bearing ultimate strength. Therein, the reinforcement effect using steel is more pronounced considering that less steel content is required to achieve similar yield and ultimate strengths as in the titanium reinforced FMLs. This characteristic is a direct result of the superior strength of steel compared to titanium. Similarly, the higher stiffness of steel compared to titanium leads to an increase of the initial joint stiffness. When considering the bearing yield strengths, titanium merely influences the strain at which plasticity of the joint begins whereas hybridization by steel leads to a decrease in strain at bearing yield strength. The subsequent plastic region up until ultimate bearing strength is defined by considerable hardening for both FMLs compared to the reference CFRP laminate.

[1]Defined as offset strength (0,5% permanent hole deformation)
[2]Defined as the maximum load carried by the joint

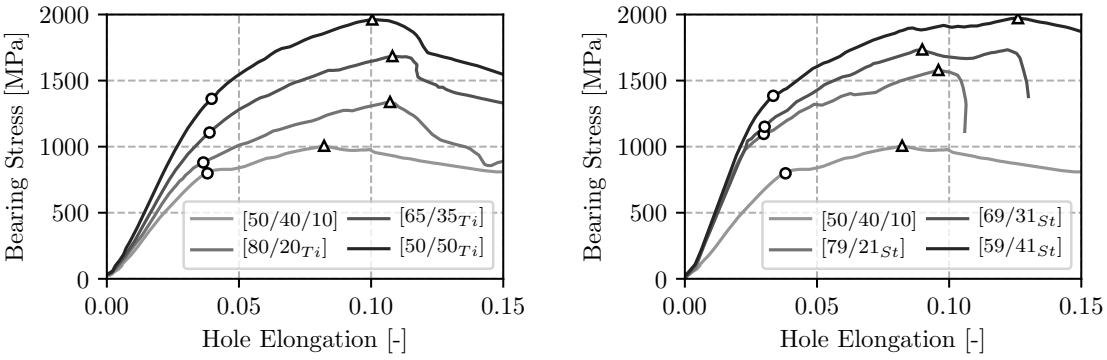

(a) CFRP-Ti FML **(b)** CFRP-St FML

Figure 3.5 Hybridization effect on bearing stress vs. hole elongation behavior of a bolted joint conforming to AITM 1-0009; reference CFRP (HTS) laminate [50/40/10] and UD-CFRP FMLs (steel 1.4310, titanium 15-3-3-3); raw data: [10]

Put simply, the observations in Figure 3.5 indicate that hybridization leads to an increase of following characteristics: joint stiffness, joint yield strength, joint ultimate strength and joint plastic hardening. The magnitude of said increase depends on the type and volume content of the metal constituent.

Influence of Metal Properties on Bearing Strength

Figure 3.6 shows the effect of varying MVF on both bearing yield strength and bearing ultimate strength for different types of reinforcing metals with different strengths. The diagrams focus on MVF between 20 % and 60 %. In addition to the bearing strength, the percentage increase in bearing strength of the UD-CFRP FMLs compared to the reference CFRP (HTS) laminate [50/40/10] is presented. In order to discuss the effects of metal strength and stiffness, titanium alloys with varying degrees of hardening Ti-6Al4V (980 MPa) and Ti 15-3-3-3 (1370 MPa & 1630 MPa) as well as the steel alloy 1.4310 with different degrees of cold working (1612 MPa & 2000 MPa) are investigated.

When considering the bearing yield strength in Figure 3.6a and the bearing ultimate strength in Figure 3.6b, it can be seen that the increase in strength with increasing metal content can be considered linear for the presented interval. The effect of metal strength is explained at the example of the three titanium alloys. While increasing the titanium strength from 980 MPa to 1370 MPa directly results in an increase in bearing strength, an additional increase of the titanium strength to 1630 MPa does not significantly improve the bearing strenght of the laminate. A further increase in bearing strength can only be achieved by increasing the MVF. Now, considering the steel FML with comparable strength (1612 MPa) but significantly higher stiffness ($E_{St}/E_{Ti} \approx 1,8$), shows an increase in bearing strength compared to the high strength titanium FML, hence indicating that both metal strength and stiffness influence the bearing behavior. Due to the lower stiffness of titanium, the stress relief of the composite plies is less pronounced than it is the case for steel at the same MVF. In this case, damage initiation in the composite plies limit the bearing strength of the joint. Increasing the stress relief in the composite plies by increasing the metal stiffness, i.e. by using steel instead

of titanium, leads to a further improvement in bearing strength. Since the metal plies now carry more load, accordingly high metal strength is required to prevent premature damage initiation in the metal component. This characteristic can be observed for both bearing yield and ultimate strength, however, it is more obvious for the latter. Comparison of the hybrid laminates with the reference CFRP laminate shows that the reinforcement effect is more pronounced for bearing ultimate strength compared to the bearing yield strength. The hybrid laminates with 50 % MVF exhibit bearing yield strengths corresponding to a strength increase of 80 % (titanium) and 140 % (steel) with respect to the reference laminate. When considering bearing ultimate strength, the strength increase at 50 % MVF reaches values of 95 % and 160 % for high strength titanium and steel reinforcement, respectively. Observations by Both [11] on a CFRP reference [67/22/11] with IM fibers and two UD-CFRP FMLs with 50 % steel (1.4324) and titanium (15-3-3-3) content, respectively, show similar results in quality, however, the reinforcement effect is less pronounced. Possibly due to the superior modulus and strength of IM fiber based composite over HTS based material. This indicates that the choice of composite material also has a significant effect on the strength increase.

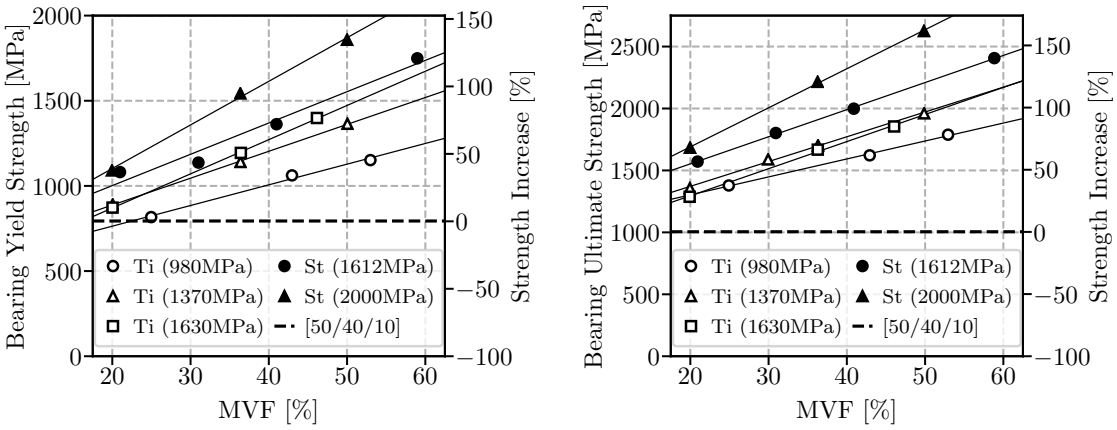

(a) Bearing Yield Strength

(b) Bearing Ultimate Strength

Figure 3.6 Hybridization effect on the bearing yield strength (a) and bearing ultimate strength (b) of UD-CFRP for different types of metals (steel 1.4310, titanium 15-3-3-3) and metal volume fractions conforming to AITM 1-0009; reference CFRP (HTS) laminate [50/40/10]; raw data: [10]

To summarize, the bearing yield and ultimate strength show a linear increase with MVF for technologically relevant metal contents (20 % - 50 %). In order to ensure optimal exploitation of the metal properties both stiffness and strength have to be chosen adequately. While the former is required for sufficient stress relief of the composite plies, the latter assures that the redirected load can be carried by the metal component. The reinforcement effect is more pronounced for bearing ultimate strength than for bearing yield strength. The magitude of the reinforcement effect, however, strongly depends on the properties and amount of metal as well as on the properties of the underlying CFRP material.

Influence of Hybridization on Joint Efficiency

In order to set the advantages of local metal hybridization into perspective, the joint efficiencies of pure composites and metals are considered in Figure 3.7. As previously described, the joint efficiency is defined as the ratio of bearing strength over ultimate tensile strength of the unnotched basis laminate. In Figure 3.7a it can be seen that the joint efficiency of a QI CFRP laminate at its peak is significantly lower than it is the case for a ductile metal. Eventhough the absolute bearing strength of CFRP-St and CFRP-Ti FMLs is larger than the strength of the QI laminate, the joint efficiency of the hybrid laminates is inferior. This is due to the fact that the bearing strength of the hybrid laminates is low compared to the unnotched strengh of the respective hybrid laminate. When considering structural applications and the idea of local metal hybridization, the original definition of joint efficency is not adequate. A more appropriate approach for locally hybridized structures is to relate the bearing strength of the locally reinforced region to the unnotched tensile strength of the monolithic basis CFRP laminate as proposed by Fink [10]. For illustration purposes the modified definition is applied in Figure 3.7b to the hybrid laminates by relating their strength to the unnotched tensile strength of the QI laminate. In this case, the joint efficiency of the hybrid laminates amounts to 105 % and 120 % and surpasses the metal joint efficiency which reveals the large magnitude of reinforcement compared to the basis structure.

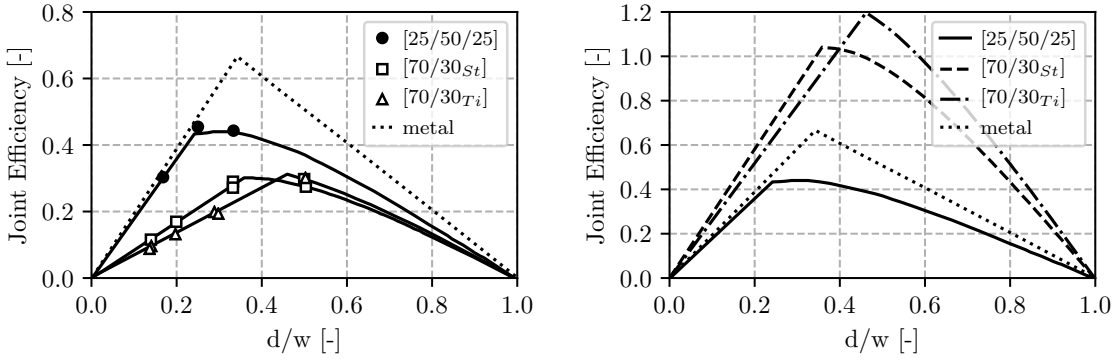

(a) Original definition of joint efficiency **(b)** Modified definition of joint efficiency

Figure 3.7 Joint efficiency as a function of d/w for sufficiently large edge distance e; CFRP and UD-CFRP FML raw data from [10], metal raw data from [68]

In conclusion, it becomes apparent that the discussion on joint efficiency should be based on a modified definition of joint efficiency for the hybrid laminates in order to capture the actual reinforcement effect with respect to the basis laminate.

Influence of Hybridization on Pitch- and Edge-Distances

When designing a mechanically fastened joint, the minimum end- and pitch-distances pose a lower limit to allowable joint geometries. Smaller minimum distances allow for a more compact joint design and increase both the mechanical and weight efficiency. In composites the minimum recommended values for the e/d and w/d ratio are 3 and 4-6, respectively. Studies by Fink [10] in Figure 3.8b confirm these general recommendations. By metal hybridization of the laminate these miminum values can be reduced

to about 3 for the w/d ratio. Regarding the e/d ratio varying recommendations are presented in literature. While investigations by Hundley [9] on CFRP-Ti FMLs in Figure 3.8a indicate that this ratio can be reduced to a minimum value of 2, both Fink [10] and Both [11] find this ratio to be 3 for CFRP-St and CFRP-Ti FMLs.

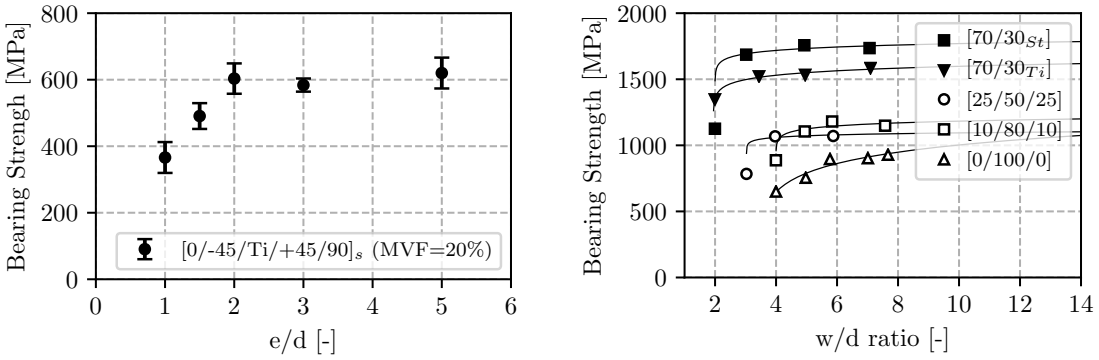

(a) Varying edge distances **(b)** Varying specimen widths

Figure 3.8 Influence of joint geometry on bearing strength: (a) bolt bearing according to ASTM D5961 in [9], (b) bolt bearing according to AITM 1-0009 in [10]

In Figure 3.9 simultanoous variation of both e/d and w/d ratios allow for a comprehensive view on the effects of specimen geometry on both bearing strength and failure type. The results indicate that for both steel and titanium reinforced laminates e/d and w/d values greater 3 lead to the favorable failure type of bearing failure which also exhibits the highest strengths. Reducing either the e/d or w/d ratio from the minimum recommended values not only leads to a change in failure type but also reduces the joint strength. Therein, small specimen widths result in net-section failure while small edge distances lead to shear failure. If both e/d and w/d are chosen too small then cleavage failure mode combining both shear and net-section failure is likely.

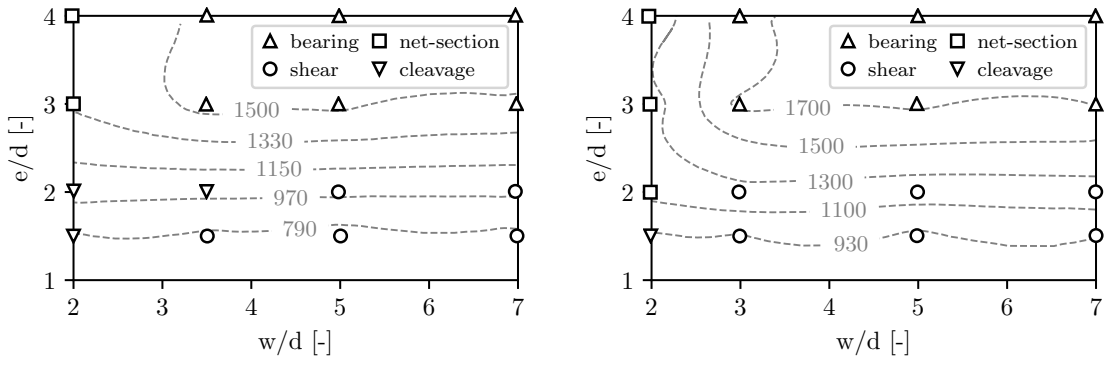

(a) Titanium hybridized laminates [70/30$_{Ti}$] **(b)** Steel hybridized laminates [70/30$_{St}$]

Figure 3.9 Influence of edge distance and specimen width on the failure type of UD-CFRP FMLs with MVF=30%; raw data [10]

Influence of Laminate Stacking and Metal Sheet Thickness

As discussed earlier in this chapter, the bearing strength of monolithic composites is very sensitive to changes in fiber orientation. By introducing metal into the laminate one would expect the bearing strength of hybridized laminates to exhibit less sensitivty to changes in fiber orientation. Fink [10] investigates a range of fiber patterns for different MVF in CFRP-Ti laminates. Therein, one result is that the upper and lower limit of bearing strengths for a certain MVF are defined by purely UD-0° and UD-90° based FMLs, respectively. As long as the metal content remains unchanged, alteration of the composite layer orientation results in bearing strengths within this range as can be seen in Figure 3.10. This behavior marks a contrast to monolithic composites where increasing the fraction of ±45° layers generally improves the bearing behavior of orthotropic laminates and relatively large deviations result from changes in the fiber orientations. The insensitivity to fiber pattern displayed by hybridized laminates is yet another advantage and offers flexibility during the design procedure especially for cases with varying loading angles.

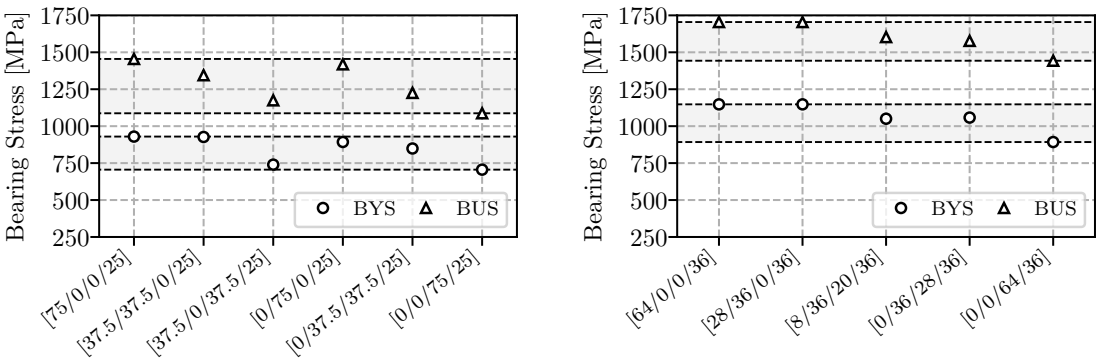

(a) MVF = 25% = const.

(b) MVF = 36% = const.

Figure 3.10 Bearing yield strength (BYS) and bearing ultimate strength (BUS) for varying fiber orientations at constant MVF in titanium reinforced composites; raw data [10]

Observations with respect to the influence of the metal sheet thickness on bearing strength indicates a favorable behavior when considering bearing yield strength. Similarly to the benefit of decreasing the number of grouped layers with identical orientation in monolithic composites, it is believed that refining the level of discretization at constant metal contents improves the material behavior. Due to the fact that damage accumulation in individual composite layers occurs more independently and that the number of interfaces at which delamination occurs increases, more energy is required in finely discretized hybrid laminates (see Figure 3.12c) to cause bearing yield failure than it is the case for coarsely discretized FMLs (see Figure 3.12d). When considering bearing ultimate strength, a coarse discretization is believed to be favorable. Since damage accumulation and delamination are well advanced near ultimate bearing failure, the metal layer stability mainly depending on its momentum of inertia is expected to have a beneficial influence [10].

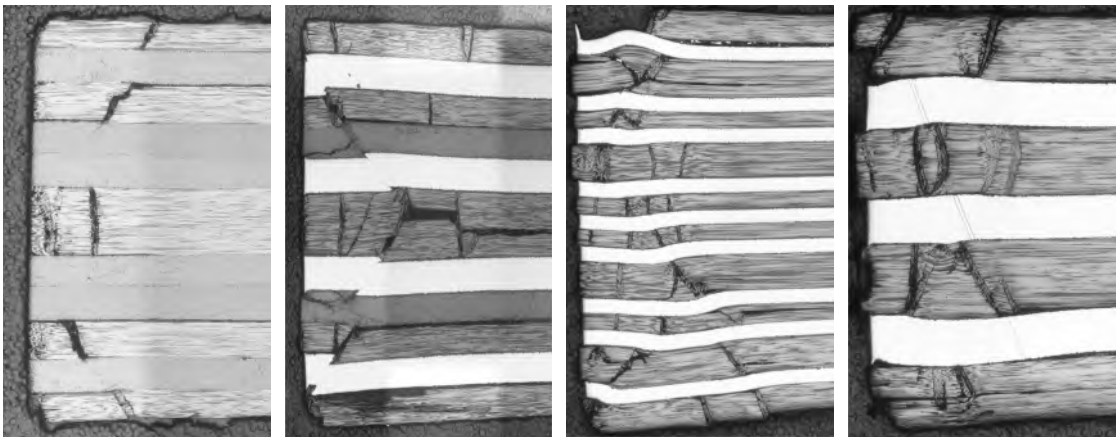

(a) [50/33/17], t_{CFRP}=0.25mm | **(b)** [50/0/17/33$_{Ti}$], t_{Ti}=0.25mm | **(c)** [70/0/0/30$_{St}$], t_{St}=0.1mm | **(d)** [70/0/0/30$_{St}$], t_{St}=0.3mm

Figure 3.11 Microsections of the bearing plane at bearing yield strength for a CFRP laminate and FMLs reinforced with steel (1.4310) and titanium (15-3-3-3) [10]

Influence of Hybridization on Damage Mechanisms

Introduction of a metallic component that exhibits isotropic and ductile material behavior as oppose to the orthotropic and brittle composite base material is expected to influence the failure mechanisms of a laminate during bearing loading. Figure 3.11 and Figure 3.12 show microsections of the bearing planes of a reference CFRP laminate and three hybridized laminates in bolt bearing configuration at bearing yield strength and bearing ultimate strength, respectively.

The microsection of a pure CFRP laminate in Figure 3.12a exhibits typical failure patterns for composite materials under bolt bearing loading that are reported repeatedly in literature [75–77]. Therein, kink-bands initiating in the 0° plies induce delamination and transverse matrix shear cracks in the neighboring layers under the washer area. Ultimate failure is a result of extensive damage accumulation under the washer and damage initiation outside the washer area through delamination, shear buckling, and transverse matrix shear cracks. All hybrid configurations have in common that damage initiation occurs by the formation of kink-bands that induces matrix shear cracks into the neighboring layers in case of composite layers and delamination in case of metal plies. Additionally, the metal plies undergo plastic deformation and a loss of stability due to bending. The titanium laminate in Figure 3.12b exhibits shear cracks in an angle of 45° triggered by damage in the adjacent 0° plies resulting in a wedge type failure. Fracture in the titanium layers is due to the low ductility as a result of the high degree of hardening. The steel layers of the CFRP-St FMLs are more ductile and thus do not suffer from shear fracture. Instead, the steel plies show pronounced plastic deformation. Despite considerable damage in both fiber and metal components under the washer area, both CFRP-St and CFRP-Ti laminates still are able to carry increasing bearing loads after reaching bearing yield strength. This is due to the lateral constraint offered by the washers which limits the loss of stability. Ultimate bearing failure occurs due to damage accumulation and extensive out-of-plane defor-

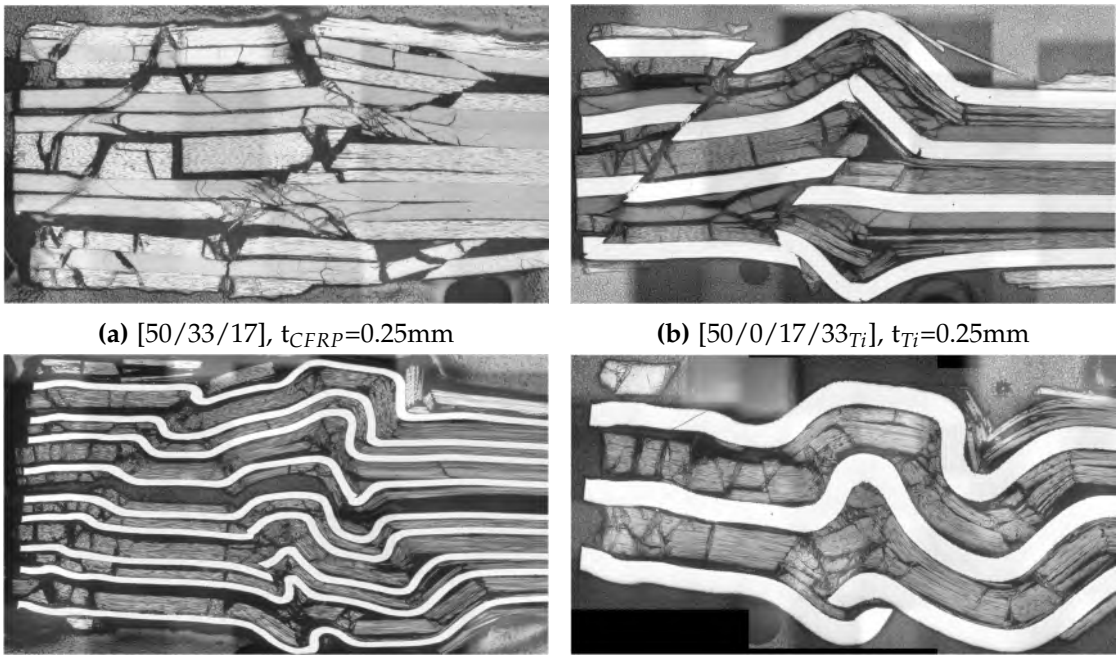

(a) [50/33/17], t_{CFRP}=0.25mm **(b)** [50/0/17/33$_{Ti}$], t_{Ti}=0.25mm

(c) [70/0/0/30$_{St}$], t_{St}=0.1mm **(d)** [70/0/0/30$_{St}$], t_{St}=0.3mm

Figure 3.12 Microsections of the bearing plane at bearing ultimate strength for a CFRP laminate and FMLs reinforced with steel (1.4310) and titanium (15-3-3-3) [10]

mations outside the washer area in all hybrid laminates. While the steel laminate with finely discretized metal plies in Figure 3.12c isolates damage in the composite plies and increases the bearing yield strength, the thick metal plies in Figure 3.12d offer out-of-plane stability as a result of their bending stiffness and lead to an increase in ultimate bearing strength [10]. Similar observations on the initiation and progression of damage are described by Hundley [9] and Yamada et al. [77].

To summarize, in addition to the relief of composite layers, introduction of the metal component leads to an isolation of composite damage, additional stability due to the out-of-plane stiffness of the metal layers and an increase in ultimate strength as a result of extensive plastic deformation of the metal prior to failure.

3.3 Bearing Behavior of Composite Joints at Low Temperature

At room temperature, numerous publications on mechanical joints are available. They cover a broad range of topics including design, damage and failure prediction, environmental effects, and fatigue just to name a few. In contrast, research on low temperature effects on the bearing behavior of mechanically fastened joints in composite structures is very limited. Publications related to low temperature effects in CFRP based-FMLs is hardly present at all. As explained in the beginning of the chapter, results for CFRP joints are studied in a effort to subsequently derive assumptions with respect to hybridized joints. In order to adapt to the lack of comprehensive data, the temperature range is extended to any condition below room temperature.

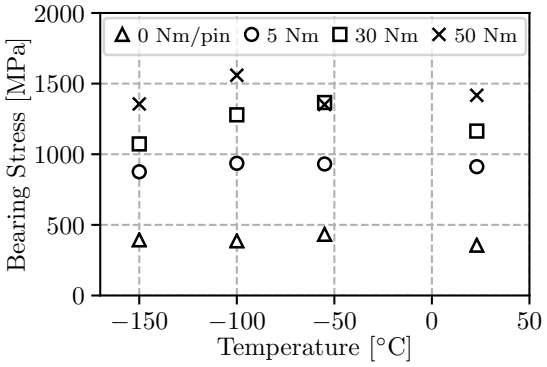

(a) Ultimate strength of bolted joints in QI configuration for different clamping torques [78]

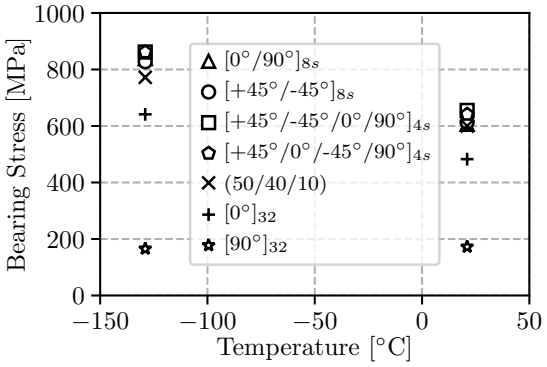

(b) Ultimate bearing strength of pinned joints with varying laminate layups [40]

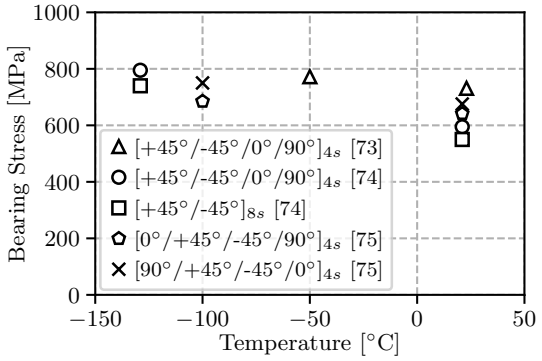

(c) Ultimate bearing strength of CFRP joints in pin bearing configuration

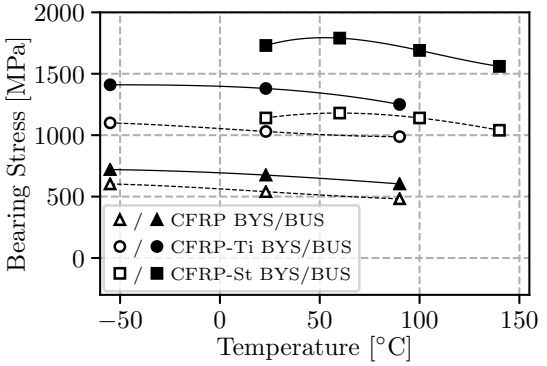

(d) Bearing yield strength (BYS) and ultimate strength (BUS) for bolted joints in FMLs [10]

Figure 3.13 Effect of temperature on the bearing behavior of pinned and bolted joints

Low temperature effects on the bearing behavior of a mechanically fastened CFRP joint were first reported in 1979 by Perry and Hyer [79] as part of the NASA program CASTS assessing composites for advanced space transportation systems at Langley Research Center. With the purpose to study the mechanical behavior of bolted joints at different temperatures, tests at temperatures including room temperature and low temperature (-157°C) were conducted for various e/d and w/d ratios. Therein, an increase of bearing ultimate strength of up to 10 % at low temperature with respect to room temperature was observed.

Scarponi et al. [78] investigated pin and bolt bearing loading for QI specimens made of 934/T300 for varying temperature levels (RT, -55°C, -100°C and -150°C) as well as varying clamping torques (0, 5, 30 and 50 Nm). As can be seen in Figure 3.13a, reducing the testing temperature down to -55°C leads to an increase in bearing strength for specimens with no or moderate clamping. Further decreasing the temperature, however, appears to be lowering the bearing strength of the specimens. Hence, no clear tendency is present. This might be partially due to very large t/d ratios during this test campaign resulting from rather thin specimens (1.15 mm)

combined with rather large hole diameters (9.8 mm) potentially evoking out-of-plane effects in the laminate.

An experimental investigation on the effects of temperature on the pin bearing strength of PETI-5/IM7 conducted by Walker [40] included various composite layups. The specimens were tested according to ASTM D5961M at room temperature and -129°C. In Figure 3.13b, all layups show a considerable increase in bearing strength by 30 % to 40 % compared to room temperature conditions except for the $[90]_{32}$ laminate that actually exhibits a slight decrease in bearing strength. Numerical analysis of the stress field in the vicinity of the hole revealed a considerable increase in thermal residual stresses. It was concluded that thermal residual stresses affect the extent to which the bearing strength changes with temperature, where they can only increase the strength degradation with decreasing temperature. Changes in fastener fit with decreasing temperature were found to have insignificant influence on the pin bearing strength.

Contrary to previous studies that applied the traditional double-lap shear configuration, Counts and Johnson [80] adapted the so-called compression test setup consisting of a specimen with a semi-ciruclar hole on one edge that is loaded by a pin, as proposed by Wang et al. [84]. Tests at -50°C on QI specimens made of PETI-5/IM7 revealed an increase in bearing strengh by about 5 % compared to RT. It was concluded that matrix embrittlement has a significant influence on the material behavior and that bearing strength exhibits a dependency on a critical delamination length and critical delamination density.

Goswami presented a comparison of experimental pin bearing test data with numerical simulation including progressive failure analysis [81]. Experimental data for a QI laminate $[+45°/\text{-}45°/0°/90°]_{4s}$ and an angle-ply laminate $[+45°/\text{-}45°]_{8s}$ were taken from Walker [40]. While the general tendencies observed by Walker could be reproduced, the accuracy of the numerical model was found to be poor which was attributed to the 2D modeling approach and rigid modeling of the pin.

Using the compression test setup, Hirano et al. [41] conducted a thorough investigation on the failure mechanisms in pinned joints for 3631/T800H at room temperature and -100°C. By microscopy of the bearing plane of QI specimens with varying stacking sequences at different loading levels, effects of both temperature and stacking seqence are studied in detail. Main findings include the previously observed increase in bearing strength, however, extended by detailed explanations regarding the initiation and progression of damage in the joint. Hirano et al. [82] applied the same approach to bolted joints of identical material and reported similar results for specimens with a clamping torque of 1.3 Nm at -100°C.

Santiuste et al. [83] conducted a computational analysis based of FEM in order to investigate the cross-effect of temperature and bolt torque on single-lap composite joints made of 3501-6/AS4 with a QI layup. Temperatures as low as -50°C were considered. Significant influence of the parameters on the stress distribution and failure were observed. Therein, torque values below those recommended by ASTM D5961

Table 3.2 Overview on investigations and results from literature on the effect of temperature on bearing stiffness, bearing yield strength (BYS), and bearing ultimate strength (BUS) in CFRP

Reference	Bearing setup	Materials	Geometry e/d; w/d; t/d	Temp.	Behavior compared to RT		
					stiffness	BYS	BUS
Perry and Hyer [79]	bolt bearing	CFRP*	3-4; 4-6; n.a.	-159°C	n.a.	n.a.	↗
Scarponi et al. [78]	pin & bolt bearing	934/T300	5; 5; 8	-150°C	↗	n.a.	↘
				-100°C	↗	n.a.	↗
				-55°C	↗	n.a.	⤫
Walker [40]	pin (ASTM D5961)	PETI-5/IM7	n.a.; 8; 0.7	-129°C	n.a.	(↗)	↗
Counts and Johnson [80]	pin (semi-circular hole)	PETI-5/IM7	4; 6; 1	-50°C	↗	-	↗
Goswami [81]	pin	PETI-5/IM7	6; 8; 0.7	-129°C	↗	-	↗
Hirano et al. [41]	pin (semi-circular hole)	3631/T800H	6; 17; 0.5	-100°C	→	-	↗
Hirano et al. [82]	bolt (semi-circular hole)	3631/T800H	6; 17; 0.5	-100°C	→	↗	↗
Santiuste et al. [83]	bolt (ASTM D5961)	3501-6/AS4	3; 6; n.a.	-50°C	↗	n.a.	↗
Fink [10]	bolt (AITM 1-0009)	Epoxy*/M40J	4; 7; n.a.	-55°C	n.a.	↗	↗
		CFRP + Ti 15-3-3-3	4; 7; n.a.	-55°C	n.a.	↗	↗

(↗) increase; (↘) decrease; (→) constant; (⤫) inconsistent; (-) pin bearing does not exhibit BYS; (n.a.) not available; (*) not specified

could already lead to damage. Furthermore, low temperature combined with low clamping torque was observed to reduce the bearing capacity.

The only results known to the author that deal with the effect of low temperature on the bearing strength of CFRP-based FMLs were presented by Fink [10]. He investigated pure CFRP laminates and CFRP-Ti FMLs with 33 % metal content at temperatures from 140°C down to -55°C in bolt bearing configuration according to AITM 1-0009. CFRP-St laminates with MVF=30 % were tested, too, however not below room temperature conditions. The pure CFRP laminate in Figure 3.13d behaves similarly to comparable laminates previously presented in literature. The CFRP-Ti laminate shows a very similar behavior compared to the pure composite specimens regarding both bearing yield and ultimate strength with decreasing temperature. Unfortunately, CFRP-St data is not available for conditions below room temperature. The evolution of bearing strength with decreasing temperature from high temperature conditions to room temperature, however, indicates an optimum in bearing strength for a temperature of 60°C. Fink contributed this behavior to the high magnitude of thermal residual stresses in the hybrid laminate. While poor mechanical properties of the matrix lower the load bearing capacity at high temperatures, thermal residual stresses lead to a decrease in bearing strength at low temperature conditions.

Table 3.2 summarizes the aforementioned investigations from literature and offers an overview on the methods as well as on the results of the respective studies. Therein, it can be seen that decreasing temperature appears to result in an increase of both joint stiffness and strength for the vast majority of investigations. It should be noted that when investigating the effects of low temperature on mechanically fastened joints both the pin and bolt bearing approach are applied equally. In general, however, the pinned joint configuration makes up for only about 10 % of the investigations on mechanically fastened joints in composites [42]. The load bearing and failure behavior of bolted and pinned joints are quite different, which is why in the following the effects of low temperature will be discussed seperately for each configuration.

Effect of Low Temperature on Bearing Behavior

The overview on literature results suggests that joint stiffness, bearing yield strength as well as bearing ultimate strength all increase with decreasing temperature. In order to study the effects of low temperature on the bearing response in detail, load-displacement curves from Hirano et al. [41, 82] for pinned and bolted joints at room temperature and low temperature are considered in Figure 3.14.

The load-displacement curve of a pinned joint in Figure 3.14a can be divided into four stages: The first stage depicts a gradual increase in the load bearing behavior due to an increase in contact area between pin and laminate. In the second stage, pin and laminate are in full contact and the load carried by the laminate increases almost linearly, followed by the third stage with a non-linear behavior. After the sudden load drop, the fourth and final stage is marked by a rather constand load [42]. These stages define the curves at both temperature levels. Compared to room temperature, however, the low temperature bearing experiment exhibits an increase in ultimate load of

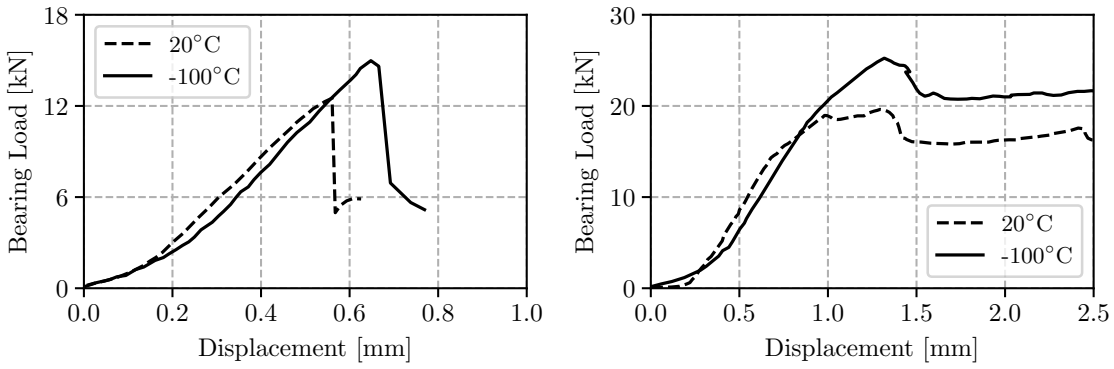

(a) Pin bearing configuration

(b) Bolt bearing configuration

Figure 3.14 Load-displacement curves for QI specimens loaded by (a) a pin and (b) a bolt with 1.3 Nm torque at room and low temperature conditions; raw data [41, 82]

about 20 %. Contrary to observations in literature [78, 81, 83], a decrease in testing temperature does not lead to an increase in joint stiffness as the slopes of the linear stage in Figure 3.14a are very similar. Eventhough not common, this observation is not entirely surprsing for a QI laminate since Sanchez-Saez et al. [85] and Walker [46] have both observed an increase in tensile and compressive strength with only moderate changes in the respective stiffness at low temperatures.

Figure 3.14b shows the typical load-displacement curve of a bolted joint for conditions at room and low temperature. The load-displacement curves can be divided into five stages, the first two being similar to the pin bearing case with a gradual load uptake in stage one and a linear behavior in stage two. While the third stage in the pin bearing case is defined by a rather small nonlinear region before ultimate failure, the bolt bearing case exhibits a knee point with a subsequent almost linear increase of load, however, with a smaller slope than in stage two. The fourth stage is marked by the load drop from the maximum bearing load defining the joints ultimate bearing strength followed by a rather constant curve shape in stage five. The qualitative behavior of the load-displacement curves is the same for room and low temperature. However, the load drop at maximum bearing load is more sudden than for the room temperature test, hence, indicating an increase in brittleness due to the decrease in temperature. Direct comparison of the curves shows an increase of load carried at the knee point by about 30 % and an increase of the maximum load carried by the joint by about 25 %.

In conclusion, reducing temperature has similar effects on both pinned and bolted composite joints. There is a significant increase in bearing ultimate strength for the pinned joint and in both bearing yield and ultimate strength for the bolted joint. The sharper load drop and less plastic deformation at high load levels after bearing ultimate strength for the bolted joint indicates that failure at low temperature is more brittle than at room temperature conditions. These observations with respect to changes in bearing strength are in line with findings in literature for CFRP laminates in both quality and quantity [10, 40, 78–80].

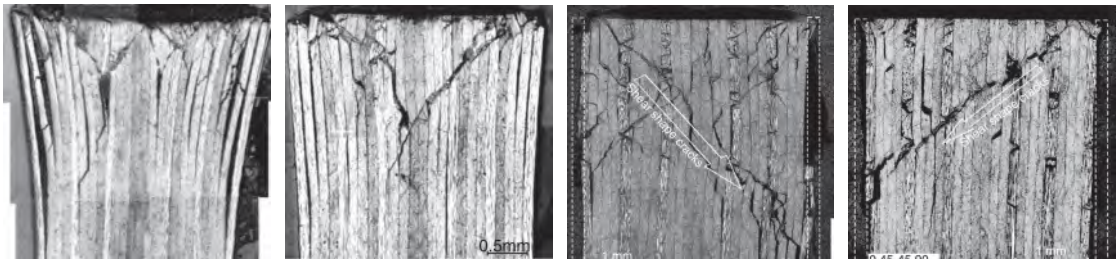

(a) Pin bearing at -100°C **(b)** Pin bearing at 20°C **(c)** Bolt bearing at -100°C **(d)** Bolt bearing at 20°C

Figure 3.15 Microsections of the bearing plane at bearing ultimate strength for a quasi-isotropic CFRP (3631/T800H) compression specimen with a semi-circular hole at 20°C and -100°C [42]

Effect of Low Temperature on Damage Mechanisms

The effects of low temperature on the damage behavior of a QI laminate are presented at the example of Figure 3.15 for both the pin and bolt bearing case from [42] where damage evolution was investigated by examining micrographs of the bearing plane for different loading levels.

Figure 3.15a and Figure 3.15b show microsections of pin bearing specimens at 20°C and -100°C. Observation of damage evolution reveals that at room temperature first damage occurs before reaching the maximum load in the form of delamination at the outermost interfaces. Ultimate failure is associated with damage accumulation due to kinking of the center 0° layers that evoke shear cracks in adjacent $\pm 45°$ and 90° plies as previously described by Fink [10]. Failure at low temperature develops similary, however, kinks and shear shape cracks are much thinner and multiple wedge type failure is observed. In addition, delamination is much more severe compared to the room temperature case. The authors conclude that the critical loads for delamination and kinking increase as the temperature decreases as in the case of compressive strength which is proportional to the matrix shear modulus [42, 86]. Yield stress and ductility of the matrix are influenced by temperature, too. At low temperature the matrix becomes stiff and sharp cracks as well as long delaminations occur. It should be noted that the interlaminar properties of CFRP are reported to increase with decreasing temperature [43,87]. Therefore, additional interlaminar effects must be present to decrease delamination resistance compared to room temperature.

The main difference between the pinned joint and the bolted joint in Figure 3.15c and Figure 3.15d is the presence of lateral constraint. As a result, much of the delaminations observed in the pinned joints are suppressed in case of the bolted joints. The change in the slope of the load-displacement curve around the knee point in Figure 3.14b is attributed to the formation and accumulation of kinks in the 0° layers of the laminate. The lateral constraint hinders the laminate from bursting out and thus allows for an additional increase of bearing load past the yielding point as previously reported by Fink [10]. Ultimate failure is associated with the formation of a through-the-thickness shear crack extending over the entire laminate that eventually leads to

the load drop at bearing ultimate strength. The effect of temperature results in an increase of bearing yield strength and bearing ultimate strength. Macroscopic and microscopic damage is almost the same for both room and low temperature. However, the authors derive that at low temperature material behavior is brittle and the stress level is high. Localized damage occurs easily at high load levels much before damage accumulation leads to ultimate failure. That is why the damaged areas are wider and damage is sharp.

To summarize, the change in material behavior with decreasing temperature significantly influences the damage mechnanisms in the CFRP joint. The matrix becomes brittle and the compressive strength of the laminate increases. As a result, the load bearing capacity of the joint increases with decreasing temperature. Distinct differences with respect to the failure mechanisms are present in the case of pin bearing where severe delamination can be observed despite delamination resistance to be reported to increase with decreasing temperature.

3.4 Strategy for Investigating the Effect of Low Temperature on the Bearing Behavior of Hybridized Composite Joints

The previous sections provide an insight on the general behavior of mechanically fastened joints, on the characteristics of local metal hybridization, and on the effects of low temperature on the bearing behavior of fastener joints in composite sructures. As explained, these fields were investigated seperately since no comprehensive research combining local metal hybridization and low temperature effects is presented in literature. With the basic understanding of these three fields, the present section aims to combine the main findings on the characteristics of local metal hybridization and low temperature effects on composite joints. This way, critical aspects can be identified and a strategy for investigating the effect of low temperature on the bearing behavior of locally hybridized joints is derived.

Summary of the Isolated Effects of Hybridization and Low Temperature

The main advantage of local metal hybridization is the increase in bearing capacity of composites by relieving composite plies and alleviating stress peaks due to isotropic material properties of metal. The stress relief is most efficient for high stiffness and high strength metals. With respect to damage mechanisms it could be observed that metal plies hinder damage propagation between composite plies, offer stability in thickness direction, and increase the ultimate bearing strength through substantial plastic deformation. At the same time, hybrid laminates exhibit significant delamination at the metal//CFRP ply interface possibly as a result of decreased interfacial properties compared to CFRP//CFRP ply interfaces.

The main aspects that are evoked by low temperature in composite joints are an increase in joint stiffness, bearing yield strength, and bearing ultimate strength. This is primarily due to the temperature dependency of the matrix that becomes stiffer, stronger and more brittle with decreasing temperature. The changes in the matrix

dominated properties of the composite material also influence the damage mechanisms that appear to be more brittle and sharp, and accompanied by substantial delamination especially in case of pin bearing joints.

Local Metal Hybridization at Low Temperature

In Chapter 1, the reasoning behind investigating hybrid laminates composed of CFRP as composite and steel as metal component is explained in detail. Simply put, the presence of a large difference in CTE of the constituents in combination with large stiffnesses of the respective materials result in significant thermal residual stresses. In Chapter 2, it was shown based on the bilinear approach that the yield strength of an unnotched CFRP-St laminate with 20 % steel content at -55°C decreases compared to room temperature conditions despite the individual strengths of the constituents increasing in the same temperature interval. This observation can be attributed solely to the substantial level of thermal residual stresses in the laminate. In contrast, a CFRP-Ti laminate exhibits an increase in yield strength with decreasing temperature as can be expected due to improving proterties of the individual constituents with decreasing temperature. Compared to the CFRP-St FML, the magnitude of thermal residual stresses in a CFRP-Ti FML is lower by a factor of 3. When considering mechanically fastened joints in either pin or bolt bearing configuration, it is appropriate to assume that thermal residual stresses influence the bearing behavior, notably the yield point of a given joint which displays the critical quantity when designing a joint. Therein, locally metal hybridized joints are expected to be affected by thermal residual stresses in two ways: Firstly, intralaminar residual stresses represent an intrinsic loading and thus can reduce the exploitable material strength. Since both thermal residual stresses and, in particular, matrix dominated material strength properties increase on ply level, the question is how the joint behavior is affected by these phenomena on laminate level. Secondly, interlaminar residual stresses increasing with decreasing temperature can negatively affect the delamination resistance of hybrid laminates that are prone to interlaminar failure as is. This reasoning defines the research hypothesis of the thesis:

> *The benefits of local metal hybridization of highly loaded mechanically fastened joints in composite structures proven at room temperature extend to low temperature despite increasing thermal residual stresses in the FML and engineering tools are capable to capture this behavior for the purpose of joint design.*

In order to study the effects of low temperature and provide design tools for hybrid joints, following four-part approach, each part associated with a working hypothesis, is chosen to answer the research hypothesis. The main idea is that temperature affects the material behavior and thus must be included in both analysis and design of FMLs.

Part I is covered in chapter 4 and mainly addresses working hypothesis I:

> *Altering interlaminar properties of a hybridized laminate at low temperature do not lead to a decrease in delamination strength of the FML.*

On mesoscale, the hybrid laminate can be divided into three entities consisting of the UD CFRP ply, the metal ply and the interfaces between single plies. The intralaminar properties of the single plies as well as the interlaminar properties of the interfaces

define the mechanical behavior of the laminate. In order to understand the material behavior on macroscale, e.g. under bearing loading, knowledge on the material behavior of the constituents is required first. While the intralaminar properties of CFRP and steel as well as the interlaminar properties of pure CFRP composites including the effects of low temperature has been addressed in academia, there is no substantial investigations offered in literature that cover the effect of low temperature on the interlaminar properties of CFRP-St laminates. In an effort to close this gap, experimental investigation of interlaminar properties in a CFRP-St laminate at low temperature is conducted by applying the fracture mechanics approach using the Double-Cantilever-Beam and End-Notched-Flexure setups. Investigation of the interlaminar properties of CFRP//CFRP and CFRP//metal interfaces paired with characterization of the intralaminar properties of the constituents allows for a first qualitative assessment of the failure behavior of locally hybridized joints. At the same time the material properties serve as input for the numerical and analytical models of this work.

Part II is covered in chapter 5 and mainly addresses working hypothesis II:

> *Despite increasing thermal residual stresses, metal hybridized laminates exhibit an absolute bearing strength at low temperature superior to monolithic laminates.*

Investigation of the reinforcement effect by metal hybridization of composite joints at low temperature is primarily based on experimental testing. Therein, three main aspects are analyzed. Firstly, the reinforcement effect itself is examined with respect to bearing yield strength and bearing ultimate strength for laminates with different degrees of orthotropy. Comparison of results for a QI and a HO laminate to results of their respective hybridizations (QI-FML, HO-FML) allows for the effects of hybridization to be discussed with respect to low temperature for relevant laminate stackings. Secondly, minimal edge-to-diameter and width-to-diameter ratios are important quantities when designing mechanically fastened joints and hybridization offers a weigth saving potential by significantly decreasing those ratios. This is why the minimum geometry ratios are determined by experimental testing. Between QI and HO laminates, former is more prone to net-section failure while latter tends to fail in shear mode. Therefore, investigation on the minimum edge distance ratio is conducted for the highly orthotropic CFRP and hybrid laminate, while the minimum width-to-diameter ratio is determined for the quasi-isotropic CFRP and hybrid laminate. Thirdly, a thorough investigation of the reinforcement effect by metal hybridization requires consideration of the damage evolution behavior in a joint. The previously considered monolithic and hybrid laminates with quasi-isotropic and highly-orthotropic layups are studied at different loading levels prior to ultimate bearing strength. Ultrasound scanning is used to quantify the area affected by damage before creating microsections of the bearing plane. The observations on intra- and interlaminar damage mechanisms in both monolithic and hybrid laminates are then used as a basis for discussing the predominant damage mechanisms at low temperature.

Part III is covered in chapter 6 and mainly addresses working hypothesis III:

> *Consideration of both thermal residual stresses and temperature dependent material properties is necessary for accurate analytical modeling of FMLs at low temperature.*

When testing composite joints, the possibilities of capturing intra- and interlaminar effects are quite limited. Methods such as digital image correlation or acoustic emission during testing as well as ultrasound or microsection analysis after testing only allow for qualitative assumptions and conclusions in retrospect. This is in particular disadvantageous when considering bearing loading with its complex interactions with respect to both load distribution as well as damage initiation and progression. Numerical modeling of the experimentally tested joints, however, allows for investigation of the laminate on mesoscale so that intra- and interlaminar strains, stresses, and damage are accessible at any given point during loading. This level of resolution is deemed necessary in particular if effects of thermal residual stresses are to be studied. The modeling approach requires incorporation of temperature effects. According to working hypothesis III, material properties determined at operating temperature do not suffice to numerically model the material behavior. Moreover, the entire manufacturing process needs to be considered in order to correctly incorporate thermal effects, e.g. thermal residual stresses. It is important to isolate parasitic thermal effects during material characterization in order to appropriately model thermo-mechanical bearing behavior of hybridized composite joints. The numerical modeling approach is to be validated against experimental data with respect to both mechanical and thermal effects. With the help of the numerical model a thorough investigation of thermal residual stresses in the vicinity of the fastener hole can be conducted in an effort to evaluate the low temperature effect on the bearing behavior of a hybridized joint. The numerical approach represents a tool for detailed analysis. Furthermore, the capabilities of the numerical model to be used as a tool within the scope of virtual testing are studied. Experimental determination of mininum possible edge distances, for instance, is very time consuming and costly, and hence represents a possible application.

Part IV is covered in chapter 7 and mainly addresses working hypothesis IV:

> *Consideration of both thermal residual stresses and temperature dependent material properties is necessary for accurate analytical modeling of FMLs at low temperature.*

While the part I-III deal with the experimental investiation of the reinforcement effect and the requirements for a numerical model to simulate the bearing beavior at low temperature, the present part builds upon those findings in a effort to develop a purely analytical design methodology that can be used as a tool for preliminary design of hybridized joints. A main requirement that is not provided by comparable tools is the incorporation of thermal residual stresses into the design process. The experimental results as well as the numerical bearing models are used in order to choose an appropriate analytical modeling approach incorporating the calculation of load distribution, stress distribution by fastener and bypass loads, incorporation of thermal residual stresses, and finally strength analysis. Therein, the main policy to be followed is to minimize required input data and maximize the number of cases that the methodology can be applied to.

Chapter 4

Experimental Determination of Material Properties

4.1 Intralaminar Properties

In the previous chapters, the thermo-mechanical behavior of FMLs was studied using analytical approaches in order to build a general understanding on the nature, influencing factors, and effects of thermal residual stresses. Furthermore, an insight on the effects of local metal hybridization as well as thermo-mechanical loading of composite joints at low temperature was given based on experimental test results in academia. The present chapter deals with the experimental determination of temperature dependent material properties of the constituents of an FML. As the hybrid laminate is divided into three entities consisting of the UD-CFRP ply, the metal ply as well as the interfaces between single plies, the present chapter addresses intra- and interlaminar properties seperately. While section 4.1 focuses on intralaminar properties of the CFRP and metal components, the interlaminar behavior is investigated in section 4.2. As material strength and stiffness govern the structural behavior, the intralaminar properties of the constituents determined in this section allow for an initial estimate on the material behavior on macroscale, i.e. bearing behavior. At the same time, the data serves as input for the numerical and analytical models introduced in the following chapters.

4.1.1 Literature Review

A number of test campaings have been conducted investigating mechanical properties of CFRP and metals at different temperature levels. A brief review of comprehensive experimental data sets[1] is given in Table 4.1, while focusing on the temperature level between room temperature and -55°C and materials similar to M21/T700GC and steel 1.4310, respectively, as they are being investigated in the following. Differentiating between fiber dominated properties (i.e. longitudinal tensile and compressive stiffness and strength) and matrix dominated properties (i.e. transverse tensile and compressive as well as shear stiffness and strength) allows for an initial classification of the material behavior. Therein, fiber dominated properties appear not to change

[1] data sheets of commercial material systems based on epoxy resin and standard/intermediate modulus carbon fibers (PAN) are considered: 2510/T700, E765/T700, NC321/NAS-S, PL350/TR50S, PL360/34-700, 8552/AS4, 8552/IM7, F593/T300

Table 4.1 Tendency of properties of standard/intermediate modulus carbon fiber in epoxy resin UD CFRP with decreasing temperature

Stiffness	RT → LT	Strength	RT → LT
E_{11}^t	⟶	X_T, R_1^t	⟶
E_{11}^c	⟶	X_C, R_1^c	⟶
E_{22}^t	↗	Y_T, R_2^t	↗
E_{22}^c	↗	Y_C, R_2^c	↗
G_{12}	↗	S, R_{12}	↗

with decreasing temperature, while matrix dominated properties show a clear tendency to increase with decreasing temperature. This behavior is commonly observed and described in several publications that offer an in-depth review on material properties [40, 63, 88]. Therein, the increase in stiffness and strength is mainly attributed to the changes in material properties of the resin with decreasing temperature, since the properties of carbon fibers show little to no dependency on temperature in the given interval. Furthermore, the increase in strength is accompanied by a decrease in failure strain, which is again more noticable regarding matrix dominated properties. Results for cold formed stainless steel indicate that decreasing temperatures lead to an increase in material yield and ultimate strength, a decrease in failure strain and a slight increase in material stiffness. In addition, it should be mentioned that a slight but distinct difference in both stiffness and strength is present regarding longitudinal and transverse properties in thin metal foils as a result of the cold forming process. Compared to the transverse direction, the longitudinal elastic modulus is smaller, while the strengh in longitudinal direction is slightly larger [11, 38, 64].

4.1.2 Experimental Procedure

As indicated in Section 2.2.3, temperature dependent material properties are deemed necessary in order to appropriatly model the material behavior of FMLs at different temperature levels and to incorporate the effect of thermal residual stresses. Thus, CFRP and metal properties at temperature levels of 23°C and -55°C are determined experimentally. Stiffness and strength as well as CTE are determined using the standards in Table 4.2. Tensile properties of the CFRP material are determined according to DIN EN 2561 and DIN EN 2597 mainly due to the larger interval considered for the calculation of moduli, which is considered more accurate for applications that include loading of the material until failure. In order to assure appropriate load introduction into the specimens, compressive testing is conducted in a hydraulic composite compression fixture (HCCF) setup according to DIN EN ISO 14126 allowing for simultaneous end- and shear-loading of the compression specimens. The longitudinal compressive strength of a UD-laminate is determined using tapered specimens. Tapering is found to alleviate the stress concentration in the gauge region and therefore results in more accurate strength prediction [89]. Due to the lower overall load levels with respect to transverse compressive properties, these specimens do not require tapering for improving the result quality. The in-plane shear properties are determined according to DIN EN ISO 14129. The choice of standards is based on a study

Table 4.2 Choice of standards for characterizing the in-plane properties of CFRP

Property	Test setup	Standard	Details in
$E_{11}^t, R_1^t, \nu_{12}$	Tensile test	DIN EN 2561	Table A.1
E_{22}^t, R_2^t	Tensile test	DIN EN 2597	
E_{11}^c, E_{22}^c, R_2^c	HCCF setup	DIN EN ISO 14126	Table A.2
R_1^c	HCCF setup & tapered specimens	DIN EN ISO 14126	
G_{12}, R_{12}	$\pm 45^\circ$ tensile test	DIN EN ISO 14129	Table A.3
CTE1, CTE2	Thermomechanical Analysis (TMA)	ISO 11359	-

on current standards for determining material properties of composites. An overview on methods for composite material characterization including a discussion on the advantages and shortcomings of the methods is presented in Appendix A. Mechanical properties of the steel foil are determined on the basis of DIN 50125 for tensile testing of thin sheet metals.

The specimens are fabricated using UD CFRP prepreg by Hexcel, namely HexPly M21/34%/UD/134gsm/T700GC, with a nominal cured ply thickness of 0.131 mm. During the course of time, identical prepreg with a nominal ply thickness of 0.26 mm was also applied. The use of the respective prepreg materials will be indicated wherever relevant. As the ply thicknesses considered here only significantly affect the shear properties determined according to DIN EN ISO 14129, the shear properties are tested for both materials, while the remaining in-plane properties are considered interchangable[2]. A total of seven plates are manufactured by hand layup, vacuum sealed, and cured in an autoclave following the manufacturer's recommended curing cycle. Cross-ply GFRP plates of 1 mm in thickness are glued onto the ends of the plates for smooth load introduction into the specimens during testing. The specimens are cut out of the plates using a diamond saw and measured with a micrometer gauge.

Testing is conducted inside a temperature chamber in a servo-hydraulic testing machine by Zwick (Zwick 1484) equipped with either a 20 kN or a 200 kN load cell depending on the load levels at hand. The air-conditioned laboratory facility provides constant contitions at $23 \pm 2°C$ and $50 \pm 10\%$ relative humidity for testing at room temperature. Cooling inside the temperature chamber for low temperature testing is done by evaporation of liquid nitrogen. In addition to the temperature sensor of the chamber, two additional resistance temperature detectors (Pt100) are inserted into the chamber in order to continuously monitor the condition on the front and back of the specimens, see Figure 4.1. Prior to testing, each specimen is kept inside the chamber for a total of 15 minutes in order to assure the specimens meet the temperature requirements. The holding time was determined in preliminary tests.

[2]The manufacturer's datasheet as well as internal tests for verification purposes show that the longitudinal tensile strength values of 0.13 mm and 0.26 mm thick UD-material differ within the range of standard deviation during testing

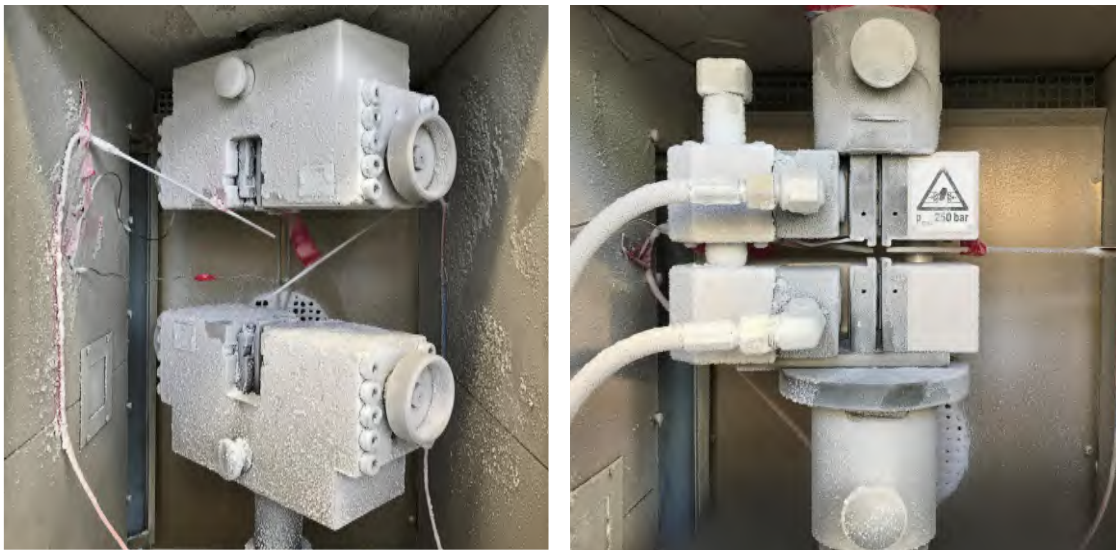

(a) Tension test setup **(b)** Compression test setup (HCCF)

Figure 4.1 Fixtures for tensile and compressive testing in the thermal chamber after low temperature testing at -55°C

4.1.3 Results and Discussion

The results of the experimental testing campaign to determine the material stiffness and strength properties as well as thermal contraction behavior of M21/T700GC and steel 1.4310 are presented hereafter. It should be noted that the room temperature mechanical properties of M21/T700GC are based on two seperate testing campaigns conducted on different material batches. While the first campaign was conducted between 2013-2016 and published by Petersen [38], the second campaign was conducted between 2019-2020 mainly for comparison purposes and therefore with a reduced sample size.

The in-plane elastic properties of M21/T700GC at 23°C (RT) and -55°C (LT) are summarized in Table 4.3. Data includes mean values, standard deviation, coefficient of variance, and sample size for in-plane elastic longitudinal, transverse, and shear properties. The respective stress-strain curves are presented in Appendix B. Agreement between batch 1 and batch 2 with respect to tensile and shear properties is good, indicating satisfactory repeatibility of both manufacturing and testing procedures as the values are within the standard deviation of the mean value for the most part. Considering compressive properties, agreement between the batches is less pronounced likely due to the high sensitivity of the compression test setup to the specimen geometry and testing procedure. Errors of 3-4 %, however, still indicate acceptable repeatability. Regarding the effect of temperature on the in-plane elastic properties, it appears as though the increasing brittleness of the matrix leads to increasing scatter in the experimental results by comparison of both standard deviation and coefficient of variance. When comparing the properties at room temperature and low temperature, a distinction between fiber dominated and matrix dominated properties is sensible. In fiber direction, the decrease in temperature leads to a slight decrease in longitudinal

Table 4.3 In-plane elastic properties of M21/T700GC at 23°C (RT) and -55°C (LT) with 0.131 mm cured ply thickness

			RT			LT
			Batch 1	Batch 2	Mean	Batch 2
E_{11}^t	Mean	MPa	125489	122296	124121	122501
	Stddev.	MPa	2710	2993	2831	4324
	C.o.V.	%	2.16	2.45	2.28	3.53
	n	-	4	3	7	8
E_{11}^c	Mean	MPa	102800	106108	103401	102413
	Stddev.	MPa	360	343	357	2658
	C.o.V.	%	0.35	0.32	0.35	2.6
	n	-	9	2	11	8
E_{22}^t	Mean	MPa	8330	8593	8382	10039
	Stddev.	MPa	81	182	106	267
	C.o.V.	%	0.98	2.11	1.27	2.66
	n	-	6	2	8	6
E_{22}^c	Mean	MPa	8260	8595	8316	10009
	Stddev.	MPa	152	31	132	176
	C.o.V.	%	1.84	0.36	1.59	1.76
	n	-	10	2	12	9
ν_{12}	Mean	MPa	0.294	0.285	0.291	0.287
	Stddev.	MPa	0.012	0.008	0.011	0.032
	C.o.V.	%	4.19	2.97	3.67	11.29
	n	-	6	3	9	8
G_{12}	Mean	MPa	4355	4306	4341	5746
	Stddev.	MPa	87	127	98	218
	C.o.V.	%	2.01	2.94	2.27	3.78
	n	-	5	2	7	6

tensile and compressive stiffness by 1.3 % and 0.9 %, respectively. As these deviations are considerably smaller than the scatter in the experimental data, it can be concluded that the temperature decrease does not influence the stiffness in longitudinal direction of a UD-ply. This behavior is in accordance with the result of the literature study at the beginning of the present chapter. Observation of matrix dominated properties reveals a strong dependency of the material stiffness on temperature effects. Therein, the temperature decrease leads to an increase of transverse and shear moduli by 20 % and 32 %, respectively. The observation with respect to matrix dominated properties is also in accordance with the findings presented in Table 4.1.

The in-plane strength properties of M21/T700GC are summarized in Table 4.4. In-plane longitudinal, transverse, and shear strengths are presented for room temperature and low temperature levels. Detailed stress-strain curves can be found in Appendix B. Similarly to the observations with respect to the behavior of longitudinal

Table 4.4 In-plane strengh properties of M21/T700GC at 23°C (RT) and -55°C (LT) with 0.131 mm cured ply thickness

			RT			LT
			Batch 1	Batch 2	Mean	Batch 2
R_1^t	Mean	MPa	2232	2200	2214	2230
	Stddev.	MPa	116	135	127	66
	C.o.V.	%	5.19	6.12	5.72	3.27
	n	-	4	5	9	8
R_1^c	Mean	MPa	1537	1442	1521	1593
	Stddev.	MPa	77	177	94	100
	C.o.V.	%	5.03	12.31	6.16	6.26
	n	-	10	2	12	9
R_2^t	Mean	MPa	(71)	86	86	93
	Stddev.	MPa	(3)	1	1	5
	C.o.V.	%	(4.75)	1.31	1.31	5.12
	n	-	(6)	5	5	6
R_2^c	Mean	MPa	202	213	207	344
	Stddev.	MPa	10	1	9	10
	C.o.V.	%	3.06	0.45	4.11	2.83
	n	-	10	2	12	9
R_{12}	Mean	MPa	78	75	77	114
	Stddev.	MPa	3	0.47	2	2
	C.o.V.	%	3.85	0.63	2.80	1.95
	n	-	4	2	6	6

material stiffness, material strength in fiber direction can be considered not to change with decreasing temperature as differences in the strength values on the two temperature levels are smaller than the respective scatter in the experiments. With respect to matrix dominated properties, transverse compressive and shear strength increase at low temperature conditions. Compared to the room temperature values the changes correspond to an increase of 66 % and 48 %, respectively. This increase in strength is based on the improved properties of the matrix at low temperatures and agrees well with the findings in Table 4.1. Considering the shear strength it should be mentioned that the values for batch 1 are based on the Iosipescu setup according to ASTM D5379 while batch 2 data is based on the $\pm 45°$ tensile setup in accordance with DIN EN ISO 14129. Both standards define the shear strength at 5 % shear strain. The results agree well and demonstrate the capabilities of the two test setups for determination of material shear strength. During testing of the transverse tensile properties E_{22}^t and R_2^t in batch 2, failure repeatedly occured either right at the edge or inside of the load introduction tabs resulting in invalid failure types. Thus, additional specimens without tabs were fabricated and tested. Failure in these specimens exhibit valid failure types as well as considerably higher strength values compared to the first batch. In addition to the stress concentration at the end of the tabs, possible causes include excessive

Table 4.5 In-plane shear properties of M21/T700GC at 23°C (RT) and -55°C (LT) with 0.262 mm cured ply thickness

			RT Batch 2	LT Batch 2
G_{12}	Mean	MPa	4644	5863
	Stddev.	MPa	43	174
	C.o.V.	%	0.93	2.98
	n	-	4	4
R_{12}	Mean	MPa	80	106
	Stddev.	MPa	0.5	0.2
	C.o.V.	%	0.67	0.22
	n	-	4	4

bending of the specimens during application of strain gauges and during application of the tabs. As a result, the transverse strength data at room temperature is based solely on batch 2 results. Testing at LT is done using specimens without load introduction tabs. Compared to the RT results, an increase in transverse tensile strength by around 8 % is observed. Due to the difficulties of testing in a thermal chamber and very small foil thickness, strain measurement for mechanical characterization of the steel foil in Table 4.6 is conducted with strain gauges which is considered to lead to slighly higher stiffness values. As the maximum strain of the strain gauges is limited, determination of stiffness and onset of plasticity ($R_{p0.2}$) is done with stress-strain data while calculation of ultimate strength values is based on force-displacement data, both of which are illustrated in Appendix B. As a result of the manufacturing process in which the steel foil is cold rolled, the material exhibits directional properties characterized by increased stiffness and earlier onset of plasticity in transverse direction at comparable ultimate strength. This behavior is previously reported for similar metal sheet material [11, 38]. The degradation of stiffness is attributed to the increase of plastic strain in the metal sheet due to the cold forming process. The physical mechanisms responsible for this behavior, however, are not fully understood. Explanatory approaches include microscopic deponding between matrix and inclusions leading to the formation of microcracks and voids in the material, which in turn tend to enlarge into cavities during cold rolling. Furthermore, the cause of stiffness degradation is associated with micro-plastic strain, changes in the dislocation arrangement, and phase transformations. Due to the kinetics of the rolling process, longitudinal properties are more affected by degradation than transverse properties of a metal sheet [90]. With respect to the qualitative behavior of the stress-strain curves it appears as though a bilinear material model in conjuction with the von Mises yield criterion is sufficent for proper modeling of the material behavior. The general stress-strain relations do not change significantly with decreasing temperature. However, the magnitude of stiffness as well as ultimate strength slightly alter at lower temperature levels, while the yield stress remains almost unchanged.

Table 4.8 shows the results of TMA analysis according to ISO 11359. In total, a temperature range between +150° to -150°C is analyzed. Determination of the effec-

Table 4.6 Stiffness and strength data for steel 1.4310 at 23°C (RT) and -55°C (LT) with a nominal sheet thickness of 0.13 mm

	RT			LT		
	Mean MPa	Stddev. MPa	C.o.V. %	Mean MPa	Stddev. MPa	C.o.V. %
E_{11}	189633	1356	0.72	184822	3674	1.99
E_{22}	197011	4076	2.07	206991	3264	1.58
$R_{p0.2,1}$	1496	6	0.46	1455	19	1.32
$R_{p0.2,2}$	1288	6	0.45	1296	42	3.25
$R_{m,1}$	1561	30	1.93	1752	9	0.53
$R_{m,2}$	1597	3	0.21	1783	15	0.86

Table 4.7 Stiffness and strength data for steel 1.4310 at 23°C (RT) and -55°C (LT) with a nominal sheet thickness 0.26 mm

	RT			LT		
	Mean MPa	Stddev. MPa	C.o.V. %	Mean MPa	Stddev. MPa	C.o.V. %
E_{11}	174894	1955	1.12	181376	1620	0.89
E_{22}	183237	2601	1.42	197780	6103	3.09
$R_{p0.2,1}$	1300	7	0.53	1215	16	1.33
$R_{p0.2,2}$	1112	51	4.56	1028	8	0.77
$R_{m,1}$	1401	14	1.00	1625	39	2.41
$R_{m,2}$	1332	10	0.77	1482	30	2.01

tive linear coefficients of thermal expansion is conducted for three temperature ranges relevant for the analysis including the stress-free temperature (132°C) of the material as the point of initiation of thermal residual stresses plus room and low temperature levels.

The failure envelopes in Figure 4.2 demonstrate how changes in material strength with decreasing temperature affect the failure characteristic of a UD ply. During bearing loading, the area in front of the bolt is subjected to a combination of global compressive and shear loads while the area at the smallest cross-section is loaded mainly in tension. Therefore, the present failure envelopes allow for an initial qualitative assessment of the effects of low temperature on the bearing behavior based on the intralaminar material properties. Effects of interlaminar properties will be addressed in the subsequent section. The failure envelopes are based on Cuntze's Failure Mode Concept[3]. Material properties for determination of the failure envelopes are taken from Table 4.4, while the mode interaction coefficient is taken from [91]. Both fracture planes in Figure 4.2 exhibit an outward shift for decreasing temperatures, indicating

[3]Details on the Cuntze Failure Mode Concept are provided in Chapter 7

Table 4.8 CTE of M21/T700GC and steel 1.4310 for temperature ranges between stress-free temperature (T_{sf}), room temperature (RT) and low temperature (LT)

				$T_{sf} \rightarrow$ RT	$T_{sf} \rightarrow$ LT	RT $\rightarrow$ LT
CTE1	M21/T700GC	Mean	$\frac{10^{-6}}{°C}$	-0.374	-0.194	0.079
		Stddev.	$\frac{10^{-6}}{°C}$	0.312	0.196	0.155
		C.o.V.	%	-83	-101	197
CTE2	M21/T700GC	Mean	$\frac{10^{-6}}{°C}$	38.478	29.655	34.494
		Stddev.	$\frac{10^{-6}}{°C}$	2.037	1.171	0.274
		C.o.V.	%	5.29	3.35	0.93
CTE1	1.4310	Mean	$\frac{10^{-6}}{°C}$	13.039	12.883	12.649
		Stddev.	$\frac{10^{-6}}{°C}$	0.281	0.093	0.277
		C.o.V.	%	2.15	0.72	2.19
CTE2	1.4310	Mean	$\frac{10^{-6}}{°C}$	14.295	13.832	13.085
		Stddev.	$\frac{10^{-6}}{°C}$	0.347	0.323	0.287
		C.o.V.	%	2.43	2.34	2.19

an increase in load bearing capacity. For a common laminate stacking comprised of 0°, ±45°, and 90° layers, the bearing capacity is expected to increase substantially. As the increase in load bearing capacity of the material is mainly driven by improved shear and transverse compressive strengths of a UD ply, the resulting increase in bearing strength is expected to decrease with increasing degree of orthotropy (e.g. a UD-0° laminate) and increase for laminates with little degree of orthotropy (e.g. a QI laminate). When considering the changes observed in metal properties at low temperatures, it is assumed that the beneficial effect of hybridization is more pronounced regarding bearing ultimate strength of a laminate as oppose to the bearing yield strength.

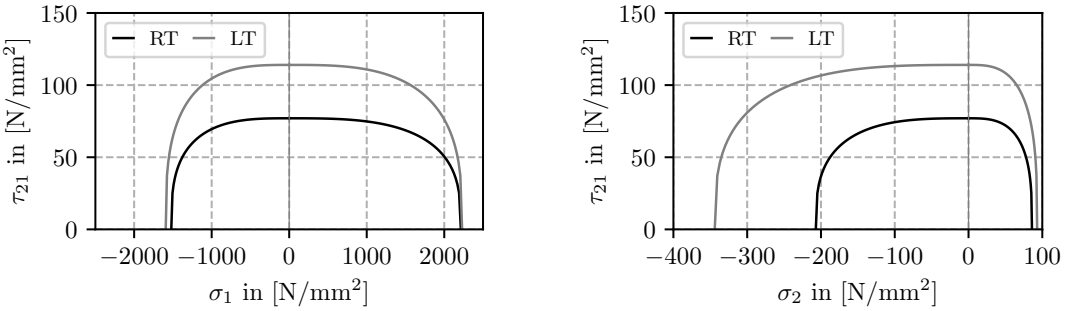

(a) Fracture plane $\tau_{21} - \sigma_1$

(b) Fracture plane $\tau_{21} - \sigma_2$

Figure 4.2 Failure envelopes for M21/T700GC in the planes $\tau_{21} - \sigma_1$ and $\tau_{21} - \sigma_2$ at 23°C (RT) and -55°C (LT) based on the Cuntze FMC

4.2 Interlaminar Properties

While intralaminar properties of CFRP and steel have been addressed in the previous section, the present section focuses on the interlaminar behavior in an FML. This topic is of particular interest as delamination represents one of the dominant failure types in FMLs. There are several aspects to this subject that will be discussed in detail including multi-material interfaces, multi-directional interfaces, thermal residual stresses, and the effect of temperature on interlaminar properties. While the first three aspects have been the subject of substantial research activities, there are only very few studies on the interlaminar behavior of CFRP-St FMLs at low temperature conditions. As oppose to other material combinations, e.g. GFRP-aluminum FMLs (GLARE), the mismatch in CTE combined with the high stiffness of both constituents leads to significant interlaminar thermal residual stresses that can in turn reduce the interlaminar strength of the composite.

In an effort to close the gap on the low temperature interlaminar behavior of CFRP-St FMLs, the present section offers an experimental investigation of the interlaminar properties in a CFRP-St laminate at low temperature, thereby addressing *Working Hypothesis I*. Both monolithic as well as hybrid interfaces, hereafter denoted CFRP//CFRP and CFRP//metal, are studied whilst focusing on aspects regarding multi-material interfaces, multi-directional interfaces, thermal residual stresses, and the effect of temperature. Similarly to the experimental characterization of intralaminar behavior, the experimental data collected on interlaminar properties is also used as input for the analytical and numerical models of this work. Results of the present section have been partly published in Koord et al. [92].

4.2.1 Literature Review

When investigating the interlaminar behavior of composites, there are two fundamentally different approaches based on which experimental test setups can be categorized. In the first approach, the tests solely allow for determination of a geometrical strength value for a given interface while the second category of test setups aims to determine a fracture toughness or an energy release rate (ERR) based on fracture mechanics [39].

The most prominent example of the former approach is the determination of apparent interlaminar shear strength (ILSS) by the short-beam method[4] in which a specimen is loaded in a 3-point bend setup. This method is commonly used as a comparative testing method for quality assurance. By adjusting the laminate layup, the method can be applied to FMLs [10]. However, due to the nature of the test setup and drawbacks, such as intralaminar damage actually initiating interlaminar failure [39], this method does not provide an independent and universal material property. Thus, while the ILSS setup is beneficial for comparative studies, it does not meet the requirements for the purpose of material characterization. The fracture mechanics approach, on the contrary, is an energy method that is based on the equilibrium of energy between the elastic energy introduced into a specimen and crack propagation at the interface. The

[4] e.g. standardized in DIN EN 2377, DIN EN 2563, DIN EN ISO 14130, and ASTM D2344

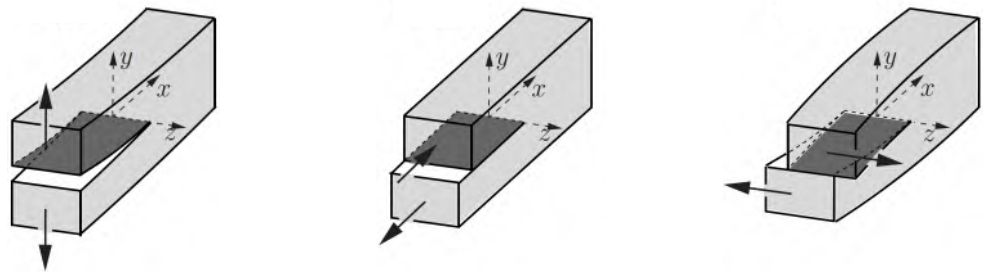

(a) Mode I (opening mode) **(b)** Mode II (shear mode) **(c)** Mode III (shear mode)

Figure 4.3 Delamination modes describing the interlaminar separation behavior [93]

energy release rate G is derived from this equilibrium as

$$G = \frac{\partial(W - U)}{\partial A} \tag{4.1}$$

where W represents the work through external forces, U the elastic energy stored in the system and A the crack surface. Once G exceeds a critical value G_c the cracked surface area increases, i.e. the crack front propagates along the interface. Hereby, interface properties are determined on meso-scale and an idealized fracture surface parallel to adjascent layers is assumed. On micro-scale, however, delamination phenomena are characterized by an interaction of resin failure and fiber-resin interface failure that propagate in direction of the smallest obstacle [38]. Thus, special care has to be taken when defining the test setup and the specimen configuration in order to assure interlaminar failure in the desired fracture plane. Depending on the specific test setup, isolation of different delamination modes, e.g. out-of-plane opening mode I or in-plane shear mode II (Figure 4.3), allow for the determination of differentiated interface properties. These properties can also be used for numerical modeling of delamination behavior, which is a great advantage of the fracture mechanics approach. Many test setups have been introduced for experimental interface characterization, of which the Double-Cantilever-Beam (DCB) and End-Notched-Flexure (ENF) setups are the most prevalent. These methods and experimental results are described in more detail in the subsequent sections. The remaining of the present section provides a literature review on aspects of multi-material interfaces, multi-directional interfaces, and the effect of temperature valuable to the discussion in the subsequent sections.

Multi-Material Interfaces

Contrary to the common specimen configuration for hybrid interface characterization, mostly within the scope of adhesive testing where the adherents themselves are made of different materials, multi-material interfaces in the present work are discussed with a focus on intrinsic FMLs without any adhesive layer. Studies by Petersen [38], Monden [39] and Both [11] deal with intrinsic CFRP-St and CFRP-Ti FMLs. The manufacturing processes are very similar combining some sort of abrasive metal pretreatment (e.g. vacuum grit blasting) followed by a chemical process (e.g. Sol-gel process) in order to activate the metal surface for improved adhesion to the CFRP matrix system within a standard prepreg manufacturing process. All testing was conducted at room temperature in DCB and ENF test setups. The results of the independent studies

are consistent in the sense that all predict a decrease in interlaminar fracture thoughness for hybrid interfaces compared to monolithic interfaces. In order to achieve decent interface toughness values, an appropriate metal pretreatment process is crucial. Monden [39] proposes alternatives to the standard pretreatment methods such as TiO_2 coating of the metal surface for improving the long-term hybrid interface behavior. Digital microscopy examination of the metal and composite surfaces after testing by Petersen [38] indicates a combination of adhesive and cohesive failure at the interface as the metal surface is partially covered with resin and fiber debris. Detailed investigation of the evolution of the energy release rate in mode I with increasing crack length conducted by Both [11] on hybrid interfaces (St//0°, Ti//0°) and the monolithic interface 0°//0° reveals that an R-curve effect is present when considering the hybrid interfaces, meaning that the energy release rate increases after crack initiation. The energy release rate of the monolithic interface, on the contrary, remains constant during the entire length of the experiment. The R-curve effect observed for the hybrid interfaces is related to fiber-bridging at the cracked interface and crack-jumping to adjacent interfaces resulting in multiple crack planes.

Multi-Directional Interfaces

Currently available standards for mode I and mode II testing, for instance in the DCB and ENF setups[5], are explicitly only valid for 0°//0° interfaces. However, most applications involve multi-directioal laminate layups and delamination is usually observed between layers of different orientations, which is why it is sensible to investigate multi-directional interfaces. Since testing of multi-directional and for that matter multi-material interfaces implies asymmetric layups with respect to the fracture plane, parasitic effects leading to flawed mode isloation should be taken into account. The effect of multi-directional interfaces in monolithic CFRP laminates is subject of several experimental and numerical studies. The results however are not consistent. Pereira et al. [94] and Chai [95] report that both mode I and mode II interlaminar properties are independant of the interface layer orientation, while Tao and Sun [96] and Bienas [97] report decreasing interlaminar toughness with increasing difference in ply-orientation. Results for FMLs with multi-directional interface layers are rare. Petersen [38] tested CFRP-St FMLs at room temperature with interfaces including St//0°, St//45° and St//90° in both DCB and ENF configuration. While the mode I energy release rate for the St//0° interface is inferior to the St//45° and St//90° interfaces, the mode II energy release rate of the St//0° interface is superior to the St//45° and St//90° interfaces. Similar observations are made by Bienias et al. [97] for GFRP aluminum and CFRP aluminum FMLs at room temperature in an ENF test setup. For both material combinations the interfaces composed of metal and 0° layers exhibit the highest mode II fracture toughness followed by metal//45° and metal//90° interfaces in descending order. Compared to the respective monolithic interfaces 0°//0°, 0°//45° and 0°//90° the general behavior with varying fiber orientation at the interface of hybrid laminates is quite similar in both studies. Apart from Petersen [38] who adjusts the specimen layup in order to reduce effects resulting from an asymmetric laminate stacking, neither of the studies on hybrid multi-directional interfaces offer a quantification of parasitic modes influencing the characterization of interface properties.

[5] as defined in ASTM D5528 or ASTM D7905

Low Temperature

Compared to the investigation of delamination effects arising from elevated temperatures, the number of studies on low temperature effects is limited. It is often assumed that matrix strength increases with decreasing temperature, thus, also interfacial fracture toughness must be increasing. However, conflicting evidence is present on the effect of low temperature on the interlaminar fracture toughness in composites. Asp [43] investigates monolithic CFRP specimens in DCB and ENF configuration at room temperature and -55°C. Despite testing asymmetric specimen layups, effects of parasitic mode interaction and thermal residual stresses on the energy release rate are not taken into account. Considering the apparant energy release rates in mode I, no noticeable effect is observed for lower temperatures. The energy release rate in mode II, however, increases significantly with decreasing temperature. Kim et al. [98] conduct DCB tests on symmetric CFRP specimens at various temperatures down to -100°C. Contrary to the results of Asp, low temperature appears to influence the energy release rate as experimentally determined G_{Ic} values increase with decreasing temperature. In addition, it is stated that there is no R-curve effect present for a $0°//0°$ interface neither at room temperature nor at low temperature conditions. Studies by Coronado et al. [99–101] on the influence of low temperature on the mode I fracture toughness considering multiple temperature levels down to -60°C indicate yet a different behaviour of monolithic CFRP interfaces. Both standard epoxy (3501-6) and toughened epoxy (8552) resins are tested with AS4 fibers. Although the specimens with toughened matrix exhibit higher absolute G_{Ic} values, the general tendency of all specimens tested is identical: the energy release rate in mode I decreases noticably with decreasing temperature.

Temperature dependent data for CFRP-steel FMLs, and for that matter for FMLs in general, with respect to static delamination strengh in terms of energy release rates is scarce, as in particular the investigation of GLARE was conducted in terms of fatigue crack growth vastly on the basis of center crack tension fatigue crack growth specimens. Within those studies the few that deal with low temperature effects indicate that lower temperatures reduce the crack growth rates in GLARE [1,102,103]. Investigation of the delamination shapes on center crack tension fatigue crack growth specimens furthermore reveals that delamination areas for low temperatures are significantly smaller than for room temperature, thus allowing for the assumption that delamination resistance increases with decreasing temperature. Burianek [22] conducts an experimental study on the face sheet delamination growth in CFRP-Ti composites including low temperature testing at -18°C. Analysis of the strain energy release rates shows that at low temperatures delamination occurs at higher energy release rates indicating an increase in delamination toughness for the hybrid surface. Similarly, Rans et al. [104] report decreasing delamination growth rates with decreasing temperature for GLARE as well as TiGr hybrid laminates at temperatures as low as -40°C.

4.2.2 Interlaminar Material Characterization

Investigation of the interlaminar behavior of hybrid interfaces is based on the DCB and ENF test setups for mode I and mode II characterization, respectively. These methods have been proven to be applicable to hybrid interfaces [11,38,39]. In addition to hy-

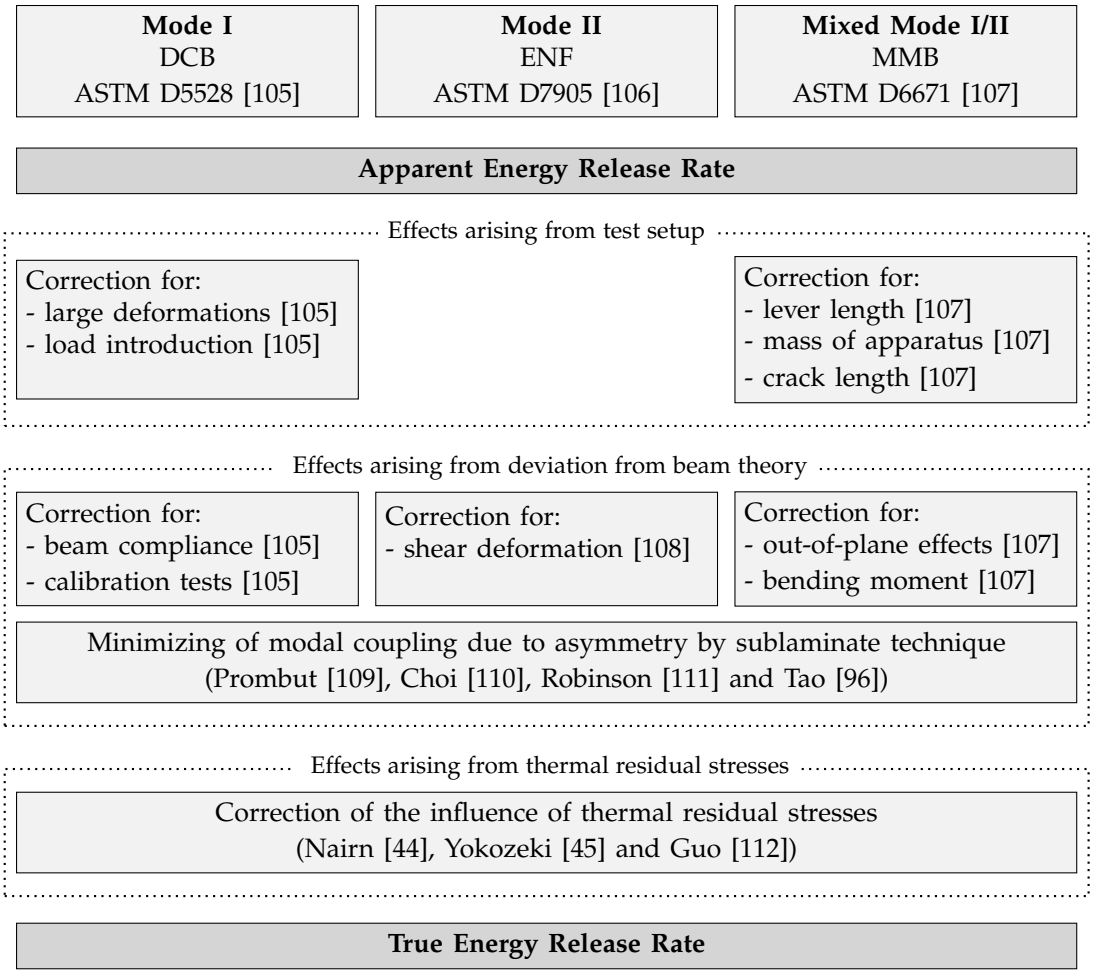

Figure 4.4 Overview on methodology for determination of the true energy release rate by correction of apparent energy release rates influenced by the test setup, deviations from the beam theory, and thermal residual stresses extended from Petersen [38]

brid interfaces, also monolithic CFRP interfaces are considered in order to allow for a comprehensive comparison of the effects of temperature on the interlaminar behavior of an FML. As determination of interface properties is sensitive to non-uniform behavior, the apparent energy release rate (aERR) resulting directly from the experiment is corrected for effects arising from the test setup, deviations from the beam theory, and thermal residual stresses, thus yielding the true energy release rate (tERR). Especially for hybrid interfaces neglecting said effects can lead to significant overestimation of the interface properties [39]. The methodology for determination of the true energy release rate is shown in Figure 4.4.

Starting with the apparent energy release rate, application of the correction methods for a given experimental test setup yields the true energy release rate. While measures like the sublaminate technique to minimize effects due to asymmetric layups are introduced during specimen manufacturing, correction for large deformations, load introduction and beam compliance are conducted during evaluation of the test results.

In turn, correcting effects arising from thermal residual stresses is usually done by applying correction terms on the energy release rate after evaluation of the test results. As the sources of deviations are manifold, the steps for determining the true energy release rate are introduced and discussed individually in the subsquent sections.

Double-Cantilever-Beam Test (Mode I)

The DCB test setup in ASTM D5528 [105] allows for determination of the mode I interlaminar fracture toughness G_{Ic} of unidirectional composites. By adjusting the laminate layup, the procedure can be applied for determining interfacial properties of hybrid interfaces [11,38,39]. As depicted in Figure 4.5a, the general setup is composed of a rectangular specimen containing a non-adhesive insert in the midplane defining the initial crack length a_0. By applying tensile forces on the hinges, the DCB specimen is opened resulting in a mode I delamination mode acting on the crack tip. Initially the specimen half-beams only deflect elastically without an increase in delamination length. Once the energy introduced at the crack tip exceeds a critical energy release rate G_{Ic} the initial crack propagates along the specimen midplane. Monitoring of synchronized load, opening displacement and crack length data allows for the determination of the critical energy release rate at initiation as well as its evolution with increasing crack length. The data reduction procedures presented in ASTM D5528 include the area method based on the beam theory (BT), modified beam theory (MBT), compliance calibration (CC) and modified compliance calibration (MCC) method. Apart from the area method, all data reduction methods include a correction for deviations from the beam theory due to shear and local deformation at the crack tip. Therein, the modified beam theory artificially increases the crack length $a + |\Delta|$, where the correction term $|\Delta|$ is determined based on a linear regression of the specimen compliance as a function of delamination length (Figure 4.6). The compliance calibration and modified compliance calibration methods introduce correction factors n and A_1, respectively, both drawn from a linear regression of delamination onset and propagation values of the specimen compliance over the crack length. The energy release rates in mode I with P as the opening load and δ as the tip opening displacement read:

$$G_I^{BT} = \frac{3P\delta}{2ba}, \quad G_I^{MBT} = \frac{3P\delta}{2b(a+|\Delta|)}, \quad G_I^{CC} = \frac{nP\delta}{2ba}, \quad G_I^{MCC} = \frac{3P^2(\delta/P)^{1/3}}{2A_1bt} \tag{4.2}$$

Due to the fact that the MBT approach yields rather conservative results, this procedure is recommended in ASTM D5528. For verfication of the experimental results, the analytical formulation of the force-displacement behavior using the corrected beam theory can be applied [113]. As the formulation is derived for a symmetric DCB specimen with identical half-beams, the application to multi-direcional and multi-material interfaces is limited. For small asymmetry effects, however, the formulation is deemed sufficiently accurate. The tip opening displacement δ_I and mode I strain energy release rate G_I are described using the cantilever longitudinal stiffness E_x, the second moment of inertia of a cantilever arm I and the thickness of a cantilever arm h:

$$\delta_I = \frac{2P(a+\chi h)^3}{3E_xI}, \qquad G_I = \frac{P^2(a+\chi h)^3}{bE_xI} \tag{4.3}$$

With the correction parameter χ, the simple beam theory is extended to account for shear deformation and for local deformations at the crack tip:

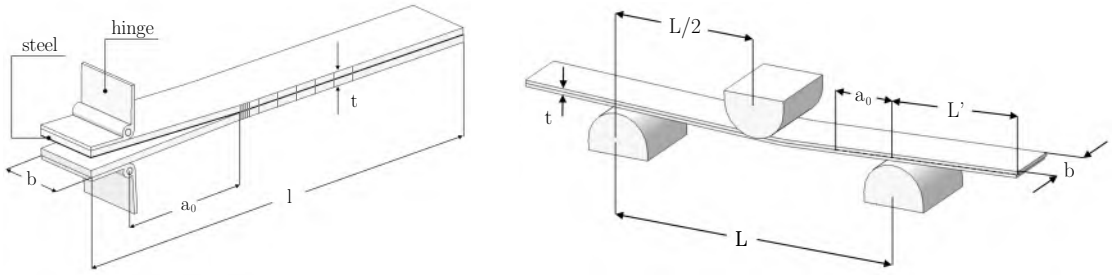

(a) Double-Cantilever-Beam (DCB) **(b)** End-Notched-Flexure (ENF)

Figure 4.5 Specimen geometry and load introduction setup for interlaminar mode I and mode II testing [11]

$$\chi = \sqrt{\frac{E_x}{11G_{xz}}\left[3 - 2\left(\frac{\Gamma}{1+\Gamma}\right)^2\right]}, \qquad \Gamma = 1.18\frac{\sqrt{E_x E_y}}{G_{xz}} \tag{4.4}$$

In the elastic regime, i.e. before crack propagation, the resulting force P and energy release rate G_I are the result of an incrementally increasing tip displacement δ_I. Once the condition $G_I = G_{Ic}$ is met, the subsequent regime of stable crack propagation can be calculated using the same equations with G_I set to G_{Ic}.

End-Notched-Flexure Test (Mode II)

The End-Notched-Flexure (ENF) test setup in ASTM D7905 [106] allows for determination of the mode II interlaminar fracture toughness G_{IIc} of unidirectional composites. Similarly to the DCB setup, the ENF setup can also be applied to hybrid interfaces by adjusting the laminate layup [11, 38, 39]. Figure 4.5b shows the ENF specimen containing a non-adhesive insert at the midplane inside a three point bend fixture. The initial delamination length a_0 is definied as the distance from the support leg to the tip of the insert. The specimen is loaded by the center stamp resulting in a mode II delamination mode in the midplane. Once the energy introduced into the specimen exceeds a critical value G_{IIc} the crack propagates along the delamination plane. As oppose to mode I testing with the DCB setup, crack propagation in the ENF setup generally initiates abrubtly and leads to an almost instantaneous failure of the cracked

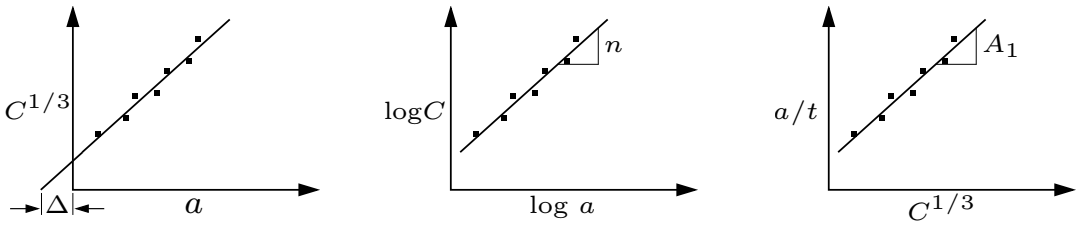

(a) MBT method **(b)** CC method **(c)** MCC method

Figure 4.6 Data reduction methods based on ASTM D5528

surface. Thus, only the critical energy release rate G_{IIc} at delamination initiation can be determined. The compliance calibration (CC) method is the only recommended data reduction procedure for ENF testing according to the standard. Therein, the ENF specimen is loaded to 50% of the maximum force from the fracture test whilst varying the crack length. The compliances of the three tests with varying initial crack lengths $(\delta/P)_{a_0=15;25;35mm}$ are plotted over the crack length cubed a^3 and CC coefficients are obtained by a linear regression analysis ($\delta/P = A + ma^3$), with A representing the intersect and m the slope of the regression function. The critical strain energy release rate in mode II results to:

$$G_{IIc}^{CC} = \frac{3mP^2a_0^2}{2b} \tag{4.5}$$

In analogy to the DCB setup, the modified beam theory can be applied for verfication of the test results [113]. Load stamp displacement δ_{II} and mode II energy release rate G_{II} are calculated as follows:

$$\delta_{II} = \frac{3P(a+0.42\chi h)^3 + 2P(L/2)^3}{96E_xI} \qquad G_{II} = \frac{3P^2(a+0.42\chi h)^2}{64bE_xI} \tag{4.6}$$

In addition to the specimen geometry and correction factors that can be adopted from the previous section on the analytical determination of the DCB specimen behavior, the distance between the supporting leg and load stamp $L/2$ is introduced. The force-displacement curve is determined analogous to the DCB case.

Specimen Manufacturing

As indicated in Table 4.9, a total of six interfaces are investigated. The interfaces are chosen in order to be able to discuss aspects of multi-material and multi-directional interfaces with respect to low temperature effects. Determination of the specific laminate layup is based on results by Petersen [38], who successfully tested hybrid interfaces at room temperature. As the laminate layup for multi-material and multi-directional interface characterization is inherently asymmetric, parasitic effects leading to undesired delamination modes affecting the DCB and ENF tests are present. Minimizing these modal coupling effects represents one component of the methodology presented to yield accurate energy release rates in Figure 4.4. Recommendations for multi-directional interfaces proposed by Prombut et al. [109] are adopted to the laminate layups presented in Table 4.9. Therein, a relatively even and symmetrically distributed energy release rate profile across the specimen width can be achieved by minimizing both the curvature due to longitudinal/transverse-bending coupling and the skewness of the crack profile due to bending-twisting coupling of the specimen arms, denoted by following conditions based on the components of the laminate ABD-matrix:

$$D_c = \frac{D_{12}^2}{D_{11}D_{22}} \leq 0.25; \quad B_t = \left|\frac{D_{16}}{D_{11}}\right| \ll 1 \tag{4.7}$$

The manufacturing process of monolithic and hybrid specimens differs only in an additional pre-treatment process for the metal layers of hybrid specimens. All specimens are fabricated using unidirectional CFRP prepreg material by Hexcel (HexPly M21/35%/134gsm/T700GC) with a cured ply thickness of 0.13 mm and austenitic cold

Table 4.9 Specimen layups for interface testing in DCB and ENF setup including bending coupling and bending-twisting coupling parameters

Interface	Layup	D_c [-]	B_t [-]	l_{DCB} [mm]	l_{ENF} [mm]	b [mm]	t_{nom} [mm]
00//00	$[0_{17}//0_{17}]$	0.006	0.036	200	150	25	4.5
00//45	$[(0_2/90)_6, 0_2//45,(0_2/90)_6,0_2]$	0.002	0.049	200	150	25	5.4
00//90	$[(0_2/90)_6, 0_2//90,(0_2/90)_6,0_2]$	0.002	0.049	200	150	25	5.4
St//00	$[0_{16}$,St$//0_{17}]$	0.006	0.036	200	150	25	4.5
St//45	$[(0_2/90)_6$,0,St$//45,(0_2/90)_6,0_2]$	0.002	0.049	200	150	25	5.4
St//90	$[(0_2/90)_6$,0,St$//90,(0_2/90)_6,0_2]$	0.002	0.049	200	150	25	5.4

worked steel 1.4310 with a nominal foil thickness of 0.13 mm. The pre-treatment process for accurate bonding between CFRP and metal layers developed at DLR [14] combines mechanical and chemical treatment by vacuum grit-blasting and sol-gel application. A total of six plates are manufactured by hand layup, vacuum sealed, and cured in an autoclave following the manufacturer's recommended curing cycle. The initial pre-crack in the midplane of the laminates is introduced by insertion of a double-layered PTFE foil of 25 µm in thickness. After the autoclave process, the specimens are cut to size by waterjet and measured using a micrometer. The DCB specimens are further processed by applying piano hinges at the ends of the free specimen sublaminates for the load introduction conforming to ASTM D5528. After manufacturing, the specimens are stored at 23±3°C and 50±10% relative humidity until testing.

4.2.3 Correction of Thermal Residual Stresses

After addressing correction methods regarding effects arising from the test setup and deviations from the beam theory, the present section focuses on the effects of thermal residual stresses on the determination of interface properties within the context of determining the true energy release rate in Figure 4.4. The layups for determining interface properties of multi-material and multi-directional interfaces are asymmetric which results in different thermal properties of the sublaminates. The difference in thermal shrinkage of the sublaminates, e.g. due to cooling of the laminate from high temperatures during curing to room or low temperature levels, leads to the build up of thermal residual stresses. As a result, non-zero forces and moments are acting on the crack tip without any external load being applied. In a DCB specimen, depending on the material properties and specific laminate layup, thermal effects can lead to either an opening or closing moment acting on the crack tip, thus affecting the measurement of energy release rate. While the influence of thermal residual stresses on monolithic CFRP specimens has been found to be negliglible [38], consideration of thermal effects is particularly important when dealing with CFRP-steel laminates, since the large difference in coefficients of thermal expansion combined with high stiffnesses of the constituents leads to an increased level of thermal residual stresses. Testing at low temperatures further increases the residual stress state.

Nairn [44] previously presented a general formulation for determining energy re-

Table 4.10 Correction terms for energy release rates in mode I and mode II due to thermal residual stresses $G^{th}_{I/II}$ in N/mm

	00//00		00//45		00//90		St//00		St//45		St//90	
	23°C	-55°C	23°C	-55°C	23°C	-55°C	23°C	-55°C	23°C	-55°C	23°C	-55°C
G^{th}_{I}	0	0	-0.019	-0.029	-0.013	-0.023	-0.048	-0.092	-0.086	-0.141	-0.060	-0.115
G^{th}_{II}	0	0	0.104	0.208	0.063	0.108	0.275	0.545	0.304	0.586	0.319	0.575

lease rates in cracked laminates with residual stresses. The approach is based on the classical lamination theory. By dividing a specimen into three sublaminates (cracked arms and intact portion of the laminate) and partitioning the stresses at the crack tip into local bending moments and normal forces, general expressions for the energy release rate are given. Based on Nairn's formulations, Yokozeki et al. [45] derived a correction method for evaluating the energy release rate in DCB and ENF specimens as special cases. Following this method, the apparent energy release rate in either mode I or mode II obtained from the experiment $G^{exp}_{Ic/IIc}$ is corrected by superimposing the respective fraction of energy release rate due to thermal effects $G^{th}_{I/II}$. Thus, the true critical energy release rates in mode I and mode II, G_{Ic} and G_{IIc}, are obtained:

$$G_{Ic} = G^{exp}_{Ic} + \underbrace{\frac{P_{max}\Delta T}{b}(\alpha_\kappa^{(1)} - \alpha_\kappa^{(2)})a + \frac{\Delta T^2}{2b}(I^{(1)} + I^{(2)} - I^{(3)}) + G_{I,tip}}_{G^{th}_{I}} \tag{4.8}$$

$$G_{IIc} = G^{exp}_{IIc} + \underbrace{\frac{P_{max}\Delta T}{b}(\alpha_\kappa^{(2)} - \alpha_\kappa^{(3)})a + \frac{\Delta T^2}{2b}(I^{(1)} + I^{(2)} - I^{(3)})}_{G^{th}_{II}} \tag{4.9}$$

Derivation of the constants is presented in Appendix B.3. The correction method has been applied repeatedly on adhesive joints with dissimilar adherents [114, 115] as well as intrinsic FMLs [11, 38, 39] and will now be applied on the present asymmetric CFRP-steel laminates to account for thermal effects on the evaluation of the interlaminar properties in mode I and mode II. The correction terms for the present laminates are calculated based on the material properties determined in the previous section and presented in Table 4.10. As recommended by Yokozeki [45], apparant energy release rates based on the CC method are used for analysis. The novelty of the present approach consists in including crack tip forces, $G_{I,tip}$, otherwise neglected. A detailed description is provided in Appendix B.3 and validation of the methodology is conducted in Chapter 6.1.

4.2.4 Experimental Procedure

The interlaminar behavior of monolithic and hybrid interfaces in mode I and mode II is characterized using the DCB and ENF setup, respectively. Testing is conducted on two temperature levels, 23°C and -55°C, inside a temperature chamber in a servo-mechanic testing machine by Zwick (Zwick 1484) equipped with a 20 kN load cell. The chamber temperature is continuously monitored using two resistance temperature

detectors (Pt100). In case of low temperature tests, the specimens are cooled inside the temperature chamber for 10 min prior to testing.

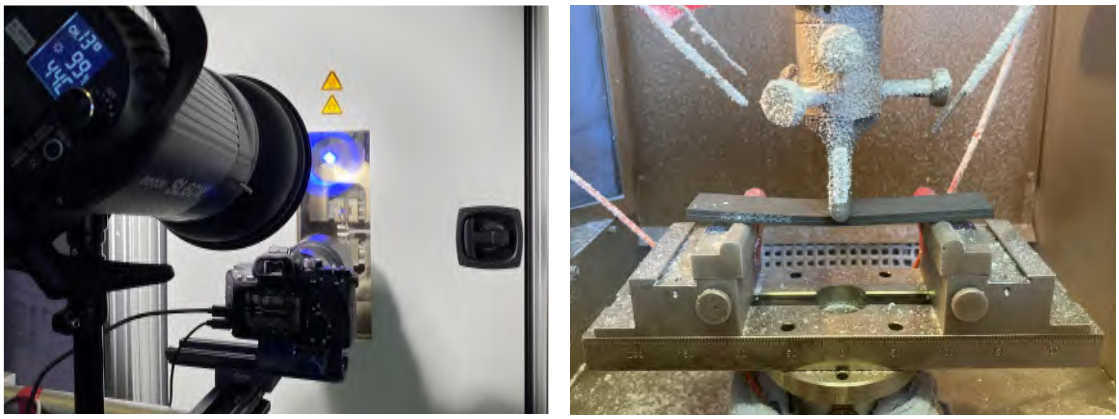

(a) Double-Cantilever-Beam (DCB) **(b)** End-Notched-Flexure (ENF)

Figure 4.7 Test setup inside a thermal chamber for a) DCB testing including camera setup and b) ENF testing

The DCB test setup is extended by a consumer fullframe mirrorless camera with a resolution of 42 mega pixel as well as a spotlight in order to assure consistent lighting conditions. Images are taken at a frequency of 1 Hz and synchronized with force, displacement, and temperature data that is provided by the testing machine for analysis of the crack propagation behavior. The setup was previously applied successfully at DLR for comparable applications [116,117]. Prior to the actual test of a DCB specimen a natural pre-crack is introduced in order to prevent measurement of wronglyfully high fracture toughness values. Studies by Pereira et al. [94] have shown that resin nests at the tip of the PTFE foil can lead to a significant error in determination of the critical energy release rate at crack initiation. The DCB specimens are inserted into the testing chamber by clamping the piano hinges between gripping jaws. After mounting the specimen inside the testing rig, the crossbeam is slowly moved until the initial pre-crack length of 40 mm defined by the PTFE foil is increased by 3 mm to a total of $a_o = 43$ mm. Thereby, a natural crack front develops, as is recommened for multi-directional interfaces. Following the introduction of the pre-crack, the actual test is conducted at a constant crosshead speed of 1 mm/min.

Characterization of mode II behavior is conducted with ENF specimens in a three-point bend setup. Since mode II testing in the ENF setup is generally associated with instable crack propagation, as oppose to the DCB test where crack propagation generally is stable, no optical monitoring of the crack position is conducted. Inside the fixture, the ENF specimens are supported by two bottom legs at a distance of 100 mm while load introduction occurs by a center stamp at a constant crosshead speed of 0.5 mm/min. Different to the DCB setup, ENF specimens require manual alignment in order to assure that the initial crack length, defined by the distance between the support leg and the crack tip, is set accurately.

4.2.5 Interlaminar Behavior in Mode I

The discussion of the results for mode I interlaminar testing is divided into four parts. First, the critical energy release rates defining delamination initiation and the importance of considering thermal effects are discussed. Then, the differences between monolithic and hybrid specimens are demonstrated based on force-displacement data, followed by an investigation on the evolution of energy release rate with increasing crack length. Finally, the fracture surfaces are compared.

Critical Energy Release Rates

In Figure 4.8, the critical energy release rates in mode I are presented for monolithic and hybrid interfaces at 23°C and -55°C. Based on the approach for determining accurate fracture toughness values in Figure 4.4, the comparison in Figure 4.8 differentiates between the apparent ERR based on the experimental test G_{Ic}^{exp}, the thermal portion due to the asymmetric layup G_I^{th} as well as the true ERR G_{Ic}.

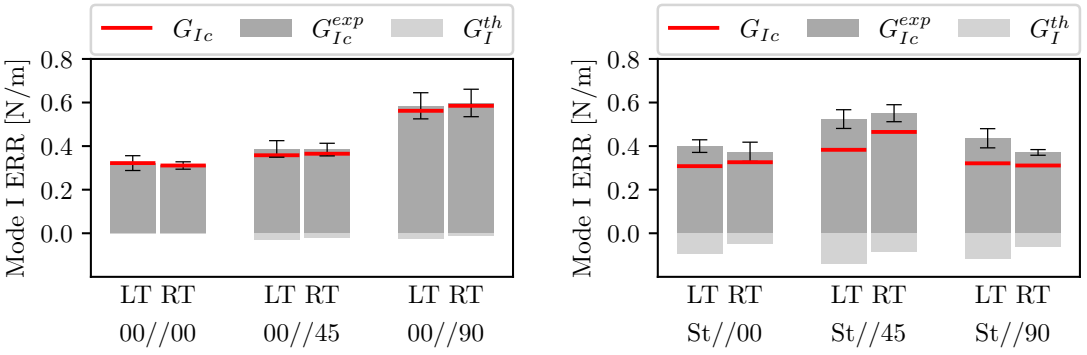

(a) Monolithic interfaces

(b) Hybrid interfaces

Figure 4.8 Mode I energy release rate (ERR) results for a) monolithic and b) hybrid interfaces including apparent ERR G_{Ic}^{exp}, thermal portion of ERR G_I^{th} and true ERR G_{Ic}

In case of monolithic interfaces in Figure 4.8a, correction of the experimentally determined ERR for thermal effects can be considered negligible since the correction terms are either smaller or of the same order of magnitude as the standard deviation in the DCB tests. For hybrid interfaces, however, the thermal correction terms cannot be neglected as the critical ERR at crack initiation would be significantly overestimated. Comparison of the true ERR values at crack initiation G_{Ic} indicates that the hybrid interfaces St//00 and St//45 exhibit comparable interfacial toughness when considering their monolithic counterparts on both temperature levels. Only the interface St//90 appears to have significant lower properties. This observation agrees well with results at room temperature by Petersen [38]. When considering the effect of low temperature on the interlaminar fracture toughness, monolithic interfaces appear to be unaffected by the change in testing temperature. Considering conflicting evidence with respect to low temperature effects on monolithic interfaces, the present results agree well with results by Asp [43] and contradict findings by Kim et al. [98] and Coronado et al. [101]. The differences at the two temperature levels for apparent ERR values of hybrid interfaces in Figure 4.8b are very small and mostly within the standard deviation of

the experiments. Considering true ERR values, the toughness of the St//45 interface appears to slightly decrease with decreasing temperature, while the interface toughness of St//00 and St//45 interfaces can be considered somewhat constant. Due to the marginal differences in toughness at different temperature levels and taking into account their magnitude with respect to the standard deviation during testing, it is concluded that, similarly to the monolithic interfaces, the interfacial fracture toughness of hybrid interfaces is not significantly affected by the decrease in temperature. It should be noted that a further decrease of the temperature level down to cryogenic temperatures for instance significantly increases intralaminar thermal residual stresses and thus the magnitude of interlaminar stresses. The question whether or not the delamination resistance that CFRP-St FMLs exhibit at RT and LT levels also extends to cryogenic temperatures can only be answered by testing at cryogenic temperautres. The appropriate tools to correctly determine cryogenic properties, however, are the same that are introduced in the present chapter.

Force-Displacement Curves

Experimentally determined force-displacement curves of the DCB tests are presented in Figure 4.9. For monolithic interfaces, analytically determined force-displacement curves based on Equation 4.3 are calculated with temperature-dependent material properties and true ERR for verification purposes.

Since the effects of thermal residual stresses due to the asymmetric layup are very small (see Figure 4.8a) the analytical methods can be applied with acceptable accuracy. In case of hybrid interfaces, however, verification by the analytical method presented is not possible as the assumption of sublaminates having identical mechanical properties is violated. In fact, the distinct kink at the beginning of the elastic regime of the hybrid interfaces in Figure 4.9 is a result of the missmatch in properties between the two sublaminates. The sublaminate containing the metal ply exhibits a curvature due to the bending moments introduced by the asymmetric layup. Thus, at the beginning of the DCB test, the curvature is eliminated before the sublaminates seperate from one another. As this behavior is a result of thermal residual stresses, the kink in the load-displacement curves of specimens tested at low temperature are on a higher load level than for those tested at RT as the difference to the stress-free temperature is greater. The behavior of the hybrid specimens in the DCB test is a good example for the necessity of including thermal effects when investigation FML structures. A detailed numerical analysis on thermal effects during interlaminar testing is presented in Chapter 6. Comparing the force-displacement curves after crack initiation indicates that an R-curve effect is likely to be present in case of 00//45 and 00//90 and to a smaller extent even in case of St//45. The behavior of the remaining interfaces is characterized by a decay in force after crack initiation, thus no R-curve effect is expected in case of 00//00, St//00 and St//90 interfaces.

Resistance Curve Behavior

Figure 4.10 shows the evolution of the apparent ERR in mode I with increasing crack length for both monolithic and hybrid interfaces at different temperature levels. Out of the interfaces considered, only the monolithic interfaces 00//45 and 00//90 exhibit a

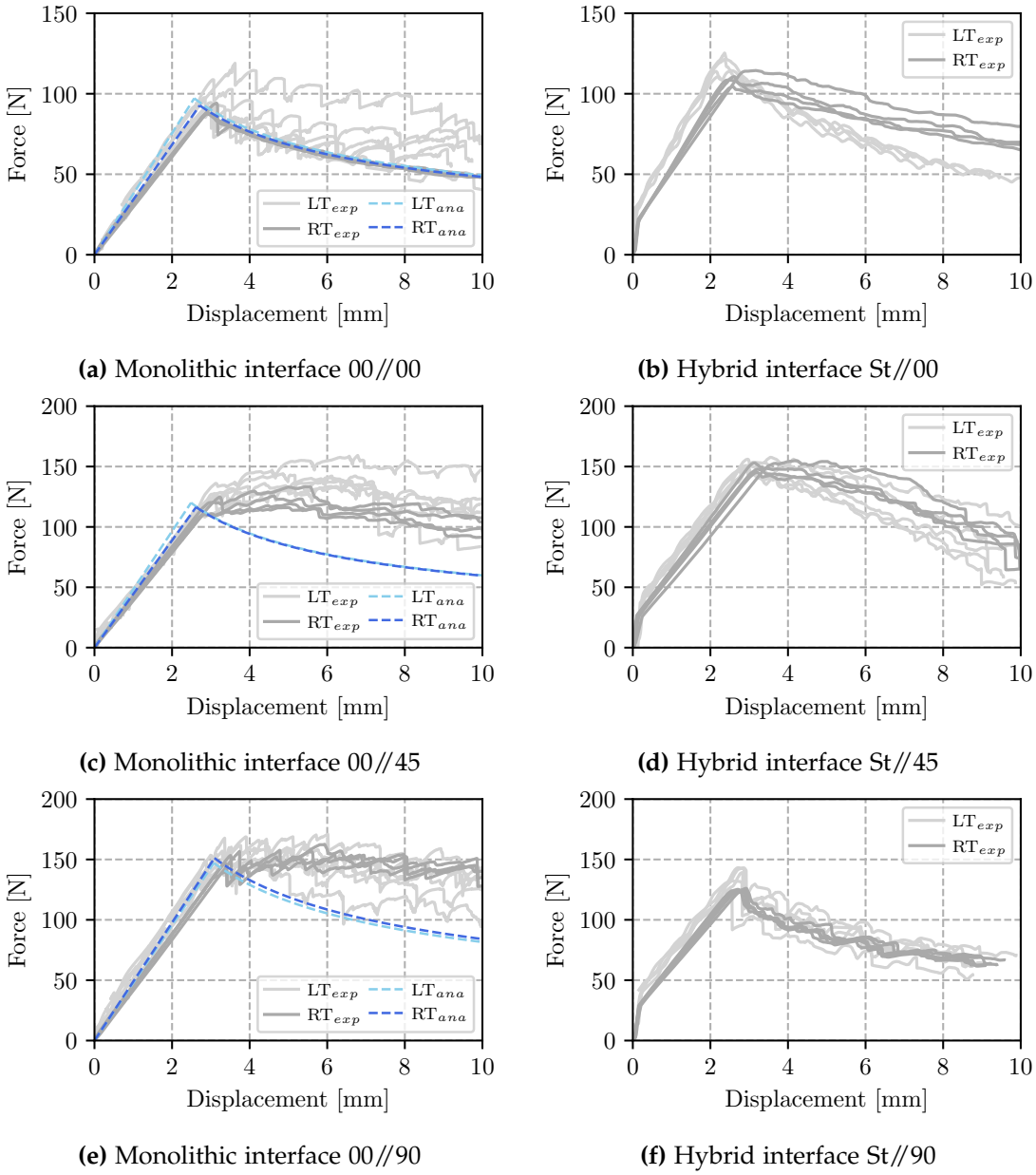

(a) Monolithic interface 00//00

(b) Hybrid interface St//00

(c) Monolithic interface 00//45

(d) Hybrid interface St//45

(e) Monolithic interface 00//90

(f) Hybrid interface St//90

Figure 4.9 Force-displacement curves of DCB tests at 23°C (RT) and -55°C (LT)

pronounced R-curve behavior as the ERR increases with increasing crack length. This behavior agrees well with the load-displacement curves of the respective interfaces in Figure 4.9. The remaining interfaces show no considerable increase in delamination

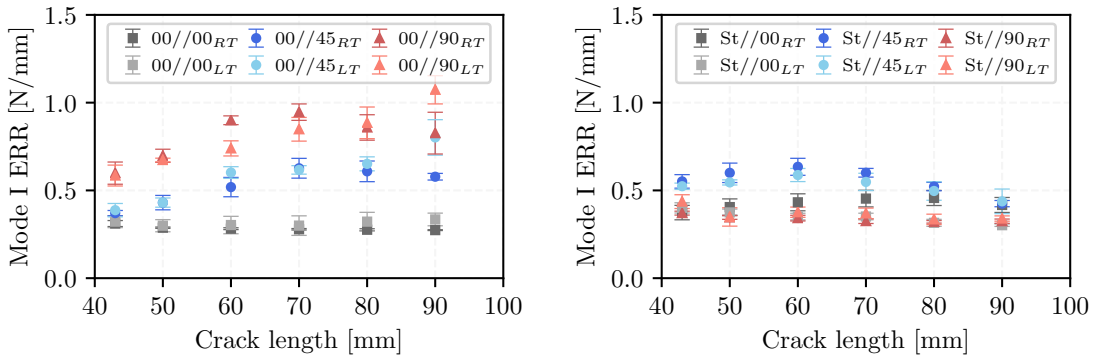

(a) Monolithic interfaces

(b) Hybrid interfaces

Figure 4.10 Evolution of apparent mode I energy release rate (ERR) with increasing crack length for a) monolithic and b) hybrid interfaces at RT and LT

resistance with increasing crack length. In case of hybrid interfaces, due to the distinct phase separation at the CFRP//metal boundary, an R-curve behavior can only occur if the crack leaves the CFRP//metal interface thus allowing for fiber-bridging to take place and/or multiple crack planes to be active. An R-curve behavior is reported by Both [11] for a St//00 interface. In the present study, however, neither the behavior of the force-displacement curve nor the evolution of ERR with increasing crack length indicate a distinct R-curve behavior for the St//00 interface. Considering the data in Figure 4.10, it can also be concluded that a decrease in temperature apparently has no influence on the R-curve behavior during mode I delamination.

Fracture Surfaces and Crack Path Analysis

In Figure 4.11, the crack paths at the specimen side of the monolithic and hybrid specimens are presented. The pictures are taken during the DCB test at crack lengths of around 70 mm. Comparison between monolithic and hybrid specimens indicate a very different behavior. In the monolithic specimens, fiber bridging and crack jumping is severely present at the 00//45 and 00//90 interfaces. Thus, the test data post crack initiation is singnificantly affected by these phenomena. However, the hybrid surfaces exhibit a crack jump only right after crack initiation but no further jumps of the crack plane during in the crack propagation regime. Comparison of the two columns in Figure 4.11 allows for analysis of the effect of temperature. In case of the hybrid interfaces, no changes are noticable by comparison of room temperature to low temperature crack paths. In case of the monolithic interfaces, the changes in crack path shape are negligible for the 00//00 and 00//90 interfaces, while the 00//45 interface exhibits more crack jumping with lower testing temperature. In general, the hybrid specimens exhibit much smoother crack paths than the monolithic specimens, which aligns well with the observations during analysis of the R-curve behavior. Therein, the presence of fiber bridging and crack plane jumping correlates with the presence of R-curve behavior in the monolithic specimens.

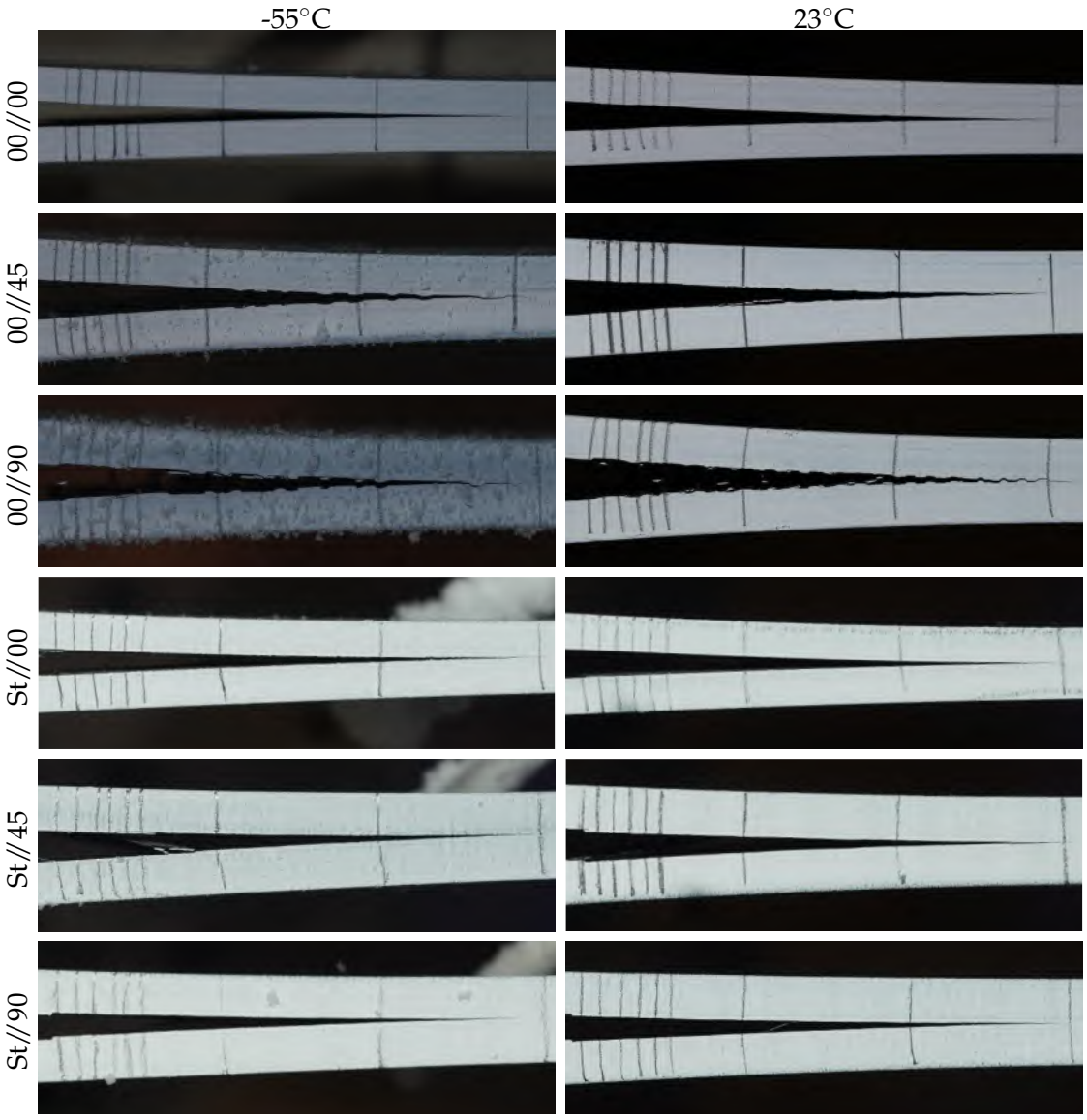

Figure 4.11 Crack paths in DCB specimens

(a) Metal surface of St//00 interface

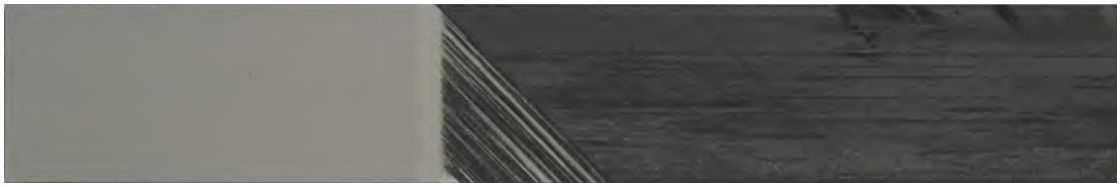

(b) Metal surface of St//45 interface

(c) Metal surface of St//90 interface

Figure 4.12 Fracture surfaces of hybrid DCB specimens

In Figure 4.12, fracture surfaces of the hybrid interfaces are presented. The metal surfaces are representative for the respective test series and are obtained by manually seperating the sublaminates after the DCB test. Comparison of interfaces tested at low and room temperature conditions shows no qualitative differences as can be expected considering the previously presented results with respect to both critical energy release rate and force-displacement data. Considering the fracture surfaces, the delamination plane in all cases leaves the initial delamination plane defined by the insert at least to some extent. In case of St//45 and St//90 specimens it is visible that crack jumping is enabled through intralaminar failure. This behavior is also reported by Petersen [38] and Both [11] for FMLs and is frequently observed in monolithic specimens [94]. As the pre-crack is defined by the foil insert, only the critical ERR determined at initiation is considered valid for the respective interfaces, e.g. as input data for delamination modeling using FEM. ERR values obtained in the crack propagation region are highly affected by crack jumping. This data does not solely represent the behavior of the initial delamination plane which explains the large deviations in the force-displacement data especially for interfaces containing 45° and 90° layers.

4.2.6 Interlaminar Behavior in Mode II

The discussion of the results of mode II interlaminar testing is conducted similarly to the mode I results by first comparing critical ERR at delamination initiation with a focus on the effects of thermal residual stresses. In addition, the force-displacement data of the ENF tests is examined before eventually investigating the fracture surfaces of hybrid specimens.

Critical Energy Release Rates

The fracture toughness values in mode II are presented in Figure 4.13 for multi-directional monolithic and hybrid interfaces at 23°C and -55°C, respectively. Based on the approach to determine true ERR values in Figure 4.4, the apparent critical ERR based on the experimental test G_{IIc}^{exp}, the thermal portion due to the asymmetric layup G_{II}^{th} as well as the true ERR G_{IIc} are quantified.

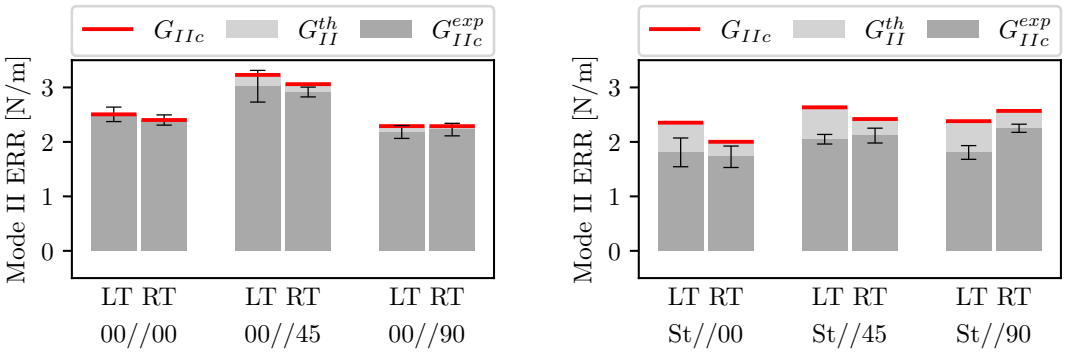

(a) Monolithic interfaces

(b) Hybrid interfaces

Figure 4.13 Mode II energy release rate (ERR) results for a) monolithic and b) hybrid interfaces including apparent ERR G_{IIc}^{exp}, thermal portion of ERR G_{II}^{th} and true ERR G_{IIc}

In case of monolithic interfaces, correction of ERR for thermal effects can be neglected similarly to the mode I case, since the portion of ERR due to thermal effects is in the same order of magnitude as the standard deviation. Compared to the mode I values, however, the thermal portion of ERR is considerably larger accounting for up to 7 % of the apparent ERR value in case of the 00//45 interface. With decreasing temperature, 00//00 and 00//45 interfaces show a slight increase in interface toughness while the critical ERR for the interface 00//90 remains constant. The increase in interface toughness observed here is consistent with the temperature dependent behavior reported by Asp [43]. As described for the results in mode I, the thermal portion of ERR is significant when considering hybrid interfaces. However, contrary to mode I loading, in case of mode II loading the portion of ERR induced by thermal effects is added to the experimentally determined apparent ERR. As reported by Petersen [38], the orientation of the specimen curvature defines whether the thermal residual stresses act in direction of the external load or opposite to it, thus either increasing or decreasing the apparent ERR value. In the present case, specimens are inserted into the test rig in a way that the metal layer is always on the lower sublaminate, therefore leading to a positive contribution that is added on top of the experimentally determined ERR. Different to the mode I case, the toughness of St//00 and St//45 interfaces increase with decreasing temperature, while the interfacial toughness of the St//90 interface slightly decreases. This behavior is somewhat similar to the behavior of the monolithic interfaces in mode II. However, compared to the monolithic interfaces, toughness properties of the hybrid interfaces exhibit slightly lower values.

As there are portions of thermally induced ERR present in both mode I and

mode II, the issue of mode interaction needs to be adressed. Especially during DCB testing, a parasitic effect of mode II loading can affect the measurements due to the relatively low loads and ERR level present during mode I testing. A numerical investigation in Chapter 6 will give more insight on this subject. In general, however, it appears favorable to aim for a symmetric sublaminate layup and preferably small differences in effective properties between the two sublaminates in order to reduce parasitic effects as much as possible. Despite correction methods being available, reducing thermal effects in the first place is considered a more effective approach, since the correction methods themselves introduce inaccuracies resulting from assumptions the analytical models are based on as well as uncertainty in the input parameters such as material properties or the stress-free temperature. With this idea in mind, recommendations for the St//00 interface regarding an improved specimen laminate layup would result in following stacking sequence: $[St, 0_{15}, St//0, St, 0_{13}, St, 0]$. As oppose to the stacking sequence $[0_{16}, St//0_{17}]$ proposed in Table 4.9, both the bending stiffness and effective thermal expansion of the sublaminates are very similar. Thus, it can be expected that thermally induced ERR values, G_I^{th} and G_{II}^{th}, decrease significantly and in some cases may even be negligible. Another benificial side effect is the fact that the center 0° layer is embedded between two metal plies. In case of crack jumping, the resulting delamination plane would still represent a St//00 interface.

Force-Displacement Curves

Force-displacement curves of monolithic and hybrid interface tests in the ENF setup at room and low temperature conditions are presented in Figure 4.14. Analytical curves based on Equation 4.6 are plotted for verification purposes using temperature-dependent material properties and true mode II ERR values. As discussed within the mode I test results, the analytical method in general shows good agreement when considering monolithic interfaces. While agreement with respect to the initial stiffness is excellent, the analytical crack growth initiation point slightly preceeds the experimentally determined point of crack growth initiation. In case of hybrid interfaces, agreement is poor with respect to both stiffness in the elastic region as well as the point of crack growth initiation. Application of the analytical methods is thus again limited to monolithic interfaces.

Fracture Surfaces

Figure 4.15 shows the fracture surface of hybrid specimens. The surfaces are representative for their respective test series and are obtained by manually seperating the sublaminates after testing. The fracture surfaces can be divided in three regions: the area of the PTFE insert on the left, the area of mode II seperation during ENF testing in the center, and the area on the right characterized by mode I seperation during manual seperation of the specimen halves. Comparison of interfaces tested at low and room temperature conditions shows no qualitative differences as can be expected considering the previously presented results with respect to both critical energy release rate and force-displacement data. Observation of the metal surface of the St//00 interface in Figure 4.15a indicates that crack propagation is limited to the initial delamination interface. This behavior differs from the behavior of the remaining specimens as crack jumping is present at least partially for the St//00 interface in mode I and in both

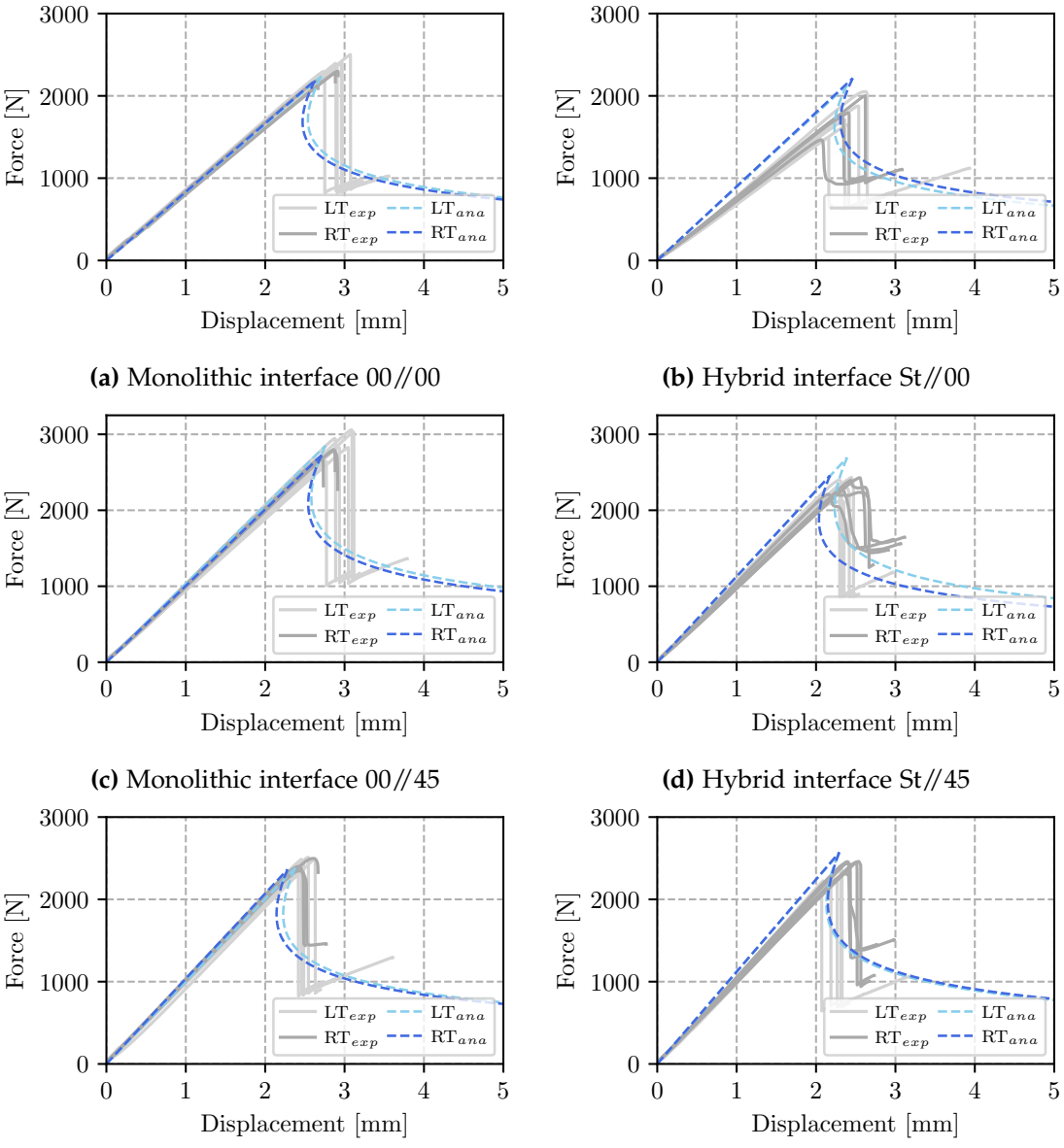

(a) Monolithic interface 00//00

(b) Hybrid interface St//00

(c) Monolithic interface 00//45

(d) Hybrid interface St//45

(e) Monolithic interface 00//90

(f) Hybrid interface St//90

Figure 4.14 Force-displacement curves of ENF tests at 23°C (RT) and -55°C (LT)

delamination modes for the St//45 and St//90 interfaces. Since the initial pre-crack is introduced by an insert foil, determination of the mode II critical ERR at crack initiation is considered valid for the respective interfaces.

(a) Metal surface of St//00 interface

(b) Metal surface of St//45 interface

(c) Metal surface of St//90 interface

Figure 4.15 Fracture surfaces of hybrid ENF specimens

4.3 Summary and Conclusions

In the present chapter, intra- and interlaminar characterization of M21/T700GC and steel 1.4310 is conducted. The intralaminar material characterization provides a comprehensive set of data including stiffness, strength and thermal expansion properties for both RT and LT conditions. Especially, LT material properties are rare. Furthermore, a recommendation for the appropriate choice of standards is provided based on a detailed discussion on the peculiarities of a multitude of composite testing standards. The data serves as input for numerical and analytical analysis in the subsequent chapters. Interlaminar material characterization is based on DCB and ENF testing. A comprehensive set of interface toughness values for monolithic, multi-material and multi-directional interfaces is provided for RT and LT conditions. Temperature dependent interlaminar properties for multi-directional hybrid interfaces is scarce, and therefore usefull to the research community. The procedure for correcting apparent energy release rates from literature is extended by a term to account for tip contact in case of hybrid DCB specimens. A detailed numerical verifictation of the necessity of the correction term is provided in Chapter 6. Furthermore, it is shown that the fracture toughness of hybrid interfaces does not decrease under low temperature conditions, despite a significant increase in thermal residual stresses acting on the inter-

face. Thereby, *Working Hypothesis I* relating to the delamination strength of CFRP-steel hybrid interfaces at low temperature conditions is confirmed.

Chapter 5

Experimental Characterization of Hybridized Composite Bolted Joints

5.1 Experimental Procedure

The investigation on the reinforcement effect by metal hybridization of composite bolted joints at low temperature is primarily based on experimental testing in the present chapter. After examining the general effect of decreasing temperatures on the bolt bearing behavior of both monolithic and hybrid laminates, the characteristics of hybrid laminates with respect to joint stiffness and strength at low temperatures are discussed in more detail. Furthermore, the effects of varying joint geometry on the failure mode are studied before eventually conducting a detailed analysis on the damage mechanisms in monolithic and hybrid laminates at low temperature. Thereby, a thorough investigation on *Working Hypothesis II* is conducted. In literature, mostly UD-CFRP-steel FMLs have been investigated in an attempt to demonstrate the theoretical maximum reinforcement effect on the bearing strength [10,11]. As described in Section 3.4, the analysis of bolted joints in the present chapter is based on the laminates presented in Table 5.1, in order to build a more profound understanding on the hybridization effect in more practically relevant laminates as well as to verify common design recommendations. The findings are then used as a basis for developing a numerical approach for detailed analysis in Chapter 6 as well as an analytical approach for the preliminary design of mechanically fastened joints in Chapter 7. Results of the present section have been partly published in Koord et al. [118].

Specimen Manufacturing

At total of 104 bolt bearing specimens are fabricated and tested using UD CFRP material (HexPly M21/35%/268gsm/T700GC) with a cured ply thickness of 0.26 mm and cold worked high strength steel sheets (St 1.4310) with identical thickness. The manufacturing process of monolithic and hybrid specimens differs only in an additional pre-treatment process for the metal layers of hybrid specimens. The pre-treatment process for proper bonding between CFRP and metal layers developed at DLR [14] combines mechanical and chemical treatment by vacuum grit-blasting and subsequent sol-gel application. Four monolithic and six hybrid plates are manufactured by hand

Table 5.1 Overview on laminate configurations

Name	Plyshares [%]	Stacking sequence [°]
QI	25/50/25	$[45/90/\text{-}45/0]_{2s}$
HO	62.5/25/12.5	$[0/45/0/\text{-}45/0_2/90/0]_s$
QI-FML	25/50/00/25	$[45/\text{St}/\text{-}45/0]_{2s}$
HO-FML	62.5/00/00/37.5	$[0/\text{St}/0/\text{St}/0_2/\text{St}/0]_s$
UD-0°-CFRP/$\text{St}_{30\%}$	70/00/00/30	$[0_2/\text{St}/0_2/\text{St}/0/\bar{0}]_s$
UD-0°-CFRP/$\text{St}_{20\%}$	80/00/00/20	$[0_2/\text{St}/0_4/\bar{\text{St}}]_s$

layup, vacuum sealed, and cured in an autoclave following the manufacturer's recommended curing cycle. After the autoclave process, the specimens are cut to size by waterjet and measured using a micrometer. Except for those specimens that are used to determine critical e/d and w/d ratios, all specimens exhibit dimensions according to AITM 1-0009 with a nominal hole diameter of 6.35 mm, a specimen width of 45 mm, and an edge distance of 25 mm. Drilling of the specimens is done using a solid carbid drill at 1200 rpm whilst tightly clamping the specimens in between aluminum plates in order to prevent delaminations at the hole edge. Due to wear on the drill blades, the drill heads are replaced after 3 and 5 drilled holes in case of hybrid and monolithic specimens, respectively. The drilling quality is monitored by ultrasonic as well as microscopic analysis. After manufacturing, the specimens are stored at 23±3°C and 50±10% relative humidity until testing.

Test Setup and Procedure

Experimental characterization of the bearing behavior is conducted in accordance with AITM 1-0009 on two temperature levels, 23°C and -55°C, respectively. As can be seen in Figure 5.1, the test rig is inside a thermal chamber. The chamber is integrated in a servo-mechanic testing machine by Zwick (Zwick 1484) and equipped with a 250 kN load cell. An extensometer is used for determination of the hole elongation. The chamber temperature is continuously monitored using two resistance temperature sensors (Pt100). The testing procedure for low temperature testing is based on a preliminary test series during which a multitude of thermocouples were applied on both the specimen and the test rig in order to quantify the cooling characteristics and to assure repeatability of the individual experiments. The test specimen is placed in between two loading plates in double-lap configuration and mechanically fastened with a torque wrench at a bolt torque of 1.3 Nm using a high strength bolt. The setup is then inserted into the test rig inside the thermal chamber and the extensometer is mounted. Due to the large thermal mass of the setup, the test starts after a cooling time of 45 min. After the test is terminated, the setup is dismounted and the load plates are inserted into a water basin for 30 min before joining them to the subsequent test specimen. This procedure assures repeatability of the experiments such that thermal effects always occur in the same manner, as for instance the change in clamping torque due to contraction of the setup during cooling. In case of room temperature testing, the waiting periods do not apply. The bearing stress is defined as the bearing load over the projected bearing surface (P/dt). Five offset strengths at permanent hole

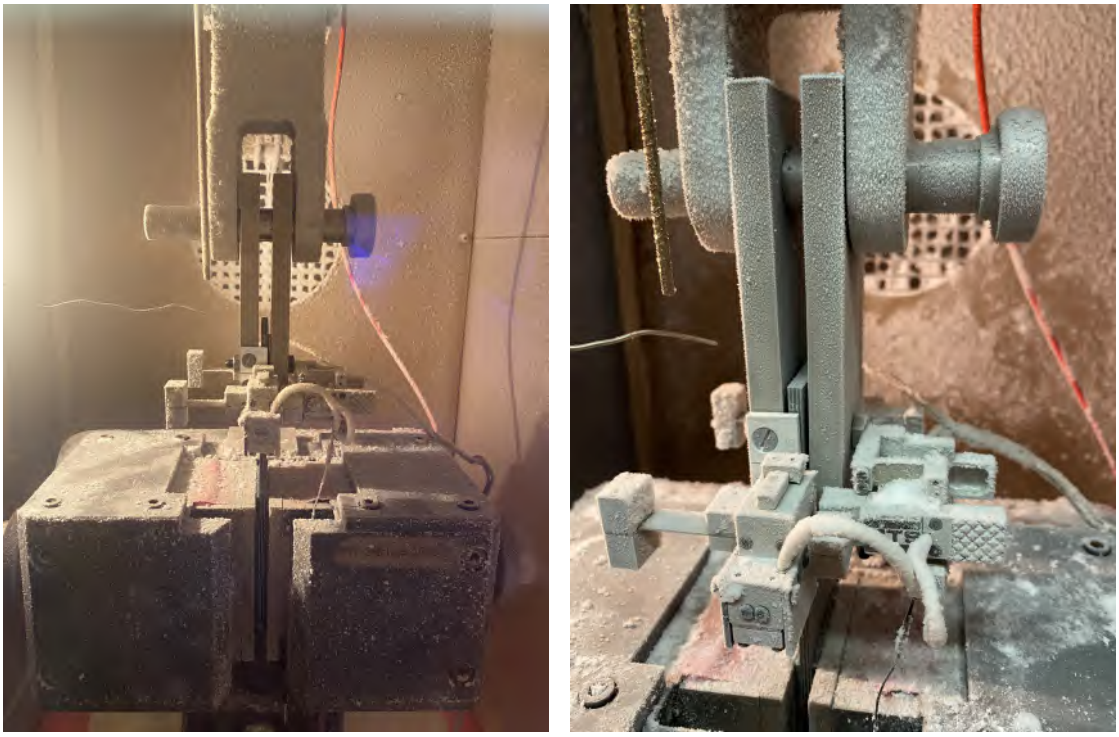

(a) **(b)**

Figure 5.1 Bolt bearing test setup conforming to AITM 1-0009 at -55°C inside a temperature chamber: Overview (a) and close up view (b) of the test rig with a test specimen in between load plates and an extensometer as well as two temperature sensors attached to the setup

deformations of 0.5, 2, 4, 6 and 10 % are considered. In addition, the bearing yield strength (BYS) at 0.5 % hole deformation and the bearing ultimate strength (BUS) at the maximum load sustained by the specimen during the test are distinguished.

5.2 Effects of Temperature on the Bearing Behavior

The present section gives an insight on the general behavior of monolithic and hybrid laminates at room and low temperature levels before addressing the characteristics of steel hybridized composite bolted joints in the subsequent sections. Two monolithic laminates (QI, HO) as well as their respective hybridizations (QI-, HO-FML) are tested at both RT and LT. The respective curves representing the load bearing behavior are presented in Figure 5.2. The diagrams exhibit identical ranges for the horizontal and vertical axes, therefore allowing for visual cross-comparison between the different laminat configurations. All test series have a sample size of n=4. The results are discussed with respect to initial joint stiffness, strength and apparent ductility.

Due to the stiffness increase with decreasing temperature on ply level, one would expect the initial joint stiffness of all laminate configurations to slightly increase with decreasing temperature. Some of the research presented within the summary of the

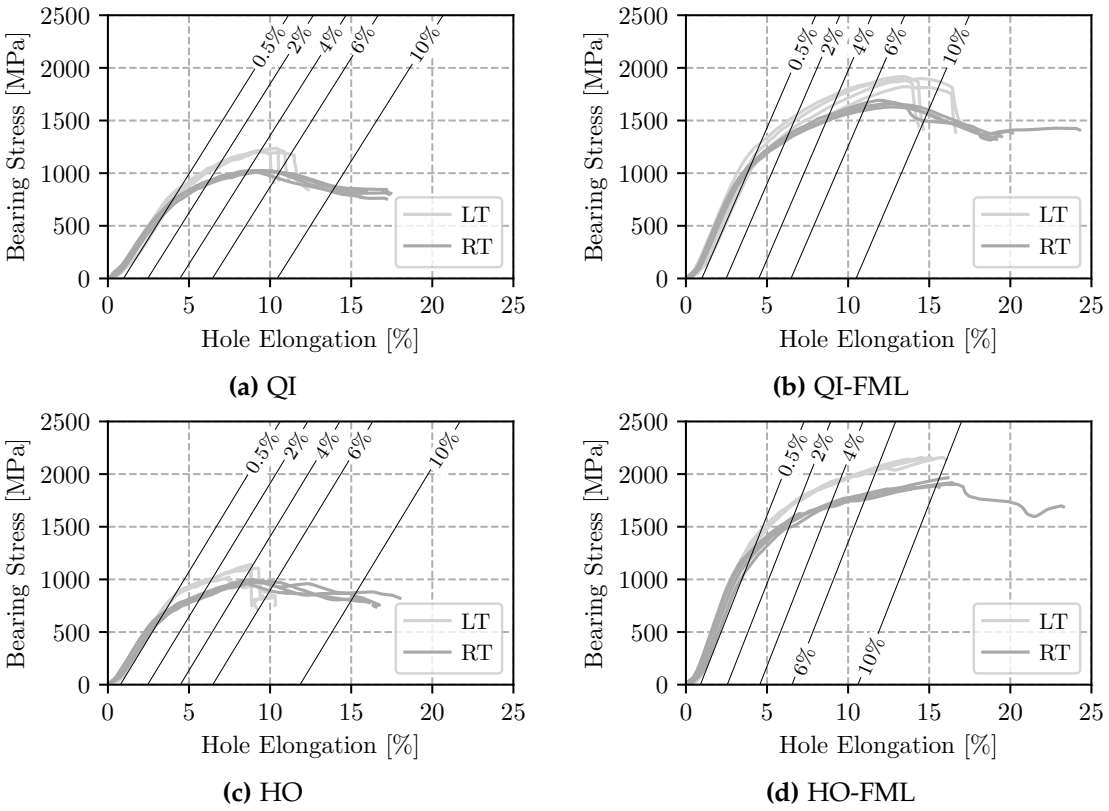

(a) QI **(b)** QI-FML

(c) HO **(d)** HO-FML

Figure 5.2 Bolt bearing behavior of monolithic (HO, QI) and hybrid (HO-,QI-FML) laminates at RT and LT including offset lines indicating permanent hole elongations at approximately 0.5, 2, 4, 6 and 10 %

literature study on the effects of low temperature on bolted joints in Table 3.2 also report increasing joint stiffness at LT. However, no effect of temperature on the initial joint stiffness is visible in Figure 5.2 as the joint stiffnesses of all configurations are very close. Comparison of the exact initial stiffness values does not indicate a consistent tendency towards increasing or decreasing stiffnesses with a temperature change either. On the other hand, the load bearing capacitiy is highly affected by the decrease in temperature. Therein, the endured bearing stress of all configurations is shifted towards higher values at LT compared to RT. In case of the monolithic laminates, the decrease in temperature also leads to an embrittlement of the material behavior. While at RT ultimate failure occurs at high bearing stress levels far beyond 10 % permanent hole elongation for both the QI and HO laminates, the behavior at LT exhibits a sudden load drop between 4 and 6 % permanent hole elongation. Depending on the metal content, hybridization with ductile metal can partially (QI-FML) or fully (HO-FML) compensate for the embrittlement caused by the temperature decrease. Thus, in contrast to the monolithic laminates the FMLs exhibit quasi-ductile behavior even at low temperatures, thereby demonstrating their favorable behavior in terms of damage tolerance.

The effect of temperature on the bearing strength in monolithic and hybrid composite bolted joints is discussed in more detail on the basis of BYS and BUS in Fig-

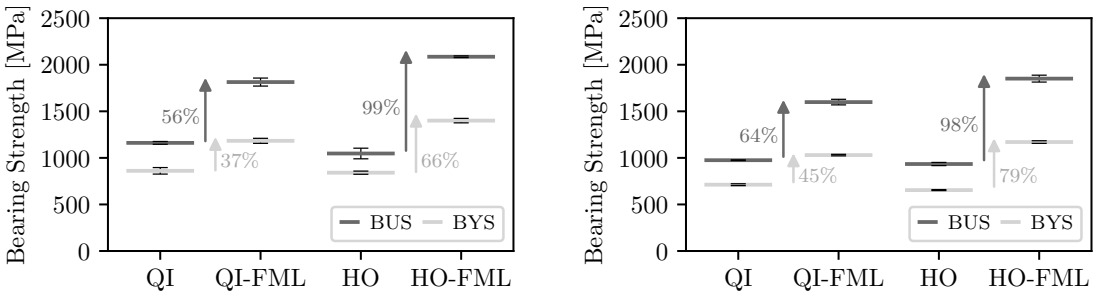

(a) Strength-increase at LT **(b)** Strength-increase at RT

Figure 5.3 Strength-increase by hybridization of QI and HO laminates at LT and RT

ure 5.3. The mean value and standard deviation of BYS and BUS are plotted for the monolithic laminates and their respective hybridized counterparts. In addition, the relative increase in strength by hybridization of each laminate is indicated for both BYS and BUS. At both temperature levels it can be seen that the strength increase by hybridization with respect to both BYS and BUS is more pronounced in case of the HO laminate compared to the QI laminate. At RT, for example, hybridization of the QI laminate results in an increase in BYS of 45 %, while hybridization of the HO laminate leads to a strength increase with respect to BYS of 79 %. This behavior can be attributed to the fact that by hybridization of the two monolithic laminates 25 % metal is introduced into the QI laminate whereas 37.5 % steel is substituted into the HO laminate. Hence, the difference in strength increase by hybridization between the HO and QI laminate is based on the difference in MVF. The effect of MVF will be discussed in more detail in the subsequent section at the example of Figure 5.7.

When differentiating between BYS and BUS, it becomes obvious that the strength increase by hybridization is more pronounced at BUS compared to BYS. For instance, the strength increase at RT in the QI and HO laminates amounts to 45 % and 79 % considering BYS, while at BUS the strength increase rates for the same laminates are 64 % and 99 %. The same behavior can be observed at LT. These results are in line with research reported by Fink [10] based on a comprehensive experimental investigation of CFRP-St and CFRP-Ti FML bolted joints at RT. Therein, the difference in strength increase between BYS and BUS is related to the failure mechanisms that are active at those stages: At BYS the strength increase by hybridization is a result of a relief of composite plies by the metal layers in combination with the isolation of damage within composite plies and suppression of damage growth through the metal sheets. At BUS, however, the dominant mechanism consists in the increase in out-of-plane stability due to the bending stiffness as well as extensive plastic deformation of the metal sheets, thus, resulting in a different strengthening rate. In Section 5.5, it will be shown that the same mechanisms are also active in the present investigation.

A very interesting observation can be made when comparing the strength increase by hybridization depending on the temperature levels. The results in Figure 5.3 indicate that the strength increase by hybridization is less pronounced at LT compared to RT. Hybridization of the QI laminate leads to an increase in BYS of 45 % at RT but

only 37 % at LT. The same tendency can be observed for the QI laminate with respect to BUS as well as the HO laminate with respect to BYS. Only the HO laminate at BUS does not follow this pattern. As the behavior at BUS is affected by significant material and geometrical non-linearities, the potential decrease in hybridization effectiveness at LT will be discussed solely with respect to BYS at this point. One possible explanation is an over-proportionate increase in material strength properties of the composite compared to the metal at LT (see Table 4.4 and Table 4.6). While matrix dominated properties of the composite increase with decreasing temperature, the yield strength of the steel material remains almost unchanged. However, it should be mentioned that fiber dominated properties, which significantly contribute to the bearing strength on laminate level, also remain almost constant when comparing RT and LT levels. Another possible explanation for the decrease in hybridization effectiveness at LT is the presence of thermal residual stresses. As discussed in Chapter 2, the magnitude of thermal residual stresses in CFRP-St FMLs increase substantially with decreasing temperature. When considering the yield strength of an un-notched FML, in some cases the presence of thermal residual stresses leads to a decrease in laminate yield strength at LT compared to RT despite the fact that the individual strengths of the consituents increase. Thus, in the present case of QI- an HO-FMLs thermal residual stresses are considered to exhibit a significant intrinsic load that limits the full exploitation of the material strength at LT, thereby reducing the effectiveness of hybridization at LT. A detailed numerical analysis in Chapter 6 will allow to quantify the contributions of these two effects.

5.3 Local Metal Hybridization at Low Temperature

In the present section, the characteristics of hybrid laminates at LT are discussed in more detail. Figure 5.4 shows the effect of hybridization at the example of representative load-displacement curves for monolithic QI and HO laminates as well as their hybridizations at LT and RT. The effect of hybridization on both initial stiffness and load bearing capacity is significant. As briefly touched in the previous section, hybridization does not only increase the stiffness and load bearing capacity of monolithic laminates but also affects the apparent ductility of the joint. The stiffness increase

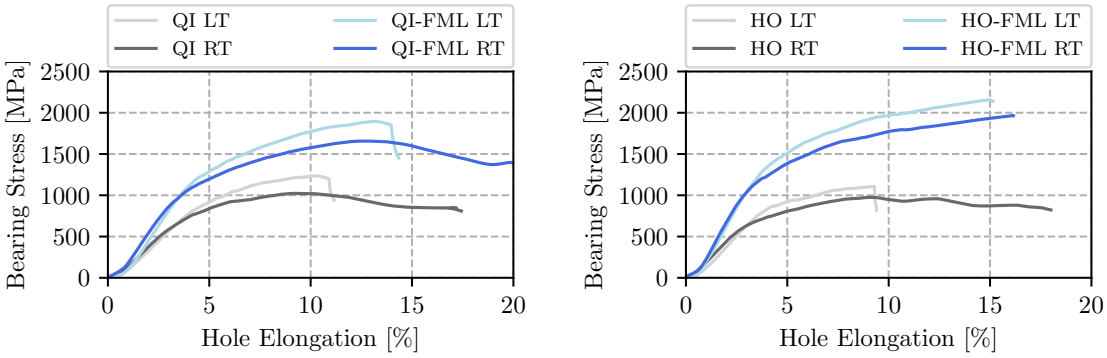

(a) Hybridization of QI laminate

(b) Hybridization of HO laminate

Figure 5.4 Effect of hybridization on monolithic QI and HO laminates at LT and RT

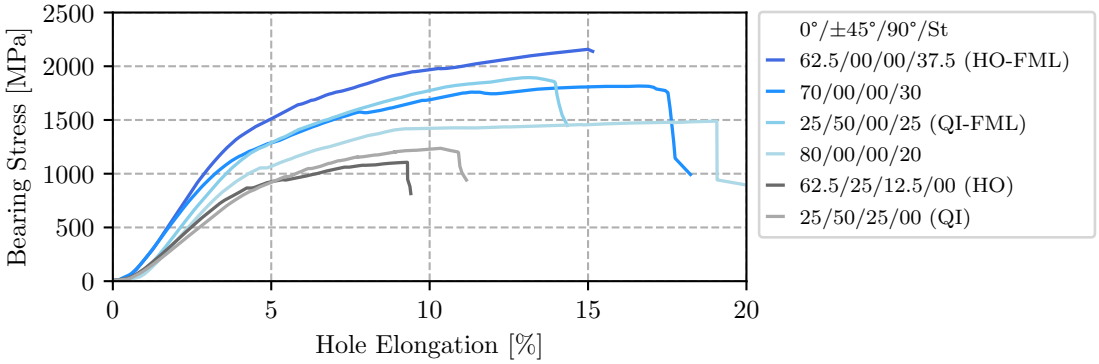

Figure 5.5 Load-displacement curve for varying MVF at LT

in the HO-FML is more pronounced due to the large MVF. Similarly, the strength increase in the HO-FML is more pronounced compared to the QI-FML. In case of the QI laminate, hybridization delays the sudden load drop observed at LT, while no load drop at all is present in the HO-FML at LT.

In order to show the bearing behavior for a gradual change of MVF, Figure 5.5 contains representative load-displacement curves of the QI- and HO-FMLs as well as two additional UD-CFRP-steel FMLs, thereby comprising MVFs from 20 % to 37.5 %. For comparison purposes, load-displacement curves of the monolithic QI and HO laminates are plotted as well. When considering the initial joint stiffness, Figure 5.5 reveals very clearly the effect of ply stiffness on meso-scale on the behavior of the joint on macro-scale. Due to the large amount of 0° layers, the monolithic HO laminate exhibits a larger initial joint stiffness than the QI laminate. Similarly, when considering the initial joint stiffness of the FMLs, a gradual increase can be observed with increasing MVF. Moreover, at MVF between 20 - 37.5 %, the initial stiffness appears to be mainly driven by the steel content since the QI-FML fits very well into the pattern despite containing significantly less 0° plies than the remaining FMLs. The increase in joint stiffness is also presented in Figure 5.6. Therein, hybridization of the QI and

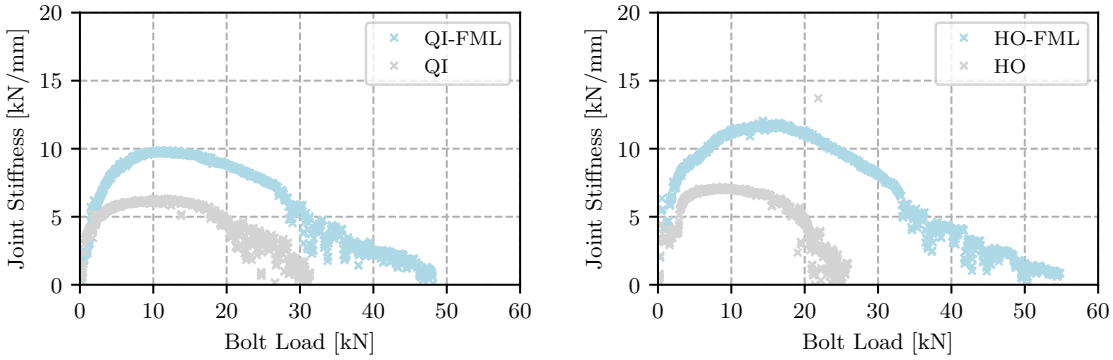

(a) Hybridization of QI laminate

(b) Hybridization of HO laminate

Figure 5.6 Effect of hybridization on the joint stiffness of monolithic QI and HO laminates at LT

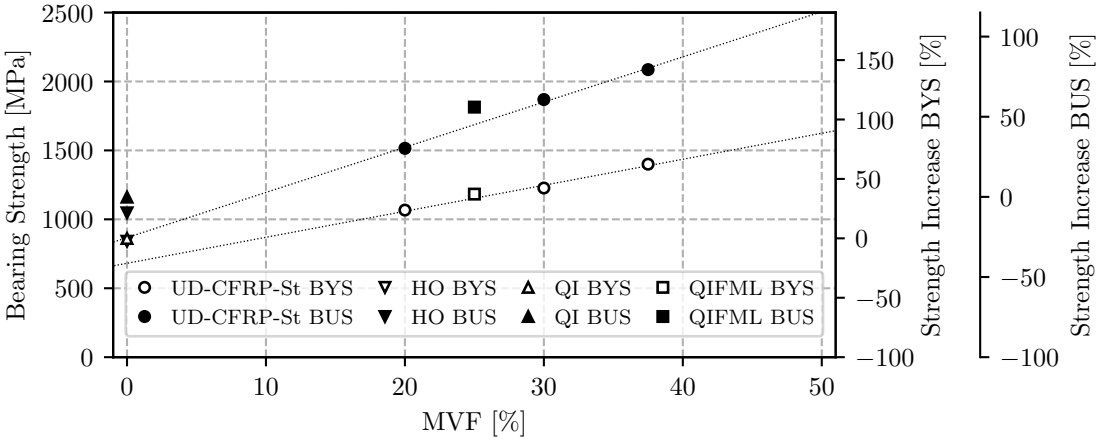

Figure 5.7 Bearing strength depending on MVF at LT

HO laminates result in both a significant increase in joint stiffness as well as a significant increase in bolt load, indicating an improvement in bearing capacity. Considering the load bearing capacity, the metal content plays a dominant role, too. As the metal content increases in Figure 5.5, the bearing capacity also generally tends to increase. As oppose to the initial joint stiffness, however, the orientation of composite plies has a noticable effect. Despite lower MVF the QI-FML endures slightly larger loads compared to the UD-CFRP-steel FML with 30 % MVF. It is assumed that in the UD-CFRP-steel FML, kink-bands once initiated in the 0° plies freely spread through neighboring 0° layers until a steel ply is reached. In the QI-FML, the combination of 0° and ±45° layers pose a greater obstacle to the spread of intralaminar damage within composite stacks in the layup and increase the amount of additional delamination at the ply interfaces as well as shear-cracks, thus, increasing the required energy for damage progression and thereby the load bearing capacity. Due to the presence of steel layers, this effect appears to be far less pronounced than in comparable monolithic laminates [10]. A detailed fractographic analysis of the bearing plane is Section 5.5 will give more insight on the damage mechanisms at LT.

In Figure 5.7, the bearing strength with respect to BYS and BUS is presented as a function of MVF. Three UD-CFRP-steel FMLs with MVF of 20, 30, and 37.5 % are considered. Additionally, the QI-FML strength with MVF of 25 % as well as the strengths of the monolithic QI and HO laminates are shown as a reference. The strength increase by hybridization regarding BYS and BUS with respect to a monolithic QI reference laminate is indicated in the secondary and tertiary axis, respectively. When considering the UD-CFRP-steel FMLs, a linear dependecy of bearing strength of the MVF can be observed for the mechanically relevant range of MVF between 20 - 37.5 %. This behavior is more pronounced for BYS than for BUS. Compared to the monolithic QI reference, hybridization by 20, 30 and 37.5 % steel results in an increase in strength by 23, 43 and 63 % with respect to BYS and 30, 61 and 80 % with respect to BUS. Similar behavior has been reported by Fink [10] for CFRP-St and CFRP-Ti FMLs at RT. The QI-FML with 25 % MVF fits quite well into the linear behavior despite significant variation from the strictly 0° layup of the UD-CFRP-steel FMLs, especially when considering BYS. At BUS, the aforementioned advantageous effect of the layup

of the QI-FML with a mixture of 0° and ±45° layers is expected to be responsible for the deviation from the linear fit. The linear relation between MVF and bearing strength with respect to BYS and BUS observed at LT, and previously reported for RT by Fink [10], is beneficial in regard to preliminary design: By relatively little testing, the basic relations between bearing strength and MVF for a hybrid material system can be established. Knowledge of this relationship allows for an initial estimate on the required MVF to achieve the necessary joint strength. Based on the estimate on MVF, subsequently a small range of configurations for local metal hybridization can be investigated following the recommendations of the ply-substitution or ply-addition technique, respectively.

5.4 Joint Geometry and Failure Types at Low Temperature

In the previous sections, it was shown that the strength increase by hybridization of monolithic laminates observed at RT level extends down to LT level. Another principle advantage of metal hybridization of composite joints is the fact that minimum required e/d and w/d ratios generally decrease in an FML. This allows for smaller distances between fasteners in multi-fastener joints and thus leads to an increase in efficiency of the joining area[1]. As reported by Fink [10] and Both [11], the minimum recommended w/d ratio in composite bolted joints decreases from 4-5 down to 3 in a CFRP-St or CFRP-Ti FML. Results by Hundley [9] indicate that the minimum e/d ratio can be reduced from 3 in composite joints down to 2 in CFRP-Ti FMLs. In order to verify if these observations extend down to LT levels as well as practically relevant laminates, bolt-bearing tests are conducted with varying joint geometry. Starting from e/d=4 and w/d=7 as recommended in AITM 1-0009, the values are gradually reduced to e/d=1.5 and w/d=2, respectively, in Figure 5.8. The QI laminate is more prone to net-section failure due to the lower tensile strength of the laminate associated with the lower fraction of 0° plies. On the other hand, the HO laminate is more likely to fail in shear-out mode resulting from the large number of 0° plies in combination with the little amount of 90° plies providing only little transverse strength. At the same time, reducing the w/d ratio provokes net-section failure of a bolted joint, while low e/d ratios tend to result in shear-out failure. Therefore, in order to consider the critical cases for QI and HO laminates, variation of w/d ratios is done using the monolithic and hybrid QI laminates, whearas e/d ratios are varied in the monolithic and hybrid HO laminates.

In Figure 5.8a, the BUS of HO and HO-FML laminates at LT is shown for varying e/d ratios at a constant w/d ratio of 7. For both HO and HO-FML it can be seen that a severe drop in BUS occurs at e/d=1.5. For e/d ratios greater 2, increasing the e/d ratio barely influences the BUS. Although the BUS of the HO-FML is consistenly about twice as high as the BUS of the monolithic HO laminate, hybridization in this case does not result in a decrease in minimum recommended e/d ratio compared to the monolithic HO laminate since the qualitative behavior of both material systems is identical. Considering the failure types, hybridization slightly extends the bearing

[1] A more detailed description of the relevance of joint geometry in both monolithic and hybrid laminates as well as the effect of joint geometry on failure types is presented in Chapter 3

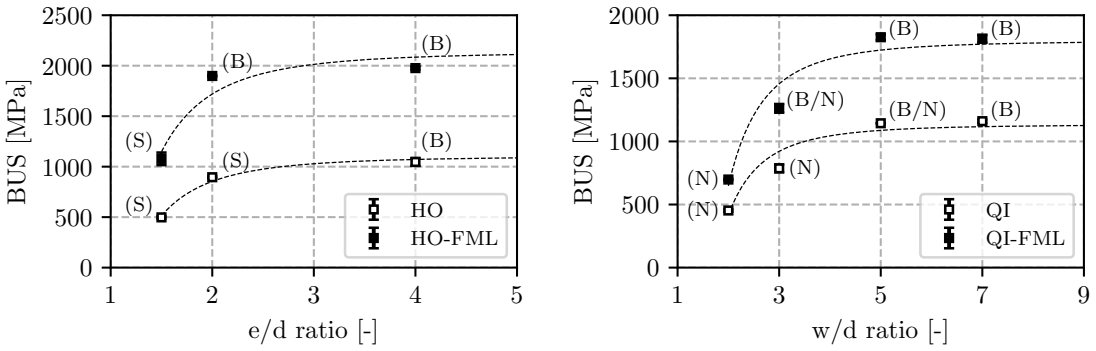

(a) Variation of e/d ratio at w/d=7=const. **(b)** Variation of w/d ratio at e/d=4=const.

Figure 5.8 Variation of e/d and w/d ratios in monolithic QI and HO laminates as well as their respective hybridization (QI-, HO-FML) at LT; Failure types: bearing (B), net-section (N) and shear-out (S)

type failure down to smaller e/d ratios compared to the monolithic HO laminate. In Figure 5.8b, variation of w/d ratios for the monolithic and hybrid QI laminates is presented. Similarly to the variation of the edge-distance, reducing the specimen width does not result in a qualitative change in strength behavior. For both QI and QI-FML, the minimum recommended w/d ratio appears to be around 4-5. This observation is not in agreement with results reported by Fink [10]. However, determination of the minimum w/d ratio by Fink is based on UD-CFRP-steel FMLs with 30 % MVF. Compared to the present QI-FML, resistance against net-section failure is much higher in those laminates due to 5 % more MVF and, more importantly, significantly more (70 % as oppose to 25 %) 0° plies with high tensile strength. This behavior shows the necessity to discuss metal hybridization with respect to the respective basis laminate rather than the mere consideration of generic UD-CFRP-steel FMLs. Furthermore, the common assumption [10, 11, 119] that pitch distances can be reduced by hybridization of CFRP laminates is challenged. This assumption is considered not to be generally valid but to be true only for certain types of laminates, i.e. UD-CFRP-steel FML. A more comprehensive study based on different types of basis laminates as well as different degrees of hybridization can give a more detailed insight on the prospects of reducing minimal pitch distances by metal hybridization.

5.5 Analysis of Damage Mechanisms

After conducting an analysis on macro-scale based on load-displacement curves and global failure modes, the present section focuses on the damage mechanisms in the laminate. In order to better understand the onset and propagation of damage in monolithic and hybrid laminates at LT, specimens are analyzed after being loaded to 0.5 %, 4 % and maximum hole elongation. Ultrasound scans are used to assess the total damaged area, while a fractographic analysis is conducted based on microsections of the bearing plane to investigate the failure patterns. The findings are then compared to the bearing behavior of monolithic and hybrid laminates reported in literature and summarized in Chapter 3.

In Figure 5.9, the C-scans of the bearing specimens loaded to different hole elongations are presented. The C-scans of the monolithic CFRP specimens are taken in reflection mode, where the transducer works in *pitch-catch* configuration. Since the metal plies exhibit different acoustic impendace properties compared to the CFRP layers, the FMLs are inspected in through transmission mode by using an additional receiver. The C-scans show planar defects such as delaminations, voids and cracks normal to the propagated pulse. Since the type of defect cannot be differentiated, the C-scans are used for a qualitative analysis of the shape and size of the damaged area.

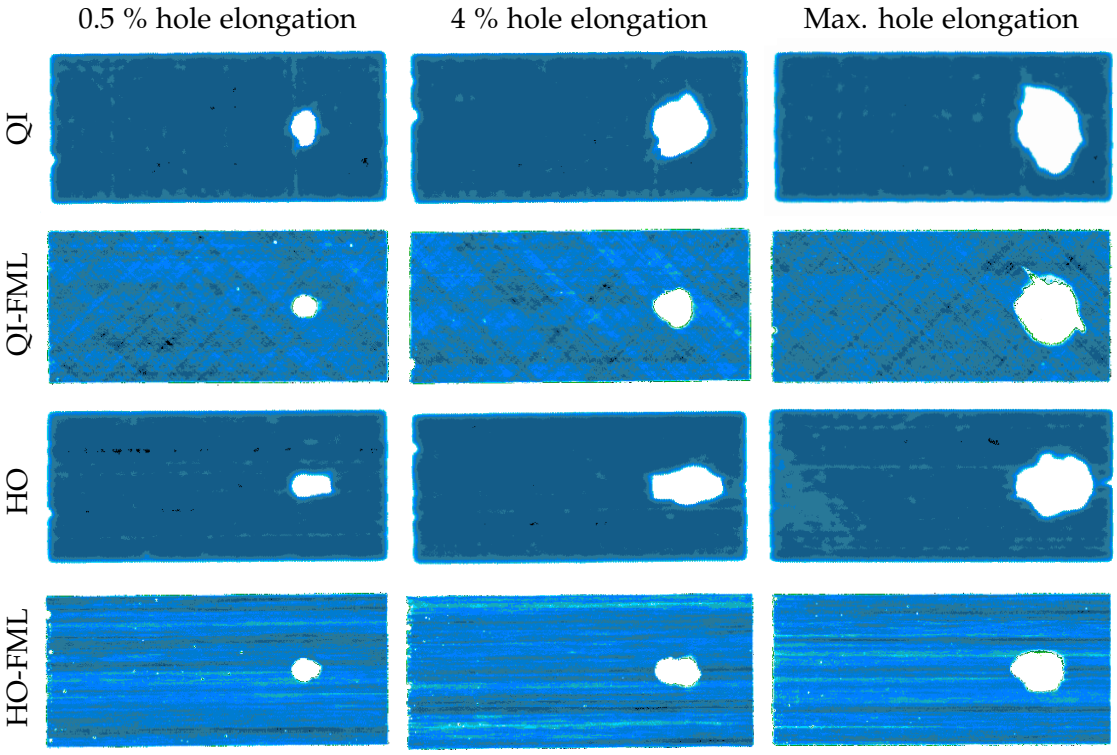

Figure 5.9 Ultrasound C-scan images (CFRP: reflection mode, FML: transmission mode) of bearing specimens at different levels of permanent hole elongation

When looking at the monolithic laminates, it can be seen that the damaged area in the QI laminate spreads out substantially in loading direction as well as in lateral direction. In comparison, the HO laminate exhibits a more directional damaged area characterized by substantially less lateral and more longitudinal expansion. Eventhough the total damaged area in the QI and HO laminate increases with increasing hole elongation, the pattern of the damaged area remains unchanged. In case of the FMLs, the damage pattern observed on the monolithic laminates translates to the QI- and HO-FML, respectively. Therein, former exhibits a more lateral damage while latter is characterized by a more directional damage pattern with mainly longitudinal expansion. The comparison of the damaged areas in monolithic and hybrid laminates is done at load levels equal to 0.5 %, 4 % and maximum permanent hole elongation. It should be mentioned that 0.5 % and 4 % permanent hole elongation effectively rep-

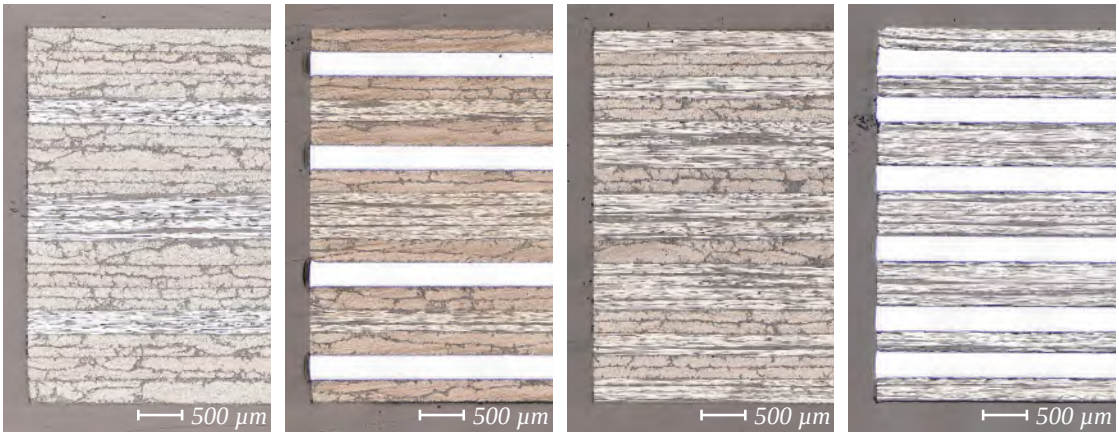

(a) QI **(b)** QI-FML **(c)** HO **(d)** HO-FML

Figure 5.10 Microsections of the bearing plane before loading

resent BYS (for all laminates) and BUS (only for monolithic QI and HO laminates), respectively (cf. Figure 5.2). Direct comparison of the C-scans show that hybridization of the QI and HO laminates results in substantially smaller damaged areas at 0.5 % and 4 % permanent hole elongation, thus emphasizing the favorable effect of metal hybdridization on damage propagation. Comparability of the C-scans at maximum hole elongation after testing is limited since these images represent different levels of permanent hole elongation: ∼8 % (QI), ∼12 % (QI-FML), ∼6 % (HO) and ∼10 % (HO-FML). However, even within this unfavorable basis for comparison, the FMLs exhibit similar (QI-FML) or significantly less (HO-FML) damaged area with respect to their monolithic counterparts, despite considerably larger permanent hole elongations and at significantly higher loads.

After inspecting ultrasound scans for gaining a first impression on the global size and pattern of the damaged area, in the following, microsections of the bearing plane are used as a basis for analyzing the damage mechanisms present in monolithic and hybrid laminates at LT. As stated in Chapter 3, there is no research presented in literature on the effect of low temperature on the damage mechanism in FMLs, notably for CFRP-St and CFRP-Ti FMLs. Therefore, research on the effects of low temperature and the effects of hybridization at room temperature on the damage mechanisms in CFRP bolted joints are summarized seperately in Chapter 3. The goal of the present analysis is, firstly, to verify if the damage mechanism in the monolithic CFRP laminates is consistent with observations in literature, and secondly, to assess if the damage mechanism present in CFRP-St laminates at RT described mainly by Fink [10] also extends to LT. For reference purposes, Figure 5.10 shows microsections at the bolt hole of specimens before loading that were sliced along the bearing plane. In Figure 5.11, microsections along the bearing plane are presented for specimens loaded to 0.5 %, 4 % and maximum permanent hole elongation. It should be mentioned that these are the exact same specimens previously inspected by ultrasound in Figure 5.9.

The first row in Figure 5.11 shows that damage in the QI laminate is initiated by fiber kinking in the 0° plies. Aside from fiber kinking no further damage is present

in the microsection at 0.5 % permanent hole elongation (BYS). Further loading to 4 % permanent hole elongation (∼BUS) leads to extensive fiber kinking in the 0° plies,

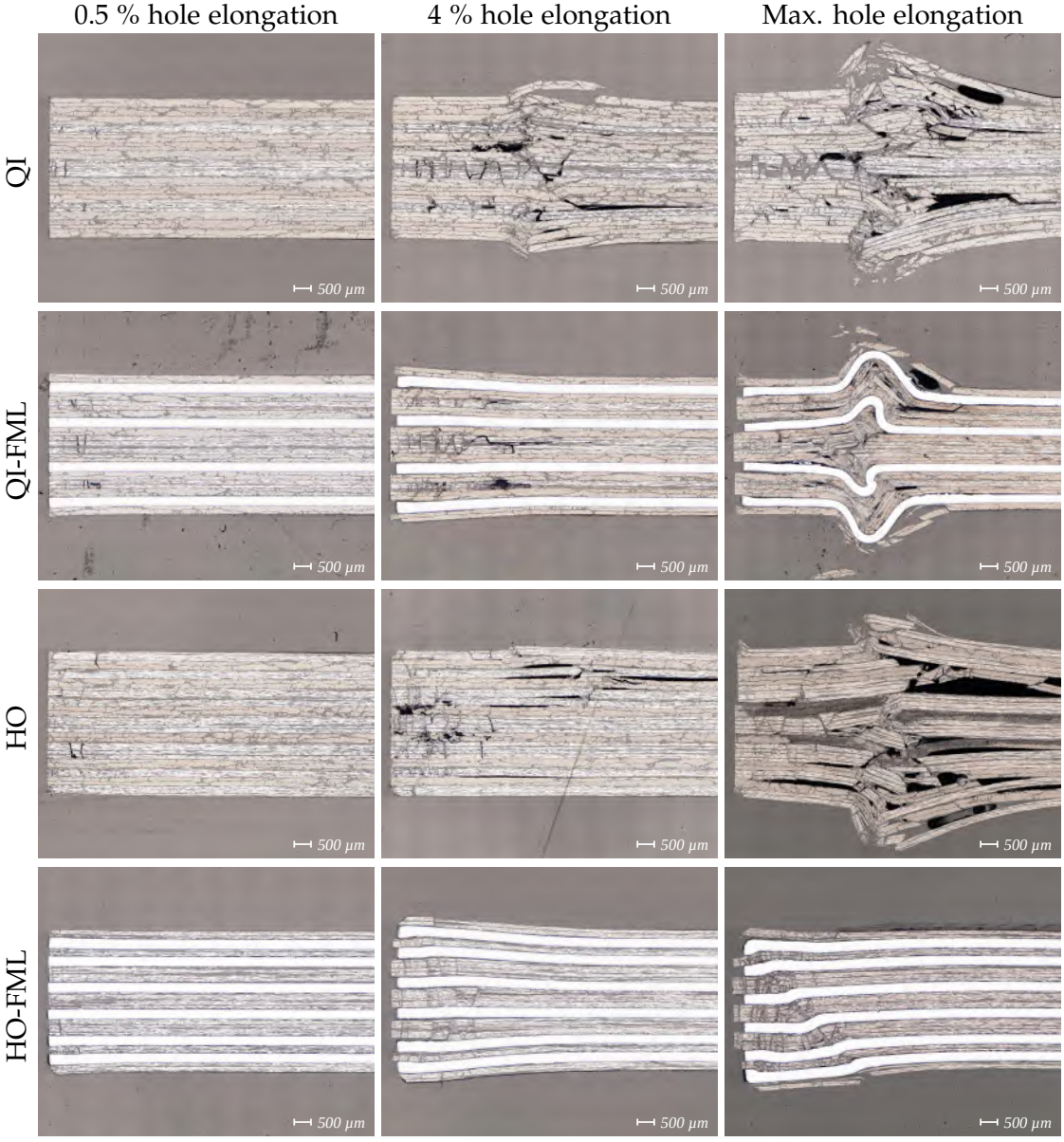

Figure 5.11 Microsections of bearing specimens along the bearing plane at varying levels of permanent hole elongation at LT

which again initiates matrix shear cracks in the neighboring ±45° plies. Only some microcracks are visible in the 90° plies. As previously reported in literature [10, 42], the lateral support by the washers largely contains damage. However, outside the washer area extensive delamination, wedge-type splitting as well as lateral bulging of the top and bottom plies of the laminate can be oberved. At maximum hole elongation (∼8 %), the damage pattern remains similiar in quality but is much more pronounced as this state represents the loss of load bearing capacity of the laminate. Compared to the QI laminate, the HO laminate in the third row in Figure 5.11 exhibits more severe

fiber kinking in the 0° plies at 0.5 % hole elongation (BYS). In addition, the kink bands provoke matrix shear failure in the neighboring ±45° plies. Similar to the case of the QI laminate, there is barely any damage visible in the 90° plies. At 4 % permanent hole elongation (∼BUS), there is extensive fiber kinking and matrix failure forming wedge-type damage patterns including some delamination. The damage in the area under the washer is mostly contained. Outside the washer area, however, the onset of lateral bulging resulting from crushing of failed plies can be observed. Moreover, severe delaminations reaching up to 15 mm into the bulk laminate are present. At maximum permanent hole deformation (∼6 %), it can be seen that while the damage under the washer area is somewhat contained, severe damage outside the washer area leads to lateral bulging and consequently to a loss of load bearing capacity of the HO laminate. To summarize, the damage mechanisms present in the QI and HO laminates at LT are characterized by fiber kinking, matrix shear cracks and delamination. Despite extensive damage accumulation in the washer area, bearing failure is triggered by laminate crushing and lateral bulging outside the washer area. These observations agree well with literature reports [41,42,82].

In the QI-FML, damage at 0.5 % permanent hole elongation (BYS) is characterized by fiber kinking in the 0° plies. There is no visible damage in the ±45° plies. Delamination between composite and steel plies can be observed in the vinicity of the hole. At 4 % permanent hole elongation, extensive fiber kinking and matrix shear cracking can be observed. Also, all CFRP-steel interfaces are delaminated under the washer area. Damage accumulation is mostly limited to the area under the washer. Additionally, the metal sheets arrest cracks in the CFRP ply package and hinder the formation of wedge-type damage patterns, which are present in the monolithic QI laminate. At maximum permanent hole elongation (∼12 %), there is large damage accumulation in the CFRP plies under the washer area. Outside the washer area, the metal plies undergo significant plastic deformation. One steel ply (second from bottom) also exhibits shear fracture. Similar to the QI laminate, outward bulging of the laminate outside the washer area likely is the reason for the loss of load bearing capacity. However, due to the extensive plastic deformation and large damage density in the CFRP plies contained in between the metal sheets, bearing failure occurs at a much higher bolt loads and larger permanent hole elongation compared to the monolithic QI laminate.

The formation of kink bands in the 0° plies of the HO-FML mark the initiation of damage at 0.5 % permanent hole elongation (BYS). In addition, the onset of delamination between CFRP and steel layers can be observed near the hole edge. Considering the microsection at 4 % permanent hole elongation, extensive fiber kinking forming a zig-zag pattern can be observed. Furthermore, delamination between most CFRP-steel interfaces as well as plastic deformation in the steel plies through outward bending is present in the area under the washer. At maximum permanent hole elongation (∼10 %), the CFRP plies exhibit substantial damage accumulation in the washer area. Failure appears to be the result of kinking in the steel plies accompanied by wedge-type damage pattern, thereby leading to a loss of stability and consequently to a loss in load bearing capacity of the HO-FML.

The damage mechanism present in the QI- and HO-FML are characterized by the

formation of kink bands in 0° plies that lead to matrix cracks in neighboring composite plies of different orientation. At higher load levels, substantial damage accumulation in CFRP stacks and delamination at the interface between composite and steel plies can be observed. Ultimate failure is the result of significant plastic deformation and out-of-plane bending of the metal plies that cause a loss of stability outside the washer area. In comparison to the monolithic laminates, the introduction of steel plies in the FMLs leads to a relief of composite plies, an isolation of composite damage, and additional stability in out-of-plane direction, thereby increasing the load bearing capacity with respect to BYS. At BUS, extensive plastic deformation and containment of composite damage between metal plies leads to an increase of bearing strength. Overall, these findings agree well with observations made by Fink [10] for CFRP-St FMLs at RT. When considering the effect of temperature, similarly to the observations made on monolithic laminates [42], delaminations in FMLs at LT are more pronounced than at RT and represent a significant contribution to the overall failure mechanism.

5.6 Summary and Conclusions

In the present chapter, an experimental study on the bearing behavior of hybridized composite bolted joints is conducted. The analysis comprises effects due to LT testing on monolothic and hybrid laminates, the reinforcement effect by steel hybridization of CFRP bolted joints, effects from varying the joint geometry as well as a detailed investigation on the damage mechanisms in monolithic and hybrid joints.

In both monolithic and hybrid bolted joints, decreasing temperatures lead to an increase in bearing strength. While monolithic laminates exhibit a brittle behavior resulting in a loss of load bearing capacity at relatively low permanent hole elongation at LT, hybrid laminates behave quasi-ductile and sustain loads at significantly higher deformations. This behavior indicates superior damage tolerance of hybrid joints compared to their monolithic counterparts.

Steel hybridization of the QI and HO monolithic laminates at LT leads to a significant increase in bearing strength with respect to BYS and BUS. However, compared to RT conditions, the strength increase is less pronounced at LT. The assumption that the presence of thermal residual stresses in the laminate limits the full exploitation of material strength is conformed in Chapter 6.

The influence of steel hybridization on joint stiffness and strength is linear for MVF between 20 - 40 %. Thus, design charts can be derived rather easily in order to determine the necessary MVF for a given joint desing. These findings at LT are in agreement with observations on similar FMLs at RT by Fink [10]. However, when it comes to the influence of hybridization on minimum e/d and w/d ratios, literature reports [10,11,119] are challenged by the present findings. The reduction of minimum e/d or w/d ratios by hybridization is not generally true but depends on the laminate stacking, as is demonstrated by the QI- and HO-FMLs in the present study.

The onset and propagation of damage in both monolithic and hybrid laminates is investigated using US analysis and optical microscopy. The basic effect regarding the increase in BYS by hybridization is associated with a relief of composite plies by the introduction of steel plies, an isolation of composite damage, and additional stability in out-of-plane direction, thereby increasing the load bearing capacity. At BUS, exten-

sive plastic deformation and containment of composite damage between metal plies leads to an increase of bearing strength. For both BYS and BUS, delamination at the CFRP-steel interface at LT are more pronounced than at RT and represent a significant contribution to the overall failure mechanism.

In summary, the results within the present chapter generally confirm *Working Hypothesis II* concerning the favorable effect of hybridization on the bearing behavior of composites. Herein, the findings on CFRP-St FMLs at RT are extended to LT conditions. However, the reinforcement effect by steel hybridization is less pronounced at LT compared to RT, which is likely due to the presence of thermal residual stresses within the hybrid laminates. The impact of thermal residual stresses on the bearing behavior is analyzed in detail in Chapter 6.

Chapter 6

Numerical Modeling of Hybridized Composite Bolted Joints

6.1 Interlaminar Material Behavior

The analysis of damage mechanisms in bolted joints in the previous chapter demonstrates the relevance of delamination effects in FMLs. Delaminations at CFRP-steel interfaces are present even at low loading levels and become increasingly dominant at higher loads, resulting in the necessity to include delamination in the design and analysis of FML bolted joints. Therefore, first of all, modeling of the interlaminar behavior in CFRP-steel laminates is discussed in the present section, while focusing on appropriate modeling techniques regarding the effect of thermal residual stresses. After introducing the material models for intralaminar material behavior in the second section, numerical models of monolithic and hybrid bolt-bearing joints are validated against experimental data and further investigated in the third section of the present chapter. The chapter emphasizes on the requirements for modeling FMLs and thus the effects of thermal residual stresses on the material behavior in an attempt to verify *Working Hypothesis III*.

Numerical modeling of interlaminar behavior can be done using Cohesive-Zone-Modeling (CZM) [120], Virtual-Crack-Closure-Technique (VCCT) [121] or the extended Finited-Element-Method (XFEM) [122]. The CZM approach does not require the definition of an initial crack, it can be applied using either an element or surface based approach, it can capture both initiation and propagation of delamination, also R-curve behavior can be modeled depending on the choice of traction-separation law [123]. VCCT is not pursued because the method requires the definition of an initial crack which is not necessarily known a prori in bolt-bearing specimens. XFEM is not implemented since the method is considered computationally too expensive and the main advantage of XFEM, namely modeling arbitrary crack paths, is not required as the delamination planes are known in general. As a result, CZM is the method of choice. Results of the present section have been partly published in Koord et al. [124].

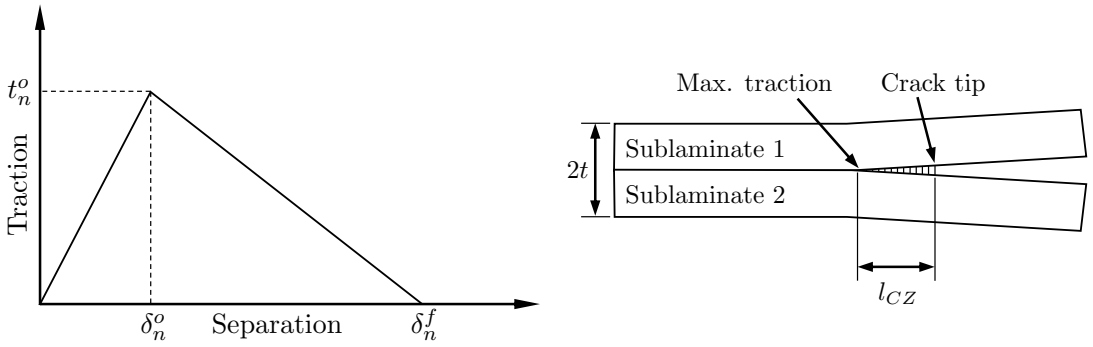

(a) Bilinear traction-separation law for CZM **(b)** Cohesive zone length adopted from [126]

Figure 6.1 Cohesive modeling

Cohesive Zone Modeling

The CZM method allows for either an element-based approach or a surface-based approach. In the former, nodal separations are interpreted, while the latter approach quantifies the separation between distinct surfaces. Either way, the cohesive behavior is based on a traction-separation law. Therein, the separation at an interface is associated with a traction, as can be seen in Figure 6.1a. Once a critical traction value, namely the interface strength t_n^o is reached, damage in the cohesive interface is initiated. Damage evolution is driven by the shape of the traction-separation law and the area under the curve, which is equal to the interface fracture toughness G_c [125]. Application of the CZM method requires the selection of numerical parameters, which is presented in the following.

Elastic Behavior

Different approaches for defining the initial stiffness K of the traction-separation law have been introduced in literature. The main goal is to define K in a way that the overall structural behavior is not affected, i.e. the cohesive stiffness does not influence the stiffness of the global model. Turon et al. [125] have proposed following relation for cases where $E_{33} \ll K$,

$$K = \frac{\alpha \cdot E_{33}}{h} \tag{6.1}$$

with h as the half-beam thickness, a numerical parameter $\alpha \approx 50$ and the laminate stiffness E_{33}. In general, with increasing cohesive stiffness K the influence on the overall structural behavior diminishes. However, excessively large stiffness values $K > 10^8$ N/mm^2 can result in significant oscillation in the delamination process, thus affecting the prediction of delamination onset as well as numerical stability of the simulation [123]. Lu et al. [127] present a study on cohesive parameters for delamination modeling. Therein, values between 10^5 to 10^6 N/mm^2 represent an adequate choice for the cohesive stiffness, assuring both accuracy and numerical stability. This recommendation also agrees with observations by Zou et al. [128] and Camanho et al. [120]. In the present simulations K is set to 10^5 N/mm^2 (see Table 6.1).

Interface Strength and Element Edge Length

Care must be taken when defining the cohesive interface strength t_n^o and the element size in the delamination region, since both parameters are connected through the cohesive zone length l_{cz}. In Figure 6.1b, the physical $l_{cz,p}$ describes the area ahead of the crack tip over which damage, i.e. microcracking at the interface, has occured, while the numerical $l_{cz,n}$ describes the area ahead of the crack tip over which degradation in the cohesive elements has started. For accurate delamination modeling a minimum number of elements is required within the cohesive zone l_{cz}. The prevaling recommendation in literature is that the fracture process zone must contain at least three elements along its length [113, 125].

Several equations for determining the characteristic length have been introduced in literature. Hillerborg et al. [129] originally formulated an equation for isotropic materials applicable to cohesive modeling in concrete structures:

$$l_{cz} = E\frac{G_c}{(\sigma_{max})^2} \tag{6.2}$$

In order to calculate cohesive zone lengths for orthotropic materials, the equation by Hillgerborg et al. was modified by Yang and Cox [130]:

$$l_{cz,I} = E_I'\frac{G_{Ic}}{(\sigma_{I,max})^2} \tag{6.3}$$

$$l_{cz,II} = E_{II}'\frac{G_{IIc}}{(\sigma_{II,,max})^2} \tag{6.4}$$

where E' is an equivalent elastic modulus for orthotropic materials. The exact value depends on the material's longitudinal, transverse, and shear moduli, as well as the specimen depth and whether plane stress or plane strain conditions are applicable. A detailed derivation and description of the calculation of E' is provided in Harper and Hallet [113]. Further modification of the equations yields following formulation that takes into account slender laminates:

$$l_{cz,slender,I} = \left(E_I'\frac{G_{Ic}}{(\sigma_{I,max})^2}\right)^{\frac{1}{4}} h^{\frac{3}{4}} \tag{6.5}$$

$$l_{cz,slender,II} = \sqrt{\left(E_{II}'\frac{G_{IIc}}{(\sigma_{II,,max})^2}\right) h} \tag{6.6}$$

with h as the half-beam thickness. For practical purposes, Harper and Hallet [113] suggest to determine both the regular orthotropic solution as well as the slender laminate solution and use the minimum value for conservatism.

Calculation of the cohesive zone length l_{cz} requires knowledge of the maximum traction value σ_{max}. Measurement of the physical interface strength is difficult. Unfolding tests with L-profile specimens is one way to experimentally determine the interface strength, as done by Petersen et al. [131]. However, interface strengths of

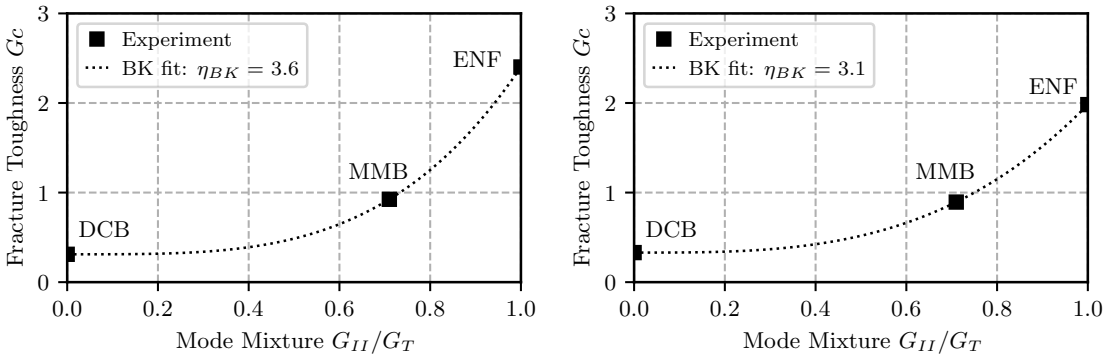

(a) Interface 00//00 **(b)** Interface St//00

Figure 6.2 Determination of interaction coefficient η_{BK} by curve fit between test results of DCB ($G_{II}/G_T = 0$), MMB ($G_{II}/G_T = 0.71$) and ENF ($G_{II}/G_T = 1$)

monolithic interfaces determined by those unfolding tests range within 79 MPa to 94 MPa, resulting in very low element lengths of 0.12 mm and 0.17 mm, respectively. These element sizes are too small in order to be used for simulation of joints and entire structures with acceptable computation times. An engineering approach for avoiding small element sizes is introduced by Turon [125]. In this approach, the maximum traction is reduced in order to assure that at least 3 elements are within the cohesive process zone, despite a larger element size. As a result, the cohesive zone is artificially increased. However, it has been demonstrated that, once a crack is initiated, only the fracture toughness value is critical for delamination simulation as crack propagation is relatively insensitive to the interface strength value. The resulting cohesive properties for the target element edge length of 0.75 mm are presented in Table 6.1.

Initiation and Propagation Criterion

Damage initiation is predicted on the basis of the quadratic stress-criterion availabe in Abaqus, which has been successfully applied in recent studies [120, 123]:

$$\left(\frac{t_I}{t_I^o}\right)^2 + \left(\frac{t_{II}}{t_{II}^o}\right)^2 + \left(\frac{t_{III}}{t_{III}^o}\right)^2 = 1 \tag{6.7}$$

In order to account for mixed-mode loading conditions, a propagation criterion containing the interaction of delamination modes is used. A study by Turon et al. [132] shows that the criterion by Benzeggagh and Kenane [133] is well suited for thermosets:

$$G = G_{Ic} + (G_{II} - G_{Ic}) \left(\frac{G_{II} + G_{III}}{G_I + G_{II} + G_{III}}\right)^{\eta_{BK}} \tag{6.8}$$

The interaction component η_{BK} can be determined by combining the results of DCB, ENF and MMB tests for a given interface. Performing a curve fit on these values, as is done in Figure 6.2, yields the interaction coefficient η_{BK} in Table 6.1. Taking into consideration the results of the delamination behavior of monolithic and hybrid interfaces in Chapter 4, where no significant change in material behavior could be

observed when reducing the testing temperature from RT to LT, the interaction coefficients determined at RT are used for the LT case, too. Nonetheless, by conducting MMB tests at LT, distinct values for η_{BK} can be obtained for LT testing as well.

Table 6.1 Summary of cohesive parameters for delamination modeling

			00//00		St//00	
			LT	RT	LT	RT
K_I=K_{II}=K_{III}		N/mm^3		10^5		
t_I^o		N/mm^2	40	20	40	20
t_{II}^o=t_{III}^o		N/mm^2	120	60	120	60
G_{Ic}^{exp}	aERR	N/mm	0.322	0.311	0.400	0.374
G_{IIc}^{exp}=G_{IIIc}^{exp}	aERR	N/mm	2.506	2.402	1.808	1.707
G_{Ic}^{th}		N/mm	0	0	-0.080	-0.044
G_{IIc}^{th}=G_{IIIc}^{th}		N/mm	0	0	0.545	0.275
G_{Ic}	tERR	N/mm	0.322	0.311	0.320	0.330
G_{IIc}=G_{IIIc}	tERR	N/mm	2.506	2.402	2.353	1.982
Initiation criterion		-		QUADS		
Propagation criterion		-		BK		
η_{BK}		-	3.6	3.6	3.1	3.1
Reference temperature		°C		132 (T_{sf})		
Testing temperature		°C	-55	23	-55	23

6.1.1 Interlaminar Behavior in Mode I

Analysis of interlaminar behavior in mode I is based on the DCB setup conforming to ASTM D5528 [105] from Chapter 4. In the following, the model setup and well as the modeling approach are introduced and discussed. As previously stated, the analysis focuses on the phenomena characteristic to the CFRP-steel interface.

Model Definition

Numerical modeling of the interlaminar behavior is done for two purposes: for validation of the experimentally determined and analytically corrected fracture toughness values based on the methodology described in Table 4.4 in Chapter 4.2, and furthermore, for investigation of the appropriate choice of modeling technique for hybrid interfaces. To save computation time, parameter variation is done using 2D models, while final validation is done on the basis of a 3D model.

Figure 6.3 shows the 3D model of the DCB setup, where the half-beams are modeled layer-wise and connected through shared nodes in Abaqus/Explicit 2021. The single layers are meshed with one element in thickness direction and an element edge-length of 2.5 mm using 8-node linear solid brick elements with reduced integration (C3D8R). The area of interest in the center part of the specimen is meshed using an

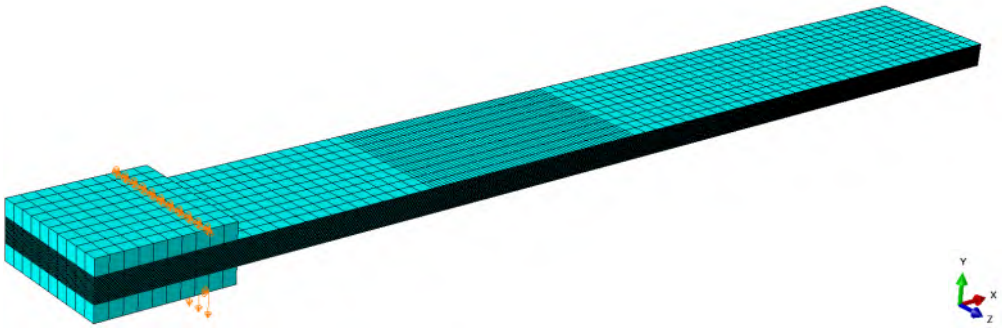

Figure 6.3 3D FE model of the DCB test setup

element edge-length of 0.75 mm in direction of crack propagation. As previously discussed, this element size in combination with the maximum interface traction assures sufficient elements to be present in the cohesive zone ahead of the crack tip, in order to accurately capture the delamination process.

The composite plies are assigned linear-elastic transverse-isotropic material properties, while the steel ply and aluminum piano hinge posses linear-elastic isotropic material behavior. The piano hinges are connected to the ends of the specimen half-beams using tie-constraints. Temperature dependent material properties are used for both engineering constants as well as cohesive parameters in Table 4.3 and Table 6.1. The cohesive behavior in the connected part of the half-beams is defined as a surface interaction based on a bi-linear traction separation law. Damage initiation and propagation are predicted by the quadratic stress criterion and BK criterion, respectively. In the region with the pre-crack, contact is defined by hard contact in normal direction and friction based contact in transverse direction with a friction coefficient of 0.1. The simulation is done in three steps. In the initial step, a uniform temperature field with $T = T_{sf}$ is applied on the model. In the second step, i.e. the cooling step, the specimen is cooled from T_{sf} down to RT or LT depending on the analysis at hand. During the second step, the translatory degrees of freedom on the hinge on the top beam are restrained, whereas the bottom half beem can move freely in accordance with the procedure during the experiments. In the third step, i.e. the loading step, the restrictions on the degrees of freedom on the top beam are still active. In addition, a displacement in y-direction is applied on the hinge of the lower half-beam, see Figure 6.3.

The 2D model of the DCB setup is built closely to the 3D model. The specimen geometry, material properties as well as boundary conditions and the simulation steps are identical. However, 2D plane-strain elements (CPE4) are used for discretezation of the model and simulation is conducted using Abaqus/Standard 2021.

Verification of Modeling Approach

CFRP-steel FMLs, similar to those discussed in the present work, have been previously subject to analysis [11,38,39]. Testing and simulation in those studies have in common that the correction for thermal residual stresses is based on the method introduced

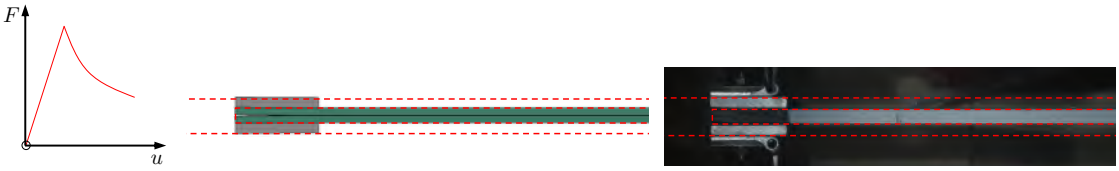

(a) Comparison of deformations in FEM and experiment after cooling to LT

(b) Comparison of deformations in FEM and experiment at LT and F_{max}

Figure 6.4 Deformation of the DCB specimen during numerical simulation and experimental testing at characteristic points of the load-displacement curve for the monolithic interface 00//00 at LT

by Yokozeki et al. [45], inferring that tip forces are not considered. In Chapter 4, the present work extends the methodology of determining the tERR[1], initially introduced by Monden [39], by the contribution of tip forces (cf. Figure 4.4). The present modeling approach postulates that both using the accurate fracture toughness value, i.e. tERR, and including a temperature step in the simulation is neccessary, even when considering RT conditions.

Numerical simulation of FMLs on meso-scale is often done without inclusion of a temperature step. As long as the effects of thermal residual stresses do not affect the goal of the investigation, this approach is acceptable. Considering the DCB setup, symmetric and balanced laminates with respect to the crack plane constitute a case where thermal residual stresses, and therefore a temperature step during simulation, can be neglected. This is the case for the monolithic specimens with a layup of $[0_{17}//0_{17}]$ for analysis of the interface 00//00. However, in case of the interface St//00 with a layup of $[0_{16}, \text{St}//0_{17}]$, the prerequisite regarding symmetry is not given. Thus, thermal effects on meso-scale are present and need to be accounted for. Which is why the numerical models considered here contain a temperature step before applying the mechanical load. Inclusion of thermal effects is especially important when dealing with delamination modeling in FMLs [38, 126, 134], yet a temperature step is not always included in numerical models [135–138].

The necessity for including a temperature step is demonstrated at the example of the monolithic interface in Figure 6.4 and the hybrid interface in Figure 6.5. The figures show the deformation of the DCB specimens at identical states during experimental testing and numerical simulation. In addition, the respective load levels are indicated on the force-displacement curve. In Figure 6.4, the example of the monolithic interface 00//00 is presented at LT. The monolithic specimen in Figure 6.4a inside the DCB test rig, after cooling to LT and before mechanical loading, is perfectly straight and shows no sign of curvature. This is sensible since the monolithic specimen is symmetric with

[1] A detailed description is provided in Chapter 4.2 and Appendix B.3

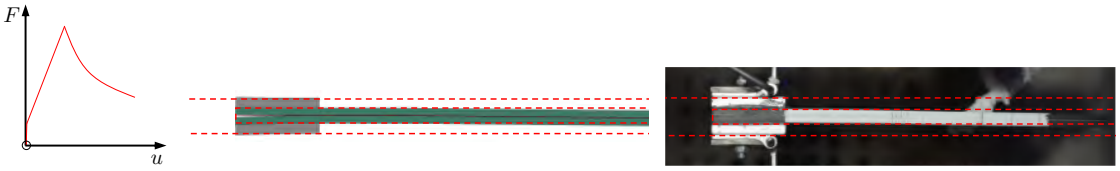

(a) Comparison of deformations in FEM and experiment after cooling to LT

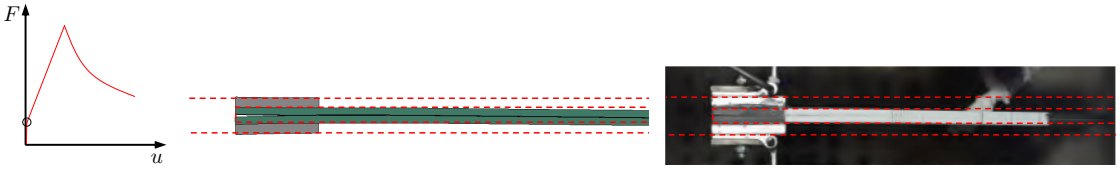

(b) Comparison of deformations in FEM and experiment after loading to kink at LT

(c) Comparison of deformations in FEM and experiment after loading to F_{max} at LT

Figure 6.5 Deformation of the DCB specimen during numerical simulation and experimental testing at characteristic points of the load-displacement curve for the hybrid interface St//00 at LT

respect to the fracture plane and exhibits no effects of thermal residual stresses on meso-scale. When loading the specimen mechanically, as is shown in Figure 6.4b, the sub-laminates separate symmetrically and the crack front starts to advance at F_{max}.

The hybrid specimen in Figure 6.5 behaves differently from the monolithic specimen. After cooling the specimen down to LT, there is a curvature visible in both the simulation and the experiment in Figure 6.5a, despite there being no mechanical load applied to the specimen. This curvature is due to the presence of thermal residual stresses. The difference in CTE between the steel ply and the composite plies of the St//00 specimen results in an inward bending of the sublaminate containing the steel ply. This effect is also present at RT, but less pronounced since the temperature difference to T_{sf} is smaller. Figure 6.6b shows the specimen from Figure 6.5a with the deformation scaled by a factor of 15. By comparison, it can be seen that the deformation state matches the model proposed by Guo et al. [112] in Figure 6.6a where bending of the sublaminates due to dissimilar layups results in contact forces at the tip of the DCB specimen[2]. The agreement between analytical theory and practical observation during testing/FE modeling serves as a first verification of the modeling approach. If no thermal step is included in the numerical model, the St//00 specimen would exhibit no curvature, thus disregarding the actual stress state of the specimen during testing.

[2]The curvature at the end of the DCB specimen is due to the difference in thermal contraction of the aluminum hinge. The tip opening is a local effect and the influence on the fracture toughness value or the shape of the force-displacement curve is negligible.

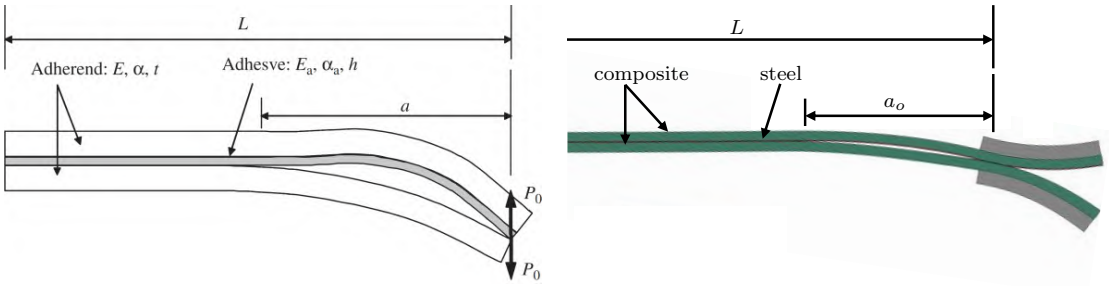

(a) Analytical model **(b)** FEM result (scale factor: 15x)

Figure 6.6 Comparison of analytical model accounting for tip contact by Guo et al. [112] and FEM simulation of St//00 interface after cooling step

The presence of thermal residual stresses in the hybrid specimen equally affects the load-displacement curve. By comparison to the behavior of the interface 00//00, a fundamental difference in the force-displacement curve of the hybrid interface St//00 can be seen in Figure 6.5. While the monolithic interface exhibits a linear slope until crack propagation at F_{max}, the hybrid interface exhibits a kink in the force-displacement curve. This kink, or knee-point, seperates the linear elastic behavior of the hybrid DCB specimen in two regions: i) a steep increase in load at practically no displacement and ii) a linear slope starting at the knee-point going up until self-similar crack propagation is initiated at F_{max}. A stepwise analysis of the FE simulation allows to explain this phenomenon:

- Cooling of the hybrid test specimen from the stress-free temperature T_{sf} during manufacturing to LT (or RT) leads to a curvature and a contact force at the tip of the sub-laminates due to the presence of meso-scale thermal residual stresses (cf. Figure 6.5a).
- The initial steep increase in the force-displacement curve up to the knee-point represents the load that is neccessary in order to overcome the contact force at the tip between the sub-laminates (cf. Figure 6.5b).
- Once the contact force is overcome at the knee-point, the sub-laminates start seperating from one another, resulting in a linear-elastic slope until the onset of crack propagation at F_{max} (cf. Figure 6.5c).

In conclusion, modeling of hybrid DCB specimens requires a profound understanding on the effects of thermal residual stresses. If neglected, errorneous modeling results are obtained as is demonstrated in the subsequent section.

Validation of Modeling Approach

Validation of the DCB models is done based on force-displacement data from the experimental results in Chapter 4. The discussion is focused on the requirement of a temperature step in the numerical model as well as the correction of fracture toughness results for thermal residual stresses based on the methodology in Figure 4.4.

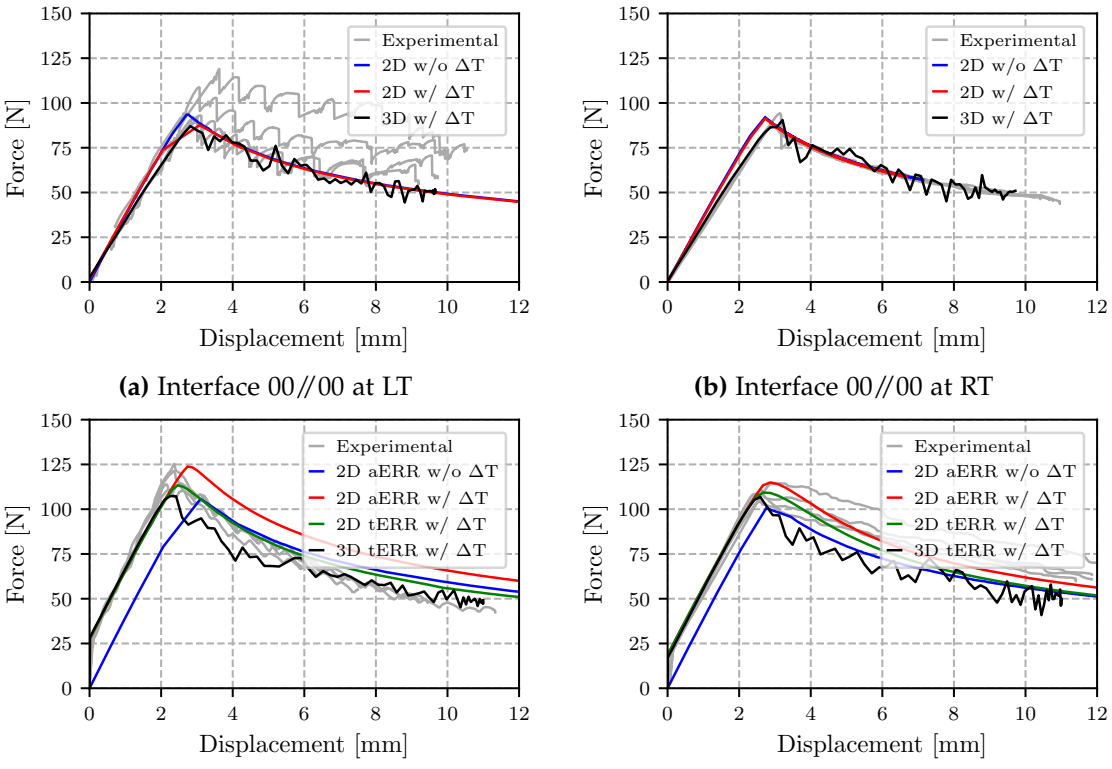

(a) Interface 00//00 at LT

(b) Interface 00//00 at RT

(c) Interface St//00 at LT

(d) Interface St//00 at RT

Figure 6.7 Experimental and numerical force-displacement diagrams of monolithic and hybrid specimens in the DCB setup

The force-displacement curves of the interface 00//00 at LT and RT are presented in Figure 6.7a and Figure 6.7a, respectively. The curves exhibit a linear slope until self-similar crack propagation is initiated at F_{max}. The delamination behavior at RT is smooth, while at LT brittle advancing of the crack front can be observed, associated with sudden load drops in the force-displacement curve. This 'stick-slip' behavior is also observed in [43] during DCB testing of monolithic specimens at -50°C. Analysis of the correct modeling approach is based on three different FE models. The first one is a 2D FE model with no temperature step (2D w/o ΔT), while the second one is a 2D FE model including a temperature step (2D w/ ΔT). The 2D models are simulated in order to gain a general understanding without excessive computation time. The third model is a 3D FE model including a temperature step (3D w/ ΔT) in an attempt to confirm the findings of the 2D study. As the interface 00//00 does not require correction for thermal residual stresses on meso-scale, tERR is equivalent to aERR (cf. Table 6.1). Both 2D FE curves result in almost identical curves at RT and LT, respectively. This indicates that inclusion of a temperature step does not alter the force-displacement curve in case of the monolithic interface. Furthermore, the numerical curves are in good agreement with the experimental result. As expected, the results demonstrate that the effect of thermal residual stresses is negligible for the 00//00 interface on meso-scale. The result of the 3D FE model confirms these findings for 3D conditions.

The force-displacement curves of the St//00 interface at LT and RT are presented

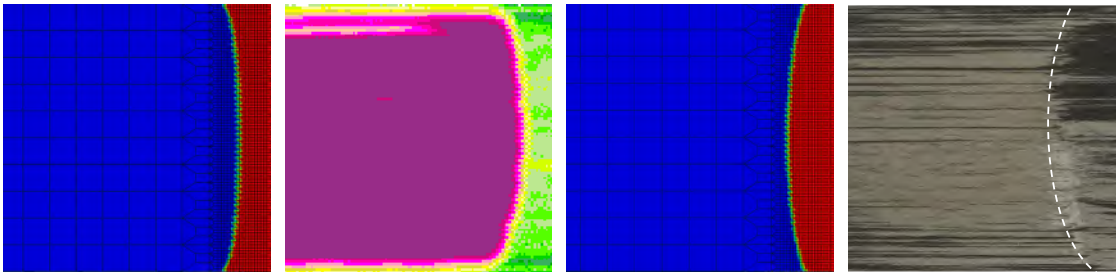

(a) 00//00 by FEM **(b)** 00//00 by US **(c)** St//00 by FEM **(d)** St//00

Figure 6.8 Comparison of crack front shapes of monolithic and hybrid interfaces at LT (FEM: fully bonded surface in blue, fully unbonded surface in red)

in Figure 6.7c and Figure 6.7d, respectively. As discussed in the previous section, the characteristic knee-point in the force-displacement curves of the hybrid interface represents a fundamental difference to the monolithic interface. In total, four numerical models are analyzed for the appropriate modeling approach for hybrid interfaces in the DCB configuration.

- 2D FE model using the uncorrected fracture toughness value (aERR) without application of a temperature step (2D aERR w/o ΔT)
- 2D FE model using the uncorrected fracture toughness value (aERR) but with application of a temperature step (2D aERR w/ ΔT)
- 2D FE model using the corrected fracture toughness value (tERR) with application of a temperature step (2D tERR w/ ΔT)
- 3D FE model using the corrected fracture toughness value (tERR) with application of a temperature step (3D tERR w/ ΔT) for confirmation of the 2D models

If the effects of thermal residual stresses are neglected altogether, as is the case for the model '2D aERR w/o ΔT', the characteristic behavior of the hybrid interface, e.g. the knee-point, is not captured accurately, resulting in a severe misprediction. If a temperature step is included but combined with the uncorrected fracture toughness in model '2D aERR w/ ΔT', then the knee-point is captured by the simulation, however, crack propagation occurs at higher loads compared to experimental data. Only when both a temperature step and the corrected fracture toughness are used, as is the case for the model '2D tERR w/ ΔT', excellent agreement between simulation and experiment can be achieved for the position of the knee-point, the subsequent linear-elastic behavior as well as the crack propagation behavior. The result of the 3D model agrees well with the corresponding 2D model considering the linear-elastic behavior until crack initiation. However, crack propagation takes place at a slightly lower load level compared to the 2D models. At increasing delamination lengths, agreement between 2D and 3D models is good.

Additional analysis of the 3D models is conducted using VCCT. Therein, the monolithic and hybrid interfaces at LT are analyzed for parasitic mode effects. Furthermore, the shape of the crack front is verified. Figure 6.8 shows the crack front predicted by

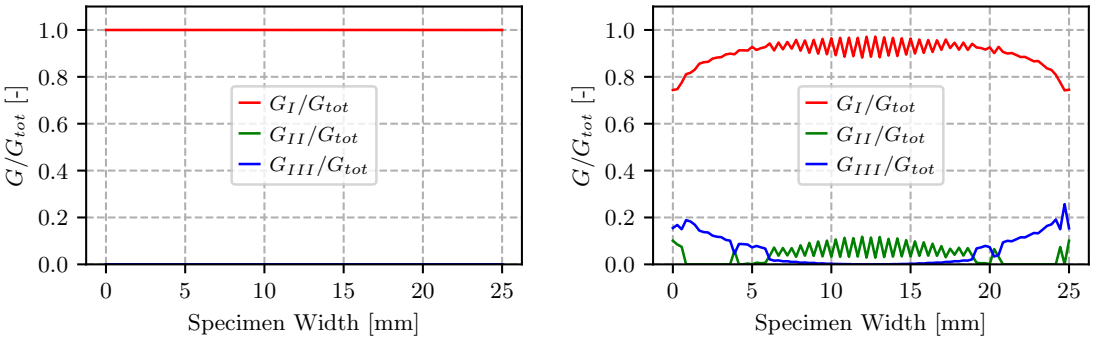

(a) Interface 00//00 **(b)** Interface St//00

Figure 6.9 Contribution of parasitic modes along the specimen width in 00//00 and St//00 DCB specimen determined by VCCT at LT

the 3D FE simulation to an ultrasonic scan (US) in case of the monolithic interface. The hybrid specimen is split in two halves after testing in order to check the fracture surface. Agreement between simulation and experiments is very good, thus demonstrating the capability of the 3D models to capture the physically correct shape of the crack front. The 2D FE analysis assumes a constant crack front, which could explain the small differences between 2D and 3D results in Figure 6.7. As for parasitic mode effects, Figure 6.9 shows the contributions of the individual ERR modes along the specimen width in the monolithic and hybrid DCB specimens at LT. Contrary to the monolithic interface, the hybrid interface appears to be affected by parasitic contributions of mode II and mode III loads near the specimen edges. In the center of the hybrid specimen, however, mode I loading is dominant again. In Table 6.2, the mode I, mode II, and mode III contributions to the total ERR determined by VCCT is summarized for the monolithic and hybrid interfaces at LT and RT, respectively. Here, the maximum values along the specimen width as well as values at the center of the specimen are compared. When looking at the maximum values, mode I loading makes up for only 68 % and 79 % of the total ERR in the St//00 interface at LT and RT, respectively. However, in the center of the specimen, the mode I contribution is at around 99 % and 97 % of the total ERR for the hybrid interfaces. Taking into account the oscillation in the center area, the mode I ratio in the specimen is still around 95 %. Here, the mode I loading is almost as pure as in the monolithic specimens. The detailed analysis by VCCT reveals that edge effects are present in the hybrid specimens. This affects data reduction since the underlying methods assume perfectly isolated modes during testing. Despite the inaccuracy introduced by parasitic mode contributions in the hybrid specimens, the general approach for data reduction and interface property derivation is considered acceptable, as the comparison in Figure 6.7 shows good agreement between numerical and experimental results. In addition, the overall isolation of the mode I contribution to the total ERR during DCB testing of the hybrid interface in Figure 6.9 is considered acceptable, given the fact that perfect mode isolation in dissimilar interfaces is not feasible. However, to further improve data reduction, the crack tip element method by Yokozeki [139] can be applied in order to account for the contribution of parasitic modes.

Table 6.2 ERR values at the center of the DCB specimens, maximum ERR values as well as the resulting mode-mixture by VCCT analysis

Interface	Temp.	G_{tot}		G_I		G_{II}		G_{III}		G_I/G_{tot}		G_{II}/G_{tot}		G_{III}/G_{tot}	
		max.	center	max.	center	max.	center	max.	center	max.	center	max.	center	max.	center
		N/mm	N/mm	N/mm	N/mm	N/mm	N/mm	N/mm	N/mm	%	%	%	%	%	%
00//00	RT	0.342	0.314	0.342	0.314	0.000	0.000	0.000	0.000	99.9	99.9	0.00	0.00	0.00	0.00
	LT	0.354	0.327	0.354	0.327	0.000	0.000	0.000	0.000	99.9	99.9	0.00	0.00	0.00	0.00
St//00	RT	0.453	0.339	0.359	0.335	0.040	0.003	0.055	0.000	79.1	98.9	8.80	1.00	12.1	0.00
	LT	0.508	0.307	0.346	0.298	0.042	0.009	0.120	0.000	68.1	96.8	8.23	3.18	23.7	0.00

In conclusion, it can bee seen that choosing the correct modeling approach, i.e. incorporating a temperature step for both the RT and LT simulation, and using the corrected fracture toughness values as CZM input, i.e. tERR instead of aERR, is crucial for accurate simulation of the delamination behavior of the hybrid interface St//00. In case of the monolithic interface 00//00, thermal residual stresses on meso-scale are negligible, therefore temperature effects on the fracture toughness can be neglected.

6.1.2 Interlaminar Behavior in Mode II

Analysis of interlaminar behavior in mode II is conducted in analogy to the approach in case of mode I loading. The model setup and well as the modeling approach are introduced and discussed, while focusing on temperature related phenomena.

Model Definition

Modeling of the ENF specimen is done almost indentical to the DCB case. For efficiency purposes, rather than modeling the entire specimen only the free length in between the mounting points is modeled. The material properties, mesh strategy as well as surface interactions are implemented identical to the DCB case. Also, the multi-step approach including a cooling and a loading step are retained. During the cooling step, the nodes at the lower left edge of the ENF specimen serve as a floating bearing (u_2=u_3=0) and the nodes of the lower right edge as a fixed bearing (u_1=u_2=u_3=0), see Figure 6.10. During the mechanical loading step, load introduction is done using a rigid center pin. Therein, a displacement along the vertical axis is applied, whilst locking the remaining translatory degrees of freedom.

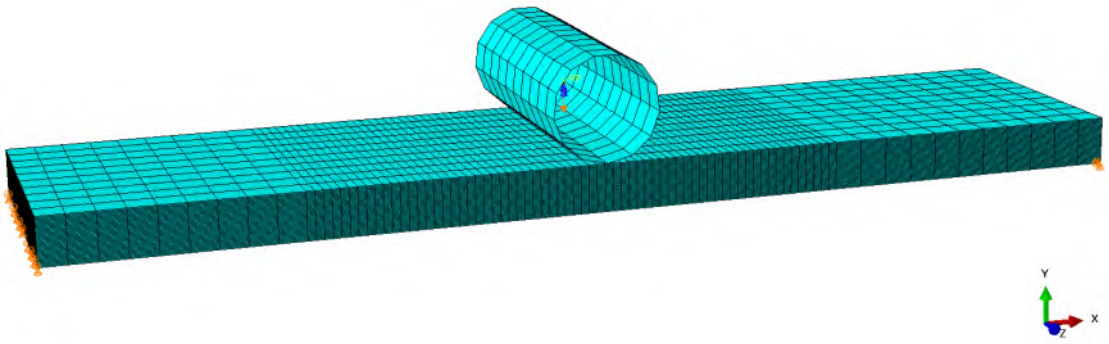

Figure 6.10 3D FE model of the ENF test setup

The 2D model of the ENF setup is defined in accordance with the 3D model. Except, 2D plane-strain elements (CPE4) are used for discretezation of the model and simulation is conducted using Abaqus/Standard 2021.

Verification of Modeling Approach

In the previous section, investigation of the DCB case demonstrates the necessity of including a temperature step and using the corrected fracture toughness value as CZM input in the simulation in order to capture the phenomena related to thermal residual stresses in a CFRP-steel FML. The present section focuses on the effects of temperature on the ENF setup.

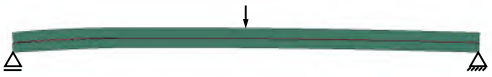

(a) Steel ply in top sublaminate after cooling to LT and before mechanical loading

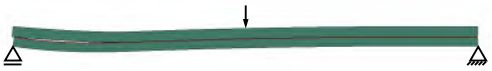

(b) Steel ply in bottom sublaminate after cooling to LT and before mechanical loading

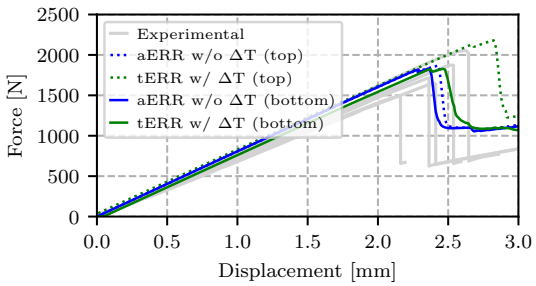

(c) Load-displacement curves at LT

Figure 6.11 Effect of the position of the steel ply in the St//00 FML on the ENF test

For this purpose, different configurations of the ENF setup are studied in Figure 6.11. Two configurations, namely one with the steel ply in the top sublaminate and one with the steel ply in the bottom sublaminate are presented in Figure 6.11a and Figure 6.11b, respectively. It should be noted, during experimental testing, the steel ply is always located in the bottom sublaminate. As oppose to the DCB case, the loading condition in the ENF setup is not symmetric with respect to the midplane of the laminate. Thus, the curvature of the specimen, and therefore the location of the steel ply, affects the mechanical behavior. The curvature of the specimen in Figure 6.11a is directed opposite to the direction of the external force, while the specimen in Figure 6.11b is curved in direction of the external force. When neglecting temperature effects, i.e. not including a temperature step and using aERR as CZM input, the resulting curves in Figure 6.11c are very close. The modeling approach oblivious to the effects of thermal residual stresses falsely yields good agreement with the experimental force-displacement curves. However, when including a temperature step and using the tERR, then only the model with the correct location of the steel ply, i.e. in the bottom sublaminate, is in agreement with experimental data. In the simulation 'tERR w/ ΔT (top)', the false curvature due to the wrong position of the steel ply results in a severe overestimation of the delamination onset. This is again an example of errorneous simulation results, when thermal effects are disregarded.

Validation of Modeling Approach

Similarly to the analysis of mode I delamination, validation of the numerical models in Figure 6.12 for mode II delamination is based on force-displacement data from the experimental results in Chapter 4. The discusson is focused on the requirement of a temperature step in the numerical model as well as the correction of fracture toughness results for thermal residual stresses.

Figure 6.12a and Figure 6.12b show the force-displacement curves of the 00//00 interface at LT and RT, respectively. The curves of the experimental tests exhibit a linear slope until unstable crack propagation is initiated at F_{max}. No substantial differences in the curve shapes between RT and LT testing conditions is observed. Three numerical models are studied at each temperature level. They include a 2D FE model with no temperature step (2D w/o ΔT) as well as a 2D FE model including a temperature step (2D w/ ΔT). The third model is a 3D FE model including a temperature step (3D w/ ΔT) in an attempt to confirm the findings of the 2D study for the 3D case. Since the 00//00 interface does not require correction for thermal residual stresses, aERR is equivalent to tERR. The shape of the force-displacement curves of both 2D FE models are almost indentical at LT and RT. This effect was previously observed at the example of monolithic specimens in the DCB setup. It is therefore also confirmed for mode II loading that inclusion of a temperature step does not alter the force-displacement curve. Overall, agreement between the 3D and 2D FE models is good, despite a slightly lower initial stiffness in the 3D case. Considering the delamination onset load, the numerical models slighly underestimate the load drop of the monolithic interface at both RT and LT. However, regarding the question of including a temperature step, the numerical results confirm that in case of the monolithic interface 00//00 thermal effects can be neglected.

Figure 6.12c and Figure 6.12d show the force-displacement curves of the St//00 interface at LT and RT, respectively. Unlike the DCB setup, there are no characteristic differences noticeable in the curve shape between monolithic and hybrid interfaces in the ENF setup. Analysis of the appropriate modeling approach for hybrid interfaces in the ENF configuration is done on the basis of the same four numerical model types as previously analysed for the DCB case: '2D aERR w/o ΔT', '2D aERR w/ ΔT', '2D tERR w/ ΔT' and '3D tERR w/ ΔT'. If the effect of temperature is completely disregarded, as is the case for '2D aERR w/o ΔT', agreement between numerical and experimental results is good. However, this agreement is deceptive. It could be wrongfully assumed that inclusion of thermal effects in delamination modeling of hybrid interfaces is negligible. However, this is not the case as shows the study on the position of the steel ply in the ENF setup. Ignoring thermal effects can potentially lead to severe mispredictions when transferring the modeling data obtained from the ENF test, e.g. aERR, into simulations of more complex structures, in particular when dealing with asymmetric CFRP-steel laminates. If a temperature step is applied but used with the aERR instead of the tERR in '2D aERR w/ dT', then the delamination onset is significantly underestimated. Applying both a temperature step and including the tERR in the simulation, as is the case for '2D tERR w/ dT', yields good agreement between numerical and experimental force-displacement curves, which is also confirmed by the 3D model '3D tERR w/ dT'.

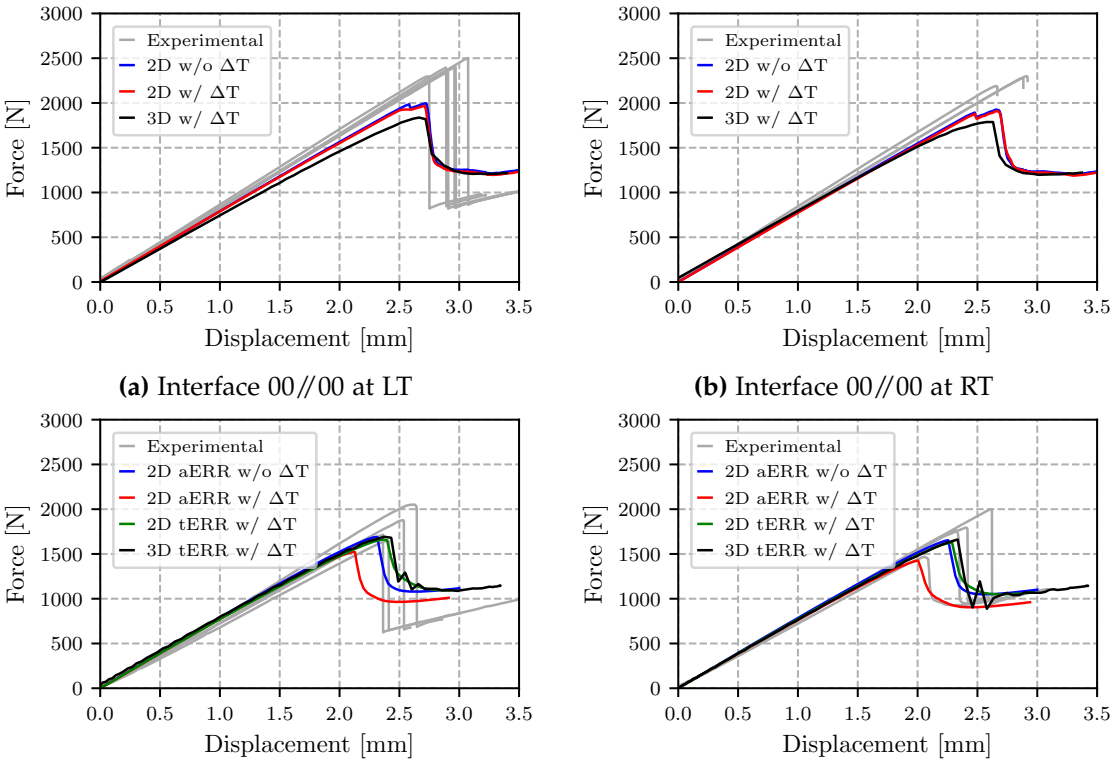

(a) Interface 00//00 at LT

(b) Interface 00//00 at RT

(c) Interface St//00 at LT

(d) Interface St//00 at RT

Figure 6.12 Experimental and numerical force-displacement diagrams of monolithic and hybrid specimens in the ENF setup

In Figure 6.13, the contribution of parasitic modes to the total ERR in case of the monolithic 00//00 and hybrid St//00 interface in the ENF setup at LT is presented. Similarly to the DCB model, the mesh in the region of interest is refined to an element edge length of 0.25 mm and analyzed using the VCCT method in order to quantify mode-mixity. In can be seen that the hybrid ENF specimen suffers from noticeable parasitic effects from mode I and mode III contributions near the specimen edges. As discussed in detail during analysis of the monolithic and hybrid DCB specimens, parasitic modes at hybrid interfaces cannot be fully eliminated due to the nature of dissimilar materials that are connected. Due to the fact that the parasitic effects are mostly limited to the area in vicinity of the specimen edges, it is also concluded for the ENF case that the methodology for data reduction as presented in Figure 4.4 is applicable to hybrid interfaces.

All in all, the study on the ENF setup confirms the findings in the context of analyzing the DCB setup. Therein, selection of the correct modeling approach, i.e. incorporating a temperature step for both the RT and LT simulation, and using the corrected fracture toughness values as CZM input, i.e. tERR instead of aERR, is crucial for accurate simulation of delamination effects for the hybrid interface. In case of the monolithic interface, however, temperature effects on delamination modeling can be neglected, since thermal residual stresses on meso-scale are negligible.

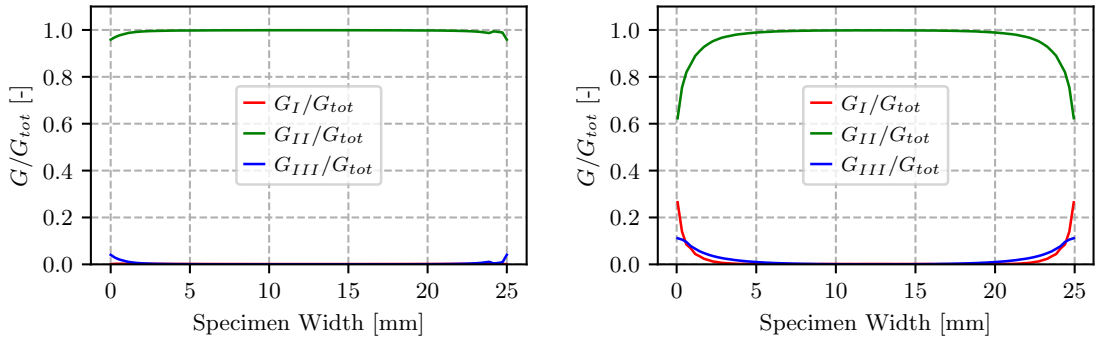

(a) Interface 00//00

(b) Interface St//00

Figure 6.13 Contribution of parasitic modes along the specimen width in 00//00 and St//00 ENF specimen determined by VCCT at LT

6.1.3 Prediction of Delamination Onset

Thus far, emphasis was laid on the understanding and modeling of phenomena related to the effects of meso-scale thermal residual stresses in hybrid interfaces. The present section deals with the question of whether or not the previously derived recommendations with respect to delamination modeling of hybrid interfaces has any significance for the practical design of composite structures. In an attempt to answer this question, the delamination onset is chosen as the relevant parameter. In Figure 6.14, the onset of delamination, comprised of the initiation force F_i and initiation displacement u_i, for the hybrid interface in both DCB and ENF setup is presented at RT and LT, respectively. The delamination onset observed during experimental testing is plotted including the standard deviation. Additionally, all numerically determined delamination onset points are indicated as well.

Comparison of the delamination onset at RT and LT in case of the DCB setup in Figure 6.14a and Figure 6.14b suggests that ignoring either one of the requirements, i.e. a temperature step and corrected fracture toughness, leads to inaccurate prediction of the delamination. For example, the error regarding delamination onset displacement u_i in model '2D aERR w/o dT' at LT is as large as 29 % compared to the experimental result. However, if both a temperature step and the corrected fracture toughness value are employed, this leads to significantly better agreement with experimental data regarding delamination onset. In Figure 6.14c and Figure 6.14d, the delamination onset for the ENF setup predicted by FEM and observed during the experiment is shown at LT and RT, respectively. Delamination onset is predicted accurately by the 2D and 3D models that include both a temperature step and the corrected fracture toughness value, since the FE results are all inside the bonds of the standard deviation during experimental testing. The slight decrease in prediction accuracy at LT compared to RT, which is present for both DCB and ENF testing, is assumed to result from the increasing effect of parasitic modes with decreasing temperature as discussed in the previous sections based on VCCT analysis (cf. Figure 6.9 and Figure 6.13)

It should be noted that the model '2D aERR w/o dT' is deceptive, because it

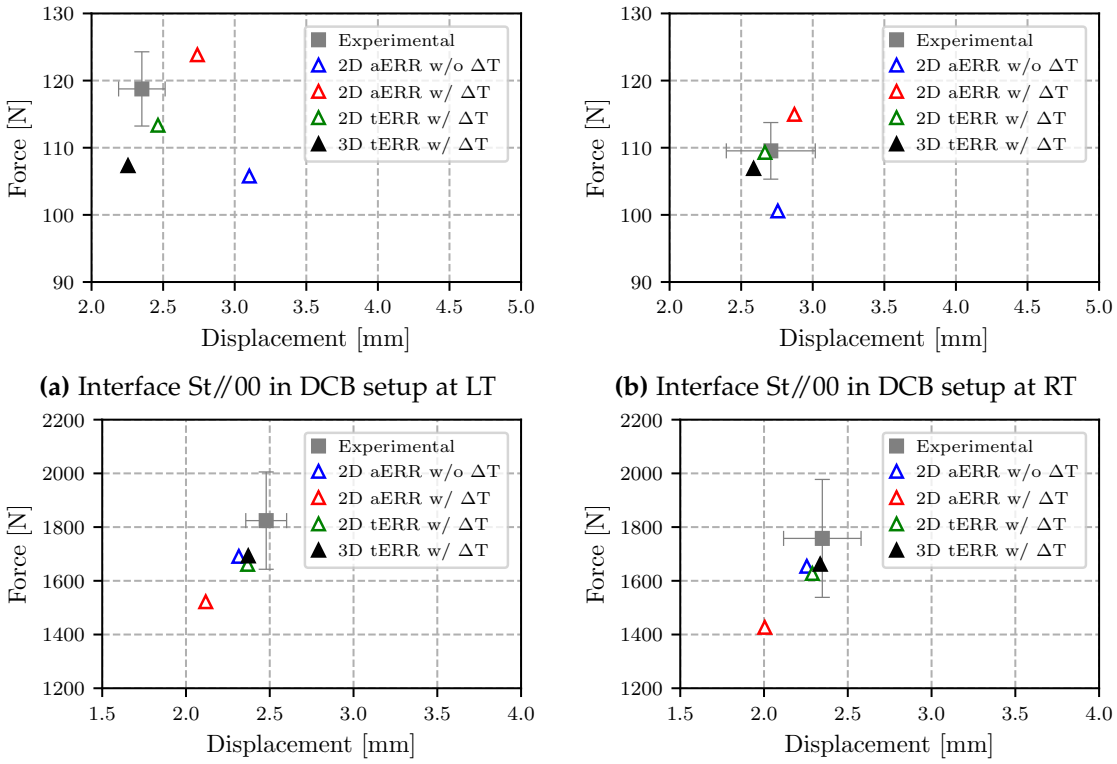

(a) Interface St//00 in DCB setup at LT

(b) Interface St//00 in DCB setup at RT

(c) Interface St//00 in ENF setup at LT

(d) Interface St//00 in ENF setup at RT

Figure 6.14 Delamination onset of the hybrid interfaces observed during the experiment and prediction by numerical simulation

falsely suggests good agreement with experimental data. However, the thermal effects present in the ENF specimen, e.g. the curvature due to thermal residual stresses and the thereof resulting parasitic effects on the fracture toughness, are not captured. Further, agreement in the force-displacement curves is limited to modeling the exact same ENF test from which the fracture toughness value is deduced. Once the CZM parameters including the fracture toughness are transferred to other problems, e.g. larger structures, results will be errorneous.

To conclude, the choice of modeling approach for hybrid interfaces not only affects the qualitative curve behavior, e.g. the knee-point in the force-displacement curve of the DCB test, or the specimen curvature after cooling but also significantly influences the accuracy with respect to delamination onset prediction.

6.1.4 Summary and Conclusions on Delamination Modeling

In the present section, awareness is raised on the peculiarities of hybrid interfaces, especially in CFRP-steel laminates, where the difference in CTE and stiffness of the constituents leads to significant thermal residual stresses. Mode I and mode II delamination analysis of hybrid interfaces is generally done using the DCB and ENF test setup in combination with asymmetric specimens [11,38,39], e.g. [0_{16},St//0_{17}]. Due to

the presence of thermal residual stresses on meso-scale, the behavior of the specimens is altered, e.g. by a characteristic kink in the load-displacement behavior during DCB testing. This kink is associated with the curvature of the sublaminates of the hybrid specimens due to thermal residual stresses, which is not present in symmetric monolithic specimens. Furthermore, the aERR derived from experimental data need to be corrected for the contribution of thermal residual stresses, since additional bending moments and shear forces are acting on the hybrid interface.

Guidance is provided for the accurate derivation of the fracture toughness value based on experimental test data. The methodology for determination of the tERR is shown in Figure 4.4. Starting with the aERR, the tERR is obtained by applying the correction methods to a given experimental test setup. While measures such as the sublaminate technique to minimize effects due to asymmetric layups are applied during specimen manufacturing, correction for large deformations, load introduction and beam compliance are done during evaluation of the test results. In turn, correcting effects arising from thermal residual stresses is done by introducing correction terms on the energy release rate after evaluation of the test results. Verification by CZM and VCCT demonstrates that by employing this methodology, the actual fracture toughness of the interface is obtained and can be subsequently used for comparison purposes or as input for delamination modeling.

Strageties for accurate modeling of hybrid interfaces are discussed. In addition to providing a comprehensive set of input data for delamination modeling of monolithic and hybrid interfaces at RT and LT, the present study underlines the importance of applying a temperature step as well as using the tERR as input for delamination modeling using CZM. While practically no meso-scale thermal residual stresses are present in the monolithic interface 00//00, the hybrid interface St//00 is highly affected by thermal residual stresses. Considering the DCB setup, only application of a temperature step allows to capture the kink in the load-displacement curve. Additionally, only by employing the tERR both delamination onset and delamination propagation is predicted accurately. Similarly, only application of both a temperature step and using the tERR yields accurate results for the St//00 interface in the ENF setup. This observation is valid for both RT and LT.

Furthermore, the effect of low temperature on the fracture toughness of hybrid and monolithic interfaces is investigated. The interlaminar fracture toughness G_{Ic} of both monolithic and hybrid interfaces remain constant between RT and LT, as the changes are in the same order or magnitude as the standard deviation during testing. No R-curve behavior is observed for either one of the monolithic or hybrid interfaces. The fracture toughness of the monolithic interface in mode II remains almost unchanged, while G_{IIc} of the hybrid interface increases with decreasing temperature. Considering the DCB and ENF test results at both RT and LT, the hybrid interfaces consistently exhibit slightly lower fracture toughness values compared to the monolithic interfaces.

Regarding future research, three main areas of interest are identified:

The correction terms introduced by Guo [112], accounting for the effects of dissim-

ilar sublaminates in contact, are derived for a two-constituent system composed of the sublaminates made of one material as well as an adhesive layer as second material. Considering the similarity of the setup, the correction method by Guo [112] is applicable to purely UD laminates with one metal layer. Nonetheless, the method should be extended to be applciable to arbitrary composite stackings, similarly to the extension by Yokozeki et al. [45] on the basis of the correction method introduced by Nairn [44].

The validation of the present data reduction, data correction and simulation methodology is solely based on one hybrid layup. Further validation is required with variation of metal volume fraction and subsequently different stacking sequences, usage of multidirectional laminates and multidirectional interfaces, as well as alternative hybrid laminates, e.g. GLARE where substantially less thermal residual stresses are present. Also, extending the low temperature level to even lower temperatures, e.g. cryogenic, can help to determine the limitations of the proposed procedure.

Instead of correcting the aERR for parasitic effects due to thermal residual stresses in order to yield the tERR, one could modify the stacking sequence of the laminates in order to minimize the effects of thermal residual stresses altogether. Therefore, in future research, the investigation of hybrid interfaces is extended to stacking sequences that exhibit less thermal residual stresses.

6.2 Bolt-Bearing Modeling Strategy

After investigating the impact of thermal residual stresses on the numerical simulation of interlaminar behavior in CFRP-steel FMLs, the present section focuses on the bolt-bearing behavior of this specific FML class. The investigation includes an examination of delamination phenomena and its effects on the bearing behavior. However, of greater significance, the necessity of including thermal effects in the numerical analysis procedure is investigated, thereby addressing *Working Hypothesis III*. For this purpose, first of all, a literature study is done in order to summarize previous research on modeling strategies. Then, a modeling strategy for simulation of the bolt-bearing behavior of CFRP-steel FMLs is derived, validated and applied to studying the reinforcement effect in FMLs.

6.2.1 Literature Review

A literature review is conducted in order to evaluate previously published modeling strategies for numerical analysis of FMLs composed of CFRP and steel/titanium. The most relevant work of the review is summarized in Table 6.3. Therein, the focus is directed towards modeling of the pin/bolt including clamping, modeling of the composite as well as metal constituent, consideration of delamination, and inclusion of thermal effects.

Pin- and bolt-bearing loading scenarios are equally considered in CFRP-St and CFRP-Ti based FML studies. In case of bolt-bearing, lateral constraint due to clamping of the bolt needs to be accounted for. This is done either by applying a concentrated force on the bolt [28,141] or a pressure [140]. Fink [37] justifies omitting application of

Table 6.3 Literature overview on strategies for numerical modeling of steel and titanium based FML bolted joints

	Van Rooijen [3]	Hundley [28]	Fink [37]	Both [11]	Cardoso [140]	Petersen [38]	Gerendt et al. [141]
Year	2006	2009	2010	2013	2016	2019	2019
Material	GLARE, GLARE + steel	CFRP-titanium	CFRP-steel, CFRP-titanium	CFRP-steel	CFRP-titanium	CFRP-steel	GFRP-steel, CFRP-titanium[1)]
Temperature	RT	RT	RT	RT	RT	RT	RT
Bolt/pin	rigid pin	rigid bolt	elastic isotropic bolt	not modeled, load BC applied	elastic isotropic bolt	rigid pin	rigid bolt
Clamping	no	bolt force applied	no	n/a	pressure applied	no	bolt force applied
Composite	3D Hashin + constant degradation (UMAT)	3D Hashin + exponential degradation (UMAT)	2D Hashin + energy based lin. degradation[2)]	2D Cuntze FMC no degradation	2D/3D Hashin + degradation[3)]	3D Cuntze FMC + constant degradation (USDFLD)	2D Puck ASPC + energy based exponential degradation (UMAT)
Metal	von Mises yield criterion + isotropic plasticity	von Mises yield criterion + isotropic plasticity	von Mises yield criterion + isotropic plasticity	von Mises yield criterion + isotropic plasticity	von Mises yield criterion + isotropic plasticity	von Mises yield criterion + isotropic plasticity	von Mises yield criterion + isotropic plasticity
Element type	reduced integrated continuum elements (C3D8R)	C3D8R	bolt: continuum element (C3D8), FML: red. int. cont. shell element (SC8R)	layered shell elements	SC8R/C3D8R	linear volume elements	reduced integrated composite volume elements (C3D8RC3)
Delamination	no	COH3D8 between CFRP // titanium	no	no	no	no	no
Thermal effects	no	no	$\Delta T = -64°C$, T_{sf}=T_{cure}=180°C	$\Delta T = -64°C$, T_{sf}=$T_{g,onset} - 20°C$	no	$\Delta T = -109°C$, T_{sf}=132°C	no

[1)] exp. data used from Fink [37]; [2)]Abaqus internal material model; [3)] 2D: Abaqus internal material model/ 3D: VUMAT

a clamping force by refering to the choice of elements (continuum shell) which do not account for stresses in thickness direction.

While the modified Hashin criterion historically dominated the modeling of composite material behavior, recent studies have introduced more advanced theories such as the Puck ASPC and Cuntze FMC. In the case of Abaqus, where only the 2D formulation of the Hashin criterion is available, researchers have resorted to implementing 3D material models. For instance, the 3D formulation of the modified Hashin criterion is implemented in UMATs [3, 28] and VUMATs [140] in order to be used with 3D continuum elements (C3D8R). However, despite using the 2D formulation of the Hashin criterion implemented in Abaqus, Fink [37] still yields good agreement between experimental and numerical results. While implementing 3D material models for application with 3D elements seems reasonable for analyzing the bolt-bearing case, the motivation behind combination of the 2D formulation of the Puck ASPC with 3D elements by Gerendt [141] is not straightforward.

Most degradation models utilize sophisticated linear or exponential formulations to represent damage progression, relying on fracture energies or degradation states. However, a simpler approach involving a constant degradation after damage initiation has proven to yield similarly good results. For instance, van Rooijen [3] employs a constant mode-wise stiffness degradation to 0, while Petersen [38] reduces the stiffness of an element to 1 % and 20 % of its original value for FF and IFF, respectively. There is greater consensus regarding modeling of the metal constituent. All references apply isotropic elasticity, the von Mises yield criterion for damage initiation, and isotropic hardening for modeling of plasticity in the steel or titanium constituent.

Most research acknowledges that delamination is a relevant failure type in FMLs. However, only few examples actually include delamination based on CZM into their bearing model [28,142]. While Fink [37], Both [11] and Petersen [38] analyze delamination in the transition zone of a locally hybridized laminate seperately from the bearing behavior, Cardoso [140] and Gerendt [141] neglect delamination altogether.

Incorporating thermal effects typically involves introducing a temperature step and utilizing temperature-dependent material properties. When thermal effects are not included, there is usually no explanation provided as to why neglecting thermal residual stresses is justified [3,28,140,141]. However, if thermal effects are included, this is generally explained by the necessity of including thermal residual stresses in order to accurately capture the stress state of the FML. Within the literature that does account for thermal effects, determination of the stress-free temperature has evolved during time. While Fink [37] assumes the stress-free temperature to be equivalent to the curing temperature, Both [134] uses an approximation for T_{sf}, whereas Petersen [38] determines the stress-free temperature experimentally based on asymmetric specimens that are reheated in an oven until the thermally induced curvature vanishes.

Considering the findings from the literature study, it is crucial to further investigate the relevance of incorporating thermal effects and delamination phenomena. The existing literature lacks a clear consensus on whether these effects should be included

in the analysis process and the extent of their impact on the load bearing behavior of CFRP-steel bolted-joints. Therefore, a thorough examination is needed in order to better understand these aspects, thereby providing an appropriate strategy for numerical modeling.

6.2.2 Bolt-Bearing Model

In the following sections, the model setup including the underlying material models and application of boundary conditions are presented in detail.

Model Setup

The bearing model in Figure 6.15 is set up as a half-model by taking advantage of the symmetry along the midplane of the laminate (x-y plane). In case of delamination modeling, the single plies are modeled individually and connected on the basis of CZM by means of cohesive surface contacts. If delamination is not included, the single plies are connected via tie-contraints. Bolt and washer a modeled as one part. Clearance between the bolt and the hole is based on the mean allowable values for the bolt and hole diameters according to AITM 1-0009. The geometry data is presented in Table 6.4. Contact between bolt and laminate is defined as hard contact in normal direction, while a friction value of 0.1 is used for the transverse behavior.

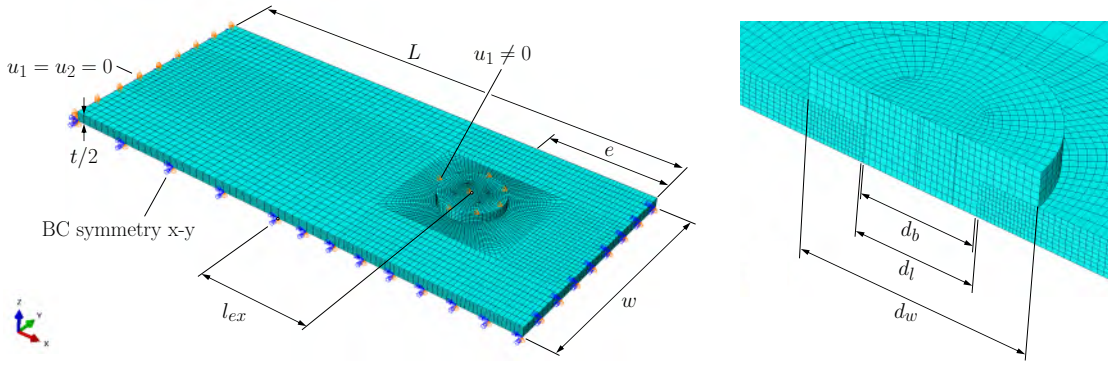

(a) Model overview **(b)** Bolt and hole dimensions

Figure 6.15 3D FE model of bolt-bearing specimens

The composite plies exhibit transversely-isotropic material behavior including damage. The steel sheets in the FML configurations are assigned isotropic elastic behavior with isotropic hardening. Despite the fact that the metal sheets exhibit slightly different stiffness and strength properties in longitudinal and transverse direction, only longitudinal properties are used for the FEM simulations for simplicity. The bolt and washer are modeled with isotropic linear elastic material behavior without damage. The material models are described in more detail in the subsequent section.

The single plies are discretized with one element in thickness direction. For defining the in-plane element size, the single plies are divided into different sections. In the

Table 6.4 Bolt-bearing test setup according to AITM 1-0009

Dimension	Value	Dimension	Value
Specimen length, L	100 mm	Bolt diameter, d_b	6.325 mm
Specimen width, w	45 mm	Hole diameter, d_l	6.362 mm
Edge-distance, e	25 mm	Washer diameter, d_w	12.7 mm
Extensometer range, l_{ex}	25 mm	Bolt torque, T	1.3 Nm

area under the washer, an element edge-length of 0.2 mm is defined. In radial direction, the element edge-length increases gradually from 0.2 mm to 0.35 mm to 0.8 mm. In the outer edges furthest away from the bolt hole, the in-plane element edge length is 1.6 mm. Discretization based on a mesh study. Bolt and washer are meshed with an element size of 0.4 mm. Steel plies are meshed using reduced integration linear brick elements (C3D8R) with hourglass control, while the composite plies are modeled using general-purpose continuum shell elements (SC8R) with reduced integration and hourglass control.

As previously mentioned, only half of the test setup is modeled in order to save computation time. Therefore, symmetry along the x-y plane is applied for both the laminate and the bolt with washer. Clamping of the specimen is simulated by restricting in-plane deformation at the back side ($u_1 = u_2 = 0$). In analogy to the experiments, load introduction is done displacement controlled. Therein, a displacement u_1 is applied on the bolt surface. In order to compare the FE results to the experimental results, a virtual extensometer with a range l_{ex} is modeled by defining reference points on the bolt and laminate according to the experimental test setup (see Figure 6.15). During post-processing, the hole elongation ε_B and bearing stress σ_B are calculated as follows:

$$\varepsilon_B = \frac{|u_1^{RP1} - u_1^{RP2}|}{d_n} \cdot 100\ \% \tag{6.9}$$

$$\sigma_B = \frac{RF_1}{t/2 \cdot d_n} \tag{6.10}$$

with the displacements at the reference points u_1^{RP1} and u_1^{RP2}, the reaction force at the bolt RF_1, the nominal hole diameter d_n and half the laminate thickness $t/2$ due to the symmetry condition. During experimental testing, a bolt torque $T = 1.3$ Nm is applied. In order to account for the clamping in thickness direction, the bolt torque is translate to an axial force F_T along the vertical bolt axis by assuming a torque coefficient of 0.2 according to [141]:

$$F_T = \frac{T}{0.2 \cdot d_b} \tag{6.11}$$

In an attempt to accurately capture the thermal effects during the experiments, the order of simulation steps is defined as depicted in Figure 6.16. During the initial step, a constant temperature field of $T = T_{sf}$ is applied. Then, the specimen is cooled from T_{sf} to RT, thereby simulating the cool-down after manufacturing and the build-up of thermal residual stresses. Determination of T_{sf} adjusted for relaxation effects is explained in more detail in Section 7.2.3. Application of the bolt torque is done

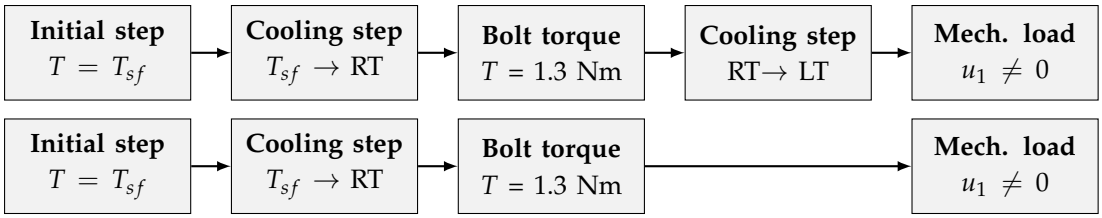

Figure 6.16 Overview of modeling steps for LT (top) and RT (bottom) FE simulation

similarly to experimental testing in a subsequent step at RT conditions. In case of LT modeling, an additional cooling step from RT to LT is included. This way, the additional build-up of stresses as well as the loss of bolt clamping due to the difference in CTE between bolt and laminate is accounted for. During both cool-down stages the bolt is free to move in longitudinal direction so that no additional forces build up. The final step consists in the application of the mechanical load for the actual bolt-bearing simulation. In case of of RT modeling, the cooling step between bolt torquing and load intrduction is omitted.

Material Model for Composites

Modeling of composite material behavior is done utilizing the built-in capabilities of Abaqus, where linear elastic behavior is defined based on engineering constants. The criteria for damage initiation in the composite plies rely on the modified Hashin criterion [143] in plane-stress[3], comprising failure mechanisms by fiber tension (F_f^t), fiber compression (F_f^c), matrix tension (F_m^t), and matrix compression (F_m^c):

$$F_f^t = \left(\frac{\sigma_{11}}{X_T}\right)^2 + \alpha \left(\frac{\tau_{12}}{S_L}\right)^2 \tag{6.12}$$

$$F_f^c = \left(\frac{\sigma_{11}}{X_C}\right)^2 \tag{6.13}$$

$$F_m^t = \left(\frac{\sigma_{22}}{Y_T}\right)^2 + \left(\frac{\tau_{12}}{S_L}\right)^2 \tag{6.14}$$

$$F_m^c = \left(\frac{\sigma_{22}}{2S_T}\right)^2 + \left[\left(\frac{Y_C}{2S_T}\right)^2 - 1\right] \cdot \frac{\sigma_{22}}{Y_C} + \left(\frac{\tau_{12}}{S_L}\right)^2 \tag{6.15}$$

The parameter α signifies the role of shear stress in initiating damage under fiber tension, adopting the modified formulation of the Hashin criterion [143], where α is set to 1. In the present case, it is differentiated between the longitudinal shear strength, denoted as S_L, which corresponds to shear forces parallel to the fibers, and the transverse shear strength, denoted as S_T, representing shear forces perpendicular to the fibers. Due to the anisotropic nature of composites, these shear strengths typically differ. However, in the present case, where shear strength is determined through $\pm 45°$ tensile tests, S_L and S_T are considered equal, and defined by the shear strength S, due to the presence of both transverse and longitudinal shear components during testing.

[3]The choice of material model is discussed in Appendix C.1

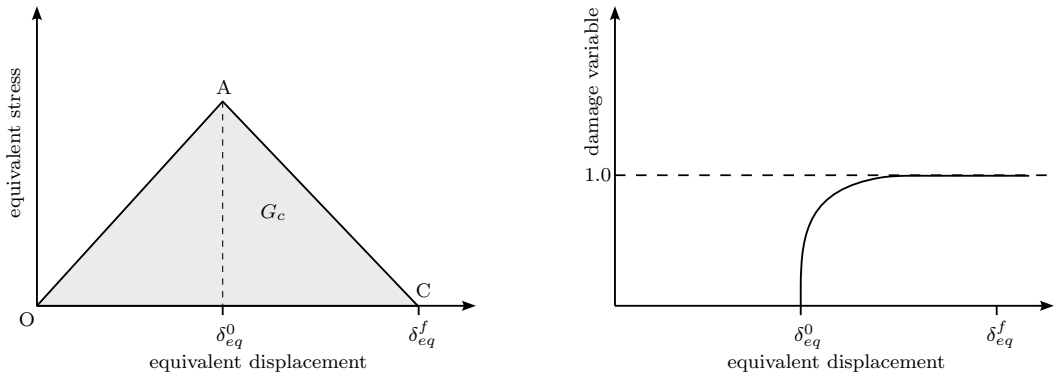

(a) Constitutve material law **(b)** Evolution of damage variable

Figure 6.17 Damage evolution for fiber-reinforced composites in Abaqus

Damage evolution is based on energy dissipation during the damage process. Therein, the damage variables d_f, d_m and d_s, each corresponding to the current states of fiber, matrix as well as shear damage, are derived from the damage variables d^t_f, d^c_f, d^t_m, d^c_m, each corresponding to the individual Hashin failure modes. The damage variables d_f, d_m and d_s are used for the stiffness degradation of the elasticity matrix. Figure 6.17a shows the constitutive material law, comprising the linear elastic regime (OA) and the degradation regime (AC). Degradation after damage initiation is linear and governed by the dissipated energy during damage. The damage variables in each failure mode are calculated using following equvalent strains:

$$d = \frac{\delta^f_{eq}(\delta_{eq} - \delta^0_{eq})}{\delta_{eq}(\delta^f_{eq} - \delta^0_{eq})} \tag{6.16}$$

The onset of degradation, at which the initiation criterion is equal to 1, is defined by δ^0_{eq}, while δ^f_{eq} denotes the fully degraded state of the material in the respective failure mode. Figure 6.17b shows the evolution of the damage variable. For each failure mode, the energy dissipated during damage is represented by the area under the triangle (OAC) in Figure 6.17a and can be obtained by the intralaminar fracture toughness, i.e. G_{ft}, G_{fc}, G_{mt} and G_{mc}. Input for the present material M21/T700GC in terms of stiffness, strength and damage are presented in Tables 6.6 and 6.7.

Material Model for Metals

Modeling of the metallic constituent of the FML is done with the functionalities provided in Abaqus. Therein, isotropic elastic material properties are employed in conjunction with isotropic hardening to incorporate plasticity. The model uses the standard Mises yield criterion with associated plastic flow:

$$\sigma_{vM} = \sqrt{\frac{1}{2}(\sigma_x - \sigma_y)^2 + (\sigma_y - \sigma_z)^2 + (\sigma_z - \sigma_x)^2 + 6(\tau^2_{xy} + \tau^2_{yz} + \tau^2_{xz})} \tag{6.17}$$

As the material model requires true stress and strain values, the nominal stresses and strains from the experimental test results are converted using following relation:

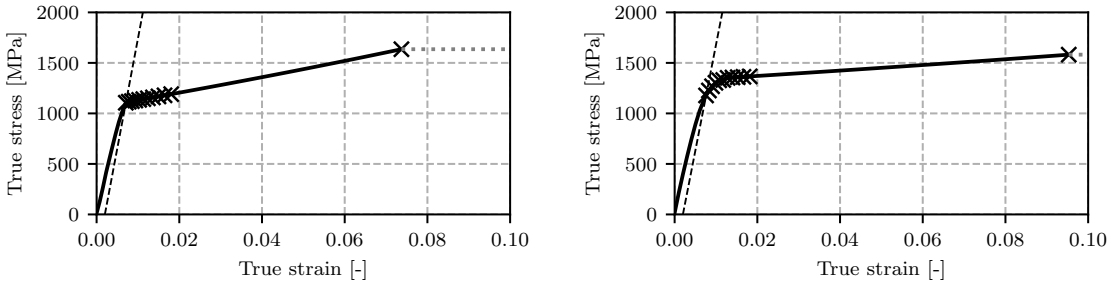

(a) Steel 1.4310 at LT **(b)** Steel 1.4310 at RT

Figure 6.18 Stress-strain behavior of steel sheets

$$\varepsilon_{true} = \ln(1 + \varepsilon_{nom}) \tag{6.18}$$

$$\sigma_{true} = \sigma_{nom}(1 + \varepsilon_{nom}) \tag{6.19}$$

Post-yielding behavior is approximated with a series of data points, consisting of yield stress of the material as a function of the true plastic strain. Since the experimental test results provide only the total strain, the plastic strain has to be calculated seperately. Therein, the plastic strain ε^{pl} is obtained by subtraction of the elastic strain ε^{el} from the total strain ε^{tot}:

$$\varepsilon^{pl} = \varepsilon^{tot} - \varepsilon^{el} = \varepsilon^{tot} - \sigma/E \tag{6.20}$$

The plasticity data for the steel 1.4310 with a sheet thickness of 0.26 mm is derived from the experimental test results in Chapter 4 and presented in Table 6.5, and visualized in Figure 6.18.

Table 6.5 Plasticity input data for 1.4310

LT		RT	
plastic strain ϵ^{pl} [-]	stress σ [MPa]	plastic strain ϵ^{pl} [-]	stress σ [MPa]
0.00000	1105.4	0.00000	1177.7
0.00070	1115.7	0.00069	1226.7
0.00146	1121.2	0.00145	1268.5
0.00230	1127.3	0.00227	1302.8
0.00322	1133.9	0.00317	1327.9
0.00423	1141.3	0.00415	1330.8
0.00534	1149.4	0.00522	1351.8
0.00656	1158.3	0.00639	1355.3
0.00789	1168.1	0.00766	1358.6
0.00936	1178.9	0.00905	1362.1
0.01097	1190.8	0.01056	1366.0
0.06665	1635.3	0.08771	1581.5

Derivation of Model Input

After presenting the model setup, now the selection process of the model input parameters is described. The vast majority of inter- and intralaminar input parameters is determined experimentally in Chapter 4. Although not explicitly required by the 2D Hashin model, the in-plane properties (E_{11}, E_{22}, ν_{12}, G_{12}) are extended to the 3D case for application in 3D material models using the assumption of transverse-isotropy (E_{22}=E_{33}, G_{12}=G_{13} and ν_{12}=ν_{13}). The shear modulus G_{23} in the 2-3 plane is defined similarly to the isotropic case:

$$G_{23} = \frac{E_{22}}{2(1+\nu_{23})} \tag{6.21}$$

For UD laminates which are homogeneous and transversely isotropic, Kuo et al. [144] derived following expression for calculating ν_{23}:

$$\nu_{23} = \frac{-E_{22}[E_{11}(\frac{1}{2}-\nu_{12})+2G_{12}\nu_{12}^2]+\Lambda}{2E_{11}G_{12}} \tag{6.22}$$

where

$$\Lambda = \sqrt{E_{22}^2\left[E_{11}\left(\tfrac{1}{2}-\nu_{12}\right)+2G_{12}\nu_{12}^2\right]^2 - 4E_{11}G_{12}\left[E_{11}E_{22}\left(\tfrac{1}{2}-\nu_{12}\right)-G_{12}(E_{11}-2E_{22}\nu_{12}^2)\right]} \tag{6.23}$$

Now that the stiffness values are defined, the selection of the strength input data is described. Longitudinal tensile and compressive strength ($R_{\parallel}^t$ and $R_{\parallel}^c$) as well as transverse compressive strength ($R_{\perp}^c$) values are taken from the experimental test results. Regarding transverse tensile ($R_{\perp}^t$) and shear strength ($R_{\perp\parallel}$), the *in-situ effect* is incorporated. The in-situ effect describes the increase in transverse tensile and shear strengths of a ply inside a laminate when constrained by neighboring plies with different orientations, compared to the strength of the same ply in a purely UD laminate. The in-situ effect was originally observed by Parvizi [145]. When applying stress based failure criteria, as is the case in the present work, consideration of the in-situ strengths is necessary for accurate prediction of matrix cracking in constrained plies. Both experimental [146–148] as well as analytical methods [149–151] have been proposed to determine the in-situ strengths. The analytical method introduced by Camanho et al. [151] proves to be efficient and accurate [152, 153], which is why it is used here for calculating in-situ strengths. The theory is based on a fracture mechanics analysis of a slit crack in a UD ply as proposed by Dvorak and Laws [149]. Therein, the slit crack representes the meso-scale effect of defects that occur at the micro-scale. As both the thickness of a ply as well as the position of the ply have an effect on the in-situ strength, the theory differentiates thin embedded plies, thick embedded plies and outer plies. In general, thinner plies exhibit higher strengths than thicker plies. Furthermore, outer plies exhibit lower strengths than fully embedded plies because the surface of the outer plies are generally unconstrained, which leads to surface cracks developing more likely in those regions. The in-situ effect is incorporated into FE analysis by replacing the strength values of UD laminates with the respective in-situ strength values. The in-situ shear strength $R_{\perp\parallel,is}$ of a ply with the thickness t is calculated by:

$$R_{\perp\parallel,is} = \sqrt{\frac{\sqrt{1+\beta_{HT}\phi G_{12}^2}-1}{3\beta_{HT}G_{12}}} \tag{6.24}$$

with

$$\phi = \begin{cases} 12\frac{R_{\perp\parallel}^2}{G_{12}} + 18\beta_{HT}R_{\perp\parallel}^4 & \text{for a thick embedded ply} \\ \frac{48G_{IIc}}{\pi t} & \text{for a thin embedded ply} \\ \frac{24G_{IIc}}{\pi t} & \text{for an outer ply} \end{cases} \tag{6.25}$$

The parameters G_{Ic} and G_{IIc} represent the interlaminar fracture toughness in mode I and mode II, respectively. The shear response factor for in-plane shear β_{HT} is set to $2.98 \cdot 10^{-8}$ MPa^{-3} according to [154]. The in-situ transverse tensile strength $R_{\perp,is}^t$ can be obtained by:

$$R_{\perp,is}^t = \begin{cases} 1.12\sqrt{2}R_{\perp}^t & \text{for a thick embedded ply} \\ \sqrt{\frac{8G_{Ic}}{\pi t\Lambda_{22}^0}} & \text{for a thin embedded ply} \\ 1.79\sqrt{\frac{G_{Ic}}{\pi t\Lambda_{22}^0}} & \text{for an outer ply} \end{cases} \tag{6.26}$$

with

$$\Lambda_{22}^0 = 2\left(\frac{1}{E_{22}} - \frac{\nu_{21}^2}{E_{11}}\right) \tag{6.27}$$

The in-situ values for thin embedded plies and for the outer ply are calculated using the strength and fracture toughness data determined in Chapter 4.

After defining the elastic and damage initiation properties, now selection of the damage evolution input is described. Damage evolution is based on the intralaminar fracture toughness. Intralaminar fracture toughness properties for M21/T700GC are not determined experimentally in the present work, since the test methods are not standardized and subject of current research. Rather, fracture toughness values in fiber direction G_{ft} and G_{fc} are taken from Gerendt et al. [141] and Furtado et al. [155] who conducted experimental tests at RT using M21/T700GC. According to the experimental tests results in the present work (Table 4.3 and Table 4.4), tensile and compressive stiffness as well as strength values in fiber direction are almost identical between RT and LT. Thus, it is assumed that the intralaminar fracture toughness values in fiber direction determined at RT can also be used for LT simulation. The matrix dominated intralaminar fracture toughness properties are derived from interlaminar properties. Czabaj and Ratcliffe [156] demonstrate that the intralaminar fracture toughness G_{mt}, tested with a compact tension specimen, and the interlaminar fracture toughness G_{Ic}, tested with a DCB specimen, is similar. The result suggests that the mode I matrix fracture toughness is independent from the fracture plane:

$$G_{mt} \approx G_{Ic} \tag{6.28}$$

Calculation of the intralaminar fracture energy for matrix compression is done following a procedure applied by Gerendt et al. [141]. Therein, the fracture energy

is derived from the mode II interlaminar fracture toughness G_{IIc} and the transverse compressive strength $R^c_\perp$:

$$G_{mc} = \frac{G_{IIc}}{\cos(\alpha_0)} + a \cdot t \cdot \eta^T \cdot R^c_\perp \cdot \cos(\alpha_0) \tag{6.29}$$

with

$$\eta^T = -(\tan(2\alpha_0))^{-1} \approx 0.3 \quad \text{for} \quad \alpha_0 = 53^\circ \tag{6.30}$$

Here, t represents the ply thickness and α_0 the compression fracture angle, which is defined to $\alpha_0 = 53^\circ$ according to [157]. Determination of the intralaminar fracture energy G_s related to shear failure is done similarly to the case of matrix tensile failure. Therein, the intralaminar fracture toughness G_s is assumed to be equivalent to the interlaminar fracture toughness G_{IIc} in mode II, according to [123,141]:

$$G_s \approx G_{IIc} \tag{6.31}$$

The intralaminar fracture energies define the evolution of the damage variable during damage progression. Similarly to [141, 158, 159], it is assumed here that the stiffness reduction associated with damage resulting from compressive loads is different from the stiffenss reduction that is associated with damage as a result of tensile loads. This effect is due to the fact that the surfaces of a crack under tensile loading are traction free, while under compressive loading the surfaces retain some load carrying capacity. However, due to the restrictions within Abaqus, where only limitation of the global damage variable is possible and no mode-wise limitation, the element damage variable is limited to 0.9, eventough a differentiation is recommended. By this approach, the continueing load carrying capacity of the CFRP under the washer region is accounted for.

Table 6.6 Material input data for M21/T700GC at RT

Elasticity	E_{11} 103.4 GPa	$E_{22} = E_{33}$ 8.3 GPa	$\nu_{12} = \nu_{13}$ 0.291	$G_{12} = G_{13}$ 4.6 GPa	ν_{23} 0.609	G_{23} 2.6 GPa
Thermal	α_{11} -0.374 $\frac{10^{-6}}{°C}$	$\alpha_{22} = \alpha_{33}$ 38.5 $\frac{10^{-6}}{°C}$				
Strength (UD)	$R^t_\parallel / X_T$ 2214 MPa	$R^c_\parallel / X_C$ 1521 MPa	$R^t_\perp / Y_T$ 86 MPa	$R^c_\perp / Y_C$ 207 MPa	$R_{\perp\parallel} / S$ 80 MPa	
Strength (in-situ)	$R^t_{\perp,is,thin}$ 113 MPa	$R_{\perp\parallel,is,thin}$ 144 MPa	$R^t_{\perp,is,outer}$ 86 MPa	$R_{\perp\parallel,is,outer}$ 118 MPa		
Fracture toughness	G_{ft} 83 N/mm [141]	G_{fc} 120 N/mm [155]	G_{mt} 0.311 N/mm	G_{mc} 13.71 N/mm	G_s 2.402 N/mm	

In Table 6.6 and Table 6.7 all input data necessary for modeling of the composite parts at RT and LT is summarized. Interlaminar properties for modeling of the cohesive behavior of monolithic and hybrid interfaces are summarized in Table 6.1. Based on findings by Völkerink et al. [123], the properties of 00//00 at St//00 interfaces are used as a conservative approximation for multi-directional interfaces. Elastic properties of the steel ply and bolt are presented in Table 6.8. Plasticity of the steel sheets is based on the input in Table 6.5.

Table 6.7 Material input data for M21/T700GC at LT

Elasticity	E_{11} 102.4 GPa	$E_{22} = E_{33}$ 10.0 GPa	$\nu_{12} = \nu_{13}$ 0.287	$G_{12} = G_{13}$ 5.8 GPa	ν_{23} 0.622	G_{23} 3.1 GPa
Thermal	α_{11} -0.194 $\frac{10^{-6}}{°C}$	$\alpha_{22} = \alpha_{33}$ 29.7 $\frac{10^{-6}}{°C}$				
Strength (UD)	$R^t_{\parallel}$ 2230 MPa	$R^c_{\parallel}$ 1593 MPa	$R^t_{\perp}$ 93 MPa	$R^c_{\perp}$ 344 MPa	$R_{\perp\parallel}$ 106 MPa	
Strength (in-situ)	$R^t_{\perp,is,thin}$ 126 MPa	$R_{\perp\parallel,is,thin}$ 147 MPa	$R^t_{\perp,is,outer}$ 93 MPa	$R_{\perp\parallel,is,outer}$ 121 MPa		
Fracture toughness	G_{ft} 83 N/mm [141]	G_{fc} 120 N/mm [155]	G_{mt} 0.322 N/mm	G_{mc} 19.69 N/mm	G_s 2.506 N/mm	

Table 6.8 Material input data for steel 1.4310

Temperature	E	ν	CTE
RT	189633 MPa	0.3	13.04 $\frac{10^{-6}}{°C}$
LT	184822 MPa	0.3	12.88 $\frac{10^{-6}}{°C}$

6.2.3 Modeling Approach for Hybrid Joints

When it comes to numerical bolt-bearing modeling, previous research has been dedicated to investigating suitable modeling strategies, encompassing various aspects such as the selection of material models [9,141], bolt modeling and torque application [160], clearance [161, 162] as well as the consideration of friction between bolt, washer and laminate [163]. Within the context of the present research, particular emphasis is placed on examining the impact of thermal residual stresses and delamination modeling. The objective of the present study is to establish a foundation for addressing the question of whether or not it is necessary to incorporate these effects into the numerical analysis process of CFRP-steel FMLs, meanwhile striking a balance between computational efficiency, accuracy, and reliability.

Study on Thermal Effects

Inclusion of a temperature step in the simulation process primarily has two effects: Firstly, due to the difference in in-plane CTE and stiffness, thermal stresses build up in the single plies of the laminate. Secondly, due to the difference in CTE in thickness direction, the bolt-torque acting on the laminate decreases as a result of larger contraction of the specimen compared to the metallic bolt and load-plates. The present section focuses on the former - the effect of intralaminar thermal residual stresses on the bearing behavior. As continuum shell (SC8R) elements are used in conjunction with the 2D Hashin criterion for modeling the composite behavior, the model is considered unfit for a detailed analysis of clamping effects.

Figure 6.19 shows the bearing response of a monolithic QI laminate and a hybrid QI-FML at LT. Experimental test results from Chapter 5 are presented with simulation results. Delamination is not modeled. For both laminates, one model including a temperature step (w/ ΔT) and one model without a temperature step (w/o ΔT)

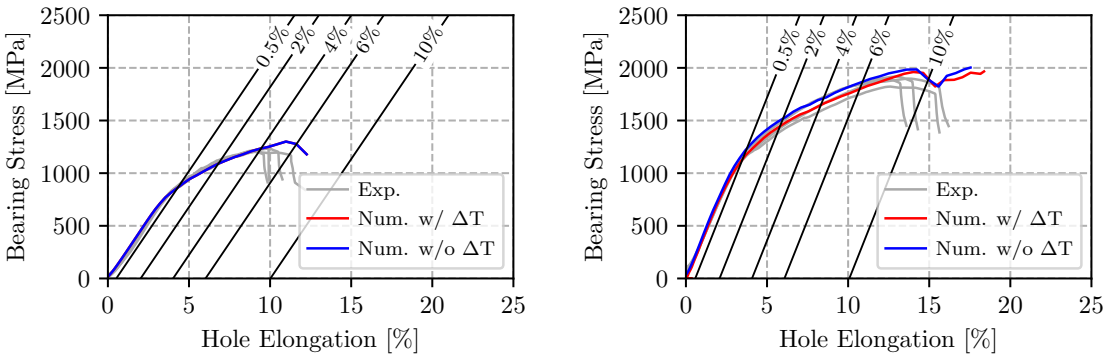

(a) QI **(b)** QI-FML

Figure 6.19 Effect of TRS on numerical strength prediction in QI and QI-FML at LT

are simulated. In the model without a temperature step, basically all temperature steps from Figure 6.16 are omitted. Inclusion of a temperature step in the simulation has no visible influence on the load-displacement curve of the monolithic QI laminate in Figure 6.19a. As the magnitude of intralaminar thermal residual stresses in monolithic laminates is quite low, this result is not surprising. However, considering the load-displacement curve of the QI-FML in Figure 6.19b, the numerical curves differ noticeably. Therein, once the linear elastic regime of the bearing response is surpassed, the model not including a temperature step (Num. w/o ΔT) exhibits higher stresses during damage progression compared to the model including a temperature step (Num. w/ ΔT). Thus, the model neglecting ΔT is consistently less conservative.

In order to better understand the cause for the different behavior of the QI-FML depending on whether or not a temperature step is included, the state of thermal residual stresses inside those laminates is analyzed in Figure 6.20. The longitudinal stress state (σ_{xx}) in a 0° ply and a steel ply after cooling to LT but before applying the bolt-load is shown in Figure 6.20a and Figure 6.20b for the cases without and with a temperature step, respectively. While the stresses in the model without application of a temperature step are close to zero (see Figure 6.20a), substantial thermal stresses are present in the composite (≈-150 MPa) and steel (≈300 MPa) plies in Figure 6.20b. Thus, prior to mechanical loading by the bolt, there is already a substantial intrinsic load present within the single plies of the QI-FML specimen. In Figure 6.20c, the stresses along the bearing plane are displayed. The numerical stresses including a temperature step (Num. w/ ΔT) in red, the numerical stresses without application of a temperature step (Num. w/o ΔT) in blue as well as the CLT result in black are shown, for each a 0° CFRP (dashed line) and a steel ply (solid line), respectively. Considering the stresses in longitudinal and transverse direction along the bearing plane, it becomes very clear that the model including a temperature step results in much higher residual stresses in both the composite and steel plies. The behavior is verified by application of CLT, which results in identical stresses in the bulk of the material. However, if no temperature step is included, the only stresses present result from the edge effects near the hole. Thus, taking into account the presence of significant thermal residual stresses in the simulation including a temperature step, it appears reasonable for the numerical simulation neglecting thermal residual stresses in Figure 6.19b to be less conservative.

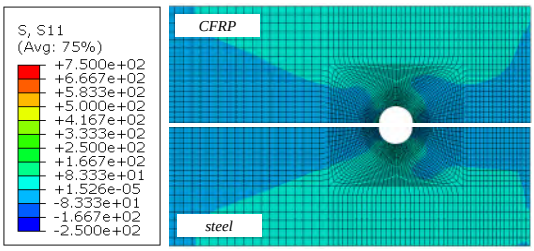

(a) Ply stresses (σ_{xx}) in QI-FML w/o ΔT

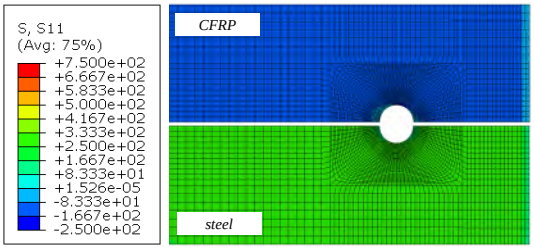

(b) Ply stresses (σ_{xx}) in QI-FML w/ ΔT

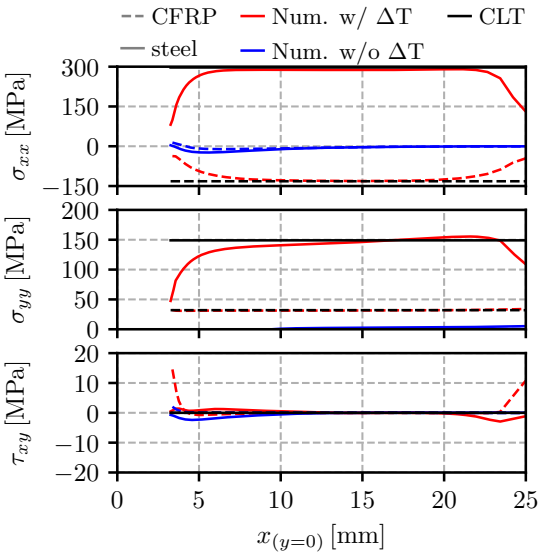

(c) Ply stresses along bearing plane

Figure 6.20 Stresses in QI-FML at LT with and without considering a temperature step

The effect of thermal residual stresses on damage onset in the composite and steel plies is analyzed in Figure 6.21 and Table 6.9. The points at which the composite damage initation criteria (F_f^t, F_f^c, F_m^t, F_m^c) are met as well as the onset of plasticity in the steel plies (PE) are indicated for both the QI- and HO-FML at LT. A small step in the beginning of the load-displacement curve can be seen in the result of the models without a temperature step. This step results from the fact that, during quasi-static loading, load is initially transferred between the washer and the laminate by surface friction. After some slippage, the bolt touches the laminate hole and the load transferred by the bolt increases. In case of the models with a temperature step, contraction of the laminate during the cool-down phase already results in contact between bolt and laminate (cf. Figure 6.15). As previously described, the bolt is free to move in longitudinal direction at this point so that no additional stresses build up, as is the case during experimental testing.

When comparing the onset of plasticity in the QI-FML, neglecting thermal residual stresses actually results is a slighly earlier prediction of plasticity. As can be seen in Figure 6.20c, tensile thermal stresses are present in the steel plies, while compressive thermal stresses are acting on the composite plies in longitudinal direction. Given that the bolt-bearing loading scenario is primarily of compressive nature (for sufficiently large specimen widths), the tensile stresses in the metal sheets act as an additional margin against the onset of plasticity. However, when there is no temperature step and thus no thermal residual stresses acting, this margin is not present. Consequently, the numerical model that neglects thermal residual stresses predicts an earlier onset of plasticity in the steel plies. This finding highlights the significance of considering the effects of thermal residual stresses on the mechanical response of the QI-FML and emphasizes the role of residual stresses in influencing the material behavior. When

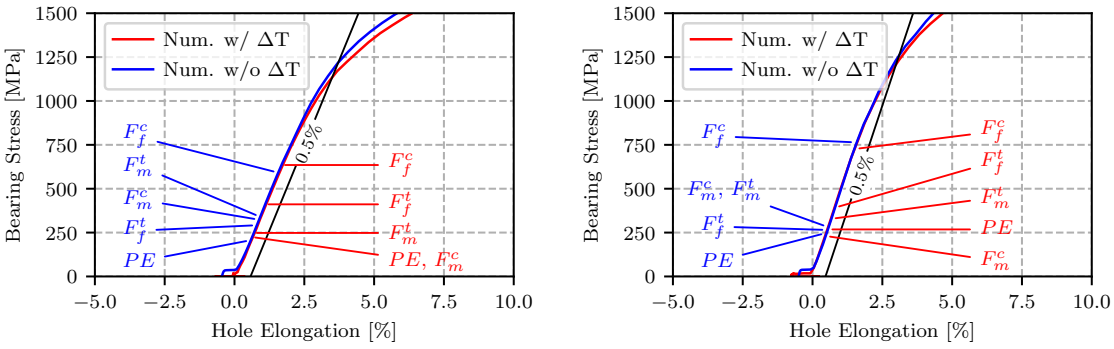

(a) QI-FML **(b)** HO-FML

Figure 6.21 Effect of TRS on numerical damage onset in QI- and HO-FML at LT

Table 6.9 Damage initiation points for QI- and HO-FML at LT

	QI-FML				HO-FML			
	w/ ΔT		w/o ΔT		w/ ΔT		w/o ΔT	
	Stress MPa	Ply -	Stress MPa	Ply -	Stress MPa	Ply -	Stress MPa	Ply -
$F_f^t = 1$	411	1	292	1	391	1	265	1
$F_f^c = 1$	635	3	591	1	727	3	764	3
$F_m^t = 1$	249	1	339	1	328	1	281	1
$F_m^c = 1$	226	1	321	1	231	1	281	1
$PE > 0$	226	2	207	2	268	4	248	2

discussing damage onset in the composite plies of the QI-FML, it should be mentioned that, due to the presence of non-0° plies, the stress state is quite complex. For a better understanding, the discussion on the impact associated with neglecting thermal effects is conducted at the example of the HO-FML in Figure 6.21b. Analysis of the effects of thermal residual stresses on damage onset in the composite plies is more straightforward in case of the HO-FML as this laminate only contains steel and 0° plies, thus allowing for a more comprehensible discussion. With respect to the onset of plasticity, the observation made at the example of the QI-FML is confirmed by the HO-FML. When thermal residual stresses are neglected by omitting the temperature step in the simulation, plasticity in the steel sheets occurs sooner. However, regarding damage onset in matrix dominated cases (F_m^t, F_m^c), the findings are not as expected. Following the logic of a positive margin with respect to F_m^c and a negative margin with respect to F_m^t due to presence of thermal residual stresses in the CFRP plies in the HO-FML, neglecting thermal residual stresses would suggest that the onset of F_m^c occurs sooner while the onset of F_m^t is retarded. Yet, when looking at Figure 6.21b the opposite is the case. Nonetheless, damage onset in the fiber dominated cases (F_f^t, F_f^c) correlates very well with the expectations concerning thermal residual stresses. In general, fiber failure is considered more relevant to the structural behavior of a bolted joint. The presence of tensile residual stresses in longitudinal direction of the composite plies results in a positive margin for F_f^c and a negative margin for F_f^t. Con-

Table 6.10 Effect of TRS on numerical strength prediction in QI- and HO-FML at LT

		QI-FML					HO-FML				
		$\sigma^f_{0,5\%}$	$\sigma^f_{2\%}$	$\sigma^f_{4\%}$	$\sigma^f_{6\%}$	$\sigma^f_{10\%}$	$\sigma^f_{0,5\%}$	$\sigma^f_{2\%}$	$\sigma^f_{4\%}$	$\sigma^f_{6\%}$	$\sigma^f_{10\%}$
Mean	MPa	1180	1450	1648	1770	1570	1400	1680	1872	1976	2151
Stdev.	MPa	27	38	52	36	176	24	11	6	11	9
C.o.V.	%	2.3	2.6	3.2	2.0	11.2	1.7	0.7	0.3	0.5	0.4
Num. w/ ΔT	MPa	1134	1446	1647	1798	1895	1208	1582	1808	1999	2207
Error	%	-3.9	-0.3	-0.1	1.6	20.7	-13.7	-5.8	-3.4	1.2	2.6
Num. w/o ΔT	MPa	1193	1505	1704	1860	1901	1215	1609	1844	2018	2240
Error	%	1.1	3.8	3.4	5.1	21.1	-13.2	-4.2	-1.5	2.1	4.1

sequently, when thermal residual stresses are neglected by omitting the temperature step in the simulation, the onset of F^c_f is expected to occur later, while the onset of F^t_f is expected to occur earlier. This behavior is confirmed by the results in Figure 6.21b. Damage onset in the individual plies occurs very localized in the vicinity of the bolt hole and at load levels much lower than the beginning of non-linearity in the global load-displacement response of the bolted joint. Therefore, the implications for global damage onset, particulary in terms of offset-strength, is limited. Nonetheless, it can be seen that neglecting thermal effects during analysis results in noticeable differences regarding damage onset in hybridized bolted joints.

After analysis of the load-displacement behavior, the intrinsic state of thermal residual stresses, as well as the onset of damage, Table 6.10 shows the offset-strength of the QI- and HO-FML at LT. Hereby, a more detailed analysis of the influence of thermal residual stresses on the bearing strength is conducted. Considering the offset-strengths of the QI-FML at LT, the numerical result including a temperature step slightly underestimates $\sigma^f_{0,5\%}$ and is extremely accurate for the offset-strengths between 2-6 % permanent hole elongation. Taking into account the complexity of the damage mechanisms present in the bolt-bearing problem, the accuracy is remarkable. Agreement between the experimental and numerical results including a temperature step in case of the HO-FML at LT is slightly less pronounced. Herein, the numerical model underpredicts the $\sigma^f_{0,5\%}$ by around 14 %, while agreement for the offset-strengths between 2-10 % is significantly better. When comparing the numerical result without inclusion of a temperature step, it becomes evident that neglecting the effect of thermal residual stresses leads to continuously less conservative results for the offset-strengths between 0.5 % and 10 %. While the deviation in case of the QI-FML is up to 5 %, dismissing a temperature step for the HO-FML leads to a difference of up to 2 %. Thus, despite the error being rather small, neglecting thermal residual stresses in the analysis process of the QI- and HO-FML leads to less conservative results, which should be taken into account when conducting FEA of CFRP-steel hybrid joints.

In summary, inclusion of a temperature step affects the bolt-bearing behavior of CFRP-steel hybridized joints in several ways. Firstly, including a temperature step is physically justified as significant thermal residual stresses of up to several houndred Megapascal build up in CFRP-steel FMLs. Although there is no tangible effect visible,

e.g. deformations due to asymmetry as is the case for the hybrid DCB specimens in section 6.1.1, both FEA and CLT confirm the presence of significant internal stresses despite no external load, e.g. a bolt-force, being applied. The presence of thermal residual stresses further affects damage initiation in the composite and metal plies of the laminate. Depending on the nature of thermal residual stresses, i.e. tensile or compressive, damage onset criteria are triggered either sooner or later, thereby influencing damage initiation and progression during bolt-bearing loading. However, the effect of thermal residual stresses on the global load-displacement curve and in particular on the bearing strength is limited. Despite the significant magnitude of thermal residual stresses, the difference in bearing strength when neglecting thermal residual stresses hardly amounts to values above 5 % for the present example cases. Nonetheless, neglecting thermal residual stresses does lead to less conservative results compared to the simulations where a temperature step is included, thus concluding that consideration of thermal residual stresses is recommended for modeling steel hybridized CFRP joints. It should be mentioned that this recommendation is valid specifically for present type of FML. For hybrid laminates with substantially less thermal residual stresses, e.g. GLARE, the thermal effects might be negligible.

Study on Cohesive Zone Modeling

Based on the literature study in Chapter 3, it has been established that delamination is a significant factor contributing to failure in FML bolt-bearing loading scenarios. The observations made for the CFRP-steel FMLs in Chapter 5 further support these findings. However, it is noteworthy that only a limited number of researchers, e.g. Hundley [8] and Masania et al. [142], have incorporated interlaminar failure into their numerical models, when simulating locally titanium/steel hybridized bolted joints in composites. On the other hand, many other studies, such as Both [11], Fink [16] or Petersen [38], primarily focus on investigating bearing failure in the hybridized region and delamination in the transition zone separately. Thereby, suggesting that interlaminar damage does not occur or is irrelevant to the bolt-bearing loading scenario, and thus contradicting observations from experimental studies in literature. Due to the lateral constraint, delamination in the washer area does not result in an immediate loss of integrity and load bearing capacity, as might be the case for pin-bearing scenarios. Therefore, in the present section, the effect of delamination on the load-displacement curve is analyzed in conjunction with a comparison of delamination phenomena in the numerical model versus experimental test. This is done in an attempt to understand whether including CZM in CFRP-steel FML bolted joints is necessary.

In Figure 6.22, experimental bolt-bearing results at LT are compared to numerical simulation results. Therein, a model without CZM, a model including cohesive behavior only at hybrid interfaces (CZM: CFRP//steel), and a model including cohesive behavior at all interfaces (CZM: all IF) are compared for a QI- and HO-FML, respectively. Implementation of cohesive behavior is described in section 6.2.2. In contrast to the approach of Masania [142], cohesive behavior at the ply interfaces is not limited to the area under the washer. Rather, cohesive behavior in the present case is implemented for the entire specimen as the experimental results indicate that delamination effects are also present outside the washer area.

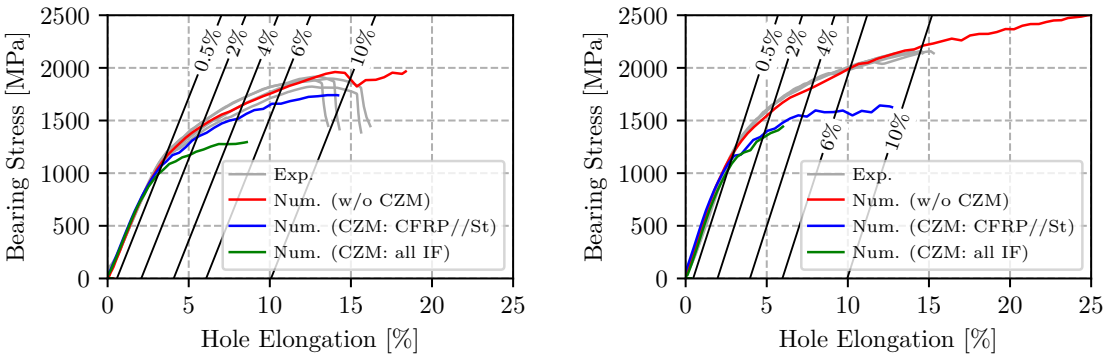

(a) QI-FML **(b)** HO-FML

Figure 6.22 Effect of CZM on numerical strength prediction in HO- and QI-FML at LT

Analysis of the load-displacement response of the numerical models shows that application of CZM does influence the global bearing behavior. In case of the QI-FML at LT in Figure 6.22a, omitting CZM leads to the highest agreement compared to the experimental result. Applying cohesive behavior only at the hybrid interfaces between CFRP and steel plies leads to less accurate but more conservative results. The model with cohesive behavior at all interfaces, i.e. both monolithic and hybrid interfaces, suffers from a premature decay in the force-displacement curve and deviates significantly from the experimental results. In Figure 6.22b, the results of the HO-FML at LT are presented. Again, the numerical model without application of CZM is the most accurate compared to the experimental force-displacement curves. Once cohesive behavior is included in the numerical models, agreement between experiment and simulation decreases. Therein, applying cohesive behavior only to hybrid interfaces or to all interfaces, i.e. both hybrid and monolithic, does not significantly alter the results. Due to the large MVF of almost 40 %, the model with cohesive behavior only at hybrid interfaces exhibits one cohesive interface less than the model in which cohesive behavior is assinged to all interfaces.

After analyzing the force displacement curves, Figure 6.23 and Figure 6.24 focus on the phenomenological delamination area. For this purpose, the models from Figure 6.22 are plotted as a wireframe model and cut along the bearing plane. The metal plies are indicated by solid black stripes along the cutting plane. The delamination is made visible through an isosurface contour plot for damage values (CSDMG) greater 0.99 in order to only show the fully delaminated region, rather than the cohesive process zone. The numerical results are compared to microsections from the bearing plane in order to assess the qualitative prediction quality regarding delamination onset and delamination area. In Figure 6.23, the comparison is done for the QI-FML at LT at 0.5 % offset-strength of the laminates. By definition, the model without CZM does not exhibit any delaminations. While Figure 6.23b shows delaminations at the CFRP//steel interfaces, in Figure 6.23b delamination at all interfaces is present. When looking at the microsection in Figure 6.23d, delamination is only present at the CFRP//steel interface but not at the monolithic interfaces. Even at the hybrid interfaces, delamination is barely visible as the structure is still intact at 0.5 % offset-strength. Nonetheless,

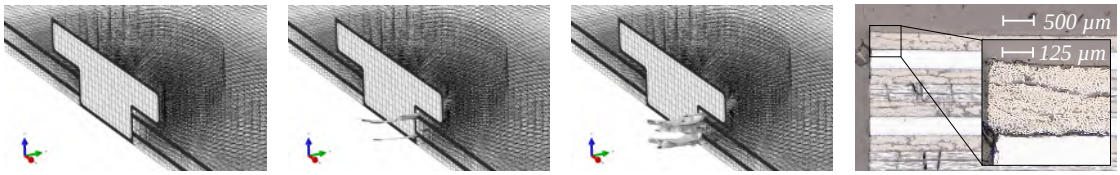

(a) w/o CZM **(b)** CZM: CFRP//steel **(c)** CZM: all IF **(d)** Microscopy

Figure 6.23 QI-FML at LT and 0.5 % offset-strength

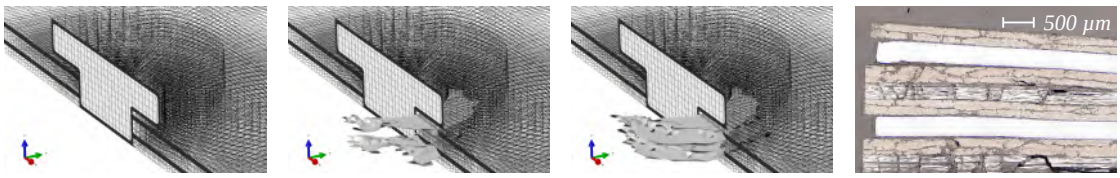

(a) w/o CZM **(b)** CZM: CFRP//steel **(c)** CZM: all I/F **(d)** Microscopy

Figure 6.24 QI-FML at LT and 4 % offset-strength

magnification of the hybrid interfaces exposes the presence of delamination. In Figure 6.24, the QI-FML is studied at 4 % offset-strength. The observations are similar in quality but more pronounced in quantity. No delamination is present in Figure 6.24a, while Figure 6.24b exhibits delamination between hybrid interfaces and in Figure 6.24c delmination is present at all interfaces. The microsection of the bearing plane in Figure 6.24d reveals that during experimenal testing, delamination is only present at hybrid interfaces while the monolithic interfaces between composite plies are still intact. Therein, the delaminated areas extend to the area under the washer, which is in good agreement with the numerical prediction. The only delamination at a monolithic interface visible in the microsection is outside the washer area at a certain distance from the bolt hole, which confirms the necessity of including cohesive behavior not only in the washer area but also in the far-field of the center hole.

In conclusion, analysis of the force-displacement curves suggests that excluding delamination effects in the washer area yields the best agreement between numerical and experimental data. Nonetheless, as the microscopy results show, delamination is indeed present in the washer area. The fact that delamination apparently only occurs at CFRP//steel interfaces suggest that incorporating cohesive behavior only at those interfaces is justified. This is valid for the bearing behavior up to 4 % offset-strength. From this point onward, delamination also occurs between composite plies, ususally triggered by preceeding intralaminar damage. However, if cohesive behavior is assigned to all interfaces, numerical results show that large deviations in the force-displacement curves occur. Thus, as a trade-off between accuracy regarding strength prediction and capturing delamination phenomena, cohesive behavior should be limited to hybrid interfaces or be omitted altogether. For future reference, discretizing the composite plies using solid elements, instead of shell elements as is the case in the present model, could improve the accuracy with respect to both the load-displacement curve as well as the phenomenological occurence of delamination. Solid elements allow for stresses in thickness direction and could thus improve the load bearing capacity when combined with surface friction after separation of cohesive surfaces.

Study on Model Robustness

In order to set into perspective the conclusions regarding the inclusion of thermal residual stresses and delamination, it is important to assess the robustness of the model by considering the effect of variations other than a temperature step and CZM on the simulation results. While the impact of thermal residual stresses, for example, is relatively modest at around 5 %, it is important to critically examine whether other factors carry more significant weight. Thus, the model input in terms of composite material strength and the choice of elements is selected, as they are expected to have a great influence on the bearing behavior. By quantifying the effects of these factors and assessing their relative impact in comparison to other influential factors, a conclusion can be drawn about the relevance of incorporating a temperature step or CZM.

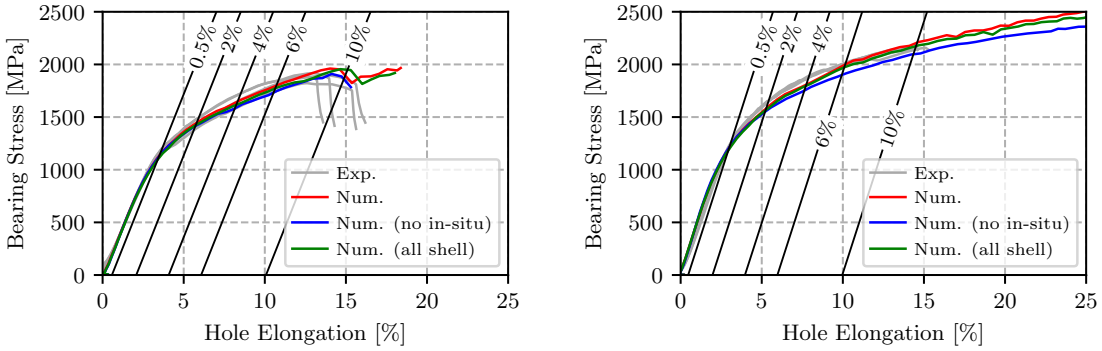

(a) QI-FML at LT **(b)** HO-FML at LT

Figure 6.25 Robustness of numerical model for varying strength and element type

In Figure 6.25, the reference FE-result from thre previous section (no CZM) is compared to a numerical model where application of in-situ properties is omitted and a numerical model where the metallic layers are modeled using continuum shell elements (SC8R) instead of continuum elements (C3D8R). The in-situ strength is selected as an influencing factor because application of in-situ properties, despite being wide-spread, is considered a rather new approach and not yet fully state of the art. Therefore, application of in-situ properties might be challenged. Furthermore, as in-situ properties alter the composite strength values, damage initiation in the composite plies of the numerical model is directly affected, and thus the bearing respose is potentially affected. While shell elements are used for the composite plies, the steel layers are modeled using solid elemets. The choice of shell elemets for the composite plies is driven by the limitation of Abaqus, whereas solid elements are selected intentionally for the steel plies since the out-of-plane stiffness of those plies are assumed to contribute to the improvement in bearing behavior by hybridization. Using shell elements instead of solid elements for the metal plies is expected to affect the simulation outcome. The modifications are applied to both the QI- and HO-FML at LT in Figure 6.25.

As can be seen for both the QI- and HO-FML, the effects from omitting in-situ strengths and using shell elements for all plies is rather low. In case of the QI-FML, almost no change is visible in the load-displacement curve. When looking at the

HO-FML, the curve of the model omitting application of in-situ strengths is slightly below the remaining curves. All in all, the effect from the choice of input strength values as well as the choice of elements is considered well below the effect of CZM and on a comparable or lower level regarding thermal residual stresses. Therefore, the discussion on thermal residual stresses and CZM is considered revelant and necessary, as these factors have a significant effect on the bearing behavior, and therefore are not negligible.

6.2.4 Validation of Modeling Stragety

After deriving a modeling strategy for CFRP-steel FML bolted joints and building an understanding on the relevant influencing factors in the previous section, now the modeling strategy is validated against all specimen configurations from the experimental test results. The experimental basis for validation is built in Chapter 5 and comprises monolithic and hybrid QI and HO stacking sequences that are tested under both RT and LT conditions. The key aspects of the modeling strategy are briefly summarized before comparing the resuls to experimental test data:

Model Setup & Bolt Modeling: The laminate is modeled layer-wise and discretized with one element in thickness direction and a refined mesh in the vicinity of the center hole. The bolt and washer are modeled as elastic materials with accurate geometry, i.e. clearance between bolt and laminate hole. Application of the bolt torque is conducted in a way that allows for a loss of clamping force when additional temperature steps are implemented, e.g. from RT to LT. Friction between bolt and laminate as well as washer and laminate is assigned. Furthermore, symmetry boundary conditions are employed in order to save computation time.

Thermal Effects: Inclusion of thermal effects by application of a temperature step is necessary for accurate modeling of CFRP-steel FML bolted joints. Therein, by application of a temperature step from the stress-free temperature to the operating temperature, the build-up of thermal residual stresses is accounted for. This way, the accurate stress state of the FML is captured, which will improve the model accuracy.

Delaminaton Modeling: When modeling for accurate strength prediction, implementation of interlaminar failure is not recommened. However, if the delamination mechanism is to be modeled, implementation of cohesive behavior only at CFRP//steel interfaces is recommended. The present modeling strategy omits application of CZM for the purpose of accuracy with respect to strength prediction.

Material Model & Element Type: Composite plies are modeled using shell elements (SC8R) in conjuction with the 2D Hashin criterion and energy-based linear degradation. Due to the ongoing load bearing capacity despite damage in the washer area, the damage variable of the composites is limited to a value of 90 %. If the material model allows for mode-wise definition of the damage variable, fiber compression and all matrix modes should be limited [141]. The steel plies can be modeled using either shell (SC8R) or solid (C3D8R) elements. Either way, an isotropic material model with hardening is implemented. Nonetheless, application of solid elements is recommended in

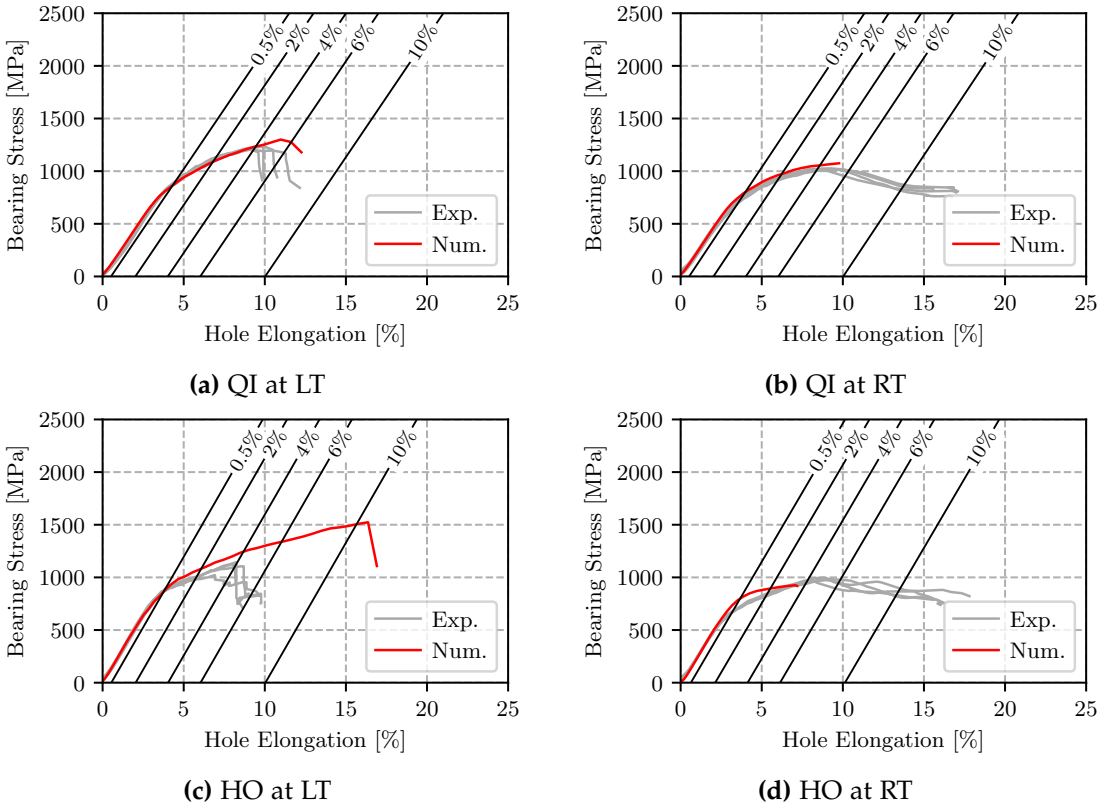

(a) QI at LT **(b)** QI at RT

(c) HO at LT **(d)** HO at RT

Figure 6.26 Validation of 3D bolt-bearing model for monolithic laminates

case out-of-plane effects occur during modeling.

In Figure 6.26, validation of the modeling strategy is conducted for monolithic stacking sequences by comparison to experimental test data at two temperature levels, namely RT and LT. In case of the QI stacking sequences, agreement is very good even for large hole elongations of up to 10 %. In case of the HO stacking, agreement is less pronounced. At LT, the numerical model sustains notably higher loads, while at RT 0.5 % offset-strength is overpredicted. Nonetheless, when considering the results for practically relevant offset-strengths of up to 4 % permanent hole deformation, the prediction quality of the present numerical models is considered good for the QI laminate (error at 0.5 % offset-strength: 0.3 % at LT and 12.4 % at RT) and acceptable for the HO laminate (error at 0.5 % offset-strength: 3.0 % at LT and 22.0 % at RT). A detailed summary of the data is provided in Table C.2 and Table C.3 in Appendix C.2.

Figure 6.27 shows the comparison of experimental and numerical data for the hybrid laminates at RT and LT. Regarding the QI-FML, agreement for both initial stiffness as well as offset-strengths up to 10 % is considered very good. When looking at the HO-FML, agreement between experimental and numerical curves at LT is better than at RT. Especially for offset-strength values greater than 4 % the deviation between numerical and experimental curve behavior increases. Furthermore, the numerical curves do not end at high hole elongation due to damage. As a result of the large MVF coupled with the ideal plasticity of the steel plies, the load-carrying capacity re-

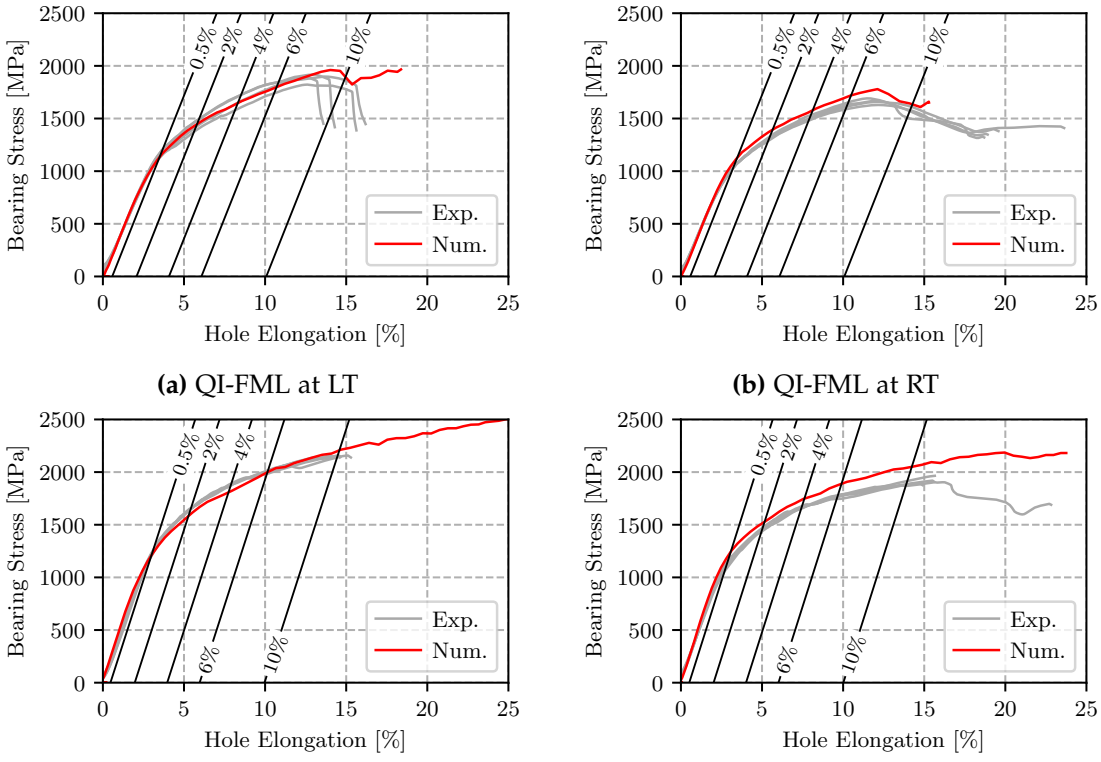

(a) QI-FML at LT

(b) QI-FML at RT

(c) HO-FML at LT

(d) HO-FML at RT

Figure 6.27 Validation of 3D bolt-bearing model for hybrid laminates

mains unaffected by damage, which deviates from physical reality. Thus, the validity of the numerical models for offset-strengths higher than 10 % permanent hole elongation is questionable. Consequently, the current modeling strategy is deemed valid only up to an offset-strength of 10 %. The prediction quality is still considered good for the QI-FML (error at 0.5 % offset-strength: -3.9 % at LT and 9.3 % at RT) and acceptable for the HO-FML (error at 0.5 % offset-strength: -13.7 % at LT and 6.4 % at RT). A detailed summary of the data is provided in Table C.4 and Table C.5 in Appendix C.2.

In conclusion, a robust modeling strategy for CFRP-steel FML bolted joints has been successfully developed, which is applicable to both monolithic and hybrid laminates. Through comprehensive comparison with experimental data covering a wide range of laminates with varying degree of orthotropy, MVF, and temperature levels, good agreement has been demonstrated, validating the high predictive quality of the approach. Reliable predictions of offset-strengths up to 4 % permanent hole deformation in case of monolithic and up to 10 % permanent hole deformation in case of hybrid laminates are consistently achieved. These findings establish a solid foundation for the precise analysis and design of CFRP-steel FML bolted joints.

6.3 Analysis of Hybridized Bolted Joints

In the present section, the previously validated numerical analysis strategy serves as a tool for conducting comprehensive investigations, thus enabling detailed analysis of the reinforcement effect in hybrid joints and facilitating virtual testing for numerical parameter determination. Therein the numerical bolt-bearing analysis tool is employed to gain a deeper understanding of the reinforcement effect in bolted joints achieved through steel hybridization in both elastic and non-elastic regimes. Furthermore, critical e/d and w/d ratios are determined as practical examples of virtual testing applications.

6.3.1 Analysis of Reinforcement Effect

In an attempt to better understand the mechanisms by which steel hybridization leads to an improved bearing behavior, the stress distribution in hybrid laminates is investigated. Figure 6.28 shows the stresses in the bolt area for a longitudinal cut along the bearing plane. Therein, the longtitudinal stress σ_{xx} is visualized for the individual plies of the QI, QI-FML, HO as well as HO-FML specimens at LT and a bearing stress of 250 MPa for illustration purposes. Due to the symmetry boundary conditions the figures show the laminate and bolt above the midplane of the laminate.

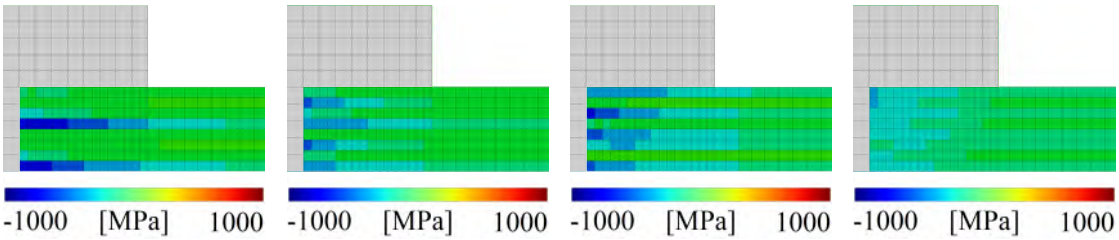

(a) QI at LT **(b)** QI-FML at LT **(c)** HO at LT **(d)** HO-FML at LT

Figure 6.28 Alleviation of longitudinal stresses σ_{xx} along bearing plane by steel hybridization at 250 MPa bearing stress

In Figure 6.28a and Figure 6.28b, the QI and QI-FML specimens are presented with a stacking sequence of $[45/90/\text{-}45/0]_{2s}$ and $[45/\text{St}/\text{-}45/0]_{2s}$, respectively. As can be seen, the 0° plies in the QI laminate exhibit high longtidutinal stresses of up to 1000 MPa at a bearing stress of 250 MPa, thereby carrying a significant portion of the load introduced into the laminate. By steel hybridization, the overall stress state at identical bearing load is greatly alleviated. The 0° plies of the QI-FML still carry significant loads. However, a substantial reduction of stress is achieved through substitution of the 90° plies by steel plies. As a result, the introduction of steel plies into the laminate leads to a relief of the composite plies. Similar observations can be made for the HO and HO-FML in Figure 6.28c and Figure 6.28d, with the stacking sequences $[0/45/0/\text{-}45/0_2/90/0]_s$ and $[0/\text{St}/0/\text{St}/0_2/\text{St}/0]_s$, respectively. By substitution of all non 0° plies with steel plies in the HO-FML, the laminate exhibits a very high overall stiffness leading to a very homogeneous stress distribution in Figure 6.28c. Therefore, in the elastic regime, where stiffness degradation from damage has minimal impact

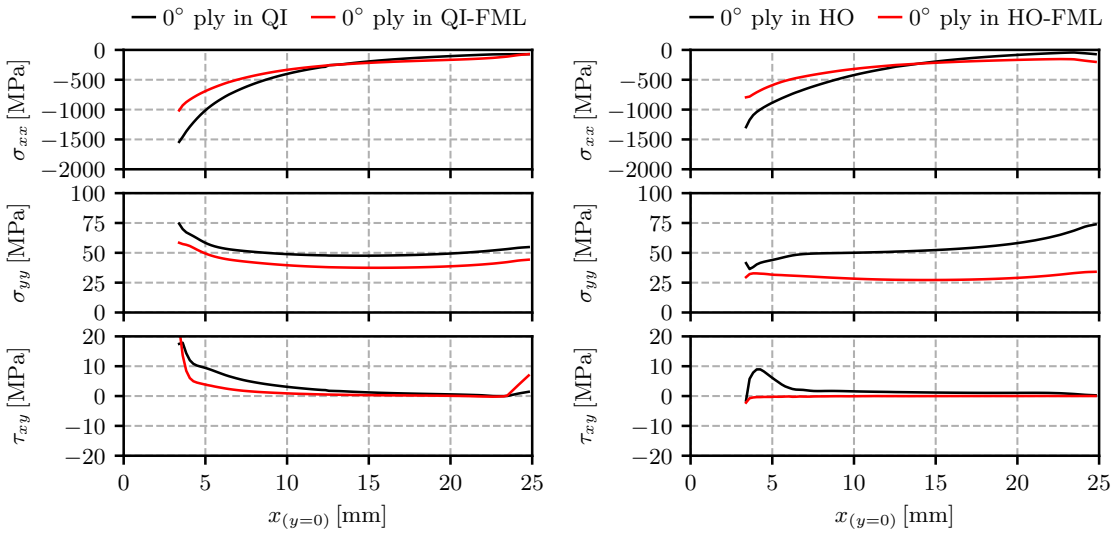

(a) QI vs. QI-FML **(b)** HO vs. HO-FML

Figure 6.29 Stresses along the bearing plane of a laminate within the 0° plies at the midplane at 250 MPa bearing stress at LT

on bearing behavior, the substitution of non-0° plies with steel in a monolithic laminate provides relief to the composite plies. This is due to the high stiffness of steel, which allows a significant portion of the loads to be transferred through the steel plies.

The relief of the composite plies is demonstrated in more detail in Figure 6.29 at the example of the 0° plies at the midplane of the QI, QI-FML, HO, and HO-FML specimens. As can be seen for both the QI and HO laminates, steel hybridization leads to a reduction in stresses in the composite plies. This is valid for all stress components in Figure 6.29, thus supporting the conclusion that introduction of steel in monolithic laminates leads to a relief of the composite plies.

6.3.2 Analysis of Damage Propagation

After analysis of the reinforcement effect in terms of stress alleviation in composite plies by steel hybridization, now the effect of hybridization on damage during bolt-bearing loading is studied. For this purpose the variables indicating the onset of damage in fiber and matrix modes, notably F_f^t, F_f^c, F_m^t and F_m^c, as well as plastic strain PE in the steel plies of the FMLs are evaluated at different load levels. The load levels comprise the elastic regime of the bolt-bearing behavior, i.e. 25 %, 50 % and 75 % of the 0.5 % offset-strength $\sigma_{0.5\%}^f$ (BYS), as well as the non-linear damage regime, i.e. the offset-strengths $\sigma_{0.5\%}^f$ and $\sigma_{4\%}^f$.

Figure 6.30 shows a cut through the bearing plane of the QI specimen at different load levels. The bolt and laminate above the midplane symmetry of the numerical model are presented. At 25 % of the BYS no damage is visible yet. The most notible stressing efforts are F_f^c (0° plies) and F_m^c (near the hole edge). During loading between

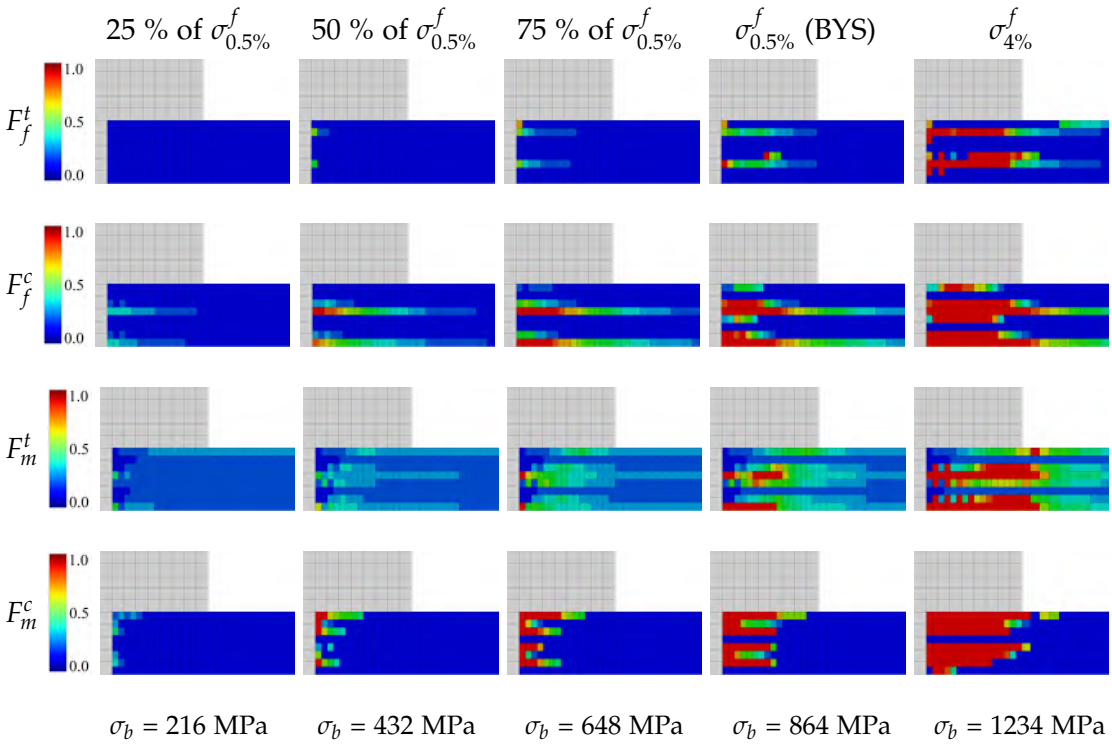

Figure 6.30 Evolution of damage onset criteria in QI at LT

50 % and 75 % of BYS, the onset and propagation of damage can be observed. Therein, fiber compressive damage F^c_f is the dominat damage mode in the 0° plies, while almost all plies suffer from matrix compressive F^c_m damage. Damage in matrix tensile mode F^t_m mode is present mainly in the 0° plies, indicating a tendency towards splitting in those plies. At 0.5 % offset-strength (BYS), significant damage is present in fiber compression F^c_f (mainly 0° plies), in matrix compression (all non-0° plies) and some matrix tensile damage in the 0° plies. The damage extends to roughly half the radius of the washer at BYS, which is in good agreement with experimental results by microcopy in Figure 6.32. Furthermore, fiber-kinking in the 0° plies observed during fractography is also indicated by fiber compressive damage in the numerical analysis in both quality and quantity. At 4 % offset-strength $\sigma^f_{4\%}$, damage accumulation in all composite plies can be observed. The area of damage accumulation is mainly limited to the area under the washer, which again agrees well with the findings during microscopy of the bearing plane. Furthermore, the angle of the damage frontline, visible as a step-wise decay over the plies in thickness direction, is an indication of wedge-type failure, which is also observed during microscopy of the bearing plane.

In Figure 6.31, the evolution of damage variables for the QI-FML at LT is presented. In addition to Hashin's damage onset variables, also the plastic strain for the steel plies is evaluated. It should be noted that while the same levels with respect to the yield strength of the bolted joint are selected for both QI and QI-FML, the actual bearing stress σ_b at those levels varies as the QI-FML exhibits a significantly higher bearing strength compared to the QI laminate. Similarly to the case of the QI laminate, there

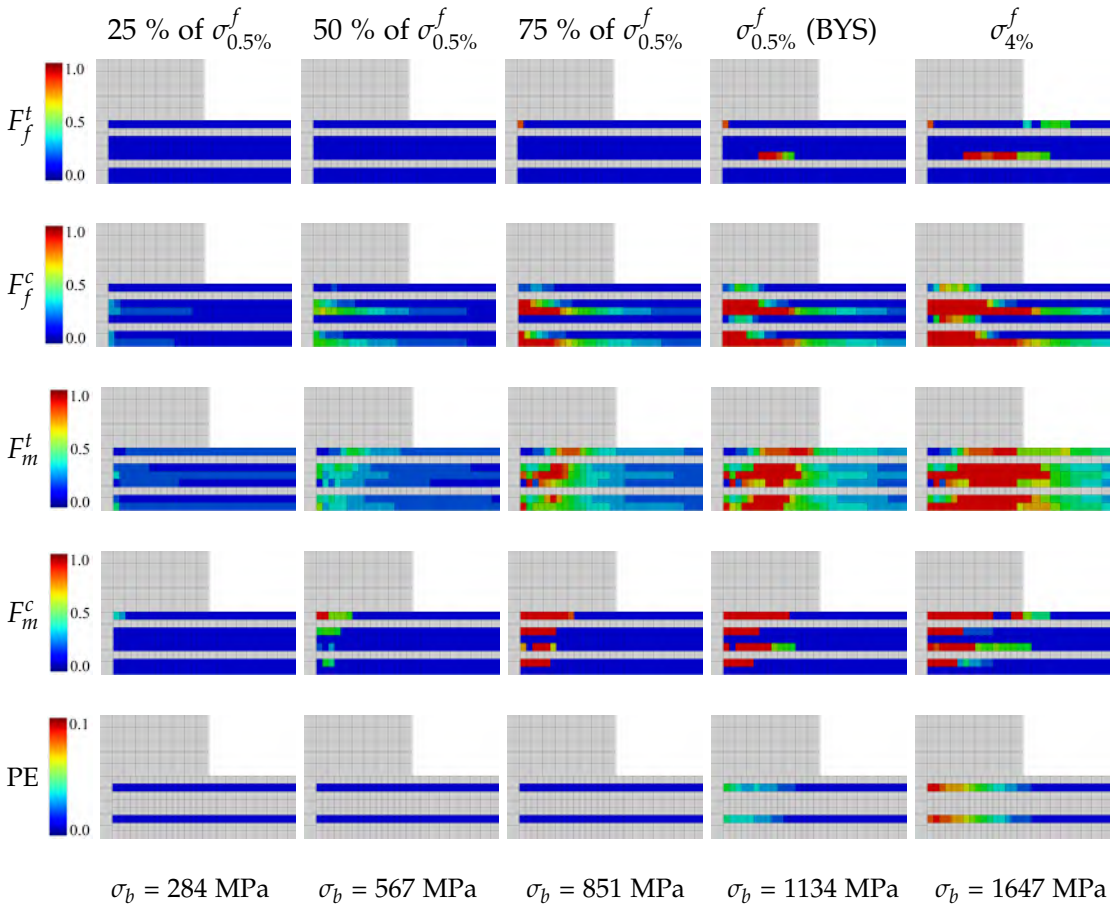

Figure 6.31 Evolution of damage onset criteria in QI-FML at LT

is no damage visible at 25 % of BYS. However, starting 50 % BYS the behvior of the hybrid laminate differs from that of the monolithic laminate. There is no damage in the 0° plies of the QI-FML despite higher bearing stress (567 MPa) than in the QI laminate (432 MPa). Therefore, the previously observed stress relief resulting from steel hybridization also appears to delay the onset of fiber compressive damage (F^c_f). In addition, the presence of steel plies significantly reduces the magnitude of matrix compressive damage F^c_m compared to the QI laminate. There is no plasticity within the steel plies up to a load level of 75 % of BYS. However, significant damage in fiber compression as well as matrix damage is present. Due to the fact that the steel plies are still intact, damage from the composite ply stacks are isolated and do not propagate along the thickness direction. The onset of non-linearity in the bolted joint at $\sigma^f_{0.5\%}$ is initiated by plasticity in the steel plies. This is a difference from the monolithic laminate, where damage accumulation under the washer area triggers yielding of the joint. Nonetheless, there is substantial damage present in the composite plies at BYS. Regarding both the quality, e.g. fiber kinking, and the quantity, i.e. damaged area, agreement between the numerical model and microscopy of the bearing plane is good. At 4 % offset-strength, substantial damage in the composite plies as well as plasticity in the steel layers is visible. Damage is mostly limited to the area under the washer, which again agrees with the findings within fractography of the bearing plane. It

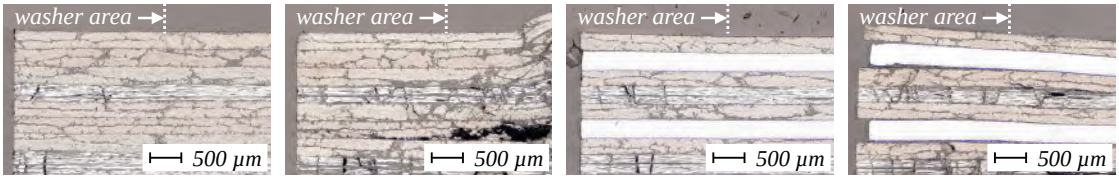

(a) QI at $\sigma^f_{0.5\%}$ **(b)** QI at $\sigma^f_{4\%}$ **(c)** QI-FML at $\sigma^f_{0.5\%}$ **(d)** QI-FML at $\sigma^f_{4\%}$

Figure 6.32 Microcopy along bearing plane of QI and QI-FML at LT

should be mentioned, however, that the microsections of the bearing plane do indeed show some damage as well as delaminations outside the washer area, which is not present in the numerical model due to the underlying modeling strategy that does not apply CZM. Similar observations can be made for the HO and HO-FML in Figure C.4 and Figure C.5 in Appendix C.2.

To conclude, examination of the damage variables within the monolithic and hybrid laminates, in order to build a deeper understanding of the underlying mechanisms responsible for the enhanced bearing capacity by steel hybridization, reveals two key aspects: Firstly, the substitution of 90° and ±45° plies with steel plies in the laminate effectively relieves the remaining composite plies. This relief occurs because the high stiffness of the steel plies enables them to carry a significant portion of the applied loads. Consequently, the initiation of damage within the composite plies is delayed to higher bearing loads. Secondly, the overall bolt bearing capacity experiences a substantial increase. This enhancement is primarily attributed to the load attraction and load-sustaining capabilities of the high-strength steel plies. Therein, the high stiffness of the steel allows for full exploitation of the steel strength. Additionally, hybridization by steel successfully isolates damage within the remaining composite stacks, resulting in reduced damage growth in thickness direction within the hybrid laminates.

6.3.3 Potential for Virtual Testing

Building upon the previous sections, where a numerical modeling strategy was derived and applied to improve the understanding of the mechanisms that contribute to the increase in bearing strength through hybridization, the present section utilizes the same modeling approach as a numerical analysis tool to determine design values. This way, the prospects of the numerical approach in regard to virtual testing are demonstrated.

In the context of virtual testing, the present numerical tool for bolt-bearing analysis is applied for the determination of design parameters, notably the critical e/d and w/d ratios. These critical ratios are used to define the minimum edge and width distances in the design of bolted joints. The conventional way of defining those values is as follows: Usually, the bearing strength is determined experimentally for a variety of e/d and w/d ratios. The critical ratios correspond to the respective edge-distance e and width w values for which a significant loss in strength and deviation from the favourable bearing failure mode can be observed. This conventional approach is ap-

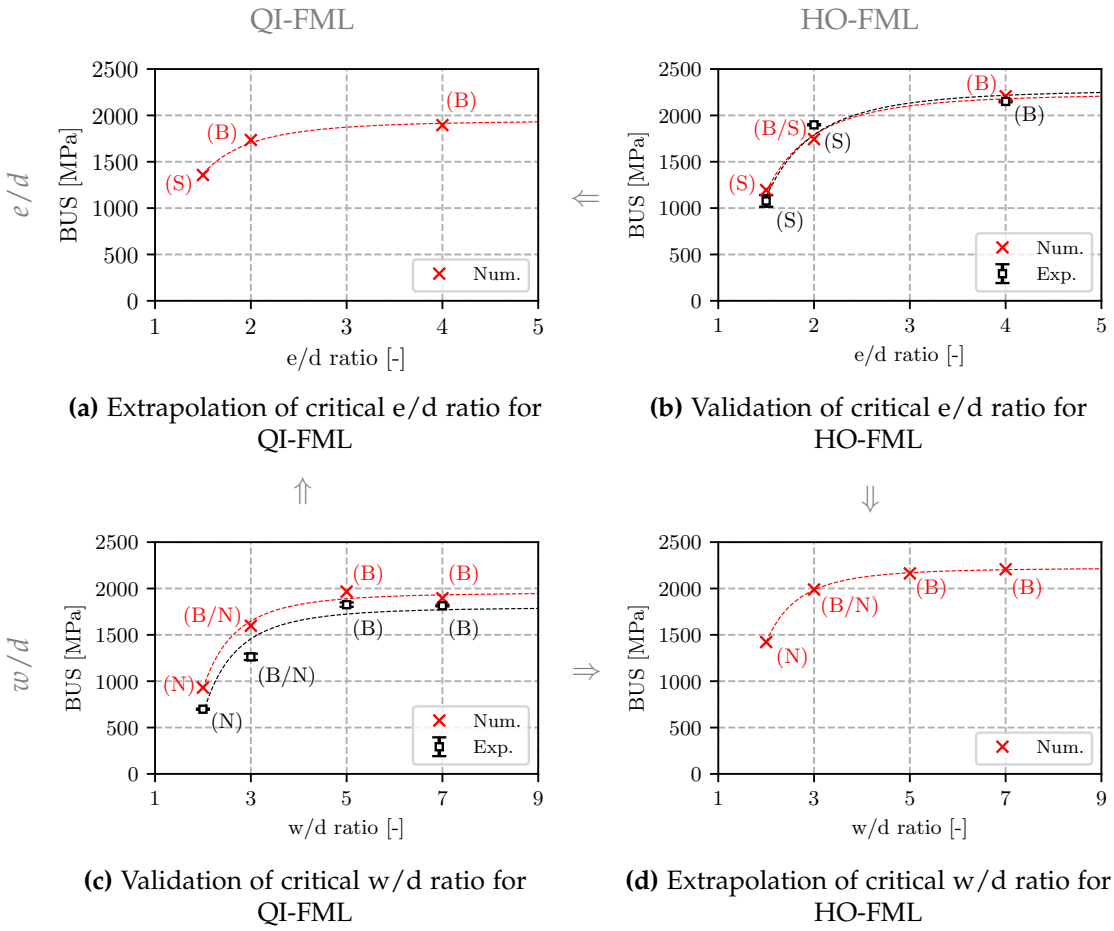

(a) Extrapolation of critical e/d ratio for QI-FML

(b) Validation of critical e/d ratio for HO-FML

(c) Validation of critical w/d ratio for QI-FML

(d) Extrapolation of critical w/d ratio for HO-FML

Figure 6.33 Validation of numerical model for variation of geometry (**b, c**) and numerical determination of critial e/d and w/d ratios by extrapolation (**a, d**) at LT

plied in Chapter 5 for determining minimum e/d and w/d ratios for the QI- and HO-FML at LT. However, since this approach requires substantial testing, the critical e/d ratio is definded only for the HO-FML, while the critical w/d ratio is only determined for the QI-FML, as those represent critical cases. By numerical simulation, i.e. virtual testing of bolt-bearing specimens according to AITM 1-0009, the remaining critical e/d ratio for the QI-FML and the w/d ratio for the HO-FML are determined. Determination of the bearing strength is based on BUS or the 10 % offset-strength, depending on which criterion is met first.

In Figure 6.33, the strategy for reducing physical testing is presented. The experimental bolt-bearing test results from Chapter 5 for different e/d and w/d ratios are used to validate the numerical tool for application to cases of varying specimen geometry. This is necessary as the validation in Section 6.2.4 only accounts for variation of orthotropy, MVF and temperature. Comparison of the bearing strength for varying e/d ratios in case of the HO-FML in Figure 6.33b shows excellent agreement with respect to both absolute bearing strength values as well as the regression line indicating the qualitative drop in bearing strength for decreasing edge distance e. In

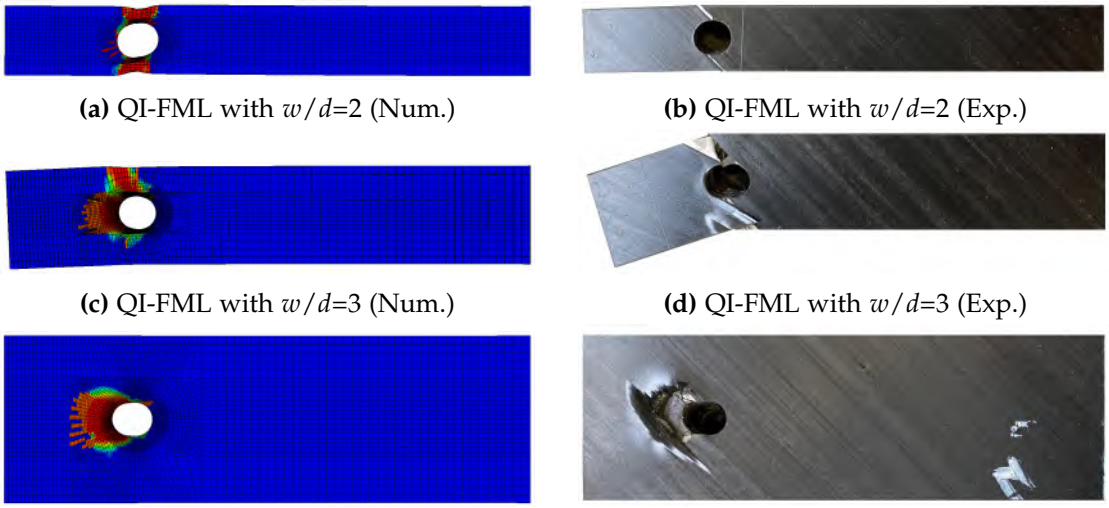

(a) QI-FML with w/d=2 (Num.)

(b) QI-FML with w/d=2 (Exp.)

(c) QI-FML with w/d=3 (Num.)

(d) QI-FML with w/d=3 (Exp.)

(e) QI-FML with w/d=5 (Num.)

(f) QI-FML with w/d=5 (Exp.)

Figure 6.34 Comparison of numerical and analytical failure pattern after testing at LT

case of the QI-FML in Figure 6.33c, the numerical model overpredicts the experimentally measured bearing strength for low specimen widths. However, the qualitative loss in bearing strength for decreasing w/d ratios indicated by the regression line is captured very well. Figure 6.34 demonstrates the capabilits of the numerical model to correcty capture the failure mode in the QI-FML at LT, despite overestimating the absolute force at failure. Thus, although some small deviation exist in the respective bearing strength, especially for low w/d values, the general conclusions remain the same. Therein, both experimental and numerical testing lead to the conclusion that in case of the HO-FML in Figure 6.33b a minimum e/d ratio of around 3-4 is valid, while for the QI-FML in Figure 6.33c the minimum w/d ratio is around 4-5. Based on the agreement between numerical and experimental data for these cases, the critical e/d ratio for the QI-FML and the critical w/d ratio for the HO-FML are determined solely based on numerical data. Evaluation of the numerically determined strength values for varying geometries yields a minimum e/d ratio of around 3-4 for the QI-FML and a minimum w/d ratio of around 4-5 for the HO-FML.

The numerical approach offers a substantial reduction in the amount of required experimental testing. Each data point in Figure 6.33a and Figure 6.33d represents the results of three individual tests, resulting in a total of 21 bolt-bearing tests that are saved compared to the conventional approach, and thereby reducing the overall testing workload for all four cases by 50 %, compared to the case in which all values are determined experimentally. The present example is a small yet compelling demonstration of the prospects of the numerical analysis tool for application in terms of virtual testing for saving time and cost during the design of mechanically fastened joints.

6.4 Summary and Conclusions

In the present chapter, both interlaminar and bolt-bearing modeling of CFRP-steel hybrid laminates is investigated in detail. The findings within this investigation contribute to a comprehensive understanding of the required modeling strategy. The numerical model resulting from the investigation serves as a potent tool for detailed analysis of the structural behavior of CFRP-steel joints.

In the first part of the chapter, interlaminar modeling of CFRP-steel hybrid interfaces is studied. A detailed analysis of thermal effects on the delamination behavior is provided, highlighting the necessity for including a temperature step in the analysis process as well as using corrected input data, notably the interlaminar fracture toughness adjusted for parasitic thermal effects during experimental testing. Thereby, also the correction methodology proposed in Chapter 4 is validated by application to experimental test results. These findings support *Working Hypothesis III*, which proposed that inclusion of thermal effects in necessary for accurate numerical modeling of CFRP-steel FMLs.

The second part of the chapter focuses on bolt-bearing modeling. Therein, a numerical simulation strategy for accurate modeling of CFRP-steel FML bolted joints is derived. Special emphasis is directed towards the question whether thermal effects need to be included into the analysis process. The numerical analysis shows that inclusion of thermal residual stresses by application of a temperature step improves the accuracy of the simulation of the bolt-bearing behavior in CFRP-steel FMLs. Thereby, application of a temperature step allows to accurately capture the intrinsic stress state in FMLs, and thus correctly model the joint behavior. This observation confirms the findings within the interlaminar analysis and further supports *Working Hypothesis III*.

The numerical modeling strategy is successfully subjected to extensive validation by comparison to experimental bolt-bearing test data for varying degrees of orthotropy, MVF, temperature levels as well as a number of different joint geometries by variation of edge- and width-distances. Thereby, allowing the numerical model to be employed as a tool for detailed analysis of hybrid bolted joints.

Using the numerical analysis tool, a better understanding of the reinforcement effect in hybrid bolted joints is built. Therein, steel hybridization of a composite structure mainly improves the bearing behavior by relieving composite plies, thereby retarding damage in the composite plies. In addition, damage in the composite stacks is isolated and prevented from propagating in thickness direction. Finally, high stiffness in combination with high strength of steel improves the load bearing capacity in CFRP-steel bolted joints at high loads. In addition to applying the numerical tool for analyzing damage behavior, it can be employed for virtual testing in order to reduce the necessity for physical testing. At the example of critical e/d and w/d ratios, the prospects of the numerical analysis tool are demonstrated in the context of numerical parameter determination by a 50 % reduction of physical tests. This approach proves to be cost-effective and time-saving, while maintaining validity of the numerically determined parameters.

Chapter 7

Analytical Modeling of Hybridized Composite Bolted Joints

7.1 Overview on Analytical Approaches

The vast number of geometrical and material design variables, especially during preliminary design stages, renders empirical design procedures for mechanically fastened joints highly effortful and expensive. In order to accelerate the design procedure, numerical and analytical design tools are employed, thus reducing the need for extensive experimental test campaigns. While being widely used for the design of small to medium-sized parts, FEA has the drawback of being rather computationally expensive. Furthermore, FEA in the context of mechanically fastened joints is used for modeling progressive damage behavior including the application of highly sophisticated failure criteria and material degradation models [141, 164, 165], rather than the mere application of a simplified analytical failure criterion on a numerically determined stress distribution [67]. Compared to FEA, analytical design methods can be even more efficient depending on the choice of analytical approach. Analytical design procedures for mechanically fastened joints range from simplified design procedures where stresses on laminate level are compared to the laminate strength, over methods applying stress concentration factors (SCF) to methods that employ approximate and exact closed-form analytical solutions. In the present chapter, a novel analytical design methodology for analyzing FML mechanically fastened joints is proposed. As oppose to other design tools, thermal residual stresses are included into the design process in order to account for the peculiarities of FMLs. After giving a general overview on different approaches for designing mechanically fastened joints, the individual modules of the analytical design methodology are presented and discussed in detail. At the end of Chapter 7, the design methodology is validated using experimental test data and compared to competing design tools.

Simplified Design Procedure

A simplified procedure that is often applied for rough estimates on the strength of mechanically fastened joints in composite structures during preliminary design has been proposed by NASA [166]. This procedure, also adopted in VDI 2014-3 [167], essentially compares stresses and strengths on laminate level, whilst differentiating the

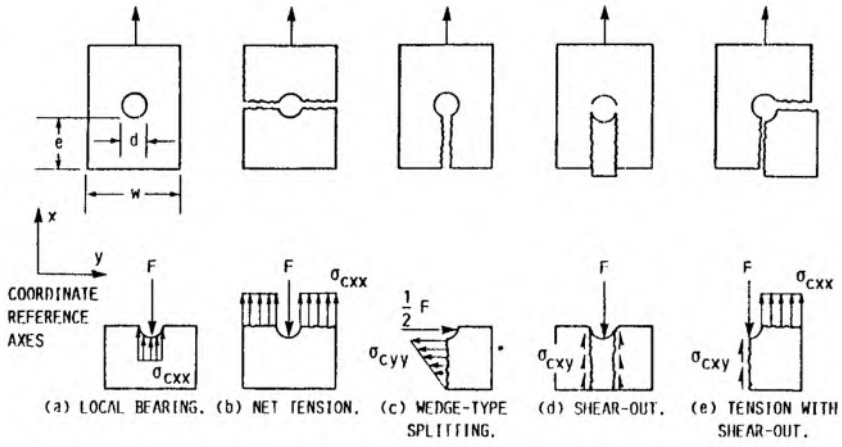

Figure 7.1 Failure modes and respective loading cases according to the simplified design procedure for composite joints by NASA [166]

basic failure modes in mechanically fastened composite joints, i.e. bearing, net-tension, shear-out, wedge-type splitting as well as cleavage failure mode. The maximum allowable bolt force F_{all} for each of the failure modes in Figure 7.1 is given by:

(a) bearing:	$F_{all} \leq d \cdot t \cdot X_C$
(b) net-section:	$F_{all} \leq (w-d) \cdot t \cdot X_T$
(c) wedge-type splitting:	$F_{all} \leq \frac{1}{2}(2e-d) \cdot t \cdot Y_T$
(d) shear-out:	$F_{all} \leq 2e \cdot t \cdot S$
(e) tension with shear-out:	$F_{all} \leq \frac{1}{2}t((w-d)X_T + 2e \cdot S)$

For example, failure in bearing mode is calculated by effectively comparing the mean bearing stress F/dt to the compressive strength X_C of the laminate. The present approach is capable of providing a rough estimate on the bearing strength. However, geometrical and material characteristics, as for instance stress concentrations or 3D-effects, are not considered. Furthermore, tensile, compressive and shear strengths in longitudinal and transverse direction are required on laminate level, thereby inhibiting simple and fast variation of materials and layups.

Design with Stress Concentration Factors

Design of mechanically fastened joints based on SCF, also known as C-Factor method, is widespread in both preliminary and detailed design stages. Depending on the approach based on which the SCF is determined, design methodologies can be further categorized in experimental, numerical or analytical. Experimental SCF definition is effortful and costly but is often used in aircraft design due to its high accuracy as well as its compatibility with knock-down factor (KDF) methods in order to include additional safety margins, e.g. for manufacturing defects, joint types, environmental effects etc. [168, 169]. Numerical or semi-analytical SCF approaches often determine the stress distribution using 2D FEA and define SCF that are subsequently used for analytical failure analysis [154].

The analytical SCF approach for composite materials is derived from the SCF method for elastic isotropic materials [170]. Given that the respective elastic isotropic SCF are determined for the same geometry as the composite material under consideration, application of an empirically determined factor (C-Factor) allows for the extension of the SCF to account for the composite orthotropy, non-homogeneity, and the non-linear material behavior. Interpretation of experimental bearing test data suggests a linear interaction between tensile stresses σ_t and bearing stresses σ_b for net-section failure in multi-row bolted joints:

$$\sigma_{max} = k_t\sigma_t + k_b\sigma_b \leq \sigma_{t,all} \tag{7.1}$$

In case of a single-bolt joint, the equation is reduced to the bearing load term. As mentioned in the beginning of the section, determination of the stress concentration factors can be done in different ways. For preliminary design purposes, the approach by Hart-Smith [170] is oftentimes sufficient enough. Therein, the tensile and bearing stress concentration factors k_t and k_b are defined as:

$$k_b = \frac{1}{w/d-1}\left[1 + C\left(\frac{w}{d} - 1.5\frac{w/d-1}{w/d+1}\Theta\right)\right] \tag{7.2}$$

$$k_t = 1 + C\left[1 + \left(1 - \frac{d}{w}\right)^3\right] \tag{7.3}$$

The parameter Θ is defined as $\Theta = 1.5 - 0.5/(e/w)$ for $e/w \leq 1$ and $\Theta = 1$ for $e/w > 1$, while C is the correlation factor between stress concentration factors observed in composites at failure and those in metallic specimens of identical geometry. The factor C can be derived from design charts based on empirical data curve fits for comparable materials and stackings [170]. However, several alternative procedures have also been proposed in literature for purely as well as semi-analytical determination of the SCF [171–174]. For the purpose of detailed design, the stress concentration factors are usually determined experimentally to explicitly account for effects due to layup, geometrical effects (i.e. e/d, w/d and t/d ratios), loading type (tension/compression), joint type (e.g. single-lap or double-lap joints) as well as fastener type (e.g. protruding or countersunk). A further cut-off condition based on the laminate bearing allowable $\sigma_{b,all}$ is applied to take into account bearing failure:

$$\sigma_b \leq \sigma_{b,all} \tag{7.4}$$

In general, $\sigma_{b,all}$ is determined empirically. For rough estimates on the bearing strength of a joint, however, the bearing allowable can be equated to the laminate compressive strength $\sigma_{b,all} = X_C$ [166]. Application of the SCF approach offers the advantage to design not only single-bolt but also multi-row joints. However, the accuracy of the approach depends on the method based on which the SCF are determined. While purely analytical formualtions for the SCF for net-section failure are availabel, determination of bearing failure often requires empirical data for acceptable results, thus limiting the applicability of the SCF method for preliminary design stages.

Exact Analytical Solutions

Exact analytical solutions based on the Lekhnitskii formalism [175] exhibit a great potential for calculating the stresses in mechanically loaded plates for subsequent failure analysis. Most of the purely analytical approaches for determining SCF are based on exact analytical solutions or their approximations. Therein, the exact analytical solution is usually solved for a characteristic point or along a characteristic path in order to derive SCF. However, exact analytical solutions are not restricted to SCF at characteristic points or paths, but allow for the calculation of stresses at any point and in any direction of a mechanically loaded plate under consideration, e.g. a pin-loaded hole or a notched laminate under tensile loading. Limitations associated with exact analytical solutions mainly result from the 2D in-plane idealization, thus not allowing for 3D effects to be incorporated, such as for instance clamping in bolted joints. However, depending on the choice of analytical model, relevant phenomena in pin-loaded composite laminates such as the effects of friction [176–185], clearance [178, 181–183], pin-elasticity [181, 186, 187], bending-extension-coupling of the plates [188] as well as finite specimen geometry [177, 182, 186, 187, 189] can be accounted for. Exact analytical solutions for determining the stress distribution in pin-loaded composite joints are reported to yield very accurate stress predictions for cases with no bending of the midplane (double-lap joints) and small clearances [154, 190]. The prospects of exact analytical solutions become more clear especially when considering the possibility of superposition of the stress distribution in pin-loaded laminates with arbitrary loading directions and the stress distribution of notched laminates, representing the common case of bearing-bypass interaction in mechanically fastened joints. Furthermore, as oppose to the previously introduced methods, application of exact analytical solutions in conjunction with CLT allows for failure analysis solely based on stiffness and strength properties of a UD single ply.

7.2 Analytical Joint Design Methodology - ajaX

As previously stated, the large number of variables in preliminary design stages renders empirical design procedures prohibitively effortful and expensive. Consideration of local metal hybridization further increases the number of variables. Therefore, reliable and efficient methods are needed which allow for the analysis of effects on the joint strength resulting from geometry and material parameter variations. A purely analytical approach is chosen because even linear-elastic FEA is computationally expensive when compared to the analytical methods considered in the following, especially for design studies with a large number of variables. The requirements for such an analysis method are:

- minimum data input
- low computation time
- applicability to FML joints

Minimum data input, preferably only stiffness and strength data of a single UD-ply, is defined in order to facilitate variation of different materials and stacking sequences. In an attempt to maximize the information gained within the analysis process

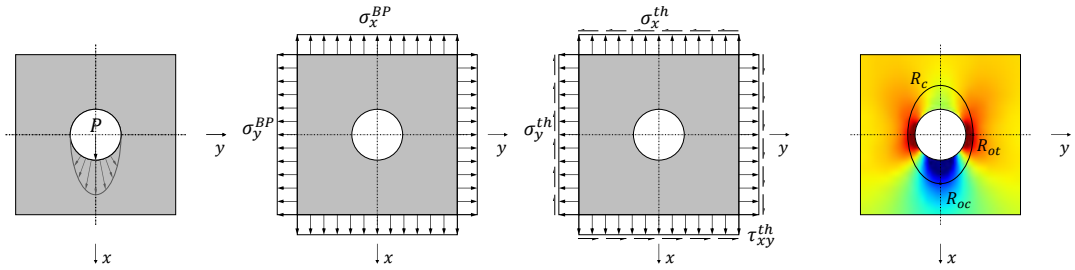

(a) Stress field due to bearing loading **(b)** Stress field due to bypass loading **(c)** Stress field due to thermal loading **(d)** Superposition & failure analysis

Figure 7.2 Schematic representation of superposition bearing, bypass and thermal loading cases and subsequent failure analysis based on the characteristic curve method

as many additional effects as possible are to be incorporated into the design process, e.g. orthotropy of the laminate, finite specimen geometries or friction. The efficiency of the tool is improved by applying purely analytical approaches to reduce computation time, while parameterability allows for automized analysis of multi-fastener joints and inclusion of thermal residual stresses in the design process takes into account the peculiarities of FMLs. In its essence, the following purely analytical design philosophy attempts to minimize required input data and computation time, while maximizing the gain in information, i.e. prediction of failure load and failure mode. The goal is to facilitate indicatory choices of joining concepts in early design stages by revealing effects of primary design variables on the overall strength of mechanically fastened joints, explicitly for the purpose of analyzing FML joints.

A design tool, **ajaX**[1], purely based on analytical methods is developed. Exact analytical solutions for calculating the stress distribution are implemented in conjunction with CLT and the characteristic curve method, thus providing a purely analytical approach for the analysis of pinned and bolted joints, see Figure 7.2. Failure analysis is done on lamina level using analytical fracture criteria, i.e. Yamada-Sun and Cuntze FMC. This allows for extensive parameter studies within preliminary design stages by simple and fast variation of geometrical, material and loading conditions, while only requiring the in-plane stiffness and strength of a UD composite ply as data input. In the following sections, the underlying methods for predicting stresses due to bearing, bypass and thermal loads as well as the methods for failure analysis are introduced, verified and validated individually. At the end of the chapter, the procedure of the design methodology is presented in detail and the design tool is validated against experimental pin-bearing and bolt-bearing test data.

7.2.1 Stress Distribution due to Bypass-Loads

The stress distribution in a composite plate with a circular center notch can be calculated using exact analytical solutions. This loading scenario represents both the case of stresses around circular cut-outs in composite structures as well as bypass stresses ocurring in multi-row mechanically fastened joints. Accurate failure analysis, how-

[1] analytical joint analysis tool

ever, requires knowledge on the accuracy of the underlying stress calculation method. Thus, the goal of the present section is to compare and evaluate existing analytical solutions from literature. Therefore, experimental testing of open-hole-tension (OHT) specimens conforming to AITM 1-0007 is accompanied by digital image correlation (DIC) as well as detailed 3D FEM. Laminates with varying degree of orthotropy (UD-0°, UD-90° and QI) as well as varying w/d ratios (3 and 5) are considered. In a first step, the results of the analytical and numerical models are validated using experimental DIC data. Subsequently, FE-data is used to evaluate the stress distribution in individual plies predicted by the analytical methods. The overall goal is to clarify to what extent the application of different exact analytical solutions presented in literature is valid for preliminary design purposes. The results of the present section have been partly published in Koord et al. [116].

Lekhnitskii Formalism

The Lekhnitskii formalism for 2D deformations of anisotropic elastic materials was introduced in 1957 [175]. In its essence, the work of Lekhnitskii represents a generalization of Muskhelishvili's solutions for the 2D deformations of isotropic elastic materials [191]. The derivation of the Lekhnitskii formalism is described in detail in [175] and frequently covered in literature [174, 192–196]. As this method constitutes the basis of the analytical methods applied for stress calculation, a brief introduction is presented herein. The starting point for the analytical solution is the fundamental equilibrium equation for a 2D plate:

$$\left.\begin{aligned} \frac{\partial \sigma_x}{\partial x} + \frac{\partial \tau_{xy}}{\partial y} + X = 0 \\ \frac{\partial \sigma_y}{\partial y} + \frac{\partial \tau_{xy}}{\partial x} + Y = 0 \end{aligned}\right\} \tag{7.5}$$

with the average normal and shear stresses σ_x, σ_y and τ_{xy} as well as the directional body forces X and Y. The second equation needed is the compatibility condition that ensures integrity and continuity during deformation and which is given by:

$$\frac{\partial^2 \varepsilon_x}{\partial y^2} + \frac{\partial^2 \varepsilon_y}{\partial x^2} - \frac{\partial^2 \gamma_{xy}}{\partial x \partial y} = 0 \tag{7.6}$$

with the average normal and shear strains ε_x, ε_y and γ_{xy}. The equilibrium equation 7.5 and compatibility condition 7.6 are connected through Hooke's law:

$$\left.\begin{aligned} \boldsymbol{\sigma} = \boldsymbol{C}\boldsymbol{\varepsilon} \\ \boldsymbol{\varepsilon} = \boldsymbol{S}\boldsymbol{\sigma} \end{aligned}\right\} \tag{7.7}$$

in which $\boldsymbol{C}$ is the stiffness matrix, $\boldsymbol{S}$ the compliance matrix and the stress and strain components are written in the vectors $\boldsymbol{\sigma}$ and $\boldsymbol{\varepsilon}$. Following Lekhnitskii's approach, the body forces in the equilibrium equation 7.5 are neglected. This allows for the stress components to be expressed in terms of an Airy's stress function $F(x, y)$ which satisfies the equilibrium condition for:

$$\sigma_x = \frac{\partial^2 F}{\partial y^2}, \quad \sigma_y = \frac{\partial^2 F}{\partial x^2}, \quad \tau_{xy} = -\frac{\partial^2 F}{\partial x \partial y} \tag{7.8}$$

By substituting the strain expression from Equation 7.7 and the Airy stress notation from Equation 7.8 into the compatibility Equation 7.6, the following biharmonic equation which represents the basic equation for the 2D problem of elasticity is obtained:

$$a_{22}\frac{\partial^4 F}{\partial x^4} - 2a_{26}\frac{\partial^4 F}{\partial x^3 \partial y} + 2(a_{12} + a_{66})\frac{\partial^4 F}{\partial x^2 \partial y^2} - 2a_{16}\frac{\partial^4 F}{\partial x \partial y^3} + a_{11}\frac{\partial^4 F}{\partial y^4} = 0 \tag{7.9}$$

with a_{ij} being components of the compliance matrix $\boldsymbol{S}$. The general solution of Equation 7.9 is given by the roots of its characteristic equation:

$$a_{11}\mu^4 - 2a_{16}\mu^3 + (2a_{12} + a_{66})\mu^2 - 2a_{26}\mu + a_{22} = 0 \tag{7.10}$$

As proven by Lekhnitskii [175], Equation 7.10 has four distinct roots which occur in complex conjugate pairs:

$$\left.\begin{aligned} \mu_1 &= \alpha_1 + i\beta_1, \quad & \mu_2 &= \alpha_2 + i\beta_2 \\ \overline{\mu}_1 &= \alpha_1 - i\beta_1, \quad & \overline{\mu}_2 &= \alpha_2 - i\beta_2 \end{aligned}\right\} \tag{7.11}$$

and are defined by the real numbers α_1, α_2, β_1 and β_2 with β_1, $\beta_2 > 0$. These parameters depend on the Young's and shear moduli and Poisson's ratio of the material, thus, describing its degree of anisotropy. The stress functions in Equation 7.8 can be rewritten as:

$$F = F_1(z_1) + F_2(z_2) + F_3(\overline{z}_1) + F_4(\overline{z}_2) \tag{7.12}$$

with the anisotropic complex coordinates $z_m = x + \mu_m y$ and $\overline{z}_m = x + \overline{\mu}_m y$ ($m = 1, 2$). Further operations yield the following expression where the stress function is the real part of the two complex functions $F_1(x)$ and $F_2(x)$:

$$F = 2\mathrm{Re}[F_1(z_1) + F_2(z_2)]. \tag{7.13}$$

Now, the analytic functions $\phi(z_1)$ and $\psi(z_2)$ are introduced as the derivatives of the complex functions $F_1(x)$ and $F_2(x)$:

$$\phi(z_1) = \frac{\partial F_1}{\partial z_1}, \quad \psi(z_2) = \frac{\partial F_2}{\partial z_2} \tag{7.14}$$

Equation 7.13 is inserted into Equation 7.8 and the derivatives of the complex function are substituted by Equation 7.14, yielding the stress components in terms of $\phi(z_1)$ and $\psi(z_2)$:

$$\left.\begin{aligned} \sigma_x &= 2\mathrm{Re}[\mu_1^2\phi'(z_1) + \mu_2^2\psi'(z_2)] \\ \sigma_y &= 2\mathrm{Re}[\phi'(z_1) + \psi'(z_2)] \\ \tau_{xy} &= -2\mathrm{Re}[\mu_1\phi'(z_1) + \mu_2\psi'(z_2)] \end{aligned}\right\} \tag{7.15}$$

The expressions in Equation 7.15 reduce the initial task of determining the stress distribution in an anisotropic 2D plate to finding expressions for the stress functions $\phi(z_1)$ and $\psi(z_2)$. By assuming boundary conditions on the hole edge that are in line with the true stress distribution in the plate, the unknowns in the expressions for the stress functions can be determined. The expressions used by Lekhnitskii to describe

the stress functions $\phi(z_1)$ and $\psi(z_2)$ are based on Fourier series. However, also other approaches can be taken when defining suitable expressions for the stress functions. Examples found in literature for the case of a circular hole in an orthotropic plate are presented in the following section.

Analytical Solutions for Stress Functions

A number of alternative expressions for the stress functions based on the Lekhnitskii formalism have been introduced in literature. In the following, a brief overview is given on solutions applicable to the OHT-case. If not stated otherwise, the following analytical approaches all consider an infinite plate with a circular center notch as well as anisotropic material properties.

By applying the Schwarz-Christoffel integral method for mapping the hole contour and the Schwartz formula for the expression of stress functions, Savin [197] proposes an alternative solution for the expression of the stress functions. Despite the fact that the solution for the stress functions by Savin differs from that of Lekhnitskii, it was found that the two approaches yield identical results for the stresses around the hole edge [194]. Both solutions are valid for anisotropic plates of infinite size.

The analytical procedure for determining stresses in an anisotropic plate proposed by Liang and Palantera [198] is based on the Lekhnitskii formalism. However, the method is capable of including in-plane loads that may be a combination of tension, compression, and shear. Furthermore, this analytical procedure is a rare example of an exact analytical solution being implemented in commercial software (Altair ESAComp™). No validation of the solution is conducted, nevertheless, it is stated that the approach is limited to cases for which $w/d>4$.

Ukadgaonker and Rao [199] extend the formulation proposed by Savin [197] by introducing a general form of mapping function and an arbitrary biaxial loading condition into the boundary conditions. Thereby accounting for arbitrary hole shapes and random uniaxial, biaxial, and shear loading conditions. Stress fields for different hole shapes and loading cases based on the exact analytical solution are presented and discussed, but no comparison to experimental or numerical data is provided in order to assess the accuracy of the approach.

Echavarria [174] introduces a solution for calculating the stress distribution around pin-loaded plates as well as plates with a circular central notch under uniaxial loading. An alternative solution for the open hole problem is given by employing simplified stress functions based on the Schwartz formula and conformal mapping. Verification by FEA shows good agreement for different geometries and degrees of anisotropy of the laminate. Further analysis recommends application of the method for cases with $w/d\geq 2.5$ [200].

Hu et al. [193] propose an analytical approach based on uniformed boundary conditions and a complex variable approach. The mapping function applied is the same as used by Ukadgaonker and Rao [199]. Results for different laminate layups as well as a comprehensive comparison to experimental DIC data and numerical models with layer-wise discretization are presented. The assessment of accuracy yields good agreement for the analytical model introduced to both experimental and numerical results with respect to both laminate as well as lamina stress and strain distributions.

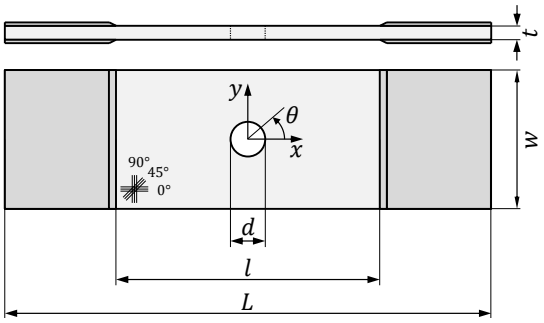

Figure 7.3 OHT test specimen geometry

Property	Unit	UD-0°	UD-90°	QI
Total length, L	mm	320	320	320
Free length, l	mm	180	180	180
Diameter, d	mm	6.355	6.355	6.355
Width, w	mm	32	32	32
w/d ratio	-	5	5	5
Thickness, t	mm	2.36	4.19	4.19
OHT Strength	kN	26.3	5.5	52.5
Std. Dev.	kN	$\pm$0.7	$\pm$0.3	$\pm$1.3

Table 7.1 Geometry data and test results

The selection at hand represents a variety of solutions for the case of a circular notch under tensile loading. The first set of stress functions was introduced by Lekhnitskii [175] in 1957 while the latest one was proposed by Hu et al. [193] in 2017. It was paid attention not to include solutions where the expressions for the stress components are obviously identical or transformations of one another. Further, it should be noted that all methods exhibit a singularity for cases of isotropic behavior which results in equal roots of the characteristic function in Equation 7.10. In order to avoid the singularity, the roots are slightly manipulated. As shows by Tung [201], changing the value of the roots by 2 % leads to a difference in the exact analytical solution of less than 0.01 %. Thus, this approach is applied whenever QI laminates are analyzed.

The results of a preliminary study on the analytical solutions are presented in Figure 7.4. In accordance with the coordinate system in Figure 7.3, an infinite plate with a center circular hole of $d = 6.355$ mm and properties of a UD-0° ply according to Table 4.3 is considered. In Figure 7.4a, the stress components σ_{xx}, σ_{yy} and τ_{xy} along the hole edge normalized by the applied load p are shown, while in Figure 7.4b the same normalized stresses are presented for a radial path perpendicular to the main loading direction at $\theta = 90°$. Two main observations are made on the basis of the preliminary study: When considering the path along the edge of the center hole in Figure 7.4a, all analytical solutions considered yield the exact same result for all stress components. This observation is surprising because all methods chose different approaches with varying boundary conditions when deriving solutions for the stress functions. Analysis of the radial path perpendicular to the loading direction in Figure 7.4b reveals that application of the analytical solutions results in one of two possible curve shapes which differ with respect to the decay of the stress concentration starting at the hole edge (r/R$\geq$1). In fact, the solutions by Lekhnitskii [175], Savin [197], Soutis and Filiou [195], Liang and Palantera [198], and Echavarria [174] yield identical curve shapes (solution A), while the solutions introduced by Ukadgaonker and Rao [199] and Hu et al. [193] are identical to one another (solution B) but vary from the curve shape of the other methods. It is assumed that the analytical expressions employed for the definition of the stress functions in Equation 7.14 are responsible for the difference in curve shapes instead of the choice of boundary condition. For example, the stress boundary conditions for the stresses around the hole edge as well as the far field stresses applied by Hu et al. [193] (solution B) and Soutis and Filiou [195] (solution A) are identical,

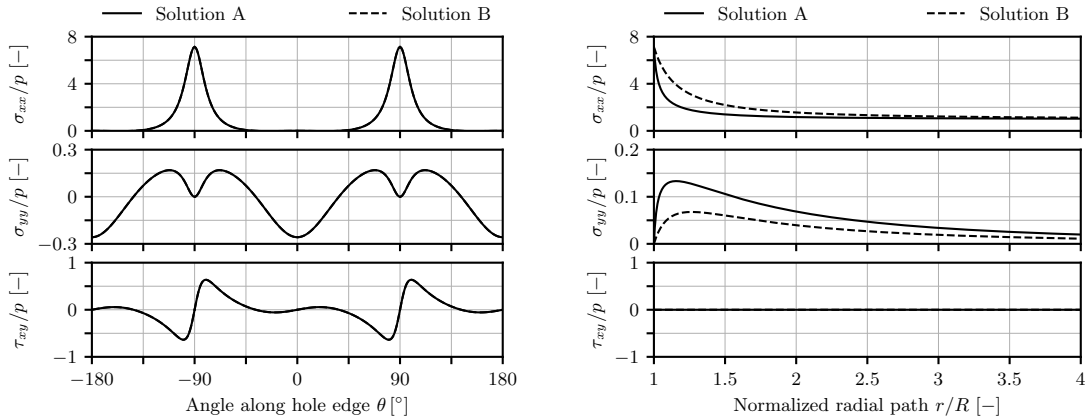

(a) Stress components along the hole edge

(b) Stress components along a radial path

Figure 7.4 Comparison of analytical solutions: Solution A represents methods introduced in [174, 175, 195, 197, 198], Solution B shows methods from [193, 199] for a plate with a circular hole loaded in tension

however, application of the respective solutions yields a different stress distribution.

In essence, while it was previously demonstrated that the solutions of Lekhnitskii [175] and Savin [197] yield identical results for the case of an infinite plate with a center hole [194], the extension of this observation to the solutions introduced by Soutis and Filiou [195], Liang and Palantera [198], and Echavarria [174] has not yet been reported in literature. Furthermore, despite the fact that the cited literature proposes different derivations, it seems as though there are only two distinct solutions available to the OHT-case. As a result of the findings within the preliminary study, hereafter, two analytical solutions will be referred to: solution A representing [174, 175, 195, 197, 198], and solution B referring to [193, 199].

Evaluation of Analytical Solutions

In order to analyze the exact analytical solutions for stress calculation, additional experimental testing and numerical simulation of OHT specimens is conducted. Specimens made of M21/T700GC with different layups ($[0]_{18}$, $[90]_{32}$ and $[-45/90/+45/0]_{4s}$) as well as varying w/d ratios (3 and 5) are manufactured and tested in accordance with AITM 1-0007. Testing of the OHT specimens is accompanied by DIC in order to determine the surface strains of the specimens for further analysis, see Figure 7.5a. In addition, 3D numerical analysis is conducted using Abaqus/Standard. Linear-elastic material properties from Table 4.3 are applied assuming transverse-isotropy for the single plies that are connected via tie-constraints. Each layer is discretized using one element (C3D8) in thickness direction. The element size is stepwise coarsened starting at the area around the hole with an element edge length of 0.25 mm. Force controlled loading is defined in order to match the instant at which DIC data is taken. Therein, the load is introduced by a concentrated force at the reference point (RF) in Figure 7.5b, which is coupled with the surface nodes of the specimen-end opposite to the boundary condition (ENCASTRE) application. Hu et al. [202] and Caminero et al. [203] demon-

(a) Experimental OHT setup

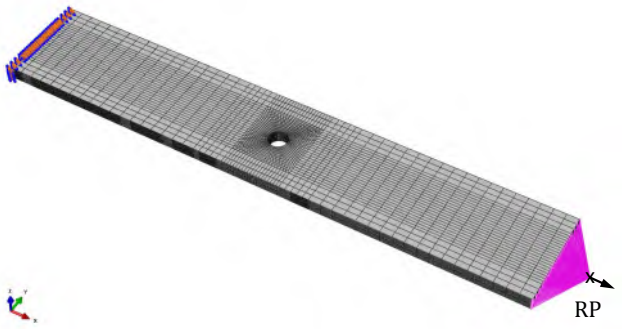

(b) 3D FE model of OHT specimen

Figure 7.5 Experimental OHT test setup including DIC system and speckle pattern around center hole (a) and numerical model including meshing pattern and boundary conditions (b)

strate that through-the-thickness stresses develop at the free edge of the center hole of OHT specimens which in turn can influence the overall stress field. Since the FE models are discretized with only one element per layer in thickness direction, these effects are not fully captured during numerical analysis. However, for failure analysis usually application of charactacteristic distances according to Chang et al. [204] or the point stress criterion by Whintey and Nuismer [205] is favored. These criteria have in common that failure analysis is conducted at a certain distance away from the hole edge. At the same time, free edge effects become vanishingly small at distances from the hole edge of about two ply thicknesses ($\approx$ 0.26 mm). Thus, in the present case through-the-thickness effects are considered to be negligible on the overall results. Especially, since the angular DIC measurements only allow for strain comparison at a distance of 0.6 mm away from the hole edge. Local damage at the hole edge, however, is expected to have a significant influence on the stress field of the OHT specimens. Since neither the analytical nor the numercial model account for the occurence of damage, noticeable differences in the stress distributions in close vicinity of the hole edge can be expected. The evaluation of exact analytical solutions for determining stresses and strains in a specimen with a circular center hole is conducted on different levels by comparison to experimental and numerical data. In an first step, the capabilities of the different approaches are assessed in a qualitative study by comparing the strain fields of the analytical and numerical methods for a representative area around the center hole to DIC data from the experimental OHT tests. Then, the strain values along characteristic paths determined by the experimental, numerical and analytical approaches are studied on laminate level. The hereby validated FE-model is then used to investigate the accuracy of the analytical solutions with respect to the stresses on lamina level. Eventually, by considering reduced width-to-diameter ratios, the applicability of the analytical solutions to finite-width specimens is analyzed.

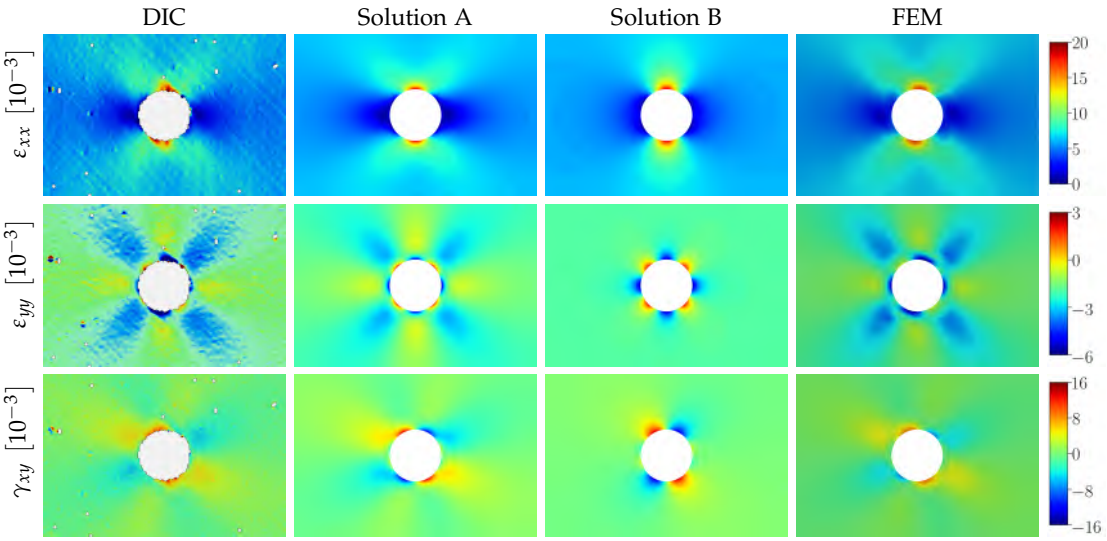

Figure 7.6 2D surface plot for QI laminate: Strain fields for ε_{xx}, ε_{yy} and γ_{xy} resulting from DIC, analytical (solution A and solution B) and FE methods are shown for a cutout of 20 mm by 30 mm around the center hole. The loading direction as well as the 0° fiber direction are parallel to the horizontal axis

In Figure 7.6, the strain fields predicted by DIC, analytical solutions and FEM are presented with synchronized colormaps for cut-outs of 20 mm by 30 mm around the center hole. While the strain components of the OHT specimen in case of DIC measurement and FE modeling is obtained directly from the result data, the stresses predicted by the analytical solutions are transformed to strains using CLT. Since DIC data represents the surface strains of the specimens, the FE results are also evaluated on the surface of the specimen. The analytical solution, however, describes the midplane strains of the laminate. Taking into account the fine discretization of the laminates and the fact that pure in-plane tensile loading is applied, the difference between surface and midplane strains is expected to be present but marginal. For example, while DIC and FEM results in Figure 7.6 capture the slight shift in strains due to the influence of the top -45° ply, the analytical solutions are perfectly symmetric.

The qualitative comparison of the 2D surface plots for the QI specimen[2] in Figure 7.6 demonstrates the high potential of exact analytical solutions for predicting strains in an OHT specimen. In fact, both analytical solutions are capable to calculate the strains in the vicinity of the hole edge, with solution A showing slightly better agreement with the DIC strain measurement. However, when considering the far-field strains at further distances from the center hole, only solution A is able to capture the strain distribution accurately. Further, the comparison for UD-0°, UD-90° and QI laminates suggests that the predictive capability of solution A is independent of the degree of orthotropy of the underlying laminate. The individual strain components ε_{xx} and ε_{yy} in longitudinal and transverse directions appear to be similarly accurate as the FE results. The shear strain γ_{xy} predicted by solution A, however, appears to be

[2]Detailed results for UD-0° and UD-90° are presented in Figure D.1 and Figure D.3 in Appendix D

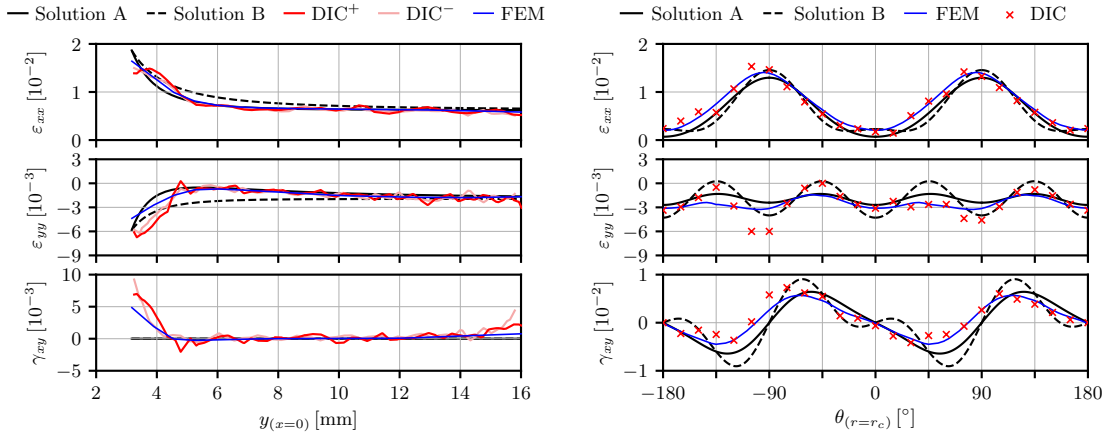

(a) Strain components along radial path

(b) Strain components along circular path

Figure 7.7 Comparison of strain components ε_{xx}, ε_{yy} and γ_{xy} for the QI specimen (a) along a radial path for x=0 and (b) along a circular path with a radius of r_c=3.7 mm

slightly more conservative compared to the DIC and FE results.

After qualitatively comparing the 2D strain fields in Figure 7.6, a quantitative study on the analysis methods for the OHT case with a QI layup[3] is presented in Figure 7.7. Strains are plotted along two characteristic paths: i) a radial path in the smallest cross-section along the positive y-axis for x=0 and ii) a circular path around the center hole with the smallest possible radius for data extraction by DIC of $r_c = 3.7$ mm. As a result of the symmetry of the OHT geometry, extraction of DIC data is conducted for both sides of the smalles cross-section at $x = 0$, with DIC$^+$ and DIC$^-$ indicating y-positions on the positive and negative part of the y-axis, respectively. Essentially, the quantitative study of the strain components along the two characteristic paths in Figure 7.7 further confirms the observations made in the previous qualitative study of the 2D surface strain fields. Therein, the individual strain components ε_{xx}, ε_{yy} and γ_{xy} determined using the analytical methods and FEM exhibit excellent agreement with DIC data to a great extent. While the numerically determined strain results represent experimental data by DIC best, solution A yields good results for the vast majority of cases under consideration despite being slightly less accurate. As expected, application of solution B results in the least accurate strain predictions considering the observations made within the study of the 2D strain fields.

Figure 7.8 exemplarily shows the assessment of ply stresses in the 0° layers of the QI laminate with w/d ratios of 5 and 3. Analytically determined ply stresses are compared with the results of the previously validated FE model along the characteristic path at the smallest cross-section for x=0. As a result of the symmetric laminate stacking, stresses in plies of identical orientation at equal distance from the midplane are identical. This is accounted for by plotting the stresses of the respective plies in the same color and therein referencing the outer-most (OM), outer (O), inner (I), and inner-most (IM) layers of a given orientation with respect to the midplane of the laminate.

[3]Detailed results for UD-0° and UD-90° are presented in Figure D.2 and Figure D.4 in Appendix D

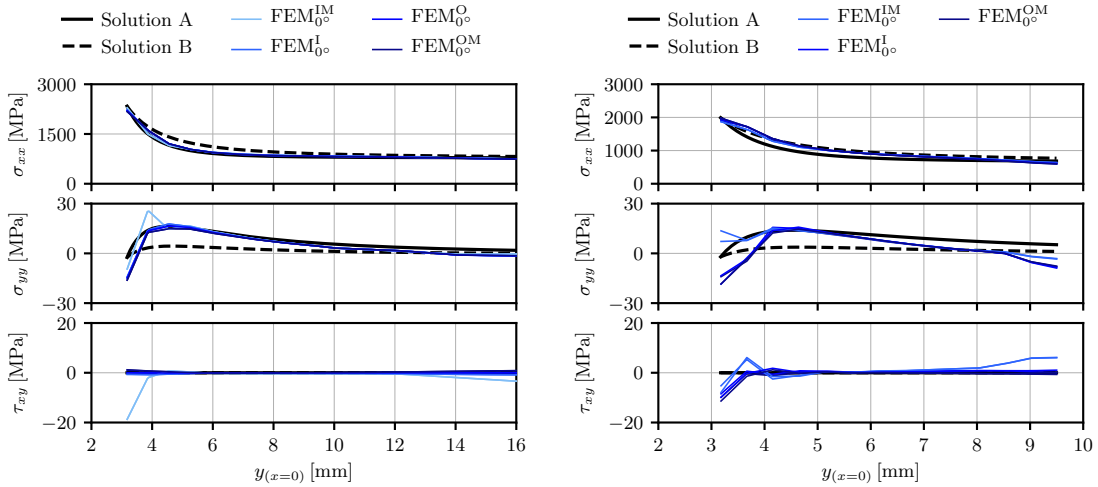

(a) Stress components for w/d=5

(b) Stress components for w/d=3

Figure 7.8 Comparison of stress components σ_{xx}, σ_{yy} and τ_{xy} for the QI specimen with w/d ratio of 3 and 5 along a radial path for x=0

Consideration of cases with small w/d ratios is important in order to quantify the lower bar of applicability of analytical models. Since all analytical models presented are derived for the case of an infinite plate with a circular center hole, by definition the applicability of the analytical models is limited to cases where the specimen geometry is large with respect to the center hole. Nevertheless, analytical solutions are frequently applied to cases with finite specimen sizes, however, different assumptions are present on the minimum w/d ratio for which the analytical solutions still yield acceptable results. Xu et al. [206] propose a minimum value of 10 for the case of an elliptical hole in a composite laminate by numerical analysis, while a minimum value of 4 can be found in the ESAComp documentation [207]. Echavarria [174] determined a minimum w/d ratio of 2.5 by experimental and numerical analysis. Since pitch distances of 4-5 are common in composite structures, a w/d ratio of 3 is defined for evaluation of the applicability of the analytical models to low w/d ratios.

A comprehensive study based on all ply orientations and stress components in the QI laminate[4] with w/d=5 reveals very good accuracy in case of solution A. Despite solution B being less accurate, sometimes by a large amount, the approach delivers more conservative results compared to solution A in most cases and thus might be relevant for cases where increased conservatism is prefered. Regarding the initially raised question, whether or not analytically determined stresses pose a relevant alternative to numerically determines stress data, it is concluded that for cases with w/d=5 the relative error compared to FE data at relevant points is generally less than 10 %. This accuracy is remarkable, especially when taking into account that the analytical approach comes with negligible computation time once the methods are implemented in program code as oppose to FE analysis which is rather computationally expensive. However, one must be aware of the limitations of the analytical models with respect to the specimen geometry and laminate stacking as well as the general implications that

[4]Detailed results are presented in Figure D.5 in Appendix D

come along with the 2D simplification of the OHT case.

Considering the specimen with a reduced w/d ratio of 3, a comprehensive study[5] on lamina level suggests that analytical solutions can be applied for analysis of specimens with w/d ratios as low as 3, granted that a slight decrease in accuracy is acceptable. Especially for application within preliminary design stages, the accuracy of the analytical solutions with errors of up to 22 % at characteristic points is considered acceptable. However, contrary to the case of w/d=5, solution B now appears to be more accurate than solution A. This observation is only valid for the characteristic paths around the center hole and along the smallest cross-section of the specimen. Observations within the qualitative study of the 2D surface plots suggest that solution B is in fact inferior to solution A when the behavior of a large area around the center hole is considered.

7.2.2 Stress Distribution due to Pin-Load

Due to the lack of availabilty of appropriate analytical models in literature, the bolt-bearing loading scenario is approximated by the analytical solution for a pin-loaded hole in a composite plate. The main difference between these two loading cases is the lack of lateral constraint in case of pure pin-loading. Therefore, the 3D stress state that is present in bolted joints is not accounted for in the 2D approach for pinned joints. However, the pin-bearing case can be considered a conservative approximation of the bolt-bearing loading scenario. As demonstrated by Takao [42], the stiffness of both bearing cases for a QI laminate in a double-lap bearing configuration is almost identical for a wide temperature range. Furthermore in Figure 7.9, the pin-bearing strength in comparison to the knee point[6] in bolted joits at 20 °C and -100 °C is lower by 18 % and 22 %, respectively, which represents a conservative but viable approximation. As the effects of variation of specimen geometry and laminate properties on pin- and bolt-bearing specimens are comparable, it is concluded that the qualitative outcome of comparative studies, e.g. between monolithic and hybrid laminate joints, is not significantly affected by the present approach.

Analogous to the procedure for the case of a notched laminate in the previous section, the accuracy of the exact analytical solutions for determining the stress distribution around a pin-loaded hole in a composite plate is investigated in order to clarify to what extent the application of different exact analytical solutions presented in literature is valid for preliminary design. For this purpose, experimental testing of pin-bearing specimens is conducted and accompanied by DIC as well as detailed 3D FE-modeling. Laminates with varying degree of orthotropy as well as varying w/d ratios are considered. After validating the results of the analytical and numerical models by comparison to experimental test data and DIC results on laminate level, FE-data is used to evaluate the stress distribution in individual plies predicted by the analytical methods. Furthermore, a correction method is employed in order to improve the accuracy of the analytical solutions for low w/d ratios. Results of the present section

[5]Detailed results are presented in Figure D.6 in Appendix D

[6]Defined by Takao as the onset of non-linearity and comparable to 0.5 % offset bearing strength

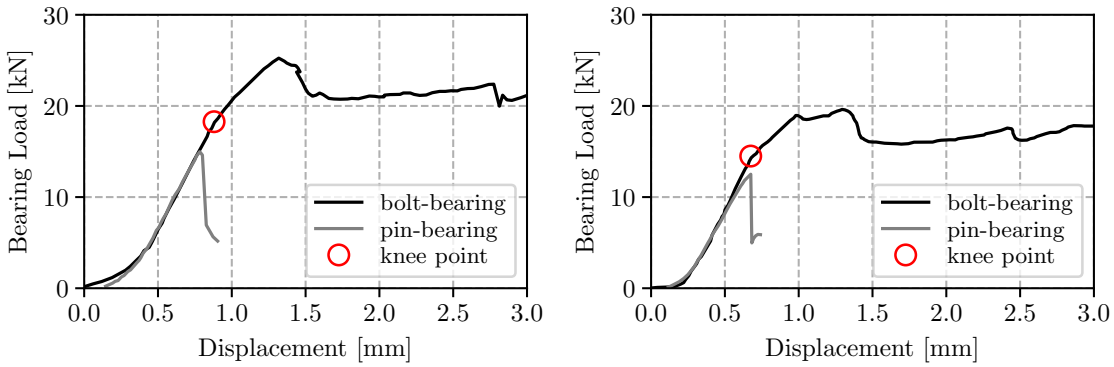

(a) Joint behavior at -100 °C

(b) Joint behavior at 20 °C

Figure 7.9 Comparison of pin- and bolt-bearing loading cases in QI CFRP laminates at room and low temperature in double-lap configuration; raw data [42]

have been partly published in Koord et al. [208].

Analytical Solutions for Stress Functions

The Lekhnitskii formalism introduced in the previous section also constitutes the basis for the analytical solutions for the case of a pin-loaded hole in a composite plate. By deriving a formulation for the stress functions in Equation 7.15, the stress distribution around a pin-loaded hole can be calculated. Different analytical solutions have been proposed in literature and will be discussed in the following. In addition to the idealizations resulting from application of the Lekhitskii formalism, the methods considered hereafter generally assume an infinitely rigid pin as well as a perfect fit between pin and hole.

Waszczak & Cruse [209] proposed an analytical calculation methodology for the stress distribution in a pin-loaded plate using stress functions, in 1973. Friction and interlaminar shear stresses are neglected. In addition, the methodology is restricted to symmetric layups, thus eliminating bending-extension coupling. Stress boundary conditions are implemented by defining a sinusoidal distribution over the loaded half of the hole, while the remaining hole contour is free of stresses. The boundary conditions are expressed as a Fourier series and the coefficients are determined by comparison to the general stress function form derived by Lekhnitskii. In the following analysis, 50 series terms are considered as a tradeoff between accuracy and computation time. The method of Waszczak & Cruse is implemented in the Bolted Joint Stress Field Model (BJSFM) which is commercially available through HyperSizer®.

The analytical solution introduced by De Jong [177, 210] incorporates friction effects by dividing the contact surface area between pin and laminate into areas of slip, non-slip as well as a transitional region. Thus, mathematical modeling is simplified by enforcing Coulomb's law of friction locally where appropriate. De Jong employs a series formulation for determining the stress distribution on the hole contour and suggests 28 series terms to be used. The series coefficients are determined by means of a displacement boundary collocation procedure. The stress functions are obtained

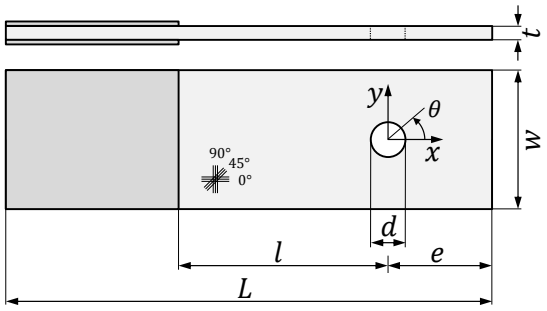

Figure 7.10 Bearing specimen geometry

Property	Unit	QI	HO
Total length, L	mm	170	170
Free length, l	mm	100	100
Diameter, d	mm	6.355	6.355
Width, w	mm	45	45
w/d ratio	-	7	7
Edge distance, e	mm	25	25
e/d ratio	-	4	4
Thickness, h	mm	4.19	4.19
Bearing strength	kN	11.58	11.87
Std. deviation	kN	$\pm$0.81	$\pm$0.91
Coeff. of variation	%	6.99	7.67
Number of specimens	-	4	4

Table 7.2 Geometry data and test results

through comparison of coefficients with the general stress function form derived by Lekhnitskii.

While the previous two methods employ series expressions, Echavarria [174, 200] proposes a closed-form solution for determining the stress distribution in a pin-loaded plate. Originally derived only for analysis of stresses on the hole contour, the solution can just as well be applied for determining the stress distribution in a pin-loaded plate. Friction effects are neglected. Stress boundary conditions are employed and expanded into a Fourier series similar to the procedure propsoed by Waszczak & Cruse. However, by determining the stress function only using the first series term, a closed-form solution is obtained.

Zhang and Ueng [179, 180] propose a closed-form solution that also takes into account effects of friction between pin and laminate. However, in contrast to the method of De Jong [210], slip and non-slip regions are not differentiated. Initially, the stress functions were defined in order to obtain a simplified formulation for calculating stresses on the contour of a pin-loaded hole. The stress functions, however, can also be used for determining the stress distribution in the entire pin-loaded plate. Solution parameters are obtained through displacement boundary conditions expressed as trigonometric series with two [179] and three [180] terms and subsequently comparing coefficients. It should be mentioned that the solution by Zhang & Ueng is derived based on a semi-infinite plate. Thus, the asumption within the Lekhnitskii formalisman of an infinite plate is not entirely satisfied. Nonetheless, this method is still considered since the resulting error is demonstrated to be insignificant [180]. Unlike the stress functions, the explicit stress formulations contain a correction factor, hence are valid for infinitely large laminates.

The approach taken by Brander [185] for calculating stresses in a pin-loaded plate is rather unconventional. Therein, stresses on the hole contour are determined by employing the explicit formulations obtained by Zhang & Ueng. Subsequently, the stress decay in the remaining portion of the plate is calculated by employing a geometrical decay coefficient (R/r). This coefficient is defined as the ratio between the hole ra-

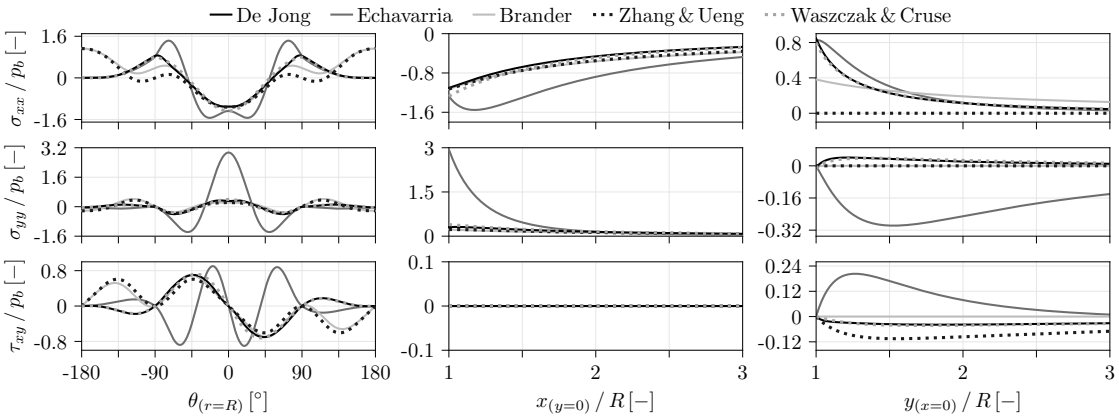

(a) Circular path with $r = R$ **(b)** Radial path along x-axis **(c)** Radial path along y-axis

Figure 7.11 Normalized stress components σ_{xx}/p_b, σ_{yy}/p_b and τ_{xy}/p_b along a circular path around the center hole with a radius $\theta_{(r=R)}$ as well as two normalized radial paths along the x-axis for y=0 and y-axis for x=0, respectively

dius R and distance to the hole center r. No physical justification for this approach is presented. However, since this method is implemented in commercial software (Altair ESAComp™) and frequently used in conjunction with the characteristic distance method for failure analysis, the accuracy of such a pragmatic approach is investigated, too. All analytical methods presented in this section are implemented in Python code and investigated in the following.

The results of a preliminary study on the analytical solutions are presented in Figure 7.11. In accordance with the coordinate system in Figure 7.10, an infinite plate with a pin-loaded hole of $d = 6.355$ mm and properties of a UD-0° ply according to Table 4.3 is considered. The stress components σ_{xx}, σ_{yy} and τ_{xy} normalized by the applied bearing stress p_b are presented for a circular path along the hole edge and for two radial paths along the x-axis for $y = 0$ and the y-axis for $x = 0$, respectively. The normalized stress curves in Figure 7.11 indicate that the methods proposed by Waszczak & Cruse and De Jong (group A) produce similar results, and the methods by Zhang & Ueng and Brander exhibit similar curve behavior (group B), while the method of Echavarria (group C) noticably differs from the first two groups. The methods in group A and B predict qualitatively and quantitatively similar stresses for angles on the loaded half of the plate (-90° $< \theta <$ 90°) along both angular and radial paths. When considering the unlaoded half of the plate (-90° $> \theta >$ 90°), the methods in group B predict tensile stresses in longitudinal direction for σ_{xx}/p_b of the same magnitude as the compressive stresses on the pin-loaded side of the hole at $\theta = 0°$. This behavior is not physically plausible. However, when failure analysis is only conducted for the loaded half of the plate, the deviations around $\theta = 180°$ do not affect failure analysis. The method proposed by Echavarria exhibits significantly higher stress peaks, e.g. by factor 10 in case of σ_{yy}/p_b, as well as qualitative deviations in the curve behavior, e.g. distributed stress peaks near $\theta = 0°$ and sign shifts in the shear stress distribution. Thus, methods from group A and B, namely Waszczak & Cruse, De Jong, Zhang & Ueng and Brander, are selected for further investigation.

Evaluation of Analytical Solutions

For the evaluation of the analytical solutions, experimental and numerical analysis of the pin-bearing scenario is conducted. Therefore, test specimens are manufactured in accordance with the geometry proposed in AITM 1-0009. Two different layups with varying degree of orthotropy are considered: a QI layup $[-45/90/+45/0]_{4s}$ and a HO layup $[0/45/0/-45/0_2/90/0]_{2s}$. The prepreg material M21/T700GC is used. Drilling of the specimens is done using a solid carbid drill at 1200 rpm whilst tightly clamping the specimens in between two aluminum plates of 5 mm in thickness. Due to wear on the drill blades, the drill heads are replaced after 5 drilled holes in order to prevent delamination and fiber pull-out at the drilling hole. The drilling quality is monitored by ultrasonic as well as microscopic analysis. Testing of the specimen is accompanied by DIC. However, optical measurement by DIC for capturing the strain field around the pin-loaded hole requires visibility of the area of interest. In the double-lap bolt-bearing setup according to AITM 1-0009, the lateral load plates cover the specimen and do not allow for optical measurement. A double-lap pin-bearing setup containing pockets in the load plates proposed by Irissaria [211] provides limited visibility of the area around the hole. In contrast, the single-lap pin-bearing setup in Figure 7.12a exhibits full visibility of the fastener hole and thus is most suitable for investigating the near- and far-field stresses around a pin-loaded hole. While the single-lap setup is expected to exhibit less pin-bending due to the reduced length of the pin, pin-tilting will be more pronounced compared to a double-lap setup. The degree of pin-tilting and pin-bending are quanitfied by evaluation of displacement data of the reference points on the setup in Figure 7.12a. Bending of the specimen frequently occurring in standard single-lap joints due to load eccentricities are compensated for by adjustment of the test-rig in order to eliminate any offset in the load line between specimen and test-rig (see Figure 7.12a). As the analytical models are valid for cases with no midplane bending, this measure is considered important regarding the comparability of results[7].

Numerical modeling of the pin-bearing tests is conducted in Abaqus/Standard. In addition to the model and material property definition in the previous section for modeling OHT specimens, the pin-bearing models contain following features: The pin is modeled as a rigid body. Clearance between pin and laminate is set to 0.035 mm based on the experimental test configuration. However, it should be mentionend that the analytical models assume a perfect fit between pin and hole. The contact formulation between pin and laminate comprises hard contact for normal behavior and penalty friction for tangential behavior. The coefficient of friction is set to 0.1 based on literature reports [141,213–215]. The same value is used for the analytical solutions that incorporate friction. The boundary conditions in Figure 7.12b include symmetry imposed on the midplane of the laminate since only half the laminate is modeled. The grip area is not modeled, thus reducing the specimen length in the numerical model to $l + e$ compared to L in the specimens in the experiment. All degrees of freedom except U1 are restricted at the specimen end. Furthermore, the pin is fully restricted by the ENCASTRE boundary condition. In order to be able to match the instant at which DIC data is taken during experimental testing, a force controlled approach is chosen. Load introduction occurs by a concentrated force at a reference point (RF),

[7] a detailed discussion is presented in [212]

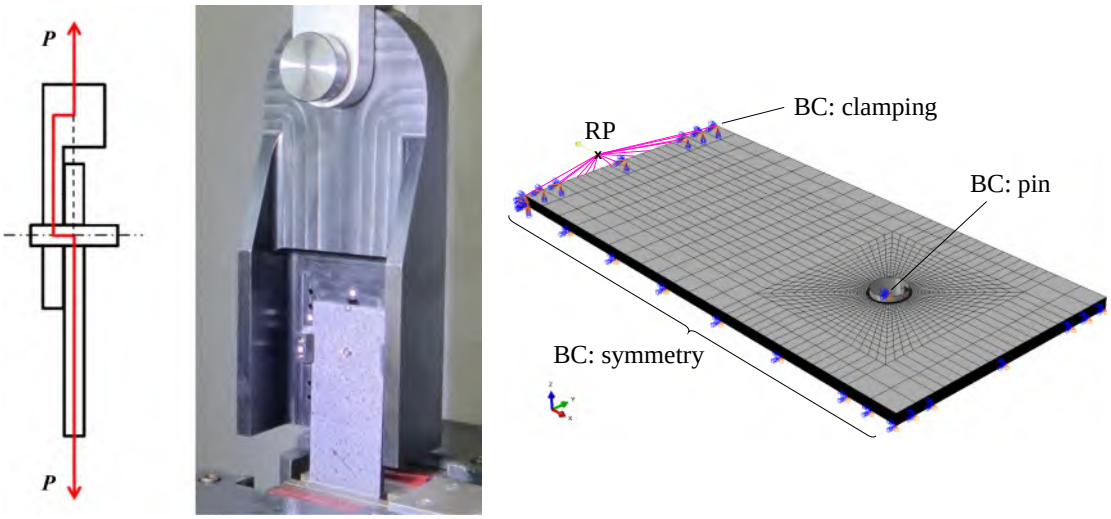

(a) Experimental pin-bearing setup **(b)** 3D FE model of pin-bearing specimen

Figure 7.12 Pin-bearing test setup including speckle pattern for DIC measurement (a) and numerical model including mesh pattern and boundary conditions (b)

which is coupled with the surface nodes of the clamped specimen-end. Based on a mesh study, a fine mesh with an element edge length of around 0.15 mm is employed in the vicinity of the hole. The mesh is coarsened stepwise to an element size of 4 mm by 5 mm in the outer regions of the specimen. In thickness direction, the area around the hole is discretized using 5 elements per ply (C3D8R) in order to capture 3D effects influencing the stress distribution around the fastened hole as observed by Hu et al. [202] as well as Caminero et al. [203]. Coarsely meshed areas further away from the center hole are discretized with one element in thickness direction. Areas of different mesh sizes in thickness direction are connected by tie-constraints. Local damage at the pin-loaded hole edge is expected to have an influence on the stress field of the pin-loaded specimens. Since neither the analytical nor the numercial model account for damage in the composite, noticable differences in the stress distribution in the vicinity of the hole edge are expected. Validation of the numerical model is done based on the load bearing behavior during the linear-elastic regime of loading as well as the surface strain distribution.

In Figure 7.13, the strain fields predicted by DIC, FEM and analytical solutions are presented with synchronized colormaps for cut-outs of 40 mm by 30 mm around the pin-loaded hole. The strain components of the pin-bearing specimen in case of DIC measurement and FE modeling is obtained directly from the result data and represent surface strains, while the stresses predicted by the analytical solutions represent mid-plane stresses and are transformed to strains using CLT. As previsouly discussed at the example of the OHT specimens, the difference between surface and midplane strains is expected to be present but marginal. Extracting strain data in close vicinity of the hole contour by DIC is quite difficult due to increased scatter as well as the fact that the shadow of the pin partly covers the area of interest. As a result, the smallest circle for which data can be extracted in case of the DIC measurements is slightly larger than the actual hole size of the specimens. In order to facilitate the comparison of DIC to

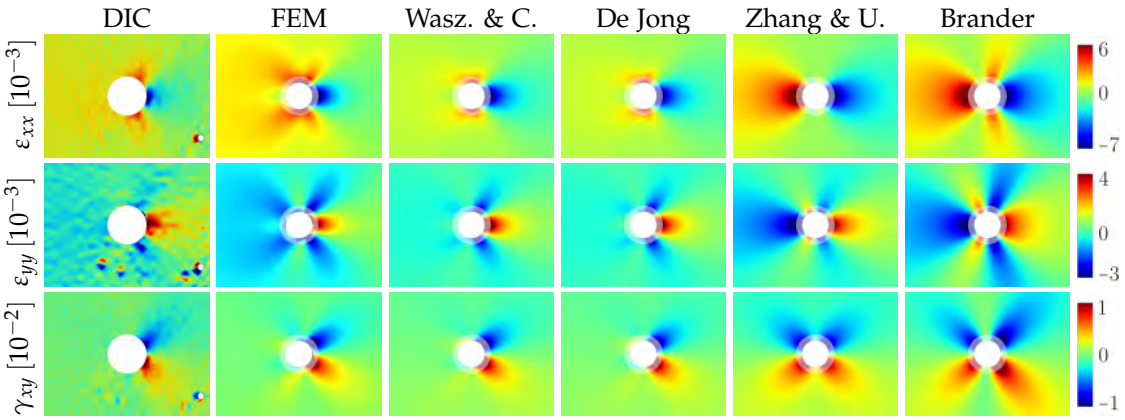

Figure 7.13 2D surface plots for QI laminate: Strain fields ε_{xx}, ε_{yy} and γ_{xy} resulting from DIC, FEM and analytical solutions are shown for a cutout of 40 mm by 30 mm around the pin-loaded hole (w/d=7, p_b=408 MPa). The loading direction as well as 0° fiber direction are alinged along the horizontal axis to the right

FE and analytical surface plots, the area that is not or only partially covered in the DIC measurements is highlighted in the 2D surface plots of the FE and analytical methods as a transparent white circle around the center hole. The principle loading direction as well as the 0° fiber direction are parallel to the horizontal axis, which is the x-axis in Figure 7.10.

The qualitative comparison of the 2D surface plots for the QI specimen[8] again shows the potential of analytical solutions for predicting strains in a pin-loaded composite laminate. The strains measured by DIC and predicted by FEM show very good agreement, with the characteristic shape of the strain distribution being somewhat more pronounced on the FE surface plots for the strain components ε_{xx}, ε_{yy} and γ_{xy}. Comparison of the strain distributions based on the analytical methods confirms the trends observed during the preliminary study. Therein, the strain fields predicted by the methods of Waszczak & Cruse and De Jong show very good agreement with FE and DIC data despite the slightly less pronounced strain decay in the analytical solution. When considering the strain fields predicted by the methods of Zhang & Ueng and Brander, agreement is acceptable for angles $-90° < \theta < 90°$. However, the strains in the area of the unloaded side of the center hole ($-90° > \theta > 90°$) are not physically plausible, especially in case of the longitudinal strain ε_{xx} and shear strain γ_{xy}. The tensile strain ε_{xx}, for instance, predicted by both Zhang & Ueng and Brander at around 180° is of the same order of magnitude as the compressive strain at $\theta = 0°$ which is neither realistic nor can it be seen on the DIC surface plot. Observation of the 2D surface plots further reveals the effect of the geometry factor (R/r) employed by Brander. Therein, the stress decay is purely driven by the geometry factor and results in increasingly inaccurate strain predictions with increasing distance from the center hole. The same observations can be made for the HO laminate in Appendix D.

[8]Detailed results for the HO laminate are presented in Figure D.7 in Appendix D

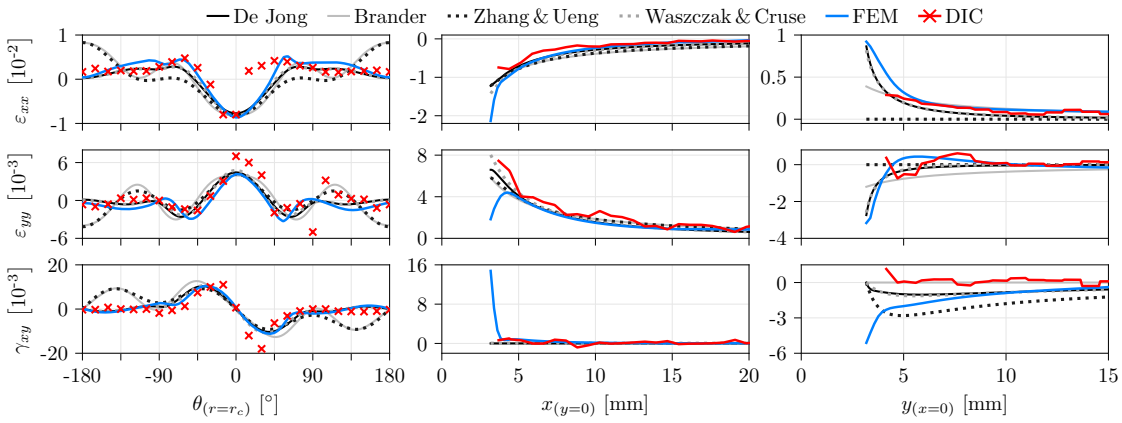

(a) Circular path with $r = r_c$ **(b)** Radial path along x-axis **(c)** Radial path along y-axis

Figure 7.14 Comparison of strain components ε_{xx}, ε_{yy} and γ_{xy} for the QI laminate (w/d=7, p_b=408 MPa) along a circular path around the pin-loaded hole with a radius of r_c=4.7 mm as well as two radial paths along the x-axis and y-axis

The quantitative comparison of strains in the QI laminate in Figure 7.14 confirms the observations made within the qualitative comparison of 2D surface plots. Strains are plotted along three characteristic paths: i) a circular path around the center hole with the smallest possible radius for data extraction by DIC of $r_c = 4.7$ mm, ii) a radial path in the bearing plane along the positive x-axis for y=0, and iii) a radial path in the smallest cross-section along the positive y-axis for x=0. In general, strain components determined by DIC, FEM and analytical methods show good agreement. Therein, experimental DIC data is almost equally well represented by FE results as well as the analytical solutions by Waszczak & Cruse and De Jong. However, the remaining analytical solutions in some cases exhibit severe inaccuracies. The scatter in DIC data for strains on the circular path between 0° and 45° is attributed to inaccuracies during DIC measurement since the effect on the strain results is very localized and the remaining points on the circular path show very good agreement.

In Figure 7.15, ply stresses in the 0° layers of the QI laminate with a w/d ratio of 7 are presented[9]. At angles close to $\theta = 0°$, agreement with the numerically determined stresses is very good for all analytical solutions, exhibiting errors generally smaller than 15 %. For increasing angles between 0° and 90°, the solution by Zhang & Ueng shows poor agreement with the numerical prediction, while the remaining methods have a very similar curve behavior and appear to be significantly more accurate. In fact, the method by Zhang & Ueng fails to capture the stress peak for σ_{xx} at $\theta = 90°$ along the smallest cross-section. This characteristic is critical regarding the design of joints, since the longitudinal tensile stresses in the 0° plies govern net-section failure. A comprehensive analysis of ply stresses for all orientations in QI and HO laminates in Appendix D confirms the general conclusions drawn from Figure 7.15. Therein, the methods by Waszczak & Cruse and De Jong exhibit good accuracy compared to numerical data, while the methods introduced by Zhang & Ueng and Brander are less accurate and partly predict unreasonable results.

[9] A comprehensive analysis of ply stresses is presented in Figure D.13 and Figure D.14 in Appendix D

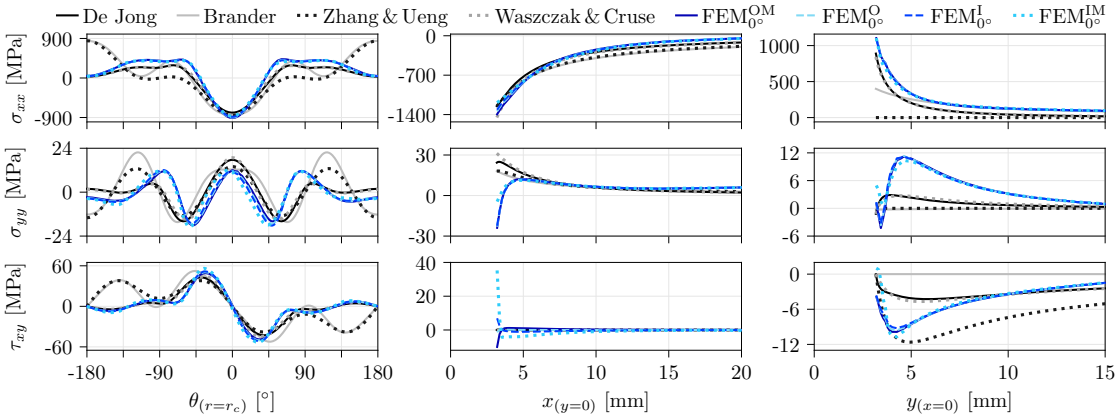

(a) Circular path with $r = r_c$ **(b)** Radial path along x-axis **(c)** Radial path along y-axis

Figure 7.15 Comparison of stress components σ_{xx}, σ_{yy} and τ_{xy} in the 0° plies of the QI laminate (w/d=7, p_b=408 MPa) along a circular path around the pin-loaded hole with a radius of r_c=4.7 mm as well as two radial paths along the x-axis and y-axis

Correction for Finite Width Effects

The analytical models presented until now all have in common that they are derived for the case of a pin-loaded hole in an infinite plate. Thus, by definition, effects arising from finite specimen geometries are not accounted for. This limits the applicability of analytical approaches to cases where the specimen geometry is large compared to the pin-loaded center hole. Different assumptions on minimum w/d ratios for which analytical models may still yield reasonably accurate results for finite width specimens are suggested in literature. The proposed values span over a range from w/d=4 as suggested by Ogonowski [216], over w/d=6 proposed by Zhang [180] up to a value of 10 defined by Xu et al. [206]. However, applying analytical models to specimens with small w/d ratios leads to increased inaccuracies and more importantly to a lack of conservatism in the stress prediction. De Jong [217] proposed a heuristic approach to approximate finite width effects for w/d ratios as low as 2.5. Therein, the solution of the case of a pin-loaded center hole in an infinite plate is superimposed with the case of a uniaxially loaded infinite laminate with a center notch, resulting in the approximation for the state of stress in a strip of finite width under pin-bearing loading (see Figure 7.16). In essence, the superposition takes into account that the far-field load is reacted at only one end of the specimen rather than at both ends. By comparison to Figure 7.12, it can be seen that this is actually a better representation of the experiment. For cases as the present one, including clearance between pin and hole, the open-hole bypass case by Soutis and Filiou [195] is to be used, while in case of zero clearance the filled-hole bypass solution by Berbinau et al. [218] can be employed.

In order to investigate the accuracy of the analytical solutions with respect to finite width specimens, the method by Waszczak & Cruse as a representative of the most accurate analytical solutions (group A) is combined with the correction method proposed by De Jong. Both 2D plots of midplane strains as well as ply stresses along characteristic paths are considered in order to assess the accuracy with respect to both the qualitative strain distribution and the quantitative stresses on lamina level, respec-

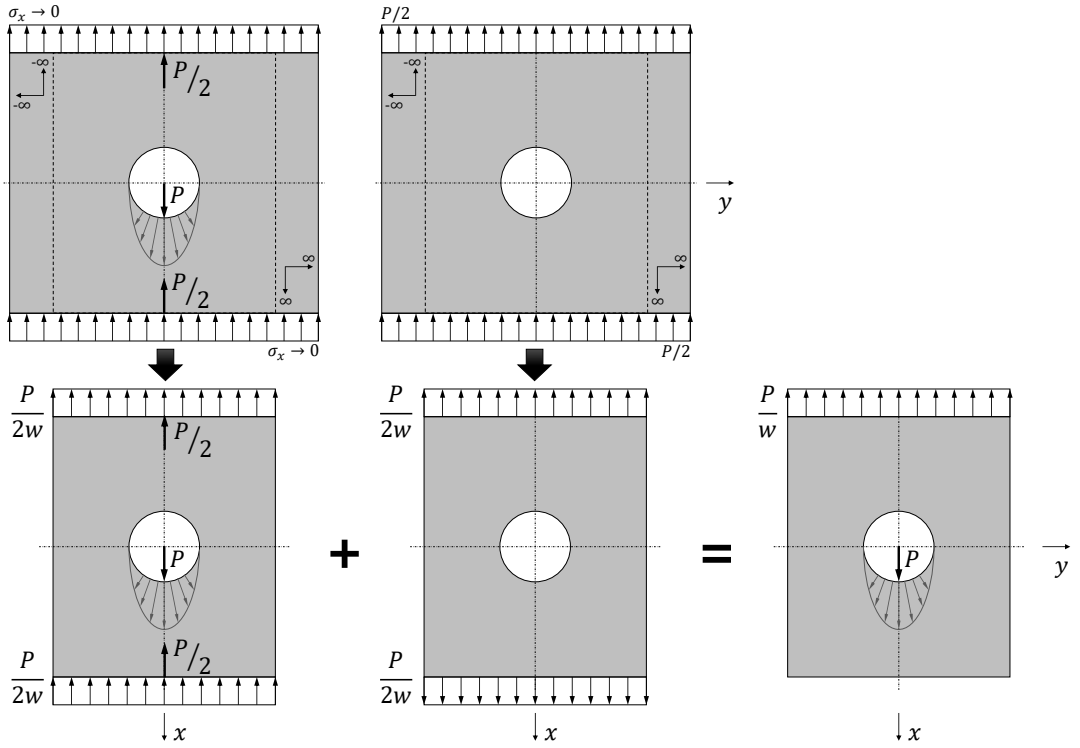

Figure 7.16 Approximation scheme of finite geometry effects for a single pin-loaded joint by superposition of the solutions of a pin-loaded infinite plate and a notched infinite plate under tensile loading introduced by De Jong [217]

tively. As demonstrated in the previous section, the analytical solutions appear to be sufficiently accurate for a w/d ratio of 7 with errors generally lower than 15 % at characteristic points. However, in composite structures pitch distances of 4-5 are very common [10]. Thus, the correction method is applied to specimens with varying w/d ratios, w/d=7 and w/d=3.

When looking at the surface strains of a QI laminate with w/d=7 in Figure 7.17a, it can be seen that the finite width correction method by De Jong leads to a significant improvement of the analytically determined strain fields for ε_{xx}, ε_{yy} and γ_{xy} compared to FE data regarding all strain components. Therein, both the strain peaks in the vicinity of the hole as well as the strain decay behavior further away from the hole are captured excellently by the analytical solution. Similar improvement by application of finite width correction can be observed when considering the ply stresses in the 0° layers of the QI laminate in Figure 7.18. Excellent agreement is present between numerically and analytically determined stresses, in particular for the analytical methods of Waszczak & Cruse and De Jong. For instance, the error in the stress component σ_{xx} at $\theta_{(r=r_c)} = 0°$ is reduced from around 15 % without correction to < 5 % with finite width correction. In Figure 7.17b, a QI laminate with a reduced w/d ratio of 3 is illustrated. Application of finite width correction on the analytical solutions results in significantly improved strain field predictions. For instance, the corrected solution is capable of capturing the butterfly shape in the strain distribution of ε_{xx} and ε_{yy},

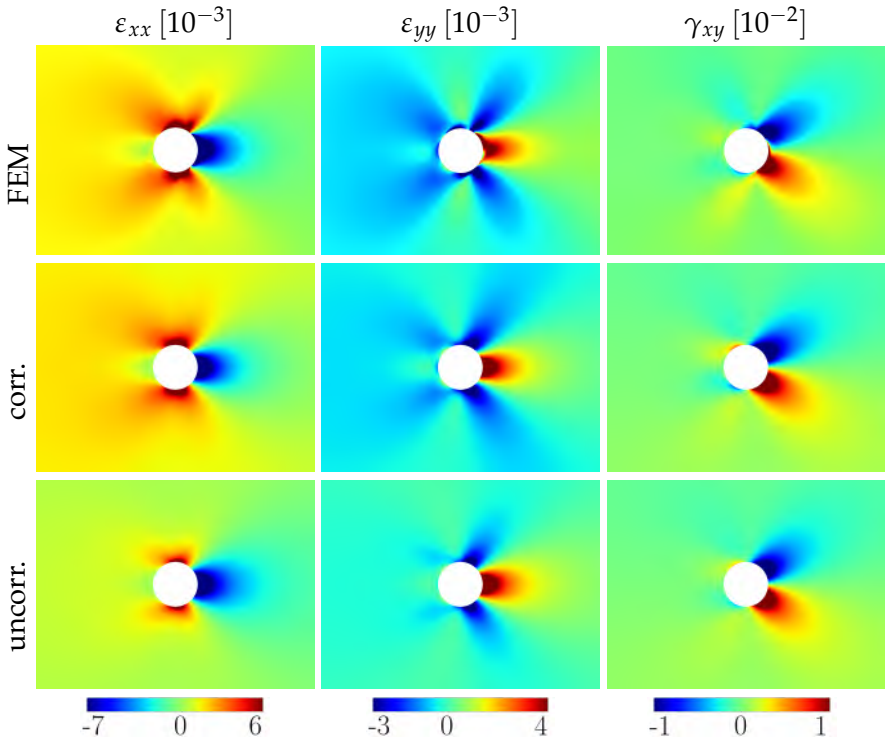

(a) 2D surface plots for QI laminate with w/d=7 for a cutout of 40 mm by 30 mm around pin-loaded hole

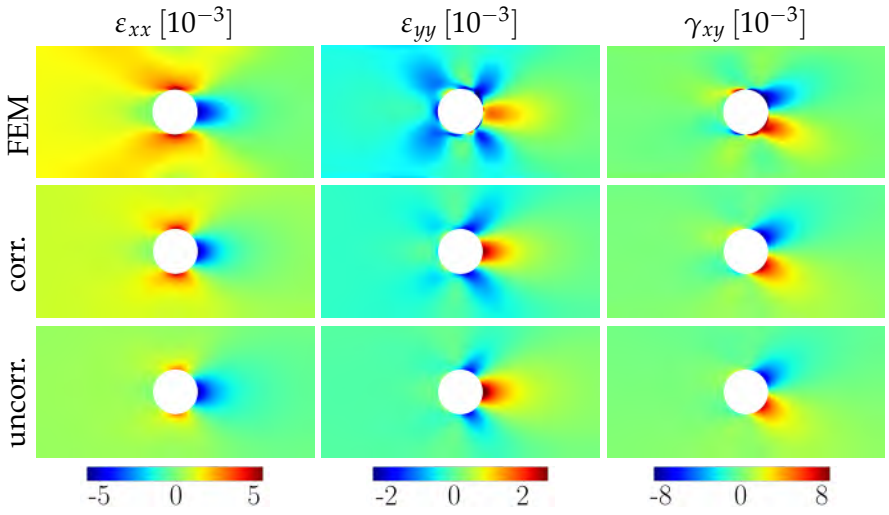

(b) 2D surface plots for QI laminate with w/d=3 for a cutout of 40 mm by 19 mm around pin-loaded hole

Figure 7.17 Surface plots for QI laminate: Strain fields ε_{xx}, ε_{yy} and γ_{xy} resulting from FEM and the analytical solution of Waszczak & Cruse without correction (uncorr.) and with correction method by De Jong (corr.) are shown. The loading direction as well as 0° fiber direction are aligned along the horizontal axis to the right

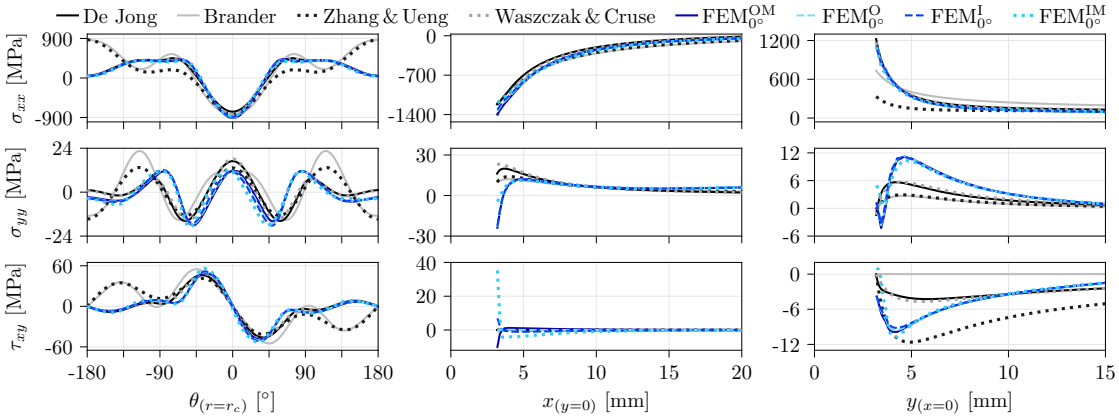

(a) Circular path with $r = r_c$ **(b)** Radial path along x-axis **(c)** Radial path along y-axis

Figure 7.18 Comparison of stress components σ_{xx}, σ_{yy} and τ_{xy} in the 0° plies of the QI laminate (w/d=7, p_b=408 MPa) along a circular path around the pin-loaded hole with a radius of r_c=4.7 mm as well as two radial paths along the x-axis and y-axis

whereas the uncorrected solution does not reproduce this charactersitic with comparable accuracy. In particular, two areas of compressive transverse strain ε_{yy} at $\pm 135°$ are correctly predicted by the corrected analytical solution. The apparent accuracy by comparison of the 2D strain fields for w/d=3 in Figure 7.17b is quite good. However, compared to the results for the QI specimen with w/d=7 in Figure 7.17a the improvement by application of the finite width correction method is slightly less pronounced. Figure 7.19 shows the ply stresses in the 0° layers of the QI specimen with w/d=3. Despite application of finite width correction, it can be seen that the relative error in the longitudinal stress component σ_{xx} at $\theta = 0°$ and 90° takes on values of up to 20 %.

In contrast to FE modeling, which is computationally expensive even for rather simple geometries, application of the analytical solutions come with negligible computation time once the methods are implemented in code. Considering this fact, the accuracy of some methods observed over the range of laminate orthotropy and geometry is remarkable. The findings indicate that in case of simple geometries the analytical solution by either Waszczak & Cruse or De Jong in conjunction with the correction method for finite widths by De Jong offers a viable alternative to numerical and experimental approaches for determining stresses down to ply level in pin-loaded composite joints. However, there are analytical solutions introduced in literature, some of which are implemented in commercial composite design tools, that lack in accuracy. Despite recommendation of the analytical approach, one must be aware of the limitations of the models with respect to specimen geometry and, in particular, 3D effects which are not considered in the present case of a pin-loaded hole. Thus, in future work analysis of analytical methods should be extended to even more geometries, e.g. variation of thickness-to-diameter ratios, as well as more laminate stackings in order to better understand the liminations with respect to stacking rules. Furthermore, an updated test setup to reduce the effects of pin-tilting and pin-bending as well as improvement in visibility and resolution of DIC data in close vicinity of the pin should be aimed for.

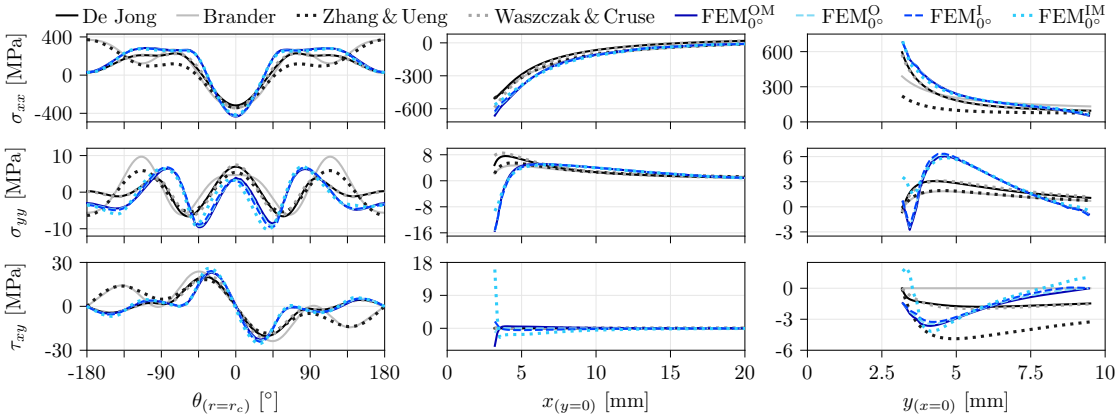

(a) Circular path with $r = r_c$ **(b)** Radial path along x-axis **(c)** Radial path along y-axis

Figure 7.19 Comparison of stress components σ_{xx}, σ_{yy} and τ_{xy} in the 0° plies of the QI laminate (w/d=3, p_b=172 MPa) along a circular path around the pin-loaded hole with a radius of r_c=4.7 mm as well as two radial paths along the x-axis and y-axis

7.2.3 Thermal Residual Stresses

The previous sections deal with the analysis of the stress prediction quality of analytical solutions for mechanically loaded monolithic laminates. Therein, thermal residual stresses are not yet considered. In fact, instead of using FMLs where substantial thermal residual stresses are present, the validation of the analytical solutions was purposefully done on monolithic UD-0°, UD-90°, QI and HO laminates in which thermal residual stresses on ply level are merely present at all or only account for a few percent of the laminate strength and therefore can be neglected. Inclusion of thermal residual stresses into the design process is dicussed in the present section. Therein, two phenomena are of particular interest: relaxation of thermal residual stresses and thermal residual stress concentrations around holes. A theoretical discussion on relaxation of thermal residual stresses is presented in Chapter 2. Therein, it is concluded that relaxation in UD plies parallel to the fiber direction can be neglected, while stress relaxation in transverse direction is significant.

In order to quantify to what extent thermal residual stresses are present in FMLs consisting of M21/T700GC and steel 1.4310, relaxation in these CFRP-steel FMLs is investigated in Figure 7.20a. Asymmetric specimens with a stacking sequence of [St, 90°_9] are fabricated using an autoclave process. Immediately after manufacturing, the specimens are cooled to room temperature in order to measure the change in curvature over time due to relaxation in the 90° plies. As can be seen in Figure 7.20b, the greater portion of relaxation processes can be considered finished after 1000 h ($\approx$ 40 d). Thus, by determining material properties, in particular the stress-free temperature T_{sf}, after a period of at least 1000 h after manufacturing of the specimen, the relaxation of thermal residual stresses is accounted for. It should be noted that the present time interval is only valid for the material combination and manufacturing process at hand. A comprehensive study by Cowley and Beaumont [52] on different asymmetric CFRP laminates with thermoplastic and toughened thermosetting matrices however also indicates that a period of 500 h to 1000 h is necessary for relaxations processes

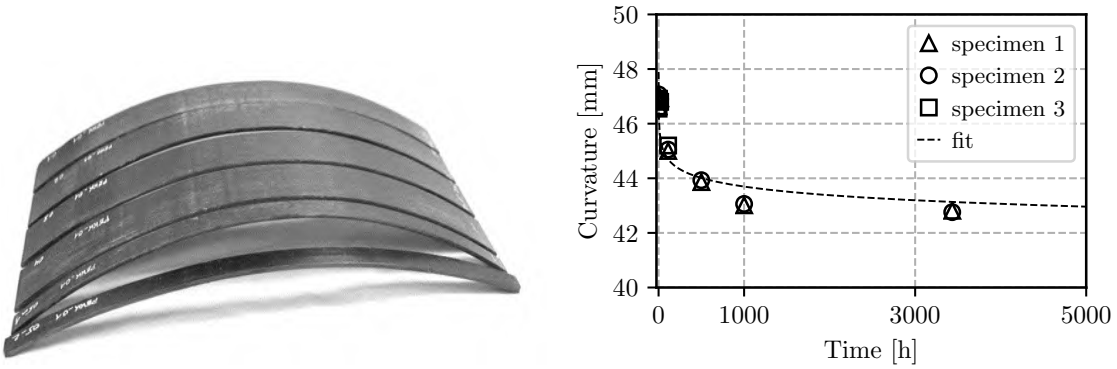

(a) Asymmetric specimens **(b)** Curvature over time

Figure 7.20 Study on the relaxation effect in CFRP-St FMLs based on curvature analysis of specimens with an asymmetric layup [St, 90_9]

to complete. After this waiting period, reheating of the specimens until the curvature is eliminated reveals the stress-free temperature T_{sf}, which is 132°C in the present case.

In Chapter 2, CLT is applied to calculate the magnitude of thermal residual stresses in the single plies of both monolithic and hybrid composite laminates. In the following, it is to be determined in which way notches locally affect the distribution of thermal residual stresses. In particular, the error between stress peaks around holes and the far-field thermal residual stresses is quantified in order to assess the effect of holes on the determination of stresses in composite laminates. For this purpose the pin-bearing FE-model from Figure 7.12b is adjusted. Instead of the mechanical load, a thermal step is introduced starting at T_{sf} down to RT and LT level, respectively. Figure 7.21 shows the stress components σ_{xx}, σ_{yy} and τ_{xy} in the 0° plies of a QI laminate at RT. While the stress decay along the bearing plane is presented in Figure 7.21a, the stresses along the smallest cross-section can be seen in Figure 7.21b. The numerically determined ply stresses in the inner-most, inner, outer and outer-most 0° plies, the mean thermal residual stress determined by CLT as well as the maximum error between these values are presented. In addition, the range of characteristic distances in compression R_{oc} and tension R_{ot} for QI laminates indicating the area for failure analysis is marked[10]. The discrepancy between thermal residual stresses determined by CLT and numerically determined thermal residual stresses that account for stress concentrations around holes increases in close vicinity of the hole. Peak relative errors of over 100 % are present as can be observed at the example of the longitudinal stress σ_{xx} along the bearing plane in Figure 7.21a. However, when considering the area where failure analysis is usually conducted, the stress peaks are reduced significantly. As a result, the error between numerically determined stresses and stresses determined by CLT are reduced significantly, too. In fact, for both paths in Figure 7.21 the relative error within the range of characteristic distances amounts to only a few percent. This observation is also valid for LT and the remaining plies of the QI laminate[11].

[10] Data based on literature study on characterisitc distances in Figure D.19 in Appendix D
[11] Detailed analysis is presented in Figure D.15 and Figure D.16 in Appendix D

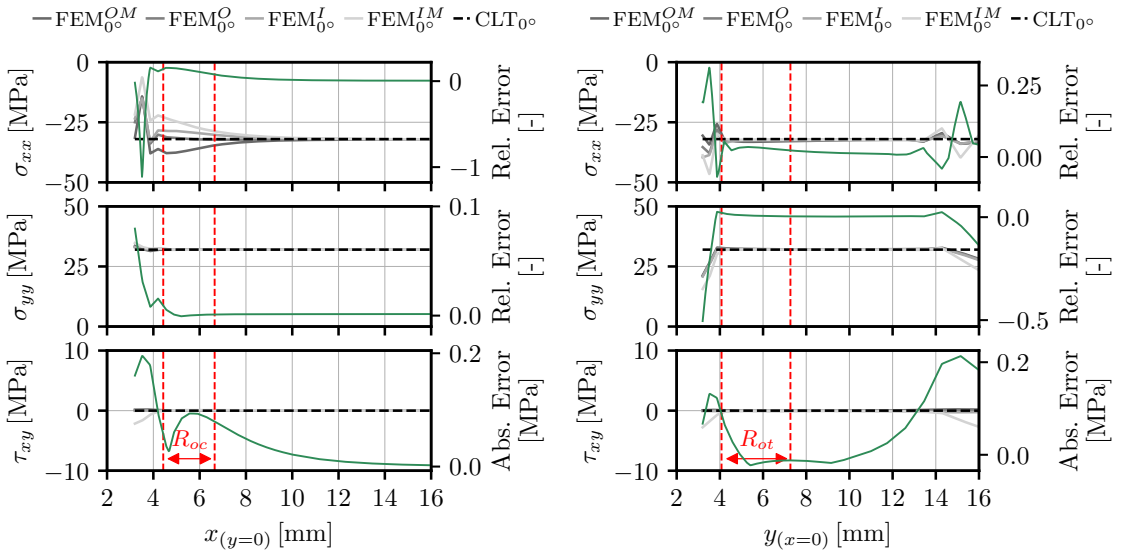

(a) Stresses along bearing plane at RT **(b)** Stresses along smallest cross-section at RT

Figure 7.21 Thermal residual stresses in the 0° plies of a QI laminate with a center notch of d=6.355 mm by FEM and CLT including range of characteristic distances in tension R_{ot} and compresssion R_{oc}

In Figure 7.22, the stress components of the 0° plies in the QI-FML determined by numerical analysis as well as CLT are presented. Due to the lack of availability of data on characteristic distances for FMLs, the values for the QI laminate are used. However, since the degree of orthotropy in FMLs is reduced by substituting composite plies with metal sheets, the characteristic distances are expected to increase. Therefore. the approximation of characteristic distances for the QI-FML with data for QI laminates represents a conservative simplification. Compared to the QI laminate, thermal residual stresses in longitudinal direction of the 0° plies σ_{xx} of the QI-FML are significantly larger. In transverse direction, the better compatibility of transverse CTE between CFRP and metal actually lead to a reduction of stresses in transverse direction σ_{yy} of the 0° plies. Substantial stresses in the metal plies are present reaching values of close to 300 MPa at LT (see Figure D.18). As previously observed at the example of the QI laminate, the stress peak at the center hole decays very rapidly such that the error between numerically determined and CLT based residual stress values becomes increasingly small. This observation is equally made for the metal sheets in the FMLs (see Figure D.18).

In conclusion, the discussion on the basis of Figure 7.21 and Figure 7.22 indicates that the error with respect to failure analysis resulting from thermal residual stresses determined using CLT rather than FEM is small when used in conjuction with the characteristic curve method because failure analysis is conducted at a certain distance away from the center hole. In future work, thermal residual stresses in notched laminates based on exact analytical solutions, for instance by application of the recently published method by Magar et al. [219], should be investigated similarly to the approach chosen for the bypass and pin-bearing loading cases in the previous sections. Investigating the internal stress state of laminates is challenging. However, by appli-

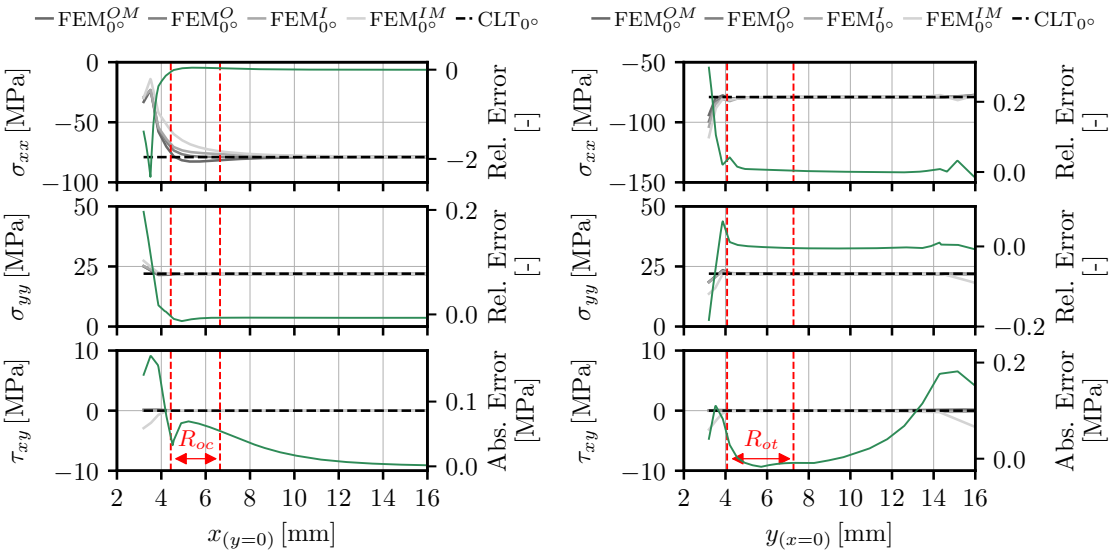

(a) Stresses along bearing plane at RT **(b)** Stresses along smallest cross-section at RT

Figure 7.22 Thermal residual stresses in the 0° plies of a QI-FML laminate with a center notch of d=6.355 mm by FEM and CLT including range of characteristic distances in tension R_{ot} and compresssion R_{oc}

cation of FBG sensors the build up of thermal strains originating from the stress-free temperature, relaxation effects ocurring over time as well as superposition of thermal and mechanical loads in an OHT specimen can be quantified. This way, FEM results regarding thermal strains can be validated.

7.2.4 Failure Analysis

Failure analysis of composite materials containing a stress concentration, e.g. notched laminates under bearing or bypass loading, requires the consideration of non-critical damage mechanisms that occur in the vicinity of the hole prior to ultimate failure. In fact, failure in notched laminates is the result of the accumulation of non-critical damage mechanisms. Therefore, evaluation of a failure criterion right at the hole edge results in overly conservative strength predictions. Both the choice of the location of failure analysis as well as the choice of an adequate failure criterion affect failure prediction and will be discussed in the following.

The Characteristic Curve Method

Many approaches have been proposed in literature to account for localized damage in composite laminates. Two of the earliest and widely used approaches are the point stress criterion and average stress criterion by Whitney and Nuismer [205], introduced in 1974, mainly for analyzing notched laminates under tensile loading. Therein, failure is predicted if either the stress at some distance away from the center notch is equal to the unnotched laminate strength or if the averaged stress over a distance away from the center notch is equal to the material strength. In both cases, a characteristic distance is introduced that was initially assumed to be independent of material

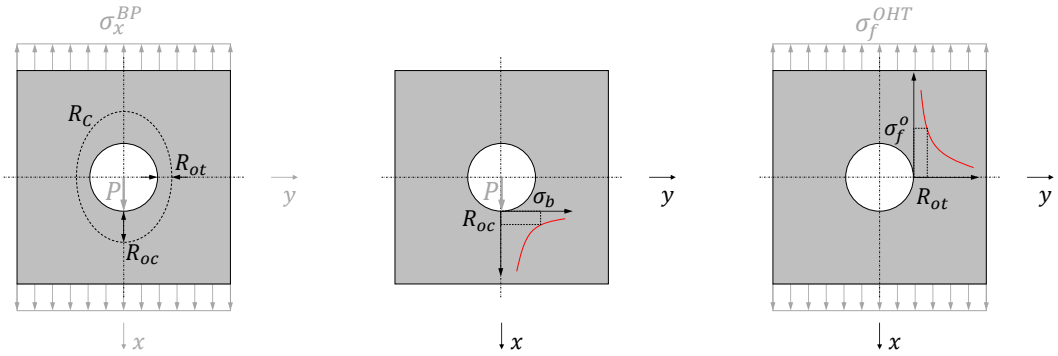

(a) Characteristic curve R_c **(b)** Characteristic distance R_{oc} **(c)** Characteristic distance R_{ot}

Figure 7.23 Schematic representation of the characteristic curve method

and stacking, but has proven to be a function of both material and stacking as well as specimen geometry [67, 154]. The characteristic curve method in Figure 7.23 for predicting ultimate failure in mechanically fastened composite joints introduced by Chang et al. [204] builds on the principles of the point stress criteron. According to the characteristic curve method, failure occurs when the stresses at any point along a curve satisfy a failure criterion. Therein, the characteristic curve is a function of the hole diameter and the characteristic distances in tension R_{ot} and in compression R_{oc}:

$$R_c = \frac{d}{2} + R_{ot} + (R_{oc} - R_{ot}) \cos\theta, \qquad \frac{-\pi}{2} \leq \theta \leq \frac{\pi}{2} \tag{7.16}$$

Based on the angle of failure θ_f for which the failure criterion is satisfied, following failure modes are differentiated:

$$\begin{aligned} 0^\circ < |\theta_f| < 15^\circ &\rightarrow \text{bearing mode} \\ 30^\circ < |\theta_f| < 60^\circ &\rightarrow \text{shearout mode} \\ 75^\circ < |\theta_f| < 90^\circ &\rightarrow \text{tension mode} \end{aligned}$$

While failure angles within these intervals represent failure in bearing, shearout and tension mode, respectively, failure angles in between these intervals indicate mixed failure modes.

Determination of Characteristic Distances

The accuracy of the characteristic curve method depends on the proper definition of the characteristic distances. The conventional approach to determine characteristic distances is based on experimental testing in combination with numerical modeling of the elastic stress field of the specimen. The characteristic distance in compression R_{oc} (see Figure 7.23b) is defined as the distance from the hole edge to a point along the bearing plane where the compressive stress in the numerical model is equal to the bearing stress at failure during experimental testing. The characteristic distance in tension R_{ot} (see Figure 7.23c) is determined by testing notched as well as unnotched laminates. Therein, R_{ot} is defined as the distance from the hole edge to a point along the smallest cross-section where the tensile stress in the numerical model evaluated at the failure

load of the notched specimen is equal to the tensile strength of the unnotched laminate.

Kweon et al. [220] propose a purely numerical approach for determining the characteristic distances in tension and compression in an attempt to eliminate the need for experimental testing. It is shown that the characteristic distance in compression R_{oc} can be calculated with an arbitray bearing load, thus eliminating the need to determine the bearing strength experimentally. According to this approach, R_{oc} is defined by the distance from the hole edge to a point along the bearing plane where the compressive stress in the laminate is equal to the bearing stress σ_b at an arbitrary load level. By comparison to the conventional approach based on experimental testing and numerical simulation, it is demonstrated that the purely numerical approach yields identical values for R_{oc} for a wide range of w/d and e/d ratios. The characteristic distance in tension R_{ot} is defined as the distance from the hole edge where the tensile stress in the numerical model is equal to the mean tensile stress of the notched laminate at an arbitrary load level. Comparison to the conventional approach shows that the purely numerical approach results in larger values for R_{ot} by more than 18 %. However, failure prediction based on characteristic distances determined using the purely numerical approach results in lower deviation from experimental test results compared to the conventional method.

With the idea in mind to create a purely analytical approach, the state of the art methods for determining characteristic distances are transformed to purely analytical methods. Therein, determination of the characteristic distance in compression R_{oc} is adopted from Kweon et al. [220]. However, instead of using a numerically determined stress field, stresses along the bearing plane are calculated based on the exact analytical solution for composite laminates under pin-bearing loading introduced in Section 7.2.2. Calculation of the characteristic distance in tension R_{ot} follows the procedure of the conventional method. However, instead of determining the strengths of the notched σ_f^{OHT} and unnotched laminate σ_f^o by experimental testing, those values are approximated. Therein, the strength of the unnotched laminate is calculated by:

$$\sigma_f^o = \sum_{i=1}^{n} x_i \, \sigma_f^i \tag{7.17}$$

In this equation, x_i denotes the ply share of a given orientation i with a tensile strength in loading direction of σ_f^i. In case of a QI laminate, for example, the approximate tensile strength of the unnotched laminate with a ply share of [25/50/25] is given by $\sigma_f^o = 0.25 \cdot X_T + 0.5 \cdot S + 0.25 \cdot Y_T$. Technically, tensile failure of an unnotched laminate largely depends on the failure strain of the 0° layers. Therefore, it would be more accurate to determine the contribution of the ±45° and 90° plies to the material strength by calculating the tensile stresses in the respective layers at the failure strain of the 0° layer. Nevertheless, this approach would require additional information for the design process and does not significantly improve the accuracy of the approximation, which is why it is not implemented. The strength of the notched laminate is approximated by the empirical relation based on Heywood [221]:

$$\sigma_f^{OHT} = \left(1 - \frac{d}{w}\right)^2 \sigma_f^o \tag{7.18}$$

Therein, the strength of the notched laminated is approximated by multiplying the strength of the unnotched laminate σ_f^o with a geometrical strength reduction factor based on the ratio between hole diameter and specimen width. Other approaches for determining the characteristic distance in tension are available, too. Such as the methods by Karlak [222], Pipes et al. [223] or Kim et al. [224] to name a few. However, those methods are typically based on empirical data. Depending on what material is analyzed, those methods yield better or worse agreement during failure analysis.

When determining characteristic distances, comparison of stresses can be conducted in different ways. While Camanho et al. [67] evaluate stresses on ply level for determining the characteristic distance in tension for OHT specimens, Kweon et al. [220] use mean stresses on laminate level for determination of characteristic distances in tension and compression. In the present approach, stresses on laminate level are used for determination of characteristic distances. Therein, a further differentiation is made:

$$\begin{array}{lcll} R_{ot} & \rightarrow & \text{OHT} & \rightarrow \quad \sigma_{xx(x=0)} = \sigma_f^{OHT} \\ R_{oc} & \left\{ \begin{array}{l} \\ \end{array} \right. & \begin{array}{l} \text{pin-bearing} \\ \text{bolt-bearing} \end{array} & \begin{array}{l} \rightarrow \quad \sigma_{xx(y=0)} = \sigma_b \\ \rightarrow \quad \sigma_{Tresca(y=0)} = \sigma_b \end{array} \end{array}$$

The characteristic distance in tension R_{ot} and the characteristic distance in compression R_{oc} in case of pin-bearing loading are determined by comparing the longitudinal stress σ_{xx} to the respective reference value. This way, the brittle nature of the failure characteristic of OHT and pin-bearing tests is accounted for. Determination of the characteristic distance in compression R_{oc} in case of bolt-bearing loading is done by evaluating the equivalent stress based on the maximum shear stress criterion (Tresca[12]), thereby accounting for quasi-ductile failure behavior with substantial interaction of stresses and accumulation of damage prior to ultimate failure under the washer area. Rather than using the van Mises equivalent stress, the Tresca equivalent stress is chosen here since it has been prevously applied with convincing accuracy in conjunction for predicting failure in composite materials by Hart-Smith [225, 226]. Furthermore, preliminary studies have shown that application of the Tresca criterion results in more accurate results compared to the van Mises equivalent stress for ductile materials or the Rankine equivalent stress for brittle materials. The validation of the analytical design methodology in the subsequent sections will give more insight on the predictive quality of the proposed failure analysis approach.

Failure Criterion

After introducing the characteristic curve method that defines the location where failure analysis is conducted, the failure criterion based on which the failure index FI is determined will be presented in the following. The Yamada-Sun failure criterion [227] is often used in conjuction with the characteristic curve method. Camanho et al. [154] propose a modification of the Yamada-Sun criterion by differentiating between tensile and compressive failure behavior. While the in-plane shear stress is considered to

[12] $\sigma_{Tresca} = \sqrt{(\sigma_{xx} - \sigma_{yy})^2 + 4\tau_{xy}^2}$

affect longitudinal compressive failure, longitudinal tensile failure is not affected by shear stresses, resulting in the following formulation:

$$FI = \left(\frac{\sigma_{11}}{X_T}\right) \qquad \text{for} \quad \sigma_{11} \geq 0 \tag{7.19}$$

$$FI^2 = \left(\frac{\sigma_{11}}{X_C}\right)^2 + \left(\frac{\tau_{12}}{S}\right)^2 \qquad \text{for} \quad \sigma_{11} < 0 \tag{7.20}$$

As oppose to the rather simple Yamada-Sun criterion, more complex failure criteria are capable of differentiating failure modes of individual plies. One example is the 2D formulation of the Cuntze FMC, where 5 individual failure modes are differentiated [91]:

$$FF1: \; f^{\parallel\sigma} = \frac{\sigma_{eq}^{\parallel\sigma}}{X_T} = \frac{\sigma_{11}^*}{X_T} \approx \frac{\sigma_{11}}{X_T} \tag{7.21}$$

$$FF2: \; f^{\parallel\tau} = \frac{\sigma_{eq}^{\parallel\tau}}{X_C} = \frac{\sigma_{11}^*}{X_C} \approx \frac{\sigma_{11}}{X_C} \overset{\sigma_{11}<0}{=} \frac{|\sigma_{11}|}{X_C} \tag{7.22}$$

$$IFF1: \; f^{\perp\sigma} = \frac{\sigma_{eq}^{\perp\sigma}}{Y_T} = \frac{\sigma_{22} + \sqrt{\sigma_{22}^2}}{2Y_T} \overset{\sigma_{22}\geq 0}{=} \frac{\sigma_{22}}{Y_T} \tag{7.23}$$

$$IFF2: \; f^{\perp\tau} = \frac{\sigma_{eq}^{\perp\tau}}{Y_C} = \frac{b_{\perp\perp}\sqrt{\sigma_{22}^2} + (b_{\perp\perp} - 1)\,\sigma_{22}}{Y_C} \overset{\sigma_{22}<0}{=} \frac{|\sigma_{22}|}{Y_C} \tag{7.24}$$

$$IFF3: \; f^{\perp\parallel} = \frac{\sigma_{eq}^{\perp\parallel}}{S} = \frac{|\tau_{12}|}{S}\sqrt{\frac{\sqrt{b_{\perp\parallel}^2\sigma_{22}^2 + S^2} + b_{\perp\parallel}\sigma_{22}}{S}} \tag{7.25}$$

The stressing efforts of the individual failure modes are then combined to the total stressing effort, i.e. the failure index FI using the interaction coefficient m:

$$FI^m = \sum_{\text{mode}=1}^{5} f^{(\text{mode})^m} \tag{7.26}$$

$$= \left(\frac{\sigma_{eq}^{\parallel\sigma}}{X_T}\right)^m + \left(\frac{\sigma_{eq}^{\parallel\tau}}{X_C}\right)^m + \left(\frac{\sigma_{eq}^{\perp\sigma}}{Y_T}\right)^m + \left(\frac{\sigma_{eq}^{\perp\tau}}{Y_C}\right)^m + \left(\frac{\sigma_{eq}^{\perp\parallel}}{S}\right)^m \tag{7.27}$$

A fundamental difference between these failure criteria is the treatment of transverse stresses. While in the Yamada-Sun criterion, transverse stresses are ignored entirely, the Cuntze FMC fully includes them into the calculation of the material stressing effort. The underlying reasoning by Yamada and Sun [227] for neglecting transverse stresses is the assumption that at ultimate failure all layers of the laminate are expected to exhibit failure in the form of cracking along the fiber direction, i.e. transverse matrix failure. Thus, the load bearing capacity of an individual ply in transverse direction is non-existing and the longitudinal stress and shear stress are considered to sustain the total applied load. However, transverse cracking of a single ply with the Cuntze

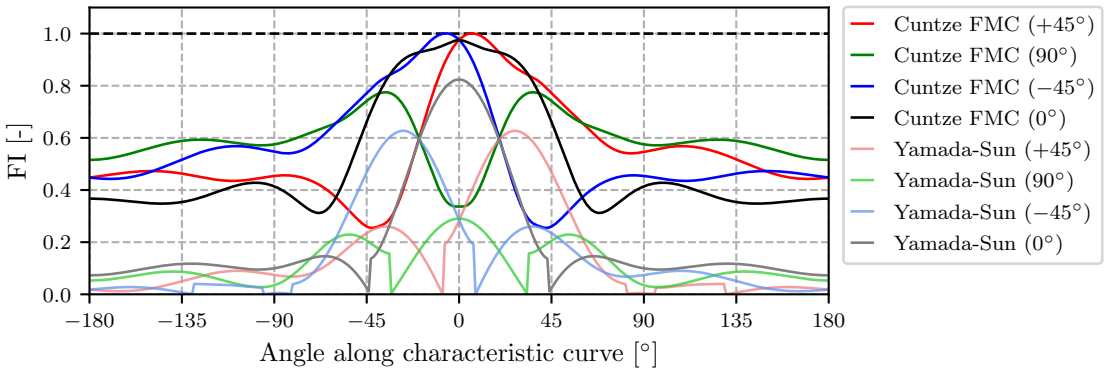

Figure 7.24 Exemplary failure indices for individual plies of a QI laminate under bearing loading determined by application of the Yamada-Sun criterion and the Cuntze FMC in 2D at equal load level

FMC directly translates to the material stressing effort. When the Cuntze FMC is used for progressive damage analysis based on continuum mechanics, load shifting from cracked plies to adjascent plies is considered, resulting in an appropriate representation of the influence of the effects of transverse cracks. However, when not coupled with progressive damage analysis, application of the Cuntze FMC ignores the prevailing load bearing capacity of a laminate with transverse cracks, therefore resulting in an overly conservative failure prediction. As can be seen in Figure 7.24, incorporation of transverse stresses by the Cuntze FMC leads to a higher FI compared to the Yamada-Sun criterion. Taking into consideration that failure analysis in the present case is conducted on an elastic stress distribution without modeling damage progression, application of the Yamada-Sun criterion is considered to be better suited for predicting failure.

In case of metal hybridized structures in the joining region, failure analysis on a thin metallic sheet is necessary. Petersen [119] observed a bi-linear behaviour for thin rolled steel sheets essentially characterised by an ideally plastic behaviour until ultimate failure, both longitudinal and transverse to the rolling direction. Hence, the von Mises yield criterion valid for ductile isotropic materials is applied to predict failure in the metal layers of an FML by comparing the equivalent von Mises stress σ_{vM} for general plane stress conditions to the yield point σ_f of the material [228]:

$$FI = \frac{\sigma_{vM}}{\sigma_f} = \frac{\sqrt{\sigma_{xx}^2 + \sigma_{yy}^2 - \sigma_{xx}\sigma_{yy} + 3\tau_{xy}^2}}{\sigma_f} \tag{7.28}$$

The validation of the analytical design methodology in the subsequent section will give more insight on the predictive quality of the choice of failure criterion.

7.3 Validation of Analytical Joint Analysis Tool

In the previous sections, the underlying theories of the elements of a purely analytical design tool (ajaX) were introduced and discussed individually with respect to

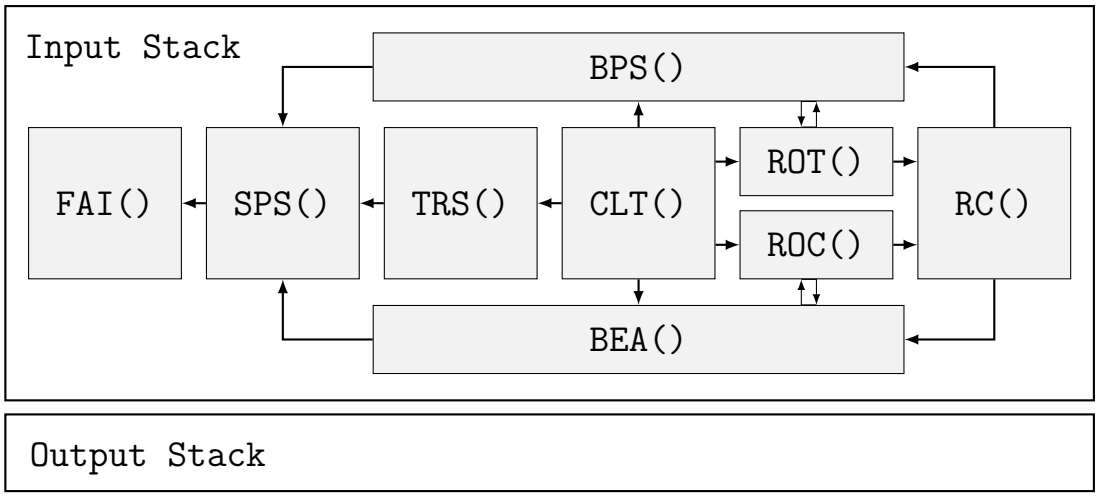

Figure 7.25 Schematic overview of design methodology

accuracy and applicability. In particular, investigation of exact analytical solutions for determining stresses was done in great detail as this element represents the main pillar of the analytical design methodology. In the following, the methodology as a whole is validated. For this purpose, experimental test data is collected for several loading scenarios, i.e. pin- and bolt-bearing, as well as two temperature levels, i.e. RT and LT, for the bolt-bearing loading scenario. Each loading scenario is applied to the QI, HO, QI-FML and HO-FML stackings from Table 5.1 in order to incorporate effects resulting from the degree of orthotropy and level of hybridization of the laminates.

7.3.1 Overview of Joint Design Methodology

The purely analytical design methodology of ajaX in Figure 7.25 is composed of three layers. The first layer is the `Input Stack`. Here, the user can define material elastic and failure data, loading conditions as well as laminate geometry and stacking sequence. Data defined in the `Input Stack` is available to all modules of the second layer. The second layer is where the analytical design procedure actually is conducted. A total of nine modules interact in order to accomplish the design task. The results of the individual modules of the second layer as well as the final joint failure prediction are transferred to the third layer, i.e. the `Output Stack`, and available for interpretation by the user.

The starting point of the design procedure is the module `CLT()` where the stiffness properties on ply level and the laminate layup are transformed to engineering constants on laminate level. This data is used by the modules for calculation of the characteristic distance in tension `ROT()` and compression `ROC()`. The former module requires the stresses in a notched laminate which is provided by the module `BPS()`, while the latter gets the stresses in a laminate under bearing loading from the module `BEA()`. The results of the modules `ROT()` and `ROC()` are combined to determine the characteristic curve in `RC()`. Once the characteristic curve is available, stresses resulting from mechanical loads can be calculated. Depending on the mechanical load-

ing scenario, the modules for calculating bypass stresses `BPS()`[13] and bearing stresses `BEA()`[14] are integrated into the design procedure. Pure bypass (uni- and biaxial), pure bearing as well as bearing-bypass interaction loading scenarios can be modeled. In the module `TRS()`, thermal residual stresses in the individual plies of the laminate are determined based on CLT. While the result of the module `TRS()` provides intralaminar thermal residual stresses on lamina level in the local ply coordinate system, the results of the modules `BPS()` and `BEA()` are defined on laminate level in the global laminate coordinate system. Thus, within the module for superposition of stresses `SPS()`, the results of `BPS()` and `BEA()` are combined and transformed to lamina level in the local ply coordinate system. The outcome of the module `SPS()` are the superimposed mechanical and thermal stresses along the characteristic curve for each material and orientation in local ply coordinates. This data is in turn processed by the module for failure analysis `FAI()` where appropriate failure criteria for composite and metallic materials are applied on ply level in order to determine the failure index and margin of safety as well as the failure mode.

Defining exact limitations of the present methodology requires extensive comparison to experimental test data by comprehensive material and geometry variation. However, similarly to comparable tools the input layup should have volume fractions greater 10 % for each orientation in the laminate. Following limitations regarding the joint geometry apply: Since the influence of the edge distance is not considered, the e/d ratio should be greater or equal 3. By incorporating the finite-width correction method, the present methodology can be applied to laminates with $w/d \geq 3$. The thickness-to-diameter ratio should be within $0.5 \leq t/d \leq 1.5$. If multi-row joints are to be considered, the present methodology can be coupled with analytical models based on 1D spring idealization for calculating the load transfer and bypass load ratios in multi-fastener joints as described in Koord et al. [229].

7.3.2 Pin-Bearing Loading Scenario

The validation of the pin-bearing loading scenario is based on the QI and HO specimen tested in section 7.2.2 as well as additional QI-FML and HO-FML specimens that are manufactured with the same manufacturing process and tested in the same pin-bearing test setup. As pin-bearing failure is sudden and brittle, the peak load F_{ult} before the sudden load drop during testing (see Figure 7.9) is considered the failure load, as is commonly done in literature [42]. Joint geometry data is taken from Table 7.2 and material properties for M21/T700GC and steel 1.4310 from Section 4.1. In Table 7.3 the experimental pin-bearing test results are compared to the failure load predicted by the analytical design methodology.

The prediction of failure by the analytical design methodology in case of the QI and HO laminates is excellent with an error of 3 % and 1 %, respectively. In case of the FMLs, the error slightly increases. However, an accuracy of ± 10 % for a purely analytical tool is still considered very good. When considering the variance during experimental testing of 7-8 %, it can be seen that the analytical results for the FMLs are

[13] Based on the exact analytical solution by Soutis and Filiou [195]

[14] Based on the solution by Waszczak and Cruse [209] with finite width correction by de Jong [217]

Table 7.3 Comparison of experimental pin-bearing test results (mean value/ standard deviation / coefficient of variance) and analytical prediction

Laminate	d [mm]	t [mm]	w [mm]	e [mm]	n [-]	Experimental test [MPa / MPa / %]	ajaX prediction [MPa]	Error [%]
QI	6.35	4.14	45	25	4	435 / 31 / 7.1 (B)	448 (B)	3
HO	6.35	4.19	45	25	4	446 / 43 / 7.7 (S)	452 (S)	1
QI-FML	6.35	4.09	45	25	3	678 / 50 / 7.4 (B)	625 (B)	-8
HO-FML	6.35	4.06	45	25	3	720 / 55 / 7.7 (B+S)	793 (S)	10

Failure modes: bearing (B), shear-out (S)

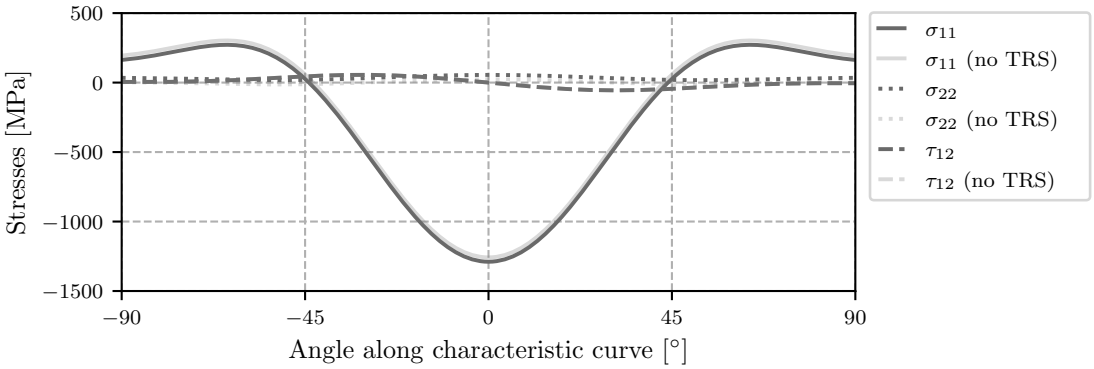

Figure 7.26 Stresses in the 0° ply of the QI laminate at FI=1 based on analytical design methodology

very close to the experimentally observed failure loads. Furthermore, taking into account the accuracy of the underlying exact analytical solution for determining stresses in pin-loaded laminates in section 7.2.2, it should be mentioned that the deviation in failure prediction is of the same order of magnitude as the error for predicting stresses. When considering the failure mode, the analytical methodology is capable of distinguishing between bearing and shear-out failure types that occured during experimental testing.

The effect of thermal residual stresses on the failure analysis is discussed at the example of the stresses in the 0° plies of the QI and QI-FML laminates at failure. In case of the QI laminate, neglecting thermal residual stresses leads to almost no change in the stress distribution at failure in Figure 7.26. Thus, it can be concluded that neglecting thermal residual stresses in the QI laminate has no significant effect on the failure prediction. When comparing the pin-bearing strength for the case when thermal residual stresses are neglected (σ_b=452 MPa) to the result for the QI laminate including the effect of residual stresses in Table 7.3 (σ_b=448 MPa), this conclusion is confirmed.

In case of FMLs, neglecting thermal residual stresses significantly affects failure analysis. As can be seen in Figure 7.27, neglecting thermal residual stresses in the QI-FML leads to less conservative longitudinal stresses in the 0° ply at an angle of 0°. As failure in the QI-FML in the present case is triggered by the steel layer, stresses

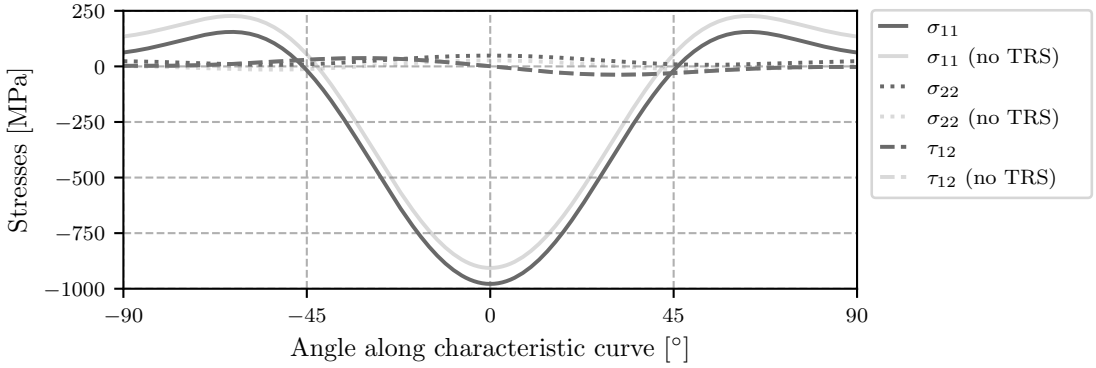

Figure 7.27 Stresses in the 0° ply of the QI-FML at FI=1 based on analytical design methodology

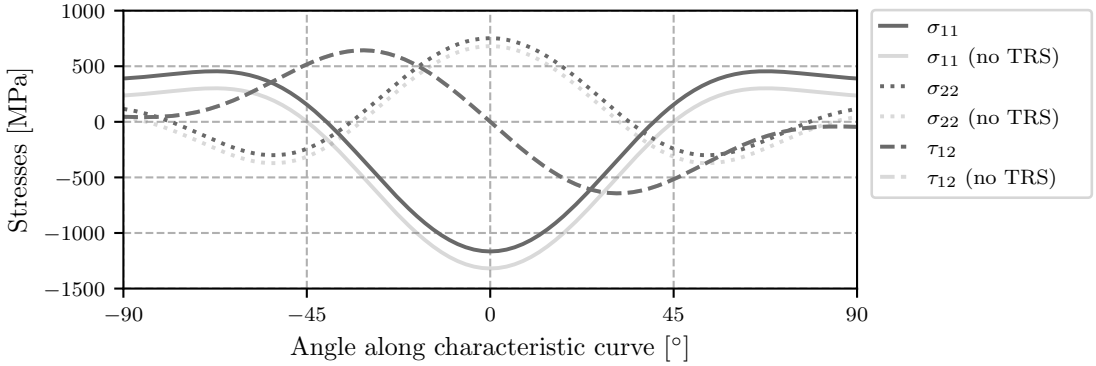

Figure 7.28 Stresses in the steel ply of the QI-FML at FI=1 based on analytical design methodology

in the steel ply are presented in Figure 7.28. It can be seen that inclusion of thermal residual stresses has the opposite effect on the steel ply, when compared to the 0° ply. Compressive residual stresses lead to an increase of the purely mechanical stresses in longitudinal direction of the steel ply σ_{11}. Thus, by incorporating thermal residual stresses into the analysis process, the predicted failure load increases from initially 571 MPa, when ingoring thermal residual stresses, to 625 MPa, when thermal residual stresses are taken into consideration. As a result, the prediction error is reduced from -16 % to -8 %.

To conclude, while the effect of thermal residual stresses on the bearing strength of pin-bearing specimens can be neglected for monolithic laminates, inclusion of thermal residual stresses in case of FMLs has a significant influence on the result. Figure 7.29 shows the experimental pin-bearing results as well as the analytical pin-bearing strength prediction with and without inclusion of thermal residual stresses. This visualization of the results further outlines the conclusion that conisderation of thermal residual stresses highly affects the failure analysis process in case of FMLs.

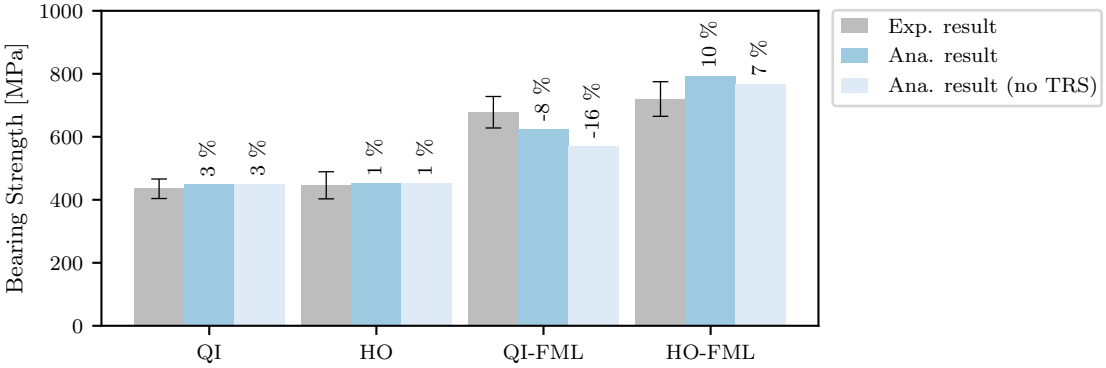

Figure 7.29 Effect of inclusion of thermal residual stresses on the accuracy of analytical pin-bearing failure prediction

7.3.3 Bolt-Bearing Loading Scenario

In the present section, test results from Chapter 5 at RT and LT are taken as a basis for validation of the analytical design methodology with respect to the bolt-bearing loading scenario at varying temperature levels. Specimen manufacturing and testing are discussed in detail in Section 5.1. Material input is taken from Section 4.1, while the laminate stacking sequence is presented in Table 5.1. The difference between failure analysis in case of pin-bearing and bolt-bearing loading lays in the definition of the characteristic curve. Failure analysis for the bolt-bearing scenario is based on characteristic distances determined using the Tresca criterion in order to better incorporate the interaction of different stress components. However, both stress prediction and failure analysis are based on 2D methods. Due to the fact that no 3D stress state is modeled, the accuracy is expected to be worse compared to the pin-bearing case. Failure analysis in case of bolt-bearing is based on the 0.5% offset strength.

Room Temperature

In Table 7.4, detailed test results of the bolt-bearing loading scenario at RT are presented together with the analytical failure prediction. The deviation between experimental result and analytical failure prediction ranges between -9 % and -21 %. Since the analytical prediction underestimates the failure strength in all cases, the methodology can be considered conservative in the present case. Compared to the pin-bearing loading scenario, failure load prediction for bolt-bearing is considerably less accurate. The analytically determined failure modes exhibit excellent agreement with experimental observations. In the present case, the analytical methodology not only captures the qualitative differences between bearing and shear-out failure modes but also correctly indicates the presence of combined bearing/shear-out mode in case of HO-FML.

When considering the stress state at failure in the metal plies in Figure 7.30, it can be seen that inclusion of thermal residual stresses noticeably affects the stresses inside the laminate and thereby failure analysis. As previously observed at the example of the pin-bearing QI-FML, taking into account the effect of thermal residual stresses aggrevates the stress state around an angle of 0° where failure occurs.

Table 7.4 Comparison of experimental bolt-bearing test results (mean / standard deviation / coeff. of variance) for 0.5% offset strength and analytical prediction at RT

Laminate	d [mm]	t [mm]	w [mm]	e [mm]	n [-]	Experimental test [MPa / MPa / %]	ajaX prediction [MPa]	Error [%]
QI	6.35	4.22	45	25	4	712 / 10 / 1.4 (B)	580 (B)	-19
HO	6.35	4.22	45	25	4	654 / 5 / 0.8 (S)	592 (S)	-9
QI-FML	6.35	4.17	45	25	4	1030 / 8 / 0.8 (B)	810 (B)	-21
HO-FML	6.35	4.16	45	25	4	1170 / 14 / 1.2 (B+S)	1025 (B+S)	-12

Failure modes: bearing (B), shear-out (S)

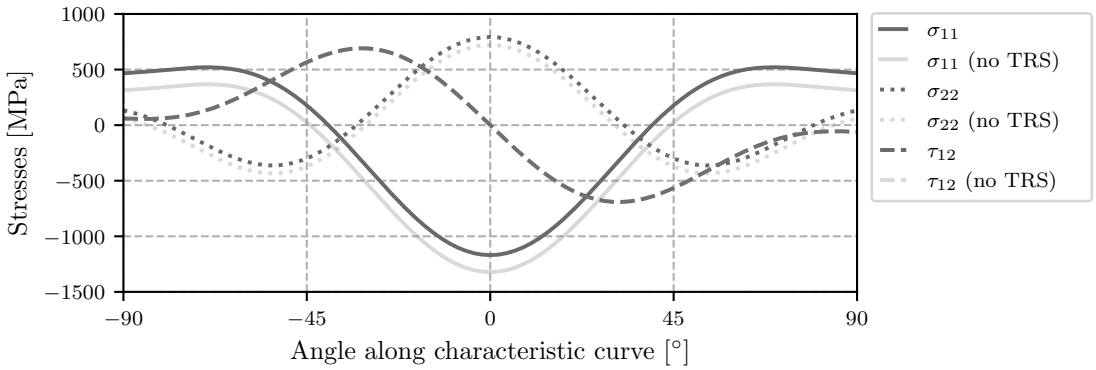

Figure 7.30 Stresses in the steel ply of the QI-FML at FI=1 at RT based on analytical design methodology

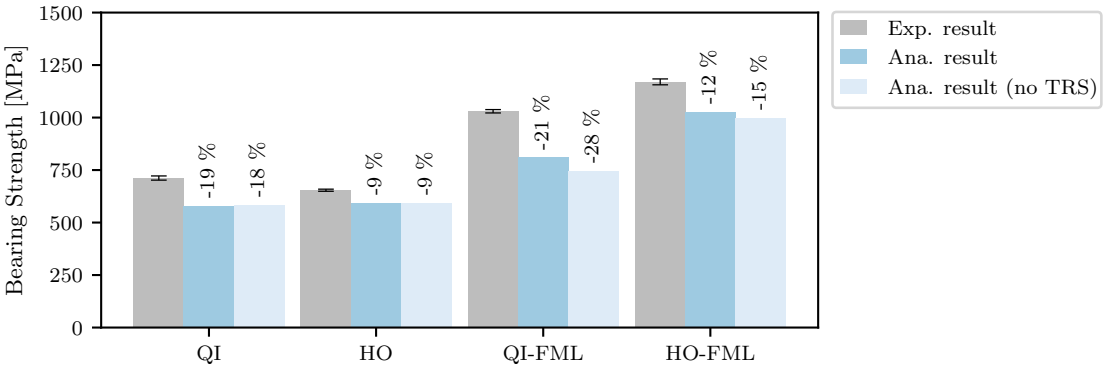

Figure 7.31 Effect of inclusion of thermal residual stresses on the accuracy of analytical bolt-bearing failure prediction at RT

In Figure 7.31, the effect of including thermal residual stresses in the design process is demonstrated. Monolithic laminates are barely affected by including residual stresses in the design process. However, when considering FMLs, incorporation of thermal residual stresses in the design process leads to an increase in strength prediction accuracy by 7 % and 3 % in case of QI-FML and HO-FML, respectively.

Low Temperature

The comparison of experimental bolt-bearing test results and analytical failure prediction at LT is presented in Table 7.4. The error of the analytical prediction ranges between -20 % and -26 %. Compared to RT level, where errors of up to -21% occur, strength prediction at LT is slightly less accurate. However, as already observed at RT level, the analytical methodology consistently underestimates the failure load and therefore can be considered conservative. Agreement between the failure modes observed during experimental testing and the analytical prediction is quite good. The qualitative differences between bearing and shear-out failure modes are generally well captured, eventhough the combined bearing/shear-out failure mode in case of HO-FML is not fully predicted by the analytical approach.

Table 7.5 Comparison of bolt-bearing test results (mean value/ standard deviation / coeff. of variance) for 0.5% offset strength and analytical prediction at LT

Laminate	d [mm]	t [mm]	w [mm]	e [mm]	n [-]	Experimental test [MPa / MPa / %]	ajaX prediction [MPa]	Error [%]
QI	6.35	4.14	45	25	4	861 / 35 / 4.1 (B)	638 (B)	-26
HO	6.35	4.19	45	25	4	841 / 17 / 2.0 (S)	670 (S)	-20
QI-FML	6.35	4.09	45	25	4	1180 / 27 / 2.3 (B)	920 (B)	-22
HO-FML	6.35	4.06	45	25	4	1400 / 24 / 1.7 (B+S)	1087 (S)	-22

Failure type: bearing (B), shear-out (S)

In Figure 7.32, the stress state at failure in the steel ply of the QI-FML is shown. As the difference between stress-free temperature and operating temperature increases, the magnitude of thermal residual stresses in the FML increases, too. Thus, the difference when including residual stresses compared to the case where residual stresses are neglected increases, too, as can be seen by comparison to the bolt-bearing loading scenario at RT in Figure 7.30.

As previously observed, including thermal residual stresses significantly affects the analytically predicted failure load in case of FMLs. This obervation also holds true for the case of bolt-bearing at LT in Figure 7.33. Inclusion of thermal residual stresses leads to an improvement in prediction accuracy by 15 % and 7 % in case of QI-FML and HO-FML, respectively.

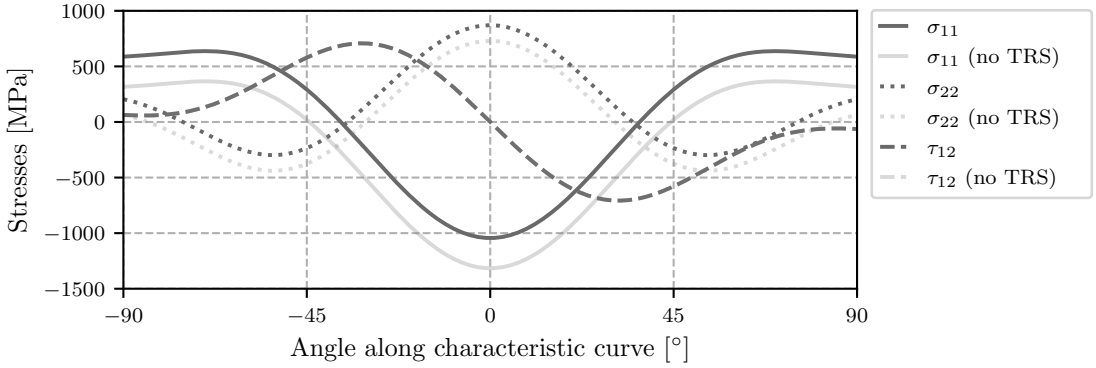

Figure 7.32 Stresses in the steel ply of the QI-FML at FI=1 at LT based on analytical design methodology

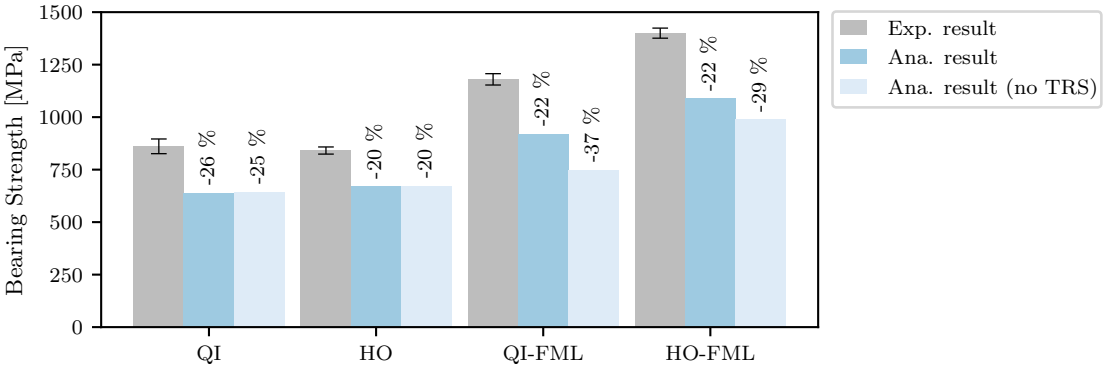

Figure 7.33 Effect of inclusion of thermal residual stresses on the accuracy of analytical bolt-bearing failure prediction at LT

7.4 Summary and Conclusions

In the present chapter, an analytical tool (ajaX) for preliminary design of pinned and bolted joints is developed. The need for creating such a tool results from the fact that currently available analytical tools generally do not incorporate the effect of thermal residual stresses, which is necessary for analyzing FMLs. Thus, one novelty of ajaX is its capability to incorporate thermal residual stresses in the strength analysis of mechanically fastened joints. The second novelty is the fact that the tool is purely analytical. Strength analysis is solely based on the joint geometry and the material stiffness and strength data. Other joint analysis tools generally require additional input such as characteristic distances for strength analysis. These values are usually determined experimentally or numerically. In ajaX, however, determination of the characteristic distances is done internally using a purely analytical approach. Figure 7.34 gives an overview of the required input for a joint analysis, the output information generated by ajaX as well as the underlying theory of the design methodology.

The methods used within the individual modules of the tool are verified and validated using numerical modeling as well as experimental testing. Moreover, the strength prediction capability with respect to bearing strength and failure type is

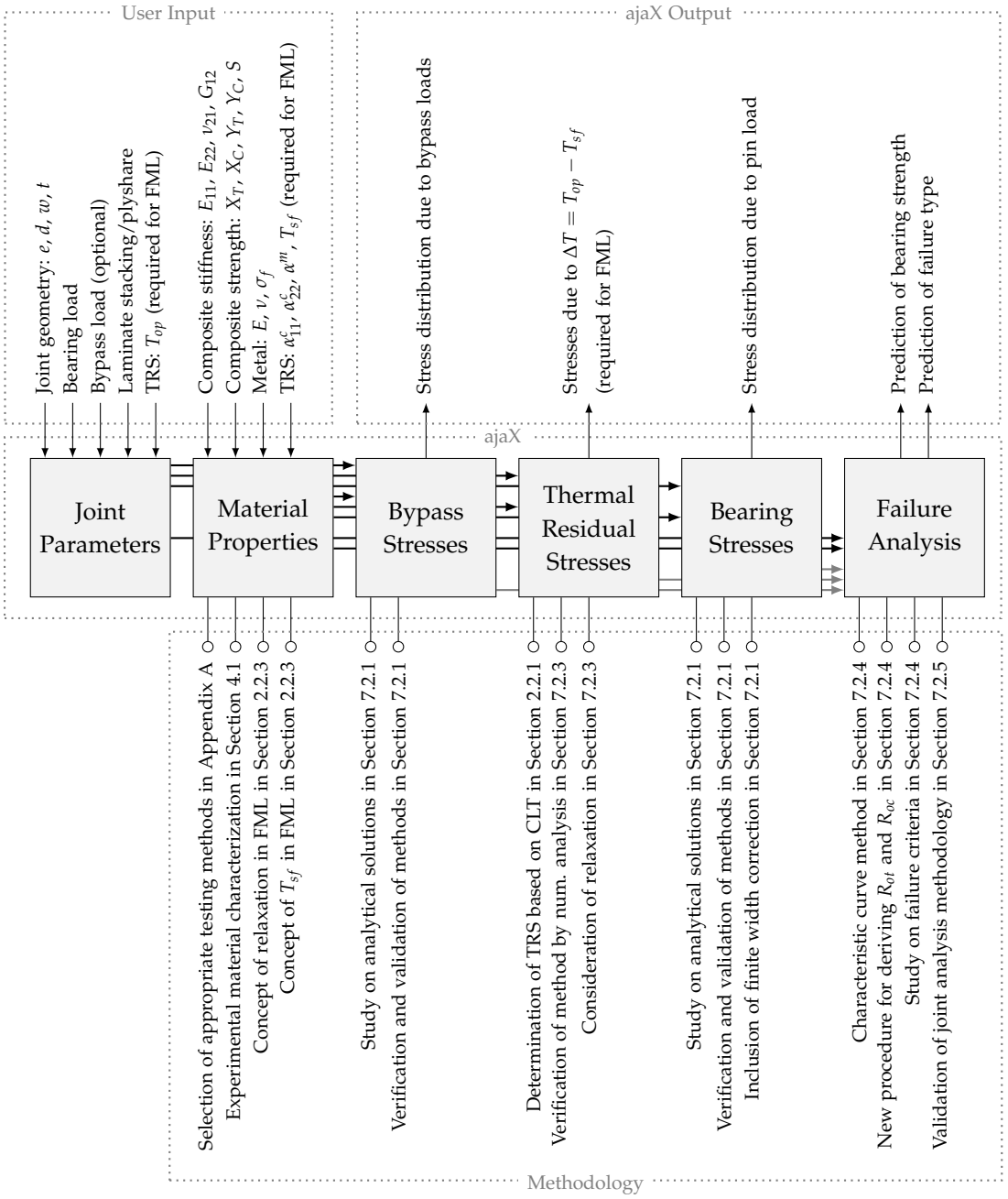

Figure 7.34 Overview of tool input/output and simplified global analysis procedure

demonstrated. Experimental pin- and bolt-bearing test results are compared to analytical predictions of failure load and failure mode for a variation of monolithic and hybrid material stackings, i.e. QI, HO, QI-FML and HO-FML, and two temperature levels, i.e. RT and LT. The prediction accuracy with regard to bearing failure load is ± 10 % (pin-bearing), ± 20 % (bolt-bearing at RT) and ± 25 % (bolt-bearing at LT). The capability of the analytical approach to predict the failure mode is excellent throughout all test cases. Considering the accuracy regarding both failure load and failure mode, it is concluded that the analytical design methodology is well capable of ac-

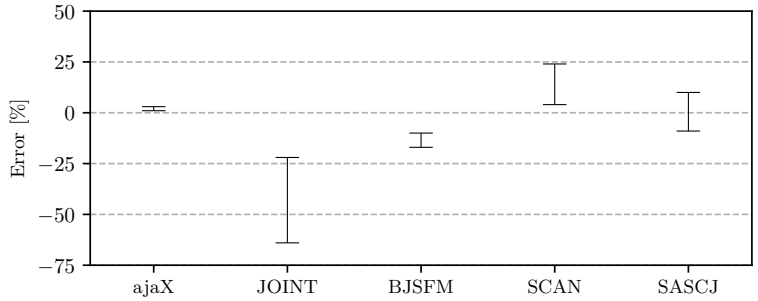

Figure 7.35 Accuracy of present approach with respect to pin-bearing strength of monolithic CFRP laminates compared to other tools evaluated at RT in [230]

couting for effects on the joint design arising from the laminate orthotropy or degree of hybridization. Furthermore, it is demonstrated that inclusion of thermal residual stresses significantly improves the prediction accuracy for hybrid laminates, thus confirming *Working Hypothesis IV*.

As the analytical design methodology is based on a 2D approach regarding both stress calculation and failure analysis, it is not surprising that the accuracy with respect to the pin-bearing loading scenario is significantly better compared to the bolt-bearing case. Nevertheless, the purely analytical tool is considered to be also suited for analysis of bolted joints during preliminary design stages. In relation to alternative tools, such as JOINT[15], BJSFM[16], SCAN[17], and SASCJ[18], the overall accuracy of the present purely analytical approach is on a comparable level as can be seen in Figure 7.35. However, ajaX requires less input data than those alternative tools and can additionally include thermal residual stresses into the design process, if needed. Especially when dealing with FMLs, consideration of thermal residual stresses in the design process appears to be necessary. Therein, incorporation of temperature effects into the design process improves the analytical strength prediction significantly. Failure in purely monolithic laminates is barely affected by thermal residual stresses, as is the consensus in the composite joint design community. In conclusion, the purely analytical joint design tool, ajaX, is considered to be suited for comparative studies on composite and FML joints within preliminary design stages. The tool allows for simple and fast variation of geometrical, material and loading conditions while only requiring in-plane stiffness and strength properties of a UD ply as data input.

[15]Composite joint analysis code: based on a simplified theory and empirical test data and stress concentration factors. Accuracy in [230]: -22 to -64 %

[16]Bolted Joint Stress Field Model: Semi-analytical tool based on exact-analytical solutions and laminated plate theory (comparable to the present approach). Accuracy in [230]: -10 to -17 %

[17]Stress Concentrations Analysis: Semi-analytical tool based on exact-analytical solutions and laminated plate theory, however, failure analysis is done on laminate level. Accuracy in [230]: +4 to +24 %

[18]Strength Analysis of Single Fastener Composite Joints: 2.5D analysis of joints based on the Lekhnitskii formalism for the plate and Timoshenko beam for the bolt deformation. Accuracy in [230]: -9 to +10 %

Chapter 8

Design Methodology for Hybridization of Composite Bolted Joints

8.1 Methodology for Local Metal Hybridization

In the previous chapters, experimental testing demostrated that the beneficial effect of hybridization on the bearing behavior of monolithic composites not only exist for room temperature conditions but also extends to low temperatures. Numerical modeling underlined the necessity of including thermal effects into the analysis process of hybrid materials. Based on those experimental and numerical results, an analytical design tool that accounts for thermal effects was developed for preliminary design of hybridized mechanically fastened composite joints. In the present chapter, the analytical design tool is incorporated into a design methodology for local metal hybridization and applied to exemplary cases.

Hybridization of a monolithic joint is always only an option in case the conventional monolithic design exhibits drawbacks. In general, these drawbacks result from the low bearing strength of monolithic laminates. Increasing the load capacity of composite joints is achieved by local laminate build-up in the joining area and/or an increase in the number of fasteners. These measures are generally accompanied by additional laminate stresses due to eccentricities, by complex geometries of adjacent structures as well as a significant increase in weight due to larger grip lengths, larger fastener diameters and heavier metallic fittings [21]. By means of local metal hybridization in the joining area, the bearing strength and the coupling stiffness are increased. Thus, not only can laminate build-up be prevented but also the possibility of reducing the number of bolts opens up, adding on to an efficient joint design [66].

In Figure 8.1, a methodology for the preliminary design of local metal hybridization is presented. Initially, in Step 1, material properties are either available or determined following the procedures outlined in Chapter 4. Subsequently, in Step 2, the analytical design process, based on ajaX, is employed to refine design parameters such as metal type, volume content or stacking sequence. These refined design solutions

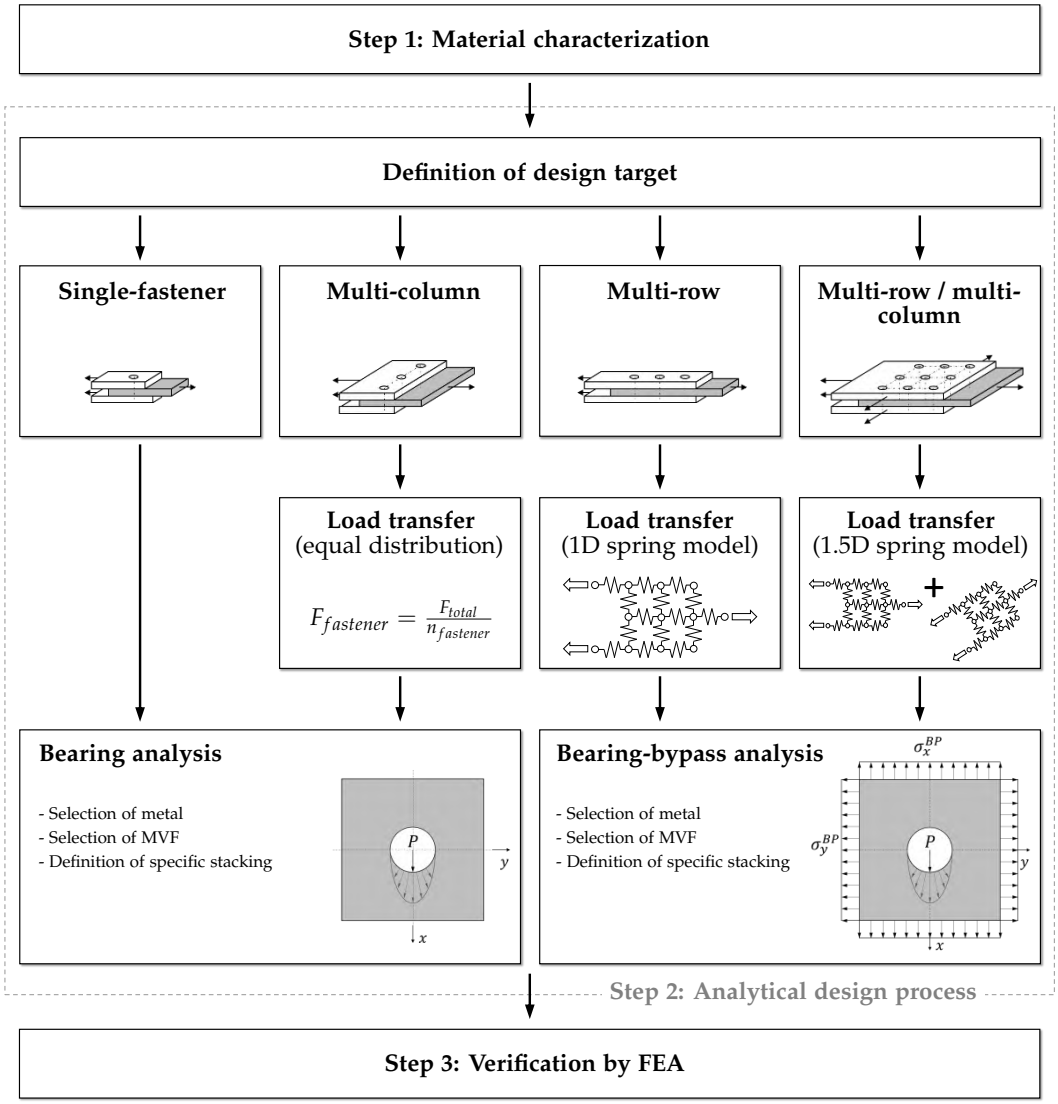

Figure 8.1 Design methodology for local metal hybridization

are then verified in Step 3 through numerical analysis, i.e. FEA.

Prior to the design of a hybridized joint, in general, a monolithic joint design is available that does not meet all requirements. The design process is a very individual task and highly depends on the requirements and the design target at hand, i.e. a highly weight-efficient joint will be different from a highly cost-effective joint design. In order to channel the vast possibilities, there are four cases differentiated in Step 2 of the design methodology in Figure 8.1: i) singe-fastener joints, ii) multi-column, iii) multi-row as well as iv) multi-row and multi-column joints. A single-fastener joint is rare in practical applications and usually serves as a simplified analysis case of a more complex structure. Multi-column joints are characterized by a main loading direction where the loads are distributed evenly between the single fasteners. In multi-row joints, load transfer between the fastener rows in uneven. A 1D-spring model can

be used to approximate the ratio of load transferred through each fastener as well as the bypass load at the respective fastener position [231]. Multi-row multi-column joints are mainly present in highly loaded structures, e.g. the joint between wing-root to center wing-box of an aircraft. In case of uniaxial loading, the columns can be seperated and treated as individual rows. However, if the joint is also loaded in transverse direction, bearing and bypass loads can be estimated by superposition of longitudinal and transverse 1D-spring models. Depending on the loading scenario either simple bearing analysis or bearing-bypass analysis is conducted.

Using the analytical design tool, ajaX, the design of the local metal hybridization is done as follows: First, a pre-selection is made for the metal type and the required MVF based on the requirements of the joint. Then, the pre-selection of metal type and MVF is analyzed in detail and transformed into distinct stacking sequences. The bearing strength of the distinct stacking sequences is determined and the final selection regarding metal type, MVF and stacking sequence is made, whilst taking into account the design objectives, e.g. regarding mechanical, weight or manufacturing requirements. After designing the joining area, the transition area, i.e. the ply-substitution scheme, needs to be defined. This is out of the scope of the present thesis as Petersen [38] provides a comprehensive design methodology for the transition area.

8.2 Application of Design Methodology

As previously mentioned, designing mechanically fastened joints is a task that highly depends on the given requirements and the design target. Therefore, the design of a hybridized joint is conducted for two example cases. The first case is rather generic and demostrates the design of a single-fastener joint with a focus on bearing strength increase, while the second case shows the design process for an aircraft wing-root/center-wing-box joint with a focus on weight optimization.

8.2.1 Single-Fastener Joint Analysis

The single-fastener case in Figure 8.1 is chosen to demonstrate the design procedure for selecting metal type, MVF, and the specific stacking sequence for hybridization by means of ply-substitution. The goal is to increase the bearing strength of the monolithic design by 50 % at minimum cost increase and otherwise constant geometry. Material properties (**Step 1**) are taken from Chapter 4. The reference joint design for a 16-ply QI laminate is derived from AITM 1-0009:

Monolithic reference design:	
Laminate plyshare	25/50/25 (QI)
Laminate stacking	$[-45,90,45,0,-45,90,45,0]_s$
Laminate thickness	4.16 mm
Laminate width	45 mm
Bolt diameter	6.35 mm
CFRP material	M21/T700GC
Loading type	Single-fastener (pin-loading)
Operating temperature	-55°C

The bearing strength is calculated using ajaX. In case of monolithic laminates, it is established in Chapter 6 and Chapter 7 that thermal effects do not need to be accounted for. Thus, input of stress-free temperature, operating temperature and CTE is not required. However, for demonstration purposes they are yet included:

Input to ajaX:	
Laminate stacking	$[-45,90,45,0,-45,90,45,0]_s$
Cured ply thickness	0.26 mm
Laminate width	45 mm
Edge distance	25 mm
Bolt diameter	6.35 mm
$X_T/X_C/Y_T/Y_C/S$	2230 MPa, 1593 MPa, 93 MPa, 344 MPa, 106 MPa
E_{11}, E_{22}, ν_{12}, G_{12}	122 GPa, 10 GPa, 0.287, 5.7 GPa
T_{sf}, T_{op}, α_{11}, α_{22}	132 °C, -55 °C, $-0.19 \cdot 10^{-6} \frac{1}{°C}$, $29.66 \cdot 10^{-6} \frac{1}{°C}$ (optional)

Step 2.1: Based on ajaX, the load that can be transferred by the joint is 12.8 kN, which equals a bearing strength of 480 MPa. Neglecting thermal effects ($\Delta T = T_{op} - T_{sf} = 0$) results in a bearing strength of 485 MPa which is a difference of around 1 %. In the following, the bearing strength including thermal effects is considered. The design target is to increase the bearing strength by 50 %, resulting in a required bearing strenght of 19.2 kN (720 MPa) compared to 12.8 kN (480 MPa) of the reference design. In a single-fastener joint, increasing the maximum transferred load is generally only possible by increasing the laminate thickness. However, metal hybridization of the joint by means of ply-substitution allows for an increase in bearing strength without increasing the laminate thickness.

Step 2.2: Three steel and three titanium alloys are considered in the following. The data is derived from Fink [37]. The difference in strength for the steel alloys is a result of different degrees of cold forming, whereas the titanium alloys Ti-15-3-3 exhibit different aging parameters.

Metal alloy options:	
Steel 1.4310	low strength: 1300 MPa (LS)
Steel 1.4310	medium strength: 1600 MPa (MS)
Steel 1.4310	high strength: 1900 MPa (HS)
Titanium Ti-6-4	low strength: 700 MPa (LS)
Titanium Ti-15-3-3	medium strength: 1000 MPa (MS)
Titanium Ti-15-3-3	high strength: 1300 MPa (HS)

In a first step, a pre-selection of metal alloy and MVF is conducted. For this purpose, the MVF of FMLs consisting of UD-0°-CFRP plies and and metal is varied in Figure 8.2. In Chapter 5, it is shown that this is a suitable way of estimating the bearing strength of steel-reinforced FMLs. In order to do so, following metal properties are required in addition to the properties of the CFRP:

Input to ajaX:	
Titanium E, ν, α	117 GPa, 0.315, $8.5 \cdot 10^{-6} \frac{1}{°C}$
Titanium yield strength	700 MPa (LS), 1000 MPa (MS), 1300 MPa (HS)

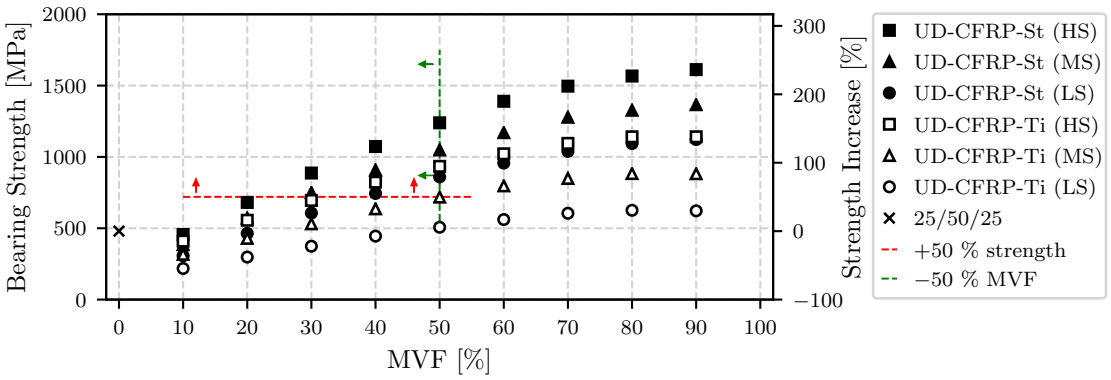

Figure 8.2 Pre-selection of metal type and MVF

Titanium sheet thickness	0.26 mm
Steel E, ν, α	190 GPa, 0.3, $12.8{\cdot}10^{-6}\,\frac{1}{°C}$
Steel yield strength	1300 MPa (LS), 1600 MPa (MS), 1900 MPa (HS)
Steel sheet thickness	0.26 mm

Figure 8.2 shows the bearing strength of laminates made up of UD-0°-CFRP plies with increasing MVF of different metal alloys. For FMLs, it is shown by experimental testing in Chapter 5 for LT as well as in Fink [37] for RT that for MVF between 20 - 50 % the increase in bearing strength is linear. Figure 8.2 is in accordance with that observation. With the target bearing strength of 720 MPa, MVF lower than 20 % appear to be insufficient. In addition, since ply-substitution is to be applied, the maximum MVF should be lower than 50 %. This is required, so that no two metal layers are neighboring and no ply-substitution occurs at the laminate surface ply. As a result, the metal alloy options are reduced to the steel alloys (HS, MS, LS) and one titanium alloy (HS). At the same time, the range of the required MVF for achieving the desired strength increase of 50 % is narrowed down to 20 % $<$ MVF $<$ 50 %.

Step 2.3: While the analysis based on UD-0°-CFRP-FMLs in Figure 8.2 is a good way to reduce the number of possible design options in terms of metal constituent and MVF, the magnitude of thermal residual stresses is still different from the stress state in the final laminate stacking. Therefore, once the number of possible metal constituents and MVF is reduced, the specific laminate stackings are determined. Based on the stacking sequence of the reference laminate, hybrid stacking sequences for the previously determined range of MVF and type of metal are derived. Derivation of the hybridized stacking sequences is based on the ply-substitution rules [37, 38]:

- Plies that contribute the least to the load bearing capacity should be substituted first (i.e. 90° before ±45° plies)
- Ply-substitution should occur symmetric to the laminate midplane
- Ply-substitution should occur in a way that the stiffness increase of the laminate is gradual
- Ply-substitution points should be seperated by at least 5-10 mm

Starting from the reference stacking, composite plies are substituted in pairs of two. In FML 1, two 90° plies are substituted by two metal plies, while in FML 2 all four 90° plies are substituted. To further increase the MVF, in FML 3 and FML 4 also 45° plies are substituted in addition to the 90° plies. It should be noted that the stacking of FML 3 and FML 4 need to be adjusted to keep the laminate balanced and symmetric. Depending on the application, e.g. if the base laminate stacking cannot be changed, the adjustment possibilities might be limited. Following the recommendations for ply-substitution results in FML 2 and FML 3 as possible stackings for local metal hybridization. The stacking sequences FML 1 and FML 4 are out of the range of the pre-selected MVF, while FML 4 also exhibits an invalid ply-substitution on the outer ply. However, the stackings are still considered for illustration purposes in Figure 8.3.

Local hybridization:

Laminate:	0°/±45°/90°/metal [%]:	Stacking sequence:
Reference	25/50/25/0	$[-45, 90, 45, 0, -45, 90, 45, 0]_s$
FML 1	25/50/12.5/12.5	$[-45, \text{metal}, 45, 0, -45, 90, 45, 0]_s$
FML 2	25/50/0/25	$[-45, \text{metal}, 45, 0, -45, \text{metal}, 45, 0]_s$
FML 3	25/37.5/0/37.5	$[-45, \text{metal}, 45, 0, \text{metal}, 0, \text{metal}, \underline{\pm 45}]_s$
FML 4	25/25/0/50	$[\text{metal}, -45, \text{metal}, 0, \text{metal}, 45, \text{metal}, 0]_s$

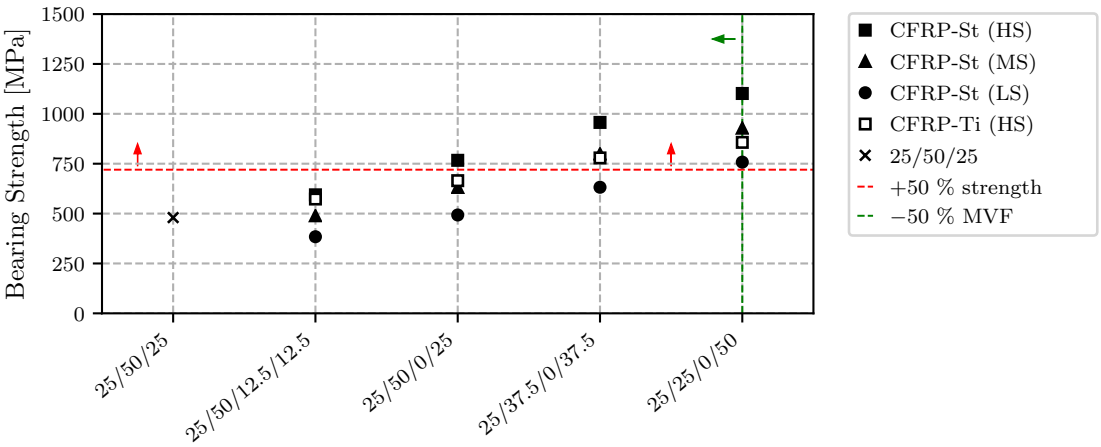

Figure 8.3 Selection of specific stacking sequence for hybridization

Figure 8.3 shows the bearing strength for the specific stacking sequences FML 1 to FML 4 with the remaining metal types for hybridization. At a MVF of 25 %, only hybridization by high strength steel leads to an acceptable increase in bearing strength of at least 50 %. At 37.5% MVF, medium strength steel, high strength steel and high strength titanium meet the required increase in bearing strength. Thus, the possible design options are reduced to the CFRP-St (HS) with 25 % MVF as well as the CFRP-St (MS) and CFRP-Ti (HS) with 37.5 % MVF. The option CFRP-St (HS) with 37.5 % MVF is omitted because hybridization with the same steel at 25 % MVF already meets the design goal.

Considering solely the increase in bearing strength of the laminate, hybridization

Table 8.1 Options for local metal hybridization of monolithic reference design

		Monolithic	CFRP-St (HS)	CFRP-St (MS)	CFRP-Ti (HS)
Plyshare	%	25/50/25	25/50/0/25	25/37.5/0/37.5	25/37.5/0/37.5
MVF	%	0	25	37.5	37.5
Stacking	°	$[-45, 90, 45, 0]_{2s}$	FML 2	FML 3	FML 3
Bolt load	kN	12.8	20.3	21.1	20.6
Bearing strength σ_b	MPa	480	767	799	779
Strength increase	%	-	60	66	62
Cost increase	%	-	149	297	623
Weight increase	%	-	98	148	75
Spec. strength σ_b/ρ	$\frac{\text{MPa}}{\text{g/cm}^3}$	300	242	202	278

by high strength steel at 25 % MVF is most efficient. When costs[1] are taken into account, CFRP-St (HS) in Table 8.1 is still the most efficient option. Compared to the titanium alloy 15-3-3 which comes at a cost of 632 €/kg, high strength stainless steel is more economical at around 15 €/kg. In addition, hybridization by high strength steel only requires two ply-substitutions, which reduces the amount of material required as well as the amount of metal pre-treatment, e.g. Sol-gel application at around 360 €/m^2. Nonetheless, the increase is cost due to hybridization in Table 8.1 remains significant. The estimation of the costs is based on the difference in raw material and Sol-gel application, while the remaining process costs, e.g. autoclave, are assumed to be the same.

If however a high weight efficiency[2] is defined as a design target, hybridization by high strength titanium CFRP-Ti (HS) is advantageous. Using titanium results in an increase in bearing strength of 62 % at only 75 % weight increase, compared to an increase in weight by 98 % when using high strength steel. Thus, despite more titanium plies in the laminate, the higher specific bearing strength of CFRP-Ti (HS) allows for a lighter design. This is in accordance with observations by Fink [37] based on bolt-bearing test results. However, as previously mentioned, the increase in specific bearing strength of the CFRP-Ti FML compared to the CFRP-St FML comes at higher manufacturing and material costs. Since the increase in bearing strength is demanded at a minimum cost increase, hybridization by CFRP-St (HS) with the distinct stacking FML 2 is selected from Table 8.1.

Based on Figure 8.4, the effects of thermal residual stresses on the design process of local metal hybridization are discussed. During the analytical analysis in Chapter 7, it is shown that inclusion of thermal effects in the analysis process alters the bearing strength by 3 % to 15 %. Therein, the inclusion of thermal effects generally leads to an improvement in accuracy. In Figure 8.4a, the bearing strength of the QI reference laminate as well as the UD-0° FMLs, namely CFRP-St (MS) and CFRP-Ti (MS), is shown with and without consideration of thermal residual stresses. Neglecting thermal residual stresses leads to an error of up to -6 % and -7 % for titanium and steel hybridization, respectively. The deviation is in the same order of magnitude as observed within the pin-bearing test results in Chapter 7, where deviations between 3 %

[1]The price estimation for steel, titanium, CFRP and Sol-gel application are taken from Fink [37]
[2]Densities: steel 7.9 g/cm^3, titanium 4.8 g/cm^3, CFRP 1.6 g/cm^3

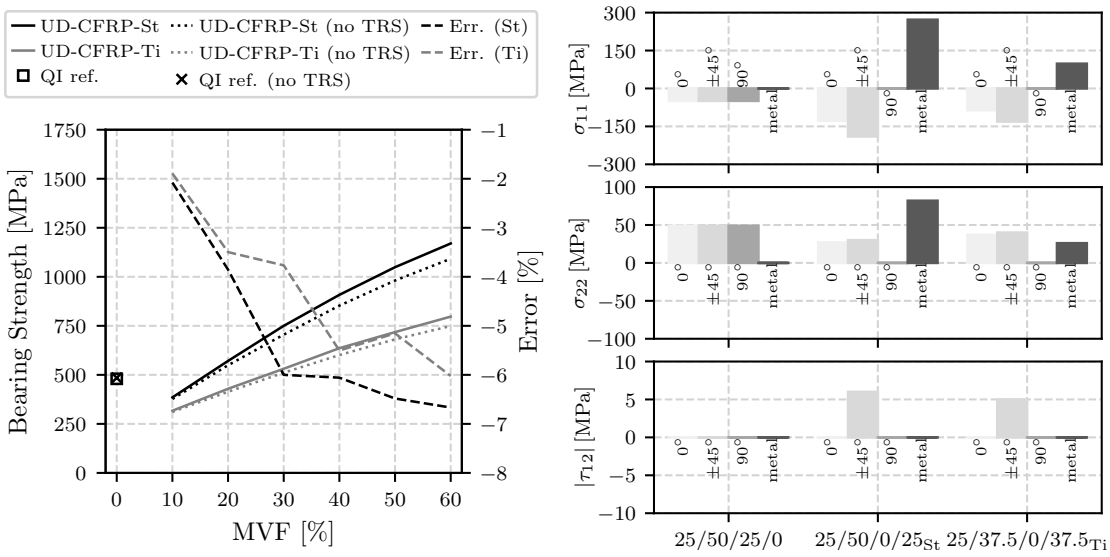

(a) Strength of UD-0°-CFRP-St/Ti (MS) **(b)** Thermal residual stresses on ply level

Figure 8.4 Effect of thermal residual stresses on the strength of UD-0°-CFRP FMLs hybridized with medium strengh steel/titanium (a) and thermal residual stresses on ply level in the individual plies of the distinct laminate stackings (b)

and 8 % are present in QI- and HO-FMLs. Considering the fact that the accuracy of the analysis tool for pin-bearing loading in FMLs is around ±10 %, the necessity of including thermal effects into the analysis process is disputable. On the one hand, the analytical prediction is more accurate when including thermal effects as demonstrated in Chapter 7. On the other hand, the error resulting from thermal residual stresses in the present case is lower than the tool accuracy itself. Figure 8.4b shows the thermal residual stresses in the individual plies of the QI reference as well as the CFRP-St (HS) and CFRP-Ti (HS) hybrid laminates in local ply coordinates. In the CFRP-St FML, for instance, the thermal residual stress state translates to 242 MPa von Mises stress which in turn makes up around 12 % of the failure stress of the steel. However, the resulting effect on the bearing strength is a redcution by about 5 %. The bearing strength itself is hardly affected despite the significant magnitude of thermal residual stresses that act in addition to the stresses due to the pin-load. Hence, inclusion of thermal effect can arguably be disregarded. However, this decision needs to be made on a case to case basis. Depending on the degree of orthotropy resulting from the stacking sequence as well as from the choice of material, the characteristic distances change and therefore the shape of the characteristic curve changes. The shape of the characteristic curve has a great influence on where failure is predicted, which in turn influences to what degree the presence of thermal residual stresses alters the analytical result. However, it should be noted that based on the experience with the design tool, inclusion of thermal effects generally improves the tool accuracy.

Step 3: The result of the analytical design process are the distict hybrid laminates in Table 8.1. In order to verify the results of the analytical design process based on ajaX (Step 2), the cases CFRP-St (HS), CFRP-St (MS) and CFRP-Ti (HS) are simulated in Abaqus. Since the present analysis considers a pin-bearing scenario, the

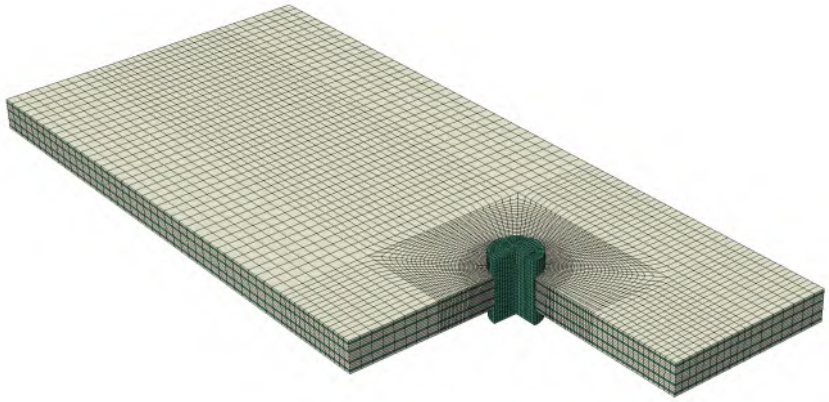

Figure 8.5 Pin-bearing model of CFRP-St (HS) derived by omitting the washers from the bolt-bearing model in Section 6.2.4 with metal (green) and composite plies (grey)

Table 8.2 Verification of analytical results for local metal hybridization

		Monolithic	CFRP-St (HS)	CFRP-St (MS)	CFRP-Ti (HS)
Plyshare	%	25/50/25	25/50/0/25	25/37.5/0/37.5	25/37.5/0/37.5
MVF	%	0	25	37.5	37.5
Stacking	°	$[-45, 90, 45, 0]_{2s}$	FML 2	FML 3	FML 3
σ_b (analytical)	MPa	480	767	799	779
σ_b (numerical)	MPa	529	851	824	680
Error	%	-10.2	-9.8	-3.0	12.7

FE-model developed in Section 6.2.2 is adjusted (see Figure 8.5) and utilized for the present analysis. Therein, the bolt is substituted by a pin. Unless stated otherwise, all modeling parameters are identical, e.g. temperature step, elements, mesh, friction. Composite properties are taken from Chapter 4 and modeled with Hashin as damage initiation criterion and energy-based degradation. For the metals, the yield strengths from Step 2 are used in conjuction with ideal-plasticity as material behavior in the numerical model. Comparison of the numerical bearing strength to the analytical prediction in Table 8.4 shows that the analytical prediction by ajaX is roughly within the ± 10 % of the numerically determined pin-bearing strength. It should be mentioned that the present error between analyical and numerical results is very similar to the previously determined error between analytical and experimental results in Chapter 7. By comparison to the numerical result in Step 3, the result of Step 2 is now verified and can be used for further detailed design of the joint.

To conclude, by application of the design methodology, a verified preliminary design for local metal hybridization of the reference laminate is now available. Limiting the design space, e.g. regarding metal type or MVF, with the analytical design tool is highly efficient as the computation time for each data point in Figure 8.2 and Figure 8.3 is less than 1 s. Further numerical and experimental analysis is still required in order for the present design to be validated. However, due to the analytical preliminary design the vast number of initially possible metal type variations as well as MVF variations has been significantly reduced. Therefore, the entire design process is

shortened and the extent of numerical analysis and experimental testing is cut down. In the present study, only metal type and MVF are varied. Further varying composite properties, laminate properties or the joint geometry within the limitations of ajaX suggests a high potential for reducing development time and cost.

8.2.2 Wing-Root Joint Design

Within the DLR-internal project ATLAs (Advanced Technology Long-range Aircraft Concepts), DLR's multidisciplinary design capabilities are demonstrated on a specific transportation task, whilst taking into account new technologies. Therein, the design of a mid-/long-lange aircraft is carried out in a seamless and automated manner from concept design to preliminary design to detailed design of components. A total of 13 DLR institutes participate in ATLAs. In particular, the following four objectives are pursued in the project: i) The development of an aircraft configuration integrating relevant technologies for society-compliant and competitive long-haul air transportation. ii) The identification of key technologies with suitable configurations. iii) Providing preliminary design tools for the configurations and technologies defined in the project plan. iv) Demonstrating the feasibility of preliminary design of the configurations defined in the project, with physically appropriate detailed representation of relevant technologies and disciplines.

In case of disciplinary modeling of technologies, individual conceptual design modeling is not sufficient to generate and evaluate robust results with appropriate confidence limits. Instead, the whole aircraft must always be considered to account for the interactions of the individual disciplines in the technology assessment. Thus, within ATLAs, design tools are developed, extended and connected for multidisciplinary overall aircraft design. This way, new technologies can be assessed with respect to their impact on aircraft level.

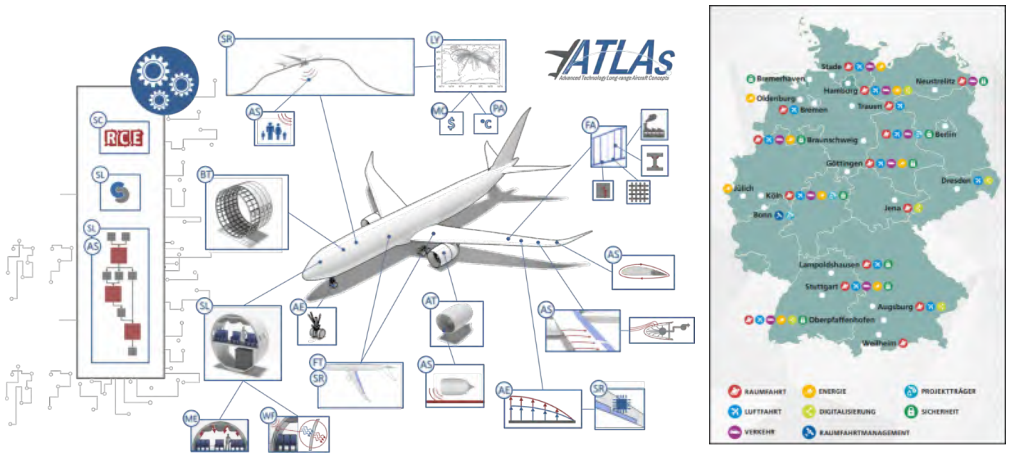

Figure 8.6 Project topics overview and participating DLR institutes

As part of the structure design branch in ATLAs, the benefits of local metal hybridization for application on the highly loaded primary joint between the center-

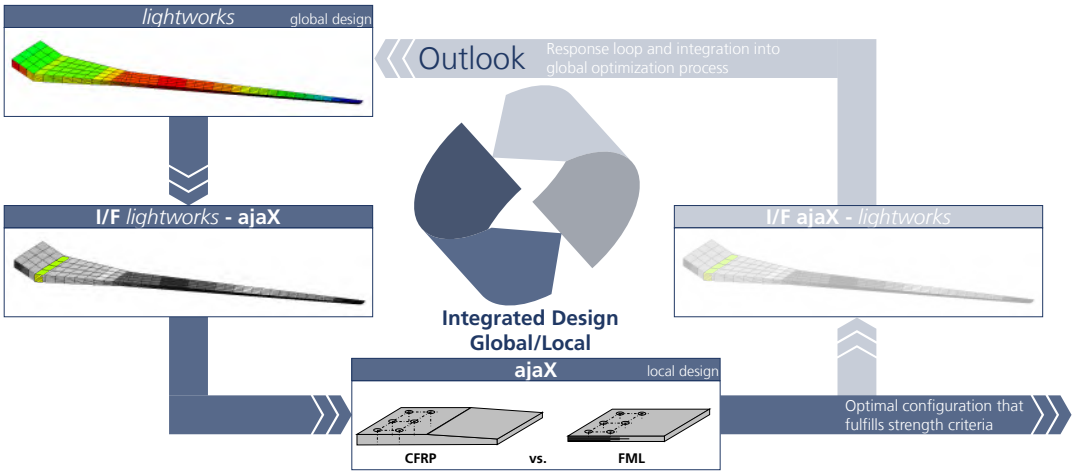

Figure 8.7 Interaction of global and local design tools

wing-box (CWB) and wing-root are investigated. In monolithic designs, the laminate build-up in the joining area resulting from low bearing strength of the basis laminate reaches far into the span-width of the wing due to manufacturing constraints, thereby affecting mass and stiffness of the entire wing. For the purpose of comparing monolithic to hybrid wing-root joint designs, an interface is created between ajaX and *lightworks* [232], see Figure 8.7. *lightworks* is a gradient-based optimization tool for composites using lamination parameters [233–235]. Therein, the laminate stiffness is defined as a linear combination of the material invariants and the lamination parameters in order to use them as continuous variables in a gradient-based optimization. In addition to failure based design criteria, e.g. maximum strain, buckling and laminate strength, also manufacturing related criteria, e.g. ply continuity and specified taper slope, are employed to derive an appropriate laminate plyshare and laminate thickness for a given wing geometry. The optimization scheme is coupled with an FE-solver (NASTRAN) for the analysis and design of a wing composed of stiffened wing covers, spars ribs and spar caps.

Currently, the design procedure consists of *lightworks* sizing the upper and lower wing-cover laminates, whereas ajaX subsequently conducts the design of the wing-root joint. During the wing-root joint analysis geometry, e.g. joining area, and laminate properties, e.g. plyshare, are rigid boundary conditions in ajaX. However, by small variations of geometric or laminate properties within *lightworks* a more overall weight efficient wing-cover design with a highly efficient CWB/wing-root joint can be achieved. Thus, in future, a design loop is to be implemented in which the output of ajaX is reused by *lightworks* in order to indentify and optimum wing-cover laminate design that takes into account the joining area.

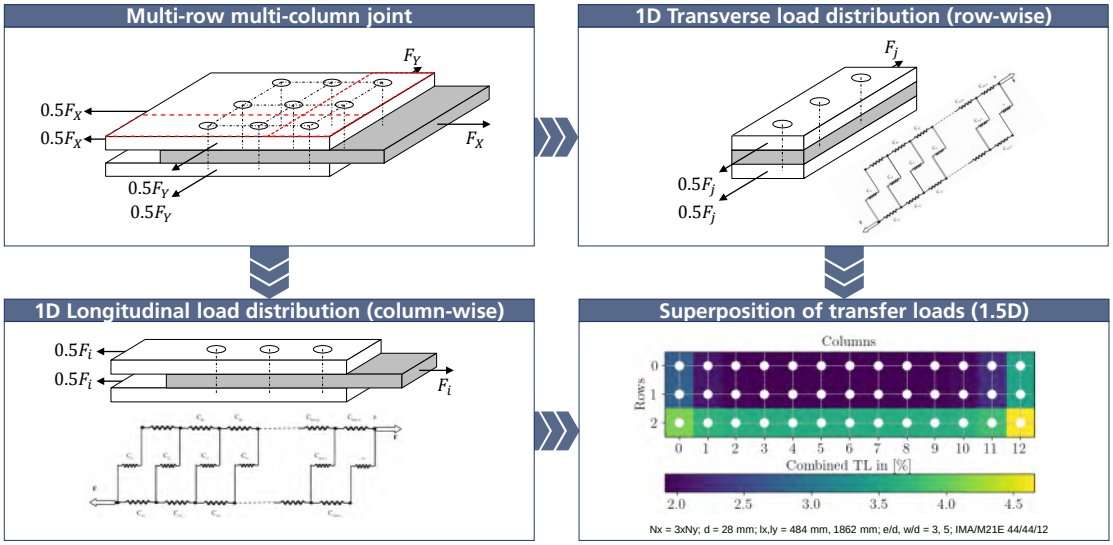

Figure 8.8 Load distribution in multiaxially loaded multi-row multi-column joint

Analysis Procedure

For the analysis of the CWB/wing-root joint, the tool *lightworks* provides geometry (maximum length and width of the joining area), material properties (stiffness, strength and ply thickness), laminate properties (plyshare and laminate thickness) as well as the loads acting on the joining area (see Table 8.3 and Table 8.4). With this data, the tool ajaX conducts a mechanical analysis of the joint as well as a weight analysis of the joining area. Data transfer between the design tools is based on JSON-format.

The analysis of the CWB/wing-root joint represents the case of a multi-row multi-column joint in Figure 8.1 and is conducted in a 3-step process. In a first step, bolt and bypass loads are derived for each fastener position of the joint based on the superposition of 1D-spring models in longitudinal and transverse direction [229]. The 1D-spring model discretizes a joint using spring elements, with pliability equivalent to the fastener flexural behavior, coupled with spring elements with a stiffness eqivalent to the stiffness of the material in between two fasteners. This way, the uneven bolt load distribution as well as the associated bypass loads are determined for each individual row. By treating each column and row individually and subsequently superponing longitudinal and transverse 1D-spring models, as shown in Figure 8.8, the bearing and bypass loads in a multi-row multi-column joint loaded in multiple directions is estimated. In the second step, the bolt and bypass loads are known for each fastener position. The analysis routine of ajaX is applied to conduct a bearing-bypass analysis and determine the failure index at each fastener position. In addition to the laminate stress and failure analysis described in Chapter 7, also shear failure of the fastener is taken into account. In the third and final step, the additional weight due to joining is determined. Therein, the additional mass of the laminate, e.g. due to either laminate build-up or hybridization, additional mass of metallic fittings as well as additional mass of the bolts is considered.

Table 8.3 Material input data

M21E/IMA						steel sheet			titanium fitting		
E_{11}	GPa	150	X_T	MPa	2610	E	GPa	190	E	GPa	117
E_{22}	GPa	8.5	X_C	MPa	1450	ν	-	0.3	ν	-	0.33
ν_{12}	-	0.35	Y_T	MPa	55	CTE	$\frac{10^{-6}}{°C}$	12.8	CTE	$\frac{10^{-6}}{°C}$	8.5
G_{12}	GPa	4.2	Y_C	MPa	285	ρ	$\frac{g}{cm^3}$	7.8	ρ	$\frac{g}{cm^3}$	4.76
CTE 1/2	$\frac{10^{-6}}{°C}$	0.15/28.7	S	MPa	105	σ_f	MPa	1982			
t_{ply}	mm	0.254	ρ	$\frac{g}{cm^3}$	1.58	t_{sheet}	mm	0.25			

The overall goal of the analysis is to assess if application of local metal hybridization to the CWB/wing-root joint is beneficial. For this purpose, the joint parameters are varied (e.g. bolt diameter, number of rows and columns, laminate thickness). Then, for each of these configurations the load distribution is determined in order to conduct a bearing-bypass analysis for quantification of the failure index. At the same time, a FML configuration is considered. Different joint configurations, in terms of bolt diameter and number of rows and columns, are analyzed for the FML joint, however, the laminate thickness is freezed to the thickness of the basis skin laminate. The failure index for the FML joint is determined in the same manner as for the monolithic CFRP joint. Subsequently to the strength analysis, all configurations with a failure index less or equal to 1 undergo a weight analysis. Therein, the additional weight that results from joining, e.g. due to fittings and fasteners, is quantified. Finally, the overall lightest configuration that can sustain the mechanical loads is selected as the analysis result. This can be either a CFRP design with or without laminate build-up, or it can be an FML design by local metal hybridization.

Analysis Input

The analysis goal is to find the lightest configuration for the connection between CWB to upper-wing-cover (UWC) and lower-wing-cover (LWC), respectively. Fur this purpose, the area that is available for joining as well as the loads acting at the wing-root are summarized in Table 8.4. Both skin laminates are made of M21E/IMA and exhibit a plyshare of 44/44/12. However, the LWC has a larger laminate thickness. The metallic fittings for connecting the CWB to the UWC/LWC are made of titanium. For hybridization of the joining area a high-strength stainless-steel is considered in order to achieve a high degree of reinforcement, see Table 8.3. Since the baseline laminate exhibits a stacking sequence that is already well suited for bearing loading, only the laminate thickness in the joining area is increased without changing the plyshare of the monolithic laminate. Ply drop-off in case of laminate build-up results in a transition area. A maximum ramp slope of 1:20 for ply drop-off is defined resulting from manufacturing constraints [235]. In case of local metal hybridization, a MVF of 40 % is applied again to achieve a high degree of reinforcement, resulting in a plyshare of 44/16/0/40. The transition region from the fully hybridized laminate in the joining area to the basis skin laminate is defined based on the design recommendations by Fink [37] and Petersen [38] in Section 8.2.1. The minimum allowable bolt distance, i.e. pitch, is set to $5d_{bolt}$ for monolithic joints and $3d_{bolt}$ for hybrid joints. The minimum

Table 8.4 Loads at wing-root and available joining area in x- (wing-span) and y-direction (wing-depth)

	Maneuver LC		Gust LC		Joining area		Laminate thickness
	X-Load	Y-Load	X-Load	Y-Load	l_x	l_y	t
	N/m	N/m	N/m	N/m	m	m	mm
UWC	-2,563,979	-135,078	-2,963,495	-241,728	0.65	3.47	12.25
LWC	2,414,719	184,871	2,909,303	223,571	0.65	3.47	20.46

edge-distance of the monolithic and hybrid joints is half the respective pitch. The bolt diameter is varied between 5 mm - 25 mm. Due to data availability the design is conducted only for room temperature conditions.

Within the project, a total of 13 loading cases are investigated. For the present analysis, two representative loading cases are selected for demonstration of the design task: A scenario with medium loading (maneuver loading case) and a scenario with high loading (gust loading case). The loads in Table 8.4 represent limit loads that are extracted from a GFEM and provide the load input to both *lightworks* and ajaX. The analysis procedure is designed to meet the following criteria:

- Design for strength of laminate at ultimate load (UL)
- Design for strength of joint
  - Laminate strength
  - Bearing failure
  - Bolt failure
- Safety factor at ultimtate load (SF=1)
- UL = 1.5 LL

The sizing in *lightworks* already accounts for laminate strength at UL. Therefore, in ajaX only the strength of the joint is analyzed. It should be noted that effects due to laminate build-up, e.g. load eccentricity and secondary bending, are not considered.

Results and Discussion

In Figure 8.9, the procedure for the design of the wing-root joint is shown. In essence, based on the input data all theoretically feasible combinations of bolt diameter, laminate thickness and number of rows and columns are analyzed using ajaX.mf. Out of all theoretically feasible combinations, those that can sustain the loads (FI$\leq$1) are further analyzed with respect to their weight in ajaX.wa. The final result is the lightest configuration that can sustain the applied loads at the wing-root.

For each of the two load cases considered, the lightest monolithic CFRP and hybrid FML configurations are presented in Table 8.5 for the connection CWB-UWC as well as CWB-LWC. The result overview contains the skin laminate thickness before and after the joint design in order to indicate the degree of laminate built-up required for the monolithic joint. Further, the total additional mass of each joint design as well as the

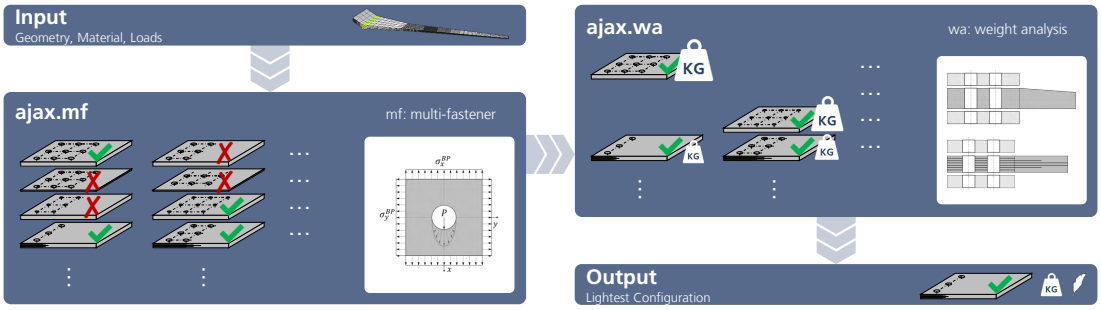

Figure 8.9 Overview of analysis procedure for the design of a wing-root joint

parameters defining the joining area, i.e. bolt diameter, number of rows and number of columns, are listed.

Considering the connection between CWB and UWC for the maneuver loading case, a monolithic design by increasing the skin laminate thickness from 12.25 mm to 15.31 mm is sufficient to transfer the loads. Compared to the hybrid design, the monolithic design is lighter. In contrast, in the gust loading case the FML design is lighter. While the monolithic design requires a laminate thickness of 23.93 mm to withstand the loads, the FML design can sustain the loads whilst maintaining the skin laminate thickness. As oppose to the maneuver loading case, now the FML design is lighter only accounting for roughly 66 % of the weight of the CFRP design. The main phenomena during the analysis process are driven by the variation of the bolt diameter. The increase in loads in the gust loading case leads to shear failure in the fasteners. Thus, compared to the maneuver loading case the bolt diameter needs to increase. However, by increasing the bolt diameter the maximum number of columns decrease due the maximum allowable pitch. Hence, also the number of fasteners in the joint decreases, and therefore the individual load per fastener increases. These counter-acting effects on the fastener shear strength are in equilibrium for bolt diameters between 19-20 mm in the present case. Nonetheless, the laminate has to withstand the bolt loads, too. Therefore, the large laminate build-up in case of the CFRP design for the gust loading case is due to both the increase in global loads as well as the decrease of fasteners available for the load transfer. The FML configuration is in advantage because of the higher bearing capacity of the laminate as well as the overall lower loads at each fastener position since the global loads are distributed over more fasteners due to the lower allowable pitch in FMLs. It should be noted, that these results represent a weight optimized solution. Hence, it is technically possible to increase the number of fasteners for the CFRP configuration in the gust loading case by increasing the number of rows. However, since the size of the metallic fittings would also increase, the decrease in laminate thickness is outweighted.

Similar observations can be made when looking at the connection between CWB and LWC in Table 8.5. In case of maneuver loading, no laminate build-up is necessary since the skin laminate is relatively thick to begin with. Thus, the CFRP configuration is significantly lighter than the hybrid counterpart. This changes when considering the gust loading case. As described for the connection CWB-UWC, the decrease in

Table 8.5 Analysis result of the monolithic CFRP and hybrid CFRP-St joint design

		Maneuver LC		Gust LC	
Joint: CWB-UWC		CFRP	FML	CFRP	FML
Skin thickness pre-design	mm	12.25	12.25	12.25	12.25
Skin thickness post-design	mm	15.31	12.25	23.93	12.25
Total additional mass	kg	**61.58**	70.52	218.87	**145.55**
Bolt diameter	mm	10	10	20	19
Number of rows (span)	-	3	3	3	3
Number of columns (depth)	-	69	114	34	59
Joint: CWB-LWC		CFRP	FML	CFRP	FML
Skin thickness pre-design	mm	20.46	20.46	20.46	20.46
Skin thickness post-design	mm	20.46	20.46	39.93	20.46
Total additional mass	kg	**74.77**	120.86	354.42	**188.88**
Bolt diameter	mm	10	10	20	13
Number of rows (span)	-	3	3	3	4
Number of columns (depth)	-	69	114	34	87
Total additional mass per wing	kg	**136.35**		**334.43**	
Additional mass w.r.t. wing-skin mass	%	1.48		3.57	

Total skin mass per wing: 9.188 kg

the total number of fasteners in the joint associated with the increase in bolt diameter leads to higher loads at each fastener position, and therefore leads to a larger laminate build-up. While increasing the number of rows is not weight-efficient for the CFRP configuration, the FML configuration benefits greatly from a 4-row design. The number of fastener in the joint increases significantly, thus the loads at each fastener position decrease. In turn, the bolt diameter can be smaller and hybridization whilst retaining the baseline skin thickness is sufficient to transfer the global loads. Adding a 4th row in the FML design is less weight-costly compared to the CFRP case, because the reduced pitch in the FML configuration also results in smaller dimensions of the fittings. While the metallic fitting of the 3-row CFRP design reaches 300 mm into span-direction, the fitting of the FML design is only 156 mm wide despite containing an additional row.

Table 8.6 shows the detailed contributions to the joint weight from the titanium fittings, the additional weight of the skin in the joining area due to either laminate build-up or hybridization, the additional weight of the skin in the transition area due to either ply drop-off or ply-substitution, as well as the additional weight from the fasteners. Regarding the more critical case of gust loads, the benefit of local metal hybridization mainly comes from the laminate periphery. While the FML skin laminate is heavier in both joining area and transition area, the weight advantage compared to the CFRP design mainly results from significantly smaller and therefore lighter

Table 8.6 Additional mass at wing-root due to joining

		Maneuver LC		Gust LC	
Joint: CWB-UWC		CFRP	FML	CFRP	FML
Total additional mass	kg	61.58	70.52	218.87	145.55
Fittings	kg	46.87	28.78	146.52	54.74
Skin in joining area	kg	2.83	14.71	23.41	28.00
Skin in transition area	kg	0.52	9.56	7.57	9.56
Fasteners	kg	11.36	17.46	41.38	53.25
Joint: CWB-LWC		CFRP	FML	CFRP	FML
Total additional mass	kg	74.77	120.86	354.42	188.88
Fittings	kg	62.63	48.08	244.72	78.97
Skin in joining area	kg	-0.53	24.57	39.09	40.30
Skin in transition area	kg	0.00	27.26	21.11	27.26
Fasteners	kg	12.68	20.95	49.50	42.35

fittings. This characteristic is also observed by Fink [37] at the example of the inter-segment joints in the Ariane 5 booster.

As the gust loading case is dimensioning, the FML design exhibits the lightest configuration for both the CWB-UWC and CWB-LWC joint. Therein, the additional weight due to joining amounts to a total of 334 kg, of which around 146 kg are contributed by the connection of the UWC and 189 kg by the connection of the LWC. Compared to the monolithic design, weight savings of around 33 % and 47 % can be achieved for the connection of the UWC and LWC, respectively. In relation to the total skin mass of a wing, the FML joints between UWC/LWC and the CWB contribute an additional 3.6 %, which is significantly lower than 573 kg or 6.2 % in case of the monolithic joint design.

Up until now, the discussion on the multi-fastener joint analysis was focused on an more overall view. At the example of Figure 8.10, a more detailed analysis is done in order to better illustrate the mechanical advantages of hybridization in a mutli-fastener joint as well as the effect of thermal residual stresses. The figure shows the bearing-bypass interaction behavior of the CFRP and FML joints in both on-axis and off-axis direction for the standard geometry according to AITM 1-0009. The increase in bearing strength by hybridization of a monolithic joint parallel to the loading direction (on-axis) is demonstrated in Chapter 5 and frequently shown in literature [11, 37, 38]. In Figure 8.10a the increase in the on-axis bearing capacity in combination with bypass loading is confirmed based on the analytical design tool ajaX. However, an additional benefit of metal hybridization of mechanically fastened CFRP joints can be seen at the example of Figure 8.10b. While the bearing strength of the CFRP joint in off-axis direction decreases significantly ($\approx$ 330 MPa), the bearing strength of the FML joint remains at a relatively high level ($\approx$ 850 MPa). The drastic decrease in bearing strength of the CFRP joint in transverse direction (off-axis) is due to the fact that the 44/44/12 stack-

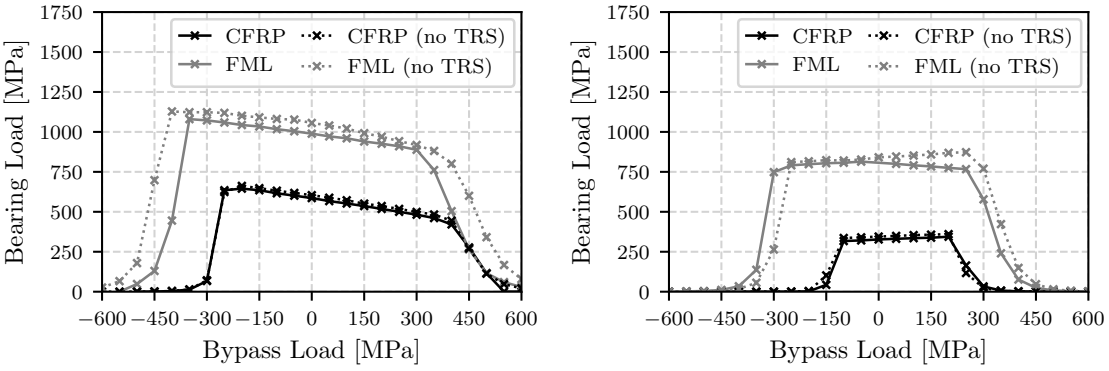

(a) Bearing-bypass interaction (on-axis) **(b)** Bearing-bypass interaction (off-axis)

Figure 8.10 Bearing-bypass interaction in CFRP (44/44/12) and FML ($44/16/0/40_{St}$) pin-bearing joint based on ajaX (geometry according to AITM 1-0009)

ing is effectively transformed into a 12/44/44 stacking, when the loading direction is turned by 90°. In highly loaded multi-fastener joints with transverse loading, this characteristic of CFRP joints can represent a major drawback. In the FML joint, however, substitution of 90° plies by steel ($44/44/12 \rightarrow 44/16/0/40_{St}$) not only improves the on-axis properties but also leads to a significant improvement of the off-axis behavior due to the isotropic behavior of metals.

Considering the effect of thermal residual stresses, observations from the previous sections are confirmed in Figure 8.10. Inclusion of thermal effects hardly affect the analysis of monolithic CFRP joints. In the FML joints, neglecting thermal effects alters both the on-axis and off-axis bearing-bypass interaction curves. The bearing cut-off line (horizontal region of high bearing strength) is shifted towards higher stresses for the on-axis as well as off-axis case. Considering on-axis loading, the drop in bearing strength of the FML joint due to bypass interaction in both the tensile and compressive regime are delayed towards higher bypass stresses. In the off-axis direction, the entire bearing-bypass interaction curve of the FML appears to be shifted toward the right side of the abscissa. For a vast portion of the curves, including thermal residual stresses in the analysis process results in a more conservative strength prediction. The error from neglecting thermal effects in the FML along the bearing cut-off line is up to 7 % and 14 % for on-axis and off-axis cases, respectively. In the areas where the bearing strength drops due to high bypass loads, the error becomes increasingly high. Similarly to the case of a single-fastener joint from the previous section, the effect of thermal residual stresses on the bearing strength predictions is in the same order of magnitude as the accuracy of the analysis tool itself. For the present case of a multi-fastener joint analysis, inclusion of thermal effects is yet recommended because the results are more conservative when taking into account thermal residual stresses in the FML (see Figure 8.10). However, especially when conducting studies that focus on the general feasibility of design concepts rather than absolute accuracy, neglecting thermal effects might be justified to facilitate the analysis process. Nonetheless, with ajaX a tool is available to estimate the impact of thermal effects in order to make such choices.

In conclusion, by the present analysis two goals are achieved. First of all, the extensions of ajaX to estimate the strength and weight of multi-fastener joints exhibit an additional capability in the overall aircraft design process. Herein, a preliminary design of detailed aspects, i.e. the wing-root joint, can be conducted and included for example into the life cycle assessment of an aircraft. Furthermore, the capability to analyze multi-fastener joints is used to assess the benefits of local metal hybridization for application on the wing-root joint. By comparison of CFRP to FML designs, the weight saving potential of local metal hybridization is demonstrated. More detailed analysis also reveals the individual contributions to the overall weight saving. Considering the computation time, analysis of one multi-row multi-column configuration takes between 9 s to 26 s depending on the number of fasteners in a joint. In total, 1040 configurations composed of 13 loading cases, two skin laminates, 20 bolt diameters (5 mm - 25 mm) for the CFRP and FML designs are considered. This does not take into account the reccuring analysis when the laminate thickness is increased for a CFRP design. Overall, around 3120 configurations are analyzed in less than 22 h accumulated computation time. The analytical design methodology allows for fast variation of a multitude of design parameters, thereby enabling comprehensive global studies as demonstated in the present section or reducing the design space by preliminary design as shown in the previous section.

8.3 Summary and Conclusions

The development and validation of the analytical joint analysis tool ajaX is conducted in Chapter 7. In the present chapter, the application of ajaX for local metal hybridization is demonstrated at the example of a uniaxially loaded single-fastener joint and a biaxially loaded multi-fastener joint. Thereby, an insight on how to approach the design of a locally hybridized composite joint is given. Furthermore, the capabilities of ajaX as well as the impact of thermal residual stresses on the design of hybrid joints are discussed.

The analysis of a single-fastener joint shows in detail how to approach the local metal hybridization of a monolithic CFRP joint. The methodology consists of preselecting metal type and MVF using UD-0°-CFRP FMLs. Based on the pre-selection, distinct laminate stackings and MVF are analyzed in order to define the local metal reinforcement in detail. Using ajaX in conjunction with this approach for preliminary design allows to reduce the vast number of initially possible solutions, e.g. with respect to metal type and MVF, for the subsequent detailed design stages based on numerical simulation and experimental testing. Thereby, the design process is shortened, which can lead to significant savings in development time and cost.

The analysis of the wing-root joint demonstrates the potential of ajaX regarding larger design studies when extended by a module for determining the load transfer in multi-fastener joints and a module for weight analysis. The design of a wing-root joint based on weight-efficiency is conducted. Further, by considering both monolithic and hybrid laminates, the benefits of local metal hybridization of the wing-root joint are demonstrated. Additionally, by conducting bearing-bypass analyses a more profound understanding of the reinforcement effect by hybridization in multi-fastner joints is

built. Similar to the single-fastener case, the design of a multi-fastener joint represents a preliminary design that is capable of accounting for material, geometry as well as thermal effects. However, further numerical simulation and experimental testing is required for detailing and validating the design. Nonetheless, by application of ajaX a significant portion of studies can be conducted in a more time- and cost-effective way.

On the question if thermal residual stresses need to be considered in the design of hybrid joints, the present analysis puts the observations from the previous chapters into perspective. By direct comparison of experimental, numerical and analytical data in the previous chapters, it is concluded that inclusion of thermal residual stresses improves the prediction accuracy of the analytical design process. This statement is still considered valid. However, for the example cases in the present chapter, neglecting thermal residual stresses in the design of the hybrid joints only leads to an error of $\approx$10 %. Thus, the error from neglecting thermal effects is roughly on the same order of magnitude as the tool accuracy itself. When conducting studies where only general tendencies are of interest, one could legitimately argue that the effect of thermal residual stresses can be neglected. However, if preliminary design with the objective of subsequent detailed design is conducted, it is strongly recommened to include thermal effects into the analysis process. As the observations in the previous chapters show, consideration of thermal residual stresses noticeably improves the tool accuracy.

Chapter 9

Conclusions and Outlook

9.1 Summary of Chapter Contents

The contents of each chapter contribute to a comprehensive exploration of the peculiarities of local metal hybridization in composite bolted joints at low temperature.

Chapter 1 serves as an introduction, providing an overview and establishing the thematic context of a specific class of FMLs, notably CFRP-steel FML, in the broad field of hybrid laminates. In Chapter 2, the theoretical foundation for dealing with thermal residual stresses is provided, covering the scales on which thermal residual stresses occur, analytical stress and strength prediction based on CLT, as well as a discussion on important factors to be considered, e.g. relaxation effects and the stress-free temperature. Application of an analytical 2D yield strength prediction model for FMLs demonstrates that, contrary to monolithic laminates, CFRP-steel FMLs exhibit significant intra- and interlaminar thermal residual stresses on ply level, which can ultimately reduce the laminate strength.

Within Chapter 3, a comprehensive literature study is presented focusing on the bolt-bearing behavior of hybridized bolted joints, with particular emphasis on CFRP-steel/titanium FMLs, as well as the impact of low temperatures. Based on the findings within Chapter 2 and Chapter 3, the *Research Hypothesis* and *Working Hypotheses* of the present thesis are formulated together with a strategy outlining how these hypotheses are to be addressed. In an effort to provide the necessary input data for the analytical and numerical tools of the thesis, Chapter 4 details the material characterization process. This step ensures a solid foundation regarding intra- and interlaminar material properties for subsequent investigations. For the determination of interlaminar properties, an existing methodology for the correction of the fracture toughness for thermal effects is extended in order to be applicable to hybrid specimens. Chapter 5 is dedicated to an experimental investigation of CFRP-steel bolt-bearing joints. The strength increase by hybridization is demonstrated for a variety of stackings, metal contents and joint geometries. Also, damage progression is analyzed in detail using ultrasound scanning and optical microscopy. This chapter provides a comprehensive characterization of the behavior of CFRP-steel bolted joints at low temperature, which has not been reported in literature before. At the same time, the experimental results serve as a basis for validating numerical and analytical tools.

Moving into the realm of computational analysis, Chapter 6 describes the development of a numerical analysis tool tailored to the detailed design of hybrid bolted joints. This tool enables precise simulations and evaluations in the context of strength prediction, progressive damage analysis and virtual parameter determination. In Chapter 7, a purely analytical tool is developed for preliminary design of CFRP-steel FML joints. The novelty of the tool consists in its applicability to FML joints by inclusion of thermal effects and failure for both composite and metallic material. Furthermore, the tool is purely analytical as oppose to semi-analytical and numerical tools, which results in lower computation times as well as less input data required for analysis. The analytical tool for preliminary design complements the numerical tool for detailed design of bolted joints, and allows for fast analysis of design parameters whilst only requireing in-plane stiffness and strength data. The potential of the tool is demonstrated in the framework of a design methodology for locally metal hybridized bolted joints in Chapter 8.

9.2 Conclusions on Research Hypothesis

As the hypotheses of the present thesis are explored across multiple chapters, the main findings regarding each hypothesis are summarized in a concise way in order to validate the *Research Hypothesis* of the present thesis:

> *The benefits of local metal hybridization of highly loaded mechanically fastened joints in composite structures, proven at room temperature, extend to low temperature despite increasing thermal residual stresses in the FML, and engineering tools are capable to capture this behavior for the purpose of joint design.*

A total of four *Working Hypotheses* are formulated in order to answer the initially raised question regarding the reinforcement effect in CFRP-steel bolted joints.

> *Working Hypothesis I: Altering interlaminar properties of a hybridized laminate at low temperature do not lead to a decrease in delamination strength of the FML.*

This hypothesis deals with the delamination strength of hybrid interfaces at low temperature. In general, literature on this topic is scarce. Due to high interlaminar stresses in FMLs, hybrid interfaces could exhibit lower delamination resistance compared to monolithic interfaces [39]. By nature, hybrid interfaces are dissimilar resulting in asymmetric specimens for characterizing the interlaminar behavior, e.g. in the DCB and ENF test setup. As a result of the asymmetry, parasitic effects are acting on the interface leading to thermal contributions to the fracture toughness values determined during testing. A framework for correcting apparent fracture toughness values from interlaminar testing is proposed in Chapter 4.2, and verified and validated using numerical and experimental data in Chapter 6.1. Thereby, true fracture toughness values for hybrid interfaces that are corrected for parasitic effects are generated. This allows for an accurate comparison of monolithic interfaces, not affected by thermal residual stresses, and hybrid interfaces, affeced by thermal residual stresses

and therefore corrected. Comparing the fracture toughness values in Chapter 4.2 confirms *Working Hypothesis I* by demonstrating comparable delamination resistance of monolithic and hybrid interfaces.

> *Working Hypothesis II: Despite increasing thermal residual stresses, metal hybridized laminates exhibit an absolute bearing strength at low temperature superior to monolithic laminates.*

For room temperature conditions, the increase in bearing strength by local metal hybridization of composite bolted joints is proven [10, 11, 38]. However, the analysis in Chapter 2, regarding the effect of increasing levels of thermal residual stresses on the laminate strength of CFRP-steel FMLs with decreasing temperature, raises the question whether the favorable reinforcement effect by steel hybridization extends to low temperature conditions. Since there is no literature on this topic for CFRP-steel FMLs, extensive experimental bolt-bearing testing is conducted in Chapter 5. Overall, the load bearing capacity by steel hybridization is significantly increased through steel hybridization also at low temperature conditions. This observation is valid for a range of varying degrees of laminate orthotropy, metal content, temperature levels as well as joint geometries, thus confirming *Working Hypothesis II*. However, the reinforcement effect in terms of percentage strength increase of the bearing yield strength by steel hybridization is less pronounced at low temperature (37-66 %) compared to room temperature (45-79 %). Further numerical analysis in Chapter 6.2 shows that thermal residual stresses affect the stress state, thereby limiting the maximum reinforcement effect with decreasing temperature. In addition to the analysis of thermal residual stresses, a comprehensive analysis of stiffness, strength, damage propagation, and virtual definition of design values is conducted, adding on to a more comprehensive understanding for designing hybridized bolted joints by including thermal effects.

> *Working Hypothesis III: Consideration of both thermal residual stresses and temperature dependent material properties is necessary for accurate numerical modeling of FMLs at low temperature.*

This working hypothesis addresses the necessity of not only including temperature dependent material properties but also thermal residual stresses into the numerical analysis process. While application of temperature dependent material properties is generally agreed upon for low temperature simulation, inclusion of thermal effects is often omitted [28, 140, 141]. During experimental testing, thermal residual stresses are present intrinsically due to the manufacturing process and different CTE and stiffness of steel and composite plies. In general, the presence of thermal residual stresses is not visible to the human eye, except for example in cases where an asymmetric layup is present, resulting in a thermally induced deformation. However, consideration of thermal residual stresses by inclusion of a temperature step during numerical analysis is crucial. This is demonstrated in great detail at the example of DCB and ENF testing of CFRP-steel interfaces, where only application of a temperature step in conjunction with the correct material properties yields good agreement between experiment and simulation. Inclusion of thermal effects is equally important for bolt-bearing modeling of CFRP-steel FMLs, as the prediction quality of the numerical tool is improved by inclusion of thermal residual stresses. By quantifying the impact of thermal residual

stresses on the strength prediction of bolted joints and comparing it to the impact on the simulation if, for instance, the choice of elements (2D/3D) or material strength input is varied, it is demonstrated that inclusion of thermal residual stresses is relevant and necessary. Simply applying material properties at a given temperature level is not sufficent for accurate modeling. These findings support *Working Hypothesis III*. However, for the purpose of providing rough estimates, the error resulting from neglecting thermal residual stresses might be accepable depending on the application at hand.

> *Working Hypothesis IV: Consideration of both thermal residual stresses and temperature dependent material properties is necessary for accurate analytical modeling of FMLs at low temperature.*

As inclusion of thermal residual stresses has proven to be necessary for the design of CFRP-steel FML joints, this working hypothesis deals with finding an appropriate approach for incorporating thermal residual stresses into an analytical design tool. For this purpose, a purely analytical design tool for preliminary design is developed from scratch. As the intralaminar thermal residual stresses influencing the bearing behavior act on ply level, the analytical tool is designed to conduct a strength prediction for a bolted joint on ply level, too. Thus, stresses due to the bolt, stresses due to bypass loads and thermal residual stresses are determined in order to be superimposed on ply level. Subsequently, failure analysis based on the characteristic curve method is conducted on the superimposed stress distribution, thereby accounting for thermal residual stresses in FML joints. Validation of the tool based on pin- and bolt-bearing test results at room and low temperature proves that inclusion of thermal residual stresses significantly improves the prediction accuracy of the analysis tool for CFRP-steel FML joints, while monolithic laminates are hardly affected at all by inclusion of thermal residual stresses, thereby confirming *Working Hypothesis IV*. Compared to alternative tools, the present tool excels through its high computational efficiency, reduced amount of required input data, and its applicability to hybrid laminates.

In summary, this thesis provides evidence for the advantages of steel hybridization in highly loaded joints, even at low temperatures, thereby extending existing literature findings and supporting the introduction of CFRP-steel FMLs into practical applications. In the process of investigating the research questions, two engineering tools have been developed: a numerical tool for detailed design and a purely analytical tool for preliminary design. By including thermal effects, both are specifically tailored to the peculiarities of CFRP-steel FMLs. With hybridization offering new design possibilities through variations in metal type, metal content, and laminate stacking, a methodology for conducting hybridization of monolithic composite joints is proposed in Chapter 8 to facilitate and streamline the design process. The potential of the analytical tool is demonstrated through two example cases: a generic single-bolt joint and a wing-root joint analysis, showcasing its ability to reduce the design space. Furthermore, a numerical analysis tool developed in Chapter 6.2 provides a capable engineering tool for detailed analysis of CFRP-steel joints. The numerical tool can be used for building an in-depth understanding on the material behavior as well as virtual testing purposes in order to reduce the need for physical testing. Examples for application cases are presented in Chapter 6. Through this thesis, a case is made for the application of local

metal hybridization, accompanied by the development of practical engineering tools for both preliminary and detailed design of such joints.

9.3 Outlook on Future Research

The outlook is divided into two parts. Firstly, recommendations for future research concerning the methodologies developed within the thesis are proposed. These recommendations aim to guide and inspire further investigation in the field. Secondly, suggestions are provided to address the essential requirements for further advancing the technology of local metal hybridization on a broader scale.

Characterization of interlaminar behavior of hybrid interfaces is challenging. Several obstacles result from the inherent asymmetry of dissimilar interfaces in accurately determining the fracture toughness. To address this, a methodology based on existing literature methods has been proposed. However, to enhance flexibility in accommodating various laminate stackings, the method by Gao et al. [192], which currently allows only a bi-material system with layers of identical orientation for the first material and one ply of the second material at the midplane, should be expanded. Extension of this method, e.g. based on CLT, would significantly improve the accuracy of the method. This would allow the characterization of not only dissimilar interfaces but also multi-directional interfaces. With the added flexibility in laminate stacking, further research on stacking sequences with reduced thermal residual stresses is possible, particularly in achieving more balanced laminates within the sub-laminates of DCB and ENF specimens whilst maintaining dissimilar interfaces at the midplane.

An efficient numerical model for bolt-bearing analysis has been developed, providing good accuracy at acceptable computation time. However, when modeling damage, 2D material models generally exhibit some limitations regarding the 3D nature of bolt-bearing loading, especially in the vicinity of the bolt. To overcome these limitations and enhance the simulation of damage progression, the application of a fully 3D material model based on state of the art concepts, e.g. such as Cuntze FMC in Appendix C.1, is recommended. Furthermore, delamination is a significant factor during damage progression. However, incorporating delamination effects into the current model leads to less accurate strength predictions. Hence, a comprehensive analysis of various modeling strategies should be conducted, e.g. by comparison of continuum shell and solid element based modeling in conjuction with cohesive elements for mesoscale progressive damage analysis as done in Völkerink et al. [236]. Such a study could provide specific recommendations based on the desired balance between accurate strength prediction and consideration of damage mechanisms, as well as computational efficiency.

The analytical tool for preliminary design of joints shows promising potential. However, further validation is necessary, specifically concerning pure bypass, combined bearing-bypass, and biaxial loading scenarios. These validations are crucial to demonstrate the tool's suitability across a range of practical applications and different loading conditions. A pragmatic approach for including thermal residual stresses into the analysis process based on CLT is implemented. However, for a more precise esti-

mation of thermal residual stresses, particularly near the center hole, it is suggested to integrate analytical solutions [219, 237, 238] based on complex functions, similar to those employed for determining stresses induced by bearing and bypass loads. This enhancement has the potential to improve the accuracy of the analytical design tool by more reliable predictions of thermal residual stresses. Apart from the methods employed for determining stresses in the laminate, the choice of methods for failure analysis is crucial for the accuracy of the design tool. Thus, in addition to the methods explored during the development of the analytical design tool, it is important to investigate alternative approaches for determining characteristic distances and alternative failure criteria in an attempt to improve the tool accuracy.

By providing engineering methods to deal with the fact that thermal residual stresses influence the material behavior, one of the more pressing concerns from industry is addressed. In particular, the analytical tool for preliminary design allows to assess the joint behavior, considering numerous influential parameters. This enables to understand and analyze hybrid joints in order to decide if application to a specific problem is beneficial, all without the need for prior practical experience with local metal hybridization. Nonetheless, following recommendations are considered to contribute to further paving the way of local metal hybridization as a technology for industrial applications on a broader scale:

Material selection, optimization and standardization: Despite numerous contributions in the field of local metal hybridization of bolted joints covering a wide range of design methodologies, guidelines and case studies, the task of designing a locally hybridized joint remains cumbersome and complex. An alternative approach to utilizing design tools, such as ajaX, is to provide standardized hybrid laminate solutions, similar to the approach taken for GLARE. This goes somewhat against the principle of local metal hybridization and undermines one of the core advantages, which is the flexibility and customizability of hybridization to specific needs, e.g. by adjsutment of metal type, metal volume content and metal sheet positioning. However, this approach offers standardized hybrid laminates which are optimized for their mechanical properties, weight, cost-effectiveness, and compatibility with composites by taking into account factors such as corrosion resistance, fatigue life, and environmental effects. This limitation in the design space facilitates easier comparison across publications and streamlines the design process. A practical starting point could involve employing common aviation stackings, such as 25/50/25, 50/40/10, or similar combinations. Should this measure encourage broader application of the technology, the experience and credibility gained in the process will lay the foundation for its future expansion.

Structural analysis, modeling and life cycle assessment: Local metal hybridization is a meso-scale measure aimed at enhancing the macro-scale structural behavior of components. Generally, state-of-the-art FEA is considered advanced enough to capture the structural behavior. Especially, since progressive damage analysis is rarely conducted, but rather linear-elastic models with geometrical non-linearity are used for the design of parts, which is subsequently validated through physical testing. However, to gain a better understanding and demonstrate the advantages of local metal hybridization, a multi-scale approach is necessary. By coupling local design considerations with global

design, e.g. such as the design of wing covers and wing-root joints, globally optimized solutions that incorporate local aspects can be developed. This integrated approach enables a more comprehensive assessment of the benefits associated with local metal hybridization. Additionally, utilizing life cycle assessment tools to evaluate the overall aircraft performance, including fuel savings resulting from direct and indirect weight reduction through local metal hybridization, can shift the discussion from a simple comparison of stiffness and strength benefits versus manufacturing effort and cost, to a broader perspective on overall aircraft level.

Manufacturing, process optimization and inspection: To be considered a viable technology for industrial application, the manufacturing of locally metal hybridized structures needs to be compatible with established manufacturing processes such as automated tape laying and fiber placement processes. In space applications, a certain degree of manual layup may be viable, but the aviation industry requires a more automated process involving the handling of metal sheets. However, for complex structures pre-curving the thin metal sheets might be necessary, which can be time-consuming and costly. Whereas, in wind-turbine applications, where thicker steel sheets can be utilized for reinforcement at the blade-root bolted joint, care must be taking in regard to compatibility with infusion processes. Another critical aspect to consider is the scalability of the metal surface treatment process, as it significantly contributes to the overall cost of local metal hybridization. While automating and industrializing abrasive and chemical surface pre-treatment processes are considered feasible, the cutting and deburring of steel plies pose challenges to avoid introducing delamination onset points. One critical aspect in advancing the technology of local metal hybridization in highly loaded composite joints is the development NDI techniques that can accurately assess integrity and detect potential damage. This becomes particularly challenging when dealing with dissimilar materials and complex composite-metal interfaces. The task becomes even more demanding when thick laminates, high metal content, and a large number of metallic plies are involved. The effective application of NDI in such cases remains an open question. However, there is potential for progress through the adaptation and improvement of ultrasonic scanning methods.

Appendices

Appendix A

Evaluation of Standards

Many test methods are available for characterizing the mechanical properties of composite materials. This section offers a brief overview on current test methods used to establish design allowables for a given material system. It will be shown that the choice of test method can significantly affect the resulting material properties. Thus, differences between standards should be taken into account when chosing the appropriate test method.

A.1 Tensile properties

Commonly used standards for determining the in-plane tensile properties of composite materials are presented in Table A.1. In their essence the methods are very similar: uniaxial tensile load is introduced at the ends of a prismatic specimen that is gripped in the test fixture. The standards are used to determine ultimate tensile strength, strain at failure, modulus and Poisson's ration. Out of the standards considered, ASTM D3039 offers the most rigorous guidance. In addition to specifying specimen geometry, test setup and procedure, and data evaluation the standard also specifies valid failure types and proposes a method to assess the degree of bending in a specimen during testing. DIN EN ISO 527 is very similar to ASTM D3039, whearas the remaining standards can be considered less detailed. While the proposed specimen and tab lengths may vary moderatly between standards, guidelines for specimen thickness and width are almost identical. In general, the differences with respect to specimen geometry, load introduction, and testing speed can be expected to have a negligible influence on the resulting properties as long as the guidelines are properly followed. However, when considering the evaluation of the data for calculating the tensile modulus, the choice of standard greatly affects the outcome. The procedure to determine the tensile modulus can be divided into strain based (ASTM D3039 and ISO 527) and load based approaches (DIN EN 2561/2597 and AITM 1-0007). While the former approach specifies a rigid interval for calculating the tensile modulus, the latter approach adjusts the interval based on the material strength. Figure A.1 indicates how the choice of standard affects the calculation of modulus for a given material system depending on the material stiffness and strength. At the example of a UD-90° specimen made of M21/T700GC, it can be seen that the intervals for determining the transverse tensile modulus in Figure A.1b are very close for the standards presented here. Considering the UD-0° specimen in Figure A.1a, however, reveals a significant

Table A.1 Selection of common standards for determining in-plane tensile properties of composite materials

Standard	Orientation	Rec. no. specimen	Testing speed mm/min	Interval of modulus calculation
ASTM D3039	0°, 90°	min. 5	2	1000 - 3000 μm/m
DIN EN ISO 527	0°, 90°	min. 5	2, 1	500 - 2500 μm/m
DIN EN 2561	0°	min. 5	n.a.	10 - 50 % F_{ult}
DIN EN 2597	90°	min. 10	0.5	10 - 50 % F_{ult}
AITM 1-0007	0°, 90°	min. 6	2	10 - 50 % F_{ult}

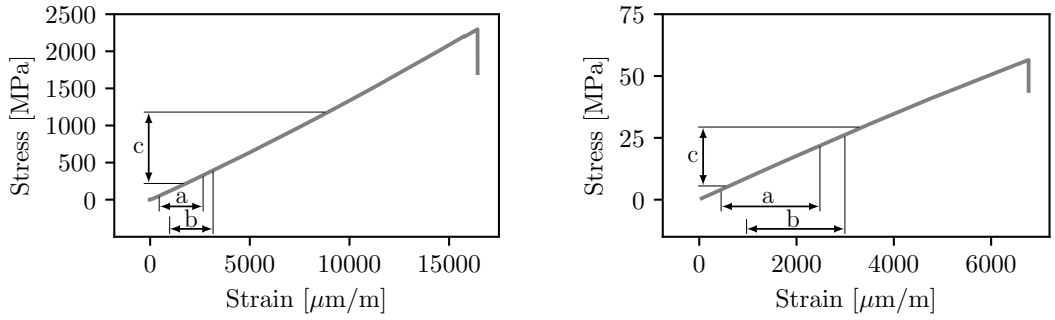

(a) UD-0° specimen

(b) UD-90° specimen

Figure A.1 Intervals of longitudinal and transverse moduli calculation for composites according to different standards (a: DIN EN ISO 527; b: ASTM D3039; c: AITM 1-0007, DIN EN 2561/2597)

difference. While the strain-based concepts determine the material modulus at the very beginning of the curve, the load-based approach covers a much greater range for calculating the modulus. In case of Figure A.1a, the strain-based approach results in a smaller modulus by around 6% (122 vs. 129 GPa). Thus, depending on the material system at hand the choice of standard greatly affects the determination of modulus, which should be taken into account when defining a test matrix for material characterization, and equally when employing these properties in numerical or analytical models.

A.2 Compressive properties

Table A.2 shows a selection of common standards for determining in-plane compressive properties of composites. Several test fixture types have been proposed in order to introduce a uniform state of uniaxial compressive stress and minimize stress concentration and bending in the specimen test section. The fixture types can be broadly classified into three groups: i) fixtures that introduce load into the test section of a specimen by pure shear at the grip area, ii) fixtures that introduce load into the test section of the specimen by compression at the end of the specimen (end-loading), and iii) fixtures that introduce load into the specimen by a combination of shear and

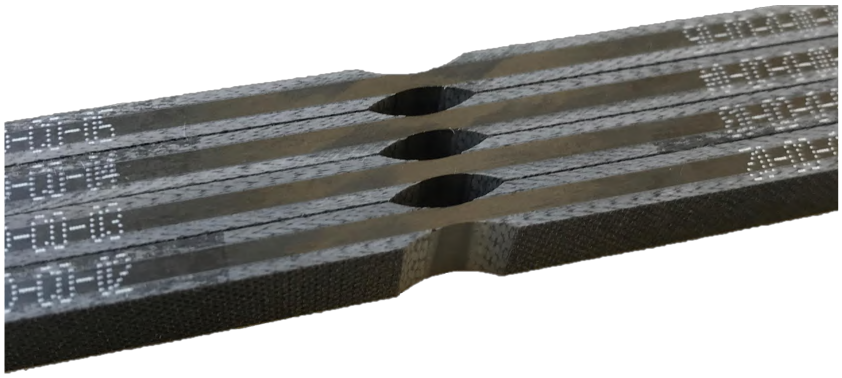

Figure A.2 Compressive specimens with tapering of the gauge region

compression. Due to their favorable load introduction aspects fixtures with combined loading are recommended by most standards. Since bending in the test section is critical, all standards propose monitoring of the degree of bending through strain gauges on both specimen surfaces. While DIN EN ISO 14126 only allows for 5 % bending, the remaining standards accept bending of up to 10 %. With respect to testing speed all standards offer very similar guidelines as the recommened testing speeds range between 1 - 1.5 mm/min. As discussed at the example of longitudinal and transverse moduli in Figure A.1, the choice of standards affects the determination of the compressive moduli. Longitudinal and transverse compressive tests[1] on M21/T700GC show that the strain based approach yields around 5 % larger values for the longitudinal compressive modulus (111 vs. 106 GPa) and 7 % smaller values for the transverse compressive modulus (9.15 vs. 8.59 GPa). In this case both longitudinal and transverse moduli are affected by the choice of method. When considering the determination of material compressive strength, both test fixture and specimen geometry influence the ultimate load at failure. Depending on the type of loading the degree of restraint of the specimen is altered, thus, influencing the material strength. Therein, the compressive strength tends to increase with the degree of restraint. With respect to specimen geometry larger gauge lengths as proposed by AITM 1-0008 (22 x 22 mm) tend to produce smaller compressive strengths. The difference in compressive strength, however, can generally be attributed to invalid failure types, e.g. buckling, that are more likely to occur in larger specimens as a comparative assessment of European and U.S. standards comissioned by the FAA has shown [239]. Experimental and numerical studies by Petersen [89] indicate that the use of tabs as recommended in many standards introduces a stress concentration at the transition of the gauge area. Compressive strengths determined using specimens with tabs resulted in artificially low strength values by around 15 %. Tapering the specimens in the gauge area (Figure A.2) leads to a more smooth stress distribution and produces more accurate compressive strength values. Tapered specimens, however, are no longer suitable for determinig the material compressive modulus. Compared to determining tensile properties of composites, compressive testing is more delicate and requires diligence when choosing the appropriate means for material characterization.

[1]Experimental tests are conducted according to DIN EN ISO 14126 using combined load introduction through a HCCF setup (Hydraulic Composite Compression Fixture), while the calculation of moduli is altered for comparing different calculation methods.

Table A.2 Selection of common standards for determining in-plane compressive properties of composite materials

Standard	Load introduction	Recommended orientation	Interval of modulus calculation
ASTM D695 [1)]	compression	0°, 90°	entire linear region
ASTM D3410	shear	0°, 90°	1000 - 3000 μm/m
ASTM D6640	combined	0°, 90° [2)]	1000 - 3000 μm/m
DIN EN ISO 14126	shear, compression or combined	0°, 90°	500 - 2500 μm/m
EN 2850	compression, combined	0°	10 - 50 % F_{ult}
AITM 1-0008	shear, combined	quasi-isotropic [3)]	10 - 50 % F_{ult}

[1)] only valid for composites with moduli < 41 GPa
[2)] not valid for strength determination of UD composites
[3)] UD specimens possible

A.3 Shear properties

Determination of the shear properties of composites is considered to be one of the most challenging areas of mechanical property testing. None of the currently available standardized methods to determine in-plane shear properties is free of deficiencies or limitations. Especially when determining the shear strength effects such like edge effects, material coupling effects, nonlinear behavior of the matrix, and imperfect stress distributions render the correct definition of the material shear strength very difficult [240]. The most commonly used standards for determining in-plane shear properties are presented in Table A.3 and can be broadly divided into three setups: $\pm 45°$ tension, V-notch specimens, and shear frame.

A number of standards are based on the tensile test (e.g. ASTM D3039) and simply alter the laminate layup to a $[\pm 45°]_{ns}$ configuration in order to produce a shear stress state. Thus, specimen preparation and testing procedure can be considered rather simple. Differences is specimen geometry between the standards is very small and the recommended number of specimens to be tested is between 5-6. The testing speed recommended by DIN 65466 appears to result in rather high strain rates compared to the other standards, in particular when considering the proposed specimen width of only 16 mm which is at the lower end of specimen widths proposed in standards. While the interval for determining the shear modulus is very similar for this test setup, the definition of the shear strength varies. This is due to the fact that strength determination by the $\pm 45°$ tesile test setup exhibits some limitations. Due to the extension of the specimen in loading direction, fiber scissoring occurs and alters the fiber orientation progressively with increasing strain at large deformations. The calculation of shear strength, however, is based on the assumption that the fiber orientation does not change, thus, resulting in errornous stregth values when considering the ultimate load at rupture as is done for instance in EN 6031, DIN 65466, and AITM 1-0002. A more accurate approach is offered in ASTM D3518 and ISO 14129 where the lower value of either shear stress at 5 % shear strain or the load at rupture, in case the specimen fails before reaching 5 % shear strain, is regarded as the material shear strength. Despite the

Table A.3 Selection of common standards for determining in-plane shear properties of composite materials

Standard	Setup	Speed mm/min	Interval of modulus calc.	Definition of strength
ASTM D3518	$\pm 45°$ tension	2	2000 - 6000 $\mu\gamma$	lower of F_{ult} or 5 % shear strain
DIN EN ISO 14129	$\pm 45°$ tension	2	1000 - 5000 $\mu\gamma$	5 % shear strain
EN 6031	$\pm 45°$ tension	1	900 - 4500 $\mu\gamma$	F_{ult}
DIN 65466	$\pm 45°$ tension	6	10 - 50 % F_{ult} 900 - 4500 $\mu\gamma$	F_{ult}
AITM 1-0002	$\pm 45°$ tension	1	900 - 4500 $\mu\gamma$	F_{ult}
ASTM D5379	V-notched beam	2	1500 - 2500 $\mu\gamma$	lower of F_{ult} or 5 % shear strain
ASTM D7078	V-notched rail shear	2	1500 - 2500 $\mu\gamma$	lower of F_{ult} or 5 % shear strain
DIN EN ISO 20337	shear frame	4	1000 - 5000 $\mu\gamma$	lower of F_{ult} or 20 % shear strain

shortcomings of the test setup, it is widely assumed that this setup matches the actual stress state and ply interaction within a structural laminate more accurately than other methods and therefore may be preferred by the designer [240]. An experimental study by Petersen [89] comparing different test setups for determining shear properties of UD composite materials supports this view by showing that methods based on the $\pm 45°$ tensile test yield very accurate results if the material strength is evaluated at 5 % shear strain. The second type of setup in Table A.3 consists of V-notched specimens in a rigid fixture (ASTM D5379) or a flexible shear rail (ASTM D7078). In this setup, a flat rectangular specimen with two symmetrical V-notches at its center is tested in a special fixture (see Figure A.3a and Figure A.3b). Due to the V-notch, the shear stress distribution in the smallest cross section is quite uniform, thus, allowing for very accurate strength measurements. Interpretation of failure based on the stress-strain history, however, is not straightforward and requires experience with the test method. While determining the material strength yield very accurate results, numerical and experimental analysis of the test setup have shown that the strain measurement exhibit significant deviations of 10 - 20 %. The two standards based on V-notched specimens differ in that ASTM D7078 requires larger specimens, thus allowing for coarser fabric material to be tested, and that the rail setup introduces pure shear loads into the specimen, thus improving the uniformity of the shear stress state.

The shear frame method in DIN EN ISO 20337 allows for the characterization of shear properties for both linear and non-linear deformation including large deformations greater than 5 % which represents the upper limit of applicability of the previously mentioned standards. A large quadratic specimen (165 x 165 mm) with corner cut-outs is clamped inside a flexible shear frame. Since no free edges exist, there is no

(a) Fixture for ASTM D5379 by *Instron*

(b) Fixture for ASTM D5379 by *Instron*

(c) Fixture for DIN EN ISO 20337 [89]

Figure A.3 Fixtures for determining in-plane shear properties of composite materials

load redistribution that could influence the test results. The determination of strength using this setup is considered very accurate but requires experience since effects of premature inter-fiber failure have to be accounted for during interpretation of the test results. The shear frame setup is considered a rather accurate method, however, application of this standard involves extensive efforts for the sample preparation and high accuracy requirements during test installation. Experimental testing at DLR [89] has shown the shear strength of M21/T700GC to vary only marginally with respect to different experimental determination methods. In fact, results for the shear strength vary by less than 5 % when comparing the preferred method for shear strength determination ASTM D5973, also known as the Iosipescu test setup, and the approach recommended by DIN EN ISO 14129, defining the shear strength to be 78 MPa and 75 MPa, respectively. Due to less complexity in both specimen preparation and testing, the $\pm 45^{\circ}$ tensile test according to either DIN EN ISO 14129 or ASTM D5973 is recommended for determination of both in-plane stiffness and strength of composites.

Appendix B

Material Characterization

B.1 Force-displacement Curves of Material Tests with Steel

Figure B.1 shows the stress-strain relations for the in-plane test results of steel with a nominal sheet thickness of 0.13 mm 1.4310 at 23°C (RT) and -55°C (LT).

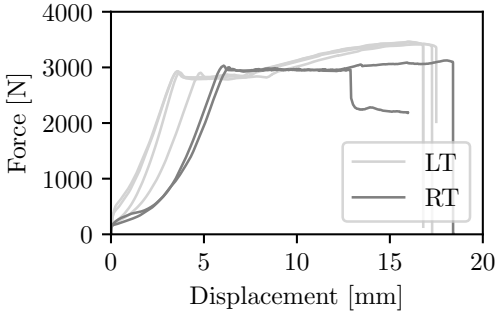

(a) Force-displacement curves

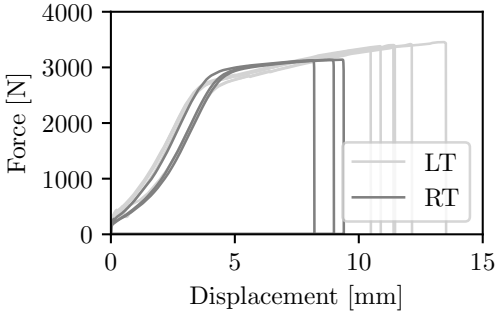

(b) Force-displacement curves

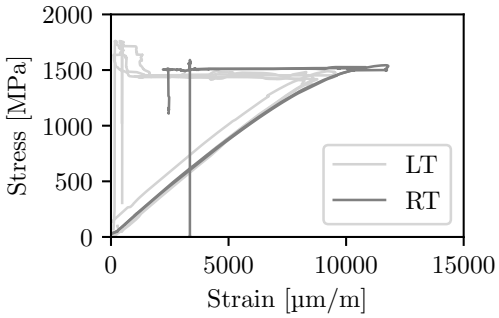

(c) Stress-strain curves

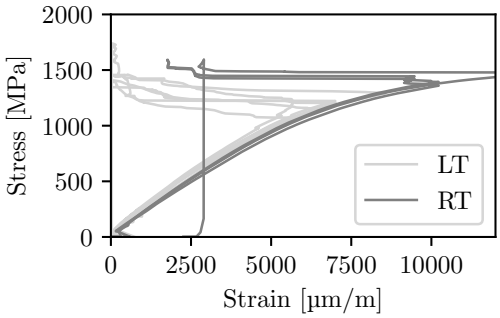

(d) Stress-strain curves

Figure B.1 Load-displacement curves of steel (1.4310) test campaign at 23°C (RT) and -55°C (LT)

B.2 Force-displacement Curves of Material Tests with CFRP

Figure B.2 shows the stress-strain relations for the in-plane test results of M21/T700GC with a cured ply thickness of 0.13 mm at 23°C (RT) and -55°C (LT).

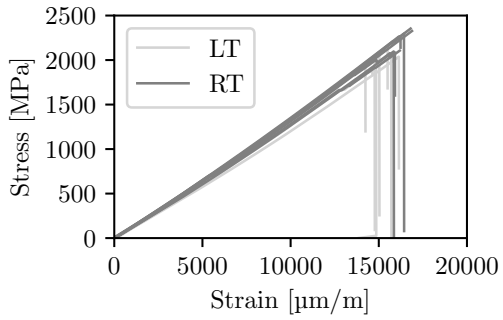

(a) Longitudinal tensile test (E_{11}^t, R_1^t)

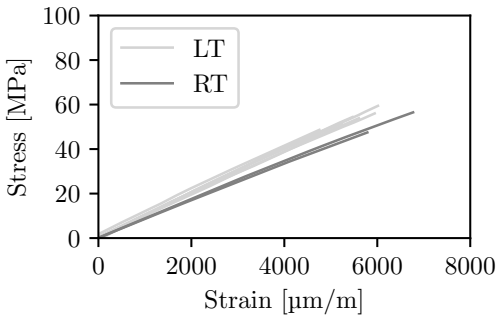

(b) Transverse tensile test (E_{22}^t, R_2^t)

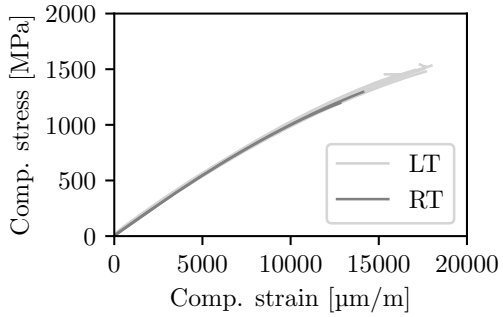

(c) Longitudinal compressive test (E_{11}^c)

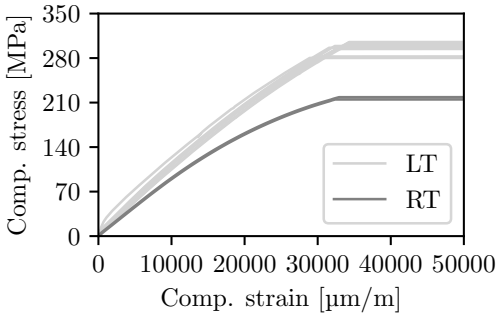

(d) Transverse compressive test (E_{22}^c, R_2^c)

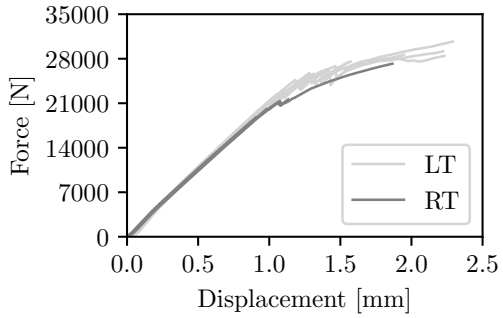

(e) Longitudinal compression test with tapered specimen (R_1^c)

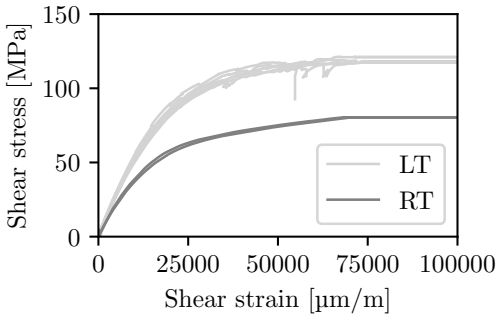

(f) In-plane shear test (G_{12}, R_{12})

Figure B.2 Load-displacement curves of M21/T700GC test campaign at 23°C (RT) and -55°C (LT)

B.3 Correction of Energy Release Rate for Thermal Residual Stresses

The present formulation for correction of energy release rates in the DCB and ENF test setup is based on the correction method proposed by Yokozeki [45]. The presence of thermal residual stresses can hinder or favor crack growth during the static crack propagation test. In the present test setup and with the present specimen stacking, crack growth during the DCB test is favored. As a result, the true energy release rate is lower than the apparent energy release rate. In case of ENF testing, the position of the metal foil is crucial. Since the loading case is defined by a directional bending load case. Depending on whether the steel foil is on the top or the bottom leg of the specimen, thermal residual stresses either favor or hinder crack growth. In the present case, the steel foil is positioned on the bottom leg, therefore, the true mode II fracture toughness is larger than the apparent fracture toughness without correction for thermal effects.

Based on Nairn's [44] general formulation, the mechanical response of linear-elastic materials subjected to combined mechanical and thermal loads can be expressed through superposition of both temperature dependent and mechanical loads. For a generally multi-layered beam consisting of the sublaminates 1 and 2 seperated by the initial crack and an intact portion (sublaminate 3), the following constitutive relations hold:

$$\begin{bmatrix} N^{(k)} \\ M^{(k)} \end{bmatrix} = \begin{bmatrix} A_{11}^{(k)} & B_{11}^{(k)} \\ B_{11}^{(k)} & D_{11}^{(k)} \end{bmatrix} \begin{bmatrix} \varepsilon_0^{(k)} \\ \kappa^{(k)} \end{bmatrix} - \begin{bmatrix} N_T^{(k)} \\ M_T^{(k)} \end{bmatrix} \Delta T \tag{B.1}$$

where

$$\begin{aligned} A_{11}^{(k)} &= b \sum_i E_i^{(k)} (z_i^{(k)} - z_{i-1}^{(k)}), \\ B_{11}^{(k)} &= \frac{1}{2} b \sum_i E_i^{(k)} (z_i^{(k)2} - z_{i-1}^{(k)2}), \\ D_{11}^{(k)} &= \frac{1}{3} b \sum_i E_i^{(k)} (z_i^{(k)3} - z_{i-1}^{(k)3}), \\ N_T^{(k)} &= b \sum_i E_i^{(k)} \alpha_i^{(k)} (z_i^{(k)} - z_{i-1}^{(k)}), \\ M_T^{(k)} &= b \frac{1}{2} \sum_i E_i^{(k)} \alpha_i^{(k)} (z_i^{(k)2} - z_{i-1}^{(k)2}), \end{aligned} \tag{B.2}$$

and

$$\begin{aligned} C_k^{(k)} &= \frac{A_{11}^{(k)}}{A_{11}^{(k)} D_{11}^{(k)} - B_{11}^{(k)2}}, \qquad C_\varepsilon^{(k)} = \frac{D_{11}^{(k)}}{A_{11}^{(k)} D_{11}^{(k)} - B_{11}^{(k)2}}, \\ D^{(k)} &= \frac{-B_{11}^{(k)}}{A_{11}^{(k)} D_{11}^{(k)} - B_{11}^{(k)2}}, \\ \alpha_\varepsilon^{(k)} &= \frac{D_{11}^{(k)} N_T^{(k)} - B_{11}^{(k)} M_T^{(k)}}{A_{11}^{(k)} D_{11}^{(k)} - B_{11}^{(k)2}}, \quad \alpha_k^{(k)} = \frac{A_{11}^{(k)} M_T^{(k)} - B_{11}^{(k)} N_T^{(k)}}{A_{11}^{(k)} D_{11}^{(k)} - B_{11}^{(k)2}} \end{aligned} \tag{B.3}$$

Therein, $N^{(k)}$ and $M^{(k)}$ represent the resultant axial force and bending moment, $E^{(k)}$ is the longitudinal Young's modulus and $\alpha^{(k)}$ the CTE in longitudinal direction. The coordinate $z^{(k)}$ defines the position from the center plane of the sublaminate (k) and B the specimen width. The general solution for energy release rate in a cracked laminate with residual stresses results to:

$$\begin{aligned} G = \frac{1}{2B}(&C_k^{(1)}M^{(1)2} + C_k^{(2)}M^{(2)2} - C_k^{(3)}M^{(3)2} + C_\varepsilon^{(1)}N^{(1)2}C_\varepsilon^{(2)}N^{(2)2} - C_\varepsilon^{(3)}N^{(3)2} \\ &+ 2D^{(1)}M^{(1)}N^{(1)} + 2D^{(2)}M^{(2)}N^{(2)} - 2D^{(3)}M^{(3)}N^{(3)}) \\ &+ \frac{\Delta T}{2B}(\alpha_k^{(1)}M^{(1)} + \alpha_k^{(2)}M^{(2)} - \alpha_k^{(3)}M^{(3)} + \alpha_\varepsilon^{(1)}N^{(1)} + \alpha_\varepsilon^{(2)}N^{(2)} - \alpha_\varepsilon^{(3)}N^{(3)}) \\ &+ \frac{\Delta T^2}{2B}(I^{(1)} + I^{(2)} - I^{(3)}) \end{aligned} \tag{B.4}$$

with

$$I^{(k)} = N_T^{(k)}\alpha_\varepsilon^{(k)} + M_T^{(k)}\alpha^{(k)2} - b\sum_i E_i^{(k)}\alpha_i^{(k)}t_i^{(k)}. \tag{B.5}$$

The equations for correcting the apparent energy release rate resulting from evaluation of the experimental load-displacement data in mode I or mode II $G_{I/II}^{exp}$ for the portion of energy release rate due to thermal effects $G_{I/II}^{th}$ yield the true energy release rates are:

$$G_{Ic} = G_{Ic}^{exp} + \underbrace{\frac{P_{max}\Delta T}{b}(\alpha_\kappa^{(1)} - \alpha_\kappa^{(2)})a + \frac{\Delta T^2}{2b}(I^{(1)} + I^{(2)} - I^{(3)})}_{G_I^{th}} \tag{B.6}$$

$$G_{IIc} = G_{IIc}^{exp} + \underbrace{\frac{P_{max}\Delta T}{b}(\alpha_\kappa^{(2)} - \alpha_\kappa^{(3)})a + \frac{\Delta T^2}{2b}(I^{(1)} + I^{(2)} - I^{(3)})}_{G_{II}^{th}} \tag{B.7}$$

When considering CFRP-steel FMLs, the correction method by Yokozeki et al. [45] contains one simplification that is incompatible with the DCB test setup of hybrid laminates. Therein, it is explicitly said that contact between the cracked arms is neglected. However, especially in case of CFRP-steel FMLs, the contact force reach a magnitude that needs to be considered. In Figure 6.6 in Chapter 6.1, an example of an adhesive specimen in DCB configuration is presented. Therein, the missmatch in CTE between adhesive and adherend results in tensile thermal residual stresses in the adhesive. The two debonded arms touch each other at the tips, which in turn leads to contact forces. Guo et al. [112] have introduced a correction method to account for the additional deformation within the debonded region due to the existance of contact forces. The total ERR is obtained by superposition of the strain energies, which is why the portion of ERR at the crack tip $G_{I,tip}$ is added onto the ERR correction terms by Yokozeki et al. [45]. The specimen configuration in Figure 6.6 from Chapter 6.1 can be translated to the case of the CFRP-steel FML investigated in the present research. Thus, by replacing the properties of the adhesive layer with properties of steel, the correction method is transferred to hybrid laminates.

The equations for the correction for tip forces from Guo at al. [112] present an approach for determining the strain energy release rate associated with this phenomenon in DCB test specimens:

$$G_{I,tip}^{th} = -\frac{EI + E_a I_a}{2\rho^2 B}\left[1 + 4\frac{EI + E_a I_a}{(h+t)^2 B}\left(\frac{1}{Et} + \frac{1}{E_a h}\right)\right] + \frac{(\Delta\alpha\Delta T)^2}{1/E_a h + 1/Et} - \frac{3E}{8\rho^2 B}\frac{II_c}{I + I_c} \tag{B.8}$$

with

$$I = \frac{Bt^3}{12} \qquad I_a = \frac{Bh^3}{12} \qquad I_c = \frac{B(t+h)^3}{12} \tag{B.9}$$

and

$$\frac{1}{\rho} = \frac{6\Delta\alpha\Delta T(1+m)^2}{(h+t)(3(1+m)^2 + (1+mn)(m^2 + 1/mn))} \tag{B.10}$$

and
$m = h/t$ and $n = E_a/E$.

While the correction method excluding tip forces has been applied repeatedly on adhesive joints with dissimilar adherents [114,115] as well as CFRP-steel FMLs [11,38, 39], the consideration of tip forces is new for asymmetric CFRP-steel laminates.

B.4 Results of Interlaminar Material Testing

In Table B.1, the results of the experimental tests in the DCB setup at 23°C (RT) and -55°C (LT) are summarized. Apparent energy release rates in mode I are presented for the data reduction procedures from ASTM D5528 including the area method based on beam theory (BT), modified beam theory (MBT), compliance calibration (CC) and modified complience calibration (MCC) method.

In Table B.2, the results of the experimental tests in the ENF setup at 23°C (RT) and -55°C (LT) are summarized. Apparent energy release rates in mode II are presented for the data reduction procedure from ASTM D7905, the compliance calibration (CC) method.

Table B.1 Apparent mode I critical energy release rates G_{Ic}^{exp} of monolithic and hybrid interfaces at different temperatures based on ASTM D5528

			G_{Ic}^{exp} at 23 °C				G_{Ic}^{exp} at -55 °C			
			BT	MBT	CC	MCC	BT	MBT	CC	MCC
00//00	Mean	N/mm	0.368	0.293	0.311	0.290	0.438	0.290	0.322	0.295
	Std. Dev.	N/mm	0.021	0.016	0.017	0.015	0.059	0.038	0.034	0.037
	C.o.V.	%	5.71	5.41	5.50	5.53	13.45	13.17	10.16	12.51
	n	-	4				6			
00//45	Mean	N/mm	0.474	0.363	0.384	0.387	0.525	0.351	0.387	0.351
	Std. Dev.	N/mm	0.041	0.026	0.029	0.036	0.046	0.037	0.038	0.039
	C.o.V.	%	8.57	7.08	7.48	9.36	8.69	10.57	9.83	11.06
	n	-	4				6			
00//90	Mean	N/mm	0.714	0.570	0.598	0.561	0.717	0.541	0.585	0.544
	Std. Dev.	N/mm	0.077	0.063	0.067	0.061	0.086	0.062	0.060	0.053
	C.o.V.	%	10.80	11.03	11.16	10.83	11.99	11.46	10.18	9.78
	n	-	4				6			
St//00	Mean	N/mm	0.414	0.358	0.374	0.367	0.384	0.357	0.400	0.409
	Std. Dev.	N/mm	0.053	0.041	0.044	0.041	0.027	0.027	0.029	0.032
	C.o.V.	%	12.9	11.4	11.7	11.1	7.03	7.65	7.27	7.92
	n	-	6				4			
St//45	Mean	N/mm	0.677	0.522	0.551	0.514	0.628	0.497	0.524	0.489
	Std. Dev.	N/mm	0.045	0.039	0.039	0.037	0.019	0.043	0.024	0.038
	C.o.V.	%	6.63	7.52	6.99	7.12	2.99	8.71	4.54	7.69
	n	-	5				5			
St//90	Mean	N/mm	0.441	0.352	0.371	0.351	0.502	0.421	0.436	0.413
	Std. Dev.	N/mm	0.017	0.014	0.013	0.010	0.043	0.044	0.039	0.037
	C.o.V.	%	3.83	4.00	3.63	2.96	8.48	10.4	9.01	8.91
	n	-	5				5			

Table B.2 Apparent mode II critical energy release rates G_{IIc}^{exp} of monolithic and hybrid interfaces at different temperatures based on ASTM D7905

			00//00	00//45	00//90	St//00	St//45	St//90
G_{IIc}^{exp} at -55 °C	Mean	N/mm	2.506	3.022	2.182	1.808	2.049	1.806
	Std. Dev.	N/mm	0.133	0.291	0.118	0.264	0.088	0.126
	C.o.V.	%	5.30	9.62	5.39	14.6	7.97	6.96
	n	-	6	6	6	4	5	5
G_{IIc}^{exp} at 23 °C	Mean	N/mm	2.402	2.916	2.226	1.707	1.897	2.114
	Std. Dev.	N/mm	0.094	0.090	0.115	0.197	0.136	0.075
	C.o.V.	%	6.93	3.08	5.18	11.5	7.16	3.56
	n	-	3	3	3	4	5	5

Appendix C

Numerical Methods

C.1 Implementation of Cuntze Failure Mode Concept

C.1.1 Material Model for Composites

The material model initially intended for simulating the composite behavior was developed at DLR by Völkerink [241] and is validated for thermoset and thermoplast materials based on OHT testing. User-defined subroutines are available in 2D and 3D formulation for both the explicit and implicit solver in Abaqus.

Constitutive Model

The continuum damage mechanics model is comprised of a linear-elastic region, followed by damage initiation and damage progression. During damage analysis, it is assumed that the effective area available for load transfer A_{eff} decreases compared to the undamaged area A_0. Based on this assumption, the nominal stress $\sigma = P/A_0$ is substituted by the effective stress $\tilde{\sigma} = P/A_{eff}$. The lamina damage tensor $\boldsymbol{M}(d)$ establishes a relationship between nominal and effective stresses:

$$\tilde{\sigma} = \boldsymbol{M}(d) \cdot \sigma \tag{C.1}$$

with

$$\boldsymbol{M}(d) = \text{diag}\left[\frac{1}{1-d_f}; \frac{1}{1-d_m}; \frac{1}{1-d_m}; \frac{1}{1-d_s}; \frac{1}{1-d_s}; \frac{1}{1-d_m};\right] \tag{C.2}$$

The damage variables d_f, d_m and d_s are associated with fiber failure and matrix failure due to transverse as well as shear loading. The scalars take values between 0 (undamaged) and 1 (completely damaged). In addition, the damage variables d_f and d_m differentiate damage from tensile and compressive stresses. The smeared damage variables read:

$$d_f = d_{ft} + d_{fc} - d_{ft} \cdot d_{fc} \tag{C.3}$$

$$d_m = d_{mt} + d_{mc} - d_{mt} \cdot d_{mc} \tag{C.4}$$

The constitutive material law, establishing a relationship between stresses and strains in case of effective and nominal stress tensor for the orthotropic continuum damage mechanics model read:

$$\tilde{\sigma} = \boldsymbol{C_0} \cdot \varepsilon^e; \qquad \sigma = \boldsymbol{M}(d)^{-1} \cdot \boldsymbol{C_0} \cdot \varepsilon^e \tag{C.5}$$

$$\begin{bmatrix} \sigma_{11} \\ \sigma_{22} \\ \sigma_{33} \\ \tau_{12} \\ \tau_{13} \\ \tau_{23} \end{bmatrix} = \begin{bmatrix} C_{1111} & C_{1122} & C_{1133} & 0 & 0 & 0 \\ & C_{2222} & C_{2233} & 0 & 0 & 0 \\ & & C_{3333} & 0 & 0 & 0 \\ & & & C_{1212} & 0 & 0 \\ & sym. & & & C_{1313} & 0 \\ & & & & & C_{2323} \end{bmatrix} \begin{bmatrix} \varepsilon^e_{11} \\ \varepsilon^e_{22} \\ \varepsilon^e_{33} \\ \gamma^e_{12} \\ \gamma^e_{13} \\ \gamma^e_{23} \end{bmatrix} \tag{C.6}$$

The individual components of $\boldsymbol{C_0}$ are defined as follows:

$$C_{1111} = E_{11}(1 - \nu_{23}\nu_{32})\Gamma \tag{C.7}$$
$$C_{2222} = E_{22}(1 - \nu_{13}\nu_{31})\Gamma \tag{C.8}$$
$$C_{3333} = E_{33}(1 - \nu_{12}\nu_{21})\Gamma \tag{C.9}$$
$$C_{1122} = E_{11}(\nu_{21} - \nu_{31}\nu_{23})\Gamma = E_{22}(\nu_{12} - \nu_{32}\nu_{13})\Gamma \tag{C.10}$$
$$C_{1133} = E_{11}(\nu_{31} - \nu_{21}\nu_{32})\Gamma = E_{33}(\nu_{13} - \nu_{12}\nu_{23})\Gamma \tag{C.11}$$
$$C_{2233} = E_{22}(\nu_{32} - \nu_{12}\nu_{31})\Gamma = E_{33}(\nu_{23} - \nu_{21}\nu_{13})\Gamma \tag{C.12}$$
$$C_{1212} = G_{12} \tag{C.13}$$
$$C_{1313} = G_{13} \tag{C.14}$$
$$C_{2323} = G_{23} \tag{C.15}$$

with

$$\Gamma = \frac{1}{1 - \nu_{12}\nu_{21} - \nu_{23}\nu_{32} - \nu_{13}\nu_{31} - 2\nu_{21}\nu_{32}\nu_{13}} \tag{C.16}$$

Damage Initiation and Propagation

Prediction of discrete damage on ply level is based on the Cuntze failure mode concept (FMC) [91] in Figure C.1. This failure theory is interactive, phenomenological and 3D stress-based. The main idea consists in seperating failure modes. Thus, each failure mechanism is associated with only one material strength and is assigned one individual stressing effort Eff. In total, five failure modes are considered. Two fiber failure (FF) modes for failure in tension (FF1) and compression (FF2) as well as three inter fiber failure (IFF) modes due to loading in tension (IFF1), compression (IFF2) and shear (IFF3) are distinguished.

The damage initiation condition for the individual failure modes are defined as follows:

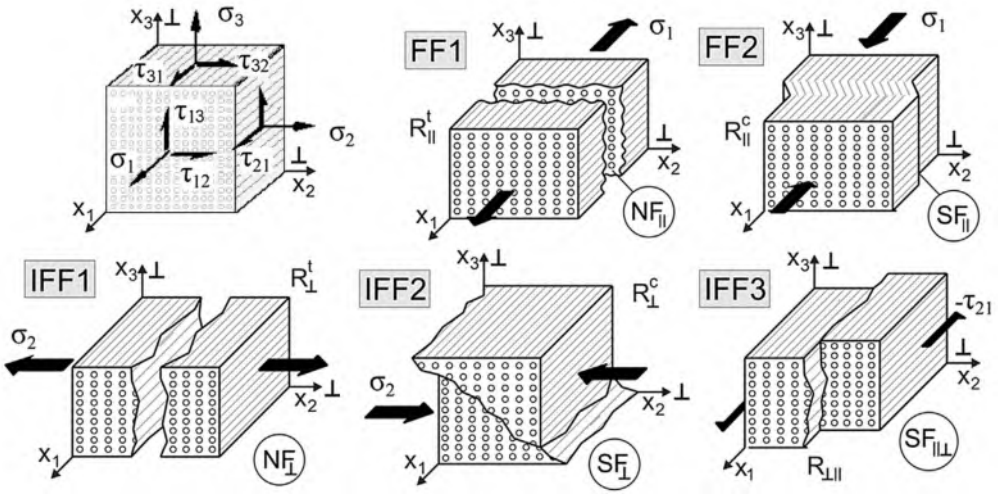

Figure C.1 Failure modes in transversely-isotropic materials according to Cuntze [91]

$$FF1: \; Eff^{\parallel\sigma} = \sigma_{eq}^{\parallel\sigma} / R_{\parallel}^{t} \quad \text{with} \quad \sigma_{eq}^{\parallel\sigma} = \sigma_1 \tag{C.17}$$

$$FF2: \; Eff^{\parallel\tau} = \sigma_{eq}^{\parallel\tau} / R_{\parallel}^{c} \quad \text{with} \quad \sigma_{eq}^{\parallel\tau} = \sigma_1 \tag{C.18}$$

$$IFF1: \; Eff^{\perp\sigma} = \sigma_{eq}^{\perp\sigma} / R_{\perp}^{t} \tag{C.19}$$

$$\text{with} \quad \sigma_{eq}^{\perp\sigma} = \left[(\sigma_2 + \sigma_3) \sqrt{(\sigma_2 + \sigma_3)^2 + 4\tau_{23}^2} \right]$$

$$IFF2: \; Eff^{\perp\tau} = \sigma_{eq}^{\perp\tau} / R_{\perp}^{c} \tag{C.20}$$

$$\text{with} \quad \sigma_{eq}^{\perp\sigma} = \left[(b_{\perp\perp} - 1)(\sigma_2 + \sigma_3) + b_{\perp\perp} \sqrt{(\sigma_2 + \sigma_3)^2 + 4\tau_{23}^2} \right]$$

$$IFF3: \; Eff^{\perp\parallel} = \sigma_{eq}^{\perp\parallel} / R_{\perp\parallel} \tag{C.21}$$

$$\text{with} \quad \sigma_{eq}^{\perp\parallel} / R_{\perp\parallel} = \left(\left[\sqrt{b_{\perp\parallel}^2 \cdot I_{23-5}^2 + 4R_{\perp\parallel}^2 (\tau_{13}^2 + \tau_{12}^2)^2} + b_{\perp\parallel} \cdot I_{23-5} \right] / 2R_{\perp\parallel}^3 \right)^{1/2}$$

$$\text{and} \quad I_{23-5} = 2\sigma_2\tau_{12}^2 + 2\sigma_3\tau_{13}^2 + 4\tau_{23}\tau_{13}\tau_{12}$$

The parameters of the Cuntze FMC for M21/T700GC ($b_{\perp\parallel}$=0.44, $b_{\perp\perp}$=1.266 and m=2.6) are adopted from Petersen et al. [91]. The stressing efforts of the individual failure modes are then combined to the global stressing effort Eff^m using the interaction coefficient m:

$$Eff^m = \left(\frac{\sigma_{eq}^{\parallel\sigma}}{R_{\parallel}^{t}} \right)^m + \left(\frac{\sigma_{eq}^{\parallel\tau}}{R_{\parallel}^{c}} \right)^m + \left(\frac{\sigma_{eq}^{\perp\sigma}}{R_{\perp}^{t}} \right)^m + \left(\frac{\sigma_{eq}^{\perp\tau}}{R_{\perp}^{c}} \right)^m + \left(\frac{\sigma_{eq}^{\perp\parallel}}{R_{\perp\parallel}} \right)^m \tag{C.22}$$

Once the global material stressing effort Eff^m reaches the value 1 at an integration point, further loading leads to degradation of the material stiffness. In a first step, the stiffness associated with the highest single effort failure mode is degraded. If further individual effort modes reach a values of 1, then the corresponding stiffnesses are

Table C.1 Damage variables associated with failure modes and fracture toughness

Failure mode	FF1	FF2	IFF1	IFF2	IFF3
Damage variable	d_{ft}	d_{fc}	d_{mt}	d_{mc}	d_s
Fracture toughness	$G_{ft} = G_{1+}$	$G_{fc} = G_{1-}$	$G_{mt} = G_{2+}$	$G_{mc} = G_{2-}$	$G_s = G_6$

degraded, too. The association of failure modes and damage variables is presented in Table C.1.

Damage evolution and displacement controlled. In order to correctly reflect the dissipated energy in the fracture process zone, the crack band approach (CBA) is employed. Therein, the dissipated energy per unit volume g_M is regularized using the intralaminar fracture toughness G_M in the respective mode M and the characteristic length of the element L_c:

$$g_M = \frac{G_M}{L_c} \quad \text{with} \quad M \in \{ft, fc, mt, mc, s\} \tag{C.23}$$

Calculation of the damage variable is done as follows:

$$d_M = \frac{\delta^f_{M,eq}(\delta_{M,eq} - \delta^0_{M,eq})}{\delta_{M,eq}(\delta^f_{M,eq} - \delta^0_{M,eq})} \quad \text{with} \quad \delta^0_{M,eq} \leq \delta_{M,eq} \leq \delta^f_{M,eq} \tag{C.24}$$

With the initiation of damage being described by the equivalent strain $\delta^0_{M,eq}$:

$$\delta^0_{M,eq} = \frac{\varepsilon^0_M}{L_c} \tag{C.25}$$

The equivalent strain at failure corresponding to $d_M = 1$ results in:

$$\delta^f_{M,eq} = \frac{2G_M}{\sigma^0_M L_c} \tag{C.26}$$

Since the stresses and strains at damage initiation (σ^0_M and ε^0_M) are not known a priori, the values are saved in the material subroutine once damage occurs. Also, as damage in the IFF modes can be caused by multiple stress components, degradation is driven by the component with the highest stress. Further details on the material model can be found in the dissertation of Völkerink [241].

C.1.2 Validation of Material Model

The material model was previously applied for modeling bonded joints and OHT specimens. Both loading scenarios, characterized by predominantly tensile loading, show very good agreement with experimental data. In contrast, bearing loading exhibits predominantly compressive loading cases. In order to verify the material model, a one-element model from Völkerink [241] is used to compare damage based on Hashin as implemented in Abaqus and the material model by Völkerink in Figure C.2. The one-element model consists of a shell element with an element edge length of 1 mm. A detailed description of the model is available in Völkerink [241]. The behavior between both material models is almost identical. The deviation in the evolution of the

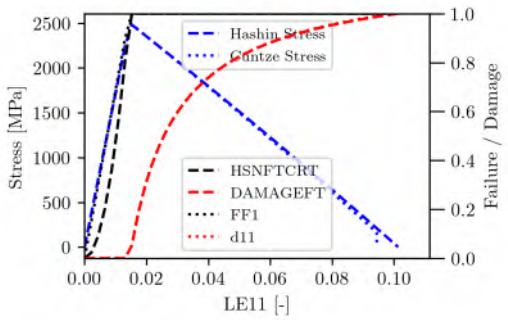

(a) Longitdudinal tensile loading σ_{11}

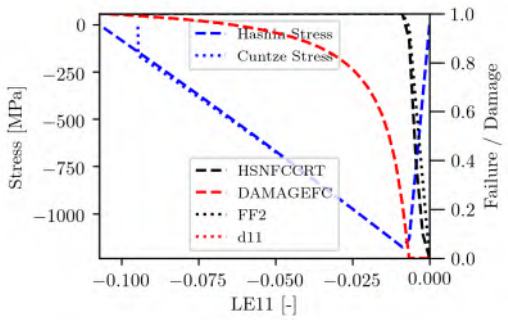

(b) Longitdudinal compression loading σ_{11}

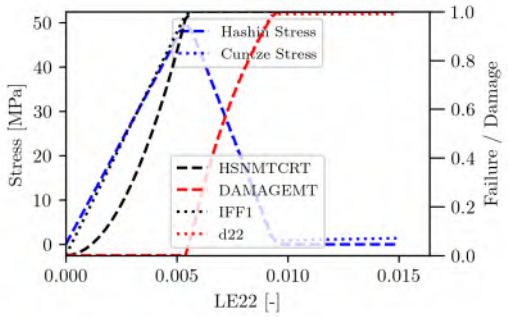

(c) Transverse tension loading σ_{22}

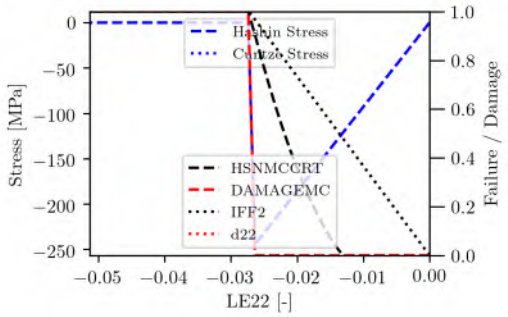

(d) Transverse compression loading σ_{22}

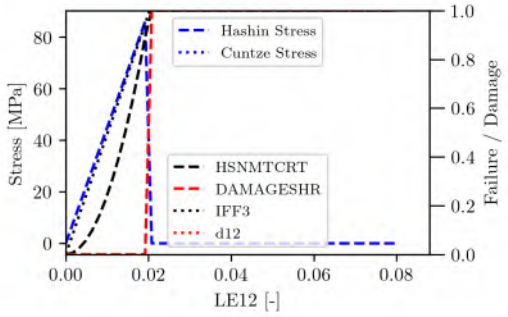

(e) Pure tensile shear loading τ_{12}

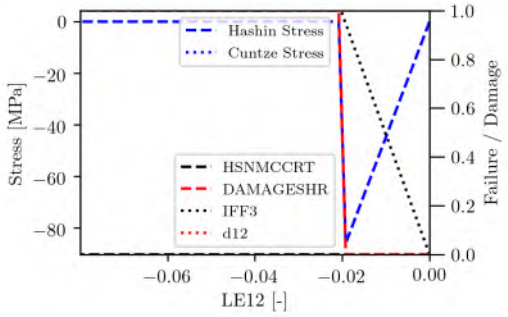

(f) Pure compressive shear loading τ_{12}

Figure C.2 Comparison of Cuntze FMC and Hashin material models

damage initiation criterion is due the fact that the Hashin criterion is formulated in quadratic form as oppose to the Cuntze FMC, which is formulated in linear form. However, the stress-strain relation as well as damage onset is practically identical for both models. Thus, for the one-element test case, both material models are considered interchangeable.

However, when the material model based on the Cuntze FMC is applied to the bolt-bearing model in Chapter 6.2, agreement between the two material models is severely decreased, as can be seen in Figure C.3. In fact, the simulation based on the Cuntze model exhibits premature failure due to a sudden drop in the load displacement curve. Therein, after damage is initiated in the Cuntze model, rapid damage

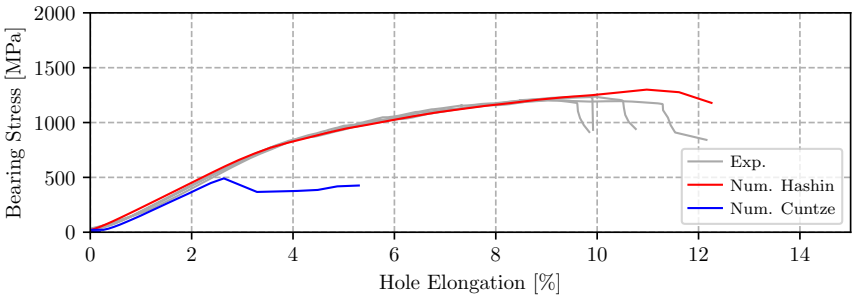

Figure C.3 Bolt-bearing loading of QI laminate at LT

propagation occurs, subsequently leading to the loss of load bearing capacity. Extensive trouble-shooting has not yet resolved the problem. However, the scope of the present work is not material modeling. Rather, the 2D and 3D formulations of the Cuntze material model were supposed to allow an investigation on modeling strategies for the bolt-bearing case. Those studies are omitted and the 2D Hashin implementation in Abaqus is used for analyzing bolt-bearing loading in CFRP-steel FMLs. Nonetheless, improvement of the material model is ongoin.

C.2 Numerical Bolt-Bearing Analysis

Table C.2 Comparison of experimental and numerical bearing strength for QI

		LT					RT				
		$\sigma^f_{0,5\%}$	$\sigma^f_{2\%}$	$\sigma^f_{4\%}$	$\sigma^f_{6\%}$	$\sigma^f_{10\%}$	$\sigma^f_{0,5\%}$	$\sigma^f_{2\%}$	$\sigma^f_{4\%}$	$\sigma^f_{6\%}$	$\sigma^f_{10\%}$
Mean	MPa	861	1060	1155	962	-	712	886	969	942	802
Stdev.	MPa	35.3	22.7	14.2	117	-	10	4	5	26	24
C.o.V.	%	4.1	2.2	1.2	12.1	-	1.4	0.5	0.5	2.8	2.9
FEM	MPa	864	1090	1234	1275	-	801	972	1055	-	-
Error	%	0.3	2.8	6.8	32.5	-	12.4	9.7	8.9	-	-

Table C.3 Comparison of experimental and numerical bearing strength for HO

		LT					RT				
		$\sigma^f_{0,5\%}$	$\sigma^f_{2\%}$	$\sigma^f_{4\%}$	$\sigma^f_{6\%}$	$\sigma^f_{10\%}$	$\sigma^f_{0,5\%}$	$\sigma^f_{2\%}$	$\sigma^f_{4\%}$	$\sigma^f_{6\%}$	$\sigma^f_{10\%}$
Mean	MPa	841	952	998	824	-	654	805	918	894	812
Stdev.	MPa	17	21	85	49	-	5	13	17	37	32
C.o.V.	%	2.0	2.2	8.6	6.0	-	0.8	1.7	1.8	4.1	3.9
FEM	MPa	866	1082	1244	1338	1505	798	894	-	-	-
Error	%	3.0	13.6	24.7	62.4	-	22.0	11.1	-	-	-

Table C.4 Comparison of experimental and numerical bearing strength for QI-FML

		LT					RT				
		$\sigma^f_{0,5\%}$	$\sigma^f_{2\%}$	$\sigma^f_{4\%}$	$\sigma^f_{6\%}$	$\sigma^f_{10\%}$	$\sigma^f_{0,5\%}$	$\sigma^f_{2\%}$	$\sigma^f_{4\%}$	$\sigma^f_{6\%}$	$\sigma^f_{10\%}$
Mean	MPa	1180	1450	1648	1770	1570	1030	1280	1460	1568	1500
Stdev.	MPa	27	38	52	36	176	8	16	23	31	38
C.o.V.	%	2.3	2.6	3.2	2.0	11.2	0.8	1.3	1.6	2.0	2.5
FEM	MPa	1134	1446	1647	1798	1895	1126	1394	1579	1720	1635
Error	%	-3.9	-0.3	-0.1	1.6	20.7	9.3	8.9	8.1	9.7	9.0

Table C.5 Comparison of experimental and numerical bearing strength for HO-FML

		LT					RT				
		$\sigma^f_{0,5\%}$	$\sigma^f_{2\%}$	$\sigma^f_{4\%}$	$\sigma^f_{6\%}$	$\sigma^f_{10\%}$	$\sigma^f_{0,5\%}$	$\sigma^f_{2\%}$	$\sigma^f_{4\%}$	$\sigma^f_{6\%}$	$\sigma^f_{10\%}$
Mean	MPa	1400	1680	1872	1976	2151	1170	1460	1626	1718	1830
Stdev.	MPa	24	11	6	11	9	14	26	11	26	26
C.o.V.	%	1.7	0.7	0.3	0.5	0.4	1.2	1.8	0.7	1.5	1.4
FEM	MPa	1208	1582	1808	1999	2207	1244	1528	1748	1889	2050
Error	%	-13.7	-5.8	-3.4	1.2	2.6	6.4	4.7	7.5	9.9	12.0

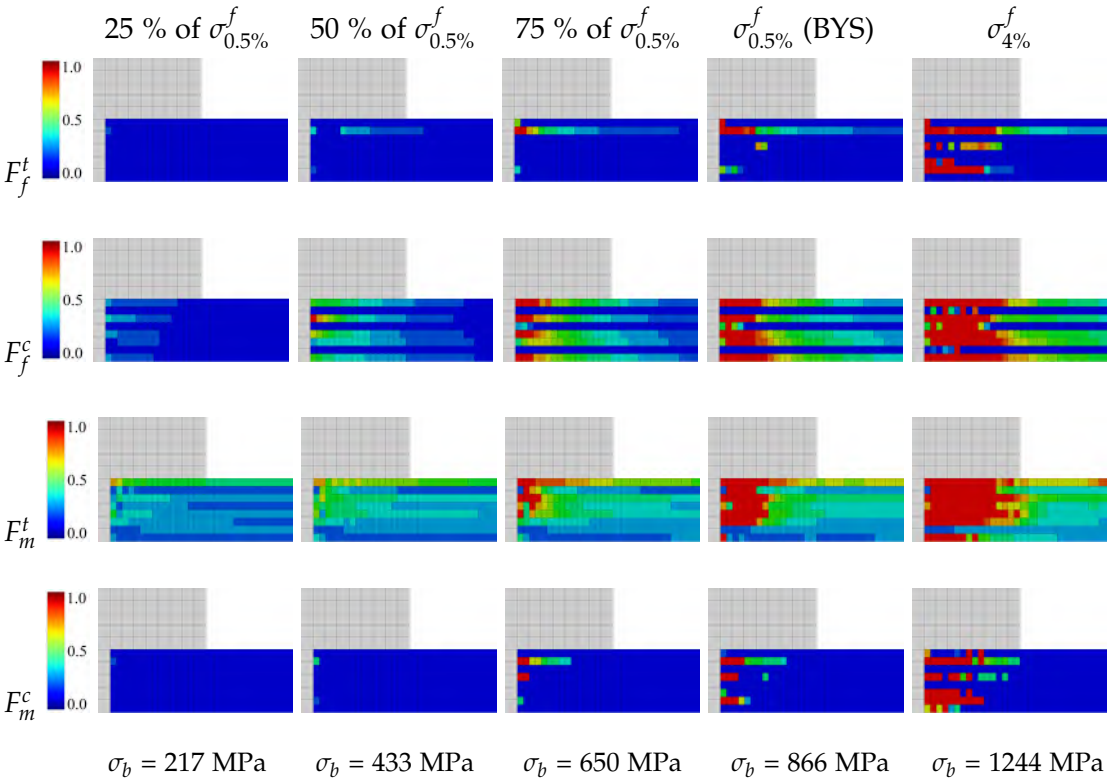

Figure C.4 Evolution of damage onset criteria in HO at LT

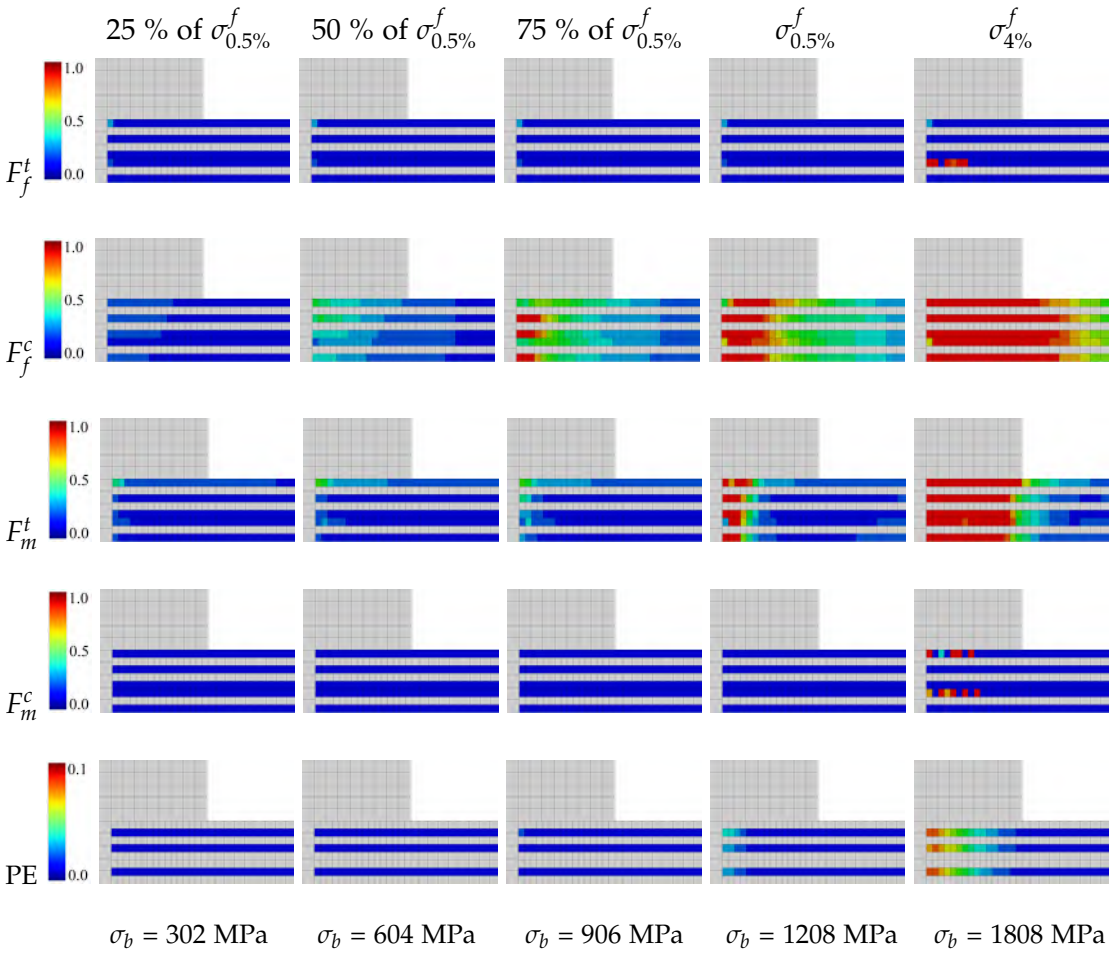

Figure C.5 Evolution of damage onset criteria in HO-FML at LT

Appendix D

Analytical Methods

D.1 Analytical Solution for Bypass Loading

Two examples of exact analytical solutions are given - one for solution A and one for solution B. The solutions are adjusted to the geometry and coordinate system given in Figure 7.3. The reader is referred to the respective original publications for a detailed description of the formulations from Chapter 7.

D.1.1 Complex parameters

The definition of the complex parameters is required for both solutions:

$$\alpha_0 = \sqrt{\frac{E_{xx}}{E_{yy}}}, \quad \beta_0 = \frac{E_{xx}}{2G_{xy}} - \nu_{xy}$$

$$\text{if } \beta_0 \geq \alpha_0: \quad s_1 = i\left(\sqrt{\frac{\beta_0 - \alpha_0}{2}} + \sqrt{\frac{\alpha_0 + \beta_0}{2}}\right)$$
$$s_2 = i\left(-\sqrt{\frac{\beta_0 - \alpha_0}{2}} + \sqrt{\frac{\alpha_0 + \beta_0}{2}}\right)$$

$$\text{if } \alpha_0 \geq \beta_0: \quad s_1 = \sqrt{\frac{\alpha_0 - \beta_0}{2}} + i\sqrt{\frac{\alpha_0 + \beta_0}{2}}$$
$$s_2 = -\sqrt{\frac{\alpha_0 - \beta_0}{2}} + i\sqrt{\frac{\alpha_0 + \beta_0}{2}}$$

The real and imaginary parts of the complex parameters are used in the following:

$$\alpha_i = \mathrm{Re}(s_i), \ \beta_i = \mathrm{Im}(s_i), \ i \in [1,2]$$

D.1.2 Solution A

The equations for solution A are taken from Soutis and Filiou [195] and adjusted to the present case. This result is a compact representation of the results in [174,175,197,198]:

$$\sigma_{xx} = p + \mathrm{Re}\left\{\frac{p}{s_1 - s_2}\left[\frac{-is_1^2}{1+is_1}\,\Omega_1 + \frac{is_2^2}{1+is_2}\,\Omega_2\right]\right\}$$

$$\sigma_{yy} = \mathrm{Re}\left\{\frac{p}{s_1 - s_2}\left[\frac{-i}{1+is_1}\,\Omega_1 + \frac{i}{1+is_2}\,\Omega_2\right]\right\}$$

$$\tau_{xy} = -\mathrm{Re}\left\{\frac{p}{s_1 - s_2}\left[\frac{-is_1}{1+is_1}\,\Omega_1 + \frac{is_2}{1+is_2}\,\Omega_2\right]\right\}$$

$$\Omega_j = \left(1 - \frac{x + s_j y}{\sqrt{\left(x + s_j y\right)^2 - R^2\left(1 + s_j^2\right)}}\right), \quad j \in [1, 2]$$

D.1.3 Solution B

The example solution for solution B is based on the formulation proposed by Ukadgaonker and Rao [199] and adjusted to the geometry and coordinate system in Figure 7.3:

$$\sigma_{xx} = p + 2\mathrm{Re}\left[\frac{2s_1^2}{R}\left(\frac{-a_3}{b_1\zeta^2 - a_1}\right) + \frac{2s_2^2}{R}\left(\frac{a_4}{b_2\zeta^2 - a_2}\right)\right]$$

$$\sigma_{yy} = 2\mathrm{Re}\left[\frac{2}{R}\left(\frac{-a_3}{b_1\zeta^2 - a_1}\right) + \frac{2}{R}\left(\frac{a_4}{b_2\zeta^2 - a_2}\right)\right]$$

$$\tau_{xy} = -2\mathrm{Re}\left[\frac{2s_1}{R}\left(\frac{-a_3}{b_1\zeta^2 - a_1}\right) + \frac{2s_2}{R}\left(\frac{a_4}{b_2\zeta^2 - a_2}\right)\right]$$

$$\zeta = \frac{z}{R}, \quad z = x + iy$$

$$a_1 = 1 + is_1, \quad a_2 = 1 + is_2$$

$$b_1 = 1 - is_1, \quad b_2 = 1 - is_2$$

$$s_1 = \alpha_1 + i\beta_1, \quad s_2 = \alpha_2 + i\beta_2$$

$$a_3 = \frac{1}{s_1 - s_2}\left[s_2\left(K_1 + \overline{K}_2\right) - \left(K_3 + \overline{K}_4\right)\right]$$

$$a_4 = \frac{1}{s_1 - s_2}\left[s_1\left(K_1 + \overline{K}_2\right) - \left(K_3 + \overline{K}_4\right)\right]$$

$$K_1 = \frac{R}{2}\left[B^* a_1 + \left(B'^* + iC'^*\right) a_2\right]$$

$$K_2 = \frac{R}{2}\left[B^* b_1 + \left(B'^* + iC'^*\right) b_2\right]$$

$$K_3 = \frac{R}{2}\left[s_1 B^* a_1 + s_2\left(B'^* + iC'^*\right) a_2\right]$$

$$K_4 = \frac{R}{2}\left[s_1 B^* b_1 + s_2\left(B'^* + iC'^*\right) b_2\right]$$

$$B^* = \frac{p}{\eta}, \quad B'^* = \frac{-p}{\eta}, \quad C'^* = \frac{(\alpha_1 - \alpha_2)\, p}{\beta_2 \eta}$$
$$\eta = 2\left[(\alpha_2 - \alpha_1)^2 + (\beta_2^2 - \beta_1^2)\right]$$

D.2 Analytical Solution for Pin-Bearing Loading

One example of an exact analytical solution is given herein. Due to its compact formulation and high accuracy, the analytical solution proposed by Waszczak & Cruse [209] is presented. All equations are adapted to the coordinate system in Figure 7.10. The stress function derivatives read:

$$\Phi_k'(z_k) = \left[\frac{A_k}{\zeta_k} - \sum_{m=1}^{\infty} m A_{k,m}\, \zeta_k^{-(m+1)}\right] \frac{\pm\zeta_k}{\sqrt{z_k^2 - R^2\left(1 + \mu_k^2\right)}}, \tag{D.4}$$

The method-specific series coefficients are defined as:

$$A_{k,m} = \begin{cases} \dfrac{\mp R\mathrm{i}\,(-1)^{(m-1)/2}\left(2 + \mathrm{i}m\mu_j\right) p_{\max}}{\pi m^2\left(m^2 - 4\right)\left(\mu_2 - \mu_1\right)} & \text{for odd } m \\ 0 & \text{for even } m \\ \dfrac{\pm R\mathrm{i}\left(1 + \mathrm{i}\mu_j\right) p_{\max}}{16\left(\mu_2 - \mu_1\right)} & \text{for } m = 2 \end{cases} \tag{D.5}$$

$$\text{with} \quad j = 3 - k \quad \text{and} \quad p_{\max} = \frac{4}{\pi}\frac{P}{dt} = \frac{4}{\pi} p_b$$

The remaining parameters are independent of the boundary conditions, thus are considered general. The complex coefficients can be expressed as:

$$A_k = \frac{P\left[\mu_k\left(\mu_j + \bar{\mu}_k + \bar{\mu}_j\right) - \dfrac{a_{12}}{a_{11}}\right]}{2\pi t\mathrm{i}\left(\mu_j - \mu_k\right)\left(\bar{\mu}_j - \mu_k\right)\left(\mu_k - \bar{\mu}_k\right)}, \tag{D.6}$$

The complex parameters describing the degree of material anisotropy read:

$$\mu_k = \begin{cases} \mathrm{i}\left(\sqrt{\dfrac{\beta + \alpha}{2}} \pm \sqrt{\dfrac{\beta - \alpha}{2}}\right) & \text{for } \beta \geq \alpha \\ \mathrm{i}\sqrt{\dfrac{\alpha + \beta}{2}} \pm \sqrt{\dfrac{\alpha - \beta}{2}} & \text{for } \beta \leq \alpha \end{cases} \tag{D.7}$$

$$\text{with} \quad \alpha = \sqrt{\frac{E_{xx}}{E_{yy}}} \quad \text{and} \quad \beta = \frac{E_{xx}}{2G_{xy}} - \nu_{xy}\,.$$

In addition, the following mapping functions are used:

$$\zeta_k(z_k) = \frac{z_k \pm \sqrt{z_k^2 - R^2\left(1 + \mu_k^2\right)}}{R\left(1 - \mathrm{i}\mu_k\right)}, \tag{D.8}$$

$$\text{with} \quad z_k = x + \mu_k y \,. \tag{D.9}$$

In contrast to series coefficients $A_{k,m}$ (eq. D.5) and complex parameters μ_k (eq. D.7), where the upper and lower sign are used for indices $k = 1$ and $k = 2$, respectively, the sign used with mapping functions ζ_k (eq. D.4 and D.8) has to be chosen so that the hole contour and arbitrary points on the laminate are mapped onto and outside the unit circle, respectively, so that

$$|\zeta_k| \geq 1 \tag{D.10}$$

By inserting the stress function derivatives from equation D.4 into equation 7.15, the stresses in a pin-loaded composite plate can be calculated.

D.3 Results for Bypass and Pin-Bearing Loading Cases

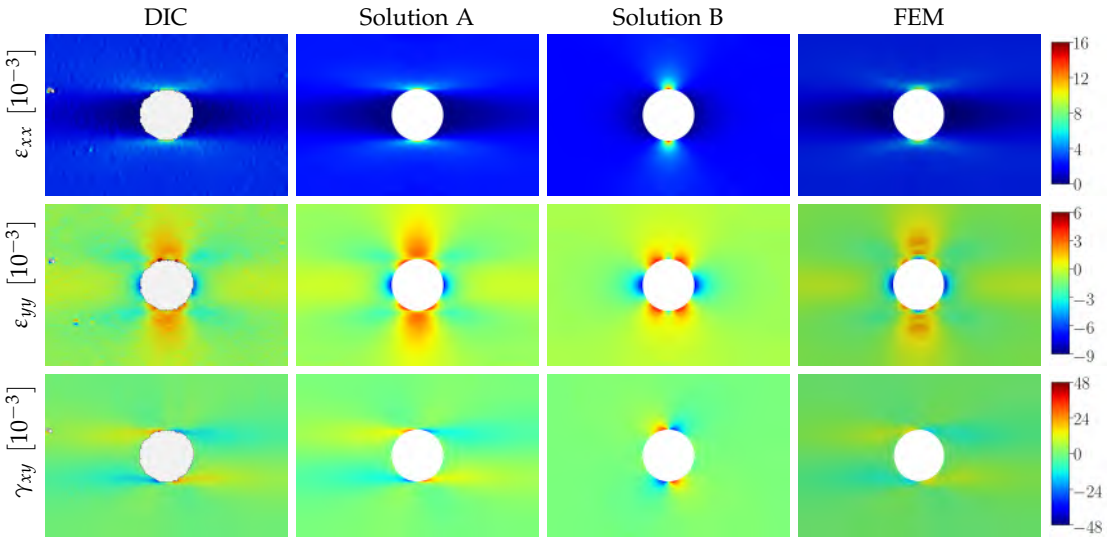

Figure D.1 2D surface plot for UD-0°: Strain fields for ε_{xx}, ε_{yy} and γ_{xy} resulting from DIC, analytical (solution A and solution B) and FE methods are shown for a cutout of 20 mm by 30 mm around the center hole. The loading as well as 0° fiber direction are aligned along the horizontal axis

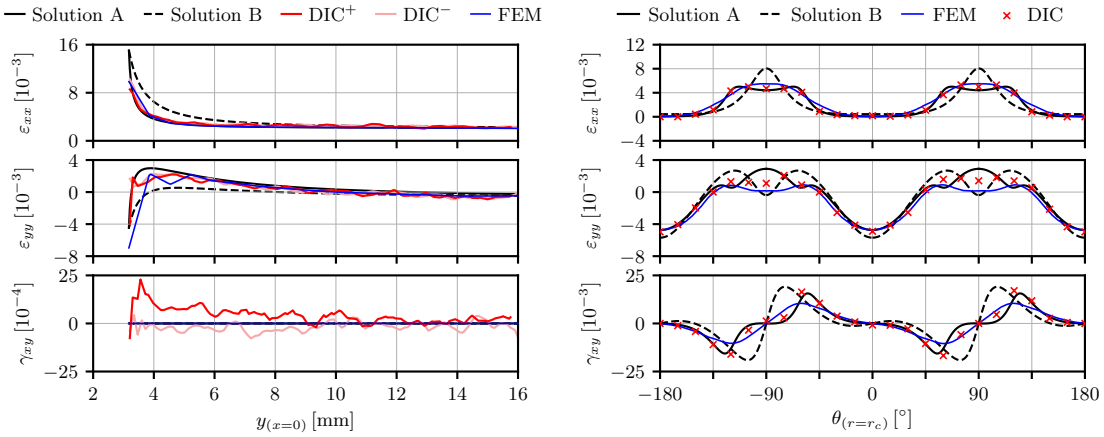

(a) Strain components along radial path

(b) Strain components along circular path

Figure D.2 Comparison of strain components ε_{xx}, ε_{yy} and γ_{xy} for the UD-0° specimen (a) along a radial path for x=0 and (b) along a circular path with a radius of r_c=3.7 mm

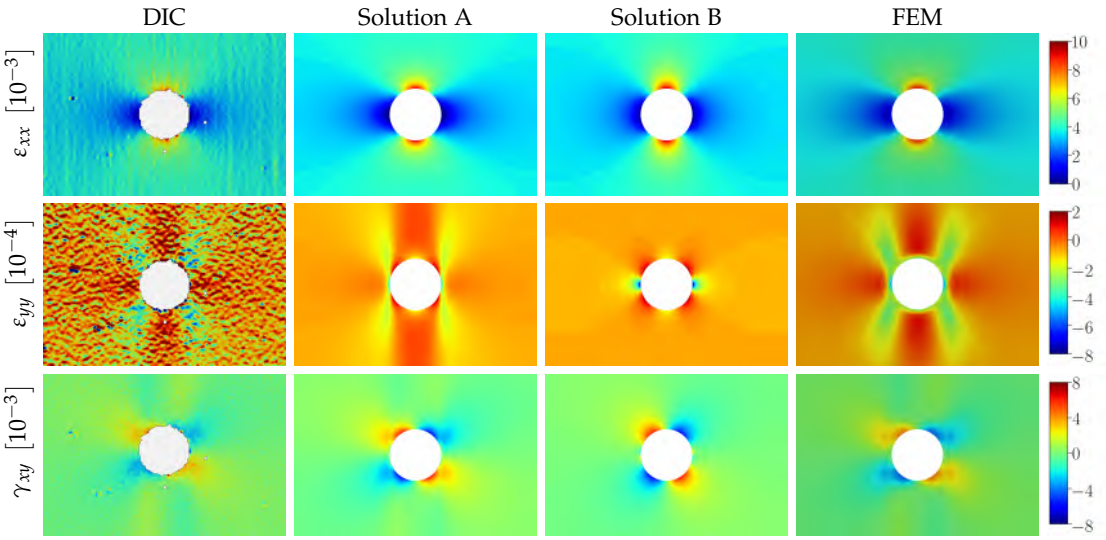

Figure D.3 2D surface plot for UD-90°: Strain fields for ε_{xx}, ε_{yy} and γ_{xy} resulting from DIC, analytical (solution A and solution B) and FE methods are shown for a cutout of 20 mm by 30 mm around the center hole. The loading direction is parallel to the horizontal axis while the fibers are oriented perpendicular to the loading direction

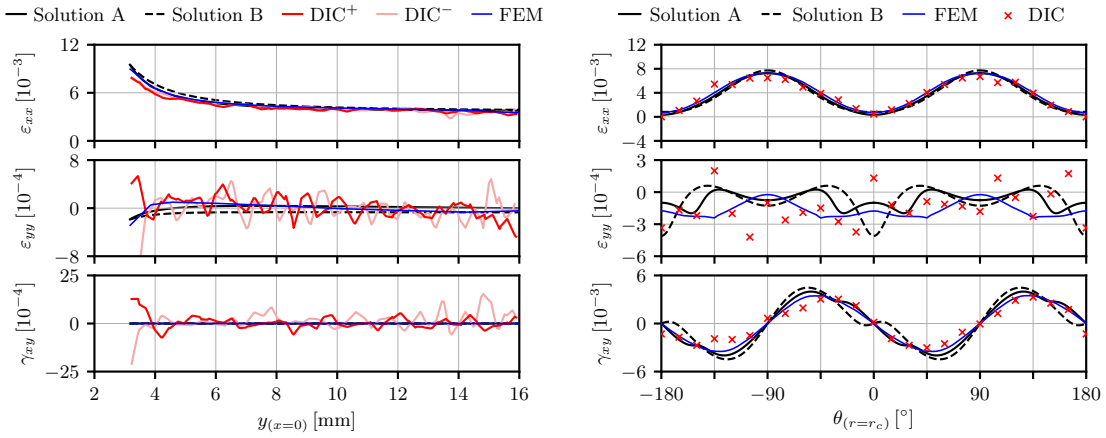

(a) Strain components along radial path

(b) Strain components along circular path

Figure D.4 Comparison of strain components ε_{xx}, ε_{yy} and γ_{xy} for the UD-90° specimen (a) along a radial path for x=0 and (b) along a circular path with a radius of r_c=3.7 mm

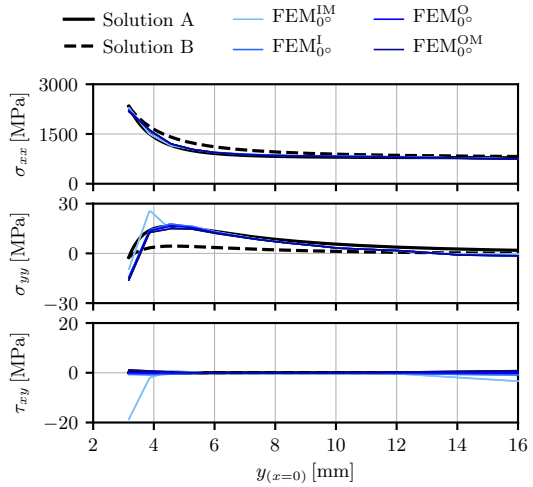

(a) Stresses along radial path for 0° ply

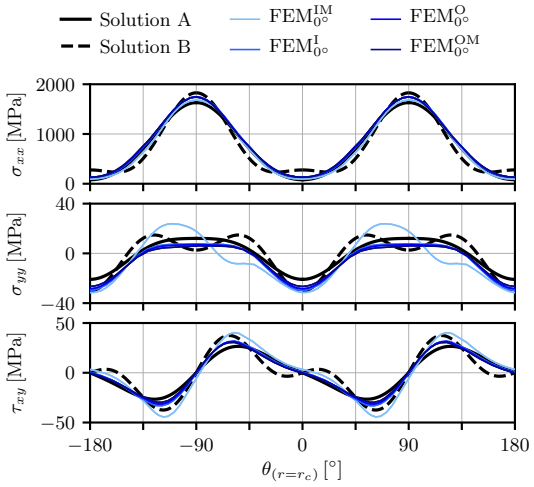

(b) Stresses along circular path 0° ply

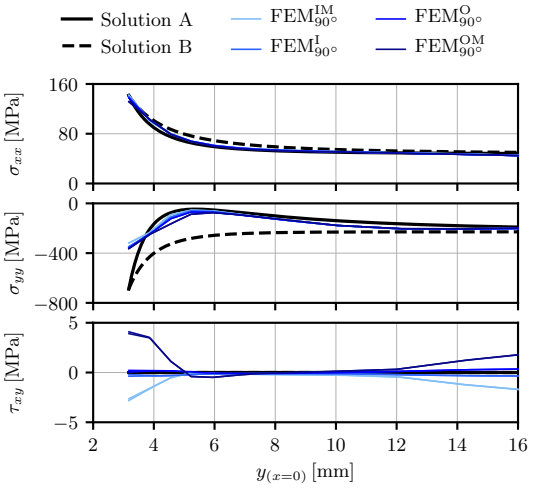

(c) Stresses along radial path for 90° ply

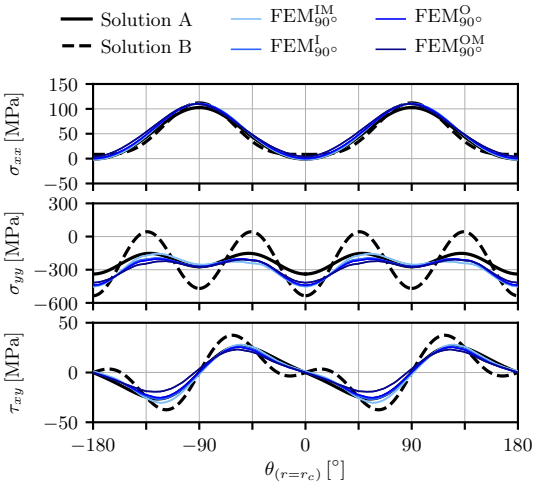

(d) Stresses along circular path 90° ply

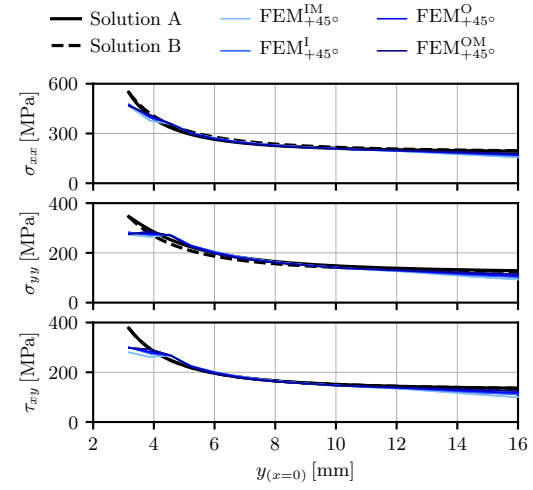

(e) Stresses along radial path for +45° ply

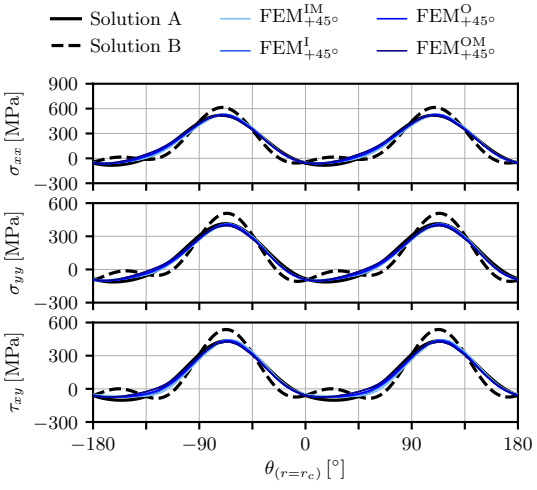

(f) Stresses along circular path +45° ply

Figure D.5 Stress components σ_{xx}, σ_{yy} and τ_{xy} for the QI specimen with w/d=5 (a) along a radial path for x=0 and (b) along a circular path with a radius of r_c=3.7 mm

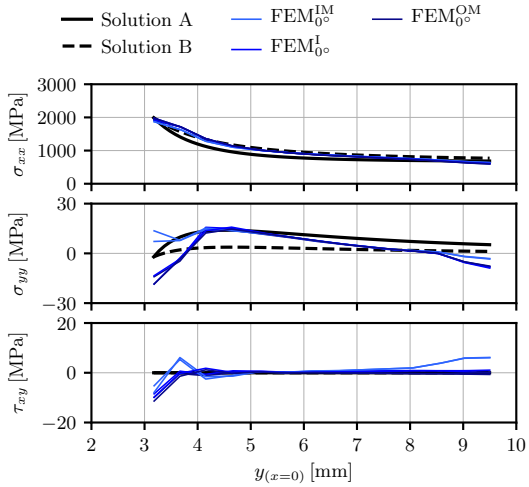

(a) Stresses along radial path for 0° ply

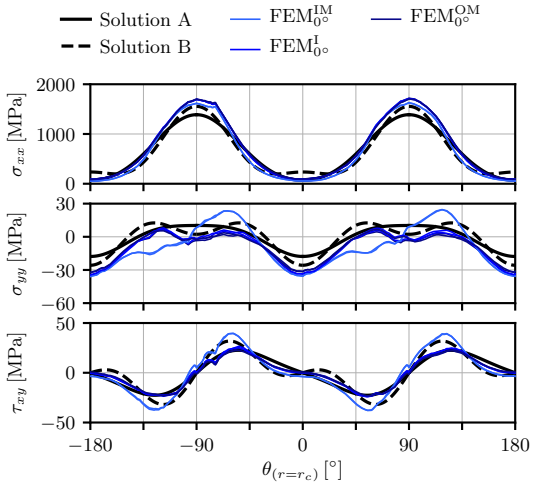

(b) Stresses along circular path for 0° ply

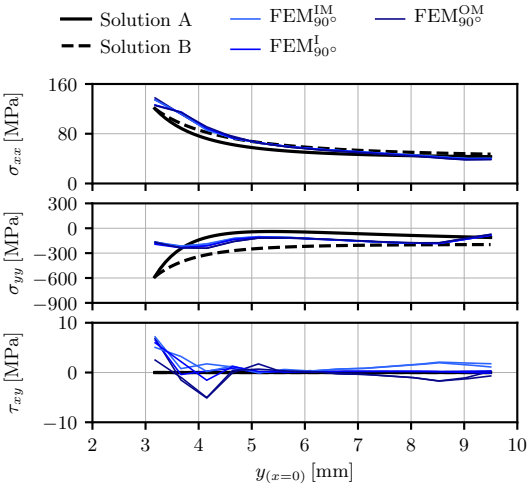

(c) Stresses along radial path for 90° ply

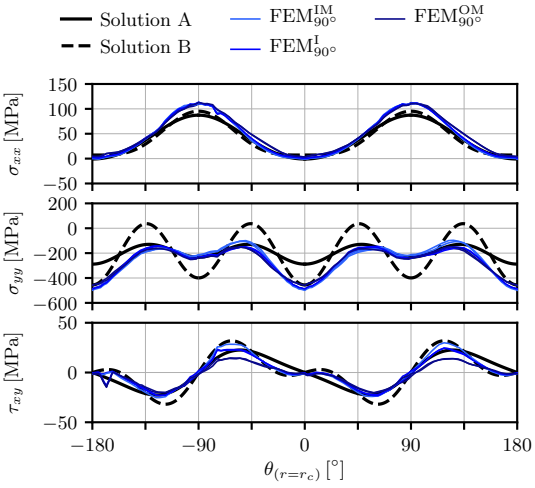

(d) Stresses along circular path for 90° ply

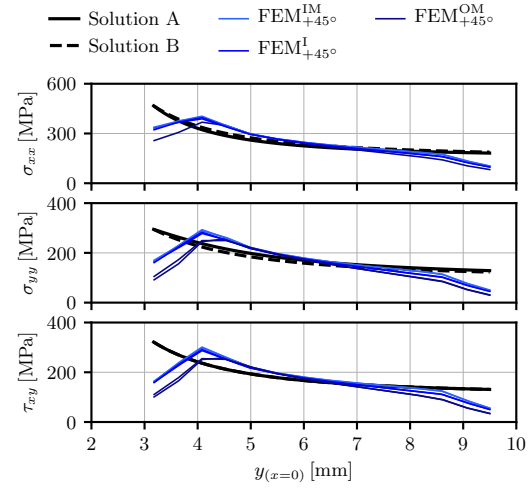

(e) Stresses along radial path for +45° ply

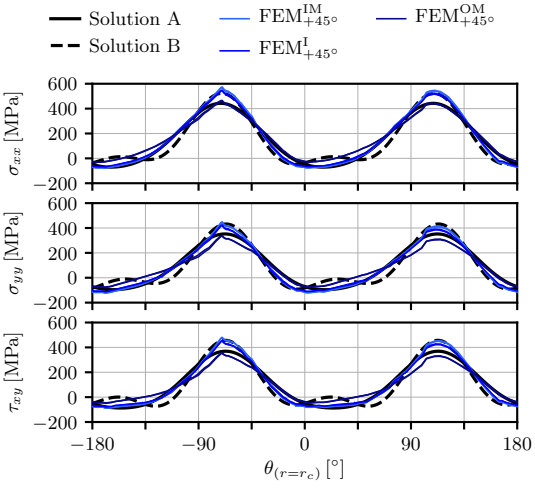

(f) Stresses along circular path for +45° ply

Figure D.6 Stress components σ_{xx}, σ_{yy} and τ_{xy} for the QI specimen with w/d=3 (a) along a radial path for x=0 and (b) along a circular path with a radius of r_c=3.7 mm

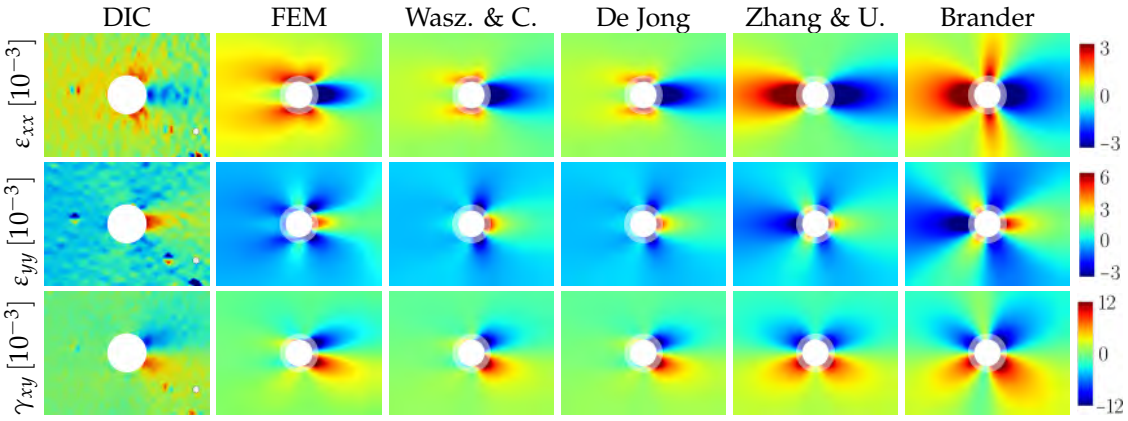

Figure D.7 2D surface plots for HO laminate: Strain fields ε_{xx}, ε_{yy} and γ_{xy} resulting from DIC, FEM and analytical solutions are shown for a cutout of 40 mm by 30 mm around the pin-loaded hole. The loading direction as well as 0° fiber direction are alinged along the horizontal axis to the right

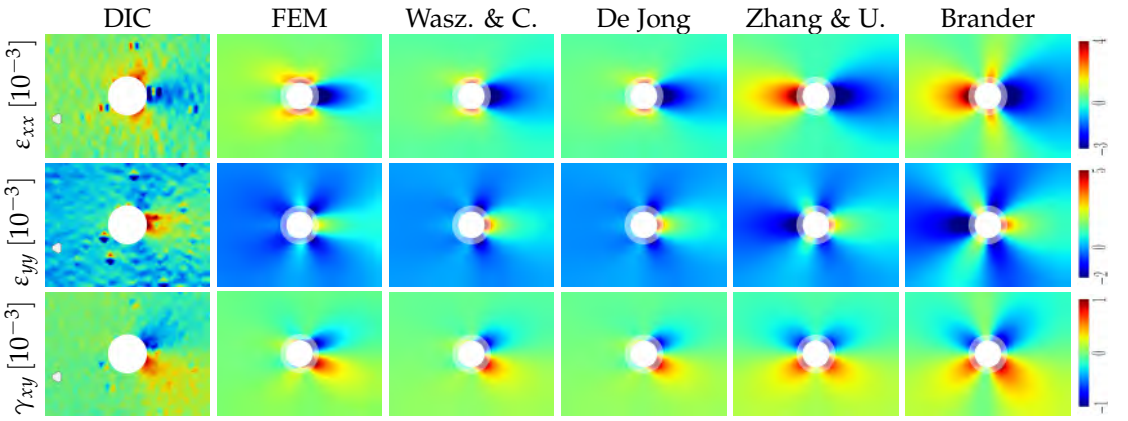

Figure D.8 2D surface plots for HO-FML laminate: Strain fields ε_{xx}, ε_{yy} and γ_{xy} resulting from DIC, FEM and analytical solutions are shown for a cutout of 40 mm by 30 mm around the pin-loaded hole. The loading direction as well as 0° fiber direction are alinged along the horizontal axis to the right

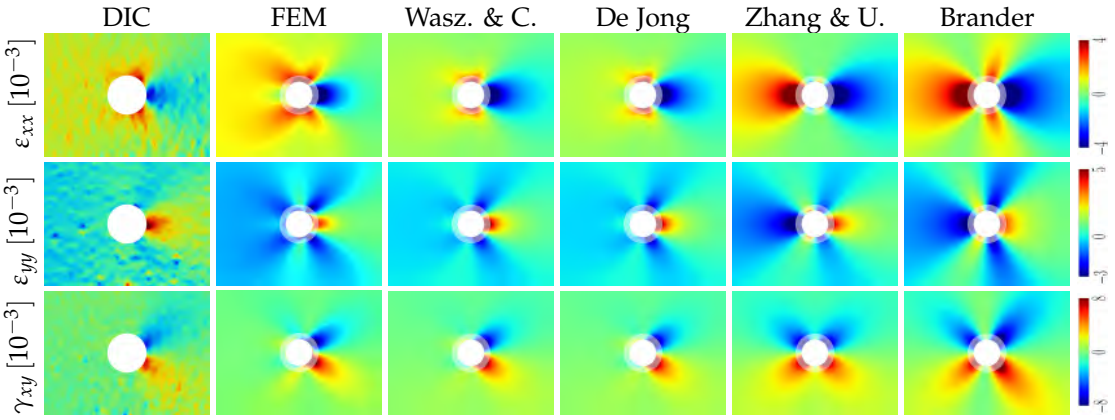

Figure D.9 2D surface plots for QI-FML laminate: Strain fields ε_{xx}, ε_{yy} and γ_{xy} resulting from DIC, FEM and analytical solutions are shown for a cutout of 40 mm by 30 mm around the pin-loaded hole. The loading direction as well as 0° fiber direction are alinged along the horizontal axis to the right

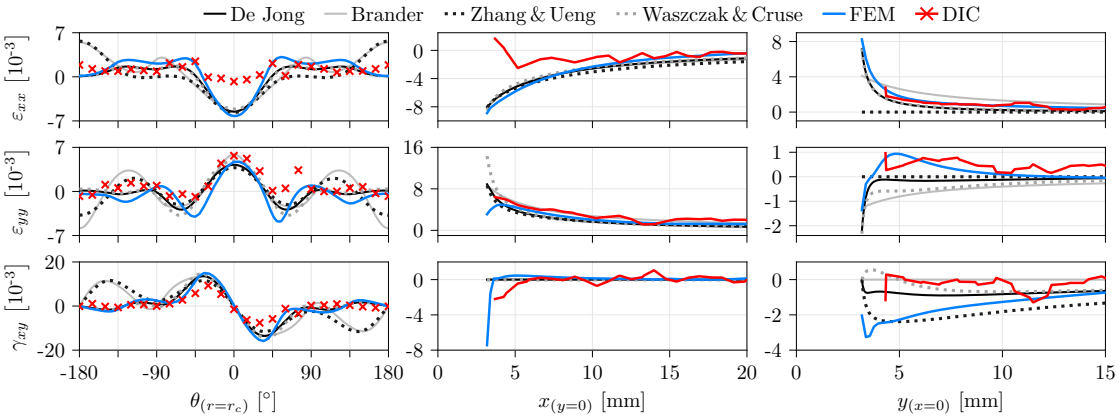

(a) Circular path with $r = r_c$ **(b)** Radial path along x-axis **(c)** Radial path along y-axis

Figure D.10 Comparison of strain components ε_{xx}, ε_{yy} and γ_{xy} for the HO laminate along a circular path around the pin-loaded hole with a radius r_c=4.7 mm as well as two radial paths along the x-axis for y=0 and y-axis for x=0, respectively

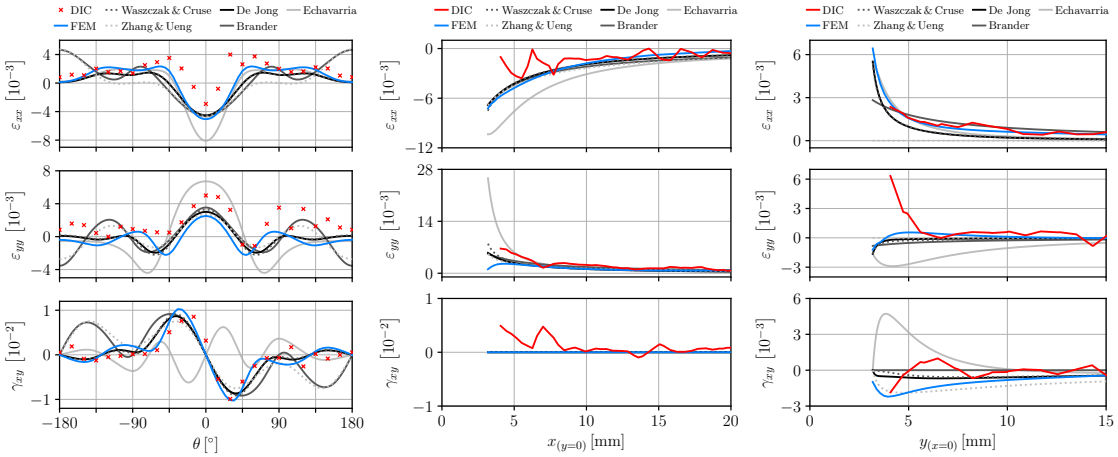

(a) Circular path with $r = r_c$ **(b)** Radial path along x-axis **(c)** Radial path along y-axis

Figure D.11 Comparison of strain components ε_{xx}, ε_{yy} and γ_{xy} for the HO-FML laminate along a circular path around the pin-loaded hole with a radius r_c=4.7 mm as well as two radial paths along the x-axis for y=0 and y-axis for x=0, respectively

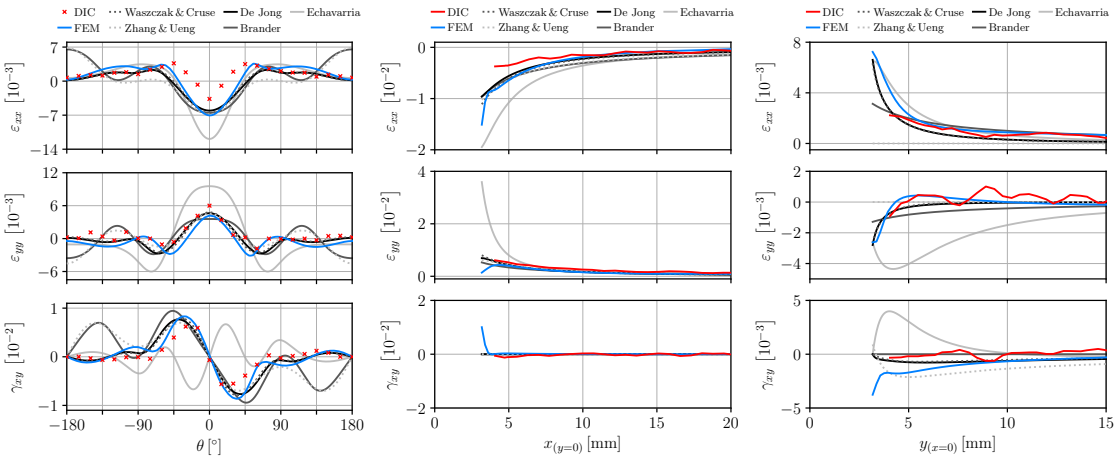

(a) Circular path with $r = r_c$ **(b)** Radial path along x-axis **(c)** Radial path along y-axis

Figure D.12 Comparison of strain components ε_{xx}, ε_{yy} and γ_{xy} for the QI-FML laminate along a circular path around the pin-loaded hole with a radius r_c=4.7 mm as well as two radial paths along the x-axis for y=0 and y-axis for x=0, respectively

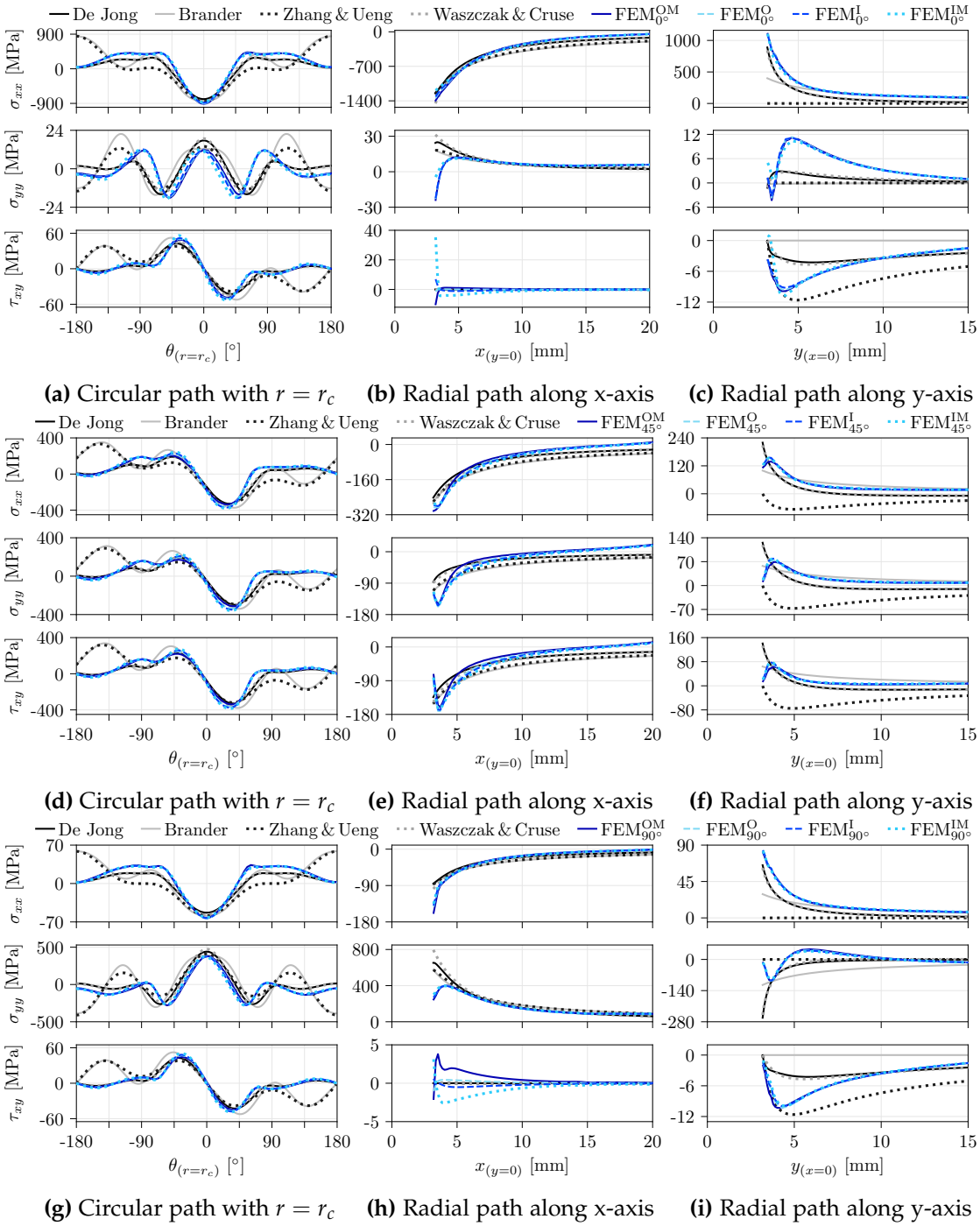

(a) Circular path with $r = r_c$ **(b)** Radial path along x-axis **(c)** Radial path along y-axis

(d) Circular path with $r = r_c$ **(e)** Radial path along x-axis **(f)** Radial path along y-axis

(g) Circular path with $r = r_c$ **(h)** Radial path along x-axis **(i)** Radial path along y-axis

Figure D.13 Comparison of stress components σ_{xx}, σ_{yy} and τ_{xy} in the single plies of the QI laminate with w/d=7 (a-c: 0° plies, d-f: 45° plies, g-i: 90° plies) along a circular path around the pin-loaded hole with a radius of r_c=4.7 mm as well as two radial paths along the x-axis for y=0 and y-axis for x=0, respectively

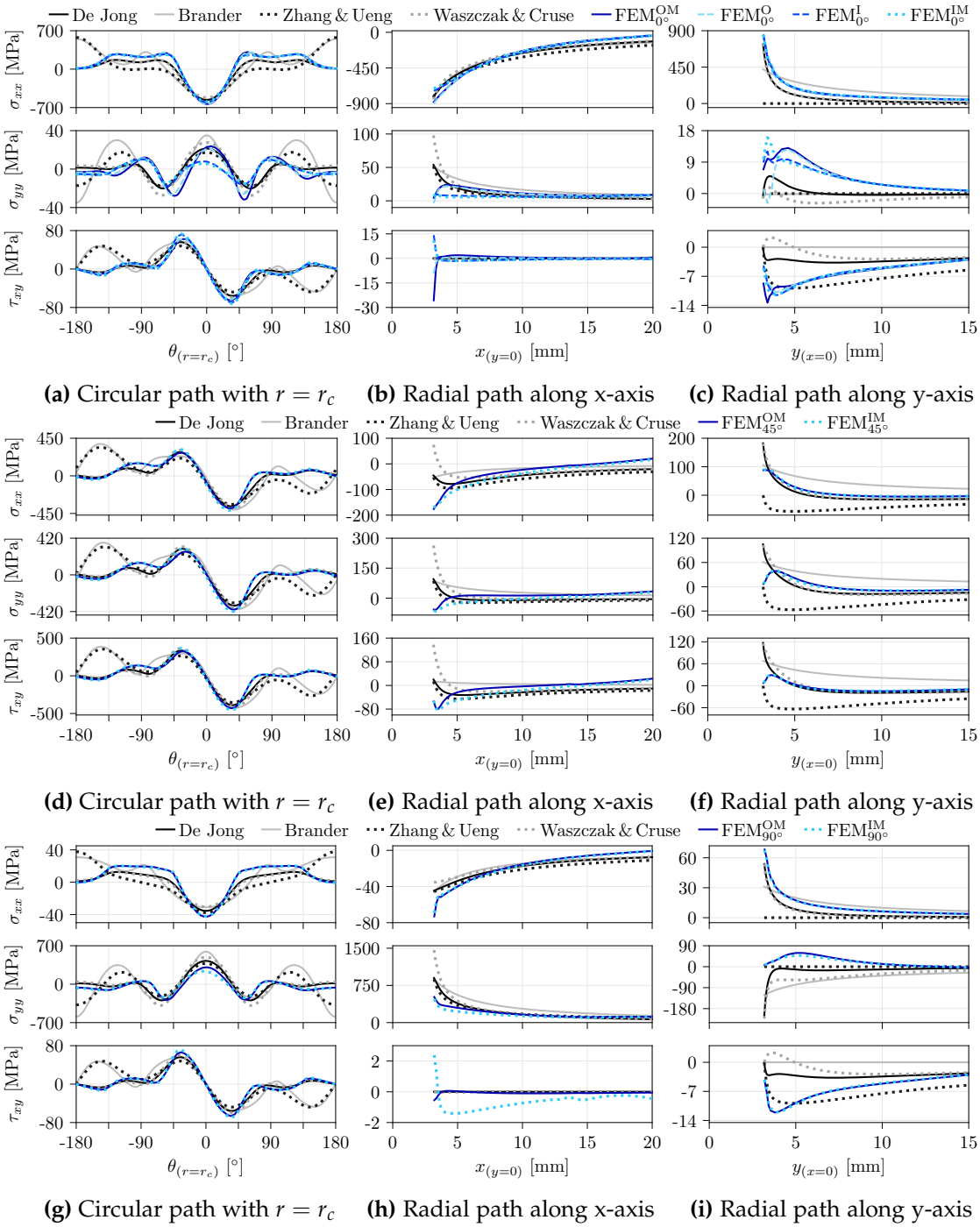

(a) Circular path with $r = r_c$ **(b)** Radial path along x-axis **(c)** Radial path along y-axis

(d) Circular path with $r = r_c$ **(e)** Radial path along x-axis **(f)** Radial path along y-axis

(g) Circular path with $r = r_c$ **(h)** Radial path along x-axis **(i)** Radial path along y-axis

Figure D.14 Comparison of stress components σ_{xx}, σ_{yy} and τ_{xy} in the single plies of the HO laminate with w/d=7 (a-c: 0° plies, d-f: 45° plies, g-i: 90° plies) along a circular path around the pin-loaded hole with a radius of r_c=4.7 mm as well as two radial paths along the x-axis for y=0 and y-axis for x=0, respectively

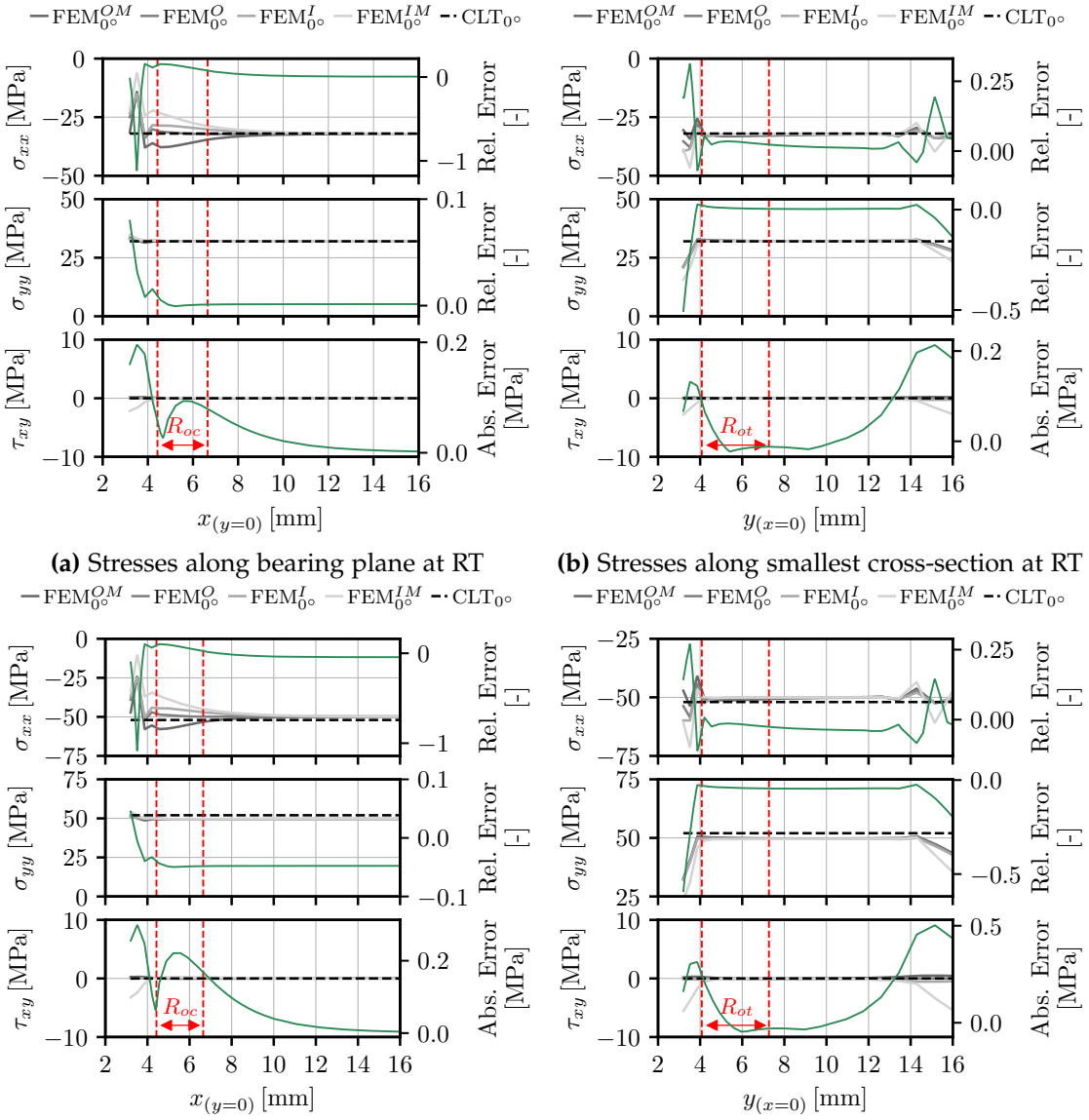

(a) Stresses along bearing plane at RT

(b) Stresses along smallest cross-section at RT

(c) Stresses along bearing plane at LT

(d) Stresses along smallest cross-section at LT

Figure D.15 Thermal residual stresses in the 0° plies of a QI laminate with a center notch of d=6.355 mm by FEM and CLT including range of characteristic distances in tension and compresssion

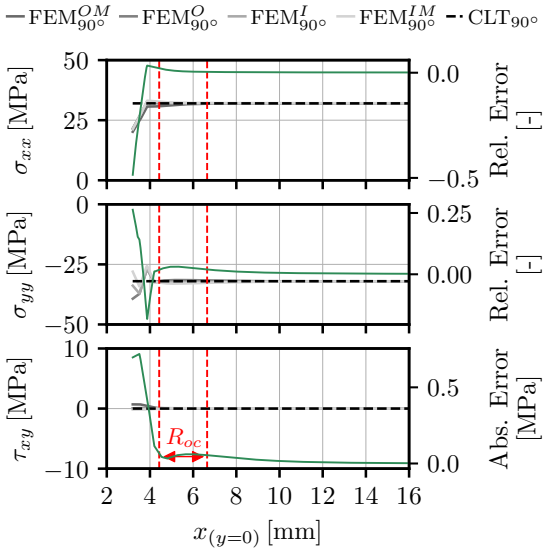

(a) Stresses along bearing plane at RT

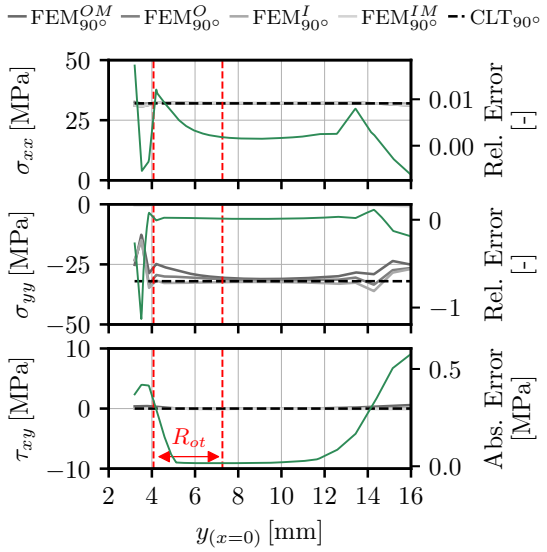

(b) Stresses along smallest cross-section at RT

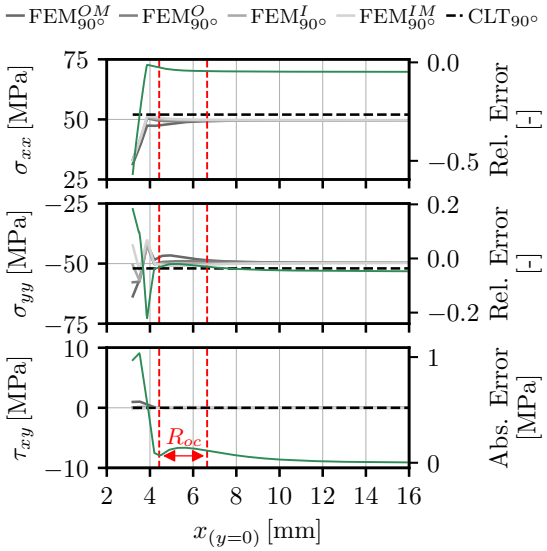

(c) Stresses along bearing plane at LT

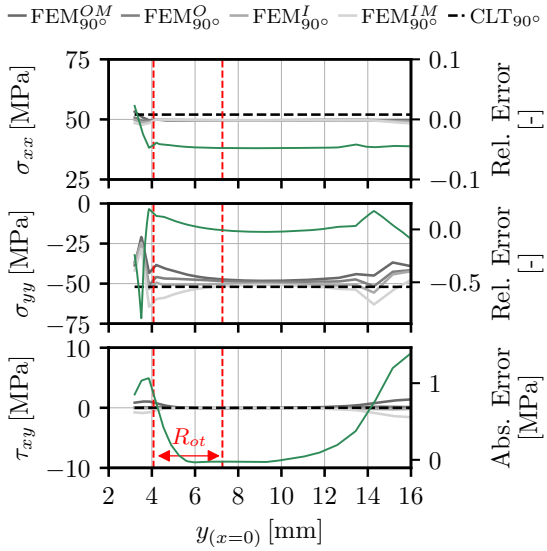

(d) Stresses along smallest cross-section at LT

Figure D.16 Thermal residual stresses in the 90° plies of a QI laminate with a center notch of d=6.355 mm by FEM and CLT including range of characteristic distances in tension and compresssion

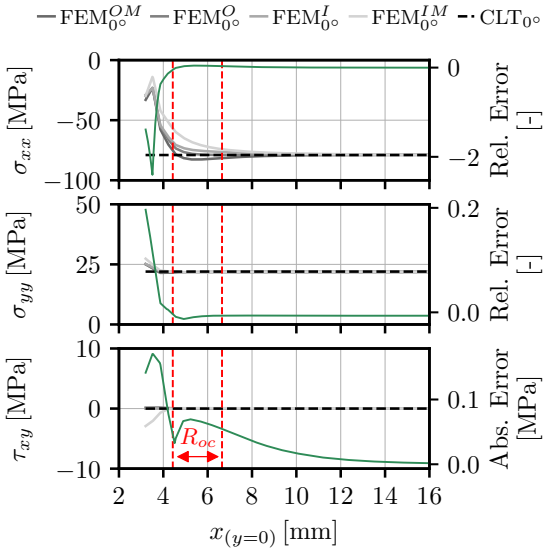

(a) Stresses along bearing plane at RT

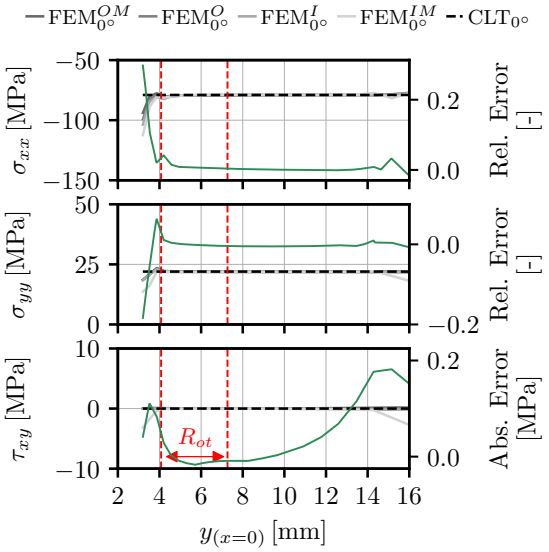

(b) Stresses along smallest cross-section at RT

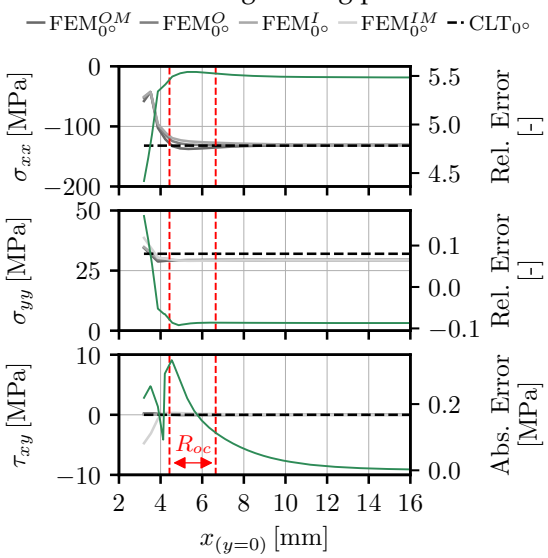

(c) Stresses along bearing plane at LT

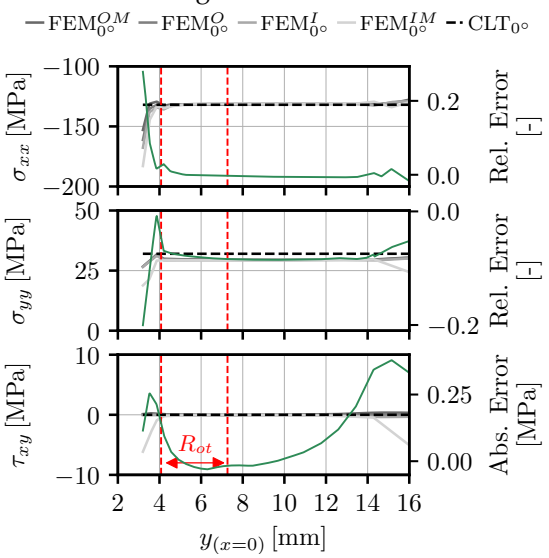

(d) Stresses along smallest cross-section at LT

Figure D.17 Thermal residual stresses in the 0° plies of a QI-FML with a center notch of d=6.355 mm by FEM and CLT including range of characteristic distances in tension and compresssion

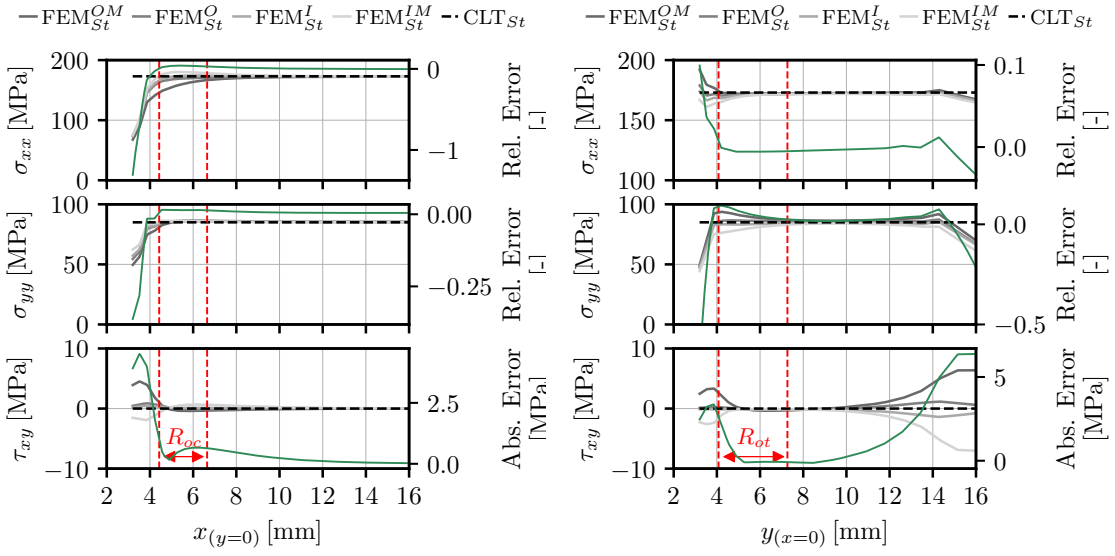

(a) Stresses along bearing plane at RT

(b) Stresses along smallest cross-section at RT

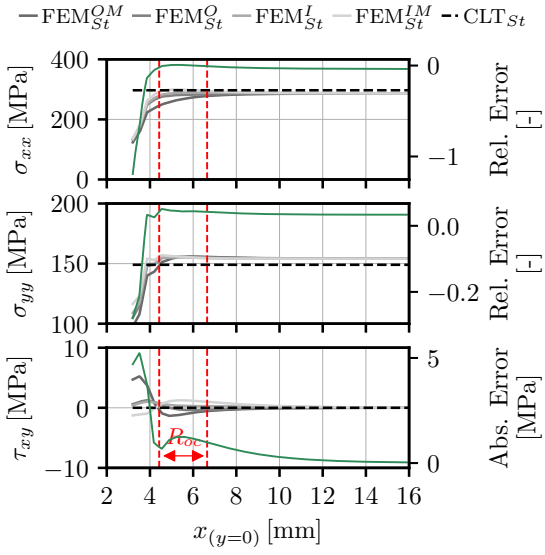

(c) Stresses along bearing plane at LT

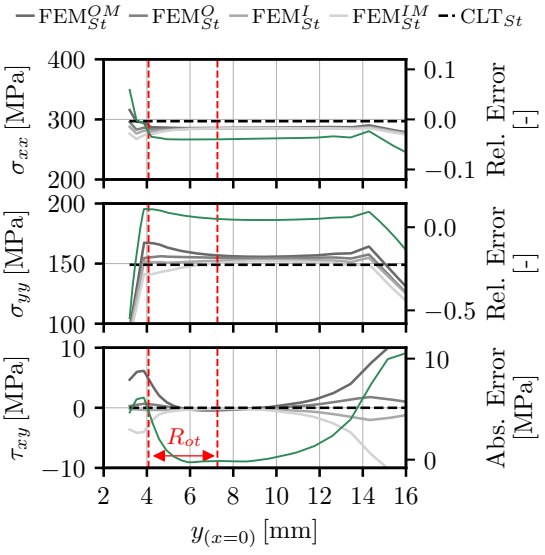

(d) Stresses along smallest cross-section at LT

Figure D.18 Thermal residual stresses in the steel plies of a QI-FML with a center notch of d=6.355 mm by FEM and CLT including range of characteristic distances in tension and compresssion

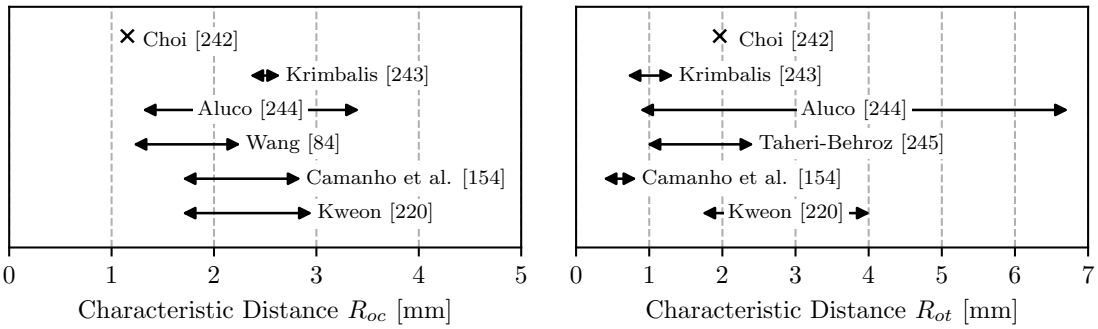

(a) Characteristic distances in compression R_{oc} **(b)** Characteristic distances in tension R_{ot}

Figure D.19 Characteristic distances in tension and compression for a QI laminate based on literature data from [84, 154, 220, 242–245]

List of Figures

List of Tables

Bibliography

[1] René Alderliesten. *Fatigue and Fracture of Fibre Metal Laminates*. Springer International Publishing, 2017.

[2] Ad Vlot and Jan Willem Gunnink, editors. *Fibre Metal Laminates*. Springer Netherlands, 2001.

[3] R.G.J. Van Rooijen. *Bearing Strength Characteristics of Standard and Steel Reinforced GLARE*. phdthesis, TU Delft, 2006.

[4] C.T. Lin, P.W. Kao, and F.S. Yang. Fatigue behaviour of carbon fibre-reinforced aluminium laminates. *Composites*, 22(2):135–141, mar 1991.

[5] C.T. Lin and P.W. Kao. Fatigue delamination growth in carbon fibre-reinforced aluminium laminates. *Composites Part A: Applied Science and Manufacturing*, 27(1):9–15, jan 1996.

[6] W. Steven Johnson, Edward Li, and Jennifer L. Miller. High temperature hybrid titanium composite laminates: An early analytical assessment. *Applied Composite Materials*, 3(6):379–390, 1996.

[7] Westre. Titanium-polymer hybrid laminates, US Patent 6114050A, 2000.

[8] J. M. Hundley, J.-M. Yang, H. T. Hahn, and A. B. Facciano. Bearing strength analysis of hybrid titanium composite laminates. *AIAA Journal*, 46(8):2074–2085, aug 2008.

[9] Jacob M. Hundley, H. Thomas Hahn, Jenn-Ming Yang, and Andrew B. Facciano. Three-dimensional progressive failure analysis of bolted titanium-graphite fiber metal laminate joints. *Journal of Composite Materials*, 45(7):751–769, dec 2010.

[10] Axel Fink. *Lokale Metall-Hybridisierung zur Effizienzsteigerung von Hochlastfügestellen in Faserverbundstrukturen*. PhD thesis, TU Braunschweig, 2010.

[11] Jan Christian Both. *Tragfähigkeit von CFK-Metall-Laminaten and unter and mechanischer und thermischer Belastung*. PhD thesis, Technische Universität München, 2013.

[12] Benedikt Kötter, Julian Karsten, Johann Körbelin, and Bodo Fiedler. CFRP thin-ply fibre metal laminates: Influences of ply thickness and metal layers on open hole tension and compression properties. *Materials*, 13(4):910, feb 2020.

[13] Daniel Stefaniak and Robert Prussak. Chances and challenges in the application of fiber metal laminates. *Advanced Materials Letters*, 10(2):91–97, dec 2018.

[14] Daniel Stefaniak. *Improving residual strength of undirectionally reinforced plastic laminates by metal layering*. PhD thesis, TU Braunschweig, 2017.

[15] Daniel Stefaniak, Robert Prussak, and Lennart Weiß. Specific challenges in the application of fibre-metal laminates. *Lightweight Design*, 10(5):24–31, sep 2017.

[16] A. Fink, B. Kolesnikov, and V. Krajeski. Design study and of the inter and segment joint and of ariane and 5 composite and booster. Technical Report IB-131-2005/09, German Aerospace Center (DLR), 2005.

[17] Alexander Pototzky. Potentials of load carrying, structural integrated conductor tracks. In *SAMPE Europe Conference 2017*, 2017.

[18] Alexander Pototzky, Daniel Stefaniak, and Christian Hühne. Potentials of load carrying conductor tracks in new vehicle structures. In *Technologies for economical and functional lightweight design*, pages 79–90. Springer Berlin Heidelberg, 2019.

[19] Robert Szlosarek, Franziska Bombis, Michel Mühler, and Matthias Kröger. Development of crash and absorbers made and of carbon and fibre-reinforced plastic. *Machine Dynamics Research*, 39(4):65–72, 2016.

[20] Alexander Pototzky, Robert Prussak, and Daniel Stefaniak. *Innovation Report 2019*, chapter Hybrid crash structures made of fiber-metal laminates - Take advantage of material specific properties. German Aerospace Center (DLR), 2019.

[21] A. Fink, P. Camanho, M. Canay, and A. Obst. Increase of bolted joint performance by means of local laminate hybridization. In *1st CEAS European Air and Space Conference*, 2007.

[22] Dennis A Burianek and S.Mark Spearing. Delamination growth from face sheet seams in cross-ply titanium/graphite hybrid laminates. *Composites Science and Technology*, 61(2):261–269, feb 2001.

[23] D. Burianek and S. Spearing. Fatigue damage in titanium-graphite hybrid laminates. *Composites Science and Technology*, 62(5):607–617, apr 2002.

[24] D.A Burianek, A.E Giannakopoulos, and S.M Spearing. Modeling of facesheet crack growth in titanium–graphite hybrid laminates, part i. *Engineering Fracture Mechanics*, 70(6):775–798, apr 2003.

[25] D.A Burianek and S.M Spearing. Modeling of facesheet crack growth in titanium–graphite hybrid laminates. part II: Experimental results. *Engineering Fracture Mechanics*, 70(6):799–812, apr 2003.

[26] D Rhymer. Fatigue damage mechanisms in advanced hybrid titanium composite laminates. *International Journal of Fatigue*, 24(9):995–1001, sep 2002.

[27] W.S. Johnson and M.W. Hammond. Crack growth behavior of internal titanium plies of a fiber metal laminate. *Composites Part A: Applied Science and Manufacturing*, 39(11):1705–1715, nov 2008.

[28] Jacob Michael Hundley. *Multi-Scale Progressive Failure Modelling of Titanium-Graphite Fiber Metal Laminates*. PhD thesis, University of California Los Angeles, 2009.

[29] Boris Kolesnikov. Trennstellenproblematik und experimentelle untersuchungen von cfk/titan-laminaten. Technical Report IB-131-99-66, Deutsches Zentrum für Luft- und Raumfahrt e.V., Institut für Strukturmechanik, 1999.

[30] Axel Fink, Boris Kolesnikov, and Lars Herbeck. Effizienzsteigerung von hochleistungsfaserverbundstrukturen durch lokale cfk/metall verstaerkung. In *Deutscher Luft- und Raumfahrtkongress 2006, 06-09.11.2006, Braunschweig*, 2006.

[31] Willard Westre, David W. Evans, Edward Li, Marc J. Piehl, and Eric Sager. Titanium foil ply replacement in layup of composite skin, 2006.

[32] Christos C. Chamis and Raymond F. Lark. Hybrid composite laminate structures, 1977.

[33] Boris Kolesnikov, Holger Wilmes, Axel Herrmann, and Arno Pabsch. Verbundmaterial mit einem verstaerkten verbindungsbereich, 2002.

[34] A. Fink, B. Kolesnikov, L. Herbeck, and S. Erwig. Verbundmaterial, 2009.

[35] Boris Kolesnikov, Axel Fink, Christian Huhne, Daniel Stefaniak, and Henrik Borgwardt. Strukturelement aus einem hybridlaminat, 2012.

[36] De Paula Francisco, Benavides Daniel Escobar, Claret Viros, and Rafael Avila Dominguez. Metallic local reinforcement for heavy loaded joints of composite components, 2007.

[37] A. Fink, P.P. Camanho, J.M. Andrés, E. Pfeiffer, and A. Obst. Hybrid CFRP/titanium bolted joints: Performance assessment and application to a spacecraft payload adaptor. *Composites Science and Technology*, 70(2):305–317, feb 2010.

[38] Enno Petersen. *Auslegung des Metalllagenauslaufs bei lokaleer Stahlhybridisierung von Kohlenstofffaser-Kunststoff-Laminaten*. PhD thesis, TU Braunschweig, 2019.

[39] Andreas Monden. *Adhäsion zwischen epoxidharzbasiertem CFK und oberflächenmodifiziertem Stahl: Grenzschichtversagen von Hybridlaminaten unter Mode I, Mode II und Mixed-Mode Belastung*. PhD thesis, Universität Augsburg, 2016.

[40] Sandra Polesky Walker. *Thermal Effects on the Bearing Behavior of Composite Joints*. PhD thesis, Virginia Univ., Graduate School of Engineering and Applied Science, United States, 2001.

[41] Noriyoshi Hirano, Yoshihiro Takao, and Wen-Xue Wang. Effects of temperature on the bearing strength of CF/epoxy pinned joints. *Journal of Composite Materials*, 41(3):335–351, may 2006.

[42] Y. Takao. Effects of temperature on the response of composite bolted joints. In *Composite Joints and Connections*, pages 295–319. Elsevier, 2011.

[43] L.E. Asp. The effects of moisture and temperature on the interlaminar delamination toughness of a carbon/epoxy composite. *Composites Science and Technology*, 58(6):967–977, jan 1998.

[44] J. A. Nairn. On the calculation of energy release rates for cracked laminates with residual stresses. *International Journal of Fracture*, 139(2):267–293, may 2006.

[45] Tomohiro Yokozeki, Toshio Ogasawara, and Takahira Aoki. Correction method for evaluation of interfacial fracture toughness of DCB, ENF and MMB specimens with residual thermal stresses. *Composites Science and Technology*, 68(3-4):760–767, mar 2008.

[46] Sandra Polesky Walker. Thermal effects on the compressive behavior of IM7/PETI5 laminates. *Journal of Composite Materials*, 38(2):149–162, jan 2004.

[47] B. Fiedler, A. Gagel, T. Hobbiebrunken, K. Schulte, M. Hojo, and S. Ochiai. Modelling of the transverse strength of fibre reinforced epoxy composite at low and high temperature. *Composite Interfaces*, 12(3-4):379–394, jan 2005.

[48] W. Schneider. Wärmeausdehnungskoeffizienten und wärmespannung von glasfaser/kunststoffverbunden — erwärmung bzw. abkühlung von wickelrohren und innendruck. *Kunststoffe*, (63):929–933, 1973.

[49] Satoshi Kobayashi, Kazuhiro Terada, Shinji Ogihara, and Nobuo Takeda. Damage-mechanics analysis of matrix cracking in cross-ply CFRP laminates under thermal fatigue. *Composites Science and Technology*, 61(12):1735–1742, sep 2001.

[50] M.M. Moure, S.K. García-Castillo, S. Sánchez-Sáez, E. Barbero, and E.J. Barbero. Matrix cracking evolution in open-hole laminates subjected to thermomechanical loads. *Composite Structures*, 183:510–520, jan 2018.

[51] Bhagwan D. Agarwal, Lawrence J. Broutman, and K. Chandrashekhara. *Analysis and performance of fiber composites*. Wiley, 2006.

[52] Kevin D. Cowley and Peter W.R. Beaumont. The measurement and prediction of residual stresses in carbon-fibre/polymer composites. *Composites Science and Technology*, 57(11):1445–1455, jan 1997.

[53] J.A. Barnes and G.E. Byerly. The formation of residual stresses in laminated thermoplastic composites. *Composites Science and Technology*, 51(4):479–494, jan 1994.

[54] M.M. Shokrieh and S.M. Kamali Shahri. Modeling residual stresses in composite materials. In *Residual Stresses in Composite Materials*, pages 173–193. Elsevier, 2014.

[55] Helmut Schürmann. *Konstruieren mit Faser-Kunststoff-Verbunden*. Springer Berlin Heidelberg, 2005.

[56] Yoshihiko Arao, Jun KOYANAGI, Yukie OKUDOI, Masanori OTSUKA, and Hiroyuki KAWADA. Residual stress relaxation in CFRP cross-ply laminate. *Journal of Solid Mechanics and Materials Engineering*, 4(11):1595–1604, 2010.

[57] Joachim Roesler, Harald Harders, and Martin Baecker. *Mechanisches Verhalten der Werkstoffe*. Vieweg + Teubner, 2008.

[58] N. J. Pagano and H. T. Hahn. Evaluation of composite curing stresses. In *Solid Mechanics and Its Applications*, pages 57–69. Springer Netherlands, 1994.

[59] R. Prussak, D. Stefaniak, C. Hühne, and M. Sinapius. Evaluation of residual stress development in FRP-metal hybrids using fiber bragg grating sensors. *Production Engineering*, 12(2):259–267, jan 2018.

[60] Robert Prussak, Daniel Stefaniak, Erik Kappel, Christian Hühne, and Michael Sinapius. Smart cure cycles for fiber metal laminates using embedded fiber bragg grating sensors. *Composite Structures*, 213:252–260, apr 2019.

[61] Robert Prussak, Daniel Stefaniak, Christian Hühne, and Michael Sinapius. Residual stresses in intrinsic UD-CFRP-steel-laminates - experimental determination, identification of sources, effects and modification approaches. *Materials Science Forum*, 825-826:369–376, jul 2015.

[62] Johannes Wiedemann, Robert Prussak, Erik Kappel, and Christian Hühne. In-situ quantification of manufacturing-induced strains in fiber metal laminates with strain gages. *Composite Structures*, 297:115967, October 2022.

[63] Till Haberle. *Thermomechanik werkstoffhybrider, faserverstärkter Schichtverbunde und Bauteile bei tiefen Temperaturen*. PhD thesis, Technische Universität Múnchen, 2001.

[64] Cryogenic materials data handbook vol. i. Technical Report AFML-DR-64-280, Air Force Materials Laboratory, 1970.

[65] B. Kolesnikov, L. Herbeck, and A. Fink. CFRP/titanium hybrid material for improving composite bolted joints. *Composite Structures*, 83(4):368–380, jun 2008.

[66] P.P. Camanho, A. Fink, A. Obst, and S. Pimenta. Hybrid titanium–CFRP laminates for high-performance bolted joints. *Composites Part A: Applied Science and Manufacturing*, 40(12):1826–1837, dec 2009.

[67] P. Camanho, P. Portela, A. Melro, and M. Lambert. Enhanced design methods for mechanically fastened joints in composite structures. In *European Conference on Spacecraft Structures, Materials and Mechanical Testing*, 2005.

[68] L. J. Hart-Smith. Design and analysis of bolted and riveted joints in fibrous composite structures. In *Recent Advances in Structural Joints and Repairs for Composite Materials*, pages 211–254. Springer Netherlands, 2003.

[69] T.A. Collings. The strength of bolted joints in multi-directional cfrp laminates. *Composites*, 8(1):43–55, jan 1977.

[70] Alaattin Aktas and M.Husnu Dirikolu. The effect of stacking sequence of carbon epoxy composite laminates on pinned-joint strength. *Composite Structures*, 62(1):107–111, oct 2003.

[71] P.A. Smith and K.J. Pascoe. The effect of stacking sequence on the bearing strengths of quasi-isotropic composite laminates. *Composite Structures*, 6(1-3):1–20, jan 1986.

[72] F. L. Matthews and P. P. Camanho. Stresses in mechanical fastened joints. In *Recent Advances in Structural Joints and Repairs for Composite Materials*, pages 67–100. Springer Netherlands, 2003.

[73] K. Shivakumar and J. Crews. Bolt clampup relaxation in a graphite/epoxy laminate. Technical report, NASA, 1982.

[74] F.L. Matthews, P.F. Kilty, and E.W. Godwin. Load-carrying joints in fibre reinforced plastics. *Plastic and Rubber Process and Applications*, 2:19–25, 1982.

[75] Pedri Camanho and Liyong Tong, editors. *Composite Joints and Connections*. Elsevier Science, 2011.

[76] Liyong Tong and Costas Soutis, editors. *Recent Advances in Structural Joints and Repairs for Composite Materials*. Springer Netherlands, 2003.

[77] T. Yamada, H. Nakatan, and S. Ogihara. Evaluation of bearing damage behavior in thin titanium films-cfrp laminate. In *ICCM19*, 2013.

[78] Claudio Scarponi, Giuseppe Marini, and Paolo Montanari. The importance of the temperature and lateral pressure on the CFRP joints strength under uniaxial loading. *Journal of Reinforced Plastics and Composites*, 16(9):825–847, jun 1997.

[79] J. C. Perry and M. W. Hyer. Investigations into the mechanical behavior of composite bolted joints. Technical Report NASA-CR-158752, NASA, 1979.

[80] W. A. Counts and W. S. Johnson. Temperature effects on ultimate bearing strength of polymeric composite joints. *Journal of Composites Technology and Research*, 24(1):17, 2002.

[81] Sanjib Goswami. A finite element investigation on progressive failure analysis of composite bolted joints under thermal environment. *Journal of Reinforced Plastics and Composites*, 24(2):161–171, jan 2005.

[82] Noriyoshi Hirano, Yoshihiro Takao, and Wen-Xue Wang. Effects of temperature on the bearing strength of CF/epoxy bolted joints. Technical report, Research Institute for Applied Mechanics, University of Kyushu, 2008.

[83] Carlos Santiuste, Enrique Barbero, and María Henar Miguélez. Computational analysis of temperature effect in composite bolted joints for aeronautical applications. *Journal of Reinforced Plastics and Composites*, 30(1):3–11, oct 2010.

[84] Hong-Sheng Wang, Chang-Li Hung, and Fu-Kuo Chang. Bearing failure of bolted composite joints. part i: Experimental characterization. *Journal of Composite Materials*, 30(12):1284–1313, aug 1996.

[85] S Sánchez-Sáez, T Gómez del Río, E Barbero, R Zaera, and C Navarro. Static behavior of CFRPs at low temperatures. *Composites Part B: Engineering*, 33(5):383–390, jul 2002.

[86] B. W. Rosen. Influence of fiber and matrix characteristics on mechanics of deformation and fracture of fibrous composite. In *FIBER COMPOSITE MATERIALS, SEMINAR OF THE AMERICAN SOCIETY FOR METALS*, 1965.

[87] Y. Shindo, K. Horiguchi, R. Wang, and H. Kudo. Double cantilever beam measurement and finite element analysis of cryogenic mode i interlaminar fracture toughness of glass-cloth/epoxy laminates. *Journal of Engineering Materials and Technology*, 123(2):191, 2001.

[88] R.P. Reed and M. Golda. Cryogenic properties of unidirectional composites. *Cryogenics*, 34(11):909–928, jan 1994.

[89] Enno Petersen. Kritische betrachtung der versuchsmöglichkeiten zur bestimmung der elastizitätsgrößen, festigkeits- und reibungswerte für den transversalisotropen werkstoff. Technical report, Deutsches Zentrum für Luft- und Raumfahrt (DLR), 2013.

[90] M. Vrh, M. Halilovič, and B. Štok. The evolution of effective elastic properties of a cold formed stainless steel sheet. *Experimental Mechanics*, 51(5):677–695, jun 2010.

[91] E. Petersen, R.G. Cuntze, and C. Hühne. Experimental determination of material parameters in cuntze's failure-mode-concept-based UD strength failure conditions. *Composites Science and Technology*, 134:12–25, oct 2016.

[92] J. Koord and C. Hühne. Effect of low temperature on interlaminar fracture toughness of multi-directional cfrp and cfrp-steel interfaces. *Composites Part B: Engineering*, 281:111540, July 2024.

[93] Dietmar Gross and Thomas Seelig. *Bruchmechanik*. Springer Berlin Heidelberg, 2016.

[94] A.B. Pereira and A.B. de Morais. Mode i interlaminar fracture of carbon/epoxy multidirectional laminates. *Composites Science and Technology*, 64(13-14):2261–2270, oct 2004.

[95] Herzl Chai. Interlaminar shear fracture of laminated composites. *International Journal of Fracture*, 43(2):117–131, may 1990.

[96] Jianxin Tao and C. T. Sun. Influence of ply orientation on delamination in composite laminates. *Journal of Composite Materials*, 32(21):1933–1947, nov 1998.

[97] Jarosław Bieniaś, Konrad Dadej, and Barbara Surowska. Interlaminar fracture toughness of glass and carbon reinforced multidirectional fiber metal laminates. *Engineering Fracture Mechanics*, 175:127–145, apr 2017.

[98] Hyoung Soo Kim, Wen-Xue Wang, and Yoshihiro Takao. Effects of temperature and fiberorientation on the mode i interlaminar fracture toughness of carbon/epoxy composites. In *ICCM12*, 1999.

[99] P. Coronado, A. Argüelles, J. Viña, V. Mollón, and I. Viña. Influence of temperature on a carbon–fibre epoxy composite subjected to static and fatigue loading under mode-i delamination. *International Journal of Solids and Structures*, 49(21):2934–2940, oct 2012.

[100] P. Coronado, A. Argüelles, J. Viña, and I. Viña. Influence of low temperatures on the phenomenon of delamination of mode i fracture in carbon-fibre/epoxy composites under fatigue loading. *Composite Structures*, 112:188–193, jun 2014.

[101] Patricia Coronado, Pedro Camanho, Antonio Argüelles, Jaime Viña, and Sara Sánchez. Low temperature and resin effects on the mode i interlaminar fracture toughness in aeronautical quality polymer composites. *Proceedings*, 2(23):1478, nov 2018.

[102] C.D. Rans and R.C. Alderliesten. The influence of temperature on crack growth in fibre metal laminates. In *12th International Conference on Fracture*, 2009.

[103] JE Schut and Alderliesten RC. Delamination growth rate at low and elevated temperatures in glare. In *25TH INTERNATIONAL CONGRESS OF THE AERONAUTICAL SCIENCES (ICAS 2006)*, 2006.

[104] C.D. Rans, R.C. Alderliesten, and R. Benedictus. Predicting the influence of temperature on fatigue crack propagation in fibre metal laminates. *Engineering Fracture Mechanics*, 78(10):2193–2201, jul 2011.

[105] Astm d5528, test method for mode i interlaminar fracture toughness of unidirectional fiber-reinforced polymer matrix composites, 2013.

[106] Astm d7905, test method for determination of the mode II interlaminar fracture toughness of unidirectional fiber-reinforced polymer matrix composites, 2019.

[107] Astm d6671, test method for mixed mode i-mode II interlaminar fracture toughness of unidirectional fiber reinforced polymer matrix composites, 2019.

[108] Klaus Friedrich. *Application of fracture mechanics to composite materials*. Elsevier Distributors for the U.S. and Canada, Elsevier Science Pub. Co, Amsterdam New York New York, NY USA, 1989.

[109] P. Prombut, L. Michel, F. Lachaud, and J.J. Barrau. Delamination of multidirectional composite laminates at $0^\circ/\theta^\circ$ ply interfaces. *Engineering Fracture Mechanics*, 73(16):2427–2442, nov 2006.

[110] N. S. Choi, A. J. Kinloch, and J. G. Williams. Delamination fracture of multidirectional carbon-fiber/epoxy composites under mode i, mode II and mixed-mode i/II loading. *Journal of Composite Materials*, 33(1):73–100, jan 1999.

[111] P. Robinson and D.Q. Song. A modified DCB specimen for mode i testing of multidirectional laminates. *Journal of Composite Materials*, 26(11):1554–1577, nov 1992.

[112] Shu Guo, David A. Dillard, and John A. Nairn. Effect of residual stress on the energy release rate of wedge and DCB test specimens. *International Journal of Adhesion and Adhesives*, 26(4):285–294, jul 2006.

[113] Paul W. Harper and Stephen R. Hallett. Cohesive zone length in numerical simulations of composite delamination. *Engineering Fracture Mechanics*, 75(16):4774–4792, nov 2008.

[114] Panayiotis Tsokanas, Theodoros Loutas, Dimitrios Pegkos, George Sotiriadis, and Vassilis Kostopoulos. Mode II fracture toughness of asymmetric metal-composite adhesive joints. *MATEC Web of Conferences*, 304:01004, 2019.

[115] Theodoros Loutas, Panayiotis Tsokanas, Vassilis Kostopoulos, Peter Nijhuis, and Wouter M. van den Brink. Mode i fracture toughness of asymmetric metal-composite adhesive joints. *Materials Today: Proceedings*, mar 2020.

[116] J. Koord, J.-L. Stüven, E. Petersen, O. Völkerink, and C. Hühne. Investigation of exact analytical solutions for circular notched composite laminates under tensile loading. *Composite Structures*, 243:112180, jul 2020.

[117] J. Kosmann, O. Vólkerink, M.J. Schollerer, D. Holzhúter, and C. Húhne. Digital image correlation strain measurement of thick adherend shear test specimen joined with an epoxy film adhesive. *International Journal of Adhesion and Adhesives*, 90:32–37, apr 2019.

[118] J. Koord and C. Hühne. Bolt-bearing behavior of hybrid cfrp-steel laminates at low temperature. *Journal of Composite Materials*, 24(287), 2024.

[119] E. Petersen, D. Stefaniak, and C. Hühne. Experimental investigation of load carrying mechanisms and failure phenomena in the transition zone of locally metal reinforced joining areas. *Composite Structures*, 182:79–90, dec 2017.

[120] P. P. Camanho, C. G. Davila, and M. F. de Moura. Numerical simulation of mixed-mode progressive delamination in composite materials. *Journal of Composite Materials*, 37(16):1415–1438, aug 2003.

[121] Ronald Krueger. Virtual crack closure technique: History, approach, and applications. *Applied Mechanics Reviews*, 57(2):109–143, mar 2004.

[122] S. Karmakov, F. Cepero-Mejías, and J.L. Curiel-Sosa. Numerical analysis of the delamination in CFRP laminates: VCCT and XFEM assessment. *Composites Part C: Open Access*, 2:100014, oct 2020.

[123] O. Völkerink, J. Koord, E. Petersen, and C. Hühne. Holistic determination of physical fracture toughness values and numerical parameters for delamination analysis considering multidirectional-interfaces. *Composites Part C: Open Access*, 8:100277, jul 2022.

[124] J. Koord, O. Völkerink, E. Petersen, and C. Hühne. Effect of low temperature on mode i and mode II interlaminar fracture toughness of CFRP-steel hybrid laminates. *Composites Part B: Engineering*, 262:110773, aug 2023.

[125] A. Turon, C.G. Dávila, P.P. Camanho, and J. Costa. An engineering solution for mesh size effects in the simulation of delamination using cohesive zone models. *Engineering Fracture Mechanics*, 74(10):1665–1682, jul 2007.

[126] Albert Turon. *SIMULATION OF DELAMINATION IN COMPOSITES UNDER QUASI-STATIC AND FATIGUE LOADING USING COHESIVE ZONE MODELS*. PhD thesis, Universitat de Girona, 2007.

[127] X. Lu, M. Ridha, B.Y. Chen, V.B.C. Tan, and T.E. Tay. On cohesive element parameters and delamination modelling. *Engineering Fracture Mechanics*, 206:278–296, feb 2019.

[128] Z. Zou, S. R. Reid, S. Li, and P. D. Soden. Modelling interlaminar and intralaminar damage in filament-wound pipes under quasi-static indentation. *Journal of Composite Materials*, 36(4):477–499, feb 2002.

[129] A. Hillerborg, M. Modéer, and P.-E. Petersson. Analysis of crack formation and crack growth in concrete by means of fracture mechanics and finite elements. *Cement and Concrete Research*, 6(6):773–781, nov 1976.

[130] Qingda Yang and Brian Cox. Cohesive models for damage evolution in laminated composites. *International Journal of Fracture*, 133(2):107–137, may 2005.

[131] E Petersen, E Kappel, J Koord, O Völkerink, and C Hühne. Determination of stresses, strains and failure types in multidirectional laminates under pure bending. *Journal of Composite Materials*, 54(28):4397–4413, jun 2020.

[132] A. Turon, P.P. Camanho, J. Costa, and C.G. Dávila. A damage model for the simulation of delamination in advanced composites under variable-mode loading. *Mechanics of Materials*, 38(11):1072–1089, nov 2006.

[133] M.L. Benzeggagh and M. Kenane. Measurement of mixed-mode delamination fracture toughness of unidirectional glass/epoxy composites with mixed-mode bending apparatus. *Composites Science and Technology*, 56(4):439–449, 1996.

[134] J. Both, D. Barfuß, and H. Baier. Mode ii delamination of cfrp-metal laminates at bolted joints. In *18TH INTERNATIONAL CONFERENCE ONCOMPOSITEMATERIALS*, 2011.

[135] Monika Kamocka and Radosław J. Mania. Numerical study of axially compressed FML profile including delamination. In *AIP Conference Proceedings*. Author(s), 2019.

[136] Hieu T.X. Truong, Marcias J. Martinez, Ozden O. Ochoa, and Dimitris C. Lagoudas. Mode i fracture toughness of hybrid co-cured al-CFRP and NiTi-CFRP interfaces: An experimental and computational study. *Composites Part A: Applied Science and Manufacturing*, 135:105925, aug 2020.

[137] Youqiang Yao, Pengcheng Shi, Mingda Chen, Gang Chen, Cong Gao, Philippe Boisse, and Yingdan Zhu. Experimental and numerical study on mode i and mode II interfacial fracture toughness of co-cured steel-CFRP hybrid composites. *International Journal of Adhesion and Adhesives*, 112:103030, jan 2022.

[138] G. Zambelis, T. Da Silva Botelho, O. Klinkova, I. Tawfiq, and C. Lanouette. Evaluation of the energy release rate in mode i of asymmetrical bonded composite/metal assembly. *Engineering Fracture Mechanics*, 190:175–185, mar 2018.

[139] Tomohiro Yokozeki. Energy release rates of bi-material interface crack including residual thermal stresses: Application of crack tip element method. *Engineering Fracture Mechanics*, 77(1):84–93, jan 2010.

[140] Claudia Cardoso. *Hybrid CFRP/Titanium bolted joints*. PhD thesis, University of Porto, 2016.

[141] Christian Gerendt, Aamir Dean, Thorsten Mahrholz, and Raimund Rolfes. On the progressive failure simulation and experimental validation of fiber metal laminate bolted joints. *Composite Structures*, 229:111368, dec 2019.

[142] Kunal Masania, Roman Geissberger, Daniel Stefaniak, and Clemens Dransfeld. Steel foilf reinforced composites: Study of strength, plasticity and ply size effects. In *20th International Conference on Composite Materials*, 2015.

[143] Z. Hashin. Failure criteria for unidirectional fiber composites. *Journal of Applied Mechanics*, 47(2):329–334, jun 1980.

[144] Y.-M. Kuo, H.-J. Lin, C.-N. Wang, and C.-I Liao. Estimating the elastic modulus through the thickness direction of a uni-direction lamina which possesses transverse isotropic property. *Journal of Reinforced Plastics and Composites*, 26(16):1671–1679, sep 2007.

[145] A. Parvizi, K. W. Garrett, and J. E. Bailey. Constrained cracking in glass fibre-reinforced epoxy cross-ply laminates. *Journal of Materials Science*, 13(1):195–201, jan 1978.

[146] F.W. Crossman, W.J. Warren, A.S.D. Wang, and G.E. Law. Initiation and growth of transverse cracks and edge delamination in composite laminates part 2. experimental correlation. *Journal of Composite Materials*, 14(1):88–108, jan 1980.

[147] Iqbal Shahid and Fu-Kuo Chang. An accumulative damage model for tensile and shear failures of laminated composite plates. *Journal of Composite Materials*, 29(7):926–981, may 1995.

[148] Donald L. Flaggs and Murat H. Kural. Experimental determination of the in situ transverse lamina strength in graphite/epoxy laminates. *Journal of Composite Materials*, 16(2):103–116, mar 1982.

[149] George J. Dvorak and Norman Laws. Analysis of progressive matrix cracking in composite laminates II. first ply failure. *Journal of Composite Materials*, 21(4):309–329, apr 1987.

[150] S.C. Tan and R.J. Nuismer. A theory for progressive matrix cracking in composite laminates. *Journal of Composite Materials*, 23(10):1029–1047, oct 1989.

[151] Pedro P. Camanho, Carlos G. Dávila, Silvestre T. Pinho, Lorenzo Iannucci, and Paul Robinson. Prediction of in situ strengths and matrix cracking in composites under transverse tension and in-plane shear. *Composites Part A: Applied Science and Manufacturing*, 37(2):165–176, feb 2006.

[152] ST Pinho, R Darvizeh, P Robinson, C Schuecker, and PP Camanho. Material and structural response of polymer-matrix fibre-reinforced composites. *Journal of Composite Materials*, 46(19-20):2313–2341, sep 2012.

[153] ST Pinho, GM Vyas, and P Robinson. Response and damage propagation of polymer-matrix fibre-reinforced composites: Predictions for WWFE-III part a. *Journal of Composite Materials*, 47(20-21):2595–2612, mar 2013.

[154] P.P. Camanho and M. Lambert. A design methodology for mechanically fastened joints in laminated composite materials. *Composites Science and Technology*, 66(15):3004–3020, dec 2006.

[155] C. Furtado, A. Arteiro, P. Linde, B.L. Wardle, and P.P. Camanho. Is there a ply thickness effect on the mode i intralaminar fracture toughness of composite laminates? *Theoretical and Applied Fracture Mechanics*, 107:102473, jun 2020.

[156] Michael W. Czabaj and James G. Ratcliffe. Comparison of intralaminar and interlaminar mode-i fracture toughness of unidirectional im7/8552 graphite/epoxy composite. In *15th US-Japan Conference on Composite Materials*, 2012.

[157] P. Maimí, P.P. Camanho, J.A. Mayugo, and C.G. Dávila. A continuum damage model for composite laminates: Part i – constitutive model. *Mechanics of Materials*, 39(10):897–908, oct 2007.

[158] P. P. Camanho and F. L. Matthews. A progressive damage model for mechanically fastened joints in composite laminates. *Journal of Composite Materials*, 33(24):2248–2280, dec 1999.

[159] Yi Xiao and Takashi Ishikawa. Bearing strength and failure behavior of bolted composite joints (part II: modeling and simulation). *Composites Science and Technology*, 65(7-8):1032–1043, jun 2005.

[160] Gordon Kelly and Stefan Hallström. Bearing strength of carbon fibre/epoxy laminates: effects of bolt-hole clearance. *Composites Part B: Engineering*, 35(4):331–343, jan 2004.

[161] M.A. McCarthy, V.P. Lawlor, W.F. Stanley, and C.T. McCarthy. Bolt-hole clearance effects and strength criteria in single-bolt, single-lap, composite bolted joints. *Composites Science and Technology*, 2002.

[162] V.P. Lawlor, M.A. McCarthy, and W.F. Stanley. An experimental study of bolt–hole clearance effects in double-lap, multi-bolt composite joints. *Composite Structures*, 71(2):176–190, nov 2005.

[163] C. T. McCarthy, M. A. McCarthy, W. F. Stanley, and V. P. Lawlor. Experiences with modeling friction in composite bolted joints. *Journal of Composite Materials*, 39(21):1881–1908, jun 2005.

[164] O. Völkerink, E. Petersen, J. Koord, and C. Hühne. A pragmatic approach for a 3d material model considering elasto-plastic behaviour, damage initiation by puck or cuntze and progressive failure of fibre-reinforced plastics. *Composite Structures*, 236:106280, aug 2020.

[165] C. Hühne, A.-K. Zerbst, G. Kuhlmann, C. Steenbock, and R. Rolfes. Progressive damage analysis of composite bolted joints with liquid shim layers using constant and continuous degradation models. *Composite Structures*, 92(2):189–200, jan 2010.

[166] Christos C. Chamis. Simplified procedures for designing composite bolted joints. *Journal of Reinforced Plastics and Composites*, 9(6):614–626, nov 1990.

[167] VDI-Fachbereich Kunststofftechnik. Development of fibre-reinforced plastics components - analysis, 2006.

[168] L. Herbeck and H. Wilmes. Design rules for a cfrp outer wing. In *ICAS 2002 23rd International Congress of Aeronautical Sciences*, 2002.

[169] H. Wilmes, A.S. Hermann, B. Kolesnikov, and I. Kröber. Festigkeitsanalysen von bolzenverbindungen für cfk-bauteile mit dem ziel der erstellung von dimensionierungsrichtlinien. In *Deutscher Luft- und Raumfahrtkongreß 1999 - DGLR-Jahrestagung*, 1999.

[170] L. J. Hart-Smith. Bolted joints in graphite epoxy composites. Technical Report CR-144899, NASA, 1977.

[171] M.M. Focht and H.N. Hill. Stress-concentration factors around a central circular hole in a plate loaded through pin in the hole. *Journal of Applied Mechanics*, 1940.

[172] R. Heywood. Designing by photoelasticity. *Chapman and Hall (London)*, 1952.

[173] S. Tan. Finite-width correction factors for anisotropic plates conatining a central opening. *Journal of Composite Materials*, 1988.

[174] Echavarria. *Analyse d'une plaque orthotrope avec trou: Application aux assemblages en bois*. PhD thesis, Ecole Polytechnique Federeale de Lausanne, 2004.

[175] S.G. Lekhnitskii. *Anisotropic plates*. New York : Gordon and Breach, 1968. translated from the second Russian edition by S.W. Tsai and T. Cheron.

[176] DW Oplinger and KR Gandhi. Stresses in mechanically fastened orthotropic laminates. In *Proceedings of the 2nd Conference on Fibrous Composites in Flight Vehicle Design*, 1974.

[177] T. De Jong. The influence of friction on the theoretical strength of pin-loaded holesorthotropic plates. Technical Report Report LR-350, TU Delft, 1982.

[178] T. De Jong and E.C. Klang. Pinned connections in composite materials. Technical Report Report LR-445, TU Delft, 1985.

[179] Kai-Da Zhang and Charles E.S. Ueng. Stresses around a pin-loaded hole in orthotropic plates. *Journal of Composite Materials*, 18(5):432–446, sep 1984.

[180] K. Zhang and C.E.S Ueng. Stresses around a pin-loaded hole in orthotropic plateswith arbitrary loading direction. *Composite Structures*, 1985.

[181] M.W. Hyer and E.C. Klang. Contact stresses in pin-loaded orthotropic plates. *International Journal of Solids and Structures*, 21(9):957–975, jan 1985.

[182] E. Madenci and L. Ileri. Analytical determination of contact stresses in mechanically fastened composite laminates with finite boundaries. *International Journal of Solids and Structures*, 30(18):2469–2484, 1993.

[183] N.A. Tomlinson. *Determination of the contact stress distribution in pin loaded orthotropic plates*. PhD thesis, Howard University, 2006.

[184] O. Aluko and H.A. Whitworth. Analysis of stress distribution around pin loaded holes in orthotropic plates. *Composite Structures*, 86(4):308–313, dec 2008.

[185] T. Brander. Mechanical joints. Technical Report heoretical background of ESAComp analyses version 4.4, ESAComp, 2012.

[186] V. Kradinov, A.Barut, and E.Madenci. Bolted double-lap composite joints under mechanical and thermal loading. Technical report, NASA, 2000.

[187] R. L. Ramkumar. Strength analysis of composite and metallic plates bolted togetherby a single fastener. Technical Report AFWAL-TR-85-3064, NASA, 1985.

[188] B Grueber, W Hufenbach, and L Krolland M Lepperand B Zhou. Stress concentration analysis of fibre-reinforced multilayered composites with pin-loaded holes. *Composites Science and Technology*, 67(7-8):1439–1450, jun 2007.

[189] M. Nguyen-Hoang and W. Becker. Stress analysis of finite dimensions bolted joints using the airy stress function. *International Journal of Solids and Structures*, 224:111023, aug 2021.

[190] P.P. Camanho and F.L. Matthews. Stress analysis and strength prediction of mechanically fastened joints in FRP: a review. *Composites Part A: Applied Science and Manufacturing*, 28(6):529–547, jan 1997.

[191] N. Muskhelishvili. *Some Basic Problems of the Mathematical Theory of Elasticity*. Springer, Leyden, The Nethderlands, 1953.

[192] Xin-Lin Gao. A general solution of an infinite elastic plate with an elliptic hole under biaxial loading. *International Journal of Pressure Vessels and Piping*, 67(1):95–104, jun 1996.

[193] Junshan Hu, Kaifu Zhang, Hui Cheng, Ping Liu, Peng Zou, and Danlong Song. Stress analysis and damage evolution in individual plies of notched composite laminates subjected to in-plane loads. *Chinese Journal of Aeronautics*, 30(1):447–460, feb 2017.

[194] R. D. B. Sevenois and S. Koussios. Analytic methods for stress analysis of two-dimensional flat anisotropic plates with notches: An overview. *Applied Mechanics Reviews*, 66(6):060802, jun 2014.

[195] C. Soutis and C. Filiou. Stress distributions around holes in composite laminates subjected to biaxial loading. *Applied Composite Materials*, 5(6):365–378, 1998.

[196] C. Filiou and C. Soutis. Compression-failure modelling under biaxial loading. Technical report, Imperial College, Progress Report II, Agreement No. SMCFU/654, DRA, 1995.

[197] G.N. Savin. *Stress Distribution Around Holes*. Nasa Technical Translation, 1968.

[198] Yuejin Liang and Markku Palanterä. Notched laminates. (Part IV Laminate Discontinuities) Version 1.5, Theoretical Background of ESAComp Analyses, 1999.

[199] V.G. Ukadgaonker and D.K.N. Rao. A general solution for stresses around holes in symmetric laminates under inplane loading. *Composite Structures*, 49(3):339–354, jul 2000.

[200] César Echavarría, Peer Haller, and Alexander Salenikovich. Analytical study of a pin–loaded hole in elastic orthotropic plates. *Composite Structures*, 79(1):107–112, jun 2007.

[201] T.K. Tung. On computation of stresses around holes in anisotropic plates. *Journal of Composite Materials*, 21(2):100–104, feb 1987.

[202] F.Z. Hu, C. Soutis, and E.C. Edge. Interlaminar stresses in composite laminates with a circular hole. *Composite Structures*, 37(2):223–232, feb 1997.

[203] M.A. Caminero, M. Lopez-Pedrosa, C. Pinna, and C. Soutis. Damage monitoring and analysis of composite laminates with an open hole and adhesively bonded repairs using digital image correlation. *Composites Part B: Engineering*, 53:76–91, oct 2013.

[204] Fu-Kuo Chang, Richard A. Scott, and George S. Springer. Strength of mechanically fastened composite joints. *Journal of Composite Materials*, 16(6):470–494, nov 1982.

[205] J.M. Whitney and R.J. Nuismer. Stress fracture criteria for laminated composites containing stress concentrations. *Journal of Composite Materials*, 8(3):253–265, jul 1974.

[206] Xiwu Xu, Liangxin Sun, and Xuqi Fan. Stress concentration of finite composite laminates with elliptical hole. *Computers & Structures*, 57(1):29–34, oct 1995.

[207] ESAComp. *ESAComp Example Cases for Version 4.6.0*.

[208] J. Koord, J.-L. Stüven, O. Völkerink, E. Petersen, and C. Hühne. Investigation of exact analytical solutions for composite laminates under pin-bearing loading. *Composite Structures*, 292:115605, jul 2022.

[209] J.P. Waszczak and T.A. Cruse. A synthesis procedure for mechanically fastened joints in advanced composite materials. Technical Report AFML-TR-73-45, Air Force Materials Laboratory, 1973.

[210] T. DeJong and H.A. Vuil. Stresses around pin-loaded holes in elastically orthotropic plates with arbitrary load direction. Technical Report LR-333, TU Delft, 1981.

[211] F.X. Irisarri, T. Vandellos, P. Paulmier, and F. Launrin. Experiments and modeling of clamping effects on the bearing strength of mechanically fastened joint in cfrp laminates. In *16th European Conference on Composite Materials*, 2014.

[212] Jan-Lukas Stüven. Comparison of analytical methods calculating the stress distribution in a pin-loaded composite plate with subsequent strength analysis. Master's thesis, Universität Bremen, 2021.

[213] Tadasu Tsukizoe and Nobu Ohmae. Friction and wear performance of unidirectionally oriented glass, carbon, aramid and stainless steel fiber-reinforced plastics. In *Friction and Wear of Polymer Composites*, pages 205–231. Elsevier, 1986.

[214] P.D. Herrington and M. Sabbaghian. Factors affecting the friction coefficients between metallic washers and composite surfaces. *Composites*, 22(6):418–424, nov 1991.

[215] Y. Yan, W.-D. Wen, F.-K. Chang, and P. Shyprykevich. Experimental study on clamping effects on the tensile strength of composite plates with a bolt-filled hole. *Composites Part A: Applied Science and Manufacturing*, 30(10):1215–1229, oct 1999.

[216] J.M. Ogonowski. Effect of variances and manufacturing tolerances on the design strength and life of mechanically fastened composite joints. volume 1. methodology development and data evaluation. Technical Report AFWAL-TR-81-3041, MCDONNELL AIRCRAFT CO ST LOUIS MO, 1981.

[217] Theo De Jong. Stresses around pin-loaded holes in elastically orthotropic or isotropic plates. *Journal of Composite Materials*, 11(3):313–331, jul 1977.

[218] P. Berbinau, C. Filiou, and C. Soutis. Stress and failure analysis of composite laminates with an inclusion under multiaxial compression-tension loading. *Applied Composite Materials*, 2001.

[219] Ashok Magar and Achchhe Lal. Stress analysis of infinite laminated composite plate with elliptical cutout under different in plane loadings in hygrothermal environment. *Curved and Layered Structures*, 8(1):1–12, jan 2021.

[220] Jin-Hwe Kweon, Hyon-Su Ahn, and Jin-Ho Choi. A new method to determine the characteristic lengths of composite joints without testing. *Composite Structures*, 66(1-4):305–315, oct 2004.

[221] E. K. Frankl. Designing by photoelasticity. r. b. heywood. chapman & hall, london 1952. 414 pp. 65s. net. *The Journal of the Royal Aeronautical Society*, 57(511):472–473, jul 1953.

[222] R.F. Karlak. Hole effects in a related series of symmetrical laminates. In *Proc. 4th Joint ASM-Metallurgical Society of AIME Symp. on Failure Modes in Composites, Chicago*. The Metallurgical Society of the American Institute of Mining, Metallurgical and Petroleum Engineers, Warrendale, Pennsylvania, 1979.

[223] R. Byron Pipes, John W. Gillespie, and Robert C. Wetherhold. Superposition of the notched strength of composite laminates. *Polymer Engineering and Science*, 19(16):1151–1155, dec 1979.

[224] Jung-Kyu Kim, Do-Sik Kim, and Nobuo Takeda. Notched strength and fracture criterion in fabric composite plates containing a circular hole. *Journal of Composite Materials*, 29(7):982–998, may 1995.

[225] L.J. Hart-Smith. Comparison between theories and test data concerning the strength of various fibre–polymer composites. *Composites Science and Technology*, 62(12-13):1591–1618, sep 2002.

[226] L J Hart-Smith. Predicting the strength of fibrous composites by an orthotropic generalization of the maximum-shear-stress (tresca) criterion. *Proceedings of the Institution of Mechanical Engineers, Part G: Journal of Aerospace Engineering*, 208(1):9–18, jan 1994.

[227] S.E. Yamada and C.T. Sun. Analysis of laminate strength and its distribution. *Journal of Composite Materials*, 12(3):275–284, oct 1978.

[228] Robert Jones. *Deformation theory of plasticity*. Bull Ridge Pub, Blacksburg, Va, 2009.

[229] J. Koord, E. Petersen, D. Stefaniak, and C. Hühne. Analytical design methodology for multi-row multi-column fastener joints in composite structures. In *SAMPE Europe Conference Southampton 2018*, 2018.

[230] V.B. Venkayya and V.A. Tischler. A review of composite joint analysis programs. In *AGARD Conference Proceedings 590*, 1997.

[231] José Andriamampianina, Feras Alkatan, Pierre Stéphan, and Jean Guillot. Determining load distribution between the different rows of fasteners of a hybrid load transfer bolted joint assembly. *Aerospace Science and Technology*, 23(1):312–320, dec 2012.

[232] Sascha Dähne, Edgar Werthen, David Zerbst, Lennart Tönjes, Hendrik Traub, and Christian Hühne. Lightworks, a scientific research framework for the design of stiffened composite-panel structures using gradient-based optimization. *Structural and Multidisciplinary Optimization*, 67(5), May 2024.

[233] Sascha Dähne and Christian Hühne. Gradient based structural optimization of a stringer stiffened composite wing box withvariable stringer orientation. In *12th World Congress on Structural and Multidisciplinary Optimization*, 2017.

[234] Tobias Bach, Sascha Dähne, Lars Heinrich, and Christian Hühne. Structural optimization of composite wings in anautomated multi-disciplinary environment. *14th AIAA Aviation Technology, Integration, and Operations Conference*, 2014.

[235] Edgar Werthen and Sascha Dähne. Design- and manufacturing constraints within the gradientbased optimization of a composite aircraft wingbox. In *6th Airframe Structural Design Conference, Bristol October 2018*, 2018.

[236] O. Völkerink, J. Koord, E. Petersen, and C. Hühne. Comparison of continuum shell and solid element-based modeling strategies for mesoscale progressive damage analysis of fiber composites. *Mechanics of Composite Materials*, 59(2):219–238, apr 2023.

[237] K.S. Rao, M.N. Bapu Rao, and T. Ariman. Thermal stresses in plates with circular holes. *Nuclear Engineering and Design*, 15:97–112, jan 1971.

[238] Mohammad Jafari and Mohammad Jafari. Effect of hole geometry on the thermal stress analysis of perforated composite plate under uniform heat flux. *Journal of Composite Materials*, 53(8):1079–1095, aug 2018.

[239] Daniel O. Adams. Comparative testing to assessthe equivalence of cen and astmtest methods for composite materials. Technical report, U.S. Department of Transportation Federal Aviation Administration, 2005.

[240] Military handbook (mil-hdbk-17-3f).

[241] Oliver Völkerink. *Simulation-driven design of bonded joints in fibre composite aircraft structures using progressive damage analyses*. PhD thesis, 2022.

[242] Jin-Ho Choi and Young-Jun Chun. Failure load prediction of mechanically fastened composite joints. *Journal of Composite Materials*, 37(24):2163–2177, dec 2003.

[243] P.P. Krimbalis, C. Poon, Z. Fawaz, and K. Behdinan. Prediction of bearing strength in fiber metal laminates. *Journal of Composite Materials*, 41(9):1137–1157, aug 2006.

[244] O. Aluko and Q. Mazumder. The accuracy of characteristic length method on failure load prediction of composite pinned joints. In *Proceedings of the World Congress on Engineering 2010 Vol II*, 2010.

[245] F. Taheri-Behrooz and H. Bakhshan. Characteristic length determination of notched woven composites. *Advanced Composite Materials*, 27(1):67–83, sep 2016.

Publications

J. Koord, C. Hühne. (2024) Effect of low temperature on interlaminar fracture toughness of multi-directional CFRP and CFRP-steel interfaces, *Composites Part B*.

J. Koord, C. Hühne. (2024) Bolt-bearing behavior of hybrid CFRP-steel laminates at low temperature, *Journal of Composite Materials*.

J. Koord, R. Prussak, D. Stefaniak, C. Hühne. (2023) Crack Analysis in CFRP by means of Fiber Optical Sensors, *SAMPE Europe Conference Madrid*.

P. Meyer, M. Vorhof, **J. Koord**, C. Sennewald, C. Cherif, C. Hühne. (2023) Anisotropic flexure hinges: Manufacturing and mechanical characterization for application in pressure actuated morphing structures, *Composites Part B*.

J. Koord, O. Völkerink, E. Petersen, C. Hühne. (2023) Effect of low temperature on mode I and mode II interlaminar fracture toughness of CFRP-steel hybrid laminates, *Composites Part B*.

O. Völkerink, **J. Koord**, E. Petersen, C. Hühne. (2023) Comparison of continuum shell and solid element-based modelling strategies for mesoscale progressive damage analysis of fibre composites, *Mechanics of Composite Materials*.

J. Koord, J.-L. Stüven, O. Völkerink, E. Petersen, C. Hühne. (2022) Investigation of Exact Analytical Solutions for Composite Laminates under Pin-bearing Loading, *Composite Structures*.

O. Völkerink, **J. Koord**, E. Petersen, C. Hühne. (2022) Holistic determination of physical fracture toughness values and numerical parameters for delaminaton analysis considering multidirectional-interfaces, *Composites Part C*.

E. Petersen, E. Kappel, **J. Koord**, O. Völkerink, D. Stefaniak, C. Hühne. (2020) Determination of stresses, strains and failure types in multidirectional laminates under pure bending, *Journal of Composite Materials*.

E. Petersen, **J. Koord**, O. Völkerink, D. Stefaniak, C. Hühne. (2020) Experimental and numerical investigation of the transition zone of locally steel-reinforced joining areas under combined tension-bending loading, *Journal of Composite Materials*.

J. Koord, J.-L. Stüven, E. Petersen, O. Völkerink, C. Hühne. (2020) Investigation of Exact Analytical Solutions for Circular Notched Composite Laminates under Tensile Loading, *Composite Structures*.

O. Völkerink, E. Petersen, **J. Koord**, C. Hühne. (2020) A pragmatic approach for a 3D material model considering elasto-plastic behaviour, damage initiation by Puck or Cuntze and progressive failure of fibre-reinforced plastics, *Journal of Computers and Structures*.

J. Koord, E. Petersen, D. Stefaniak, C. Hühne. (2018) Analytical design methodology for multi-row multi-column fastener joints in composite structures, *SAMPE Europe Conference Southampton*.